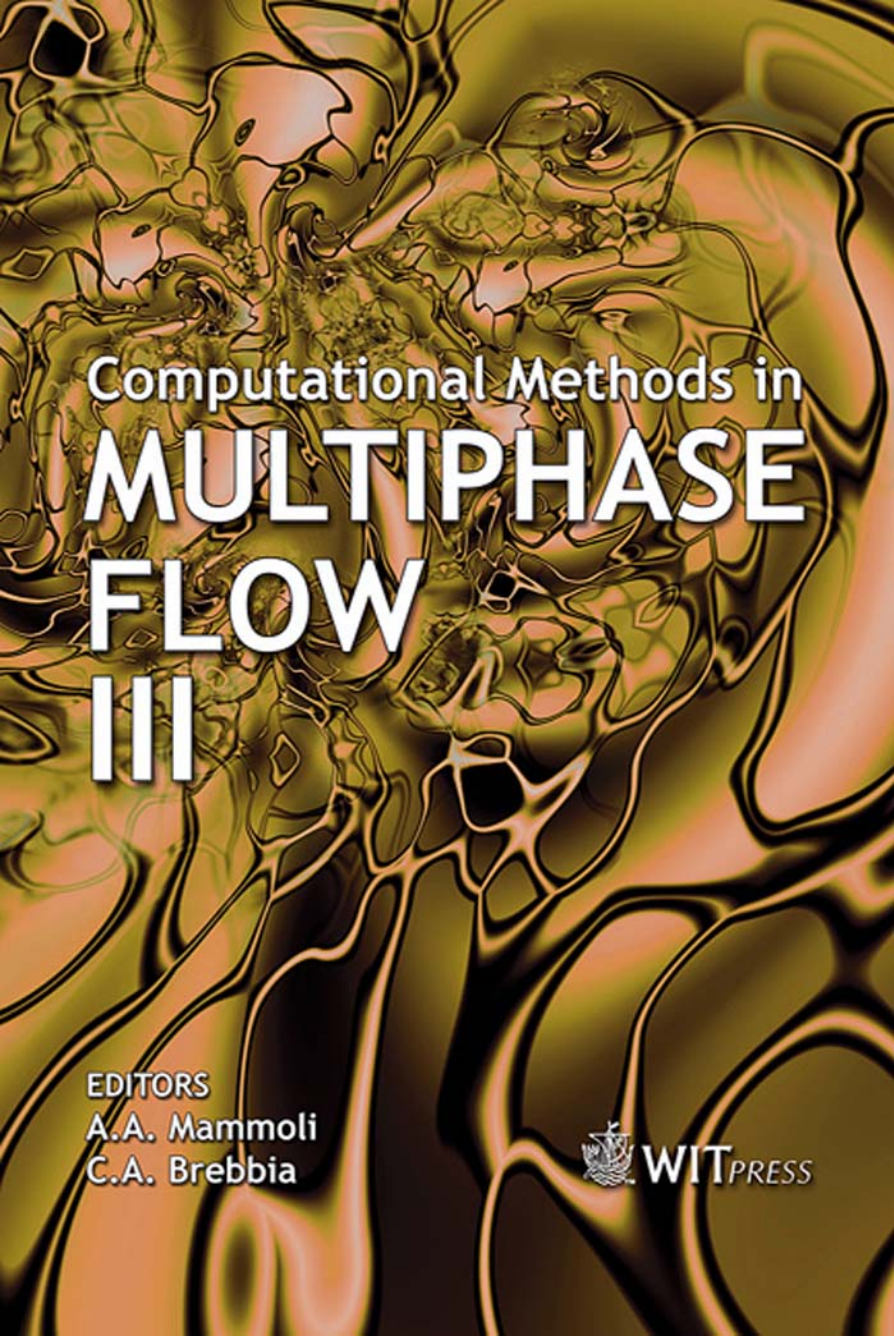
Computational Methods in
MULTIPHASE
FLOW
III
EDITORS
A.A. Mammoli
C.A. Brebbia
WIT PRESS

COMPUTATIONAL METHODS IN MULTIPHASE FLOW III

WIT PRESS

WIT Press publishes leading books in Science and Technology.
Visit our website for new and current list of titles.
www.witpress.com

WIT eLibrary

Home of the Transactions of the Wessex Institute.
Papers presented at Computational Methods in Multiphase Flow III are archived in the WIT eLibrary in volume 50 of WIT Transactions on Engineering Sciences (ISSN 1743-3533).

The WIT eLibrary provides the international scientific community with immediate and permanent access to individual papers presented at WIT conferences.
http://library.witpress.com

FLUID MECHANICS

Editorial Board

THIRD INTERNATIONAL CONFERENCE ON COMPUTATIONAL METHODS IN MULTIPHASE FLOW

MULTIPHASE FLOW III

CONFERENCE CHAIRMEN

C. A. Brebbia
Wessex Institute of Technology, UK

A.A. Mammoli
University of New Mexico, USA

INTERNATIONAL SCIENTIFIC ADVISORY COMMITTEE

M Gorokhovski
M I Ingber
C Koenig
W-Q Lu
S Parameswaran
C Petty
N C Shapley
L Skerget
Z Wu

Organised by:
Wessex Institute of Technology, UK
and
University of New Mexico, USA

Sponsored by:
WIT Transactions on Engineering Sciences

COMPUTATIONAL METHODS IN MULTIPHASE FLOW III

EDITORS

A.A. Mammoli
University of New Mexico, USA

C. A. Brebbia
Wessex Institute of Technology, UK

WIT PRESS Southampton, Boston

A.A. Mammoli
University of New Mexico, USA

C. A. Brebbia
Wessex Institute of Technology, UK

Published by

WIT Press
Ashurst Lodge, Ashurst, Southampton, SO40 7AA, UK
Tel: 44 (0) 238 029 3223; Fax: 44 (0) 238 029 2853
E-Mail: witpress@witpress.com
http://www.witpress.com

For USA, Canada and Mexico

Computational Mechanics Inc
25 Bridge Street, Billerica, MA 01821, USA
Tel: 978 667 5841; Fax: 978 667 7582
E-Mail: infousa@witpress.com
http://www.witpress.com

British Library Cataloguing-in-Publication Data

A Catalogue record for this book is available
from the British Library

ISBN: 1-84564-030-6
ISSN: 1746-4471 (print)
ISSN: 1743-3533 (on-line)

The texts of the papers in this volume were set individually by the authors or under their supervision. Only minor corrections to the text may have been carried out by the publisher.

Printed in Great Britain by Athenaeum Press Ltd.

Preface

The topic of multiphase flow is broad, encompassing a variety of fluids, transported solids and flow regimes. A common feature is that there is generally a dispersed, or discontinuous phase, carried by a continuous phase. The interactions between particles or deforming drops in the disperse phase dominate the overall behavior of the flow. Much of the research has focused on understanding these complex interphase interactions, through a wide array of theoretical, computational and experimental techniques. Research in multiphase flows is driven by the challenge of understanding such complex phenomena, as well as by practical considerations dictated by technological needs.

Despite recent advances in experimental and computational capabilities, multiphase flows still present many open questions. While for individual, rather restricted classes of flows (such as, for example, rigid spheres in a Newtonian fluid) there exist several models which provide good simulation under a certain set of conditions, these are not robust. Difficulties arise especially when the scale of the disperse phase is comparable to the scale of the characteristic dimension of the flow itself. In this case, boundary conditions are particularly difficult to impose. Modeling has been approached from all length scales, from the particle level, with direct numerical simulation, to the continuum level via constitutive equations of varying complexity, while some recent work was aimed at combining various length scales within the same model.

Similarly, experimental work can focus of many aspects of the flow process, from phase distributions, to small-scale interactions between two particles, to macroscopic fluid and flow properties. The presence of multiple phases renders optical observation difficult for moderate and high concentrations of the disperse phase, so non-invasive techniques have been adapted and devised to achieve the capability of seeing inside the flow, sometime in real-time. For low concentrations, optical observation and PIV are still the preferred choice.

A recent area of research is multiphase flow in porous media, in which the carrier phase and the dispersed phases (drops, bubbles, particles) interact with each other and with the porous phase, thereby adding another level of complexity. These flows are increasingly important, particularly in the energy sector (geological sequestration of greenhouse gases, enhanced oil recovery, fuel cells).This research area is becoming treatable due to constantly increasing computing capacity, as well as improved experimental diagnostics This book covers a broad spectrum of the most recent research in multiphase flow, ranging from basic research, to industrial

applications, to the development of new numerical simulation techniques.

Hoping that the readers finds this collection of papers useful in pursuing their activity, the authors wish to acknowledge the invaluable help of the Scientific Advisory Committee in selecting the papers and ensuring their quality.

The Editors
Portland, Maine, 2005

Contents

Section 7: Particle image velocimetry

Section 8: Macroscale constitutive models

Section 9: Large eddy simulation

Section 10: Finite volumes

Section 11: Interface tracking methods

Section 1
Suspensions

This page intentionally left blank

Modelling of coagulation efficiencies in rotating systems

M. Breitling & M. Piesche
Institute of Mechanical Process Engineering,
University of Stuttgart, Germany

Abstract

Under the influence of an induced shear and centrifugal field, inter-particle collisions of solid particles in liquids as well as viscous forces result in agglomeration, breakage, and erosion. There is a permanent alteration of the particle size distribution which is described mathematically by the method of population balances. Due to the uniform surface charge of the dispersed particles, a self-induced agglomeration does not take place automatically which means that coagulant agents need to be added to the suspension. The influence of these electrolytes is taken into account by the so-called coagulation efficiency. In the course of this work, two different models are developed describing the collision efficiency locally and in dependence on apparatus geometry, operating conditions, particle combination (species and mass), coagulant agents and material properties. It is shown that in highly rotating systems particle collisions result in small agglomerates although being exposed to large centrifugal forces and shear forces.
Keywords: coagulation efficiency, populations balances, centrifuge, suspension, multiphase flow.

1 Introduction

In mechanical separation units rotating apparatuses are relatively common. Especially highly rotating disc stack centrifuges become increasingly popular due to their good separation efficiency and the disbandment of filter media. Since the separation is exclusively caused by different densities of the phases, disc stack centrifuges are adapted for the separation of all kinds of dispersed systems (emulsions, aerosols, and suspensions). By using coagulating agents which induce the formation of agglomerates, the separation of very small particles becomes more efficient.

With regard to the flow field in a single gap of a disc stack centrifuge, fig. 1 and table 1, inter-particle collisions of solid particles in liquids as well as viscous forces result in agglomeration, breakage and erosion. There is a permanent

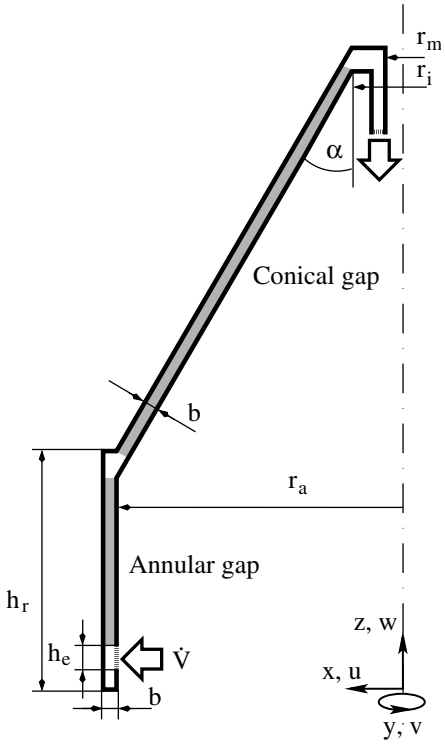

Figure 1: Sketch of a single gap of a disc stack centrifuge.

Table 1: Geometry data.

Angle of the conical gap	$\alpha = 30°$
Height of the outer annular gap	$h_r = 71$ mm
Height of the inlet	$h_e = 6$ mm
Width of the gap	$b = 4$ mm
Radius of the outer annular gap	$r_a = 100$ mm
Radius of the inner annular gap	$r_m = 20$ mm
Radius of the end of the conical gap	$r_i = 30$ mm

alteration of the properties of the dispersed particles, namely the size distribution which cannot be described mathematically by commonly used Euler–Euler or Euler–Lagrangian approaches. In order to take this alteration into consideration, the method of population balances is used. It describes particle numbers N with certain properties $\underline{e} = (e_1, e_2, \ldots, e_n)$ in dependence on time t and position $\underline{x} = (x_1, x_2, x_3)$. Assuming incremental differences of particle properties and a sufficient large number of dispersed particles, the particle number density function f is defined by

$$f(\underline{x}, \underline{e}, t) = \frac{dN}{dx_1 dx_2 dx_3 de_1 de_2 \cdots de_n} \,. \tag{1}$$

For laminar flow patterns, the particle interactions are examined locally in a single gap of a disc stack centrifuge with respect to particle species (non-aggregated particles and agglomerates), particle mass m, and time. The population balance in cylindrical co-ordinates (x, y, z) is then given by

$$\frac{\partial f(\underline{x}, m, t)}{\partial t} = -\frac{1}{x}\frac{\partial}{\partial x}(x u_l \cdot f) - \frac{1}{x}\frac{\partial}{\partial y}(v_l \cdot f) - \frac{\partial}{\partial z}(w_l \cdot f) + S^+ - S^- \tag{2}$$

with velocity components in radial, azimuthal and axial directions (u_l, v_l, w_l). The source term S^+ describes particle interactions resulting in particles or agglomerates of mass m by coagulation of smaller particles or by breakage and erosion of larger ones. The sink term S^- indicates the loss of particles of size m. Except for coagulation efficiencies, their specific inter-particle kinetics have been investigated sufficiently for laminar flows, see Lu and Spielman [1], Schuetz [2], and Smoluchowski [3].

2 Microscopic model

Generally, the coagulation efficiency is defined to be the probability with which a particle collision results in an agglomerate. With respect to the microscopic model, particle trajectories are derived from microhydrodynamic investigations. Since inertia plays a negligible role on the microscale, the hydrodynamic force balances the centrifugal and colloidal forces. The motion of the particles dictates the evolution of the suspension microstructure. The multiparticle configuration in turn shapes the forces $\underline{F}$ acting on the particles. Solving the mobility problem of two particles, so-called limiting trajectories can be determined defining a capture cross section, see fig. 2. The ratio of the curvilinear particle flux through this section to that of the rectilinear particle flux corresponds to the collision efficiency.

2.1 Particle trajectories

Neglecting torques acting on each particle $\alpha = 1, 2$, trajectories can be determined from the mobility problem, Batchelor [4], Kim and Karrila [5]. For cylindrical co-

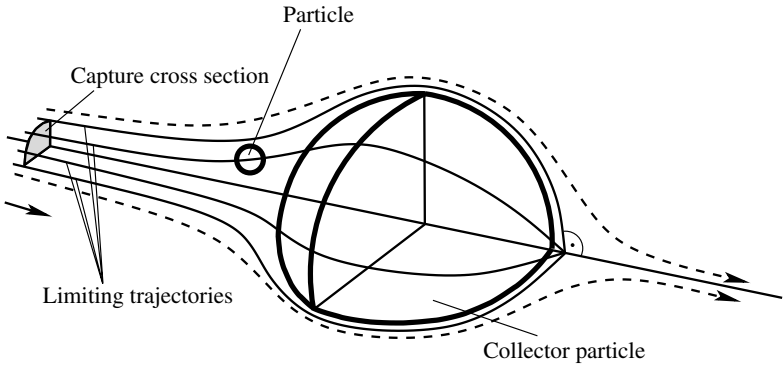

Figure 2: Sketch of particle trajectories and the capture cross section.

ordinates the coupled system of non-linear equations is given by

$$\frac{dx_\alpha}{dt} = u_l - \mu^{-1}\sum_{j=1}^{3} a_{1j}^{(\alpha 1)} F_{1j} - \mu^{-1}\sum_{j=1}^{3} a_{1j}^{(\alpha 2)} F_{2j} - \sum_{j=1}^{3}\sum_{k=1}^{3} E_{jk}\tilde{g}_{1jk}^{(\alpha)} \tag{3}$$

$$\frac{dy_\alpha}{dt} = \frac{1}{x_\alpha}\left[v_l - \mu^{-1}\sum_{j=1}^{3} a_{2j}^{(\alpha 1)} F_{1j} - \mu^{-1}\sum_{j=1}^{3} a_{2j}^{(\alpha 2)} F_{2j} - \sum_{j=1}^{3}\sum_{k=1}^{3} E_{jk}\tilde{g}_{2jk}^{(\alpha)} \right] \tag{4}$$

$$\frac{dz_\alpha}{dt} = w_l - \mu^{-1}\sum_{j=1}^{3} a_{3j}^{(\alpha 1)} F_{1j} - \mu^{-1}\sum_{j=1}^{3} a_{3j}^{(\alpha 2)} F_{2j} - \sum_{j=1}^{3}\sum_{k=1}^{3} E_{jk}\tilde{g}_{3jk}^{(\alpha)} \tag{5}$$

with $\underline{\underline{E}}$ being the rate of strain tensor, $a_{ij}^{(\alpha\beta)}$ and $\tilde{g}_{ijk}^{(\alpha)}$ being the scalar mobility functions of the grand mobility matrix (Kim and Karrila [5]) and μ being the dynamic viscosity.

2.1.1 External forces

In combination with the centrifugal force, the colloidal force

$$F_{\alpha,colloid} = -\frac{d}{d\,|\underline{r}|}\left(V_{attr} + V_{rep}\right) \tag{6}$$

balances the microhydrodynamic force. Applying the DLVO theory (Verwey and Overbeek [6], Derjaguin and Landau [7]), the total potential energy of interaction is the sum of the energies of repulsion V_{rep} (Hogg et al. [8]) and attraction V_{attr} (Ho and Higuchi [9]). In eqn (6), $|\underline{r}|$ represents the distance of two spherical particles.

2.1.2 Flow field

Because of the very fine grid needed for a good resolution of the flow field in the vicinity of the particles, numerical calculations are still inapplicable. Therefore,

analytical expressions for laminar flows are used for the outer annular gap and the conical gap, see hatched areas in fig. 1.

2.2 Limiting trajectories

With eqns (3)–(5) limiting trajectories can be determined. They define a capture cross section upstream from the collector particle through which all trajectories of smaller particles terminate on the surface of the collector particle. In analogy to Higashitani et al. [10], all limiting trajectories end at the rear stagnation point of the collector particle. Assuming a circular capture cross section, limiting trajectories have the radial distance y_c from the streamline of the stagnation point.

2.3 Coagulation efficiency

The coagulation efficiency is defined to be the ratio of curvilinear particle flux J to that of rectilinear particle flux J_S that is given by Smoluchowski [3]. For circular capture cross sections, it can be shown that the coagulation efficiency corresponds to the ratio of the capture cross section and the collision cross section

$$\alpha = \frac{J}{J_S} = \left(\frac{y_c}{a_1 + a_2} \right)^2 . \tag{7}$$

with a_α being the radius of particle α.

3 Macroscopic model

For separation apparatuses, a continuous alteration of the particle spectrum takes place as large particles are removed. Thus, a separation coefficient needs to be included when describing the particle interactions by population balances. It gives local information about whether a particle of mass m is already settled out at a given place or not. The combination of both coefficients—the coagulation efficiency and the separation coefficient—is called the integral coagulation efficiency. Based on the investigations of Loeffler [11], the integral coagulation efficiency is modelled in dependence on apparatus geometry, local flow field, particle combination (species and size) and liquid properties.

3.1 Trajectories and particle velocities

Applying the method of Euler–Lagrange, particle trajectories are calculated by integrating the momentum equation on a spherical particle. In order to obtain the velocity components of the flow field in a single gap of a disc stack centrifuge, the commercial CFD tool FLUENT has been used, Breitling et al. [12]. Several assumptions have been made:

- the steady flow is rotationally symmetric,
- the liquid properties are constant, and

- the influence of the gravitational force is negligible compared to the centrifugal force.

The dimensionless equations of particle motion in cylindrical co-ordinates are then given by

$$\frac{dU_s}{dT} = \frac{1}{1+\frac{1}{2}(1-\Delta)} \cdot \left[18\,\frac{Re}{St}\,(U_l - U_s) - \frac{\partial P}{\partial X_s}(1-\Delta) + Re \cdot (X_s + 2V_s) \right] \tag{8}$$

$$\frac{dV_s}{dT} = \frac{1}{1+\frac{1}{2}(1-\Delta)} \cdot \left[18\,\frac{Re}{St}\,(V_l - V_s) + Re\,(Y_s - 2\,U_s) \right] \tag{9}$$

$$\frac{dW_s}{dT} = \frac{1}{1+\frac{1}{2}(1-\Delta)} \cdot \left[18\,\frac{Re}{St}\,(W_l - W_s) - \frac{\partial P}{\partial Z_s}(1-\Delta) \right] \tag{10}$$

$$\frac{dX_s}{dT} = Re \cdot U_s \tag{11}$$

$$\frac{dY_s}{dT} = Re \cdot \frac{V_s}{X_s} \tag{12}$$

$$\frac{dZ_s}{dT} = Re \cdot W_s \tag{13}$$

with the dimensionless variables

$$T = \frac{\mu t}{\varrho_l b^2}, \qquad \Delta = 1 - \frac{\varrho_l}{\varrho_s}, \qquad P = \frac{p}{\mu\omega}, \tag{14}$$

$$St = \frac{\varrho_s d_s^2 \omega}{\mu}, \qquad Re = \frac{\varrho_l b^2 \omega}{\mu}, \tag{15}$$

$$U_{l/s} = \frac{u_{l/s}}{\omega b}, \qquad V_{l/s} = \frac{v_{l/s}}{\omega b}, \qquad W_{l/s} = \frac{w_{l/s}}{\omega b}, \tag{16}$$

$$X_s = \frac{x_s}{b}, \qquad Y_s = y_s \qquad \text{and} \qquad Z_s = \frac{z_s}{b} \tag{17}$$

that depend on time t, pressure p, liquid and solid densities ϱ_l and ϱ_s, particle diameter d_s, and the angular velocity ω.

3.2 Adhesion constraint

The so-called critical impact velocity v_{crit} of the smaller particle (superscript f) characterizes the transition between adhesion and rebound. If the magnitude of the real particle velocity $\underline{v}^f$ exceeds v_{crit}, coagulation will not take place. Therefore, it is necessary to prove in advance the adhesion constraint when calculating the integral coagulation efficiency. The critical impact velocity can be derived by the

conservation equations of momentum and energy. Its dimensionless and non-linear conditional equation is given in dependence on the impact parameter k

$$\lambda^3\psi\left[k^2(1+\lambda^3\psi)-\lambda^3\psi\right]\cdot V_{crit}^2-\lambda^3\psi\cos\varphi\cdot V_{crit}+ \left[k^2(1+\lambda^3\psi)-1\right]-\frac{12}{\pi}\frac{(1+\lambda^3\psi)}{{d^C}^3\,\varrho^C{\underline{v}^C}^2}\cdot\Delta E_A=0. \tag{18}$$

The dimensionless parameters are defined by

$$V_{crit}=\frac{v_{crit}}{\left|\underline{v}^C\right|},\qquad \lambda=\frac{d^f}{d^C}\le 1\qquad \text{and}\qquad \psi=\frac{\varrho^f}{\varrho^C} \tag{19}$$

where the superscript C represents the collector particle. The angle between the particle velocity vectors φ is obtained by the definition of the scalar product. In order to determine the difference of repulsive and attractive energies before and after the impact ΔE_A, the following assumptions have been made:

- the particle diameters are much bigger than the size of deformation due to the impact and
- the deformation depths of each particle are equal.

In analogy to Dahneke [13], Hiller [14], Krupp [15], Tsouris and Yiacoumi [16], ΔE_A can be derived. Together with eqn (18), the critical impact velocity can now be calculated. The necessary adhesion constraint is then given by

$$\left|\underline{v}^f\right|<v_{crit}\ . \tag{20}$$

3.3 Integral coagulation efficiency

Only if eqn (20) is true, coagulation of two particles will take place. The integral coagulation efficiency can be determined as a function of the modified Stokes number

$$\widetilde{St}=\frac{\varrho^f\ {d^f}^2\left|\underline{v}^f\right|\cdot\underline{v}_l^2}{18\,\mu\,d^C\,\left(\underline{v}_l-\underline{v}^f\right)^2} \tag{21}$$

In analogy to Loeffler [11], the integral coagulation efficiency is defined by

$$\alpha^\star=\left(\frac{\widetilde{St}}{\widetilde{St}+\gamma_1}\right)^{\gamma_2} \tag{22}$$

with $\gamma_1=0.65$ and $\gamma_2=3.7$. When particles have diameters less than $1\ \mu$m, perikinetic interactions are dominant compared to orthokinetic interactions. For

small Peclet numbers ($Pe < 1$), the integral coagulation efficiency is determined by Russel, Saville and Schowalter [17]

$$\alpha^\star = 2.52 \cdot Pe^{-2/3} \tag{23}$$

where the Peclet number is defined by

$$Pe = \frac{6\pi\mu\, d^f d^C \left|\underline{v}^C - \underline{v}^f\right|}{k_B T} \tag{24}$$

with the absolute temperature T and the Boltzmann's constant k_B.

4 Results

For a flow rate of $\dot{V} = 117$ l/h and an angular velocity of $\omega = 173$ s^{-1}, the (integral) coagulation efficiencies have been calculated in a single gap of a disc stack centrifuge. The geometry corresponds to that given in table 1 and the suspension consists of a glycerine/water-mixture ($\varrho_l = 1156$ kg/m^3, $\mu = 0.01$ Pas) with glass spheres ($\varrho_s = 2465$ kg/m^3). For a mean porosity of 40% the density of the resulting agglomerates is $\varrho_s = 1940$ kg/m^3 and the concentration of the coagulant agent (NaOH and $CaCl_2$) corresponds to 1 g/l.

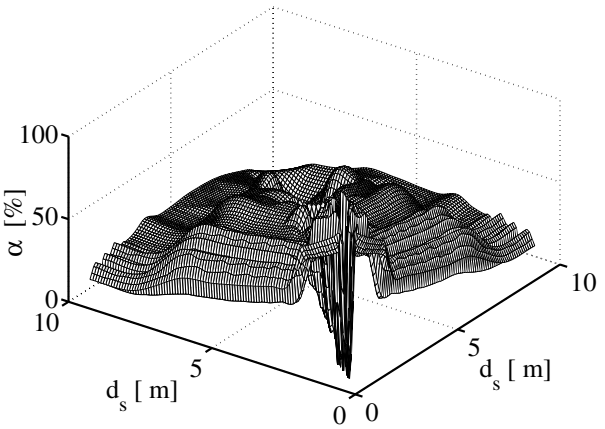

Figure 3: Integral coagulation efficiency $\alpha^\star$ in dependence on particle diameters at a defined position in the annular gap.

In fig. 3, the integral coagulation efficiency is shown in dependence on particle sizes at a defined position in the annular gap. For a combination of small particles with different sizes the integral coagulation efficiency has maximum values as the relative velocity is high. Due to the additional precipitation of larger particles in the

centrifuge this behaviour decreases, which means in turn that the integral coagulation efficiency becomes lower. For particles with same diameters, the coagulation efficiency vanishes since the critical impact velocity is very small. This behaviour corresponds to experimental investigations.

Comparing the microscopic and macroscopic models directly becomes very complex as there are too many parameters influencing the efficiencies respectively. Therefore, the local particle size distributions calculated by the method of population balances with different models for the (integral) coagulation efficiency are regarded. An example of these distributions at radius $r = 59$ mm in the conical gap shows fig. 4. They fit well with the experimentally gained mass distribution at the same position in the gap. Differences between the calculated distributions appear only at large particles. For particles with $d_s > 10$ μm, the distribution determined with the macroscopic model is displaced towards smaller particles as the model contains an additional separation coefficient.

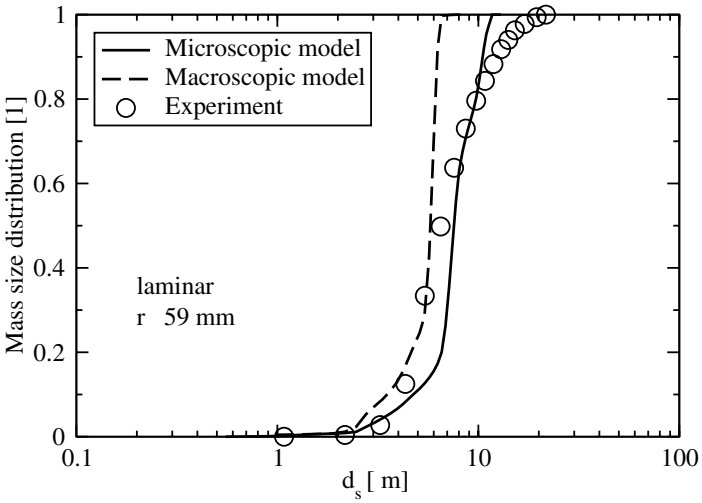

Figure 4: Comparison between microscopic and macroscopic model.

In summary, both methods are suited for predicting the (integral) coagulation efficiency in dependence on flow pattern, apparatus geometry, liquid and solid behaviour. Whilst the macroscopic model only considers particles that have not been separated at a given position, the microscopic model can be used only for analytical flow patterns.

References

[1] Lu, C.F. & Spielman, L.A., Kinetics of floc breakage and aggregation in agitated liquid suspensions. *Journal of Colloid and Interface Science*, **103**, pp. 95–105, 1985.

[2] Schuetz, S., (ed.) *Modellbildung und Simulation von Partikelwechselwirkungen bei dispersen Stoffsystemen am Beispiel von Flockungsprozessen*. VDI Verlag GmbH: Duesseldorf, 1999.
[3] Smoluchowski, M., Versuch einer mathematischen theorie der koagulationskinetik kolloidaler loesungen. *Zeitschrift fuer Physikalische Chemie*, **82**, pp. 129–169, 1917.
[4] Batchelor, G.K., Brownian diffusion of particles with hydrodynamic interaction. *Journal of Fluid Mechanics*, **74**, pp. 1–29, 1976.
[5] Kim, S. & Karrila, S.J., (eds.) *Microhydrodynamics: Principles and selected applications*. Butterworth–Heinemann: Boston, 1991.
[6] Verwey, E.J.W. & Overbeek, J.T.G. *Elsevier Publishing Company*.
[7] Derjaguin, B. & Landau, L.D., Theory of the stability of strongly charged lyophobic sols and of the adhesion of strongly charged particles in solutions of electrolytes. *Acta Physicochim (USSR)*, **14**, pp. 633–662, 1941.
[8] Hogg, R., Healy, T.W. & Fuerstenau, D.W., Mutual coagulation of colloidal dispersions. *Transactions Faraday Society*, **62**, pp. 1638–1651, 1966.
[9] Ho, N.F.H. & Higuchi, W.I., Preferential aggregation and coalescence in heterodispersed systems. *Journal of Pharmaceutical Sciences*, **57**, pp. 436–442, 1968.
[10] Higashitani, K., Ogawa, R., Hosokawa, G. & Matsuno, Y., Kinetic theorie of shear coagulation for particles in a viscous fluid. *Journal of Chemical Engineering of Japan*, **15(4)**, pp. 299–305, 1982.
[11] Loeffler, F., (ed.) *Staubabscheiden*. Georg Thieme Verlag: Stuttgart, 1988.
[12] Breitling, M., Janoske, U. & Piesche, M., Numerische simulationen transienter und turbulenter strömungen zum abscheideverhalten in tellerseparatoren. *Chemie Ingenieur Technik*, **75**, pp. 184–188, 2003.
[13] Dahneke, B., The capture of aerosol particles by surfaces. *Journal of Colloid and Interface Science*, **37(2)**, pp. 342–353, 1971.
[14] Hiller, R., (ed.) *Der Einfluss von Partikelstoss und Partikelhaftung auf die Abscheidung in Faserfiltern*. VDI Verlag GmbH: Duesseldorf, 1981.
[15] Krupp, H., Particle adhesion. theory and experiment. *Advances in Colloid and Interface Science*, **1**, pp. 111–239, 1967.
[16] Tsouris, C. & Yiacoumi, S., Particle flocculation and filtration by high–gradient magnetic fields. *Separation Science and Technology*, **32**, pp. 599–616, 1997.
[17] Russel, W.B., Saville, D.A. & Schowalter, W.R., (eds.) *Colloidal dispersions*. Cambridge University Press: Cambridge, 1989.

The study of asphaltene precipitation in dilute solution by calorimetry

A. Miadonye, L. Evans & T. M. McKenna
Department of Engineering, Cape Breton University, Sydney, Canada

Abstract

Hydrocarbon solvents are often used in the transport of heavy petroleum. Because of the weak dispersion forces formed, it requires less energy for the molecules to change phases and to precipitate asphaltenes out of the solution, leading to problems in the pipeline transportation. In this study, the calorimetric method was used to study the energy change for various mixtures of non-polar solvents with heavy petroleum, and with heavy petroleum which contained a non-polar additive. The amount of asphaltene precipitation was measured for various petroleum-toluene solutions mixed with either hexane or naphtha. It was observed that the lower the concentration of toluene in petroleum, the greater the amount of precipitate. Comparing the enthalpy of mixing with the weight percent of asphaltene precipitation showed that the lower the weight percent asphaltene, the lower the enthalpy of mixing in hexane and naphtha. The presence of toluene lowers the enthalpy of mixing and reduced the precipitation of asphaltenes.
Keywords: dispersion forces, asphaltene precipitation, enthalpy of mixing, hydrocarbon solvents, calorimetry, heavy petroleum, bitumen.

1 Introduction

The widely acceptable method for reducing heavy oil viscosity, particularly for enhanced recovery, pipeline transportation and refinement is the addition of liquid hydrocarbon condensates, which frequently leads to complex phase transformations, and precipitation of asphaltenes in the resulting solution [1-3]. Asphaltenes are well known for their contribution to problems occurring in petroleum processing. Transportation and drilling processes are affected by the deposition of asphaltenes as they flocculate from petroleum and aggregate in areas such as reservoirs, storage vessels, pipelines and valves. Extensive

asphaltene precipitation has the potential to halt production thus, remediation strategies are required. Branco et al [4] has shown that the increase in production of heavy petroleum has given rise to the growing concern on the effect of asphaltene deposition on process facilities. While calorimetric methods offer valuable information into the heat effects and phase changes surrounding the determination of asphaltene precipitation [5,6], it has proven very difficult to provide standard evaluations due to the heteroatom content of asphaltenes [7,8].

This study is aimed towards relating the heat of mixing with asphaltene precipitation when bitumen is blended with hydrocarbon solvent. The intermolecular forces observed in these solute-solvent interactions consist mainly of dispersion forces, and the induced polarity of these molecules is weak. Creation and destruction of these bonds provide the framework for this study, as the chemical and/or physical changes can be measured in the form of heat. In this study, different bitumen and bitumen blended with additive are mixed with various hydrocarbon solvents and their heats of mixing are determined. In addition, the weight percent of asphaltene precipitation at various mixing concentrations is correlated with heat of mixing.

2 Experimental

2.1 Materials and chemicals

The materials used in this study were Kerrobert, Cold Lake and Underground Test Facilities bitumen from Syncrude Canada Ltd, Alberta and two heavy crude oils from Irving Oil Refinery Ltd, New Brunswick, as solutes, and Light Straight Run Naphtha, Heavy Straight Run Naphtha, Gas Oil, from Irving Oil Refinery Ltd, New Brunswick, Toluene and Hexane purchased fro Aldrich (with purity grade of 99.9%), as the solvents. For standardization procedure for the calorimeter THAM (Tris[hydroxymethyl]aminomethane) was dissolved in 0.1 M Hydrochloric Acid.

2.2 Calorimetry

The Parr 1455 Solution Calorimeter used in this study employs a microprocessor-based thermometer along with a 0.0008 heat leak constant for precise temperature measurements and calculations. The calorimeter was interfaced with a desktop PC for automatic data acquisition and analysis, and the results were obtained within atmospheric pressure and a 25ºC jacket temperature. Heat capacity of the system, C_{sys}, was obtained from the Tris/HCl samples at 25.05ºC $\pm 0.05^{O}$C in accordance with the procedure and equation given in the manufacturer's manual. This constant was used throughout the experiments to calculate the heat values (Q) and hence the enthalpy of mixing (ΔH).

In a typical procedure, the bitumen sample is weighed into the rotating glass sample cell and placed in the calorimeter dewar (solvent chamber). When both solute and solvent attain equilibrium temperature (25.05^{O}C $\pm 0.05^{O}$C), the solute is released into the solvent chamber and heat of mixing is recorded and plotted as

shown in Figure 1. This plot, of the temperature of the solvent versus time before and after the solute is added (Figure 1), known as a thermogram is produced and a trendline is drawn for both before and after the mixing occurs.

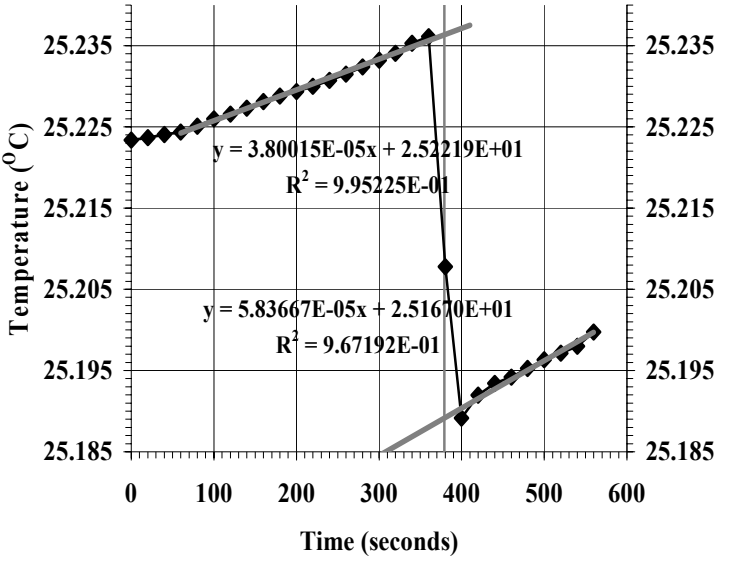

Figure 1: Typical Thermogram Plot for mixing 2.68g ColdLake in 85.44g toluene (100mL).

Using the equations obtained from the pre and post reaction trendlines, the initial and final temperatures are obtained and used to calculate the temperature change, ΔT_C, and hence the heat of the reaction, Q_{rxn}, as given in Equation 1.

$$Q_{rxn} = \Delta T_c * C_{sys} \tag{1}$$

This heat of mixing, ΔH_{mixing}, at the temperature of mixing, is then obtained by dividing the negative of the energy of the system, by the mass of the solute (Equation 2).

$$\Delta H_{mix} = -Q_{rxn} * m_{solute} \tag{2}$$

Different weights of solute samples were used with standard solvent volume of 100mL.

3 Results and discussion

Heats of mixing were obtained for the mixing of toluene with hexane, and HSR naphtha to provide a reference enthalpy of mixing for the bitumen/solvent mixtures being studied. Since no enthalpy of mixing is available in the literature to compare our toluene-naphtha results, we decided to repeat the experiment for methanol-water mixtures. Figure 2 shows the consistency in results obtained for enthalpy of mixing for miscible hydrocarbon solvents and miscible polar solvents. Our results are in good agreement with the literature values. The hexane-toluene mixtures and methanol-water mixtures provide excellent reference standards for endothermic and exothermic processes respectively.

The hexane-toluene mixtures provide an increase in heat of mixing until the solution becomes saturated with toluene, the heat of mixing then decreases. The naphtha-toluene mixtures behave in a much similar manner, however a more consistent and stable increase and decrease in heat of mixing. The water-methanol mixtures are highly miscible and also consistent but, exothermic as a result of the presence of similar heteromolcular interactions and molecular packing. For hydrocarbon solvents, the enthalpy of mixing for hexane-toluene mixtures is higher than for naphtha-toluene mixtures. This increase in enthalpy could be attributed to the rupture of the homomolecular interactions within both components.

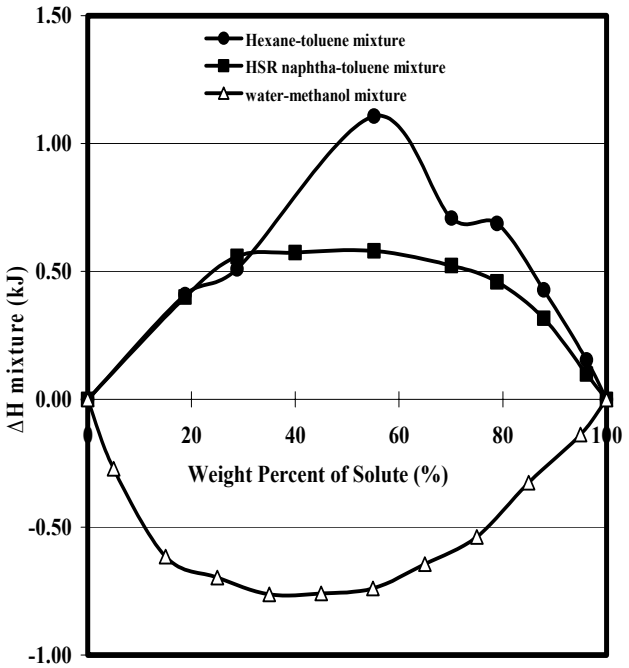

Figure 2: Solute-solvent mixtures possessing high levels of miscibility.

With toluene used as the solvent, enthalpy of mixing values was determined for various solutes. These solutes occupy three different classes: hydrocarbon diluents, heavy crude oils, and bitumen. The results for various solutes-toluene mixtures are shown in Figure 3.

The largest enthalpies of mixing were obtained for toluene with hexane and with the two naphthas. The results show that lower enthalpies of mixing are associated with higher molecular weight solutes. As clearly illustrated in Figure 3, the more complex the solute hydrocarbon chains the lower the enthalpy of mixing for the system. This is in agreement with results given in Figure 2 for naphtha-toluene mixtures, and identifies with the increasing absence of homomolecular interactions in the components. The results for enthalpies of mixing obtained for different bitumen-solvents systems at various bitumen weight percent are shown in Figure 4. Bitumen-naphtha systems show higher enthalpy of mixing at low bitumen concentration which decreases sharply with increase in concentration. Bitumen-toluene systems have low enthalpy of mixing which remains consistent with increase in bitumen concentration. In bitumen viscosity reduction, low solvent volume is preferred for economic reasons, and toluene, identified by several researchers as excellent solvent for bitumen [1,3,4,6], is shown to exhibit consistent enthalpy of mixing over a broad range of bitumen concentration.

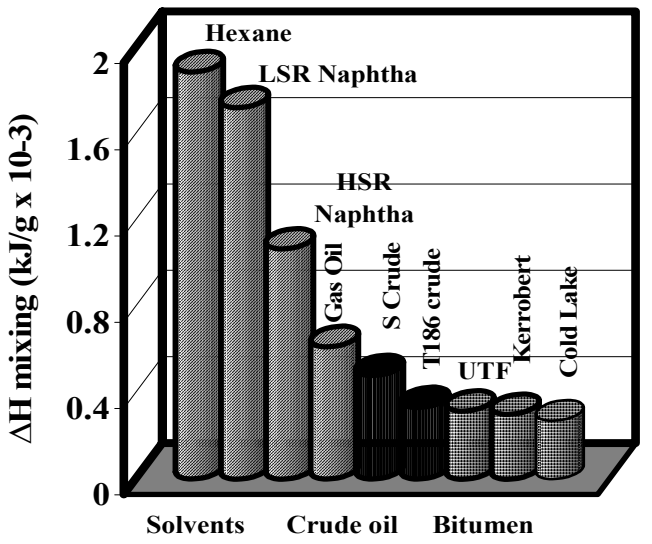

Figure 3: Enthalpy of mixing for a variety of hydrocarbon liquids with toluene.

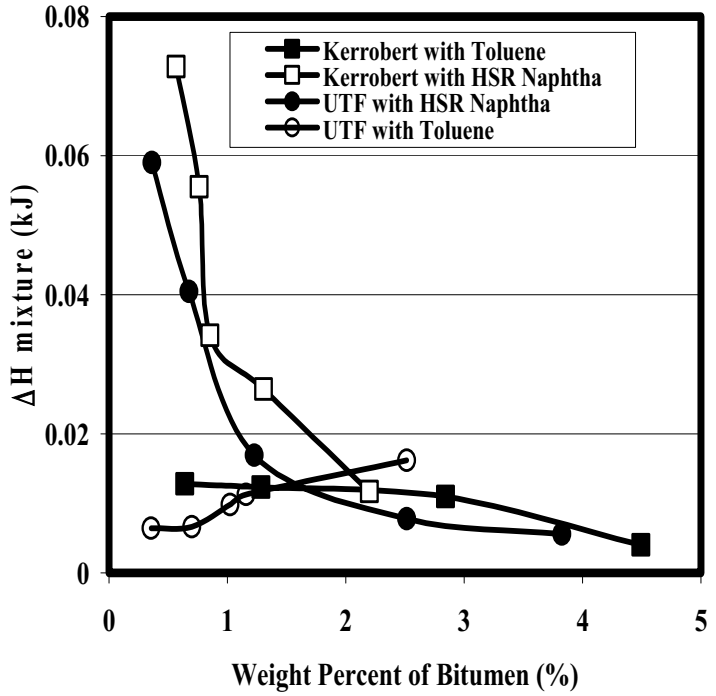

Figure 4: Enthalpy of mixing for various bitumen and solvent systems.

Toluene has been widely documented as completely miscible with bitumen [1,4,6,9]. In order to elucidate the effect of asphaltenes on enthalpy of mixing, we used toluene as additive to dissolve bitumen. Various amounts of UTF bitumen were dissolved in 10 ml of toluene and mixed with 90 ml of both hexane and HSR naphtha. The solution was filtered and the weight percent asphaltenes precipitated was determined. In Figure 5 it is shown that the lower the percent toluene in UTF bitumen, the greater the amount of asphaltenes precipitated. The same volumes were used for both hexane and naphtha solvents.

There was less precipitate with naphtha, but the same trend was observed, as the percent toluene in UTF bitumen increased the amount of precipitate decreased. The weight percent asphaltene precipitation and enthalpy of mixing for each solvent are depicted respectively in Figures 5 and 6. With a decreasing heat of mixing coupled with decreasing toluene concentration, asphaltene precipitation increases. Comparing the enthalpy of mixing values for the solution with the weight percent of asphaltenes that came out of solution, in Figure 6, showed that the greater the weight percent asphaltene, the lower the enthalpy of mixing. The trend is more pronounced with hexane than naphtha, but with reduced effect.

Since these values are positive, it is observed that the mixing of the UTF-toluene blend with hexane becomes less endothermic with increasing amounts of UTF bitumen. The presence of toluene in bitumen leads to a prevalence of dipole-dipole interactions due to polar components of asphaltenes.

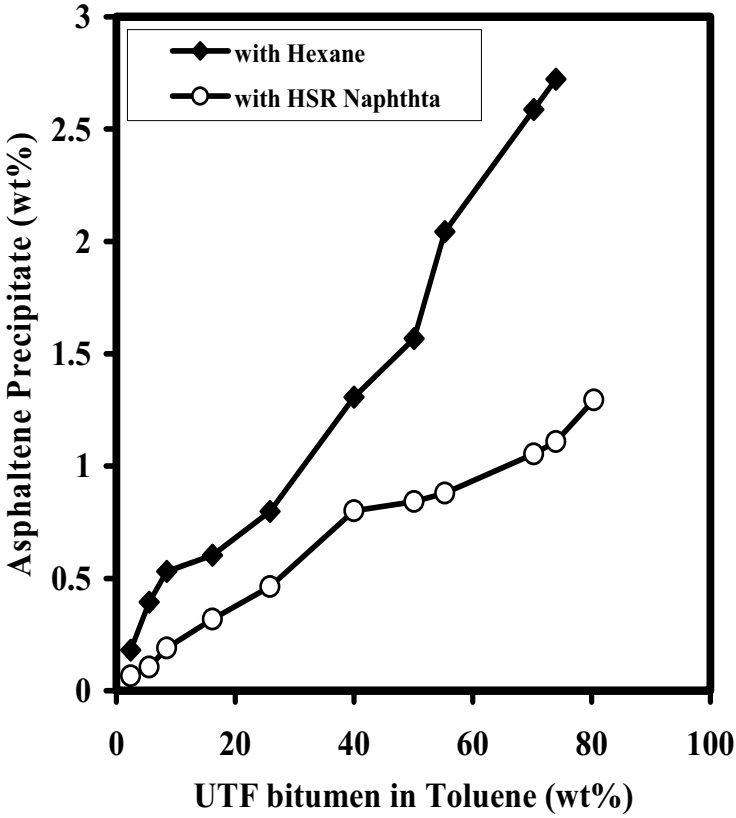

Figure 5: Comparison of asphaltene precipitation in different solvents for bitumen + toluene additive.

Addition of "non-solvent" breaks down this homomolecular interactions while weaker heteromolecular interactions are promoted. For naphtha, hydrogen bonding is arguably predominant and like dipole-dipole interactions results in lower asphaltenes precipitation. On the contrary, molecular packing and heteromolecular interactions in the hexane-bitumen+toluene system lead to flocculation and precipitation of the asphaltenes.

4 Conclusion

Using calorimetry we have been able to illustrate the relationship exiting between the enthalpy of mixing and aspaltenes precipitation, and the nature of molecular interactions affecting these properties in bitumen-diluents mixtures. It was observed that the lower the concentration of toluene in petroleum, the greater the amount of precipitate. Lower weight percent of asphaltenes precipitation, is associated with lower enthalpy of mixing in hexane and naphtha solvents. This phenomenon was more pronounced with hexane, and for all the

solvents enthalpy diminished with increase in solvent concentration. The enthalpy of mixing increases with increase in petroleum concentration, particularly with the bitumen, and therefore higher tendency of asphaltene precipitation. The presence of toluene lowers the enthalpy of mixing and reduced the precipitation of asphaltenes.

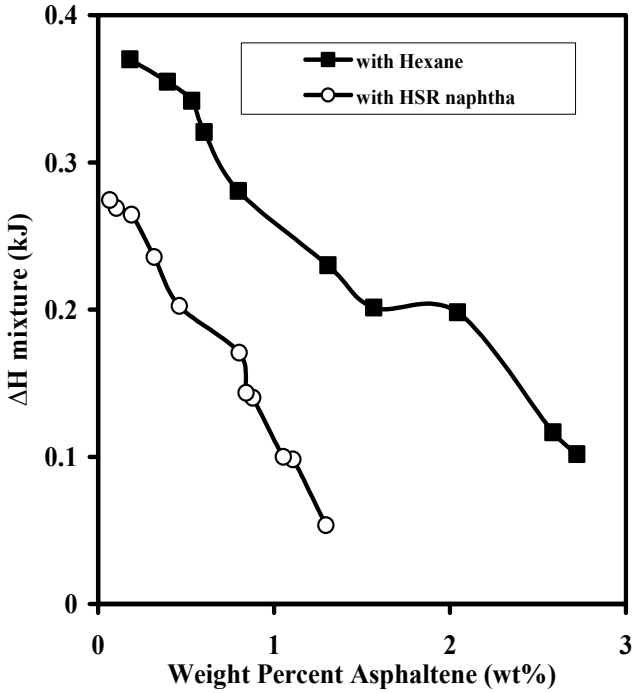

Figure 6: Comparison of enthalpy of mixing with amount of asphaltenes precipitated in UTF + toluene additive.

Acknowledgements

We wish to acknowledge the financial support provided by the Cape Breton University RAP grant and NSERC, Canada, through which the project was made possible. The bitumen samples were made available by Alberta Research Council and Syncrude Canada Ltd, and the heavy oil and refinery solvents by Irving Oil Refinery Ltd, Saint John, NB, Canada.

References

[1] Wallace, D., Henry, D., Miadonye, A., & Puttagunta, V.R., Viscosity and solubility of mixtures of bitumen and solvent. *Fuel Sci. & Tech. Inter.*, **14(3)**, pp. 465-478, 1996.

[2] Turta, A., Fisher, D., Singhal, A.K. & Najman, J., Variation of oil-solvent mixture viscosity in relation to onset of asphaltene flocculation and deposition. *J. Can. Pet. Tech.*, **38(13)**, pp. 55-60, 1999.

[3] Miadonye, A., & Britten, A., Generalized equation predicts of viscosity of heavy oil-solvent mixtures. *Computational Methods and Experimental Measurements*, **10**, pp. 165-177, 2001.

[4] Branco, V., Mansoori, G., Xavier, L., Park, S. & Manafi, H., Asphaltene flocculation and collapse from petroleum fluids. *J. Pet. Sci. and Eng.*, **32**, pp. 217-230, 2001.

[5] Zhang, L., Yang, G., & Que, G., The conglomerating characteristics of asphaltene from residue during thermal reaction. *Fuel*, **84**, pp. 1023-1026, 2005.

[6] Akbarzadeh, K., Alboudwarej, H., Svrcek, W.Y. & Yarranton, H.W., A generalized regular solution model for asphaltene precipitation from *n*-alkane diluted heavy oils and bitumens. *Fluid Phase Equilibria*, **232**, pp. 129-140, 2005.

[7] Porte, G., Zhou, H. & Lazzeri, V., Reversible description of asphaltene colloidal association and precipitation. *Langmuir*, **19**, pp. 40-47, 2003.

[8] Alboudwarej, H., Beck, J., Svrcek, W.Y., Yarranton, H.W. & Akbarzadeh, K., Sensitivity of asphaltene properties to separation techniques. *Energy & Fuels*, **16**, pp. 462-469, 2002.

[9] Sanchez, J. & Mansoori, G., In situ remediation of heavy organic deposits using aromatic solvents. *Proc. of the 68th Annual SPE Western Regional Meeting*, Bakersfield, CA, pp. 11-15, May 13, 1998.

This page intentionally left blank

Section 2
Bubble and drop dynamics

This page intentionally left blank

A homogenous cavitation transport model in turbo machinery

I. Biluš, L. Škerget, A. Predin & M. Hriberšek
Faculty of Mechanical Engineering, University of Maribor, Slovenia

Abstract

Cavitating flows are complex three-dimensional flows with a phase change in the low-pressure regions. These are very sensitive to bubble formation processes and to velocity/pressure pulsations caused by turbulence. The presented cavitation model derived from a reduced Rayleigh–Plesset equation accounts for some of these effects. The model is based on the additional generic transport equation for the vapour phase. The cavitation influence over the mixture density and viscosity is included in the model, which is implemented in commercial, general purpose CFD code and validated on practical flow examples.
Keywords: cavitation, numerical simulation, turbo machinery.

1 Introduction

Flow simulation using the numerical method known as Computational Fluid Dynamics has become one of the important topics of attention in cavitating fluid flow investigations. Cavitation is a phase transformation which occurs in fluid systems under certain conditions. If the dynamic alteration of the absolute static pressure reaches or drops below the vapour pressure of the liquid, vapour bubbles are formed inside the fluid and can collapse as they are convected into the higher-pressure regions. Cavitation results in flow continuity disturbance, operating characteristics drop and the appearance of other undesirable effects such as noise, vibration and solid surface erosion.

This cavitation phenomenon was first observed when a difficulty arose with a ship's propellers (the torpedo boat Daring) at the end of the nineteenth century because high speeds could not be reached despite the enlargement of the screw area. In 1910 Sir Charles Pearson built the first tunnel channel, for cavitation phenomenon research [1] and cavitation has been investigated since then.

However, owing to this phenomenon's complexity and high number of influential parameters, cavitation has never been completely defined or solved mathematically.

Accordingly this, present paper introduces a two-phase cavitation transport model, which was developed, improved and verified on practical flow examples. The presented simplified homogenous fluid model enables specification of those major parameters that affect the cavitation phenomenon thus making it useful for important practical examples, such as simulation of flow over a hydrofoil and for cavitation swirl simulation in a pump intake pipe. Numerical simulation results are compared with available experimental cavitation study results made on a NACA hydrofoil and with the results of cavitation swirl analyses made at the industrial water pump's entrance eye. The influence of diffusive term on the vapour fraction transport equation, the influence of the turbulent model and of the averaged fluid properties on the numerical simulation results are analyzed under different operating regimes and boundary conditions.

2 Mathematical model

2.1 The governing equations

The flow conditions for single phase turbulent flow could be modelled using the equations system, which presents a mathematical and physical model of the conservation laws: a continuity equation, a vapour mass fraction conservation equation, a momentum equation and a turbulence equations closure model, which connects the Reynolds stresses with the averaged flow values (RANS).

In the case of the two-phase flows, two separate equations systems must be considered, with conservation equations for both phases, and equations for interaction between them. The homogenous two-phase systems [2] are, basically, simplified multiphase systems that could be modelled using a single- phase equations system, where the average mixture values, are considered.

Averaging the Navier–Stokes equation system, turbulent models arise. In the common practice we use the models where the Reynolds averaged equations closure problem is circumvented by applying Boussinesque approximation, in which we assume proportionality between the deviatory parts of the Reynold's stress tensor and the strain rate tensor. This assumption is analogous to the constitutive relationship [3]. In this way, the standard two-equation $k - \varepsilon$ turbulence model was introduced.

The $k - \omega$ turbulence model was suggested with the specific dissipation rate ω as an alternative to ε. Wilcox presented his $k - \omega$ model based on Kolmogoroff's formulation in 1988; with the disadvantage of being highly sensitive to ω specified in the freestream. Menter proposed the $k - \omega$ baseline (BSL) model for the same reason, combining the $k - \omega$ model by Wilcox in the inner region of the boundary layer and the standard $k - \varepsilon$ in the outer region, and the free stream. The BSL model combines the advantages of the Wilcox and $k - \varepsilon$ models, but still fails to properly predict the onset and amount of flow separation from the smooth surfaces. The main reason for this deficiency is that both models do not

account for the transport of the turbulent shear stress. This results in an overprediction of the eddy – viscosity. Proper transport behaviour can be obtained by a limiter to the formulation of the eddy–viscosity included in the SST turbulence model which will be analysed in our case.

2.2 Cavitation modelling

The species conservation equation defines the transport phenomenon for the arbitrary variable C. In differential form it could be written as

$$\frac{\partial C}{\partial t}+\left(u_i\frac{\partial}{\partial x_i}\right)C=D\frac{\partial^2}{\partial x_i^2}C+I \tag{1}$$

where D represents the substance diffusivity, and I defines the substance sources. The additional transport equation will be used in order to describe transport of vapour phase inside the fluid domain. In the following, a special attention will be given to formulation of physical properties, vapour diffusivity and especially production (vaporisation) and condensation of the vapour phase.

The basis for numerical description of phase change, i.e. generation and condensation of vapour bubbles, is description of transport phenomena for a single spherical bubble.

It could be done using the well-known Rayleigh–Plesset equation

$$R_B\frac{d^2R_B}{dt^2}+\frac{3}{2}\left(\frac{dR_B}{dt}\right)^2=\frac{p_B-p}{\rho_L}+\frac{4\upsilon_L}{R_B}\dot{R}_B-\frac{2\sigma}{\rho_L R_B} \tag{2}$$

where first term presents the driving term, the second term is the viscous term and the last one on the left side of equation is the surface tension term. The inertia term is on the right hand side of equation.

In the homogenous two-phase flow model formulations there is no slip between the vapour and liquid phase, i.e. the phases share the same velocity field. The distribution of the vapour phase is obtained by solving an additional transport equation for vapour phase and the influence of the vapour phase on the motion of the mixture is accounted by applying mixture density and mixture viscosity as physical properties. In order to avoid the necessity of solving additional transport equation for the motion of vapour phase the homogenous two – phase flow model introduced by Singhal [4] was adopted and extended with diffusion term:

$$\frac{\partial}{\partial t}(\rho f)+\vec{\nabla}\cdot(\rho\vec{u}f)=\vec{\nabla}\cdot(\rho\Gamma\vec{\nabla}f)+R_e+R_c \tag{3}$$

where the vapour mass fraction f

$$f=\frac{m_V}{m_V+m_L} \tag{4}$$

is governed by the generic transport equation where source terms R_e and R_c denote vapour generation and condensation rate. They are functions of the flow parameters (flow pressures and velocities) and the fluid properties (density, evaporation pressure, surface tension). Γ represents the diffusivity of the variable f.

The introduced homogenous two – phase flow model is limited to source terms (R_e and R_c) definition [4, 5],

$$R_e = C_e \frac{V_{ch}}{\sigma} \rho_L \rho_V \left[\frac{2}{3} \frac{p_V - p}{\rho_L} \right]^{1/2} (1 - f) \tag{5}$$

$$R_c = C_c \frac{V_{ch}}{\sigma} \rho_L \rho_L \left[\frac{2}{3} \frac{p - p_V}{\rho_L} \right]^{1/2} f \tag{6}$$

where C_e and C_c are constants, and V_{ch} the local relative velocity between the liquid and vapour which can be assumed by $V_{ch} = \sqrt{k}$. The empirical constants C_e and C_c have been calibrated using empirical data, covering a very wide range of flow conditions, and do not require adjustments for different problems [4].

2.3 Two-phase mixture properties

According to the theory of homogenous transport models, we are solving one system of equations for water–water vapour mixture. Homogenous mixture properties are defined by the following equations. The mixture density ρ is determined using the mixing rule

$$\rho = \alpha \rho_V + (1 - \alpha) \rho_L \tag{7}$$

Similar formulation is used for the viscosity definition

$$\upsilon = \alpha \upsilon_V + (1 - \alpha) \upsilon_L \tag{8}$$

where $\eta = \rho \upsilon$. Both formulations are linear in α.

3 Experimental analysis

3.1 Flow around the hydrofoil

The first part of the experimental analysis was performed in a tunnel for Kaplan turbine testing at the Turboinstitute in Ljubljana [6]. The tunnel was equipped with a mechanism for variation of the blade attack angle, vacuum pump and with a transparent Plexiglas window for flow visualisation at different operating regimes defined with Reynolds number

$$\mathrm{Re} = \frac{uL}{\upsilon} \tag{9}$$

and the cavitation coefficient

$$\sigma = \frac{p - p_V}{\frac{1}{2} \rho u^2} \tag{10}$$

3.2 Unstable pump cavitation operating regime

The numerical model was verified for the cavitation operating regime simulation of the conventional centrifugal turbopump.

An unstable operating regime is brought about by a combination of unacceptably low flowrates and inadequate NPSH provision. A strong recirculatory motion occurs within an impeller and the adjacent pipework. This induces a rotating motion on the cavities which are ejected along the wall of the inlet pipe before returning to enter the impeller eye [7].

The cavitation swirl in the intake pipe was analysed in the Laboratory for Turbine Machinery at the University of Maribor. The measurement testing system was manufactured to conform to ISO 2548 recommendations for cavitation tests using pump NPSH variation.

4 Computational results and comparison with experiments

The present section includes results comparison for listed cavitation examples. Diagrams and photographs are given showing different operating regimes.

4.1 Calculation parameters and convergence

Information about the boundary layers of the calculating domain is defined by the following boundary conditions:

- wall condition,
- inlet condition,
- opening condition
- outlet condition,
- symmetry condition.
- frozen rotor on the interface rotating – stationary.

The conventional and SST turbulence models were used for calculation and for results comparison, for presented mixture properties models. Simulation was performed for different values of the diffusion coefficient Γ. Diffusion represents the velocity of scalar quantity propagation from the molecular point of view. In the cases of reduced and no convection examples which, in general, depend on liquid properties and/or on the properties of the phase they are currently calculated by transport equation. The calculation was repeated for different values of Γ from this reason.

The target residual was $r=10^{-5}$ for the hydrofoil and $r=10^{-4}$ for the pump example. No equation relaxation was used.

4.2 Flow around the hydrofoil

In order to set up an accurate numerical model for the computation of governing equations the numerical simulation for single phase flow around the blade profile NACA 4418 was performed analysing the 3D volume with a size of 1200*1000*5 mm, closed on all sides. The area was divided into hexahedrons. In each node of the flow element the dependent variables pressure, velocity, turbulent kinetic energy, dissipation of the turbulent kinetic energy and the vapour fraction are calculated.

Test calculations were performed for different mesh refinement factors and numerical method consistency was concluded.

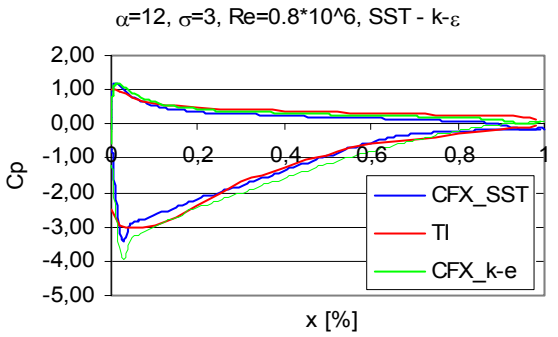

Figure 1: The distribution of pressure coefficient $C_{p.}$

4.2.1 The turbulence model influence

Turbulent flow modelling is one of the important subjects in the present analysis. To follow the general idea of the article and keep the computational cost as low as possible without loosing too much accuracy, the eddy viscosity based two-equation turbulence models were selected. Among them, the k – ε model as a standard engineering, and the SST model as advanced two equation model were selected for computations.

The results of turbulence model influence on numerical analyses results is shown in figure 1. Figure 1 shows the influence of the turbulence model on distribution of pressure coefficient C_p along the blade for operating regime $\alpha=12°$, $\sigma=3$, $Re=0.8*10^6$, where α represents the blade inclination angle and C_p is defined as

$$C_p = \frac{p - p_{st}}{\frac{1}{2}\rho u^2} \tag{11}$$

It is obvious, that the turbulence model influences the pressure coefficient curve considerably at the blade suction side and that the SST model follows the measured curve (red) better.

4.2.2 The diffusion coefficient influence

In the introduced transport equation, the determination of diffusion term, among other terms, presents one of the major uncertainties. The reason is the physical origin of the diffusion coefficients as it models interactions at microscopic level. In the presented transport equation the role of diffusion coefficient is mainly in accounting for the motion of vapour bubbles from regions of higher concentration to regions with lower concentration. Since no suitable data can be found in the open literature, cavitation cloud visualization results with diffusivity coefficient influence analysis is presented in figure 2, for three different operating regimes:

a) $\alpha=8°$, $\sigma=2$, $Re=1.5*10^6$;
b) $\alpha=10°$, $\sigma=2$, $Re=1*10^6$;
c) $\alpha=16°$, $\sigma=2$, $Re=8*10^5$.

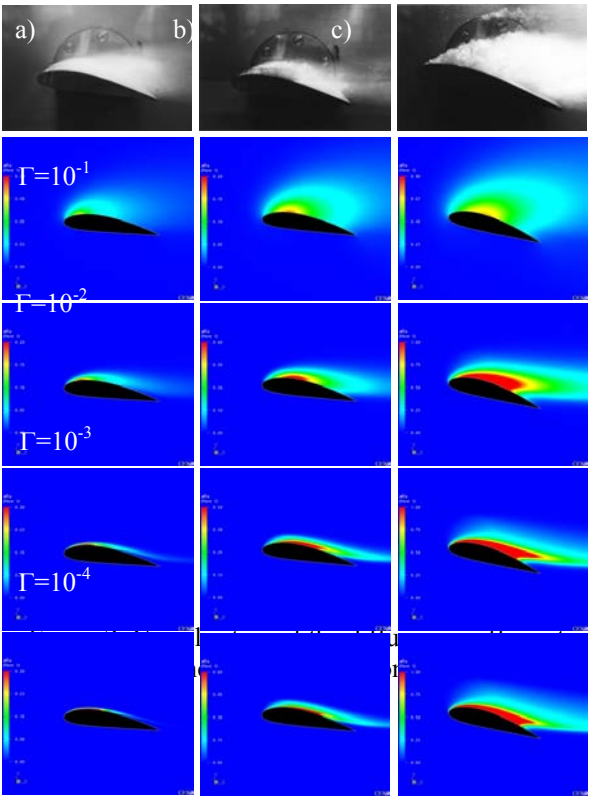

Figure 2: Visualisation of the diffusion coefficient influence on the cavitation cloud.

The parametric analysis accession was used in order to find an appropriate value of Γ based on known experimental results. Therefore, calculated cavitation cloud areas are shown for different values of Γ at three different Reynolds number values.

It is obvious from figure 2, that the diffusion term of the transport equation could not be neglected, since a diffusive transport phenomenon affects the two-phase region. It could be concluded, that the diffusion parameter should have a value in the range $10^{-3} \leq \Gamma \leq 10^{-2}$.

4.3 Unstable pump cavitation operating regime

Conclusions from the previous chapter regarding the turbulence model and diffusion coefficient will be used for analysis in the present chapter.

The influence will be analysed of relative pressure in the water reservoir and convection term height on cavitation swirl with stress laid on method stability.

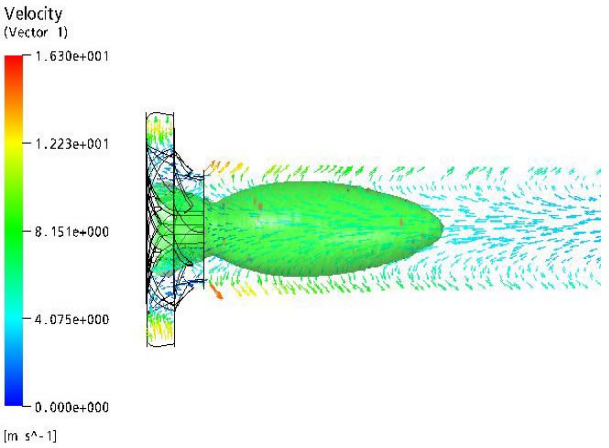

Figure 3: Unstable cavitating operating regime.

Figure 3 shows the unstable cavitating operating regime with a strong recirculating cloud at the inlet pipe walls.

Strong recirculatory motion with an active flow area in the middle of the pump is shown in figure 3. It is obvious, that cavitation swirl takes place in the low-pressure region of the active flow area. Figure 4 shows the cavitation visualisation comparison between two different operating regimes.

It could be concluded from the results shown in figure 4, that the introduced cavitation model follows the experimental results and presents a useful method for cavitation prediction for very complex flow pattern examples. It is validated, that the used frozen rotor interface between the rotating part of the grid and the stationary part of the grid might be used for impeller – pipe connections, despite the fixed relative positions of the grid parts.

5 Conclusions

It can be concluded that the presented homogenous two-phase model gives acceptable results for the flow pattern around the blade profile and for cavitation swirl, under different operating regimes [8].

The presented mathematical model is suitable for the prediction of cavitation cloud around a hydrofoil (shape, position and dimensions) and for cavitation announcement in turbomachinery.

The distinct advantage of the presented mathematical model compared to similar ones [9, 10], is in its source term defining parameters, since they are easily measured.

The used conventional two-equation turbulent model k-ε is suitable for turbulent cavitation flow conditions determination but SST turbulence model defines the characteristics closer to experimental values.

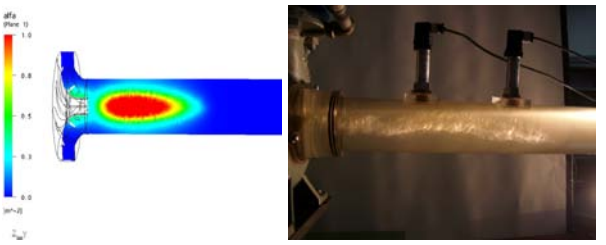

a) p=35000 Pa, Re=$5.5*10^4$

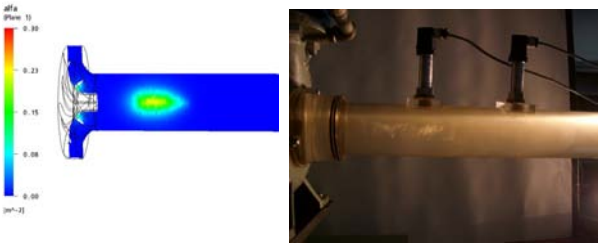

b) p=50000 Pa, Re=$5.5*10^4$

Figure 4: Cavitation swirl visualisation.

The influence of vapour diffusion in the water is not neglectable, since diffusion coefficient remarkably defines cavitation propagation for different convection term values. The assumed constant density of vapour and liquid do not cause important disagreements. The convection at the bubble interface does not influence the vapour phase fraction. The presented model is convergent and stable up to Re=$1.5*10^6$ since no under relaxation parameters were used. The presented homogenous cavitation model therefore presents an accurate and computationally fast numerical tool for cavitation prediction of turbomachinery.

References

[1] Knap R. T., Cavitation, McGraw-Hill Book Company, New York.

[2] Wallis G. B., One Dimensional Two Phase Flow, McGraw-Hill Book Company, New York, 1970.

[3] Voigt K. L., Comparison of Turbulence models for Numerical Calculation of Airflow in an annex 20 Room, Technical University of Denmark, 2000.

[4] Singhal, A. K., Athavale, M. M., Mathematical Basis and Validation of the Full Cavitation Model, Journal of Fluids Engineering, Vol. 124, pp. 617–624, 2002.

[5] Dular, M., Širok, B., Stoffel B., Bachert, B., Numerical simulation of cavitation on a single hydrofoil in a cavitation tunnel, Slovene Society for Mechanics, Kuhljevi dnevi 2003, Zreče, pp. 93–102, 2003.

[6] Vujanič, V., *Analysis of the flow around the hydrofoil in the cavitation tunnel*, Master degree work, Faculty for Mechanical Engineering, Ljubljana, 1992.
[7] Grist, E. *Cavitation and the Centrifugal Pump*, Taylor & Francis, London, 1999.
[8] Biluš, I., *Homogenous cavitation transport models in turbomachinery*, Dissertation, Faculty of Mechanical Engineering, Maribor, 2005.
[9] Sauer, J., *Instationar kavitierende Stromungen – Ein neues modell, basierend auf front Capturing (VoF) und Blasendynamik*, Dissertation, Universitat Karlsruhe, Karlsruhe, 2000.
[10] Lindau, J. W., Kunz, R. F., High Reynolds Number, unsteady, Multiphase CFD Modelling of Cavitation Flows, *Journal of Fluids Engineering*, Vol. 124, pp. 607-616, 2002.

Mixing in a gas/liquid flow countercurrent bubble column

T. A. Bartrand, B. Farouk & C. N. Haas
Drexel University, Philadelphia, USA

Abstract

This paper presents results of experimental and numerical investigations into the hydrodynamics of a bench scale bubble column reactor. Countercurrent bubble column reactors are the reactors most commonly used in water treatment for effecting the mass transfer of ozone to the aqueous phase. The experimental reactor is a glass cylinder with an internal diameter of 17 cm and height of 1.8 m. Gas is introduced at the bottom of the column via a 2.5 cm spherical diffuser and water is introduced to the top of the column through a manifold packed with glass spheres. Residence time distribution (RTD) studies were conducted for a range of gas flow rates chosen to span the dispersed flow bubble regime. A computational fluid dynamics computer code was used to model flow in the bubble column. Numerical studies were performed to refine and validate the CFD model and to gain insights into the fluid dynamics of countercurrent flow bubble columns. Investigations identified a gas flow rate within the ideal bubbly flow regime at which large-scale hydrodynamics and phase distribution were significantly different from those encountered at lower gas flow rates. These results will be used in subsequent studies in which ozone mass transfer and chemistry are included.
Keywords: countercurrent, bubble column, dispersion, CFD.

1 Introduction

In water and wastewater treatment, bubble contactors are used frequently for dissolution of gaseous ozone into the aqueous phase because of their simple design, low energy requirements (excluding the energy required in ozone generation) and familiarity to the industry and regulatory agencies (Langlais et al. [1]). Full-scale contactors typically employ baffled chambers in which

ozonated gas is contacted with untreated water in both countercurrent and cocurrent fashion. Reducing operating costs and minimization of deleterious by-products associated with reaction of ozone with bromide and natural organic matter (NOM) require the minimization of ozone dose and the optimization of ozone transfer and contact with untreated water.

This study investigates the use of computational fluid dynamics (CFD) for detailed study of countercurrent bubble column flow. Despite a rich literature on bubble column reactors, few studies have explored the details of countercurrent flow and fewer studies applied CFD to countercurrent flow.

1.1 Dispersion in bubble column reactors

Rising bubbles promote liquid-phase hydrodynamic dispersion and influence mixing of the phases and mass transfer rates. To date, most analyses have characterized liquid dispersion in bubble columns via a single Peclet number, though dispersion varies axially in bubble columns (Bischoff and Phillips [2]). Among the many relations developed for predicting axial dispersion in bubble columns, only three (Table 1) were developed explicitly for countercurrent operation.

Table 1: Summary of countercurrent bubble column dispersion relations.

Relation	Study
$E_L \propto \frac{u_g^2 d_c}{v_b}$	Bischoff and Phillips [2][a]
$P_e = \frac{(2u_g + v_b)d_c}{E_L} = 3.0 \pm 0.3$	Reith et al. [3][b]
$P_e^{-1} = \frac{4.88}{H}\left[0.00185 + 9.7\frac{u_g^{1/2}}{u_L^{5/3}}\left(\frac{\nu_L}{d_b}\right)^{7/6}\right]$	Kim et al. [4][c]

[a] Based on analysis of data from numerous small diameter cocurrent, countercurrent and nonflowing liquid phase bubble columns. Only valid in the ideal bubbly flow regime.
[b] Based on experimental data taken in 5 cm and 14 cm cocurrent and countercurrent bubble columns (air/tap water). The term $2u_g + v_b$ is the relative velocity between phases.
[c] Developed for co- and countercurrent flow in a 15 cm circular bubble column. Units of H must be m and all other units must be dimensionally consistent.

In the relations shown in Table 1, P_e is the Peclet number, defined as

$$P_e = \frac{u_L d_c}{E_L}, \tag{1}$$

E_L, is axial dispersion, u_g and u_L are superficial gas and liquid velocities, v_b is bubble terminal rise speed, d_c is column diameter, and H is column height.

In pilot studies of bubble columns of differing diameter and with a non-flowing liquid phase, the column diameter influences mixing due to the dependence of large-scale fluid structure (circulation) on column diameter but did not influence gas phase holdup (Forret et al.[5], Krishna et al. [6], Ruzicka

et al [7]). Column height can also influence transition from homogeneous to heterogeneous bubbly flow and dispersion in columns with non-flowing liquid phase, with transition occurring earlier as column height is increased (Ruzicka, et al. [8]). Minor vertical misalignment of tall cylindrical bubble columns can drastically change column hydrodynamics; a reactor tilt of only 0.5° resulted in a three order of magnitude difference in dispersion in pilot studies of air injected into water in a 2.44 m tall pilot scale bubble column (Rice and Littlefield [9]).

In full scale reactors, the arrangement of baffles dominates reactor hydrodynamics (T_{10}/θ); gas injection scheme (distribution of gas injection between reactor compartments) plays a less significant role (Do-Quang et al. [10]). The spacing of spargers and their proximity to reactor walls influence reactor hydrodynamics, given the tendency of bubble plumes to migrate toward each other (Freire et al. [11]) or toward reactor walls (Machina et al. [12]).

Using drift flux analysis and experimentation, Hasan et al. [13] observed that holdup in bubble columns differs significantly for cocurrent and countercurrent modes of operation. For countercurrent operation in the ideal bubbly flow regime, Argo and Cova [14] determined that gas superficial velocity influences on dispersion more than liquid superficial velocity.

1.2 Review of prior numerical studies

Numerous CFD studies have been made of bubble columns with non-flowing liquid phase for exploring the submodels best suited for reproducing bubble column hydrodynamics in general and momentum exchange between phases and bubble break-up and coalescence in specific. Significant differences between reported studies are treatment of the dispersed phase (Eulerian (e.g., Olmos et al. [15]; Pfleger et al. [16]; van Baten and Krishna [17]) or Lagrangian (e.g., Laín et al. [18])), distribution of bubble diameters (monodisperse (e.g., Pfleger et al. [16]) two size groups (e.g., van Baten and Krishna [17]) or a distribution of bubble diameters (e.g., Olmos et al. [15])) and bubble drag model.

Among researchers who have performed CFD studies of ozone bubble contactors, Cockx et al. [19] modelled relevant physics in the greatest detail. That study used an Eulerian-Eulerian approach with a monodisperse gas phase (3 mm bubble diameter) and uniform drag coefficient of 1.0.

2 Experimental and numerical methods

2.1 Experimental methods

Tracer studies were performed in the countercurrent flow bubble column shown in Figure 1. Water enters the column via two ports at the bottom of the collar that encloses the top of the column. The space between the column and collar is packed with 7 mm glass beads. Water flows out of the column through four symmetric ports located approximately 3 cm below the bottom of the diffuser. The volume of the column below the diffuser is also packed with glass beads. Air flows into column via a spherical 2.5 cm diameter fine porous diffuser and leaves the reactor at the water surface.

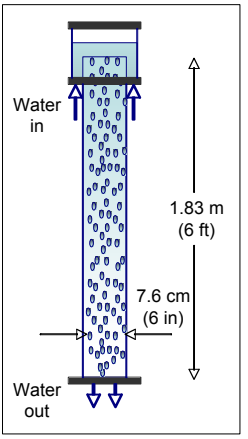

Figure 1: Experimental apparatus.

Step tracer studies (NaCl tracer) were performed at a liquid flow rate of 6.6 L/min and at gas flow rates of 0, 0.5, 1, 2, 3 and 3.5 L/min. Gas flow was observed to be in the ideal bubbly regime at all gas flow rates, though, as will be described later, the liquid phase flow field and distribution of bubbles in the column changed significantly over the range of gas flow rates. During tracer studies, samples were taken at 15s intervals from a port approximately 6 cm downstream of the column's water discharge ports. All calculations were performed using conductivity rather than NaCl concentration since calibration studies confirmed linear dependence of conductivity on concentration over the anticipated concentration range. Prior to tracer studies the column was operated at the test water and gas flow rates for at least 3 theoretical residence times. During tracer experiments tracer was introduced to the column via step feed for 3 theoretical residence times, then tracer feed was replaced with tap water and tracer was washed out for at least three residence times.

2.2 Numerical model

Numerical studies were performed with the commercial finite volume CFD package CFX (ANSYS Europe Ltd. [20]) on a 480,000 element 3-dimensional unstructured mesh. Mesh density was chosen based on a grid resolution study and generated to provide high resolution at column walls and near the diffuser.

An Eulerian-Eulerian two phase formulation was employed. The gas phase was approximated as monodisperse (2 mm diameter) with drag coefficient from the Grace model (Clift et al. [21]) and with bubble-enhanced turbulence (Sato and Sekoguchi [22]). Dirichlet water and air inlet boundaries were specified and gas escaped from the top of the column via a degassing boundary (no slip for the liquid phase, sink term for the gas phase).

All calculations were 3-dimensional and unsteady. A second order upwind transient scheme with relatively small time steps (0.05 s) was required to achieve convergence to an RMS residual of 1×10^{-5} within 10 iterations per time step. To

produce representative "quasi-steady" results for inclusion in this paper, calculations were performed for approximately 10s of simulation time, after which variations in bubble plume shape became minor and bubble plume was seen to rotate in the column, though not with a fixed period.

3 Experimental observations

As gas flow rate was increased during tracer studies, the behaviour of the bubble plume changed significantly, despite though no increase in bubble break-up or collisions was observed. At low gas flow rates, the plume rises vertically and increases in diameter with height, as shown in Figure 2(a). At higher gas flow rate (Figure 2(b)), the bubble plume rotates while rising, tending to migrate away from the column centreline and toward the wall. At some distance above the sparger (typically between 0.6 and 1 m), the plume expands to fill the entire column.

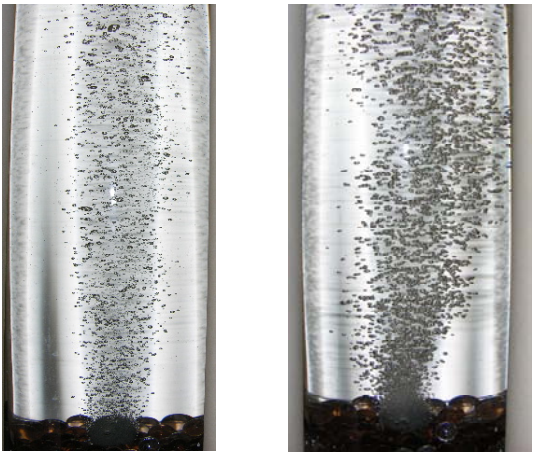

(a) Low Q_g (b) High Q_g

Figure 2: Bubble plume shapes.

Residence time distributions (RTDs) corresponding to the range of gas flow rates tested are presented in Figure 3.

The parameters θ and F are the normalized time (time/theoretical hydraulic residence time) and the normalized concentration, given as

$$F = \left(\frac{C_{\text{Tracer}} - C_0}{C_{\text{Tracer,in}} - C_0} \right) \text{ for tracer feed or } \left[1 - \left(\frac{C_{\text{Tracer}} - C_0}{C_{\text{Tracer,in}} - C_0} \right) \right] \text{ for washout} \quad (2)$$

where C_{Tracer} is the measured tracer conductivity, C_0 is the conductivity of the tap water feed (background) and $C_{\text{Tracer,in}}$ is the conductivity of the tracer at column inlet. The early portion of the RTD curves indicate that increased gas flow rates promote earlier breakthrough. This is due, in part, to "gulfstreaming" (upward flow of liquid phase in the bubble plume) and reduction of the effective column cross sectional area through which downward-flowing liquid passes.

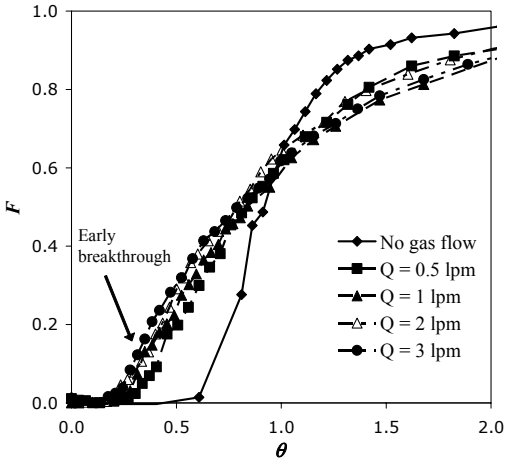

Figure 3: RTDs for $0 < Q_g < 3$ L/min.

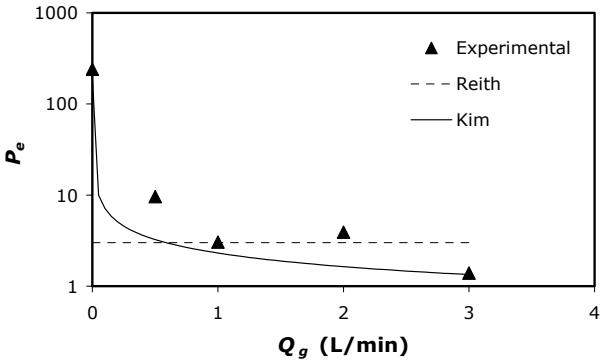

Figure 4: Experimental and predicted Peclet number.

Axial dispersion was estimated via RTD analyses (Haas et al. [23]). Candidate RTD models (inverse Gaussian, Gamma, two stream gamma and two stream inverse Gaussian) were fit to data and best-fit models were identified. F-tests were performed to ensure use of more highly parameterized models was justified by improvement in fit. For 0.5 l/min $\leq Q_{gas} \leq$ 2 l/min, a single stream inverse Gaussian distribution provided the best fit to RTD data. For 0 and 3 l/min gas flow, a two-stream inverse Gaussian distribution provided a statistically-significant better fit than the single stream model at 90% confidence level. Peclet number was estimated from the variance of the inverse Gaussian distribution via the relation

$$\sigma^2 = \frac{2}{P_e} - \frac{2\left(1-e^{P_e}\right)}{P_e^2} \tag{3}$$

Figure 4 shows Peclet number calculated from experimental data and the relations found in Table 1. Experimental Peclet number falls sharply as gas flow

increases from 0 to 0.5 L/min, is relatively constant (around 3.0) for moderate gas flow rate and falls as gas flow rate increases above 2 L/min. The Kim expression fits experimental data well at low and high gas flow rates and the Reith expression fits the data at moderate gas flow rate.

In summary, three trends identified in RTD analyses indicate changed hydrodynamics as gas flow is increased above 2 L/min: early breakthrough observed in the RTD, significant improvement in RTD fit when a two-stream model is used, and significant reduction in Peclet number.

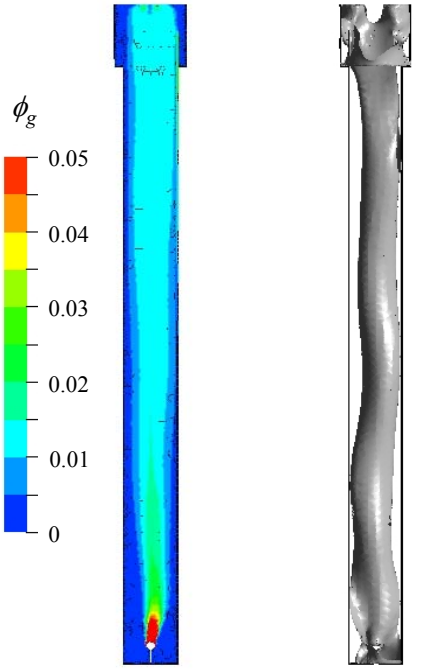

(a) Gas volume fraction (b) Plume shape

Figure 5: Phase distribution.

4 Numerical studies

Contours of gas volume fraction, ϕ_g, predicted at a gas flow rate of 2 L/min are shown in Figure 5(a). The plume does not rise symmetrically, but migrates in the column and finally migrates to the wall near the top of the column. The plume region, shown in Figure 5(b) is defined as the region within which the liquid phase velocity is upward. Note that there is upflow of liquid in the bubble plume over the entire reactor height and that the plume twists as it rises in the column. These figures illustrate non-axisymmetric plume rise and significantly different plume shape near the sparger compared with higher locations. In drinking water treatment, non-asymmetric flow as illustrated in Figure 5 creates the potential for short-circuiting of raw water and retards ozone mass transfer via poor mixing in the bubble plume and reduced contact of bubbles with raw water.

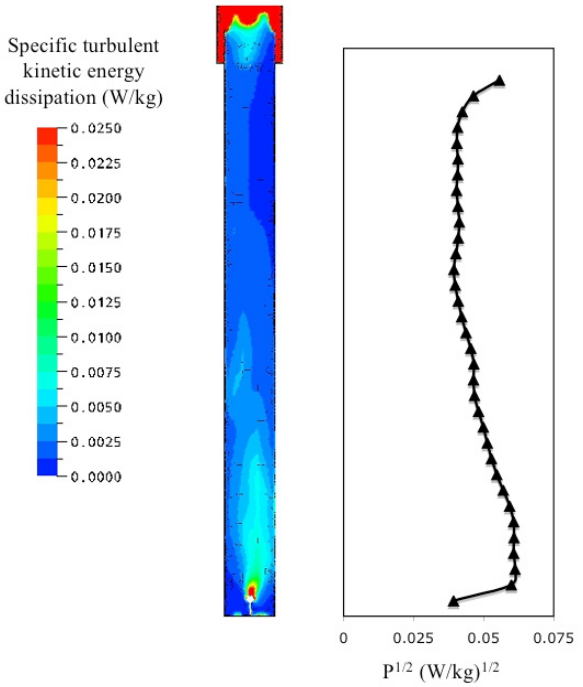

Figure 6: Spatial variations in mixing.

Axial variation in mixing in the column is shown in Figure 6. Neglecting large-scale fluid motion, local mixing intensity is approximately proportional to the square root of the rate of turbulent energy dissipation (Droste [24]). Figure 6(a) shows contours of turbulent kinetic energy dissipation on a column midplane and Figure 6(b) is a plot of mean dissipation as a function of axial location. Average turbulent dissipation at axial location *k,* is calculated by:

$$\overline{\dot{P}}_k = \frac{\sum_{i=1}^{\#\text{elements}} \left(\phi_g\right)_{i,k} \left(\dot{P}\right)_{i,k} A_{i,k}}{\sum_{i=1} \left(\phi_g\right)_{i,k} A_{i,k}} \tag{4}$$

where $A_{i,k}$ is area of element i at axial location k. Mixing is non-uniform both axially and radially. Mixing is highest near the sparger ($z < 0.5$ m) and uniform in the rest of the column, except near the top where entrance effects dominate the flow. Mixing intensity is high inside the bubble plume and much lower outside the bubble plume. These results explain early breakthrough of tracer at high gas flow rates (Figure 3) – the flow field is partitioned into a well-mixed portion rising in the bubble plume and a poorly mixed stream flowing downward.

5 Discussion

Experiments and numerical studies were used to explore mixing phenomena in a countercurrent bubble column operating in the ideal bubbly regime. Nonuniform

distribution of the gas phase and mixing became pronounced for gas flow rate higher than 2 L/min. At high gas flow rate the liquid flow field was partitioned into a fast-flowing stream flowing through a restricted area and a second stream dominated by large scale hydrodynamics. These findings indicate that dispersion relations for bubble column reactors are specific to the column mode of operation and height of bubble column. In very tall columns, axial variations in dispersion will be minor, but large-scale hydrodynamics may be different than in smaller reactors. The proposed numerical model was adequate to reproduce significant features in the flow field and results of CFD studies provided explanation for the unexpectedly early breakthrough of tracer during tracer studies at high gas flow rates.

In subsequent studies additional experiments with a greater range of gas flow rates will be performed to allow characterization of the entire ideal bubbly flow regime. In concert with these studies, numerical tracer studies will be performed at several gas flow rates.

Acknowledgements

The authors gratefully acknowledge the Koerner Family Fellowship and the L.D. Betz Endowment for Environmental Engineering for support of this research.

References

[1] Langlais, B., D.A. Reckhow, and D.R. Brink, eds. *Ozone in Water Treatment: Application and Engineering*. ed. AWWARF and Compagnie Général des Eaux. 1991, Lewis Publishers, Inc.: Chelsea, MI. 569.

[2] Bischoff, K.B. and J.B. Phillips, *Longitudinal Mixing in Orifice Plate Gas-Liquid Reactors.* Industrial and Engineering Chemistry Process Design and Development, 1966. **5**(4): p. 416-21.

[3] Reith, T., S. Renken, and B.A. Israël, *Gas Hold-up and Axial Mixing in the Fluid Phase of Bubble Columns.* Chemical Engineering Science, 1968. **23**: p. 619-29.

[4] Kim, J.-H., R.B. Tomiak, and B.J. Mariñas, *Inactivation of Cryptosporidium Oocysts in a Pilot-Scale Ozone Bubble-Diffuser Contactor. I: Model Development.* Journal of Environmental Engineering, 2002a. **128**(6): p. 514-21.

[5] Forret, A., et al., *Influence of Scale on the Hydrodynamics of Bubble Column Reactors: an Experimental Study in Columns of 0.1, 0.4 and 1 m Diameters.* Chemical Engineering Science, 2003. **58**: p. 719-24.

[6] Krishna, R., et al., *Influence of Scale on the Hydrodynamics of Bubble Columns Operating in the Churn-Turbulent Regime: Experiments vs. Eulerian Simulations.* Chemical Engineering Science, 1999. **54**: p. 4903-11.

[7] Ruzicka, M.C., et al., *Homogeneous-Heterogeneous Regime Transition in Bubble Columns.* Chemical Engineering Science, 2001. **56**: p. 4609-26.

[8] Ruzicka, M.C., et al., *Effect of Bubble Column Dimensions on Flow Regime Transition.* Chemical Engineering Science, 2001. **56**: p. 6117-24.

[9] Rice, G.R. and M.A. Littlefield, *Dispersion Coefficients for Ideal Bubbly Flow in Truly Vertical Bubble Columns.* Chemical Engineering Science, 1987. **42**(8): p. 2045-53.
[10] Do-Quang, Z., C.C. Ramirez, and M. Roustan, *Influence of Geometrical Characteristics and Operating Conditions on the Effectiveness of Ozone Contacting in Fine-Bubbles Conventional Diffusion Reactors.* Ozone Science and Engineering, 2000. **22**(4): p. 369-78.
[11] Freire, A.P.S., et al., *Bubble Plumes and the Coanda Effect.* Intenational Journal of Multiphase Flow, 2002. **28**(8): p. 1293-1310.
[12] Machina, D.W., J.A. McCorquodale, and J.K. Bewtra, *Numerical and Physical Modeling of Air Diffuser Plume.* Journal of Environmental Engineering, 1992. **118**(2): p. 253-67.
[13] Hasan, A.R., C.S. Kabir, and S. Srinivasan, *Countercurrent Bubble and Slug Flows in a Vertical System.* Chemical Engineering Science, 1994. **49**(16): p. 2567-74.
[14] Argo, W.B. and D.R. Cova, *Longitudinal Mixing in Gas-Sparged Tubular Vessels.* Industrial and Engineering Chemistry; Process Design and Development, 1965. **4**(4): p. 352-9.
[15] Olmos, E., C. Gentric, and N. Midoux, *Numerical Description of Flow Regime Transition in Bubble Column Reactors by a Multiple Gas Phase Model.* Chemical Engineering Science, 2003. **58**: p. 2113-21.
[16] Pfleger, D., et al., *Hydrodynamic Simulations of Laboratory Scale Bubble Columns Fundamental Studies of the Eulerian-Eulerian Modeling Approach.* Chemical Engineering Science, 1999. **54**: p. 5091-99.
[17] van Baten, J.M. and R. Krishna, *Eulerian Simulation for Determination of the Axial Dispersion of Liquid and Gas Phases in Bubble Columns Operating in the Churn Turbulent Regime.* Chemical Engineering Science, 2001. **56**: p. 503-12.
[18] Laín, S., D. Bröder, and M. Sommerfeld, *Experimental and Numerical Studies of the Hydrodynamics in a Bubble Column.* Chemical Engineering Science, 1999. **54**: p. 4913-20.
[19] Cockx, A., et al., *Use of Computational Fluid Dynamics for Simulating Hydrodynamics and Mass Transfer in Industrial Ozonation Towers.* Chemical Engineering Science, 1999. **54**: p. 5085-90.
[20] ANSYS Europe Ltd., *CFX-5.7.1*. 2004: Abingdon, UK.
[21] Clift, R., J.R. Grace, and M.E. Weber, *Bubbles, Drops and Particles*. 1978, New Nork, NY: Academic Press. 380.
[22] Sato, Y. and K. Sekoguchi, *Liquid Velocity Distribution in Two-Phase Bubble Flow.* International Journal of Multiphase Flow, 1975. **2**(1): p. 79-95.
[23] Haas, C.N., et al., *Predicting Disinfection Performance in Continuous Systems from Batch Disinfection Kinetics.* Water Science and Technology, 1998. **38**(6): p. 171-9.
[24] Droste, R.L., *Theory and Practice of Water and Wastewater Treatment*. 1997, New York: J. Wiley and Sons.

A contribution to the problem of the continuous dewatering process

J. Mls
Faculty of Science, Charles University, Prague, Czech Republic

Abstract

Because of its energetic efficiency, gravity thickening is one of the most convenient processes of lowering the volume of suspensions. One of the problems that has to be solved when designing equipment for, say, a digestion tank for the continuous process of suspension dewatering, is to determine the optimum height of the compression zone of the given suspension. This paper presents a solution for this problem. The suspension is considered as a two-phase continuum where both the phases are independently movable. The behaviour of such a system can be described by a set of partial differential equations of general Darcian mechanics. Making use of the known hydromechanical characteristics of the investigated two-phase system, a problem with a set of two ordinary differential equations and related boundary conditions was formulated and numerically solved. The unknown functions of the problem are the liquid-phase pressure and the solid-phase concentration. The method of solution is described and the achieved results are visualized and presented.

1 Introduction

The process of compression of a suspension has to be studied in detail when various industrial technologies are designed, particularly when the optimum height of the compression zone of sedimentation tanks has to be determined, e.g. Tuček and Koníček [6]. The previous reduction of the suspension volume minimizes, for example, the space of digestion tanks and improves the efficiency of filtration or centrifugation. The gravity thickening is, because of its low energetic demands, one of the most convenient processes of lowering volume of suspensions and significantly increasing the concentration of their solid phase.

WIT Transactions on Engineering Sciences, Vol 50, © 2005 WIT Press
www.witpress.com, ISSN 1743-3533 (on-line)

During the sedimentation process of a suspension, a sharp interface develops separating the upper zone of free sedimentation from the lower zone of compression. The position of this interface results from the balance of mass exchange between both the zones. It is also affected by the behaviour of the suspension under compression. The sedimentation zone is characterized by zero value of the effective stress of the solid phase. On the other hand the effective stress of the solid phase is negative in the zone of compression. In the case of compressible suspensions, the negative solid-phase stress may increase the liquid-phase pressure which pushes the liquid phase out of the zone of compression and continues the required solid-phase thickening.

There are several possible approaches to describe the mechanism of such processes in suspensions. Mls et al. [4] suggested to solve the problem by means of the theory of water seepage through porous media, particularly applying the Darcy law. Toorman [5] presented a discussion of two different approaches and suggested a possible unification.

2 The applied theory

Under certain assumptions imposed on the flow velocities and the hydraulic conductivity, Mls [3] formulated the following system of partial differential equations governing the Darcian mechanics of two-phase media.

$$\frac{\partial}{\partial t}\big(\rho_w(\mathbf{x},t)\, n(\mathbf{x},t)\big) + \frac{\partial}{\partial x_j}\big(\rho_w(\mathbf{x},t)\, w_j(\mathbf{x},t)\big) = 0, \tag{1}$$

$$\frac{\partial}{\partial t}\big(\rho_s(\mathbf{x},t)\, (1-n(\mathbf{x},t))\big) + \frac{\partial}{\partial x_j}\big(\rho_s(\mathbf{x},t)\, v_j(\mathbf{x},t)\big) = 0, \tag{2}$$

$$\begin{aligned}\frac{\partial}{\partial t}\big(\rho_w(\mathbf{x},t)\, w_i(\mathbf{x},t)\big) + g\,\frac{\partial x_3}{\partial x_i}\,\rho_w(\mathbf{x},t)\, n(\mathbf{x},t) \\ + n(\mathbf{x},t)\,\frac{\partial p}{\partial x_i}(\mathbf{x},t) + g\,\rho_w(\mathbf{x},t)\, n(\mathbf{x},t)\, K_{ij}^{-1}(\mathbf{x},t)\, u_j(\mathbf{x},t) = 0\,,\end{aligned} \tag{3}$$

$$\begin{aligned}\frac{\partial}{\partial t}\big(\rho_s(\mathbf{x},t)\, v_i(\mathbf{x},t)\big) + g\,\rho_s(\mathbf{x},t)\big(1-n(\mathbf{x},t)\big)\,\frac{\partial x_3}{\partial x_i} - \frac{\partial \tau_{ij}}{\partial x_j}(\mathbf{x},t) \\ + \big(1-n(\mathbf{x},t)\big)\,\frac{\partial p}{\partial x_i}(\mathbf{x},t) - g\,\rho_w(\mathbf{x},t)\, n(\mathbf{x},t)\, K_{ij}^{-1}(\mathbf{x},t)\, u_j(\mathbf{x},t) = 0,\end{aligned} \tag{4}$$

$i = 1, 2, 3$ and the summation rule has been used. In these Equations, t is time, $\mathbf{x} = (x_1, x_2, x_3)$ are space coordinates with x_3 axis oriented vertically upwards, ρ_w and ρ_s are densities of the liquid phase and the solid phase respectively, n is porosity of the medium, $\mathbf{w}$ and $\mathbf{v}$ are the volumetric flux-density vectors of the liquid phase and the solid phase respectively, g is the gravitational acceleration, p is the liquid-phase pressure, K is the hydraulic-conductivity tensor, $\mathbf{u}$ is the relative flux-density vector of the liquid phase satisfying

$$\mathbf{u} = \mathbf{w} - \frac{n}{1-n}\,\mathbf{v}, \tag{5}$$

and τ is the effective solid-phase stress. To simplify expressions concerning the solid phase, it is convenient to introduce the volume fraction of the solid phase. It will be denoted s. According to its definition, it holds

$$s(\mathbf{x}, t) = 1 - n(\mathbf{x}, t). \tag{6}$$

In the theory, both the phases are supposed to be independently movable. The first two Equations are expressions of the continuity axiom, and the Equations (3) and (4) are equations of motion of the liquid phase and the solid phase respectively.

3 The constitutive equations

Consider following process. A suspension of given volume fraction of the solid phase is continuously charged to the upper part of a vertical cylinder. Due to its higher density, the solid phase moves downwards at a higher rate than the liquid phase. Consequently, the relative flux density of the liquid phase is positive (i.e. oriented upwards) everywhere in the suspension column which makes the volume fraction of the solid phase to increase downwards. The discharge of the suspension at the bottom of the cylinder reflects exactly the total charge of the solid phase and the bottom value of the solid-phase volume fraction. More exactly, denote s_i and Q_i the initial value of the solid-phase volume fraction and the total charge of the suspension at the input, and s_b the value of the solid-phase volume fraction at the bottom of the cylinder. Then it holds for the total discharge Q_b of the suspension at the bottom

$$Q_b = \frac{s_i}{s_b} Q_i \,.$$

The mass balance of the liquid phase gives

$$(1 - s_i)\, Q_i = (1 - s_b)\, Q_b + Q_t \,,$$

where Q_t is the discharge of the liquid phase over the top of the cylinder.

Making use of Equations (1) to (4), the described process can be studied in detail. Generally this system consists of eight equations containing 14 unknown functions: τ, $\mathbf{w}$, $\mathbf{v}$, p and s, hydraulic conductivity K is supposed to be a known constitutive function. Densities ρ_w and ρ_s of the liquid phase and the solid phase are known constants. As the considered problem is one-dimensional, the system of governing equations reduces to four equations with five unknown functions: τ, w, v, p and s. Consequently, it is sufficient to add two constitutive equations in order to complete the solved system to a closed one. These two equations will characterize the particular suspension under consideration, e.g. Handová and Sladká [1].

The first constitutive equation is the hydraulic conductivity which will be defined as a function of the solid-phase volume fraction s. The described process

evidently satisfies the condition

$$\frac{\partial s}{\partial t}(m,t) \geq 0$$

for every value of a material coordinate m and for every time t. Hence, it is a monotonous process defined by Mls [2] as a process satisfying for every two values m_1 and m_2 and every two times t_1 and t_2 the inequality

$$\frac{\partial s}{\partial t}(m_1,t_1)\,\frac{\partial s}{\partial t}(m_2,t_2) \geq 0\,.$$

The monotonous process enables us to exclude the effect of hysteresis and allows for the assumption, that the effective solid-phase stress is a function of the solid-phase volume fraction.

If we further suppose that the investigated suspension is a mixture of kaolin and water, the results obtained by Mls [2] can be used to define the required constitutive equations in the following form

$$K(s) = A_1\, s^{A_2}, \tag{7}$$

and

$$\begin{aligned} &\tau(s) = 0 && \text{for } s \leq B_2, \\ &\tau(s) = g\,(\rho_s - \rho_w)\left(B_1\,\ln\left(\frac{s+B_1}{B_2+B_1}\right) - s + B_2\right) && \text{for } s > B_2\,, \end{aligned} \tag{8}$$

where $A_1 = 1.048 \times 10^{-7}$, $A_2 = -2.468$, $B_1 = 3.055 \times 10^{-2}$ and $B_2 = 3.834 \times 10^{-2}$. In this case, the units are $[k]$ = m/s and $[\tau]$ = Pa.

4 The solved problem

Consider the above described process of continuous suspension thickening in a vertical cylinder allowing for the control of the suspension discharge. A visible interface develops in the suspension column separating the lower part of the column, the zone of compression, from the overlying zone of free sedimentation. At the top of the column, there is a layer of outflowing water, more precisely a layer of suspension with negligible solid-phase concentration. Suppose that the values of s_i, Q_i and s_b are given. Denote S the cross section of the column. This set of data together with the above constitutive equations determine the uniquely the thickening process.

The problem being one-dimensional, we denote x the coordinate oriented vertically upwards. The continuous process with the prescribed constant data determines steady state values of all the involved functions; we solve a steady-state problem. It is also evident that it is sufficient to restrict our consideration to the zone of compression. Under the above conditions, the height of this zone is an unknown value. On the other hand, the value of the solid-phase volume fraction

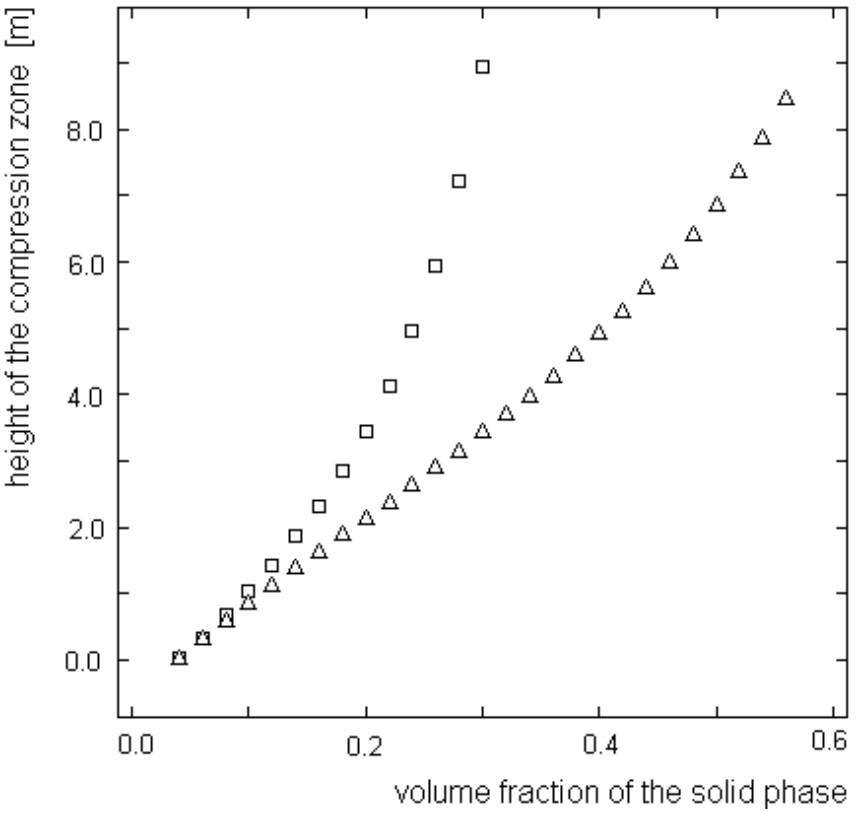

Figure 1: The dependence of the height of compression zone on the volume fraction of the solid phase.

at the unknown upper boundary is determined by the constitutive equations; this defines a free-boundary problem.

In the case of one-dimensional steady-state flow, functions w and v can be found solving the first two equations of the system (1) to (4) and the given conditions. Their expression is

$$v = \frac{Q_i}{S}\, s_i \tag{9}$$

and

$$w = \frac{Q_i}{S}\, \frac{s_i}{s_b}\, (1 - s_b)\,. \tag{10}$$

The one-dimensional steady-state form of Equations (3) and (4) reads

$$g\, \rho_w\, n(x) + n(x)\, \frac{\mathrm{d}p}{\mathrm{d}x}(x) + g\, \rho_w\, \frac{n(x)}{K(s(x))}\, u(x) = 0. \tag{11}$$

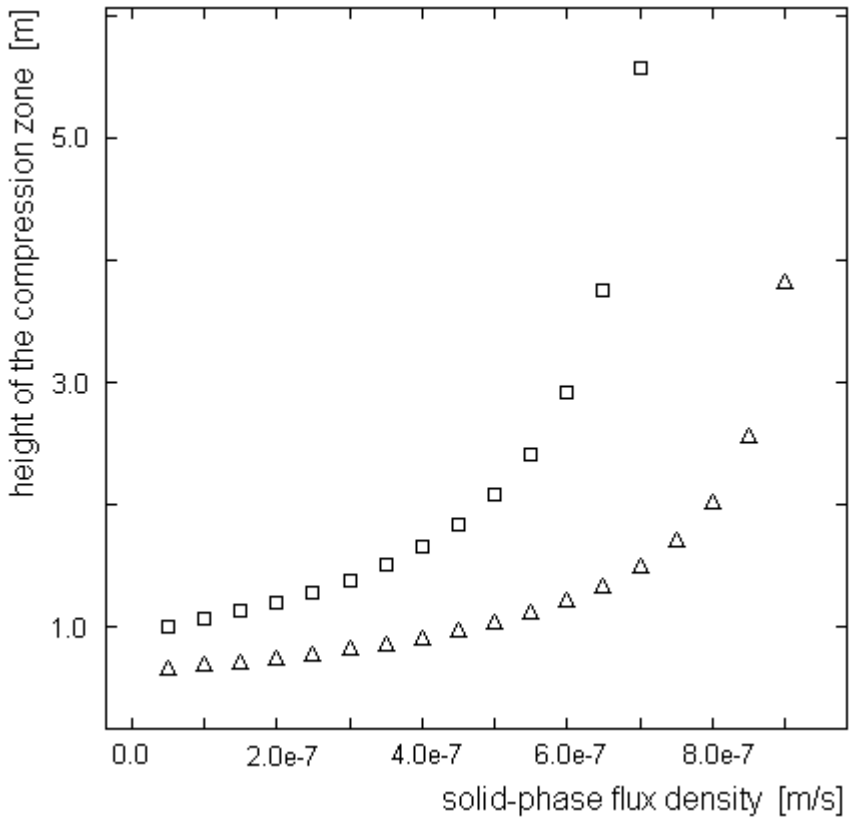

Figure 2: The dependence of the height of compression zone on the solid-phase flux density.

and

$$g\,\rho_s\,(1-n(x))-\frac{\mathrm{d}\tau}{\mathrm{d}x}(s(x))+(1-n(x))\,\frac{\mathrm{d}p}{\mathrm{d}x}(x)--g\,\rho_w\,\frac{n(x)}{K(s(x))}\,u(x)=0. \quad (12)$$

Two unknown functions, the solid-phase volume fraction and the liquid-phase pressure, remain in the system. Making use of Equation (6) and constitutive equations (7) and (8), Equations (11) and (12) build a system of two nonlinear ordinary differential equations with the above unknown functions s and p.

5 Numerical solution

Several problems for the system (11) and (12) have been formulated and numerically solved. The required degree of dewatering, expressed by s_b, is the initial value of function s. The value of liquid-phase pressure p is known at the top

of the compression zone. In order to find the unknown height of the compression zone, the given value B_2 of the solid-phase volume fraction can be utilized. Consequently, the problem can be solved using the shooting method and iterating for the height x_H of the compression zone satisfying

$$s(x_H) = B_2$$

and for the prescribed value of the liquid-phase pressure at x_H.

The computed dependence of the height of compression zone x_H on the prescribed solid-phase flux density is shown in Figure 1. Triangles denote the values for $s_b = 0.1$ and squares denote the values for $s_b = 0.15$.

The height of the compression zone necessary to reach a prescribed degree of dewatering is firmly dependent on the given flux density of the solid phase. Figure 2 shows the dependence of the height of compression zone x_H on the solid-phase volume fraction s_b for two different values of solid-phase flux density. Triangles belong to $v = 3.5 \times 10^{-7}$ m s^{-1}and squares belong to $v = 5.0 \times 10^{-7}$ m s^{-1}.

Acknowledgements

This paper is based upon work supported by the Grant Agency of the Czech Republic, under grant No. 205/01/0992. The author also wishes to express his thanks to Prof. Z. Koníček and Dr. Z. Handová from the Czech University of Technology for a valuable discussion and for the possibility to use their experimental data.

References

[1] Handová Z. & Sladká, A., Evaluation of Sedimentation Characteristics of Activated Sludges, *Proceedings of Sludge and Waste '88*, ČSVTS; Brno, 1988.

[2] Mls, J., Determination of hydromechanical characteristics of a suspension, *Computational Modelling of Free and Moving Boundary Problems III*, eds. L.C. Wrobel, B. Šarler and C.A. Brebbia, Computational Mechanics Publications; Southampton, Boston, pp. 237–244, 1995.

[3] Mls, J., A Continuum Approach to Two-Phase Porous Media *Transport in Porous Media,* **35**, pp. 15–36, 1999.

[4] Mls J., Koníček, Z. & Handová, Z., Mathematical Formulation of Two-Phase System Mechanics, *Proc. of the Workshop 92, Fluid Mechanics*, ČVUT; Praha, 1992.

[5] Toorman, E. A., Sedimentation and Self-Weight Consolidation: General Unifying Theory, *Géotechnique*, **46** , pp. 103–113, 1996

[6] Tuček, F & Koníček, Z., Estimation of the Area of Secondary Settler and Degree of Thickening in Biological Stage of Waste Water Plant, *Vodní Hospodářství,* **8**, 1989

This page intentionally left blank

Numerical modelling of the Riemann problem for a mathematical two-phase flow model

D. Zeidan
Department of Mathematics, Al-Zaytoonah University of Jordan, Jordan

Abstract

We report preliminary results obtained using Godunov methods of a centred type for hyperbolic systems of conservation laws for which the analytical solution of the Riemann problem is too difficult to develop. For this purpose, we consider a mathematical model used for modelling an unsteady compressible non-equilibrium mixture two-phase flow which results in a well-posed initial value problem in a conservative form. The mathematical two-phase flow model consists of six first-order partial differential equations that represent one-dimensional mass, momentum and energy balances for a mixture of gas-liquid and gas volume concentration, gas mass concentration and the relative velocity balances. This system of six partial differential equations has the mathematical property that its six characteristic roots are all real with a complete set of independent eigenvectors which form the basic structure of the solution of the Riemann problem. The construction of the solution of the Riemann problem for the model poses several difficulties. Since the model possesses a large number of non-linear waves, it is not easy to consider each wave separately to derive a single non-linear algebraic equation for the unknown region, the star region, between the left and right waves. We propose numerical techniques of a centred type specifically developed for high speed single-phase gas flows. A main feature of centred methods is that they do not explicitly require the solution of the Riemann problem. This is a desirable property which guarantees that the methods can handle the solution of the Riemann problem numerically and resolve both rarefaction and shock waves for the model in a simple way with good accuracy. Finally, we present some numerical simulations for the gas-liquid two-phase flow Riemann problem to illustrate the efficiency of the proposed schemes.
Keywords: gas-liquid two-phase flow, thermodynamically compatible system, mathematical model, well-posed initial value problem, Riemann problem, Godunov methods, TVD SLIC scheme.

WIT Transactions on Engineering Sciences, Vol 50, © 2005 WIT Press
www.witpress.com, ISSN 1743-3533 (on-line)

1 Introduction

Mathematical and numerical development of two-phase fluid flow models are of considerable practical importance for scientific and industrial problems. Yet, little work has been dedicated to the specific study of the Riemann problem when modelling two-phase flow. The Riemann problem is very useful for a better understanding of the physical and mathematical meanings of the two-phase flow models. In this paper we are concerned with numerical solutions for a class of systems of conservation laws for which the analytical solution of the Riemann problem is too difficult to develop. Systems of this class are thermodynamically compatible, i.e., are generated by one thermodynamic potential alone and have an additional conservation law as a consequence [1, 2, 3]. Furthermore, these systems can be reduced to symmetric hyperbolic systems of balance equations in conservative form [4]. This results in fully hyperbolic conservative systems of governing equations which provide a well-posed initial value problem as in the case of time-dependent two-phase flow equations. The system of equations is a mathematical model which describes gas-liquid two-phase flow as a whole. This model is derived using an approach initiated by Romensky [4] and developed in detail [7] for two-phase media with different velocities of motion of phases and interphase friction. Desirable features of the hyperbolic conservative model include the existence of real eigenvalues and a complete set of linearly independent eigenvectors in a process without dissipation. This allows the application of numerical methods originally developed for high speed single-phase gas flows such as Godunov-type methods which make use of the wave propagation information to construct numerical schemes. To achieve this, one either solves the Riemann problems exactly or provides a minimum amount of information on wave propagation directions. Due to these features, one can formulate a single wave solution such as shocks, contacts and rarefactions to solve the Riemann problem exactly for the hyperbolic conservative model. Thus, depending on the type of non-linear wave, there can be up to sixteen wave patterns involved in the construction of the solution of the Riemann problem.

In general the hyperbolic conservative two-fluid model has a complex mathematical structure due to the fact that it contains a large number of waves in addition to the closure relations. The complexity of the structure of the model makes it very difficult to develop an analytical solution for the Riemann problem or to use Godunov numerical methods of upwind-type. This leads us to consider numerical approximation to the model by using methods that do not require the knowledge of any analytical results of the Riemann problem. We propose to use Godunov methods of centred-type such as the First-Order Centred (FORCE) scheme and the second-order Slope Limiter Centred (SLIC) scheme [6]. Centred methods do not explicitly require the condition of wave propagation information to construct the schemes which make them easy to understand and implement. A comprehensive presentation of Riemann solvers and upwind and centred methods is given in [5]. The numerical methods will give insight into the Riemann problem for the hyperbolic conservative model and will resolve both rarefactions and shocks as we shall see through the numerical results presented in this paper.

Explicit details about the mathematical and numerical analysis of the mathematical two-phase flow model described in this paper can be found in the PhD thesis of the author [7].

2 Mathematical two-phase flow model-hyperbolic conservative model

The mathematical hyperbolic conservative two-fluid model considered in this paper is given by the following set of equations in one-space dimension [7]

$$\frac{\partial \mathbb{U}}{\partial t} + \frac{\partial \mathbb{F}}{\partial x} = \mathbb{S}. \tag{1}$$

Here $x \in \mathbb{R}$, $t > 0$ and $\mathbb{U}$, $\mathbb{F}$ and $\mathbb{S}$ are a vector-valued function, the flux vector and the source term vector, respectively. The components of $\mathbb{U}$ are the conserved quantities

$$\mathbb{U} = \left[\rho, \rho\alpha, \rho u, \rho c, u_r, \rho\Big(\mathcal{E} + \frac{u^2}{2}\Big)\right]^T. \tag{2}$$

These represent the mass for the mixture, the volume concentration for the gas phase, the momentum for the mixture, the conservation law for the mass concentration of the gas phase with no phase transition, the balance law for the relative velocity and the energy conservation law for the mixture. The flux vector $\mathbb{F}$ is a function of $\mathbb{U}$

$$\mathbb{F}(\mathbb{U}) = \begin{pmatrix} \rho u, & \rho u\alpha, & \rho u^2 + \mathcal{P} + \rho u_r \mathcal{E}_{u_r}, & \rho uc + \rho \mathcal{E}_{u_r}, & uu_r + \mathcal{E}_c, \\ & & \rho u\Big(\mathcal{E} + \frac{u^2}{2}\Big) + \mathcal{P}u + \rho \mathcal{E}_{u_r}\Big(uu_r + \mathcal{E}_c\Big) & & \end{pmatrix}. \tag{3}$$

In the above expressions, the variables denote the usual quantities: ρ is the mixture density, α and c are the volume fraction and the mass concentration of the gas phase, u, $\mathcal{P}$, u_r and $\mathcal{E}$ are the mixture velocity, pressure, relative velocity between the two phases and the mixture internal energy, respectively. The source term vector is a function of $\mathbb{U}$

$$\mathbb{S}(\mathbb{U}) = \left[0, -\frac{\rho}{\tau}, 0, 0, -\kappa c(1-c)u_r, 0\right]^T. \tag{4}$$

Additionally, several physical closure laws must be given which involve the source terms, the pressure, the equations of state for the mixture and for the phases and the mixture relations. We do not state these closure laws here (see instead [7] for details).

The mathematical structure of the model is more clearly revealed and the nature of the characteristic analysis is simplified in terms of primitive variables [7]. One

possible primitive formulation would be

$$\mathbb{W} = \Big[\rho, \alpha, u, c, u_r, \mathcal{S}\Big]^T. \tag{5}$$

Thus, in quasi-linear form we have

$$\frac{\partial \mathbb{W}}{\partial t} + \mathbb{A}(\mathbb{W})\frac{\partial \mathbb{W}}{\partial x} = \mathbb{Q}(\mathbb{W}). \tag{6}$$

For a more comprehensive discussion of the mathematical properties of the hyperbolic conservative two-fluid model we refer to [7]. The model was shown to be hyperbolic (using perturbation methods) in processes without dissipation with six real eigenvalues. Four of these eigenvalues correspond to the left and right sound waves while two of these eigenvalues are equal to the mixture velocity corresponding to the convective waves. In addition the characteristic fields corresponding to the acoustic waves were shown to be genuinely non-linear while the last two are linearly degenerate.

3 Numerical modelling of the Riemann problem

The Riemann problem for the hyperbolic conservative two-fluid model is the initial value problem for the conservation laws in processes without dissipation

$$\left.\begin{array}{l} \partial_t \mathbb{U} + \partial_x \mathbb{F}(\mathbb{U}) = 0, \\ \mathbb{U}(x,0) = \left\{ \begin{array}{ll} \mathbb{U}_{\mathcal{L}} & \text{if } x < 0, \\ \mathbb{U}_{\mathcal{R}} & \text{if } x > 0, \end{array} \right. \end{array}\right\} \tag{7}$$

where $\mathbb{U}$ and $\mathbb{F}(\mathbb{U})$ are vectors of conserved variables and fluxes given by (2) and (3), respectively. As anticipated in the previous section there are six real eigenvalues. Two of these eigenvalues are equal to the mixture velocity. Thus there are six waves separating six constant states. In terms of a choice of primitive variables given by (5), these six constant states are: $\mathbb{W}_{\mathcal{L}}$ (left data), $\mathbb{W}^{\star}_{\mathcal{L}1}$, $\mathbb{W}^{\star}_{\mathcal{L}2}$, $\mathbb{W}^{\star}_{\mathcal{R}2}$, $\mathbb{W}^{\star}_{\mathcal{R}1}$, $\mathbb{W}_{\mathcal{R}}$ (right data). The states $\mathbb{W}^{\star}_{\mathfrak{s}1,2}$ ($\mathfrak{s} = \mathcal{L}, \mathcal{R}$) are the unknowns of the problem and they cover the star region and emerge from the interaction of the data states $\mathbb{W}_{\mathcal{L}}$ and $\mathbb{W}_{\mathcal{R}}$. The star region is divided into four subregions. The multiple middle wave is the contact discontinuity while the two-left and two-right non-linear waves are either shock or rarefaction waves, see [7] for details. Therefore, depending on the type of the non-linear waves there could be sixteen waves patterns to construct for the solution of the Riemann problem in the star region. The main step in solving the Riemann problem is the determination of the solution in the star region. This depends on suitable relations through the left and right waves connecting $\mathbb{W}^{\star}_{\mathcal{L}1}$, $\mathbb{W}^{\star}_{\mathcal{L}2}$ to $\mathbb{W}_{\mathcal{L}}$ and $\mathbb{W}^{\star}_{\mathcal{R}2}$, $\mathbb{W}^{\star}_{\mathcal{R}1}$ to $\mathbb{W}_{\mathcal{R}}$, respectively. In practice the determination of the solution in the star region is too difficult to develop because it typically requires iterations for the non-linear equations.

Since the model possesses a large number of non-linear waves it is not easy to analyse the star region mathematically. In addition, the number of non-linear equations will depend on the number of the non-linear waves considered. These facts motivate us to consider numerical approximations by using modern Riemann-problem shock-capturing methods of centred-type. Determining the analytical explicit solution of the Riemann problem is very useful for a better understanding of the physical and mathematical meaning of the model and to develop an efficient numerical method.

As mentioned before, we considered two methods, namely, a FORCE scheme and a SLIC scheme. Both methods advance the solution via the conservative formula

$$\mathbb{U}_i^{n+1} = \mathbb{U}_i^n - \frac{\Delta t}{\Delta x}\Big[\mathbb{F}_{i+\frac{1}{2}} - \mathbb{F}_{i-\frac{1}{2}}\Big], \tag{8}$$

where $\mathbb{F}_{i+\frac{1}{2}}$ is the inter-cell numerical flux corresponding to the inter-cell boundary at $x = x_{i+\frac{1}{2}}$ between i and $i+1$. The flux of the FORCE scheme is written as

$$\mathbb{F}^{\text{FORCE}}_{i+\frac{1}{2}} = \frac{1}{2}\Big[\mathbb{F}^{\text{LF}}_{i+\frac{1}{2}} + \mathbb{F}^{\text{RI}}_{i+\frac{1}{2}}\Big], \tag{9}$$

where $\mathbb{F}^{\text{LF}}_{i+\frac{1}{2}}$ is the Lax–Friedrichs flux and $\mathbb{F}^{\text{RI}}_{i+\frac{1}{2}}$ is the Richtmyer flux. The FORCE scheme is a first-order centred method and has half the numerical viscosity of the Lax–Friedrichs method. The SLIC scheme is a second-order TVD scheme that is an extension of FORCE scheme. The scheme is of the slope limiter type and results from replacing the Godunov flux by the FORCE flux in the MUSCL–Hancock Method [5]. The TVD version results from limiting the slopes in data construction. We refer to [7] for further detail on the centred methods for two-phase fluid flow problems.

4 Numerical simulations

Numerical results for the gas-liquid mixture two-phase flow Riemann problem (7) are now presented. They were obtained using centred methods with no source terms in (7) (i.e. no influence for dissipation). Physically this means that we look at the experiment at a time when the relaxation of volume concentration and interfacial friction are negligible.

The results illustrate typical wave patterns: two-left rarefactions and two-right shocks separated by contact discontinuities with high pressure in the left side and with low pressure on the right side resulting from the solution of the Riemann problem for the hyperbolic conservative two-fluid model. The left and right states of the Riemann problem are: $\mathcal{P}_{\mathcal{L}} = 0.1$, $\mathcal{P}_{\mathcal{R}} = 0.0001$, $\alpha_{\mathcal{L}} = 0.4$, $\alpha_{\mathcal{R}} = 0.6$, $u_{\mathcal{L}} = 0.0 = u_{\mathcal{R}}$, $u_{r\mathcal{L}} = 0.0 = u_{r\mathcal{R}}$, $c_{\mathcal{L}} = 0.08175$, $c_{\mathcal{R}} = 0.00150$ and $\mathcal{S}_{\mathcal{L}} = 0.0 = \mathcal{S}_{\mathcal{R}}$.

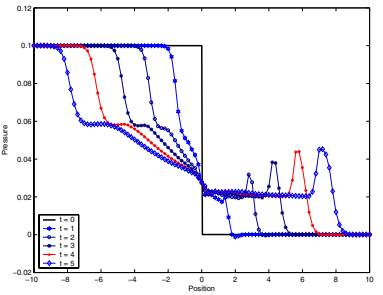

Figure 1: Time-evolution of the pressure using the TVD SLIC scheme on a mesh of 100 cells.

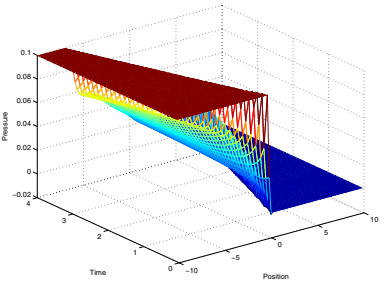

Figure 2: Pressure distribution in the three-dimensional results from the numerical modelling of the gas-liquid mixture two-phase flow Riemann problem at time $t = 4.0\ s$ on a mesh of 1000 cells.

A precise description of the other parameters involved is given in [7]. The numerical solutions are computed with 100 and 1000 computational cells representing a coarse and fine mesh, respectively, on the spatial domain $-10 \leq x \leq 10$ with Courant number coefficient $C_{\text{CFL}} = 0.9$ and with transmissive boundary conditions together with the SUPERBEE limiter. As mentioned before, it is difficult to construct an exact solution for the Riemann problem in general. However, for given states on the left and right the solution is composed of six waves which are either two-rarefactions, two-shocks or multiple contact discontinuities. Since we do not have an analytical solution, numerical evidence [7] shows that there are two-left rarefactions and two-right shock waves separated by contact discontinuities for the considered gas-liquid mixture two-phase flow Riemann problem as displayed in figure 1.

Figure 1 shows the time-evolution of the pressure wave propagation profile for different time values $(t = 0, 1, 2, 3, 4, 5)$ using the TVD SLIC scheme. However, for all different times the waves move away from the origin and they need a closer look to be identified. From the results plotted in figure 1, one can exhibit the two-left rarefaction-like waves propagating to the far left in the high pressure region, a

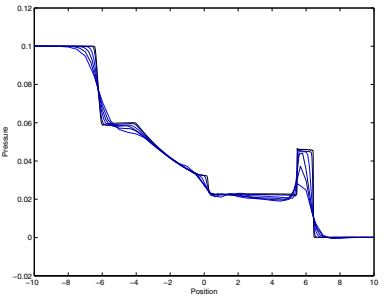

Figure 3: Grid-convergence study of the pressure profile, at time $t = 4.0\ s$, computed with the SLIC scheme with SUPERBEE limiter.

shock-like wave propagating to the far right in the low pressure region and contact-like wave in the middle of the structure which remains approximately constant. In order to demonstrate the behaviour of these waves, the results for the pressure in three-dimension are presented in figure 2 on a mesh of 1000 cells at $t = 4.0\ s$. In figure 3 we study the convergence of the SLIC scheme as the mesh is refined for the pressure profile at time $t = 4.0\ s$. The results demonstrate that the SLIC scheme approach the reference solution without introducing any spurious oscillations. Thus, numerical evaluation suggest that the TVD SLIC scheme with fine mesh (i.e. using 1000 computational cells) is the reference solution for the gas-liquid mixture two-phase flow Riemann problem.

Figure 4 displays the pressure profile at $t = 4.0\ s$ for the gas-liquid mixture two-phase flow with a mesh of 100 computational cells. The different methods are plotted for the sake of comparison, as shown in figure 4. We emphasise that these oscillations are not of a numerical nature but rather due to some existing non-linearity effects within our two-fluid model system in the absence of any source terms (which may here introduce some dissipative or regularising effect) [7].

From the plot of the pressure shown in figure 4, we see that Lax–Friedrichs, FORCE and SLIC schemes seem to produce the same wave structure in the pressure variable as the reference solution. This structure arises due to the existence of two-left rarefactions and shock-like wave separated by a contact discontinuity as mentioned earlier.

Concerning the shock-like wave in figures 1, 2, 3 and 4, we observe that the structure of the pressure shock waves propagation depends on the value of the initial pressure on the right side. To find an explanation of this phenomenon, we have plotted the pressure contours for the Riemann problem at $t = 4.0\ s$ as shown in figure 5.

In particular, figures 4 and 5 reflect the following dynamics: as the mixture velocity is the same in both sides at $t = 4.0\ s$, the decreasing pressure in the right side leads to a shock-like wave propagating to the far right in the low pressure region. Clearly the SLIC scheme is able to handle the gas-liquid mixture

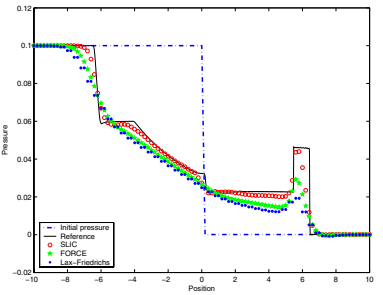

Figure 4: Comparison between the TVD SLIC, FORCE, Lax–Friedrichs scheme on a mesh of 100 cells with the reference solution computed by the TVD SLIC scheme using a mesh of 1000 cells.

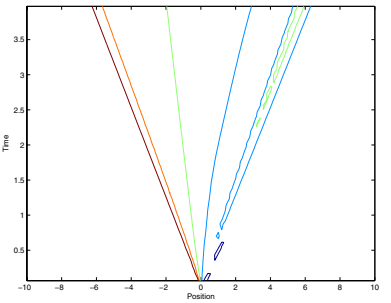

Figure 5: Effect of the initial pressure on the shock-like wave at time $t = 4.0\ s$.

two-phase flow Riemann problem without generating any oscillation and the accuracy of the coarse mesh solution is totally satisfactory. From figure 4 we observe that the results for the Lax–Friedrichs scheme look substandard to those of the FORCE scheme. The numerical results of the SLIC scheme are better to those of the FORCE scheme. In particular, we see that the coarse mesh solution is able to approximate the fine mesh solution very well.

5 Conclusions

Godunov methods of centred-type have been proposed for a mathematical model which describes unsteady compressible non-equilibrium mixture two-phase flow. The model is given by a non-linear hyperbolic system of conservation law for which its mathematical structure prevent us from developing an analytical solution for the Riemann problem or from using Godunov methods of upwind-type. The associated Riemann problem is solved numerically and its solution is obtained by centred methods. The concept of centred methods totally avoids the explicit solution of the Riemann problem and are not biased by the wave propagation direc-

tions. Taking advantage of these properties, the methods are applied to the simulation of the gas-liquid mixture two-phase flow Riemann problem with particular focus on the discontinuities expected to appear for the numerical modelling of the Riemann problem. Numerical results show that the approximate solutions are in good agreement with the reference solution. In particular, the SLIC scheme gives a very accurate solution of the wave propagation as demonstrated through the considered two-phase flow problem. Moreover, the scheme is robust with an ability to capture solutions accurately. Finally, Godunov methods of centred-type seem to be very useful for developing new mathematical models together with closure laws and to study Riemann problem two-phase flows.

References

[1] Godunov, S. & Romensky, E., Thermodynamics, conservation laws and symmetric forms of differential equations in mechanics of continuous media. In *Computational Fluid Dynamics Review*, John Wiley & Sons: New York, pp. 19–31 1995.

[2] Müller, I. & Ruggeri, T., *Rational Extended Thermodynamics*, Springer–Verlag: New York, 1998.

[3] Romensky E., Hyperbolic systems of thermodynamically compatible conservation laws in continuum mechanics. *Mathl. Comput. Modelling*, **28**, 115–130, 1998.

[4] Romensky E., Thermodynamics and hyperbolic systems of balance laws in continuum mechanics. In *Godunov Methods: theory and applications*, ed. E.F. Toro, Kluwer Academic/Plenum Publishers pp. 745–761, 2001.

[5] Toro E. F., *Riemann Solvers and Numerical Methods for Fluid Dynamics.* A Practical Introduction. Springer–Verlag, Berlin, 1999.

[6] Toro E. F. & Billett S., Centred TVD schemes for hyperbolic conservation laws. *IMA. J. Numerical Analysis*, **20**, 47–79, 2000.

[7] Zeidan D., *Mathematical and Numerical Study of Two–Phase Flow Models*, PhD Thesis, Manchester Metropolitan University, UK, 2003.

This page intentionally left blank

Droplet collisions using a Level Set method: comparisons between simulation and experiments

S. Tanguy, T. Ménard & A. Berlemont
CNRS-UMR6614-CORIA, Rouen University, France

Abstract

Level Set methods are based on defining a continuous function where the zero level curve is the interface. That function is initialized as the signed distance to the interface in the computation field. Solving a convection equation allows one to follow the interface displacements in a given velocity field. One advantage is its ability to represent topological changes and geometrical information on the interface, such as the normal vector or curvature, which are obtained through a level set function gradient. To avoid the spreading and stretching of a level set, a re-distancing algorithm is applied to ensure that the function remains the signed distance to the interface.

The Level Set method is coupled with the projection method for the direct numerical simulation of the incompressible Navier-Stokes equations. Spatial derivatives are estimated with the 2nd order central scheme, but convective terms are approximated by the 5th order WENO scheme discretization in order to get a robust behavior of the solution. Temporal derivatives are approximated with the Adams Bashforth scheme. The linear system deduced from the Poisson equation is solved with a multigrid algorithm for preconditioning the conjugate gradient method. To handle interface discontinuities the ghost fluid method is used. Numerical codes have been developed for 2D, 2Daxi and 3D geometries, with MPI parallelization. The results are presented for head-on droplets collisions in a coalescence regime and a reflexive regime with 2D axi-symmetric code, and for off-center droplets collision code in a separation regime for a large impact parameter with 3D code. Simulations provide realistic and various droplet collision behaviors and they correspond to experimental observations.
Keywords: Level Set, ghost fluid, interface tracking, droplet collision simulation.

WIT Transactions on Engineering Sciences, Vol 50, © 2005 WIT Press
www.witpress.com, ISSN 1743-3533 (on-line)

1 Introduction

Numerical simulations for interface tracking can be carried out using either "front tracking" methods or "front capturing" methods. Front tracking methods (Nobari et al. [1]) are based on the Lagrangian tracking of marker particles that are attached to the interface motion. They appear suitable when irregularities on the interface curvature are not too large, but they are not well adapted to describing topological changes of the interface. Moreover on 3D geometries they rapidly require too large computer resources and they do not appear of interest for industrial purpose. We have thus developed a front capturing method.

Two main approaches can be used in front capturing methods, namely the Volume of Fluid method (VOF) and the Level Set method. The VOF method describes the volumetric fraction of each phase in grid cells. The main difficulty of the method is that 2D interface reconstruction appears quite difficult, and 3D reconstruction is numerically prohibitive on 3D domain. A consequence can be some uncertainties on the interface curvature and thus on the surface tension forces. Nevertheless, let us mention that realistic and predictive simulations can be carried out (Rieber and Frohn [2], Gueyffier et al. [3]). Interface reconstruction can be avoided by assuming a continuous volumetric fraction throughout the whole computational domain, which means that an interface thickness is introduced (Benkenida and Magnaudet [4]). The method is then quite similar to the Level Set method in its continuous force formulation. Osher and Sethian [5] proposed a Level Set method which describes the interface with the zero level curve of a continuous function defined by the signed distance to the interface. To describe the interface discontinuities, two approaches can be used, namely the Continuous Surface Force ("delta" formulation), which assumes that the interface thickness is 2 or 3 grid meshes wide, and the ghost fluid method (GFM), which has been derived by Fedkiw et al. [6] to capture jump condition on the interface.

We first present the Level set method and its coupling with incompressible Navier Stokes equations. The Ghost Fluid Method is described and results are then presented and compared with experiments for different droplet collision configurations, leading to different collision regimes, namely coalescence, separation after minor deformation and separation with the formation of satellites in the break up process. Simulations are carried out with the 2D-axi code for head-on collisions and the 3D code for off-center collisions.

2 Numerical approach

2.1 Level set method

Level Set methods are based on the use of a continuous function ϕ to describe the interface between two mediums [7,8]. That function is defined as the algebraic distance between any point of the domain and the interface, and the interface is thus described by the 0 level of that function. Solving a convection equation determines the evolution of the interface in a given velocity field $\mathbf{V}$:

$$\frac{\partial \phi}{\partial t} + \mathbf{V}.\nabla\phi = 0 \tag{1}$$

Specific care is put on the discretization method, as discontinuities are often observed in the results. To avoid singularities in the distance function field, we thus use 5th order WENO scheme for convective terms.

One advantage of the level set method is its ability to represent topological changes both in 2D or 3D geometry quite naturally. Moreover, geometrical information on the interface, such as normal vector **n** or curvature κ, are easily obtained through:

$$\mathbf{n} = \frac{\nabla\phi}{|\nabla\phi|} \qquad \kappa(\phi) = \nabla \cdot \mathbf{n} \tag{2}$$

Some problems arise when the level set method is developed, namely high velocity gradient can produce wide spreading and stretching of level set, and ϕ will no longer remain a distance function. A redistancing algorithm [8] is then applied to keep ϕ as the signed distance to interface. The algorithm is based on the iterative resolution of the following equation:

$$\frac{\partial d}{\partial \tau} = \text{sign}(\phi)(1 - |\nabla\phi|) \text{ where } d(x,t,\tau)_{\tau=0} = \phi(x,t) \tag{3}$$

where τ is a fictitious time. We solve equation (3) until steady state is reached, thus close to the exact steady state solution namely either sign(ϕ)=0, meaning that we are on the droplet interface, or $|\nabla d| = 1$ which mathematically defines a distance function. We then replace ϕ (**x**,t) by d(**x**,t,τ_{steady}).

It is well known that numerical computation of eqns. (1) and (3) can generate mass loss in under-resolved regions. This is the main drawback of level set methods, but to improve mass conservation two main extensions of the method can be developed, namely the particle level set (Enright et al. [9]) and a coupling between VOF and Level Set (Sussman and Puckett [10]). These extensions have not been carried out here, but we have quantified mass loss in the simulations and ensured that it was negligible (<1%).

2.2 Projection method

The Level Set method is coupled with projection method for the direct numerical simulation of the incompressible Navier-Stokes equations expressed as follows:

$$\frac{\partial \mathbf{V}}{\partial t} + (\mathbf{V}\cdot\nabla)\mathbf{V} + \frac{\nabla p}{\rho} = \frac{\nabla(2\mu\mathbf{D})}{\rho} + \mathbf{g} \qquad \mathbf{D} = \tfrac{1}{2}(\nabla\mathbf{V} + \nabla\mathbf{V}^T) \tag{4}$$

$$\nabla \cdot \mathbf{V} = 0 \tag{5}$$

p is the pressure, ρ and μ are the fluid density and viscosity respectively. Spatial derivatives are estimated with 2nd order central scheme, but convective terms are approximated by 5th order WENO scheme discretization in order to get a robust behavior of the solution. Temporal derivatives are approximated Adams Bashforth formulation. Linear system deduced from Poisson equation is solved with a multigrid algorithm for preconditioning conjugate gradient method (Tanguy [11]).

2.3 Discontinuities: ghost fluid method

The interface is defined by two different phases and discontinuities must be taken into account for density, viscosity and pressure. For example, the pressure jump related to surface tension σ and to the interface curvature reads (Brackbill et al. [12])

$$[p] = \sigma\kappa(\phi) + 2[\mu]\ (\nabla u.\mathbf{n}, \nabla v.\mathbf{n}, \nabla w.\mathbf{n}).\mathbf{n} \tag{6}$$

where [.] represents a jump in the variable considered.

Specific treatment is thus needed to describe the jump conditions numerically. Two different approaches can be used to represent the above conditions, namely the continuum surface force (CSF formulation) or the Ghost Fluid Method (GFM). The CSF approach has been proved to be robust and leads to interesting results, but two main problems can be noticed. Smoothing the Heaviside function introduces an interface thickness which depends on the mesh size, and thus an uncertainty on the exact location of the interface. To overcome that smoothing, the **G**host **F**luid **M**ethod, has been developed by Fedkiw et al. [6]. The formalism respects jump discontinuities across the interface, and avoids an interface thickness. Discretization of discontinuous variables is more accurate, and spurious currents in the velocity field are thus much lower than with CSF methods. We have used this procedure to discretize all discontinuous variables, namely density, viscosity, pressure and viscous tensors ([11], Kang et al. [13]).

In the GFM, ghost cells are defined on each side of the interface and appropriated schemes are applied for jump conditions. As above defined the distance function defines the interface, and jump conditions are extrapolated on some nodes on each side of the interface. Following the jump conditions, the discontinued functions are extended continuously and then derivatives are estimated. Let us consider variable f which is discontinuous across the interface such as the jump of f is $[f]_\Gamma = a(x)$.

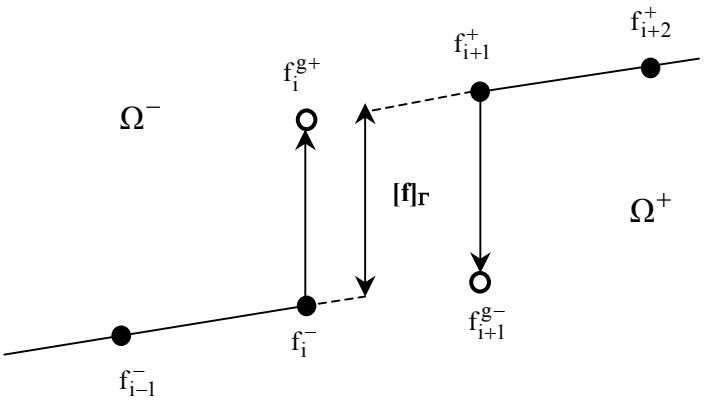

The f derivative is then expressed in cells i which are crossed by the interface by:

$$\left.\frac{\partial f}{\partial x}\right|_{i+\frac{1}{2}} = \frac{f_{i+1} - f_i}{dx} - \frac{a_\Gamma}{dx} \qquad a_\Gamma = \frac{a_i|\phi_{i+1}| + a_{i+1}|\phi_i|}{|\phi_i| + |\phi_{i+1}|} \tag{7}$$

where Ghost values f_{i+1}^{g-} and f_i^{g+} are defined by:

$$\begin{aligned} f_{i+1}^{g-} &= f_{i+1}^{+} - a_\Gamma \\ f_i^{g+} &= f_i^{-} + a_\Gamma \end{aligned} \tag{8}$$

The method is applied for any kind of discontinuities, with assumption that the interface can be localized inside a grid mesh and that the jump of the discontinuous variables is known. More details can be found in Liu et al. [14] on implementing the Ghost Fluid Method to solve the Poisson equation with discontinuous coefficients and obtain solution with jump condition. All the simulations presented here are thus carried out with the Ghost Fluid Method. Numerical codes have been developed for 2D, 2Daxi and 3D geometries, and MPI parallelization is used.

3 Results

Experimental droplet collision studies (Ashgriz and Poo [15], Qian and Law [16]) are providing us with different correlations to decide what happens when droplet collision occurs. The main parameters are the surface tension coefficient σ, liquid viscosity μ_l, liquid density ρ_l, droplet relative velocity U_c, the impact parameter I, and the ratio of droplet diameters Δ. The following non-dimensional numbers are thus defined by most authors to characterize droplet collisions, namely:

$$We = \frac{\rho_l U_c^2 D_s}{\sigma} \qquad Oh = \frac{\mu_l}{\sqrt{\rho_l \sigma D_s}} \qquad \Delta = \frac{D_s}{D_b} \qquad I = \frac{2b}{D_s + D_b} \tag{9}$$

where *We* is the Weber number and *Oh* the Ohnesorge number, and it is assumed that D_b is the bigger droplet diameter and D_s is smaller droplet diameter. The impact parameter I characterizes the eccentricity of the collision, and b is defined as the distance from the center of one droplet to the relative velocity vector placed on the center of the other droplet.

Several simulations have been carried out for head on droplet collision (2D-axi), off center droplet collisions (3D), for different Weber number and Ohnesorge number. Different collision regimes have thus been observed, namely coalescence, coalescence followed by separation with or without formation of satellites, and all the comparisons with experimental studies are in very good agreement and some of them are very impressive (Tanguy and Berlemont [17]).

Some results are now described in order to illustrate the ability of the method to comply with experimental observations. As previously mentioned, mass conservation might not be satisfied in Level set methods and we thus evaluated mass loss during all simulations to check that it was negligible (<1%). Moreover we carried out convergence tests to check that coalescence and break-up of interface was independent of the mesh size [17].

3.1 Coalescence followed by separation for head-on collisions

Collision has been observed by Ashgriz and Poo [15] for two identical water droplets, with a Weber number equal to 23, and impact parameter nearly equal to zero (0.05). Simulation results are presented for water droplets, with the same Weber number, and with an impact parameter equal to 0, a droplet radius of 400 μm, and a droplet relative velocity of 1.44 ms^{-1}. The grid size is 60x120 in the 2Daxi configuration.

Comparisons between our results and experimental visualization are shown on figures 1.a and 1.b.

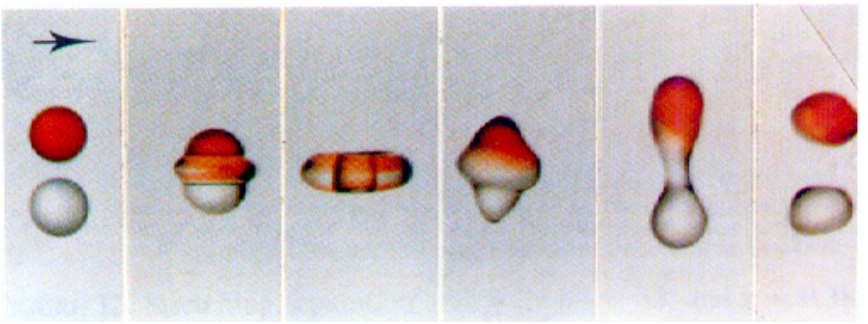

(a)

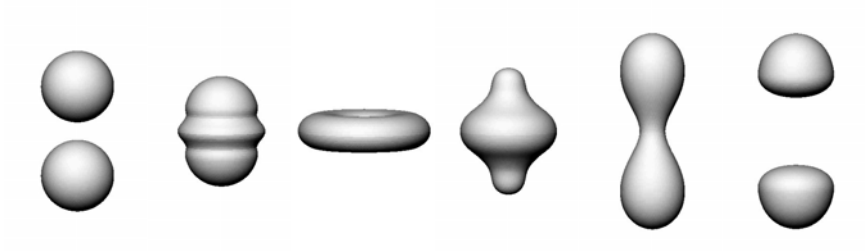

(b)

Figure 1: (a) Head on collision, We=23, from Ashgriz and Poo [15]; (b) Head on collision, We=23, Oh=0.0047, our simulation.

The qualitative agreement between simulation and experiments in the different pictures is quite good. The final state is well predicted (two droplets without satellites) and moreover, the liquid phase behavior during the collision process is very similar in both image sequences.

3.2 Head on collision for two droplets with different sizes

Experimental conditions given by Ashgriz and Poo [15] are the Weber number (We=56), the droplet radius ratio (0.5) and the impact parameter (0.). We thus chose one radius equal to 400 μm, the smallest radius is 200 μm, and the relative velocity for We=56 is equal to 3.175 ms^{-1}. The grid size is 60x240.

As can be observed on figures 2.a and 2.b the agreement between the experimental pictures and the simulation results is very impressive. The shape evolution of the liquid phase is quite identical on both image sequences, and the last images of the two resulting droplets prove the quality of the whole collision process simulation.

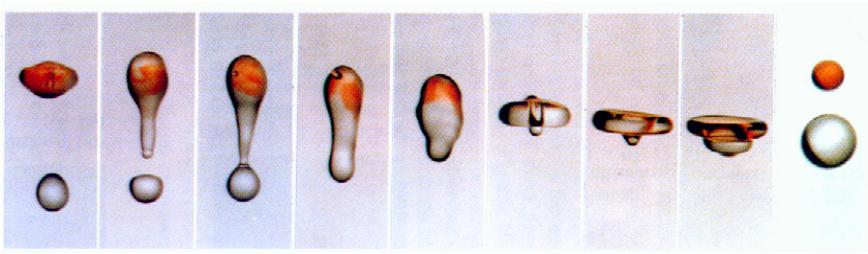

(a)

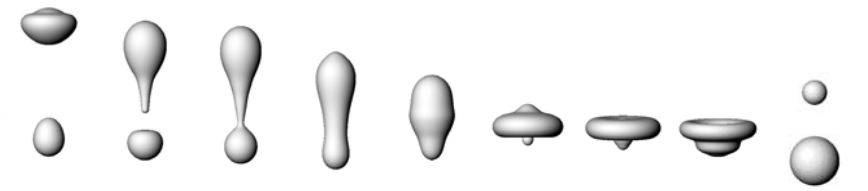

(b)

Figure 2: (a) Head on collision, We=56, radius ratio 0.5 from Ashgriz and Poo [15]; (b) Head on collision, We=56, Oh=0.0047, radius ratio 0.5, simulation.

3.3 Off-center collision

In order to check the method in 3D configurations, collision between two droplets with non-zero impact parameter has been studied. We chose ethanol droplet, droplet radius is 100μm, impact parameter is 0.5 and relative velocity is 2.94 ms^{-1} which gives a Weber number equal to 60. The grid size is 64x128x256 and symmetry condition is imposed on the parallel direction of the droplet velocity vectors. MPI parallelization is used and calculations are carried out on 8 processors on IBM 1600 cluster.

The chosen initial configuration is in the transition regime between separation with one satellite and separation with three satellite. Simulation results are presented on Figure 3.a. Collision process leads to coalescence followed by separation with formation of two satellites.

Ashgriz and Poo [15] showed a collision with very similar behavior as shown on figure 3.b, but with a slightly different configuration, namely water droplets, We=83 and impact parameter is 0.43. A difference appears on image 2 in figures 3.a and 3.b where the thin membrane is broken in the simulation but seems to experimentally remain during the collision.

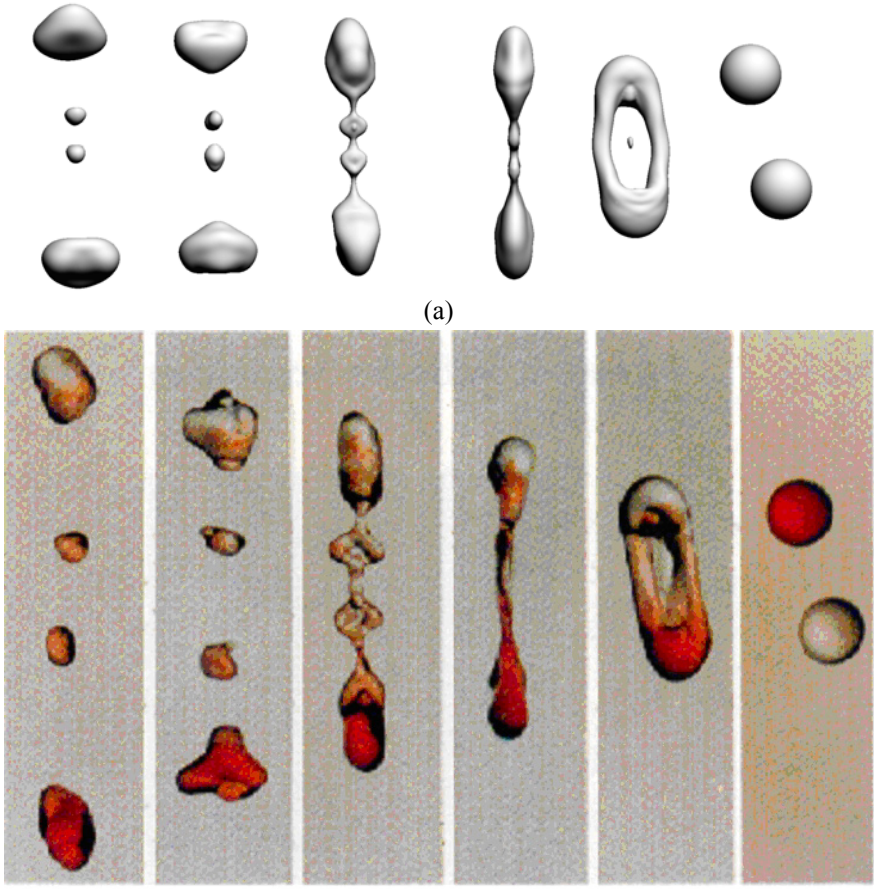

(a)

(b)

Figure 3: (a) 3D simulation, ethanol droplet, We=60,Oh=0.02, I=0.5; (b) Water droplet, We=83, I= 0.43 from Ashgriz and Poo [15].

The numerical description of very thin liquid layers in the collision process is a difficult problem to handle. As shown on figure 4 the thin membrane which is observed in the 3D simulation first breaks near the liquid ring, and then the bridge on the center of the liquid shape is elongated until it also breaks and a small droplet appears in the center. The ring is then stretched until its two sides collapse on the vertical axis and the small droplet is captured and merges with the whole liquid. Ashgriz and Poo [15] never seem to observe this behavior. We can assume that the break-up in the interface topology is induced by under-resolved numerical simulation of the very thin interface. However, while it remains quite impossible to check the spatial convergence of the results in 3D configurations, such behavior has also been observed in 2D simulations, namely for We=23 in the above results. Refining the grid can, in some cases, allow the interface motion to be described without any rupture, but we found some cases

where the membrane break-up occurs at the same time on the same location whatever the grid size we used (the finest grid mesh was less than 2 μm). We observed that these thin membranes rupture during head-on droplet collisions for quite small Weber numbers.

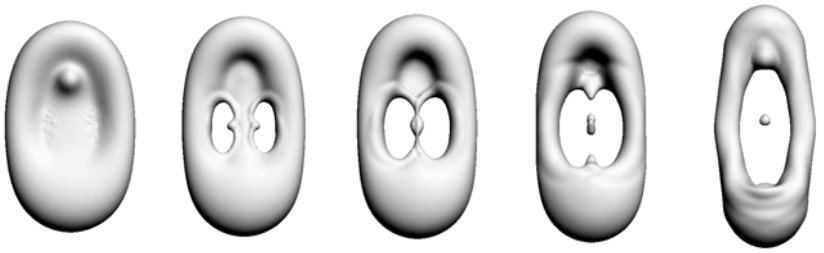

Figure 4: Thin membrane break in 3D simulation.

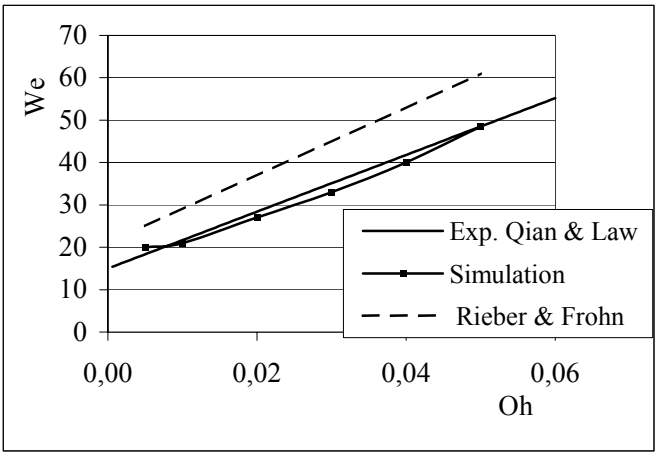

Figure 5: Comparison between simulation and experiments for transition between coalescence and separation in (Oh,We) space for droplet head on collision.

3.4 Quantitative comparison

Quantitative comparisons can be biased by a lack of experimental operating conditions or detailed measurement data. However experimental studies (Qian and Law [16]) provide the critical Weber versus Ohnesorge number for the transition between coalescence regime and separation regime for droplet head on collision. Figure 5 compares our results with Qian and Law [16] experimental correlation, and Rieber and Frohn [18] simulations. The agreement between our simulations and experimental data is very satisfactory and confirms that Level Set method with Ghost Fluid approach are accurate tools numerical simulations of droplet collisions.

References

[1] Nobari M.R., Jan Y.J., Tryggvason G., Head-on collision of drops – a numerical investigation. *Physics of Fluids* Vol 8, 1, 1996.

[2] Rieber M., Frohn A., Navier-Stokes Simulation of droplet collision dynamics. *Aerosol Sci*., Vol. 26, Suppl. 1, pp. S929-S930, 1995.

[3] Gueyffier D., Li J., Nadim A., Scardovelli S. et Zaleski S., Volume of Fluid interface tracking with smoothed surface stress methods for three-dimensional flows. *J. Comput. Phys*., 152, 423-456, 1999.

[4] Benkenida A., Magnaudet J., A method for the simulation of two-phase flows without interface reconstruction *Comptes Rendus de l'Academie des Sciences* Series IIB, vol. 328, iss. 1, pp. 25-32(8), 2000.

[5] Osher S., Sethian J.A. Fronts propagating with curvature-dependent speed: algorithms based on Hamilton-Jacobi formulations. *J. Comp. Phys*. 79, 12-49, 1988.

[6] Fedkiw R., Aslam T., Merriman B., Osher S., A non-oscillatory eulerian approach to interfaces in multimaterial flows (The Ghost Fluid Method). *J. Comp. Phys*. 152, 457-492, 1999.

[7] Sethian J *A Level Set Method and fast marching methods*. Cambridge Univ. Press, 1999.

[8] Sussman M Fatemi E Smereka P Osher S, An improved Level Set method for incompressible two-phase, *Computers and Fluids*, 27, 1997.

[9] Enright D Fedkiw R Ferziger J Mitchell I. A Hybrid Particle Level Set Method for Improved Interface Capturing, J. *Comp. Phys.* 183, 83-116,2002

[10] Sussman M., Puckett E.G., A coupled level set and volume-of-fluid method for computing 3D and axisymmetric incompressible two-phase flows. *J. Comp. Phys*. 162, 301-337,2000.

[11] Tanguy S. Développement d'une méthode de suivi d'interface. Applications aux écoulements diphasiques, PhD thesis, Université Rouen, Laboratoire CORIA CNRS UMR 6614, 2004.

[12] Brackbill J.U. , Kothe D. , Zemach C. A continuum method for modeling surface tension. *J. Comp. Phys.* **100**, 335-354,1992.

[13] Kang M Fedkiw R Liu X D A Boundary Condition Capturing Method for Multiphase Incompressible Flow, *J. Sci. Comput.* 15, 323-360,2000.

[14] Liu X.D., Fedkiw R., Kang M., A Boundary Condition Capturing Method for Poisson equation on irregular domains, *J. Sci. Phys.,* 151-178, 2000.

[15] Ashgriz N., Poo J.Y. Coalescence and separation in binary collisions of liquid drops. *J. Fluid Mech.* 221, 183-204, 1990.

[16] Qian J., Law C.K. Regimes of coalescence and separation in droplet collision. *J. Fluid Mech.* 331, 59-80, 1997.

[17] Tanguy S., Berlemont A. Application of a Level Set Method for simulation of droplet collisions, *Int. J. Multiphase Flow*, under printing.

[18] Rieber M., Frohn A. Navier-Stokes Simulation of droplet collision dynamics. *Aerosol Sci.*, Vol. 26, Suppl. 1, pp. S929-S930, 1995.

An indirect boundary integral equation for confined Stokes flow of drops

G. Zhu[1], A. A. Mammoli[1] & H. Power[2]
[1] *Department of Mechanical Engineering, University of New Mexico, USA*
[2] *School of Mechanical, Materials and Manufacturing Engineering, University of Nottingham, UK*

Abstract

An indirect boundary integral formulation is used to model the viscous flow of drops in a container. The indirect formulation results in well-conditioned linear systems, suitable for solution using iterative methods. The formulation is tested using several benchmarks. The tests allow the determination of the range of viscosity ratio and capillary number which can be treated accurately using the formulation. The convergence behavior is also tested, and it is shown that it is relatively independent of the systems size, and that the method is suitable for treating systems with large numbers of drops. Finally, the method is applied to a typical problem, that of the flow of one or more drops through a contraction. The outcome of the passage through the contraction is highly dependent on the viscosity ratio and the capillary number.

1 Introduction

Multiphase flow in porous media is currently one of the more challenging topics in fluid mechanics. In many cases (gas sequestration in aquifers, oil recovery, filtration), one continuous phase carries drops and particles of different phases. The interaction of the multiphase fluid with the porous formation at the scale of the droplet size or pore size determines the macroscopic characteristics of the flow. An experimental treatment of the phenomenon presents considerable difficulties due to the small scales involved, on the order of a few microns. As a consequence, Insight into the interaction may be obtained using simulation. Boundary integral techniques appear suitable for this type of problem, characterized by very complex, evolving geometries. Recently, several types of acceleration methods have

WIT Transactions on Engineering Sciences, Vol 50, © 2005 WIT Press
www.witpress.com, ISSN 1743-3533 (on-line)

been developed for the solution of the large fully populated linear systems produced by the discretization of the BIE [1]. However, these acceleration methods require that the linear system is well-posed. For the case of suspensions of rigid particles, the completed double layer boundary integral equation has been applied widely. In this, the flow field is represented by a distribution of double layer potentials on the particle surfaces and point forces and torques located inside each particle. The unknown particle surface velocity is related to various moments of the respective particle hydrodynamic potential distribution, resulting in an invertible linear system. In the case of drops, the surface velocity is not a simple rigid body motion, so the velocity conditions cannot be expressed in relation to the translation and rotation rate of the particle. On the other hand, the jump in surface traction across the interface can be related to the surface tension and curvature of the drop. The change in nature of the surface boundary conditions from specified velocity to specified traction suggest a different representation of the flow field from the case rigid particles, which nevertheless should still result in Fredholm second-kind integral equations. The strategy for achieving this is described in section 2. The method is benchmarked and tested in section 3. Finally, an application problem is shown in section 4.

2 Numerical formulation

Consider a volume Ω_0 bounded by a surface Γ_0, in which n drops, with the i^{th} drop defined by volume Ω_i and surface Γ_i. In the volume defined by $\Omega_0 \setminus \Gamma_0$, the velocity is represented by a distribution of double layer sources on the container boundary and single layer sources on the drop boundaries:

$$u_i(\mathbf{x}) = \int_{\Gamma_0} K_{ij}((\mathbf{x},\mathbf{y})\phi_j(\mathbf{y})d\Gamma_y + \sum_{p=1}^{n}\int_{\Gamma_p} Q_{ij}((\mathbf{x},\mathbf{y})\psi_j(\mathbf{y})d\Gamma_y, \qquad (1)$$

where the double and single layer hydrodynamic kernels K_{ij} and Q_{ij} are well-known and easily found [2]. One key feature of this formulation is that the velocity field is continuous across the drop surfaces (unlike the gradient of velocity, since the derivative of the single layer kernel in not necessarily continuous across the drop surfaces [2]). In fact, differentiation of the velocity field inside and outside the surface of drop q, followed by a limiting process to obtain the surface stress on either side of the interface yields:

$$\begin{aligned} t_i^{(e)}(\mathbf{x}) = &-\frac{\mu}{2}\psi_i(\mathbf{x}) - \mu\int_{\Gamma_q} K_{ji}(\mathbf{y},\mathbf{x})\psi_j(\mathbf{y})d\Gamma_y \\ &- \sum_{p=1}^{n}(1-\delta_{pq})\,\mu\int_{\Gamma_p} K_{ji}(\mathbf{y},\mathbf{x})\psi_j(\mathbf{y})d\Gamma_y \\ &+ \mu\int_{\Gamma_0} T_{ij}(\mathbf{x},\mathbf{y})\phi_j(\mathbf{y})d\Gamma_y, \end{aligned} \qquad (2)$$

$$t_i^{(i)}(\mathbf{x}) = \frac{\lambda\mu}{2}\psi_i(\mathbf{x}) - \lambda\mu \int_{\Gamma_q} K_{ji}(\mathbf{y},\mathbf{x})\psi_j(\mathbf{y})d\Gamma_y$$
$$- \sum_{p=1}^{n} (1-\delta_{pq})\,\lambda\mu \int_{\Gamma_p} K_{ji}(\mathbf{y},\mathbf{x})\psi_j(\mathbf{y})d\Gamma_y$$
$$+ \lambda\mu \int_{\Gamma_0} T_{ij}(\mathbf{x},\mathbf{y})\phi_j(\mathbf{y})d\Gamma_y, \tag{3}$$

in which μ is the viscosity of the continuous fluid, $\lambda\mu$ is the viscosity of the drops (assumed equal in all drops for clarity), $\mathbf{n}$ is the unit normal vector pointing outside the drop, and the kernel T_{ij} is obtained by differentiating K_{ij}. It should be noted that although T_{ij} is hypersingular, it is not necessary to evaluate it on Γ_0, and poses no particular difficulty. The traction parallel to the drop surface is exactly opposite, while in the direction normal to the surface there is a traction jump due to surface tension, so that the expressions for outside and inside traction can be related by:

$$t_i^{(i)}(\mathbf{x}) + t_i^{(e)}(\mathbf{x}) = \gamma n_i(\mathbf{x})\frac{\partial n_j(\mathbf{x})}{\partial x_j} + \Delta\rho g_k x_k n_i(\mathbf{x}), \tag{4}$$

where γ is the surface tension, and the second term on the right-hand side of the equation is a normal traction which accounts for buoyancy [3]. The final step is to apply the boundary conditions. For $\mathbf{x} \in \Gamma_0$, where a velocity field $U_i(\mathbf{x})$ is assumed known, Eq. 1 can be taken to the boundary through the usual limiting process, resulting in:

$$U_i(\mathbf{x}) = \frac{1}{2}\phi_i(\mathbf{x}) + \int_{\Gamma_0} K_{ij}(\mathbf{x},\mathbf{y})\phi_j(\mathbf{y})d\Gamma_y + \sum_{p=1}^{n}\int_{\Gamma_p} Q_{ij}(\mathbf{x},\mathbf{y})\psi_j(\mathbf{y})d\Gamma_y. \tag{5}$$

For $\mathbf{x} \in \Gamma_i$, incorporation of Eqs. 2 and 3 into 4 yields:

$$-\frac{1}{1+\lambda}\gamma n_i(\mathbf{x})\frac{\partial n_j(\mathbf{x})}{\partial x_j} - \frac{1}{1+\lambda}\Delta\rho g_k x_k n_i(\mathbf{x}) = \frac{1}{2}\psi_i(\mathbf{x})$$
$$-\beta\left[\sum_{p=1}^{n}\int_{\Gamma_p} K_{ji}(\mathbf{y},\mathbf{x})\psi_j(\mathbf{y})d\Gamma_y + \int_{\Gamma_0} T_{ij}(\mathbf{y},\mathbf{x})\phi_j(\mathbf{y})d\Gamma_y\right], \tag{6}$$

where $\beta = (\lambda-1)/(\lambda+1)$. Eqns. 5 and 6 are both Fredholm equations of the second kind, and the problem is well posed except for limiting values of λ. In this work, the surfaces are discretized using an adaptive meshing algorithm and triangular elements with constant source density and quadratic geometry. Curvature at a given point is calculated by fitting a quadratic patch to the surface neighboring the point, using least squares. The principal curvatures and average curvature are then easily evaluated.

3 Benchmarks and convergence testing

Two benchmarks are performed, both in creeping flow regime. One ensures correct functioning of the traction jump due to curvature and surface tension, the other ensures correctness of the formulation. In the first benchmark, an originally ellipsoidal neutrally buoyant drop is allowed to deform following the traction jump due to surface tension, in a quiescent fluid. At steady state, the drop should acquire a spherical shape, whether or not a container is present. The presence of a container slows the transition to a spherical shape.

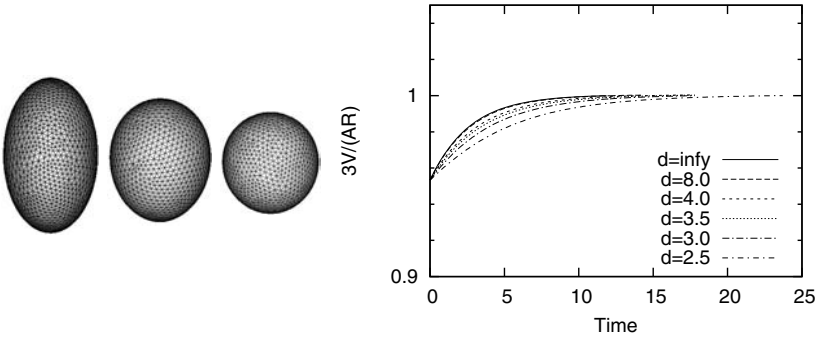

Figure 1: Relaxation of the shape of a drop in a quiescent fluid, from an initial ellipsoid to a sphere (left); ratio of volume to surface area as a function of time, for various container sizes.

The outcome of the simulation is shown in Fig. 3. The surface appears smooth, indicating proper functioning of the meshing and curvature algorithms. The ratio of volume to surface area correctly asymptotes to $R/3$ for all cases. The relaxation to spherical shape is fastest in an infinite fluid, and slows with decreasing container size, as expected. Volume is conserved (to within 0.2%), as is inherent in the incompressible formulation.

The second benchmark test is the motion of a buoyant Newtonian drop in a Newtonian fluid. Quantitative analysis of the solution accuracy are possible because of the analytical solution for this particular problem, namely Hill's spherical vortex. The velocity field inside and outside the sphere is in excellent agreement with the theoretical results. The z velocity profile is shown as a function of r in the direction normal to the direction of motion. The change in velocity gradient at the interface is consistent with the viscosity ratio $\lambda = 2$. Furthermore, It was shown by Batchelor [4] that for small RE the drop remains spherical, and the simulation results are in excellent agreement with this. The rise velocity U_b can be calculated using the

Hamdamard-Ribczynksi formula [5],

$$U_b = \frac{2R^2 g \Delta\rho}{9\mu} \left[\frac{\lambda + 1}{\lambda + \frac{2}{3}} \right] \tag{7}$$

which asymptotes to the Stokes velocity for $\lambda \to \infty$ and to the velocity of a rising bubble for $\lambda \to 0$. The simulation results are compared to the analytical solution in Fig. 3.

For a mesh with 816 elements, the simulation yields acceptable results in the range $0.01 < \lambda < 10$. With a finer mesh (2950 elements), the range is extended to $0.0001 < \lambda < 100$. In general, best accuracy is obtained for viscosity ratios close to unity. For small drop to carrier fluid viscosity ratios (λ), accuracy remains good. On the other hand, for large ratios, very fine meshes are required to obtain sufficient accuracy. This is likely a consequence of the null space for the ψ distribution, which emerges as β approaches unity, resulting in increasingly poorly conditioned systems.

Finally, the convergence behavior of the GMRES solver is plotted as a function of mesh refinement in Fig. 3. For $\lambda = 1$, convergence is rapid and relatively independent of mesh refinement. For large and small viscosity ratios λ, the number of GMRES iterations increases, possibly due to the emergence of the null space of the integral operator. In such cases, alternative formulations which better approach the problem should be sought [6, 7]. As the drop approaches the contraction, the number of iterations also increases, in this case because elements on different surfaces become very close giving rise to large off-diagonal entries in the coefficient matrix. This effect may be countered effectively with lubrication-type formulations [8].

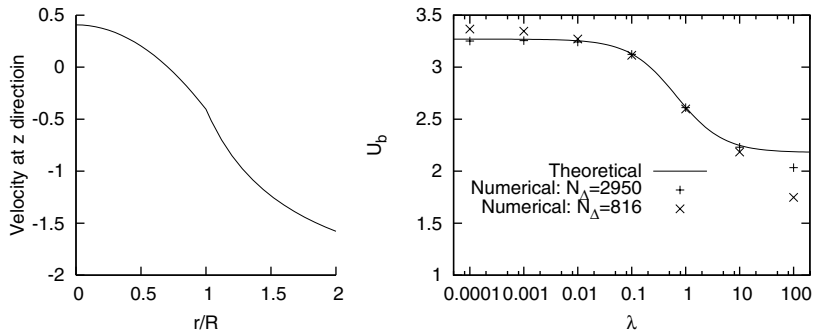

Figure 2: Velocity in the direction of motion (relative to centroidal motion) as a function of radial distance in the direction perpendicular to the axis of motion for a viscous drop rising in a viscous fluid (left); Predictions of drop velocity as a function of viscosity ratio in comparison to analytical result (right).

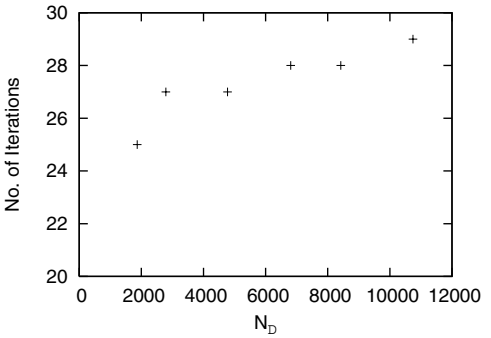

Figure 3: Convergence of the GMRES solver as a function of the number of degrees of freedom, for $\lambda = 1$.

4 Flow of a drop in a contraction

Much can be learned about multiphase flow in porous media by studying the creeping flow of individual drops in an emulsion. Specifically, flow inside pores has strong elongational characteristics, which promote drop breakup [9]. What is of interest is the nature of the steady-state emulsion that emerges, in terms of its drop size distribution. In turn, the drop size distribution, in conjunction with the characteristics of the porous medium, results in a flow which is essentially viscoelastic, so that Darcy's law may be inadequate in predicting macroscopic characteristics of the flow. The extent to which this is true is an important aspect of this research, as well as the determination of an alternative macroscopic model. Here, some examples are given to illustrate the above points, and to provide impetus for further research.

The simulation geometry consists of a cylinder in which a toroidal shaped contraction is placed, as described in fig. 4. Poiseuille boundary conditions are applied at either end of the cylinder. A drop is placed upstream of the contraction, and its behavior is observed as the flow progresses.

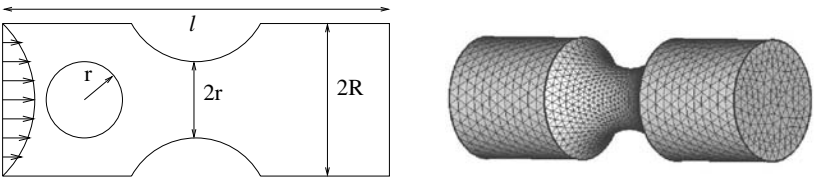

Figure 4: Model geometry: cross-section (left) and typical mesh (right).

First, the effect of the capillary number (Ca = $U\mu/\sigma$, where U is the average fluid velocity at the inlet, μ is the dynamic viscosity and σ is the surface tension) and ratio between drop viscosity and carrier fluid viscosity on the drop shape is considered, for a fixed viscosity ratio of 0.5. This effect can be observed by traversing Fig. 4 horizontally.

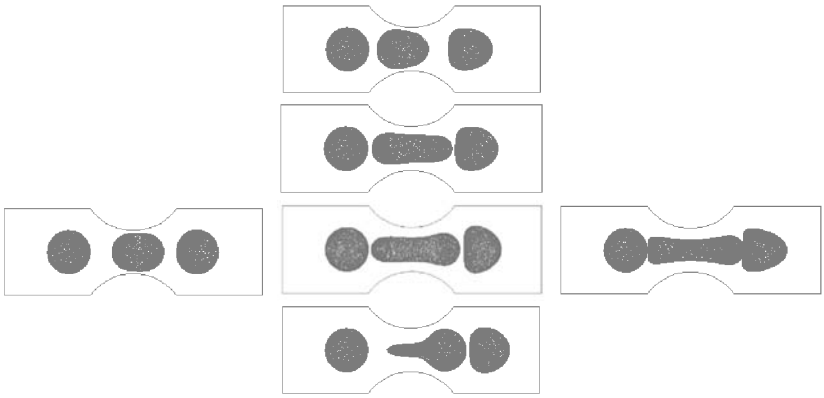

Figure 5: Evolution of drop shape as a function of Ca (0.01, 0.1 and 1.0 left to right) and λ (50, 5, 0.5 and 0.05 top to bottom). In each plot, snapshots of the drop shape before entering the contraction, in the contraction and after exiting the contraction are shown.

Clearly, the larger viscous forces at high capillary numbers result in stronger deformation of the drop. In the case of fixed physical parameters, such as in the injection of supercritical CO_2 in saline aquifers, higher Ca can be achieved through increasing the flow rate. Also interesting is the fact that large drop deformation can induce drop breakup, and as a consequence the reduction in the drop size distribution. It is also possible that, for very small capillary numbers, a drop whose size is larger than the pore size may become trapped and effectively reduce the permeability of the medium. The other parameter of interest is the ratio of drop viscosity to carrier fluid viscosity λ. For a fixed value of Ca, the effect of viscosity ratio, visible by traversing Fig. 4 vertically, is to reduce the extent of drop deformation. Thus, the tendency for drop breakup increases with increasing Ca and decreasing λ. In the case of $\lambda = 0.05$ and Ca$= 0.1$, the drop forms a tail, evidence of instability.

A parameter of high interest is the pressure required to drive the drop through the contraction. This is also a function of Ca and λ, as can be observed in Fig.4. Although a drop has the potential to deform and pass through the contraction, the surface tension acts to retain the drop's spherical shape, and as a consequence the pressure drop across the contraction increases during passage of the drop through the contraction. At low Ca (dominant surface tension forces), the pressure to drive the flow at a constant flux oscillates substantially, with a net increase of energy

expenditure in comparison to a flow with no drop. As Ca increases, the pressure oscillation decreases, and the net energy expenditure decreases with respect to the flow without a drop (the decrease is due to the lower viscosity of the drop). For a fixed Ca, increasing the viscosity of the drop results, predictably, in an increase in the pressure required to drive the drop through the contraction, and consequently in a higher energy expenditure.

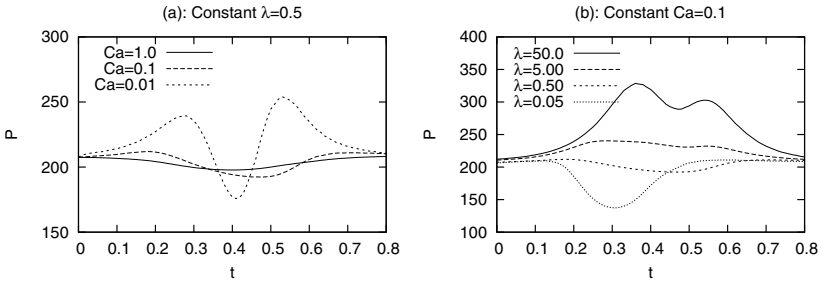

Figure 6: Pressure drop between ends of cylinders as drop moves through contraction, a function of Ca (left) and λ (right).

5 Conclusions

A second-kind boundary integral formulation is developed for the treatment of the flow of emulsions. From a numerical point of view, the method is successful. The number of GMRES iterations is relatively independent of the number of elements used in the model simulation. When the viscosity ratio becomes very large or very small (rigid particle and bubble respectively) a null space for the double layer kernel emerges and the number of iterations increases substantially. We therefore conclude that the method in its present form is well-suited for viscosity rations $0.1 < \lambda < 10$. The iteration count also increases as drop surfaces become close to the container boundary. This is a problem with most BEMs, and can be effectively dealt with a lubrication formulation where a traction is applied to each element, with the traction cast as a function of relative velocity between surfaces.

With the limitations noted, the formulation performed very well in accuracy benchmarks involving the calculation of the surface tension forces. An elliptical drop in a quiescent fluid becomes spherical under the action of the surface tension. The presence of a container slows the relaxation to a spherical shape increasingly with decreasing container size. This benchmark shows that the surface curvature calculation is implemented correctly, and that the method accounts for the interaction between container walls and drop surface correctly. A second benchmark serves the dual purpose of a quantitative verification of the accuracy of the BIE formulation and its implementation, as well as of a test for determine the range of

usability of the method. The ratio of drop viscosity to carrier fluid viscosity can range from 0.1 to 10 and provide accurate results.

The method was used to perform a preliminary investigation on the behavior of drops passing through a contraction. For low Ca, the drop tends to retain its shape, and passage through the contraction requires a substantial increase in applied pressure differential between the ends of the tube. At high Ca, which can be produced by high flow rate, high viscosity, or low surface tension, the relative amplitude of the pressure drop oscillation is reduced. In general, some of the physical parameters are fixed. For example, in CO_2 injection the viscosity and the surface tension cannot be altered easily, while the flow velocity can.

The capillary number is also a factor in determining the deformation and breakup of the drop. High capillary number and low drop viscosity act to break up the drop as it passes through pores, thereby reducing the mean value of the drop size distribution. A full scale parameter study of this effect is currently being conducted.

References

[1] Zinchenko, A.Z. & Davis, R.H., An efficient algorithm for hydrodynamical interaction of many deformable drops. *J Comp Phys*, **157**, pp. 539–587, 2000.
[2] Ladyzhenskaya, O.A., *The Mathematical Theory of Viscous Incompressible Flow*. Gordon and Breach Science Publishers, Inc.: New York and London, 1963.
[3] Pozrikidis, C., *Boundary Integral and Singularity Methods for Linearized Viscous Flows*. Cambridge University Press: Melbourne, 1992.
[4] Batchelor, G.K., *An introduction to fluid dynamics*. Cambridge University Press: Cambridge, 1967.
[5] Happel, J. & Brenner, H., *Low Reynolds Number Hydrodynamics, with Special Applications to Particulate Media*. Prentice-Hall: Edgewood Cliffs, NJ, 1962.
[6] Power, H. & Wrobel, L.C., *Boundary Integral Methods in Fluid Mechanics*. Computational Mechanics Publications: Southampton and Boston, 1995.
[7] A. R. M. Primo, L.C.W. & Power, H., An indirect boundary-element method for slow viscous flow in a bounded region containing air bubbles. *J Eng Math*, **37**, pp. 305–326, 2000.
[8] Mammoli, A.A., Towards a reliable method for predicting the properties of multiphase fluids. *Engrg Anal Bound Elem*, **26**, pp. 861–870, 2002.
[9] Stone, H.A., Dynamics of drop deformation and breakup in viscous fluids. *Ann Rev Fluid Mech*, **26**, pp. 65–102, 1994.

This page intentionally left blank

Simulations of pressure pulse-bubble interaction using the boundary element method

K. C. Hung[1], S. W. Fong[1], E. Klaseboer[1], C. K. Turangan[1], B. C. Khoo[2,3] & T. G. Liu[1]
[1] *Institute of High Performance Computing, Singapore*
[2] *Department of Mechanical Engineering, National University of Singapore*
[3] *Singapore-MIT Alliance, Singapore*

Abstract

The Boundary Element Method (BEM) is used to simulate the interaction of a bubble with a pressure pulse which resembles a shock wave. The main advantage of this model lies in its enormous speed-up in calculation as compared with other existing methods. The pulse in question is in the form of a step-pulse function with variable width and is incorporated into the Bernoulli equation. Its interaction with a bubble induces the formation of a high-speed jet that accelerates in the pulse direction. Since the dynamic response of the bubble is assumed to be mainly inertia-controlled, the compressibility effect of the surrounding water is neglected. The validation of this methodology comes from the reasonable agreement of the results with those from other established numerical simulations; namely, the Arbitrary Lagrangian Eulerian (ALE) method, the Free Lagrange Method (FLM), and experiments. Detailed comparisons in terms of bubble-shape transformation, collapse times, and jet velocities are discussed.
Keywords: boundary element method, shock wave, bubble collapse, jet impact, jet velocity.

1 Introduction

Nonlinear bubble dynamics has been the subject of intense investigation in recent years. Often emphasis is placed on the asymmetrical collapse and the formation of a high speed jet of a single gas bubble in an incompressible fluid. This is because this phenomena is perceived to be the main cause of erosion in hydraulic

machinery [1], initiation of explosives [2, 3], photoluminescence [4], ultrasonic cleaning and disinfection [5], and extracorporeal shock wave lithotripsy (ESWL) for intra-organ stones removal. The resulting jet and impact blast wave have been identified as possible mechanisms of kidney stone fragmentation [6, 7].

To better understand the event of asymmetrical collapse of the bubble interacting with shock wave, several experiments were carried out [2, 8]. But due to constraints in temporal and spatial resolution of experimental diagnostics, it is argued that numerical simulations offer many advantages, particularly in their abilities to capture specific events that signify the collapse phenomena. Jamaluddin [9] modeled the interaction of a spherical bubble with a step shock of various strengths in an axisymmetric geometry using FLM. The simulations are similar to those conducted by Ding and Graceweski [10] using ALE.

This work uses the BEM to simulate such phenomenon. Previous works on BEM include the growth and collapse of a single spherical bubble near a planar rigid boundary [11, 12], near a curved boundary [13], and a single or multiple bubbles near a free surface [14, 12]. In this case, we model the disturbance in the form of a step pressure pulse. This pulse is incorporated into the reference pressure as a function of time and space. We are, therefore, exploiting the capabilities of BEM in predicting the interaction of a planar pressure pulse with spherical bubble. We focus on the jet formation in the shock-induced collapse and compare our results with other numerical and experimental works.

2 The boundary element method and pressure pulse-bubble interaction model

Very briefly, the mathematical framework for a collapsing bubble in water due to a pressure impulse is presented in this section. We consider a stationary spherical bubble in an infinite medium with no other boundaries. A pressure pulse is moving with a constant velocity U_s and a width W_s towards the bubble in the direction of the z-axis as depicted in Fig. 1(a). The pressure pulse is assumed to have the simplest possible form with an amplitude P_s along the width W_s, and P_{ref} , the atmospheric pressure, anywhere else.

A velocity potential Φ is introduced, and thus allowing the velocity vector $\boldsymbol{u}$ be written as:

$$\boldsymbol{u} = \bigtriangledown\phi \tag{1}$$

In the whole fluid domain the Laplace equation is assumed to be valid. Furthermore, the unsteady Bernoulli equation can be applied anywhere in the fluid, as well as on the bubble surface:

$$p_g = p_\infty - \rho \frac{D\phi}{Dt} + \frac{1}{2}\rho \left|\boldsymbol{u}\right|^2 \tag{2}$$

where p_g is the pressure inside the bubble, p_∞ is the reference pressure, ρ is density of the medium, and the material derivative $\frac{D\phi}{Dt}$ is equal to $\frac{\partial}{\partial t} + u \bullet \bigtriangledown$.

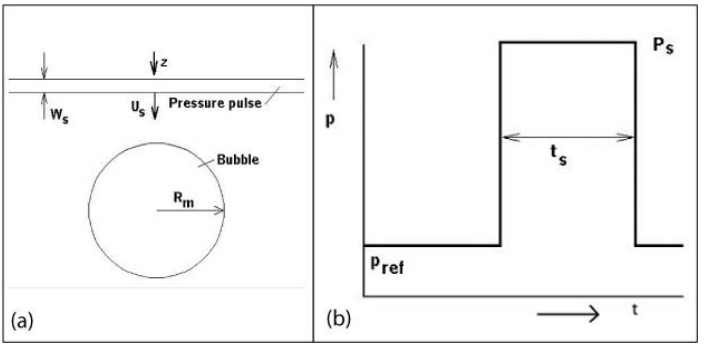

Figure 1: (a) Schematic diagram of a pressure pulse with width W_s moving with a velocity U_s towards the bubble in the downwards z-direction. The initial bubble radius is R_m. (b) Schematic diagram of a pressure pulse with duration t_s and strength P_s as a function of time t.

The pressure pulse is incorporated into Equation (2) in the p_∞ term as such:

$$p_\infty = \begin{cases} P_{ref} & z < z_0 + t\,U_s - W_s, \\ P_s & z_0 + t\,U_s - W_s < z < z_0 + t\,U_s, \\ P_{ref} & z > z_0 + t\,U_s. \end{cases} \tag{3}$$

The Laplace equation is solved via the Boundary Element formulation. The reader is referred to [15] for more details. It is noted that all equations are non-dimensionalised in this work (we attach a postscript ' to the non-dimensionalised terms). The initial radius R_m, which is also the maximum bubble radius, is used to scale all lengths. The pressure p_{ref} is used to non-dimensionalise all pressure terms. Time is non-dimensionalised with:

$$t_{ref} = R_m \sqrt{\frac{\rho}{p_{ref}}} \tag{4}$$

and the potential, Φ, with:

$$\Phi_{ref} = R_m \sqrt{\frac{p_{ref}}{\rho}} \tag{5}$$

2.1 Pressure pulse (shock) velocity

If the pressure pulse represents a shockwave, the amplitude of the shockwave P_s and its speed U_s are not independent. In water, it is assumed that the Tait equation of state applies. The density behind the shock, or post-shock density, is therefore:

$$\rho^* = \left(\frac{P_s}{B} + 1\right)^{\frac{1}{n}} \rho_{Rd} \tag{6}$$

where ρ_{Rd} = 999.96 kg/m^3 is the water reference density at zero pressure, and B and n are constants with values 3.31×10^8 and 7 respectively. As described by Ball [2], the post-shock water particle velocity, u^*, can be calculated from

$$u^* = u_u + \sqrt{\left(\frac{\rho^* - \rho_u}{\rho^* \rho_u}\right)(P_s - P_u)} \tag{7}$$

where the subscript u refers to the pre-shock condition. It is known that for most solids and liquids the shock velocity U_s is near-linearly proportional to the velocity of the material behind the shock u^*:

$$U_s = a_k + A_k u^* \tag{8}$$

where a_k is the local isentropic sound velocity and A_k is the shock density ratio parameter. For water, a_k = 1480 m/s and A_k = 1.815 (based on shock Hugoniot data [16]).

3 Results in comparison with other methods and experiments

In this section, BEM simulations of the response of a gas bubble to a step pressure pulse that resembles a shockwave are presented. The problem under consideration involves a single air bubble of various initial spherical size immersed in water under standard atmospheric conditions and imploded by a planar pressure pulse. Nine cases have been simulated: bubbles with initial bubble radii of 0.1, 1.0 and 10.0 mm are collapsed by a step pressure pulse of strength 0.528 GPa, 1.011 GPa and 2.06 GPa. These cases are similar to those examined by Jamaluddin [9] using a Free Lagrange Method (FLM) and those of Ding and Gracewski [10] using an Arbitrary Lagrangian Eulerian Method (ALE). For details on FLM, the reader is referred to [17, 9, 18]; and for ALE, details are found in [10]. One case example is given special attention in the following section; the case with initial bubble radius of 1.0 mm and a pressure pulse with very large width and strength of 0.528 GPa. In addition, other cases of bubbles interacting with various pulse strengths are conducted and the results concerning the jet velocities are presented in Section 3.2.

3.1 Case Study: 0.528 GPa pressure pulse acting on a bubble of 1.0 mm radius

The case shown in this section corresponds to a strong shock wave interacting with a bubble. A bubble with an initial radius of 1.0 mm is selected. This example has been specially chosen in order to show the capacity of the developed numerical scheme to deal with a very strong shock wave. The reference pressure is $P_{ref} = 10^5 Pa$. The calculations were carried out using both BEM and FLM methods with a shock profile as shown in Fig. 1(b).

The shock expanse is assumed to be very wide for both the BEM and FLM simulations and with a width W's set to a value of 100. The shock propagates through the water from top to bottom and the elapsed time is measured from the first contact between the bubble and the shock front ($t' = 0$). For a shock strength of 0.528 GPa, the particle velocity behind the shock reaches a value of u^* = 259 m/s, and therefore P_s' = 5280 and U_s' = 195.0. Only 50 nodes, which are equally distributed along the bubble surface, are used in BEM simulation as compared to the large number of nodes used in FLM and ALE. This is the main reason attributing to the much higher computational efficiency of BEM.

When the pressure pulse strikes the upstream bubble wall, the impact subsequently imparts a large momentum on the gas-water interface. This creates a high pressure region in the water around the impact location, and forces the bubble boundary to form an accelerating jet in the direction of the pulse. Fig. 2(a) depicts the BEM results on the bubble evolution as a result of its interaction with the pressure pulse. At all times prior to $t' = 0$, the velocity anywhere on the bubble surface is identically zero. The results are plotted with a time interval of 0.22 μs. In Fig. 2(b) the corresponding results are shown for the FLM method (with a time interval of 0.2 μs); these bubble shapes were taken directly from Jamaluddin [9].

On the FLM method, the pressure pulse front represents the Mach contour front, whereas for the BEM method, the horizontal line in Fig. 2(b) represents the pulse front, which is always maintained as a straight line. Physically, the transmitted shock inside the bubble propagates slower than the pressure pulse front as shown correctly by the FLM simulations due to the lower acoustic impedance of air compared to that of water. Due to its simplicity, these features are not reproduced with the BEM method.

At time t = 0 (first image of Fig. 2(a)), the pulse has just reached the upper bubble interface. In the following few images, the bubble surface is flattening at the top as the fluid behind the shock responds to the pressure pulse. As the pulse propagates downwards, the upstream bubble wall deforms rapidly to produce an accelerating jet for both methods. In the sixth image of Fig. 2(a), the leading edge of the pressure pulse has completely passed the bubble. The whole bubble is now submerged in a region of very high pressure; the shock width is very large for this particular case. Due to this pressure difference and liquid inertia, the bubble contracts further while the jet continues to approach the opposite bubble wall, as shown in the last images of Figs. 2(a) and (b).

Although the simulations by BEM omitted the wave propagation inside the bubble, very reasonably similar topographical features of the bubble surface with those of FLM is obtained, providing support to the use of BEM in simulating transient bubble dynamics such as pressure pulse-bubble interaction problems. The jet impacts at $t = 1.6\ \mu s$ for the FLM method and at $t = 1.74\ \mu s$ for the BEM method. Apart from bubble shapes, velocity vector plots are also shown in Fig. 2. Similar plots are also presented by Jamaluddin [9], and are in good agreement with the Fig. 2(a) (not reproduced here). Some non-physical (small) velocity vectors are observed in the region preceding the shock front. These are due to the incompress-

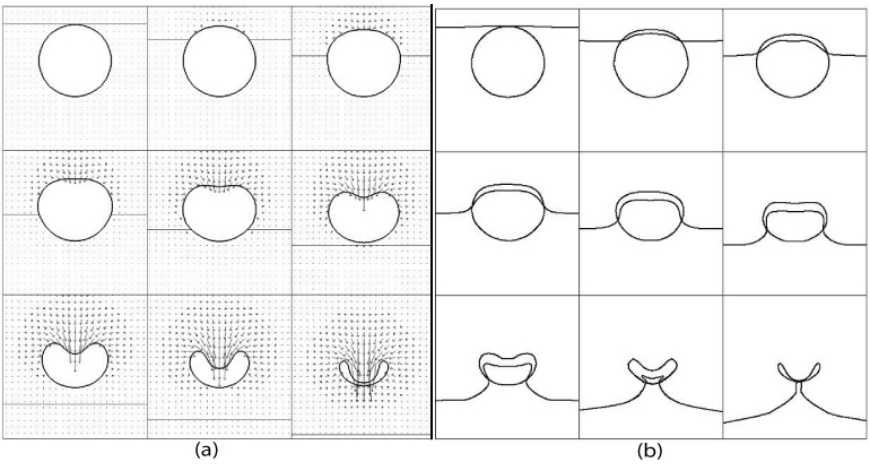

Figure 2: (a) BEM simulation of the interaction of a very wide pressure pulse of 0.528 GPa with a bubble of radius 1.0 mm. The dimensionless parameters are: P'_s =5280, W'_s =1000 and U'_s =195. The time interval between each plot is 0.22 μs. Also indicated are velocity vector plots. (b) FLM simulation of shock-bubble interaction derived from [9], using the same parameters. The time interval between each plot is 0.2 μs. The horizontal line indicates the Mach contour front (inside and outside the bubble).

ible nature of the BEM method. These velocities are small with respect to the jet tip velocity. Remarkably, in spite of its simplicity, the BEM method produces fairly similar results as obtained in the FLM simulation.

In order to make a more quantitative comparison between the FLM and BEM methods, the time history of the jet tip velocity u_{jet} (the velocity at the upper part of the bubble) for this particular case is compared to that of [9]. Jamaluddin [9] took the average of the absolute velocity of a few particles at the tip of the jet; in our simulations, the velocity of a single node on the tip of the jet (on the axis of symmetry) is recorded as a function of time. The results are presented in Fig. 3 for comparison. There are limited differences between the two methods and the general trend is similar. The jet tip velocity reaches a maximum value of about $u_{jet,max} = 2000$ m/s for the BEM method and about 2200 m/s for the FLM method, just before jet impact. This particular case was also compared to the numerical results of Ding and Gracewski [10], who implemented an Arbitrary Lagrangian Eulerian (ALE) method. The results in terms of bubble shape are very similar to those obtained with the BEM and FLM methods. The results concerning the jet tip velocity with the ALE method, which depict some 'oscillations' in the initial period, are also indicated in Fig. 3. Although there are observed differences between the three methods, the general trend is similar and clear.

3.2 Comparison of jet tip velocity for several pressure pulse strengths and bubble sizes

Ding and Gracewski [10] conducted a numerical study of the behavior of a single bubble with initial bubble radii of 0.1, 1.0 and 10.0 mm and applied step pressure pulses with strength 0.528 GPa, 1.011 GPa and 2.06 GPa for all three bubble sizes using the ALE method. Jamaluddin [9] simulated the same nine cases, using the FLM method. All nine cases have been compared to the numerical results obtained with the present BEM method. Since the dimensionless BEM model is independent of the bubble radius, the results will only depend on the dimensionless shock strength P_s'. Since the results are in essence fairly indistinguishable for the different bubble sizes, it is therefore reckoned that only the results for a bubble radius of 1.0 mm will be shown. Fig. 4 shows the dimensionless jet tip velocity–time history plot for BEM, FLM and ALE. The comparisons show a reasonably good agreement between the BEM and FLM/ALE results.

3.3 Comparison with experimental result

Although experimental results such as those conducted by Bourne and Field [4] focused only on the shock-induced collapse of 2D dimensional bubbles, where an amount of air was trapped in air filled cavity in gelatin, comparisons with their results can still be relevant in terms of trends observed and the magnitude of collapse times and jet velocities. Four cases will be considered: two bubbles with a radius of 6 mm each are imploded with a shockwave with strength of 0.26 GPa and 1.88 GPa, and two bubbles with radius of 3 mm each are imploded with 1.88 GPa and 3.49 GPa shockwave. Their results are shown in Table 1.

Table 1: Experimental results for four cases according to Bourne and Field [4].

Case	R_m (mm)	P_s (mm)	t_{coll} (μs)	$u_{jet,max}$ (m/s)
1	6.0	0.26	100	100
2	6.0	1.88	7	1700
3	3.0	1.88	3	5000
4	3.0	3.49	2	Unknown

As the shock width W_s was not recorded in the experiments, we carry out our simulation with varying W_s as shown in Table 2. The results seem to depend considerably on the value of W_s'. It is probable that the shock width increases with increasing shock strength. This can possibly explain the differences and trends observed between the experimental and numerical results. Although the results differ, the order of magnitude of the values of t_{coll} and $u_{jet,max}$ between experiments and numerics are comparable.

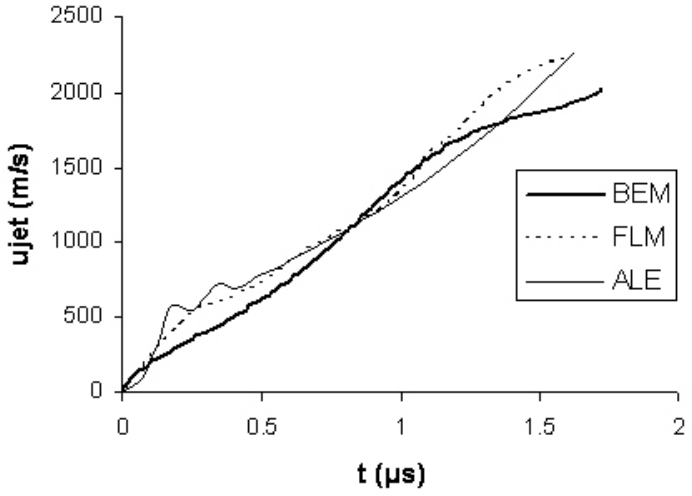

Figure 3: Plots of the jet tip velocity u_{jet} vs time for the BEM, FLM and ALE methods.

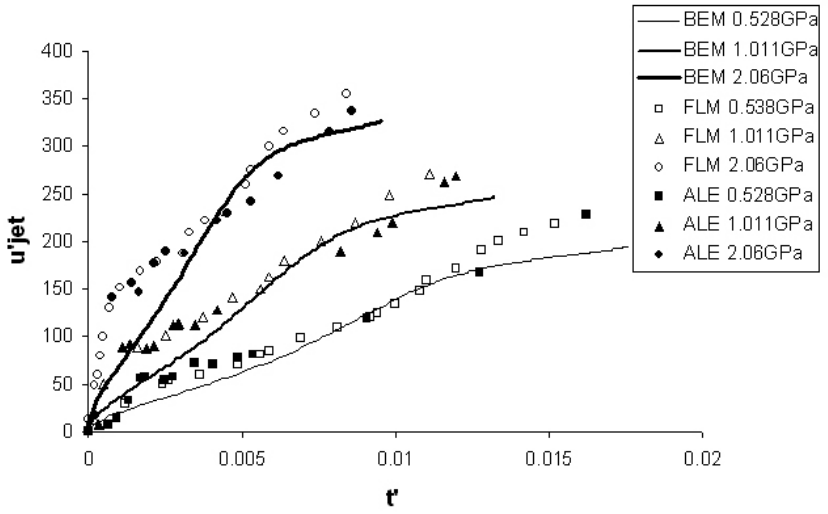

Figure 4: Comparisons of dimensionless jet tip velocity u'_{jet} as a function of dimensionless time t' for the BEM simulations.

4 Discussion and conclusion

The dynamics of a pressure pulse that may resemble a shock wave and its interaction with a spherical bubble were investigated numerically in this study.

Table 2: Numerical parameters and results concerning collapse times and jet velocities for the cases in Table 1.

Case	P'_s	U'_s	W'_s	t_{coll} (μs)	$u_{jet,max}$ (m/s)
1a	2600	175	1000	14	1600
1b	2600	175	1	19	800
1c	2600	175	0.2	80	250
2a	18 800	269	1000	5.8	3100
2b	18 800	269	0.5	7.9	1700
3	18 800	269	1000	2.9	3100
4	34 900	332	1000	2.9	4200

Several important assumptions were made to simplify the mathematical model for studying the general problems of shock-bubble interaction. One of the key assumptions is the neglect of compressibility of the water surrounding the bubble. The problem hence became amendable to solutions by the boundary element method, which is computationally much more efficient. In other words, it was assumed that the dynamic response of the bubble to an impinging shock wave was mainly inertia controlled. Another assumption in the formulation was related to the effects of internal shock waves in the bubble. These effects were neglected in the current approach, since they were thought to be of secondary importance. The boundary element formulation inherently accounted for these simplifications, and when compared with other methods such as the Free Lagrange Method (FLM) or the Arbitrary Lagrangian Eulerian Formulation (ALE), it shows a phenomenal reduction in terms of computational time and effort (our BEM simulations typically take 10 seconds as compared to a few days for FLM and ALE). The efficacy and accuracy of the proposed approach were compared with cases reported by Jamaluddin [9] using a FLM method and Ding and Gracewski [10] who used an ALE method. Bubble shapes, collapse times and jet velocities all showed very reasonable agreement for a wide range of parameters such as bubble radii, shock strengths and shock widths.

References

[1] Leighton, T., *The Acoustic Bubble*. Academic Press/The University Press: Cambridge, United Kingdom, 1994.

[2] Ball, G.J., Howell, B.P., Leighton, T.G. & Schofield, M.J., Shock-induced collapse of a cylindrical air cavity in water: A free-lagrange simulation. *Shock Waves*, **10**, pp. 265–276, 2000.

[3] Bourne, N.K., On the collapse of cavities. *Shock Wave*, **11**, pp. 447–455, 2002.

[4] Bourne, N.K. & Field, J.E., Shock-induced collapse and luminescence by cavities. *Philosophical Transactions of The Royal Society of London A*, **357**, pp. 295–311, 1999.
[5] Kalumuck, K.M., Chahine, G.L., Frederick, G.S. & Aley, P.D., Development of high erosity cavitating and acoustically enhanced water jets for well scale removal. *10th American Waterjet Conference*, Houston, Texas, 1999. Paper 61.
[6] Coleman, A.J., Saunders, J.E., Crum, L.A. & Dyson, M., Acoustic cavitation generated by an extracorporeal shock-wave lithotripter. *Ultrasound in Medicine & Biology*, **13**, pp. 69–76, 1987.
[7] Kodama, T. & Takayama, K., Dynamic behaviour of bubbles during extracorporeal shock-wave lithotripsy. *Ultrasound in Medicine & Biology*, **24(5)**, pp. 723–738, 1998.
[8] Bourne, N.K. & Field, J.E., Shock-induced collapse of single cavities in liquids. *Journal of Fluid Mechanics*, **244**, pp. 225–240, 1992.
[9] Jamaluddin, A.R., *Free-Lagrange Simulations of Shock-Bubble Interaction in ESWL*. Ph.D. thesis, School of Engineering Sciences, University of Southampton, United Kingdom, 2004.
[10] Ding, Z. & Gracewski, S.M., The behaviour of a gas cavity impacted by a weak or strong shock wave. *Journal of Fluid Mechanics*, **309**, pp. 183–209, 1996.
[11] Best, J.P., The formation of toroidal bubbles upon the collapse of transient cavities. *Journal of Fluid Mechanics*, **251**, pp. 79–103, 1993.
[12] Zhang, Y.L., Yeo, K.S., Khoo, B.C. & Chong, W.K., Three-dimensional computation of bubbles near a free-surface. *Journal Computational Physics*, **146**, pp. 105–123, 1998.
[13] Tomita, Y., Robinson, P.B., Tong, R.P. & Blake, J.R., Growth and collapse of cavitation bubbles near a curved rigid boundary. *Journal of Fluid Mechanics*, **466**, pp. 259–283, 2002.
[14] Blake, J.R., Taib, B.B. & Doherty, G., Transient cavities near boundaries: Part 2. free surface. *Journal of Fluid Mechanics*, **191**, pp. 197–212, 1987.
[15] Ramachandran, P.A., *Boundary Element Methods in Transport Phenomena*. WIT Press: Canada, US, 1993.
[16] Marsh, S., *LASL Shock Hugoniot Data*. University of California Press: United States of America, 1980.
[17] Ball, G.J., A free-lagrange method for unsteady compressible flow: simulation of a confined cylinder blast wave. *Shock Waves*, **5**, pp. 311–325, 1996.
[18] Jamaluddin, A.R., Turangan, C.K., Ball, G.J. & Leighton, T.G., Free lagrange simulations of the jetting collapse of air bubbles with application to extracorporeal shock wave lithotripsy. *Proceedings of Royal Society of London A*. In preparation.

Section 3
Flow in porous media

This page intentionally left blank

Multilevel adaptive modeling of multiphase flow in porous media

H. Gotovac, R. Andričević, B. Gotovac, M. Vranješ & T. Radelja
Department of Civil and Architectural Engineering, University of Split, Croatia

Abstract

Multiphase flow in porous media is characterized by zones of sharp gradients that include the development of sharp interfaces and narrow transition zones. Numerical modeling of these problems usually shows difficulties in resolving all space and temporal scales, numerical oscillations and artificial dispersion and obviously needs a demanding computational request with very fine grid and small time steps. Adaptive numerical modeling is one of the most promising options. In the last decade adaptive collocation methods have become very popular due to using a highly localized basis functions as wavelets or splines. In this paper we present the lesser-known localized Fup (**F**inite **up** function) basis functions with compact support and **A**daptive **F**up **C**ollocation **M**ethod (AFCM) appropriate for application to multiphase flow problems in porous media. The numerical procedure is designed through a well-known method of lines (MOL). Space discretization and grid adaptation are obtained by Fup collocation transform and corresponding adaptive strategy, while time integration is reduced to a solving system of differential-algebraic equations. Furthermore, the method enables an adaptive multilevel evolution of a solution with all resolved spatial and temporal scales and desired level of accuracy using the whole family of Fup basis functions. The numerical method is tested and verified with classic Buckley-Leverett 1-D multiphase flow problem in porous media.
Keywords: atomic functions, Fup basis functions, method of lines, adaptive collocation method, multiresolution approach, multiphase flow in porous media.

1 Introduction

Many physical and engineering problems exhibit a wide range of space and/or temporal scales. Moreover, lot of variables associated to these problems show

variability and/or different time/space scales through transient simulation of processes or a variety of types of intrinsic heterogeneity. One of the most demanded examples in water resources includes unsaturated and multiphase flow problems among many others. These examples are characterized by zones of sharp gradients that include the existence of sharp interface and narrow transition zones.

Numerical modeling of such processes (e.g. Class et al., [1]) usually shows difficulties resolving numerical oscillations and dispersion and obviously requires a huge computational effort with very fine mesh or grid and small time steps. In modern numerical analysis there is a development of adaptive methods which possess the property of accurate description of very fine space and time scales with a low computational cost. The wavelet adaptive methods of Galerkin (e.g. Beylkin and Keiser, [2]; Chiavassa et al., [3]) and collocation type (e.g. Bertoluzza, [4]; Vasilyev and Paolucci, [5]; Hesthaven and Jameson, [6]; Holmstrom, [7]; Vasilyev and Bowman, [8]; Cruz et al., [9]), among others, deserve special attention. The Galerkin wavelet oriented methods have three potential difficulties: treatment of boundary conditions, handling nonlinearities and solving problems with complex domains.

The main feature of wavelets is to ease the possibility of grid space adaptation and multiresolution data compression. It enables solving problems with a sharp interface and narrow transition zone which change their locations and steepness in time and space. This demands the use of non-uniform grids that dynamically adapt to the changes in solution. Any function, signal or data values can be represented by the linear combination of basis functions in multiresolution fashion with different scales/frequencies and locations. It means that specific frequencies are associated with a particular space interval that is not possible in classic Fourier transform.

Instead of wavelet basis functions, it is possible to use any other functions with compact support (non-zero values only in one part of the domain) in the proposed collocation method (Vasilyev and Paolucci, [5]). There is also the usage of the spline adaptive collocation method (for instance Ramachandran and Duduković, [10]; Bhattacharya and Joseph, [11]; Wang et al., [12]). With the exception of wavelets and splines, there is a relatively little known class of atomic or R_{bf} basis functions (Rvachev's basis functions, Rvachev and Rvachev, [13]; B. Gotovac, [14]). R_{bf} or atomic functions are classified between classic polynomials and spline functions. However, in practice, their application as basis functions is still closer to splines or wavelets. Procedures for calculation of function values are given by B. Gotovac and Kozulić [15], together with an illustration of basic possibilities for their application in practice. Recently, an application of Fup basis functions has been shown (one type of atomic basis functions) in signal processing (for instance Kravchenko et al., [16]; Zelkin et al., [17]), for initial value problems (B. Gotovac and Kozulic, [18]) and in the non-adaptive collocation method for boundary value problems (Kozulic and B. Gotovac, [19]; H. Gotovac et al., [20]).

The main objective of this paper is to establish the Fup adaptive approach and show the basic application to multiphase flow problems. The numerical

procedure is designed through a well-known method of lines (MOL). Space discretization and grid adaptation on the dyadic grid are obtained by the Fup collocation transform, differentiation is solved with the classical finite difference operator, while time integration is reduced to the solving system of DAE equations with the appropriate method that depends on stiffness of the problem. Algebraic equations are corresponding to boundary conditions and differential equations are related to differential equations of the considered problem. This method uses the whole family of $Fup_n(x)$ basis functions so that the Fup order is closely related to the order of the finite difference operator. Furthermore, this method enables adaptive multiresolution evolution of solution with all resolved spatial/temporal scales and the desired level of accuracy. The numerical method is tested and verified with the classic 1-D Buckley – Leverett problem.

2 Fup basis functions

Atomic or Rvachev's basis functions - R_{bf} have a compact support and they are infinitely derivable functions (B. Gotovac and Kozulic, [15]). They are classified between classical polynomials and spline functions, but in practice their application as basis functions is closer to splines and also wavelets.

Atomic functions are defined as finite solutions of differential-functional equations of the following type:

$$Ly(x) = \lambda \sum_{k=1}^{M} C_k \, y(ax - b_k) \tag{1}$$

where L is a common linear differential operator with constant coefficients, λ is a scalar different than zero, C_k are solution coefficients, $a>1$ is a parameter of the length of finite function support, b_k are coefficients which determine displacements of finite basis functions.

The simplest and most studied among atomic basis functions is the up(x) function (Fig. 1a). Function up(x) is a smooth function with the compact support [-1,1], which can be expressed in an integral form:

$$up(x) = \frac{1}{2\pi} \int_{-\infty}^{\infty} e^{itx} \prod_{j=1}^{\infty} \left(\frac{\sin(t\,2^{-j})}{t\,2^{-j}} \right) dt \tag{2}$$

The above expression can also be considered as inverse Fourier transform. Eqn (2) is not suitable for calculation of function up(x) values. B. Gotovac and Kozulic [15] provided an improved expression for calculation of function up(x) values in an arbitrary point $x \in [0,1]$ in the following form:

$$up(x) = 1 - \sum_{k=1}^{\infty} (-1)^{1+p_1+\ldots+p_k} \; p_k \sum_{j=0}^{k} C_{jk}(x-0, p_1 \ldots p_k)^j \tag{3}$$

where coefficients C_{jk} are rational numbers determined according to the following expression:

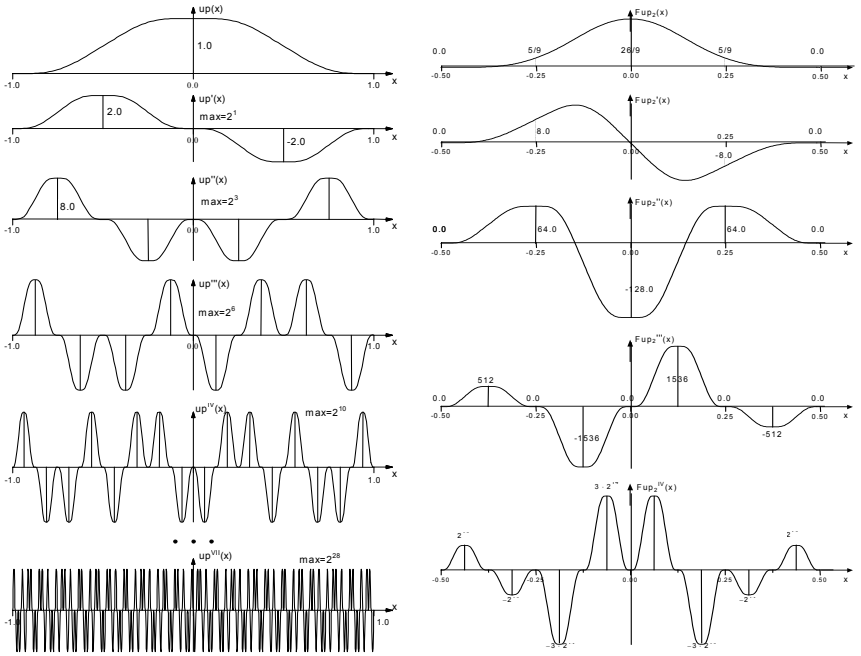

Figure 1: Left, function up(x) and its first four and the seventh derivative; right**,** function $Fup_2(x)$ and its first four derivatives.

$$C_{jk} = \frac{1}{j!}\, 2^{j(j+1)/2}\, up\left(-1+2^{-(k-j)}\right);\ \mathbf{j = 0,1,\ldots,k} \qquad \mathbf{k = 1,2,\ldots,\infty} \tag{4}$$

Expression *(x-0, p_1 ... p_k)* in Eqn (3) is the difference between the real value of coordinate *x* and its binary form with *k* bits, where p_1 ... p_k are the digits 0 or 1 of the binary development of the coordinate *x* value. Therefore, the accuracy of coordinate *x* computation, and thus the accuracy of up(x) function in an arbitrary point, depends upon the accuracy of a computer. In binary-rational points, the up(x) values are calculated exactly in the form of a rational number. Those points of the function up(x) support we called characteristic points.

From (1) it can be concluded that the derivatives of the function up(x) can be calculated simply from the values of the function itself. The general expression for the derivative of the *m*-th degree is:

$$up^{(m)}(x) = 2^{C_{m+1}^2} \sum_{k=1}^{2^m} \delta_k\, up(2^m x + 2^m + 1 - 2k)\,,\ m \in N \tag{5}$$

where $C_{m+1}^2 = m(m+1)/2$ is the binomial coefficient and δ_k are the coefficients of value ± 1 which determine the sign of each term. They change according to the following recursive formulas:

$$\delta_{2k-1} = \delta_k \ , \ \delta_{2k} = -\delta_k \ , \ k \in N \ , \ \delta_1 = 1 \tag{6}$$

Figure 1a shows the up(x) function and its derivatives. It can be observed that the derivatives consist of the up(x) function compressed to the interval of length 2^{-m+1} and with ordinates ″extended″ with the factor $2^{C^2_{m+1}}$.

Functions $Fup_n(x)$ can be defined as finite solutions of differential functional equations, similarly as function up(x) (Eqn. 1). These functions are used in this paper as basis functions. The best way for calculating functions $Fup_n(x)$ is that we represent them in the form of a linear combination of displaced up(x) functions. $Fup_n(x)$ functions and their derivatives retain the properties of up(x) functions, but they are more suitable for numerical analyses. Index *n* denotes the greatest degree of a polynomial which can be expressed accurately in the form of the linear combination of basis functions obtained by displacement of the $Fup_n(x)$ function by a characteristic interval 2^{-n}.

$$Fup_n(x) = \sum_{k=0}^{\infty} C_k(n)\ up\left(x - 1 - \frac{k}{2^n} + \frac{n+2}{2^{n+1}}\right) \tag{7}$$

where coefficient $C_0(n)$ is:

$$C_0(n) = 2^{C^2_{n+1}} = 2^{n(n+1)/2} \tag{8}$$

and other coefficients of linear combination in (7) are determined as $C_k(n) = C_0(n) \cdot C'_k(n)$, where a recursive formula is used for calculation of auxiliary coefficients $C'_k(n)$:

$$\begin{aligned} &C'_0(n) = 1 \ , when \ \ k = 0; \ \ i.e. when \ \ k > 0 \\ &C'_k(n) = (-1)^k C^k_{n+1} - \sum_{j=1}^{min\left\{k\,;\,2^{n+1}-1\right\}} C'_{k-j}(n) \cdot \delta_{j+1} \end{aligned} \tag{9}$$

Fig. 1b shows the $Fup_2(x)$ function and its first four derivatives. It can be observed that intervals of the third derivative (n+1) correspond to the compressed up(x) function.

3 Fup collocation transform

Fup collocation transform (FCT) is a very efficient numerical tool for describing various type of signals, functions or data collection by linear combination of the Fup basis functions. It is a discrete type of transform related to the classic discrete Fourier transform where coefficients of linear combination are called Fup or "Fourier" coefficients. Classic discrete Fourier transform (DFT) presents any signal by linear combination of basis functions with a different frequency. Each frequency is quantified with a particular Fourier coefficient. The frequency domain can show what range of frequencies mainly present the chosen signal. However, the main disadvantage of DFT lies in the unresolved location of

important frequencies due to non–localized properties of the classic trigonometric basis functions. This essential problem of classic DFT becomes a natural advantage of transform designated by basis function with compact support. It means that specific frequencies are associated with a particular space interval that is not possible in the classic Fourier transform. Fup coefficients are associated with a specific resolution level (length of the compact support is called scale or frequency) and point in space domain.

This procedure is also well known as multiresolution analysis (MRA). This transform is obtained through the collocation procedure and therefore called Fup collocation transform. The great efficiency of FCT lies in the property of transform that keeps only significant Fup coefficients that accurately describe the chosen function. Other Fup coefficients present residual between function and their Fup presentation that is less than the prescribed threshold. In this way, we decompose any function in multiresolution fashion by only few significant Fup basis functions with appropriate scales (frequencies) and locations with the desired level of accuracy and at near minimal computational cost.

The multilevel expansion of function *u(x)* can be expressed in the following way:

$$u(x) = \sum_{j=0}^{J\to\infty} \sum_{k=-n/2}^{(2^{j\min+j}+n/2)} d_k^j \varphi_k^j(x) \tag{10}$$

where j shows the resolution level from the chosen minimal j_{min} to maximal level J needed for Fup presentation (10) with a desired level of accuracy defined by threshold ε, n is Fup order, d_k^j are Fup coefficients, φ_k^j are Fup basis functions and k denotes the index of the collocation point in the current level. We consider a set of dyadic grids:

$$G^j = \left\{ x_k^j \in R : x_k^j = 2^{-j} k, k \in Z \right\} \quad , \quad j \in Z \tag{11}$$

where x_k^j are the grid collocation points. Each level has the 2^j+1 collocation points, 2^j+1 internal and n external Fup basis functions, respectively. Every internal basis function is associated with a corresponding internal collocation point, while external basis functions are associated to boundary collocation points.

Level G^{j+1} has nearly two times more collocation points than the previous level G^j. Note that even numbered collocation point of G^{j+1} already exists in G^j $(x_{2k}^{j+1} = x_k^j)$. It implies that the relation $G^j \subset G^{j+1}$ is valid. The example of a dyadic grid is presented in Fig. 2. If a grid contains all possible points (Fig. 2), it is a regular grid. The grid is the irregular grid if at least one collocation point at any resolution level is omitted. If we define the domain $\Omega = [X_1, X_2]$, then the characteristic interval is equal to the distance between adjacent collocation points:

$$\Delta x_j = \frac{X_2 - X_1}{2^j} \tag{12}$$

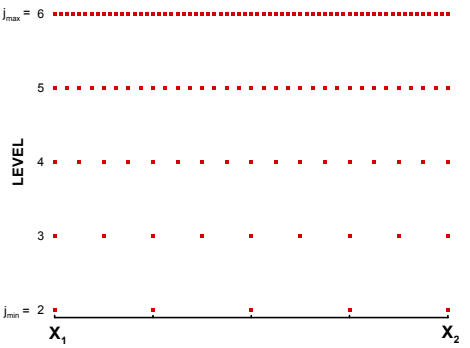

Figure 2: Example of the dyadic grid.

The location of each basis function is actually presented by the location of the vertexes of the basis function and defined by $b_k^j = X_1 + k\Delta x_j$. Calculation of basis function values should be done in the following way:

$$\varphi_k^j(x) = Fup_n\left(\frac{x - b_k^j}{2^n \Delta x_j}\right) \tag{13}$$

Note that higher levels include smaller scales or higher frequencies, which represent properties of the chosen function only in the sensitive zones that will be discussed below. The grid is completely defined with the chosen parameters: j_{min}, X_1, X_2, n and ε. The influence of the threshold ε depends on the collocation procedure. For example, we consider the test function:

$$f(x) = -\tanh\left(\frac{x - 2/3}{0.02}\right) \tag{14}$$

For illustrative purposes we choose the relatively high threshold $\varepsilon=0.07$. Other parameters are $j_{min}=2$, $X_1=0$, $X_2=2$ and $n=4$. Zero level is the coarsest level that is always present in the grid and corresponding to the $j_{min}=2$.

The key step of the FCT is the transfer from the current level to the next level. Firstly, we set all possible collocation points in the next level according to Eqn (11) and Fig. 3 and check the residual between true function and approximation from the previous levels. For even collocation points residual is zero and these points are rejected from the grid. For odd collocation points residual is nonzero and we reject only the points where the residual is less than the prescribed threshold. Each kept point must be surrounded with $n+2$ basis functions that enable consistent approximation for transfer to the next possible level. It means that for each kept point we should add $n+2$ additional closest points. Furthermore, if points near the boundary are present in the grid, external basis

functions should be added. All these points are called basic collocation points and are presented in Fig. 4 for test function (14).

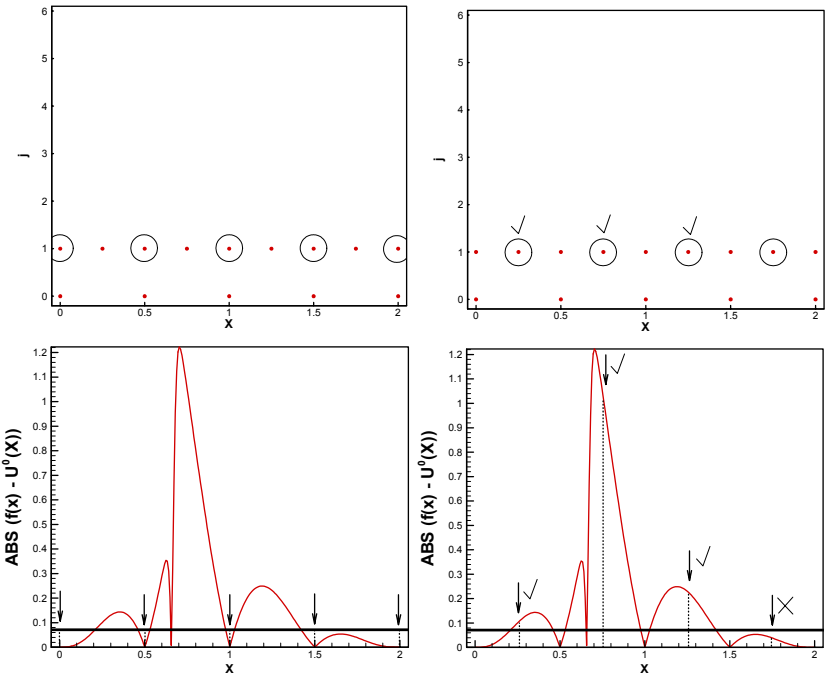

Figure 3: Adaptive selection of collocation points of the first level.

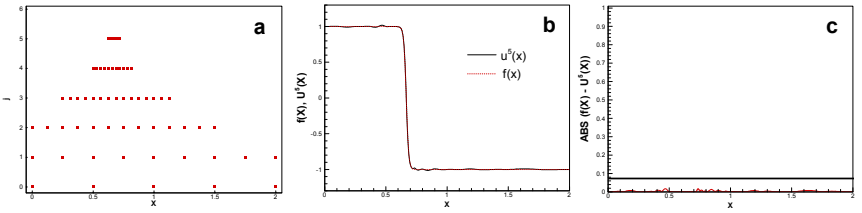

Figure 4: a) adaptive collocation grid, b) function (14) and their Fup presentation and c) difference between function and Fup approximation.

It means that Figure 4 shows the multilevel approximation to a maximum of five levels. Obviously, higher levels include only higher frequencies and a more detailed description of the chosen function. Collocation points are added only in the front region where the residual from the previous level is greater than the prescribed threshold. Eventually, the residual between true function and five level approximations is less than the threshold within the whole domain. In this way, we decompose any function in multilevel fashion by only a few significant

Fup basis functions with appropriate scales (frequencies) and locations with a desired level of accuracy and at near minimal computational cost.

4 Fup adaptive collocation method

In this section we present the adaptive Fup collocation method (AFCM) and its main properties. Generally, the main feature of this method lies in adaptive change of the grid during the time. In that way, the grid follows all changes of the solution resolving all spatial and temporal scales. It enables the very efficient modeling of problems with layers, fingers, sharp interfaces or narrow transition zones that exhibit a wide range of different spatial and temporal scales during the time evolution. Moreover, due to the simple nature of the collocation method, the handling of nonlinearities and general boundary conditions are straightforward tasks. The adaptive approach also enables getting the solution with the desired accuracy and low computational cost.

The adaptive Fup collocation method is designated through the well-known method of lines (MOL). It means that space and time evolution of the solution are divided. After every chosen time step space discretization on dyadic grid is obtained by Fup collocation transform and the corresponding adaptive strategy. Time integration is reduced to solving the system of differential-algebraic equations (DAE) written in general form suitable for groundwater flow and transport problems:

$$A(t,u)\frac{\partial u}{\partial t} = F\left(t,x,u,u^{(m)}\right) \tag{15}$$

$$0 = G\left(t,x,u,u^{(m)}\right) \tag{16}$$

where u is the solution, m is derivative order, and A, F and G are linear or nonlinear operators depending on the considered groundwater problem. Eq. (15) represents time–dependent partial differential equations which describe the time evolution of the solution while Eq. (16) presents boundary conditions (Dirichlet, Neumann or Chauchy mixed type). Algebraic equations are corresponding to boundary conditions and differential equations are related to partial differential equations of the considered problem.

The numerical algorithm consists of three basic steps, which will be explained below in detail:

1. The grid adaptation procedure that dynamically changes the grid.
2. The calculation of spatial derivatives that enables writing the DAE system (15-16) in the general form suitable for numerical time integration.
3. The performance of time integration with obtained non–uniform multilevel grid and adaptive time step – dt.

4.1 Adaptive strategy

The grid adaptation strategy consists of the next steps:

1. Knowing the functions' values from initial data or previous time step to perform the Fup collocation transform (FCT). In that way we get the basic grid required for Fup function presentation with the desired accuracy that is defined by threshold ε.
2. For each basic point x_k^j we add a specific number of points left and right at the same level $\left(x_{k+i}^j,\ i=-N_L,...,N_R\right)$. These points are included to guarantee an accurate approximation of a possible movement of sharp solution features (Fig 5a, $N_L = N_R = 2$).
3. For each basic point x_k^j we add points at the specific number of higher levels $\left(x_{2^l\left(k-N_L^U\right)-2^l+1}^{j+l},...,x_{2^l\left(k+N_R^U\right)+2^l-1}^{j+l},\ l=1,...,M\right)$. Note that N_L^U and N_R^U must be less or equal to N_L and N_R, respectively, because it is impossible to add points in the higher levels without the existence of corresponding points in the lower levels. These points are included to guarantee accurate approximation if the solution becomes steeper in this part of the domain (Fig 5b, $N_L^U = N_R^U = M = 1$). All additional points are shown in Fig. 5c.
4. Basic and additional points create the total grid.
5. If there are more dependent variables, we find the total grid for all variables as the union of all particular grids.
6. The effective grid is constructed from the total grid in the following way. All collocation points at the zero level are kept. At the other levels only odd numbered collocation points are kept. It makes it possible that the effective grid does not have more collocation points at the same location by levels, which is not consistent for the time integration algorithm. Note that cardinal basis functions make it possible that total and effective grids are the same. This procedure reduces the number of collocation points (approximately 50% for 1 – D, but 25% for 2 – D and only 12.5% for 3 – D problems, respectively).

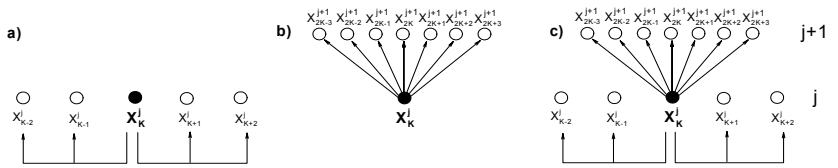

Figure 5: Additional points at the same level (a), level above (b) and at the same and above level (c).

4.2 Calculation of spatial derivatives

Time integration algorithm (DAE system 15 – 16) required many calculations of spatial derivatives on an adaptive grid in operators *F* and *G*. An efficient

algorithm needs fast and accurate calculation of spatial derivatives from function values at collocation points. Generally, there are two different approaches:

1. Find the derivatives using Fup collocation transform on an adaptive grid (Vasilyev and Paolucci, [5]).
2. Find the derivatives using finite difference differentiation on an adaptive grid (e.g. Jameson, [21], Cruz et al., [9]).

The first approach uses Fup basis functions for all actions: compression, interpolation and differentiation. Unfortunately, this consistent approach is too slow, especially for nonlinear problems and higher dimensions. The second approach requires the finite difference differentiation. We construct here the classical finite difference operator on an adaptive non–uniform grid. It enables that for adaptive time step Δt and non–uniform grid write equations (15 – 16) in the general form.

4.3 Time integration

Time integration is reduced to solving the system of the differential – algebraic equations (16 – 16) with initial conditions from initial data or previous time step. System (15 – 16) changes after every grid adaptation. Adaptation strategy directly influences the size of the time step that represents the time increment while grid remains unchanged. The basic hypothesis behind the algorithm, during the time step Δt, is that the solution does not move outside the border of the adapted non–uniform grid.

If we apply the collocation procedure to system (15 – 16), then we obtain a discrete form of DAE system of equations which can be solved by public domain subroutine DASPK (Li and Petzold, [22]). It uses the implicit Petzold - Gear (BDF) method with variable order (up to the fifth order) and step size (Acsher and Petzold, [23]). The routine is appropriate for systems of stiff equations, and attempts to keep the global error proportional to a user-specified tolerance. This tolerance should be smaller by few orders than threshold ε because we want to keep global numerical accuracy closely related to the space approximation error. Note that Jacobian is numerically evaluated.

5 Buckley – Leverett problem

The Buckley – Leverett problem arises from the analysis of the multiphase flow which is especially important in the oil industry. In that case we consider the two-phase flow of water and oil. Oil production is a very complex process in which numerical modeling can play a key role. The usual stimulation method consists of water injection into surrounded wells that pushes oil under pressure to the production well. Since water and oil are immiscible fluids, it is necessary to solve a motion of saturation interface between water and oil. The problem is solved with respect to water saturation. Phase saturation is generally defined as the ratio of phase volume and total volume. In certain cases, it is possible to consider the three-phase flow of water, oil and gas.

The Buckley – Leverett problem describes one of the simplest multiphase flow examples. The complexity of these processes lies in the complicated interaction between two fluids at the microscopic scale which is caused by gradient pressure fluctuations. The problem is described by the following non-dimensional saturation equation:

$$\frac{\partial s^*}{\partial t}+\frac{\partial F\left(s^*\right)}{\partial x}=\upsilon\frac{\partial}{\partial x}\left(G\left(s^*\right)\frac{\partial s^*}{\partial x}\right) \tag{17}$$

and related functions are defined by:

$$F\left(s^*\right)=\frac{s^{*2}}{s^{*2}+\left(1-s^*\right)^2} \tag{18}$$

$$G\left(s^*\right)=4s^*\left(1-s^*\right) \tag{19}$$

since domain, initial and boundary conditions are:

$$\upsilon=0.01; x\in[0,1] \tag{20}$$

$$s^*(x,0)=\begin{Bmatrix}1-3x, & 0\le x\le 1/3\\ 0, & drugdje\end{Bmatrix} \tag{21}$$

$$s^*(0,t)=1; \frac{\partial s^*(1,t)}{\partial x}=0 \tag{22}$$

where s^* is non-dimensional water saturation, t and x are non-dimensional space and time coordinates, while $F(s^*)$ is a function which shows flow ratio between two phases.

The problem is characterized by strong nonlinearities and a narrow saturation front. Moreover, the DAE system (15-16) is very stiff and requires small time steps. There is no analytic solution, but numerically the problem is solved by Kurganov and Tadmor [24] and Alves et al. [25] who used the high resolution finite difference scheme. The adaptive algorithm uses next parameters: $N_L=N_R=2$, $N_L^U=N_R^U=2$, $M=1$, $n=4$, $\varepsilon=10^{-4}$, $j_{\min}=4$.

Figure 6 shows the multilevel adaptive solution of the moving saturation front. Initial conditions are relatively simple, except one point where the saturation front has derivative discontinuity. It is the reason why we need five levels for this simple bilinear function.

At the early stages of the process the saturation front moves very slowly since at approximately $t = 0.1$ reaches final steepness and sharpness with eight levels and nearly 200 collocation points (Fig. 7). Furthermore, front travels with variable velocity and around the same number of points.

This example clearly presents the ability of the method to handle such strong nonlinear problems and a narrow saturation front which changes sharpness and location both in space and time. The adaptive grid dynamically follows all solution changes and shows a wide range of all space and time scales that characterize these complex problems.

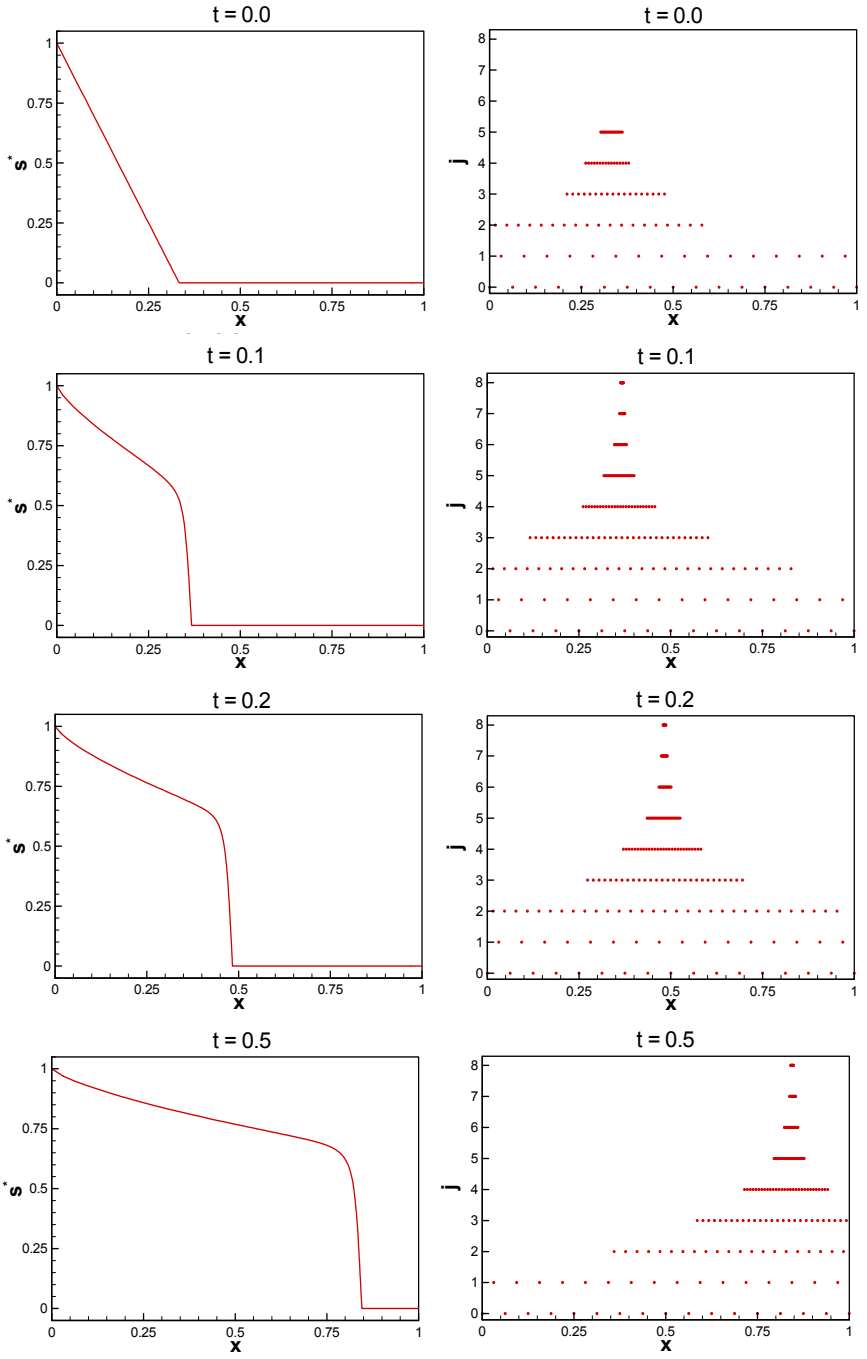

Figure 6: Saturation front (left) and adaptive grid (right).

Efficiency of the method is usually described by the compression coefficient that is defined as the ratio between the number of collocation points in the non-adaptive and adaptive algorithms. Namely, the non-adaptive algorithm requires all points in the maximum level which is needed for the same accurate solution in comparison with the described adaptive algorithm. Figure 7 shows the values of the compression coefficient during this time. Mostly, the compression coefficient is about twenty which shows the elegancy and robustness of the proposed method.

The method is tested and verified in Figure 8 by comparison at $t = 0.2$ between the solution of AFCM and Kurganov and Tadmor [24]. Figure 8 shows practically perfect similarities between the two solutions. The AFCM solution is free of numerical oscillation, while classic numerical dispersion is reduced to a negligible level and related to the prescribed threshold.

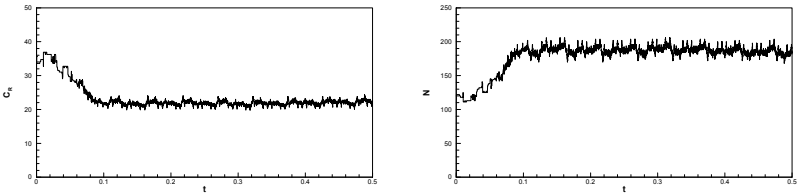

Figure 7: Compression coefficient (left) and number of collocation points through simulation time (right).

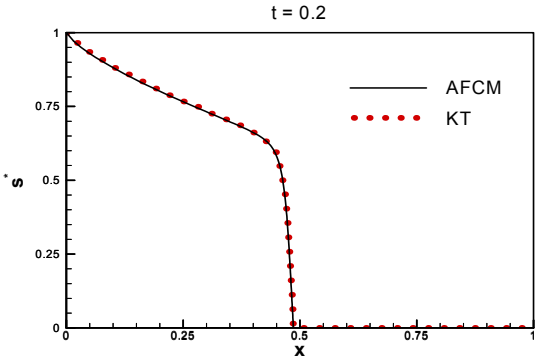

Figure 8: Comparison between AFCM and Kurganov and Tadmor [24].

6 Conclusions

Many physical and engineering problems exhibit a wide range of space and temporal scales. Water resources examples include multiphase flow, density driven flow and transport, reactive transport, thermal convective problems or turbulent flow among many others. All examples are characterized with zones of sharp gradients that include the development of fingering and layering and the

existence of sharp interfaces and narrow transition zones. One of the most demanding examples mentioned is multiphase flow. Numerical modeling of multiphase flow usually shows difficulties in resolving numerical oscillations and artificial dispersion and obviously needs a demanding computational request with a very fine mesh or grid and small time steps.

The main objective of this paper is to establish the Fup adaptive approach and show its application to multiphase flow problems. The numerical procedure is designed through the well-known method of lines (MOL). Space discretisation and grid adaptation on the dyadic grid is obtained by the Fup collocation transform, differentiation is solved with the classical finite difference operator, while time integration is reduced to the solving system of DAE equations with the appropriate method that depends on the stiffness of problem. The method enables adaptive multilevel evolution of solution with all resolved spatial and temporal scales and the desired level of accuracy using the whole family of the Fup basis functions. The numerical method is tested and verified on the classic 1-D Buckley – Leverett problem.

References

[1] Class, H., Helmig, R., Bastian, P., Numerical simulation of non-isothermal multiphase multicomponent processes in porous media. 1. En efficient solution technique, Advances in Water Resources, 25, 553-590, 2002.

[2] Beylkin, G., Keiser, J.M., On the Adaptive Numerical Solution of Nonlinear Partial Differential Equations in Wavelet Bases, Journal of Comp. Physics, 132, 233-259, (1997).

[3] Chiavassa, G., Guichaoua, M., Liandrat, J., Two adaptive wavelet algorithms for nolinear parabolic differential equations, Computers & Fluids, 31, 467-480, 2002.

[4] Bertoluzza, S., Adaptive wavelet collocation method for the solution of Burgers equation, Transport Theory and Statistical Physics, 25, 339-352, 1996.

[5] Vasilyev O.V., & Paolucci S., A fast adaptive wavelet collocation algorithm for multidimensional PDEs. Journal of Computational Physics, 125, 16-56, 1997.

[6] Hesthaven, J.S., Jameson, L.M., A wavelet Optimized Adaptive Multi – domain method, Journal of Comp. Physics, 145, 280-296, 1998.

[7] Holmstron M., Solving hyperbolic PDEs using interpolation wavelets, Journal of Scientific Computing, 21, 405-420, 1999.

[8] Vasilyev O.V., Bowman, Second Generation wavelet collocation method for the solution of the partial differential equations, Journal of Computational Physics, 165, 660-693, 2000.

[9] Cruz, P., Mendes, A., Magalhes, F.D., Using wavelets for solving PDEs: and adaptive collocation method, Chemical Eng. Science, 56, 3305-3309, 2001.

[10] Ramachandran, P.A., Duduković, M.P., Solution by triple collocation for periodic operation of heat regenerators, Comp. & Chemical Eng., 8(6), 377-388, 1984.
[11] Bhattacharya, A., Joseph, B., Simulation of fixed – bad gas solid reactors using an adaptive spline collocation method, Comp. Chem. Eng., 12(4), 351-352, 1988.
[12] Wang, R., Keast, P., Muir, P., A High order global spatially adaptive collocation method for 1-D parabolic PDEs, Applied Num. Math, 50, 239-260, 2004.
[13] Rvačev V.L., Rvačev V.A., Pro odnu finitnu funkciju. DAN URSR. Ser. A, No. 6, 705-707, 1971.
[14] Gotovac B., Numerical modelling of engineering problems by smooth finite basis functions, PhD Theses, pp. 255, Zagreb, 1986 (in Croatian).
[15] Gotovac B., Kozulić V., On a selection of basis functions in numerical analyses of engineering problems, Int.J.Eng.Model. 12 (1-4), 25-41, 1999.
[16] Kravchenko V.F., Basarab, M.A., Perez-Meana, H., Spectral properties of atomic functions used in digital signal processing, Journal of Communications Technology and Electronics, 46, 494-511, 2001.
[17] Zelkin, E.G., Kravchenko, V.F., Basarab, M.A., Interpolation of signals with a Finite spectrum by Fourier tranforms of atomic functions and application of this interpolation to Antenna synthesis problems, Journal of Communications Technology and Electronics, 47, 413-420, 2002.
[18] Gotovac B., Kozulić V., Numerical solving the initial value problems by R_{bf} basis functions, Structural Engineering & Mechanics, 14(3), 263-285, 2002.
[19] Kozulić V., Gotovac, B., Numerical analysis of 2-D problems using Fup basis functions, Int. J. Eng. Mod., 13 (1-2), 7-18, 2000.
[20] Gotovac H., Andričević R., Gotovac B., Kozulić V., Vranješ M., An improved collocation method for solving the Henry problem, Journal of Contaminant Hydrology 64, 129-149, 2003.
[21] Jameson, L.M., A Wavelet-optimized, very high order adaptive grid and order numerical method, Siam J. Sci. Comp, 19(8), 1980-2013, 1998.
[22] Li S., Petzold, L., Design of new DASPK for sensitivity analysis, Internet communication, 2004.
[23] Ascher, U., Petzold, L., Computer Methods for Ordinary Differential Equations and Differential-Algebraic Equations, Society for Industrial and Applied Mathematics, Berkeley, 297 p., 1998.
[24] Kurganov, A., Tadmor, E., New high resolution central scheme for nonlinear conservation laws and convection-diffusion equations, Journal of Comp. Physics, 160, 241-282, 2000.
[25] Alves, M.A., Cruz, P., Mendes, A., Magalhes, F.D., Pinho, F.T., Oliviera, P.J., Adaptive multiresolution approach for solution of hyperbolic PDE's, Comp. Methods. Appl. Mech. Eng., 191, 3909-3928, 2002.

A three-dimensional finite element method for simulating gas and water two-phase flow induced by excavation in sedimentary rock

H. Li[1], P. G. Ranjith[2], Y. Narita[1], Y. Kawahara[1] & M. Sato[1]
[1]*Geoscience Research Laboratory, Kanagawa, Japan*
[2]*Department of Civil Engineering, Monash University, Australia*

Abstract

This paper describes the developed software MGF2 (Mine Gas Flow 2-Phase)-3D and its applications. Based on the finite element method on two-phase seepage flow like methane gas and underground water, MGF2 has been mainly applied to simulate the gas gushing problems for disaster prevention during coal mining and excavation processes in sedimentary rock for nuclear waste disposal. The partial differential simultaneous equations for two-phase permeable flow, sorption/diffusion formulations and their finite element discretization as well as two examples of practical application using MFG2 are described in this paper.
Keywords: two-phase flow, finite element method, three-dimensional, diffusion/adsorption.

1 Introduction

Nowadays, environmental and disaster-prevention problems are becoming more and more outstanding in the engineering of energy resources, coastal construction and nuclear waste underground disposal. Multiphase flow analysis [1] is also becoming more and more important in the environmental remediation of soil and subsurface water pollutions, coal seam gas extraction, carbon dioxide geo-sequestration, etc. The projects to simulate and predict gas coupled with water permeable flow phenomena induced by excavation in sedimentary rock are increasing. In China, coal, the mining and consumption of which are bringing large quantities of greenhouse gas to the atmosphere, is unfortunately by far the main primary energy resource, which makes it an urgent need to enhance the coal bed methane production as the most reliable means to reform current energy

structure in this largest developing country. In Japan, prominent budgets for the research and development of carbon dioxide geological and coal-seam sequestration are known. So far, although there are a few simulators on multiphase flow within the above fields, e.g., TOUGH2 [2], GEM [3], COMET [4], they are all based on the finite difference or finite volume method. It is not only scholarly significant but also of commercial potential from the point of domestic technical support and simulation consultancy to develop a simulator based on the finite element method.

2 Fundamental theory on the two-phase flow

2.1 The domination simultaneous equations of water and gas two-phase flow

In order to grasp the behaviour of subsurface co-existing gas and water in the gas phase and liquid phase respectively, the simulation should be carried out on the basis of not separately and singly dominant equations, but simultaneously coupled dominant equations with consideration of mechanical and physical interaction between the two gas and water phases.

$$\nabla\cdot\left[b_g\frac{k_g}{\mu_g}\kappa_{ij}\left(\nabla p_g+\gamma_g\nabla Z\right)+R_s\cdot b_w\frac{k_w}{\mu_w}\kappa_{ij}\left(\nabla p_w+\gamma_w\nabla Z\right)\right]+q_s+\left(q_g+R_s\cdot q_w\right)$$
$$=\frac{d}{dt}\left(\Phi b_g S_g+R_s\cdot\Phi b_w S_w\right) \tag{1}$$

$$\nabla\cdot\left[b_w\frac{k_w}{\mu_w}\kappa_{ij}\left(\nabla p_w+\gamma_w\nabla Z\right)\right]+q_w=\frac{d}{dt}\left(\Phi b_w S_w\right) \tag{2}$$

where

$\nabla\cdot$ is divergence operator of vector field;
∇ is gradient operator of scalar field;
b_n (n = g or w, i.e., gas or water) is flow shrinkage factor (-); $b=1/\beta$, where β is formation volume factor (-), which is the ratio of the volume (m^3) at a certain state V to that at the standard state V_s, i.e., $\beta=V/V_s$. Since V is the function of pressure, $\beta_n=\beta_n(p_n)$. So is b. $M_n=k_nK/\mu_n$ is phase mobility; $k_n\in[0,1]$ is phase relative permeability (-), which is the function of phase saturation;
$k_n\in[0,1]$ is phase relative permeability (-), which is the function of phase saturation;
K is abstract permeability tensor (m^2);
μ_n is phase viscosity (kg/m/sec).
p_g is pressure of gas (Pa);

p_w is pressure of water (Pa); the difference of pressure in the gas and water is called the capillary pressure dependent on the saturation of water or gas;

$\gamma_n = \rho_n \cdot g$, where $\rho_n = \rho_n(p_n)$ is phase mass density (kg/m^3) and g is gravitational acceleration (9.8 m/sec^2);

Z is elevation (m);

$R_s = R_s(p_w)$ is gas solubility (-) in water;

q is positive for a source or negative for a sink term with regard to gas (sm^3/m^3/sec); particularly in this paper, it will represent the diffusive flow rate of the desorbed methane from the microscopic primary porosity in the coal matrix to the macroscopic permeable natural cleat network [5];

Φ is the porosity effective for water or gas permeable flow and if necessary $\Phi = \Phi(p_w)$;

The phase saturation (-) must of course satisfy $S_g + S_w = 1$.

2.2 Finite element discretization

Discretizing Equation (1) and (2) by the Galerkin finite element method yields

$$\left[A_g\right]_{mk}\left\{p_g\right\}_k + \left[F_g\right]_{mk}\frac{\partial\left\{p_g\right\}_k}{\partial t} + \left[H_g\right]_{mk}\frac{\partial\left\{S_w\right\}_k}{\partial t} = \left\{Q_g\right\}_m - \left\{G_g\right\}_m + \left\{D_g\right\}_m + \left\{C_g\right\}_m \tag{3}$$

$$\left[A_w\right]_{mk}\left\{p_g\right\}_k + \left[F_w\right]_{mk}\frac{\partial\left\{p_g\right\}_k}{\partial t} + \left[H_w\right]_{mk}\frac{\partial\left\{S_w\right\}_k}{\partial t} = \left\{Q_w\right\}_m - \left\{G_w\right\}_m + \left\{D_w\right\}_m \tag{4}$$

where

$$\left[A_g\right]_{mk} = \sum_{e=1}^{N}\int_{V_e}\frac{\partial N_m}{\partial x_i}\left(\frac{k_{rg}}{\mu_g} + R_0\frac{k_{rw}}{\mu_w}\right)K_{ij}\left(\frac{p_g^{\nu,n+1}}{P_0}\right)\frac{\partial N_k}{\partial x_j}dV_e\ ;$$

$$\left[F_g\right]_{mk} = \sum_{e=1}^{N}\int_{V_e} N_m\left(\phi + p_g^{\nu,n+1}\beta_r\right)\left\{1 + (R_0 - 1)S_w^{\nu,n+1}\right\}\frac{1}{P_0}N_k dV_e\ ;$$

$$\left[H_g\right]_{mk} = \sum_{e=1}^{N}\int_{V_e} N_m\phi(R_0 - 1)\frac{P_g^{\nu,n+1}}{P_0}N_k dV_e\ ;$$

$$\left\{Q_g\right\}_m = \sum_{e=1}^{N}\int_{S_e} N_m\left(-u_g - R_0 u_w\right)_i n_i\left(\frac{p_g^{\nu,n+1}}{P_0}\right)dS_e\ ;$$

$$\left\{G_g\right\}_m = \sum_{e=1}^{N}\int_{V_e}\frac{\partial N_m}{\partial x_i}\left(\frac{k_{rg}}{\mu_g}\gamma_g + R_0\frac{k_{rw}}{\mu_w}\gamma_w\right)K_{i3}\left(\frac{p_g^{\nu,n+1}}{P_0}\right)dV_e\ ;$$

$$\{D_g\}_m = \sum_{e=1}^{N} \int_{V_e} N_m \left(q_g + R_0 \cdot q_w\right) dV_e \ ;$$

$$\{C_g\}_m = \sum_{e=1}^{N} \int_{V_e} N_m (q_s)\, dV_e \ ;$$

$$[A_w]_{mk} = \sum_{e=1}^{N} \int_{V_e} \frac{\partial N_m}{\partial x_i} \left(\frac{k_{rw}}{\mu_w}\right) K_{ij} \frac{\partial N_k}{\partial x_j} dV_e \ ;$$

$$[F_w]_{mk} = \sum_{e=1}^{N} \int_{V_e} N_m S_w \beta_r N_k dV_e \ ;$$

$$[H_w]_{mk} = \sum_{e=1}^{N} \int_{V_e} N_m \phi N_k dV_e \ ;$$

$$\{Q_w\}_m = \sum_{e=1}^{N} \int_{S_e} N_m \left(-u_w\right)_i n_i dS_e \ ;$$

$$\{G_w\}_m = \sum_{e=1}^{N} \int_{V_e} \frac{\partial N_m}{\partial x_i} \frac{k_{rw}}{\mu_w} \gamma_w K_{i3} dV_e \ ;$$

$$\{D_w\}_m = \sum_{e=1}^{N} \int_{V_e} N_m (q_w)\, dV_e \cdot$$

Additionally, the coefficient matrix of each time differential term needs to be diagonally concentrated.

Using the addition and subtraction method, the time differential terms with regard to saturation can be eliminated from (3) and (4) so that the pressure will be sought. The saturation can then be renewed by substituting the sought pressure into either (3) or (4).

2.3 Formulations of sorption/diffusion

In the case of coal bed gas extraction, e.g., methane adsorbed on the internal surface of the primary porosity will at first be desorbed and diffuse into the secondary fractures, then permeable flow occurs coupled with water [6, 7].

The source or sink term of gas adsorption/diffusion is

$$q_s^m = \rho_0 \cdot q_s = \rho_0 (1-\phi) \left(-\frac{\partial C}{\partial t}\right) \doteq \rho_0 (1-\phi) \frac{C^n - C^{n+1}}{\Delta t} = \rho_0 \frac{1-\phi}{\tau} \left\{C^n - C^{n+1}\right\} \quad (5)$$

where

$$C^{n+1} = C^n \cdot \exp\left(-\frac{1}{\tau}\Delta t\right) + C_e \cdot \left[1 - \exp\left(-\frac{1}{\tau}\Delta t\right)\right] = C_e + \left(C^n - C_e\right) \exp\left(-\frac{1}{\tau}\Delta t\right) \quad (6)$$

q_s^m is massive source/sink of gas sorption/diffusion (kg/m^3/sec);

ρ_0 is gas density under the standard status (gas pressure = 1 atm) (kg/m^3);

τ is sorption time (sec), which is decided by the diffusion coefficient and the Warren/Root shape factor [5];

C_L is Langmuir concentration (-) or (St. m^3/m^3)

P_L is Langmuir pressure (Pa)

C is instant concentration (-), i.e., gas volume under standard status contained in unit volume of coal matrix at present time (St. m^3/m^3);

P_d is desorption pressure（Pa）

C_e is equilibrium concentration decided by Langmuir formula, which is the boundary condition of fracture for diffusion (St m^3/m^3);

$$C_e = \begin{cases} \dfrac{C_L \cdot P_d}{P_L + P_d}, & if\ p_g \geq P_d \\ \dfrac{C_L \cdot p_g}{P_L + p_g}, & if\ p_g < P_d \end{cases} \tag{7}$$

3 Application to the practical projects

After MGF2-3D was developed, it was verified by some simple and self-evident computation examples, where special attention was paid to the mass conservation from the change of the contents to the temporal accumulative flow rates. Then the following two projects were carried out.

3.1 Gashing gas predictive simulation contributing to the ventilation design for underground excavation of a nuclear waste disposal site

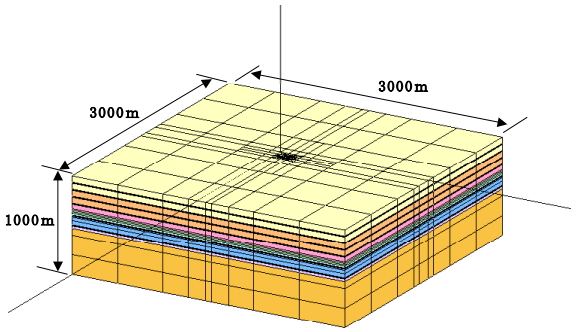

Figure 1: Model appearance.

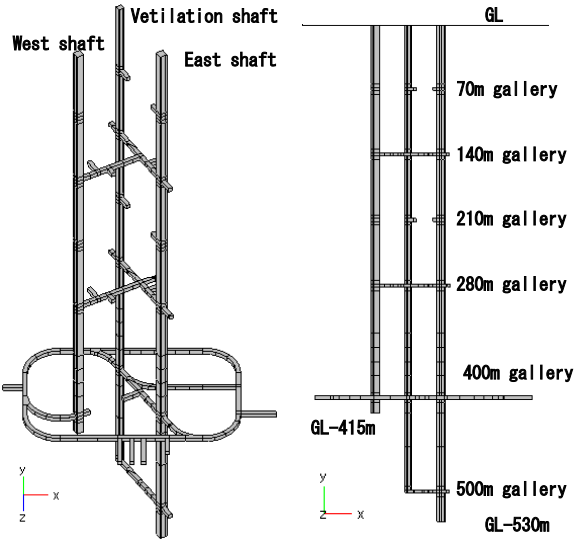

Figure 2: Excavation system.

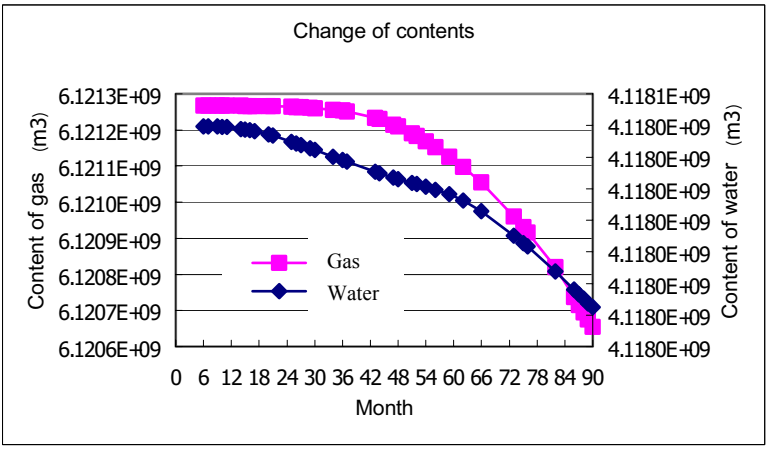

Figure 3: Change of gas content with time.

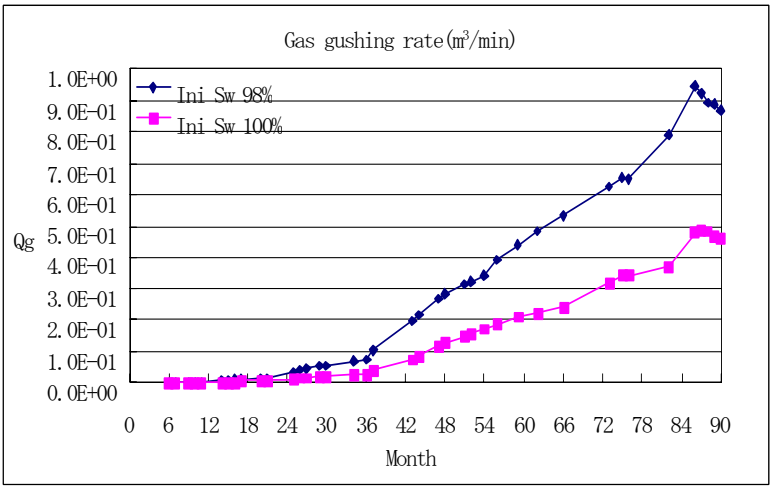

Figure 4: Gas gushing rate results.

3.2 Simulation to predict gas flow induced by both boring and excavation in a mine

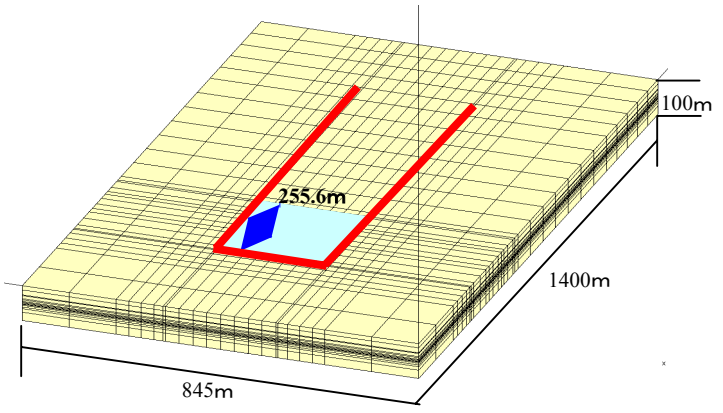

Figure 5: Model appearance.

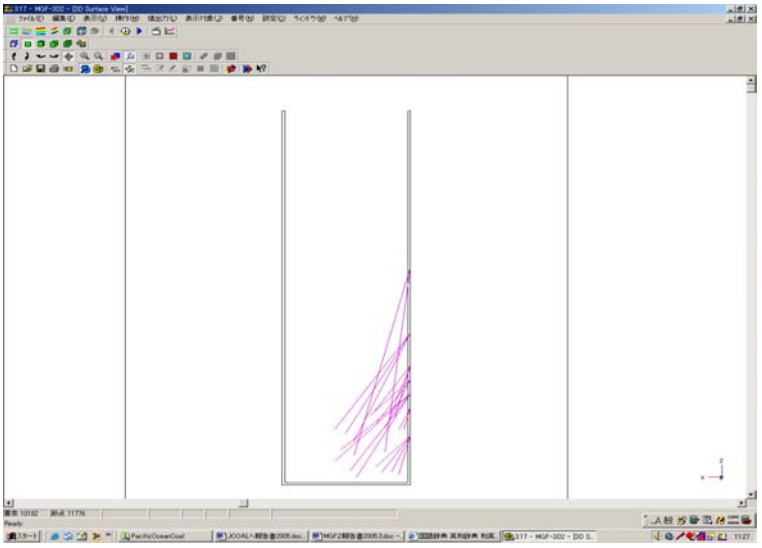

Figure 6: Boring distribution.

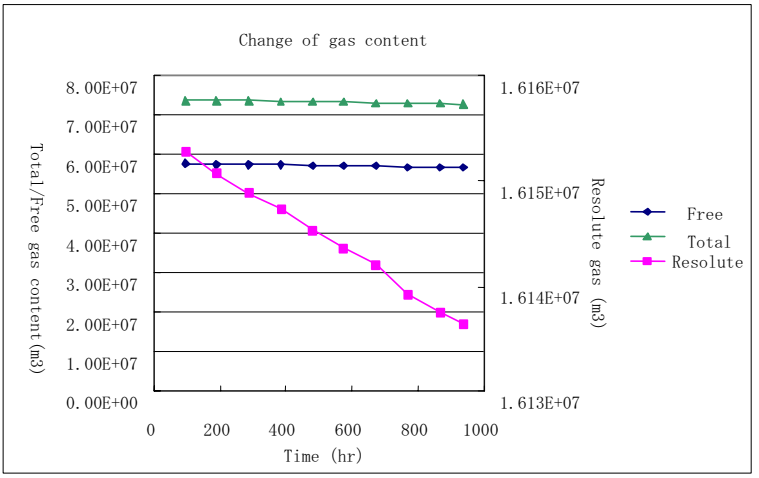

Figure 7: Result example one.

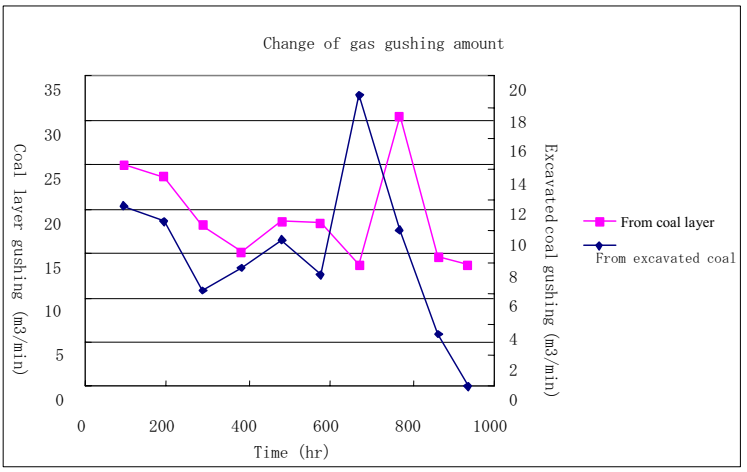

Figure 8: Result example two.

4 Conclusion

The solver of MGF-3D2, which is based on finite element method, has been integrated into developed pre-post processor, a user friend interface at the level of commercial simulator. In addition, the manual in Japanese, English and Chinese has also been made. It is expected that MGF-3D2 would play an active role in the engineering over the related fields.

References

[1] Helmig, R., *Multiphase flow and transport processes in the subsurface*, Springer-Verlag, 1997.
[2] Lawrence Berkeley Laboratory, *TOUGH User's Guide*, 1987.
[3] Computing Modeling Group, Ltd., *GEM fact sheet,*
[4] http://www.cmgl.ca/software/gem.htm.
[5] Advanced Resources International, Inc., *COMET2 User's Guide*, 1998.
[6] Warren, J. E. and Root, P. J., *The behavior of naturally fractured reservoirs,* SPEJ, 1963.
[7] Ertekin, T. et al., *Numerical simulation of the transient behavior of coal-seam degasfication wells*, SPE Formation Evaluation 1(2): pp. 165–183, 1986.
[8] Ertekin, T. et al., The unsteady-state nature of sorption and diffusion phenomena in the micropore structure of coal: Part 1-Theory and mathematical formulation. SPE Formation Evaluation 5(1): pp. 81–88, 1990.

This page intentionally left blank

Section 4
Interfaces

This page intentionally left blank

Influence of the interfacial pressure jump condition on the simulation of horizontal two-phase slug flows using the two-fluid model

J. N. E. Carneiro, A. J. Ortega & A. O. Nieckele
Pontifícia Universidade Católica de Rio de Janeiro, Brazil

Abstract

The two-fluid model has been widely used on the simulation of two-phase flows in pipelines. The model consists of two sets of conservation equations of mass and linear momentum for the liquid and gas phases on its transient, one-dimensional form. The slug capturing methodology involves the numerical solution of the equations using a finite volume formulation, which is capable of naturally predicting the onset of slugging from the stratified flow regime, as well as the growth and collapse of the slugs. However, the existence of a region where the flow equations are ill-posed restricts the range to which a valid solution is obtained. The ill posedness region depends on the modeling of the interfacial closure relations. In the present work, the influence of an interfacial pressure-jump condition in the solution was investigated.
Keywords: slug-flows, one-dimensional, horizontal, pressure-jump.

1 Introduction

Two-phase flow in the slug pattern can be found in several engineering applications, such as flow of hydrocarbons through pipelines, liquid-vapor flow in power-plants, etc [1]. The slug is a flow pattern which is highly intermittent, it is formed by sequences of large gas bubbles followed by packs of liquid (slug) flowing in random fluctuating frequencies [2,3].

The slug pattern can be formed in horizontal and inclined pipelines from a stratified pattern by basically two mechanisms: the natural growth of

hydrodynamic instabilities and by the accumulation of liquid due to irregularities on the pipeline. In the first case, small perturbations in the form of small waves naturally emerge. These waves can grow to larger waves of the size of the pipeline cross-section [4]. The growth mechanism is the classic Kelvin-Helmholtz instability (KH) [5,6]. These waves can continue to grow, capturing the liquid that flows in front of them until the cross section becomes saturated with liquid, thus forming the *slugs*. At inclined pipelines, the slug can be formed due to the delay and sub-sequent accumulation of liquid at the down points of the pipeline, leading to a cross section completely filled with liquid. This type of slug pattern induced by the terrain is called "*severe slugging*" and it can be formed when a slightly inclined pipeline joins a riser, that is, a vertical pipeline [7]. The flow in the slug pattern can also be formed by a combination of the mechanisms described above. Small undulations of the terrain can lead to slug formation in addition to the ones formed by the inherent instabilities of the flow. In theses cases, the slug formed by one mechanism interacts with those formed by the other, leading to a complex slug pattern.

The intermittence of the flow in the slug pattern causes large instabilities, which propagates through out the pipeline and any other equipment connected to it. This often increases the design problems and it usually leads to a reduction of the efficiency and/or size of a processing plant. Thus, it is important to be able to predict the beginning and subsequent development of the slug pattern, as well, as the prediction of its characteristics such as size and frequency.

There are several methods to predict the slug formation, among them, the "*slug capturing*" methodology can be mentioned, which is based on the one-dimensional two fluid model [8], to predict two-phase flows. In this model, each phase is described by a set of mass, momentum and energy conservation equations, which are obtained by an average process for each phase. The "*slug capturing*" methodology was employed by Issa and Kempf [9], to predict the transition of a stratified flow to a slug pattern, and by Oliveira and Issa [10] who investigated numerical aspects of the solution of the two-fluid model, presenting methodologies to limit the volume fraction within physical limits. In 2003, Bonnizi and Issa [11,12] presented two papers employing the *"slug capturing"* model. At the first one, the slug pattern for a three phase fluid was obtained with the multi-fluid model, while the second one concerns the entrainment of small bubbles of gas in the liquid.

One of the problems in predicting the slug formation is related to the fact that, when a slug is formed the gas volume fraction becomes zero, and as a result the gas momentum equation becomes singular. To solve this problem Oliveira and Issa [10] proposed a non-conservative approach to model the gas momentum equation. Ortega and Nieckele [13] have also addressed the same issue, and they concluded that although the non-conservative approach damps some of the instabilities, it is too dissipative. In their study, the slug formation problem was investigated by neglecting the pressure jump across the interface. However, Banerjee [14] mentioned that the absence of this term can turn the equation ill posed. Therefore, the objective of the present work consists on investigating the influence of the pressure jump on the prediction of the slug regime.

2 Mathematical modelling

The mathematical model selected is based on the "*slug capturing*" technique, in which the slug formation is predicted as a result of a natural and automatic growth of the hydrodynamic instabilities [9]. Both stratified and slug pattern are modeled by the same set of conservation equations based on the two-fluid model. Additionally, closure relations are also included. The liquid is considered as incompressible, while the gas follows the ideal gas law, $\rho_g=P/(RT)$, where R is the gas constant and T is its temperature, which was considered here as constant. Two different hypotheses were considered concerning the pressure distribution. Initially the pressure P was considered constant long the cross section, being the same, for the liquid P_ℓ, gas P_g and interface ($P=P_g=P_\ell$). Then, a pressure jump was considered at the interface, proportional to the ratio of the surface tension σ and the curvature radius R, which can be determined from the variation of the liquid level h as

$$P_\ell = P_g - \frac{\sigma}{R} \Rightarrow P_\ell = P - \sigma \frac{\partial^2 h}{\partial x^2} \tag{1}$$

The governing mass and momentum equations in the conservative form can be written as

$$\frac{\partial(\rho_g \alpha_g)}{\partial t} + \frac{\partial(\rho_g \alpha_g u_g)}{\partial x} = 0 \quad ; \quad \frac{\partial(\rho_\ell \alpha_\ell)}{\partial t} + \frac{\partial(\rho_\ell \alpha_\ell u_\ell)}{\partial x} = 0 , \tag{2}$$

$$\frac{\partial(\rho_g \alpha_g u_g)}{\partial t} + \frac{\partial(\rho_g \alpha_g u_g^2)}{\partial x} = -\alpha_g \frac{\partial P}{\partial x} - \rho_g \alpha_g g \,\mathbf{sen}(\beta) - \\ - \rho_g \alpha_g g \frac{\partial h}{\partial x} \mathbf{cos}(\beta) - F_{gw} - F_i \quad , \tag{3}$$

$$\frac{\partial(\rho_\ell \alpha_\ell u_\ell)}{\partial t} + \frac{\partial(\rho_\ell \alpha_\ell u_\ell^2)}{\partial x} = -\alpha_\ell \frac{\partial P}{\partial x} - \rho_\ell \alpha_\ell g \,\mathbf{sen}(\beta) - \\ - \rho_\ell \alpha_\ell g \frac{\partial h}{\partial x} \mathbf{cos}(\beta) - F_{\ell w} + F_i + \alpha_\ell \sigma \frac{\partial^3 h}{\partial x^3} \quad , \tag{4}$$

where $\alpha_g+\alpha_\ell=1$. The subscripts g, ℓ, and i concern the gas, liquid phases and interface, respectively. The axial coordinate is x, ρ and α are the density and volumetric fraction, u is the velocity. The pipeline inclination is β, h is the liquid level inside the pipe, and g is the gravity acceleration. The third term on the right side of eqs. (3) and (4) are related with the hydrostatic pressure at the gas and liquid, respectively. The term $F=\tau S / A$ is the friction force per unit volume between each phase and the wall and between the phases (at the interface), where τ is the shear stress, S is the phase perimeter and A is the pipe cross section area.

The shear stress is $\tau = f\rho|u_r|u_r/2$, where u_r is the relative velocity between the liquid and wall, the gas and wall, or gas and liquid. Closure relations are needed to determine the friction factor *f*.

The flow was considered in the laminar regime, when the Reynolds number **Re**, was smaller the 2100 ($\mathbf{Re}_g$; $\mathbf{Re}_i$ and $\mathbf{Re}_\ell$ for the gas, interface and liquid, respectively). The Hagen-Poiseulle formulas were employed for the gas-wall and interface friction factor and the correlation of Hand [15] for the liquid-wall friction factor:

$$f_g = 16/\mathrm{Re}_g \;\;,\;\; f_i = 16/\mathrm{Re}_i \;\;,\;\; f_\ell = 24/\mathrm{Re}_\ell^s\,, \tag{5}$$

while the correlation of Taitel and Dukler [16] was adopted for the turbulent gas-wall and interface friction factor and the Spedding and Hand [17] correlation for turbulent the liquid-wall friction

$$\begin{aligned} f_g &= 0.046\left(\mathrm{Re}_g\right)^{-0.25},\;\; f_i = 0.046\left(\mathrm{Re}_i\right)^{-0.25} \\ f_\ell &= 0.0262\left(\alpha_\ell\,\mathrm{Re}_\ell^s\right)^{-0.139}\;\;, \end{aligned} \tag{6}$$

where α_l is the *hold-up* (liquid volumetric fraction). The Reynolds numbers are defined as

$$\mathbf{Re}_g = \frac{4A_g u_g \rho_g}{\left(S_g + S_i\right)\mu_g}, \qquad \mathbf{Re}_i = \frac{4A_g\left|u_g - u_\ell\right|\rho_g}{\left(S_g + S_i\right)\mu_g}, \tag{7}$$

$$\mathbf{Re}_\ell = \frac{4A_\ell\; u_\ell\;\rho_\ell}{S_\ell\;\mu_\ell}, \qquad \mathbf{Re}_\ell^s = \frac{\rho_\ell Us_\ell D}{\mu_\ell}, \tag{8}$$

where μ is the absolute viscosity and *D* is the pipe diameter. The last Reynolds in eq. (8) is based on the liquid superficial velocity, i.e., the ration of the liquid volume flow rate to the total cross section area of the pipe:

$$Us_\ell = \frac{Q_\ell}{A} \qquad \text{or} \qquad Us_\ell = \alpha_\ell\; u_\ell\,. \tag{9}$$

Figure 1 presents a sketch of the pipeline, with a cross section area *A* and diameter *D*. The areas and wetted perimeters of the gas and liquid are A_g, S_g and A_ℓ, S_ℓ, respectively, and the interface width is S_i. All these geometric parameters depend only on liquid height *h* [17]:

$$S_g = D\,\mathbf{cos}^{-1}(\xi)\;;\quad S_\ell = \pi\; D - S_g\;;\quad S_i = D\sqrt{1-\xi^2} \tag{10}$$

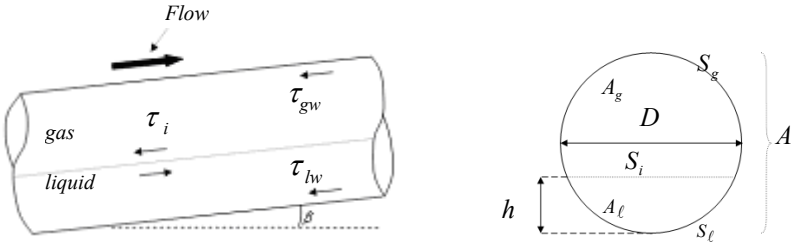

Figure 1: Sketch of the pipe, and its cross section.

$$A_g = \frac{D}{4}\left[S_g - \xi\ S_i\right] \quad ; \quad A_l = \frac{\pi\ D^2}{4} - A_g\ ; \xi = 2\ (D\ /\ h) - 1. \quad (11)$$

Further, the liquid height is a geometric function of the gas volumetric fraction (α_g=A_g / A), and can be obtained by the solution of

$$\alpha_g = \frac{1}{\pi}\left[\cos^{-1}(\xi) - \xi\ \sqrt{1-\xi^2}\right] \quad (12)$$

3 Numerical method

The conservation equations were discretized by the Finite Volume Method [18]. A staggered mesh was employed, with both phases' velocities stores at the control volume faces and all other variables at the central point. The interpolation scheme *upwind* and the implicit *Euler* scheme were selected to evaluate the space and time derivates, respectively.

A conservative approach was selected to discretize the conservation equations, based on the analysis of Ortega and Nieckele [13], who investigated the advantages/disadvantages of employing a conservative or non-conservative. The set of resulting equations consists of two momentum equations, one pressure equation (global mass conservation) and one gas volumetric fraction (gas mass conservation). These equations were solved sequentially, through an iterative method [13].

Since the gas momentum equation becomes singular when the gas volumetric fraction becomes zero, this equation was not solved when a slug was formed (α_g<0.02), and the gas velocity was arbitrarily set to zero, as recommended by Issa and Kempt [9] and Bonizzi and Isaa [11].

The time step was specified to guarantee a Courant number equal to 0.5 [9], therefore, the time step was obtained from Δt= 0.5 Δx_i | $u_{\max}$ |, where u_{max} is the

maximum velocity in the domain. For each time step, due to the non linearities of the problem, the sequence of conservation equations were solved in an iterative process, until convergence was obtained, that is, until the residue of all equations became smaller than 0.0001.

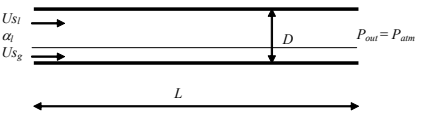

Figure 2: Problem test configuration.

4 Results

Figure 2 illustrates the problem configuration. It is exactly the same as the one investigated by Issa and Kempf [9] and Bonizzi [19]. The pipeline is horizontal, with length equal to L=36 m, and internal diameter D = 0.078m. The flow was considered isothermal at a reference temperature T = 281.15 K. The outlet pressure P_{out} was kept constant equal to the atmospheric pressure. The gas phase is air (gas constant, R = 287 N m /(Kg K) and the absolute viscosity is $\mu = 1.796\times 10^{-5}$ Pa-s) and the liquid phase water (density, $\rho = 998.2$ kg/m^3, absolute viscosity is $\mu = 1.139 \times 10^{-3}$ Pa-s). At the inlet the superficial liquid and gas superficial velocities, U_{sl} and U_{sg} , were specified as constant, as well the gas volumetric gas fraction α_g.

The initial condition was defined as a stratified steady state flow, that is, constant liquid height along the pipeline, with constant liquid and gas velocities. The pressure distribution was obtained by integrating the following equation, resulting from a combination of the momentum equation of the liquid and gas phase, for the equilibrium stratified flow,

$$\partial P / \partial x = -(\tau_{\ell w} S_\ell + \tau_{gw} S_g) / A . \qquad (13)$$

A map of flow pattern [16] can be seen in fig. (3), for the pipeline configuration adopted at the present work. This map shows the range of gas and liquid superficial velocities which leads to the different flow patterns (bubbles, slug, annular, stratified). Based on the analysis presented by Bonizzi [19], at the same map, an additional curve was plotted, separating the regions where the system of equations is well and ill posed.

For the first case the boundary condition employed by Issa and Kempf [9] was selected: Us_g=2.0 m/s; Us_ℓ=1.0 m/s, α_l=0.4. For the second case, the following superficial velocities were defined Us_g= 6.53 m/s, Us_ℓ=0.53 m/s and α_g=0.606 [19]. The location of these conditions in the Taitel and Dukler [16] flow pattern map indicates that slugging is expected. In addition, the cases were selected to lie above the well-ill posedness boundary (IKH limit).

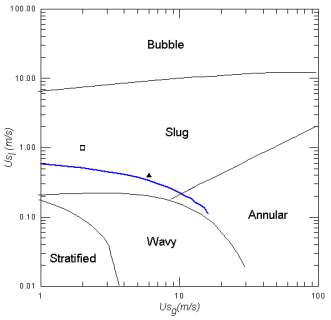

Figure 3: Flow pattern map [16]. Location of test cases on the map.

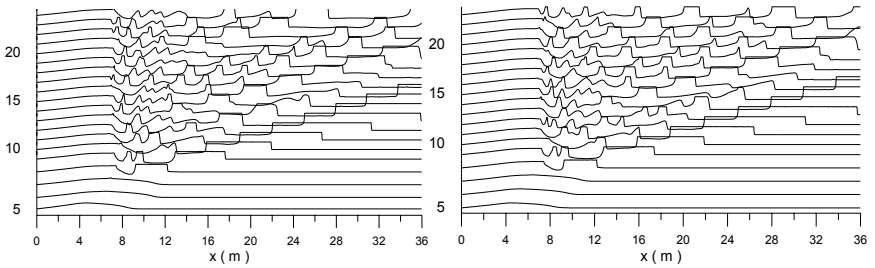

(a) without pressure jump (b) with pressure jump

Figure 4: Successive hold-up profiles in time. Case 1: Us_g = 2 m/s, Us_ℓ= 1 m/s.

As suggested by Issa and Kempf [9], for Case 1, a uniform mesh was specified in the domain, with 1250 nodes (Δx/D=0.37). Figure 4 illustrates for Case 1, the liquid holdup distribution along the pipe, for different time instants, considering the pressure jump at the interface and not considering it. The results show that the methodology is indeed capable of predicting several characteristics of the slug flow for both cases. If appropriate initial and boundary conditions are given, the flow develops naturally into an intermittent state as a result of the growth of instabilities that arise in the process of solution of the equation system. It can be seen that for the present situation, the pressure jump is negligible, and the holdup evolution is similar for both pressure conditions.

Transient phenomena such as growing, merging and collapsing of slugs are well captured by the methodology. After some simulation time, trains of slugs can be formed and the flow develops into a statistically steady state as observed in fig. 4. It is also to be noted that the shorter slugs are usually unstable and tend to disappear along the pipe. Some waves can momentarily bridge the pipe section, but are not stable enough to maintain as a coherent slug, collapsing and being absorbed by faster slugs. The merging process occurs until the liquid slug is long enough to be stable, traveling towards the pipe outlet. These aspects are

well connected to the physics of the slug flow observed experimentally in several previous works [20].

The average slug velocity U_{slug} and average slug length L_{slug} were also computed. Table 1 presents the results obtained with and without the pressure jump. It can be seen that the presence of the pressure jump in the momentum equation is irrelevant, since the results are almost the same with and without it. Further, it can be observed that a reasonable agreement was obtained with the empirical correlation for the translational velocity of Bendiksen [21].

Dukler and Hubbard [22] found out that the stable liquid slug length is dependent only with the pipe diameter, being typically in the range between 12D–30D. The mean liquid slug length calculated in cases 1 and 2 lie within that range.

Table 1: Average slug velocity and slug length.

	Case 1			Case 2		
	with ΔP	without ΔP	Empirical [20,21]	with ΔP	without ΔP	Empirical [20,21]
Slug velocity [m / s]	3.6	3.7	3.6	8.4	9.2	8.5
Slug length [D]	14D	16D	12-30D	26	28	12-30D

In well posed cases, successive grid refinements produce flows which asymptotically tend towards a unique solution. However, when boundary and initial conditions lead to an ill-posed problem, grid refinements will produce a diverging solution. In this sense, numerical diffusion may mask the ill-posedness of the equations system.

The role played by numerical diffusion in the solution is illustrated in fig. 5. The coarse grid (Δx/D = 1.15) was not able to capture smaller wave lengths appearing in the region where slugs are generated (approximately at 7 m from pipe inlet). However, the slug velocity and length were approximately the same as with the finer mesh.

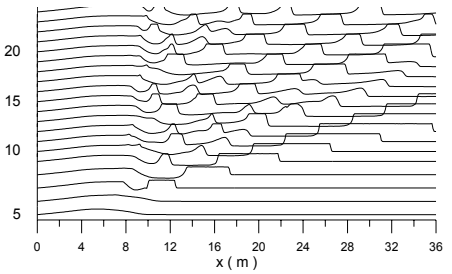

(a) with pressure jump (Δx/D=1.15)

Figure 5: Successive hold-up profiles in time. Case 1: Us_g = 2 m/s, Us_ℓ= 1 m/s.

Figure 6 illustrates the evolution of the liquid holdup for Case 2, with and without the pressure jump. The same coarse mesh as employed for Case 1, was employed for this case. Once again, it is observed that the pressure jump is too small for these cases; therefore the solution is not affected by it. The holdup time evolution obtained agreed well with literature results [19]. The slug velocity and slug length are shown in Table 1, and again a good agreement with the literature correlation was obtained.

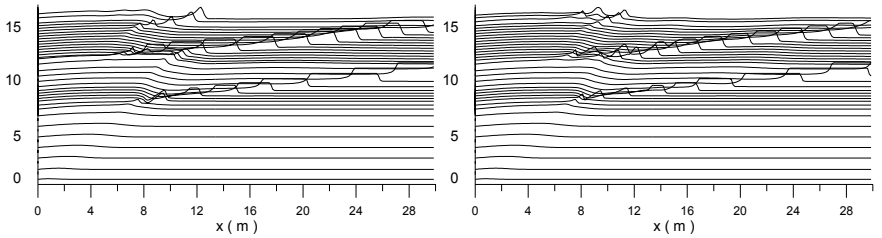

(a) without pressure jump (b) with pressure jump

Figure 6: Successive hold-up profiles in time. Case 2: Us_g = 6.53 m/s, Us_ℓ = 0.53 m/s.

5 Final remarks

Although the hypothesis of pressure equality for both phases is an approximation, the consideration of an interfacial pressure-jump condition seems to bring no difference for the solution. This is because slug flow is a long wave length phenomena, and as already pointed out by stability analysis carried out in the past [23], the effect of surface tension is negligible in that cases.

Acknowledgement

The authors thank CNPq for supporting the development of this work.

References

[1] Dukler, A.E.; Fabre, J., Gas–liquid slug flow-knots and loose ends. Proceedings of 3rd International Workshop Two-Phase Flow Fundamentals, Imperial College, 1992.

[2] Fabre, J.; Liné, A., Modeling of two-phase slug flow, Annual Review of Fluid Mechanics, 24, pp. 21–46, 1992.

[3] Woods, B.D.; Hurlburt, E.T.; Hanratty, T.J., Mechanism of slug formation in downwardly inclined pipes, International Journal Multiphase Flow, 26, pp. 977–998, 2000.

[4] Ansari, M. R., Dynamical behavior of slug initiation generated by short waves in two-phase air-water stratified flow, ASME Heat Transfer Division 361, pp. 289–295, 1998.
[5] Lin, P.Y.; Hanratty, T.J., Prediction of the initiation of slugs with linear stability theory, International Journal Multiphase Flow, 12, pp. 79–98, 1986.
[6] Fan, Z.; Lusseyran, F.; Hanratty, T.J., Initiation of slugs in horizontal gas-liquid flows, AIChE Journal, 39, pp. 1741–175, 1993.
[7] Jansen, F.E.; Shoham, O.; Taitel, Y., The elimination of severe slugging, International Journal Multiphase Flow, 22, pp. 1055–1072, 1996.
[8] Ishii, M., Thermo-Fluid Dynamic Theory of Two-Phase Flow, Eyrolles, Paris, 1975.
[9] Issa, R.I.; Kempf, M.H.W., Simulation of slug flow in horizontal and nearly horizontal pipes with the two-fluid model, International Journal Multiphase Flow, 29, pp. 69–95, 2003.
[10] Olivera, P.J.; Issa, R.I., Numerical aspects of an algorithm for the Eulerian simulation of two-phase flow, International Journal of Numerical Methods in Fluids, 43, pp. 1177–1198, 2003.
[11] Bonizzi, M.; Issa, R.I., A model for simulating gas bubble entrainment in two-phase horizontal slug flow, International Journal of Multiphase Flow, 29, pp. 1685–1717, 2003.
[12] Bonizzi, M.; Issa, R.I., On the simulation of three-phase slug flow in nearly horizontal pipes using the multi-fluid model, International Journal of Multiphase Flow, 29, pp.1719–1747, 2003.
[13] Ortega, A. J., Nieckele, A.O., Simulation of horizontal two-phase slug flows using the two-fluid model with a conservative and non-conservative model, Proceedings of 18th International Congress of Mechanical Engineering, Ouro Preto, MG Brazil, Paper 0153, 2005.
[14] Banerjee, S., Mutifield Models, Short courses Modelling and Computation of Multiphase Flows, Part I, Zurich, Switzerland, 2002.
[15] Hand, N.P. Gas–liquid co-current flow in a horizontal pipe, Ph.D. Thesis, Queen`s University Belfast, 1991.
[16] Taitel, Y.; Dukler, A.E., A model for predicting flow regime transitions in horizontal and near horizontal gas–liquid flow, AIChE Journal, 22, pp. 47–55, 1976.
[17] Spedding, P.L.; Hand, N.P., Prediction in stratified gas–liquid co-current flow in horizontal pipelines, International Journal Heat Mass Transfer, 40, pp. 1923–1935, 1997.
[18] Patankar, S.V., Numerical Heat Transfer and Fluid Flow, Hemisphere Publishing Corporation, 1980.
[19] Bonizzi, M., Transient One-dimensional Modelling of Multiphase Slug Flow, Doctoral Thesis, Dept. Mechanical Engineering, Imperial College London, 2003.
[20] Barnea, D., Taitel, Y., Two-phase slug flow. Advances in Heat Transfer, 20, pp. 83–132, 1990.

[21] Bendiksen, K., Experimental Investigation of the motion of long bubbles in inclined tubes, International Journal of Multiphase Flow, 10, pp. 467–483 , 1984.
[22] Dukler, A.E.; Hubbard, M.G., A model for gas-liquid slug flow in horizontal and near horizontal tubes. Industrial Engineering Chemical Fundamentals, 14, pp. 337–347, 1975.
[23] Barnea, D., Taitel, Y., Interfacial and structural stability of separated flow. International Journal of Multiphase Flow 20, pp. 387–411, 1994.

This page intentionally left blank

Interfacial phenomena during crystal growth: solute redistribution, double-diffusive convection and non-isothermal phase-change

W.-Q. Lu, K. Shi & J. Liu
Graduate School of the Chinese Academy of Sciences, Beijing, China

Abstract

A simplified mathematical physical model with axisymmetric dual reciprocity boundary element method (ADRBEM) and finite element method (FEM) is used to numerically simulate the interfacial phenomena during crystal growth: the solute segregation, redistribution and non-isothermal phase change on the interface between crystal and thawing fluid, and the double-diffusive convection driven by the solute gradient and thermal gradient. Some interesting flow physical phenomena are found.
Keywords: solute redistribution, non-isothermal phase change, double-diffusive convection.

1 Introduction

The vertical Bridgman process in a circular ampoule has been used widely for growing the high quality II–IV semiconductor family such as HgCdTe, HgZnTe and CdZnTe, etc. Solute segregation, diffusion and redistribution will occur at the phase interface during the crystal growth, so a solutal gradient is generated. Hence, the double-diffusive convection is driven by the solute gradient together with the thermal gradient in the fluid phase. Simultaneously, the variation of solute concentration on the phase-change interface produces non-isothermal phase-change characters. The growth quality of the crystal is largely controlled by these interfacial phenomena. However, the devoid of literature is detailed numerical simulation works for some basic problems, such as the factors to affect the region of solute redistribution, the non-isothermal phase change and double-diffusion convection phenomena. The main objective of this paper is to

explore an effective numerical method of modeling these problems, and gain some knowledge of the above phenomena.

2 Solute redistribution and non-isothermal phase-change

2.1 Physical model

In some kinds of crystal growth process by the vertical Bridgman method (VBM), for example the process of a slowly pulling rate in microgravity environment, the natural convection in the melt is negligible. The heat transfer in the crystal and melt is controlled by heat conduction. The heat transfer between the crystal, melt and surroundings is simplified as follows: the heat flux is applied on the top, and there is heat output at the bottom. It remains adiabatic on the sidewall. The mass transfer is simplified as the form of mass diffusion. The solute diffusion in the crystal is negligible. The shape of crystal-melt interface remains planar.

As shown in Fig. 1, the field is described in terms of the stationary axisymmetric cylindrical coordinate systems (r, x) with origin located at the centerline of the bottom. The position of the interface is represented by the function $X = x(t)$. The simplified mathematic physical controlling equations are described as the follows.

$$\nabla^2 T_c = \frac{1}{\alpha_c}\frac{\partial T_c}{\partial t} \qquad \nabla^2 T_m = \frac{1}{\alpha_m}\frac{\partial T_m}{\partial t} \tag{1}$$

$$\nabla^2 C_m = \frac{1}{D_m}\frac{\partial C_m}{\partial t} \tag{2}$$

where T, C, α and D represent temperature, concentration, thermal and concentration diffusivity, respectively. Subscripts c and m represent crystal and melt. The initial and boundary conditions are:

$$T(0 \le x \le L_c, 0) = T_0, \qquad C(0 \le x \le L_c, 0) = C_0,$$

$$\partial C / \partial x\big|_{x=0,L_c} = 0, \qquad \partial C / \partial r\big|_{r=0,R} = 0,$$

$$\partial T / \partial r\big|_{r=0,R} = 0, \quad Q\big|_{x=L_c} = Q_2, \quad Q\big|_{x=0} = Q_1,$$

$$K_c \partial T / \partial x\big|_c = K_m \partial T / \partial x\big|_m + \rho_c \Delta H V_I, \; -D_m \partial C_m / \partial x\big|_X = (C_m - C_c) V_I,$$

$$C_c(X,t) = kC_m(X,t) \quad , \; T_c(X,t) = T_m(X,t) = T_p(C_m(X,t))$$

where C_0, T_0 and T_p represent initial concentration, initial and melting temperature, respectively. Q_1 and Q_2 represent the heat flux applied on the bottom and at the top of the field, respectively, and ΔH and V_I represent the latent heat and moving velocity of phase change interface respectively. ρ_c, C_m, C_c represent the density of crystal, melt and crystal concentration of the solute on the phase change interface, respectively. k and K are the segregation coefficient and thermal conductivity respectively.

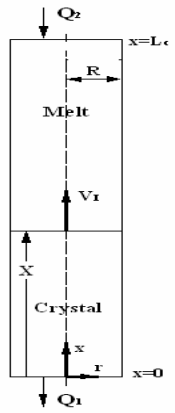

Figure 1: Schematic of the system.

2.2 ADRBEM with augmented items

The calculating domain is chosen as an axisymmetric cylindrical domain, i.e. crystal phase: $0 \le r \le R$, $0 \le x \le X$; melting phase: $0 \le r \le R$, $X \le x \le L_c$. In order to compare with one-dimensional experimental data, $L_c / R = 20$ is chosen, so that the numerical results at the centerline in this spindly cylinder can represent one-dimensional numerical results.

Considering equations (1) and (2) as the following representative equation

$$\nabla^2 u = b \tag{3}$$

where b may be a function of position, potential or time.

Employing dual reciprocity theory, Eq. (3) can be converted to the pure boundary integral equation.

The choice of function f is very important for the calculation by DRBEM. However, in early ADRBEM, it is impossible to arrange nodes on the symmetrical axis because of the singularity of function f used in early ADRBEM. In [1], the singularity is avoided by integral averaging and selecting different assemblage of functions f. In this calculation, the marked B-11 type f function is chosen [1]:

$$\begin{cases} f = \sqrt{r_i^2 + (x - x_i)^2}\left(1 - \dfrac{1}{4} \cdot \dfrac{r_i^2}{r_i^2 + (x - x_i)^2}\right) & r = 0 \\ f = \sqrt{r_i^2 + (x - x_i)^2}\left(1 - \dfrac{1}{4} \cdot \dfrac{r_i}{r}\right) & r \neq 0 \end{cases} \tag{4}$$

Further, the right-hand side of Eq. (3) is interpolated using a combination of monomials and radial basis functions:

$$b = \sum_{i=1}^{N+M} \alpha_i f(r_i, x_i) + \sum_{k=1}^{N_p} \beta_i p_i(r_i, x_i) \tag{5}$$

$$\nabla^2 \phi_i = p_i \qquad (i = 1,2 \cdots\cdots N_p) \tag{6}$$

ϕ_i can be solved after p_i is given. In the present calculation, we choose p_i as: $p_1=1$, $p_2=x-x_0$ ($N_p=2$), and can obtain: $\phi_1 = \left[r^2 - r_0^2 + (x-x_0)^2\right]/6$, $\phi_2 = (x-x_0)^3/6$. r_0, x_0 is determined by the geometrical condition: $r_0 = (r_{\min} + r_{\max})/2$, $x_0 = (x_{\min} + x_{\max})/2$.

The interpolation of the augmented items including r_0, x_0 shows that the geometrical condition plays a more important role. Therefore, it will be more flexible and accurate to calculate the problem when the computational domain has larger ratio between axial length and radial length.

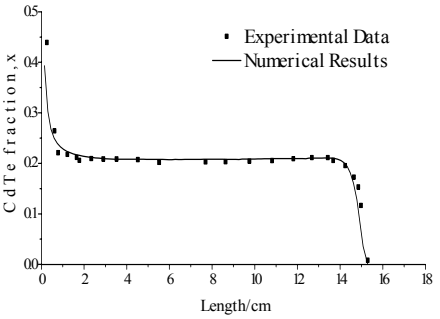

Figure 2: Validation of the method.

2.3 Numerical results

In order to compare with the experimental data of [2], the same parameters as [2] are chosen as follows. Material: $Hg_{1-x}Cd_xTe$, $C_0=x=0.202$, $L_c=15.3$ cm, $V_1=1.12$ μm/s, $D_m=6.0\times10^{-5}$ cm^2/s, $k=3.63$. The numerical results and experimental data are drawn in Fig. 2. As shown in Fig. 2, the experimental data can be well fitted by numerical results. This shows that ADRBEM with augmented items is reliable for the calculation of this problem.

In the following calculation, the effect of different moving velocity on the solute redistribution process is numerically simulated. The calculating parameters are chosen as [3]: Material: $Cd_{1-x}Zn_xTe$, $C_0=0.04$, $L_c=7.6$ cm, $V_1=1.0$ μm/s, $D_m=1.0\times10^{-4}$ cm^2/s, $k=1.35$. The numerical results are drawn in Fig. 3. Fig. 3 shows the variation of axial solute redistribution during the crystal growth with the velocity: the initial, final transient regions both become shorter and the steady growth region becomes longer as the velocity increases. The longer the length of the steady growth region, the higher the quality of the crystal. Since the velocity of interface during the crystal growth is controllable by changing the pulling velocity, it is possible to increase the length of the steady

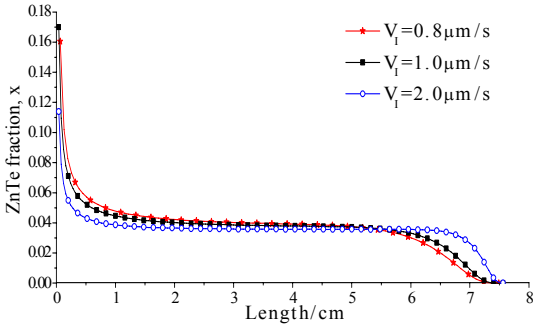

Figure 3: The effect of the interface moving velocity on solute redistribution region.

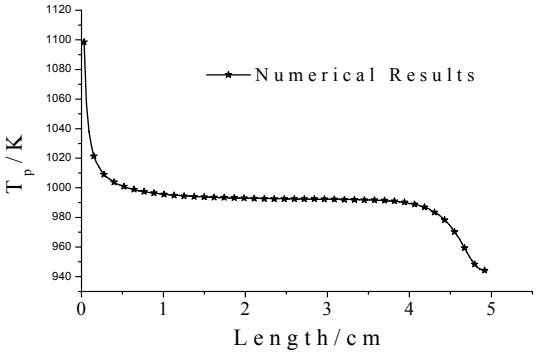

Figure 4: The phase-change temperature variation.

growth region by increasing the velocity of the interface. But in the real crystal growth process a fast velocity will lead to some shortages: structure disfigurement, great thermal stress, etc. So it is necessary to choose an appropriate velocity.

Finally, calculate non-isothermal phase-change phenomena. On the HgTe-CdTe quasi-binary phase diagram (k>1), the melting temperatures can be represented in terms of a cubic polynomial in the mole fraction of CdTe: $T_p(°C) = a_1 + a_2 C_m(X,t) + a_3 C_m^2(X,t) + a_4 C_m^3(X,t)$, where the coefficients $\{a_i\}$ take the values {670.49, 671.46, -375.07, 110.54}. The thermophysical properties data for $Hg_{1-x}Cd_xTe$ are given by [4]. Present numerical non-isothermal phase-change characters are drawn in Figures 4 and 5.

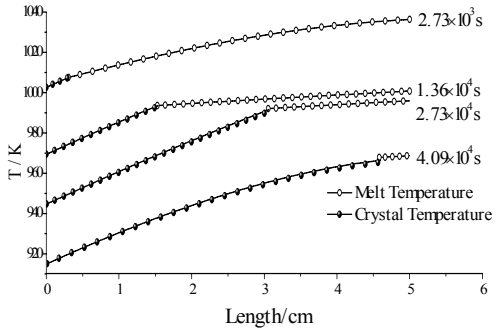

Figure 5: The temperature distribution at different time.

As shown in Fig. 4, the phase change temperature distribution presents three different regions like the axial solute redistribution: initial and final transient region of phase change are obviously non isothermal while the steady growth region of phase change are almost isothermal with time. Because of the difference of thermal conductivity between crystal and melt, the phase-change point becomes the turning point of the temperature distribution as shown in Fig. 5. At the same time the variation of phase change temperature occurs with time marching in the initial transient region and the final transient region

3 Double diffusion convection in vertical circular cylinder

3.1 Physical model

The physical system is a vertical circular cylinder with a height of H and a radius of R. Initially the fluid in the cylinder is at rest and isothermal ($T=T_0$) and isoconcentration ($C=C_0$)，and at $t=0$ the temperature on the side wall changes impulsively to $T=T_w$ and the concentration on the bottom wall varies to $C=C_w$, this temperature and concentration are maintained thereafter. The flow is assumed to be axisymmetric, incompressible, laminar and Newtonian. The computational domain is drawn in Fig. 6. The heat generation, viscous dissipation, chemical reactions and thermal radiation are neglected. The Boussinesq approximation is used; the thermophysical properties of the fluid are assumed to be constant except $\rho(T,C)=\rho_0(1-\beta_T(T-T_0)-\beta_C(C-C_0))$. Here, $\rho_0=\rho(T_0,C_0)$, $\beta_T=(-1/\rho_0)(\partial\rho/\partial T)_C$ and $\beta_S=(-1/\rho_0)(\partial\rho/\partial C)_T$ are the density at temperature T_0 and concentration C_0, the thermal expansion coefficient, and the solutal expansion coefficient, respectively. The control equations can be written by vorticity (ω)-stream function(ψ) in dimensionless form as follows.

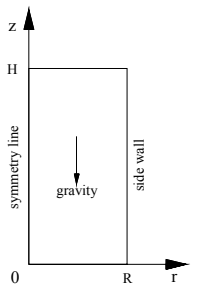

Figure 6: Computational domain.

Equation of motion:

$$\frac{\partial\omega}{\partial t}+\frac{1}{r}\frac{\partial\psi}{\partial z}\frac{\partial\omega}{\partial r}-\frac{1}{r}\frac{\partial\psi}{\partial r}\frac{\partial\omega}{\partial z}-\frac{\omega}{r^2}\frac{\partial\psi}{\partial z}=\left(\frac{\partial^2\omega}{\partial r^2}+\frac{1}{r}\frac{\partial\omega}{\partial r}+\frac{\partial^2\omega}{\partial z^2}-\frac{\omega}{r^2}\right)-Gr_T\frac{\partial T}{\partial r}-Gr_S\frac{\partial C}{\partial r} \quad (7)$$

Stream function equation: $$\frac{\partial^2\psi}{\partial r^2}+\frac{\partial^2\psi}{\partial z^2}-\frac{1}{r}\frac{\partial\psi}{\partial r}=r\omega \quad (8)$$

Energy equation: $$\frac{\partial T}{\partial t}+\frac{1}{r}\frac{\partial\psi}{\partial z}\frac{\partial T}{\partial r}-\frac{1}{r}\frac{\partial\psi}{\partial r}\frac{\partial T}{\partial z}=\frac{1}{\mathrm{Pr}}\left(\frac{\partial^2 T}{\partial r^2}+\frac{1}{r}\frac{\partial T}{\partial r}+\frac{\partial^2 T}{\partial z^2}\right) \quad (9)$$

Solute equation: $$\frac{\partial C}{\partial t}+\frac{1}{r}\frac{\partial\psi}{\partial z}\frac{\partial C}{\partial r}-\frac{1}{r}\frac{\partial\psi}{\partial r}\frac{\partial C}{\partial z}=\frac{1}{\mathrm{Pr}\,Le}\left(\frac{\partial^2 C}{\partial r^2}+\frac{1}{r}\frac{\partial C}{\partial r}+\frac{\partial^2 C}{\partial z^2}\right) \quad (10)$$

where $Gr_T=\frac{g\beta_T\Delta T H^3}{\nu^2}$, $Gr_S=\frac{g\beta_S\Delta C H^3}{\nu^2}$, $\mathrm{Pr}=\frac{\nu}{\alpha}$ and $Le=\frac{\alpha}{D}$. In the above equations, lengths are nondimensionalized by H, stream-function by $H\nu$, vorticity by ν/H^2, time by H^2/ν, temperature by $\Delta T=T_0-T_w$ and concentration by $\Delta C=C_0-C_w$.

The initial and boundary conditions are: $\psi=\omega=0$, $T=C=0$ for $r\neq 1/A$ and $t=0;\psi=0,\frac{\partial T}{\partial r}=\frac{\partial C}{\partial r}=0$ on $r=0$ for $t\geq 0;\psi=0$, $\frac{\partial C}{\partial z}=0, T=-1$ on $r=1/A$ for $t\geq 0;\psi=0,\frac{\partial T}{\partial z}=0, C=-1$ on $z=0$ for $t\geq 0;\ \psi=0,\ \frac{\partial T}{\partial z}=\frac{\partial C}{\partial z}=0$ on $z=1$ for $t\geq 0$. The average rates of heat and mass transfer across the side wall are expressed in dimensionless form by the Nusselt and Sherwood numbers:

$$Nu=\int_0^1\left(\frac{\partial T}{\partial r}\right)_{r=r_1}dz,\ Sh=\int_0^{1/A}\left(\frac{\partial C}{\partial r}\right)_{z=0}dz \quad (11)$$

3.2 Finite element scheme

The control equations are solved by the finite element method. The elements are rectangular elements with four nodes in which the bilinear function is constructed: $\Phi=b_1+b_2\zeta+b_3\eta+b_4\zeta\eta$. The relaxation iterative is used in the calculation and the vorticity on the wall is calculated by the Thom formula. The code has been used [5] to study the steady double-diffusive convection in a vertical rectangular and annular cavity with horizontal temperature and solution

gradients; the results in the rectangular cavity agree well with the previous studies [6]. The mesh 101×101 and time step 2.0×10^{-5} are chosen in this computation.

3.3 Numerical results

The parameters are chosen as: $Gr_T=10^7$, $Pr=7.0$, $Le=5.0$ and aspect ratio $A=H/R=2$. The effect of the buoyancy ratio ($N=Gr_S/Gr_T$) on double diffusive convection is investigated. Fig. 7 displays the thermal driven convection course under the conditions of $Gr_T=10^7$ and $N=0$. It is seen that a vertical thermal boundary layer develops very rapidly on the sidewall. After the full development of the vertical thermal boundary layer, a cold intrusion begins to form and moves continuously along the bottom wall towards the symmetry line. New intrusions successively produce and this process acts to generate the temperature stratification in the cavity. On the other hand, from the picture of solutal field, it is observed that the solutal boundary layer along the bottom wall is squeezed and the solutal field travels along the symmetry line due to the intrusion induced by thermal buoyancy.

Figures 8 and 9 illustrate the evolvement of double-diffusive convection in the cases of $N=1$ and $N=-1$. When $Gr_T>0$, for $N=1$, it must be $Gr_S>0$ ($\beta_S>0$, ρ increases with decreasing C). Contrarily, $Gr_S<0$ ($\beta_S<0$, ρ decreases with decreasing C) in the case of $N=-1$. In this paper, isoconcentration ($C=0$) at $t=0$ changes impulsively to $C=-1$ on the bottom, than the concentration at the bottom remains at $C=-1$. This induces the fluid density to become heavier for $N=1$ and lighter for $N=-1$ near the bottom. In the case of $N=1$, the fluid in the solutal boundary layer along the bottom is pushed to the symmetry line, it will amass there and be difficult to move upward due to its biggish density. Fig. 8(b) shows that the cold intrusion near the bottom wall is cumbered and the rate of the development of solutal field along the symmetry line slows down in contrast to the nature convection in Fig. 7(b). At the same time, flow turns upward before it approaches the symmetry line, as shown in Fig. 10. Finally, it will form a dead region because of slow flow and inefficient heat transfer in the neighborhood of the symmetry line near the bottom. Fig. 11 shows the temperature distribution on that region in the cases of $N=1$, 0, -1. It is clearly seen that the temperature remains higher for $N=1$ because of the above reason. On the contrary, in the case of $N=-1$, being squeezed up and pushed to the symmetry line by the cold intrusion, the fluid will move upward rapidly because of the low density, as shown in Fig. 9. At the same time, the flow in the cavity will be chaotic and the waves near the bottom will appear due to the opposite direction of thermal and solutal buoyancy. The dead region and the irregular and disorganized flow must be avoided for good quality of practical crystal growth.

The average Nusselt number Nu at the sidewall and the average Sherwood number Sh at the bottom wall for different cases are presented in Figs. 12 and 13, respectively. It is observed that the Nu numbers change little as the buoyancy ratio N varies. In addition, it is observed that the variation of Sh numbers shows much difference. This is associated with the different patterns of the thermal and solutal boundary layers in the different cases.

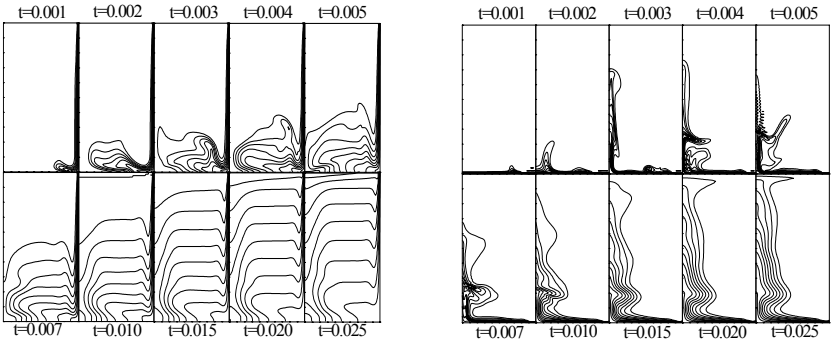

(a) Temperature fields (b) Concentration fields

Figure 7: Thermal convection (N=0).

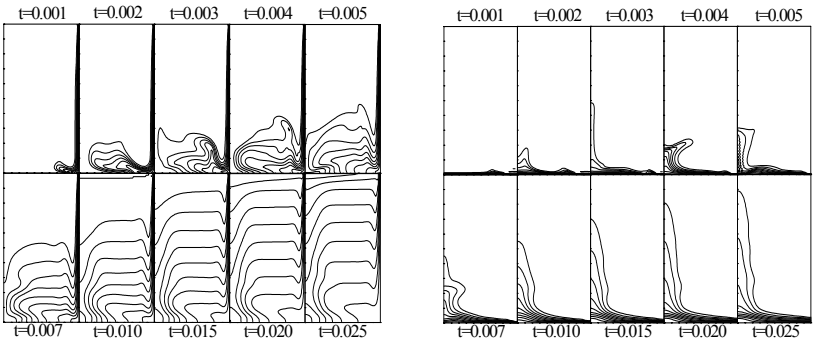

(a) Temperature fields (b) Concentration fields

Figure 8: The double-diffusion convection for N=1.

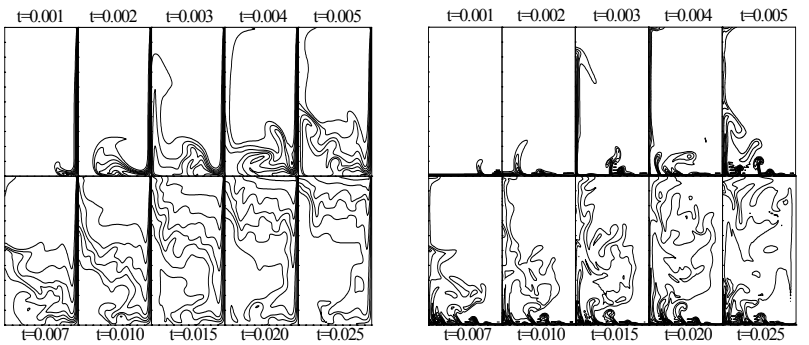

(a) Temperature fields (b) Concentration fields

Figure 9: The double-diffusion convection for N= –1.

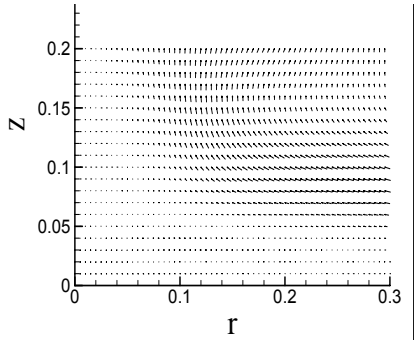

Figure 10: Velocity vector graph for N=1 at t=0.020.

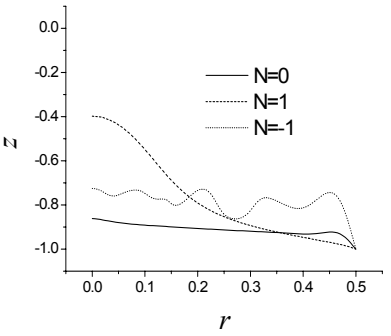

Figure 11: Temperature profile at z=0.05 and t=0.020.

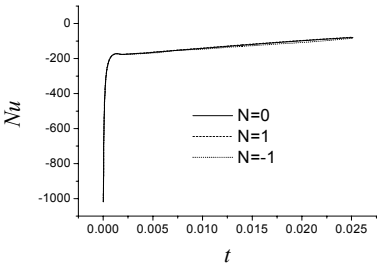

Figure 12: The average Nu at the sidewall.

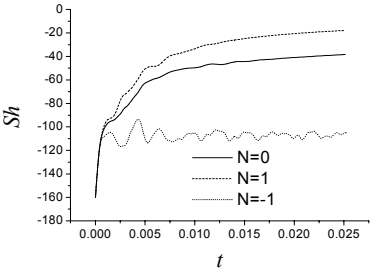

Figure 13: The average Sh at the bottom wall.

4 Conclusions

1) The problem of solute segregation and redistribution is calculated using DRBEM with augmented items. The calculating results can be fitted by the experimental data, so it is reliable to use this method.

The variation of the solute redistribution with the growth velocity during the CdZnTe growth process is simulated. Numerical results show that the solute redistribution can be divided into three regions, i.e. initial transient region, steady growth region and the final transient region. Some factors such as increasing or decreasing growth velocity can affect the length of three regions. Numerical results show that the initial and final transient regions both become shorter and the steady growth region becomes longer as the velocity increases.

For the numerical example of HgCdTe growth process, the phase change temperature obviously decreases with the phase-change interface time marching in the initial transient region and final transient region. This draws the important phenomena of non-isothermal phase change.

2) Numerical solutions are obtained for the transient process of the double-diffusive convection with horizontal temperature and vertical solutal gradients in

a vertical circular cylinder by FEM. The presented results exhibit a comprehensive and direct perception of the transient process of double-diffusive convection; at the same time, new features of double-diffusive convection are observed for different buoyancy ratios (N=Gr_S/Gr_T).

Due to the cold intrusion on the bottom, the solutal in the solutal boundary layer will be pushed to the symmetry line by the cold intrusion and then move upward.

In the case of N=1, a dead region forms in the neighborhood of the symmetry line near the bottom. In the case of N= –1, irregular and disorderly flow occurs and waves appear near the bottom wall continuously. These phenomena are worth noticing for practical crystal growth processes.

Under the condition of double-diffusive convection, since the different patterns of the thermal and solutal boundary layers exist in different cases, the variation of heat transfer rate (Nu) along the sidewall is almost the same while the mass transfer rate (Sh) along the bottom changes much with buoyancy ratios.

Acknowledgement

The project is supported by the National Natural Scientific Foundation of China (Grant No. 50336040).

References

[1] Bai, F.W. & Lu, W.-Q, The selection and assemblage of approximation functions and disposal of its singularity in axisymmetric DRBEM for heat transfer problems. *Engineering Analysis with Boundary Elements*, **28**, pp. 955–965, 2004.

[2] Wang, Y. & Li, Q.-B., etc, The choice of the initial velocity during the growth process of HgCdTe using VBM*, Infrared Technology*, **22**, pp. 25–28, 2000.

[3] Liu, X. & Jie, W.-Q., etc, *Numerical analysis of CdZnTe Crystal growth by the vertical Bridgman method using the accelerated crucible rotation technique*, Journal of Crystal Growth, 219, (2000), 22–31.

[4] Kim, D.H. & Brown, R.A., Modelling of the dynamics of HgCdTe growth by the vertical Bridgman method, *Journal of Crystal Growth*, **114**, pp. 411–434, 1991.

[5] Shi, K.F. & Lu, W.-Q., Double-diffusive Convection in an Annular Vertical Cavity, *Journal of the Graduate School of the Chinese Academy of Sciences,* **22** (2)，pp. 152–156, 2005.

[6] Lin, W.X. & Armfield, S.W., Direct Simulation of Natural Convection Cooling in a Vertical Circular Cylinder, *International Journal of Heat and Mass Transfer,* **42,** pp. 4117–4130, 1999.

This page intentionally left blank

Phase-field simulation of two-phase micro-flows in a Hele-Shaw cell

Y. Sun & C. Beckermann
Department of Mechanical and Industrial Engineering, University of Iowa, USA

Abstract

A two-phase diffuse interface model previously developed by the authors is used to simulate the buoyancy-driven flow and Rayleigh-Taylor instability of fluid layers inside a Hele-Shaw cell. The model assumes that the two phases coexist inside the diffuse interface with different properties and velocities. A separate momentum equation is used to calculate the slip velocity between the two phases within the diffuse interface. This two-phase approach is coupled with a phase-field equation for calculating the interface motion. The model is validated by comparing the calculated interface evolution, before any topology changes occur, to available results from a sharp interface model. Then, the flows and interface topology changes are investigated for fluid layers with a large density and viscosity contrasts. The convergence of the results with respect to the interface width is examined in detail. It is shown that the two-phase model converges better than standard diffuse interface models that assume a single velocity inside the diffuse interface.

1 Introduction

Two-phase flows featuring topology transitions and other interface singularities have become an area of increasing research interest over the last decade [1-3]. In such flows, multiple length and time scales emerge and capillary stresses cannot be neglected. For the nano-scale phenomena introduced by interface singularities, conventional sharp interface models fail to work. Diffuse interface approaches have been proposed to overcome these difficulties [1, 4, 5]. In diffuse interface models, the interface is viewed as a region of finite extent over which the properties vary smoothly from one phase to the other.

WIT Transactions on Engineering Sciences, Vol 50, © 2005 WIT Press
www.witpress.com, ISSN 1743-3533 (on-line)

All thermodynamically derived diffuse interface models [1, 2, 4] assume the existence of a single velocity and pressure at any point inside the diffuse interface between two phases. Moreover, single thermophysical properties (e.g., density and viscosity) are assumed to exist and their variation across the diffuse interface is postulated in some *ad-hoc* manner. For large differences in these properties between the phases, such diffuse interface models can give results that are very dependent on the choice of the interface width [6] and the way the property variations are specified [7]. Based on an atomic-scale ensemble averaging approach, a so-called "two-phase" diffuse interface model was recently developed by the present authors [6]. As opposed to thermodynamically derived diffuse interface models, the two phases are assumed to coexist inside the diffuse interface with different properties, velocities, and pressures. The phase interactions are modelled explicitly through the inclusion of interfacial forces in the momentum equations for each phase. Capillary stresses inside the diffuse interface are included in the model as well. One unique feature of the model is that the results are independent of the diffuse interface width for simple shear flows. This allows for artificially large interface widths and hence significantly improves computational efficiency.

In the present study, the two-phase diffuse interface model from [6] is applied to a buoyancy-driven flow inside a Hele-Shaw cell that features interface topology transitions. The motion of the interface between the two phases is calculated using a phase-field equation [8]. The two-phase model is compared to a mixture model that assumes a zero slip velocity inside the diffuse interface and is equivalent to thermodynamically derived models. The objective of this paper is to examine the differences in the predictions between the two-phase and mixture diffuse interface models for large density and viscosity contrasts between the phases. The convergence of the results from the two models with respect to the interface width is compared in detail.

2 Model equations

2.1 Two-phase model

The present study considers the flow of two viscous fluids of different properties (i.e., density and viscosity) inside a Hele-Shaw cell. The cell has a gap of width b that is much smaller than the cell length L (i.e., $b << L$), as illustrated in Fig. 1. The two-phase diffuse interface model of Sun and Beckermann [6] is simplified in the following using the standard Hele-Shaw approximations [9].

2.1.1 Continuity

In the absence of phase change, the two-phase continuity equations are given by

$$\nabla \cdot \boldsymbol{u} = (\rho_1 - \rho_2)\nabla \cdot \left[\frac{\phi(1-\phi)}{\rho} \Delta \boldsymbol{u} \right] \tag{1}$$

$$\frac{\partial \phi}{\partial t} + \boldsymbol{u} \cdot \nabla \phi + \rho \nabla \cdot \left(\frac{\phi(1-\phi)}{\rho} \Delta \boldsymbol{u} \right) = 0 \tag{2}$$

where ρ_1 and ρ_2 are the densities of phases 1 and 2, respectively, $\rho = \rho_1\phi + \rho_2(1-\phi)$ is the mixture density, $\boldsymbol{u} = [\rho_1\phi\boldsymbol{u}_1 + \rho_2(1-\phi)\boldsymbol{u}_2]/\rho$ is the mixture velocity averaged across the gap width b, $\boldsymbol{u}_1$ and $\boldsymbol{u}_2$ are the gap averaged velocities of the two phases, and ϕ is the phase field. The phase field varies in a hyperbolic tangent fashion across the diffuse interface, as illustrated in Fig. 2, and takes on constant values of $\phi = 1$ and $\phi = 0$ inside phases 1 and 2, respectively. It can be viewed as an atomic-scale volume fraction [5]. The parameter δ in Fig. 2 is a measure of the interface width, with ϕ varying from 0.95 to 0.05 within 6δ. The concept of a slip velocity, $\Delta\boldsymbol{u} = \boldsymbol{u}_1 - \boldsymbol{u}_2$, inside the diffuse interface is illustrated in Fig. 3. In the so-called mixture model, $\Delta\boldsymbol{u}$ is equal to zero.

Note that the right-hand side of Eq. (1) is generally non-zero for $\rho_1 \neq \rho_2$. Hence, the present two-phase approach introduces compressibility inside the diffuse interface, even though the individual phases are incompressible. Equation (2) is the evolution equation for the phase-field, ϕ. This advection equation also contains an extra term due to the slip velocity [6]. To solve it numerically, Eq. (2) is rewritten as

$$\frac{\partial\phi}{\partial t} + \boldsymbol{u}\cdot\nabla\phi + \rho\nabla\cdot\left(\frac{\phi(1-\phi)}{\rho}\Delta\boldsymbol{u}\right) = M\left[\nabla^2\phi - \frac{\phi(1-\phi)(1-2\phi)}{\delta^2} - |\nabla\phi|\nabla\cdot\left(\frac{\nabla\phi}{|\nabla\phi|}\right)\right] \quad (3)$$

where M is a purely numerical parameter. The right-hand side of Eq. (3) maintains the hyperbolic tangent phase-field profile across the diffuse interface, while cancelling out any curvature-driven interface motion. The reader is referred to [3, 8] for a detailed discussion of this technique.

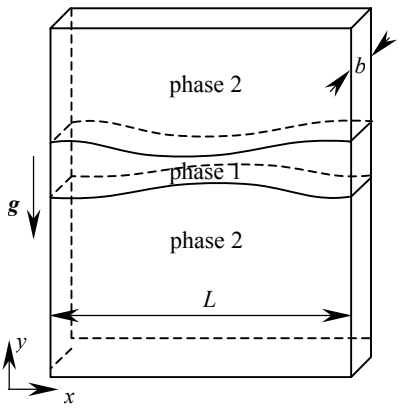

Figure 1: Schematic of the two-phase Hele-Shaw cell problem (after [2]).

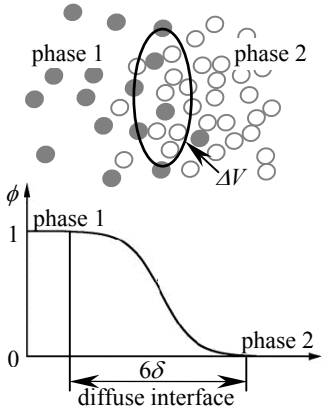

Figure 2: Schematic illustration of the diffuse interface and the phase field variation normal to the interface.

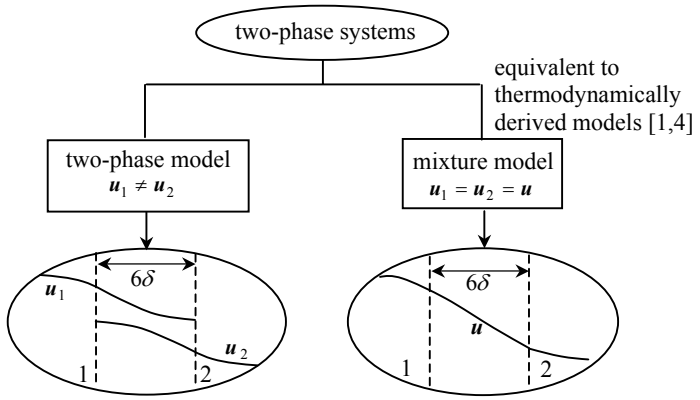

Figure 3: Illustration of the two-phase and mixture approaches.

2.1.2 Momentum

The momentum equations for the mixture velocity and the slip velocity are given, respectively, by

$$\boldsymbol{u} = -\frac{b^2}{12\mu} k_{rel}\left[\nabla p + \frac{\sigma\delta}{\phi(1-\phi)}\nabla^2\phi\nabla\phi - B\rho\boldsymbol{g}\right] \tag{4}$$

$$\Delta\boldsymbol{u} = -\frac{b^2}{12}\frac{\mu_2-\mu_1}{\mu_1\mu_2}\left[\nabla p + \frac{\sigma\delta}{\phi(1-\phi)}\nabla^2\phi\nabla\phi\right] + \frac{b^2}{12}\frac{\rho_1\mu_2-\rho_2\mu_1}{\mu_1\mu_2}\boldsymbol{g} \tag{5}$$

where $\mu = \mu_1\phi + \mu_2(1-\phi)$ is the mixture viscosity, μ_1 and μ_2 are the viscosities of phases 1 and 2, respectively, p is the mixture pressure, σ is the surface tension, and $\boldsymbol{g}$ is the gravitational acceleration. In Eq. (4), the relative "permeability", k_{rel}, is given by

$$k_{rel} = 1 + \frac{(\rho_2\mu_1 - \rho_1\mu_2)(\mu_1-\mu_2)}{\rho\mu_1\mu_2}\phi(1-\phi) \tag{6}$$

and the relative "kinetic" density, B, by

$$B = 1 + \frac{(\rho_2-\rho_1)\mu(\rho_2\mu_1-\rho_1\mu_2)\phi(1-\phi)}{\rho^2\mu_1\mu_2 + \rho(\rho_2\mu_1-\rho_1\mu_2)(\mu_1-\mu_2)\phi(1-\phi)} \tag{7}$$

These two factors are different from unity only inside the diffuse interface. Note that, $k_{rel}=1$ for $\mu_1=\mu_2$ and $B=1$ for $\rho_1=\rho_2$. The term $\sigma\delta\nabla^2\phi\nabla\phi/\phi(1-\phi)$ represents the surface tension force and is equivalent to the capillary stress term in thermodynamically derived models [1, 4] (see Ref. [6] for detail). Equation (5) shows that the slip velocity is non-zero only in the presence of property differences between the phases.

2.2 Mixture model

Setting $\Delta\boldsymbol{u}=0$, the mixture velocity, $\boldsymbol{u}$, becomes solenoidal (i.e., $\nabla\cdot\boldsymbol{u}=0$), and the last term on the left-hand side of Eq. (3) vanishes. The relative permeability, k_{rel}, and kinetic density, B, in Eq. (4) are both equal to unity.

3 Problem description and validation

The physical problem considered in the present study is adopted from [2]. As illustrated in Fig. 1, an unstable stratification is introduced by surrounding a layer of a light fluid, phase 1, by a heavy fluid, phase 2. The initial locations of the interfaces are given by $(x, y_1(x,0))$ and $(x, y_2(x,0))$, where [2]

$$\begin{cases} y_1(x,0) = \pi - (0.5 + 0.1\cos x) \\ y_2(x,0) = \pi + (0.5 + 0.1\cos x) \end{cases} \qquad 0 \le x \le 2\pi \tag{8}$$

Here, x and y are nondimensionalized by $L_0 = L/2\pi$. Periodic boundary conditions are applied in both the x and y directions. Under gravity, the upper interface is unstable and the upper heavy fluid flows downwards through the layer of light fluid. The lower interface is stable and resists motion. Ultimately, the two interfaces meet and pinch off. The equations are nondimensionalized using L_0, $t_0 = \mu_2 L/2\pi b^2(\rho_1 - \rho_2)g$, $u_0 = L_0/t_0$, and $p_0 = (\rho_1 - \rho_2)gL/2\pi$ as the length, time, velocity, and pressure scales, respectively. Two dimensionless parameters, the Bond number, $Bo = (\rho_1 - \rho_2)g(L/2\pi)^2/\sigma$, and the Atwood number, $At = (\mu_2 - \mu_1)/(\mu_2 + \mu_1)$, characterize the interface motion [2, 3]. Symbols denoting dimensionless variables are dropped in the following.

The numerical implementation of the present models (not described here due to space limitations) is validated by comparing results to the boundary-integral, sharp interface solution provided by Lee et al. [2]. The governing parameters for the validation case are [2]: density ratio $r_\rho = \rho_1/\rho_2 = 0.9$, viscosity ratio $r_\mu = \mu_1/\mu_2 = 1$, and $Bo = 25$. The mesh size is 250×250 grid points and $\delta = 0.04$. Calculated interface contours before pinch-off (at $t = 0$, 4, 6, and 7.5) are compared in Fig. 4. Note that a boundary-integral solution cannot be obtained during and after pinch-off [2]. It can be seen that the results from the present two-phase and mixture models almost overlap. This can be expected because in this example the viscosity ratio is equal to unity and the density ratio is also close to one. The diffuse interface results are in good agreement with the sharp interface solution, except near the pinch-off time (i.e., at $t = 7.5$). At that time, the diffuse interfaces are starting to overlap. Similar differences between diffuse and sharp interface results near the pinch-off have also been observed by Lee et al. [2]. They used a Cahn-Hilliard type (mixture) diffuse interface model with concentration as the order parameter.

The differences between the diffuse and sharp interface results before pinch-off can be attributed to the diffuse interface model results not being fully converged with respect to the interface width, δ. Identical results can only be expected for $\delta \to 0$. Figure 5 compares the convergence behaviour of the two-phase and mixture models with respect to δ. The calculated y intercept of the upper interface (i.e., the $\phi = 0.5$ contour), y_δ, at $t = 7.5$ is used as the figure of merit. The reference intercept, y_0, is obtained from the sharp interface solution of [2]. It can be seen that for a finite interface width, y_δ differs significantly from the sharp interface result. The two-phase and mixture models show both a

linear convergence behaviour with respect to δ. However, for a given interface width, more accurate results are obtained by the two-phase model, even though the density contrast is small and $r_\mu = 1.0$ in this case.

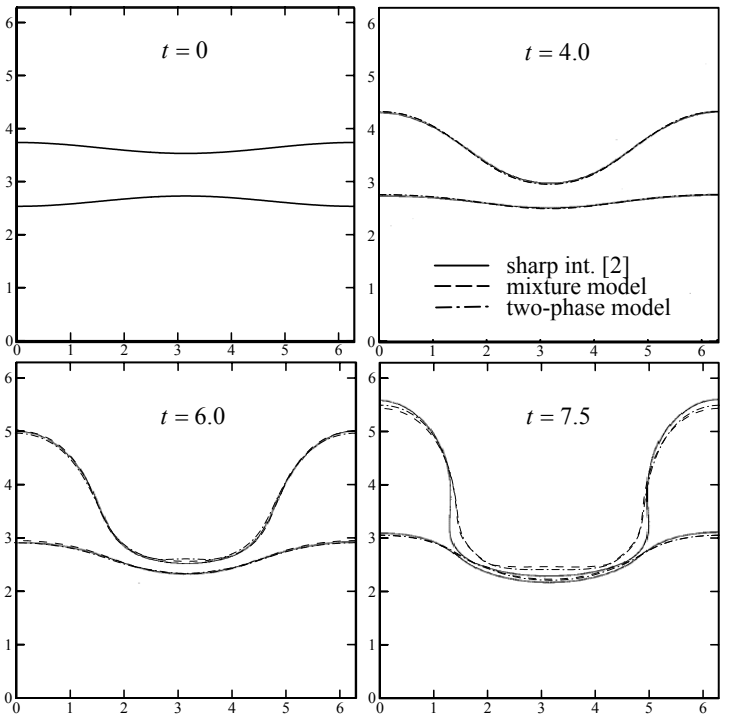

Figure 4: Evolution of interfaces: comparison between sharp and diffuse interface solutions ($r_\rho = 0.9$, $r_\mu = 1.0$, $Bo = 25$, and $\delta = 0.04$).

4 Results for large property contrasts between the phases

The two-phase and mixture models can be expected to differ more significantly for larger property contrasts between the two phases than in the previous test case. In the example of this section, the density and viscosity ratios are chosen to be $r_\rho = 0.01$ and $r_\mu = 0.1$. These ratios should be viewed as corresponding to a much less dense and less viscous phase 1 (middle fluid layer) compared to phase 2. The Bond number is kept unchanged by adjusting $\boldsymbol{g}$. The focus in the following discussion is on (i) the topology transition around the pinch-off time and (ii) the convergence of the results with respect to the interface width.

The calculated evolution of the phase-field contours for this example is shown in Fig. 6 for both the two-phase and mixture models. It can be seen that

the pinch-off occurs earlier for the two-phase model than for the mixture model. Also, at $t = 2.0$, two satellite drops appear for the two-phase model, while only a single but larger droplet occurs for the mixture model. The difference in the pinch-off time can be attributed to the presence of a highly asymmetric (with respect to $\phi = 0.5$) velocity distribution across the diffuse interface for the mixture model. For that model, the velocity inside the diffuse interface is dominated by phase 2, because that phase has a much larger density and viscosity. Since phase 2 is more viscous than phase 1, the velocity of phase 2 near the interface is generally less than that of phase 1. Hence, the asymmetric velocity distribution slows down the interface motion. The two-phase model effectively prevents this asymmetry because a slip flow is allowed inside the diffuse interface.

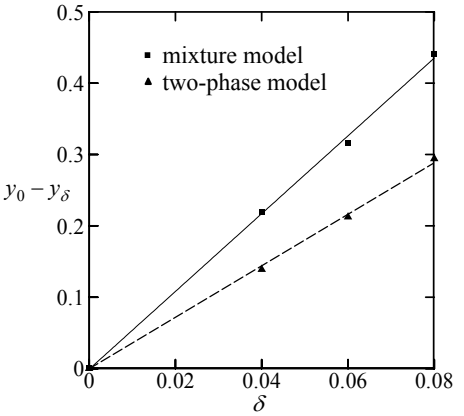

Figure 5: Convergence of y intercept of the upper interface at $t = 7.5$ wrt. δ ($r_\rho = 0.9$, $r_\mu = 1.0$, and $Bo = 25$).

The differences in the calculated velocities between the two-phase and mixture models can be better observed in Fig. 7. This figure compares results from the two models at different times, but in each case the results correspond to times right before and after the pinch-off. It can be seen that the velocities near the interface inside of phase 1 are generally smaller for the mixture model (Fig. 7a) and than for the two-phase model (Fig. 7b). This is particularly evident near the centre of the main vortex. Again, the smaller phase 1 velocities for the mixture model can be attributed to the more viscous and dense phase 2 extending its influence far across the diffuse interface into phase 1. The slip velocities inside the diffuse interface, $\phi(1-\phi)\Delta\boldsymbol{u}$, calculated by the two-phase model are shown in Fig. 7c. It is apparent that the velocity of phase 1 inside the diffuse interface is much larger than that of phase 2, which is due to the density and viscosity being smaller in phase 1 than in phase 2 [see also Eq. (5)]. Since $\boldsymbol{u} = \left[\rho_1\phi\boldsymbol{u}_1 + \rho_2(1-\phi)\boldsymbol{u}_2\right]/\rho$, the mixture velocity for the two-phase model is

therefore more symmetric across the interface, even though $\rho_1 << \rho_2$. Also note that it is the slip velocities shown in Fig. 7c that are responsible for the compressibility effect in the two-phase model, as discussed in connection with the continuity equation.

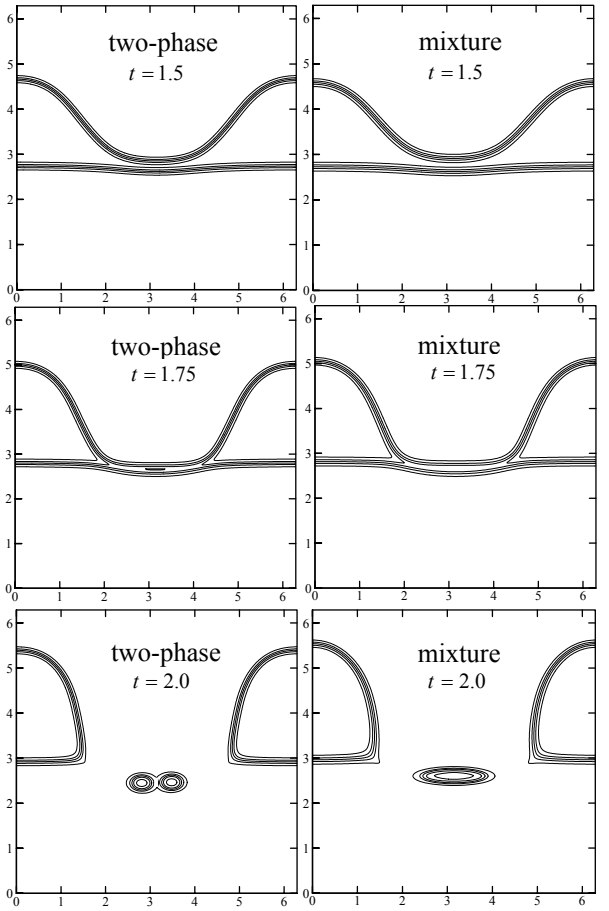

Figure 6: Evolution of phase-field contours ($\phi = 0.1$, 0.3, 0.5, 0.7, and 0.9) near the pinch-off: comparison of two-phase and mixture models ($r_\rho = 0.01$, $r_\mu = 0.1$, $Bo = 25$, $At = 0.82$, and $\delta = 0.04$).

A comparison of the convergence behaviour of the pinch-off time with respect to the interface width between the two-phase and mixture models is shown in Fig. 8. In each simulation, the grid spacing was adjusted such that $\Delta x/\delta = 0.628$, implying that the simulations with a smaller interface width required a finer grid. It can be seen that for both models, the pinch-off time

decreases in an approximately linear fashion with decreasing interface width. Best straight-line fits to the calculated results show that the pinch-off times from the two models converge to approximately the same value (~1.7) in the limit of $\delta \to 0$. As already noted in connection with Fig. 5, at a given interface width, the results from the two-phase model are much more accurate than those from the mixture model. For example, the pinch-off time for the mixture model with $\delta \approx 0.03$ is approximately the same as for the two-phase model with $\delta = 0.06$. Hence, the two-phase model offers a significant advantage relative to a standard mixture approach for large property contrasts between the phases. The remaining dependence of the two-phase model results on the interface width can be attributed to the presence of δ in the capillary stress term in the momentum equation.

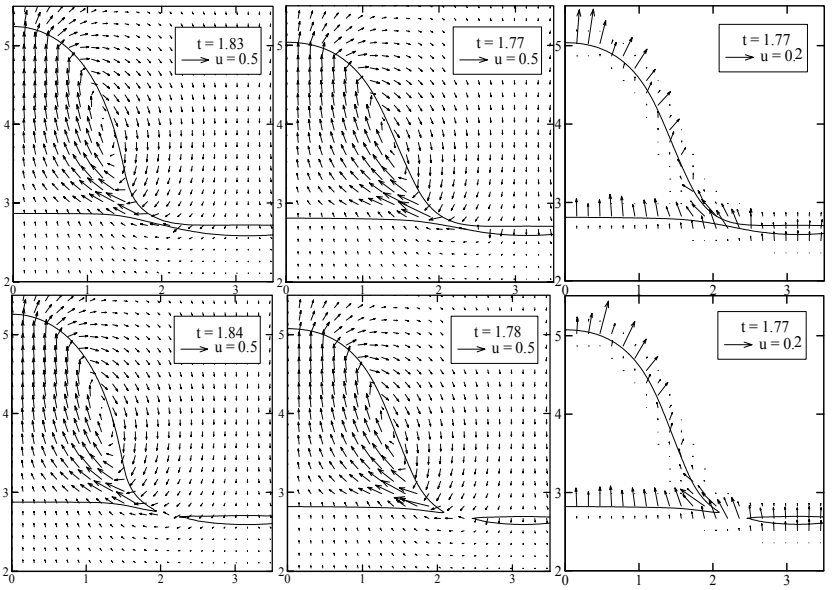

(a) $\boldsymbol{u}$: mixture (b) $\boldsymbol{u}$: two-phase (c) $\phi(1-\phi)\Delta\boldsymbol{u}$: two-phase

Figure 7: Velocity vectors before (upper panels) and after (lower panels) pinch-off ($r_\rho = 0.01$, $r_\mu = 0.1$, $Bo = 25$, $At = 0.82$, and $\delta = 0.04$).

5 Conclusions

The present study shows that, in the presence of large property contrasts between the phases, the use of a two-phase approach in diffuse interface modeling of micro-scale two-phase flows offers a significant advantage relative to standard models that assume a single velocity inside the diffuse interface. The two-phase

approach strongly reduces the dependence of the results on the width of the diffuse interface. Even though the present study examines only a simplified set of diffuse interface equations for Hele-Shaw flows, a similar advantage can be expected for the full Navier-Stokes version of the two-phase model as presented in [6]. Future work should focus on developing methods to overcome the remaining interface width dependencies due to the capillary stress term in the momentum equation. The ultimate goal of such work should be to achieve complete convergence of the results for a finite interface width (since only finite interface widths can be resolved numerically), along the same lines as in the thin-interface phase-field models of Karma and Rappel for solidification [10]. Only then can diffuse interface models be used reliably for the simulation of complex two-phase flows.

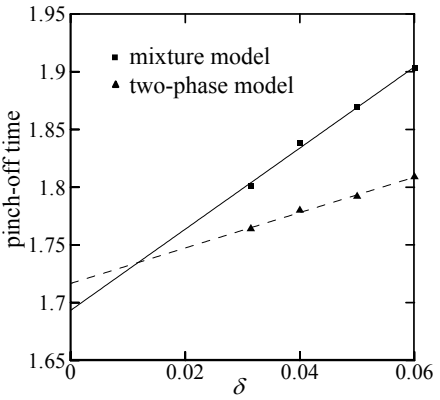

Figure 8: Convergence of pinch-off time wrt. δ ($r_\rho = 0.01$, $r_\mu = 0.1$, $Bo = 25$, and $At = 0.82$).

Acknowledgement

This work was supported by the U.S. National Science Foundation under Grant No. DMR-0132225.

References

[1] Jacqmin, D., Calculation of two-phase Navier-Stokes flows using phase-field modeling. *J. Comput. Phys.*, **155**, pp. 96-127, 1999.

[2] Lee, H.-G., Lowengrub, J.S. & Goodman, J., Modeling pinchoff and reconnection in a Hele-Shaw cell. I. The models and their calibration & II. Analysis and simulation in the nonlinear regime. *Phys. Fluids*, **14**, pp. 492-513 & pp. 514-545, 2002.

[3] Folch, R., Casademunt, J., Hernández-Machado, A. & Ramírez-Piscina, L., Phase-field model for Hele-Shaw flows with arbitrary viscosity contrast. I. Theoretical approach & II. Numerical study. *Phys. Rev. E*, **60**, pp. 1724-1733 & pp.1734-1740, 1999.

[4] Anderson, D.M., McFadden, G.B. & Wheeler, A.A., Diffuse-interface methods in fluid mechanics. *Ann. Rev. Fluid Mech*., **30**, pp. 139-165, 1998.

[5] Beckermann, C., Diepers, H.-J., Steinbach, I., Karma, A. & Tong, X., Modeling melt convection in phase-field simulations of solidification. *J. Comput. Phys.*, **154**, pp. 468-496, 1999.

[6] Sun, Y. & Beckermann, C., Diffuse interface modeling of two-phase flows based on averaging: mass and momentum equations. *Physica D*, **198**, pp. 281-308, 2004.

[7] Anderson, D.M., McFadden, G.B. & Wheeler, A.A., Phase-field model of solidification with convection. *Physica D*, **135**, pp. 175-194, 2000.

[8] Sun, Y. & Beckermann, C., Interface tracking using the phase-field method (in preparation).

[9] Saffman, P.G. & Taylor, G., The penetration of fluid into a porous medium or Hele-Shaw cell containing a more viscous liquid. *Proc. R. Soc. London A*, **245**, pp. 312-329, 1958.

[10] Karma, A. & Rappel, W.-J., Phase-field model for computationally efficient modeling of solidification with arbitrary interface kinetics. *Phys. Rev. E*, **53**, pp. R3017-3020, 1996.

This page intentionally left blank

Section 5
Turbulent flow

This page intentionally left blank

Stabilization of heat transfer in a turbulent film flow

S. Sinkunas[1], J. Gylys[1] & A. Kiela[2]
[1]*Department of Thermal and Nuclear Energy, Kaunas University of Technology, Lithuania*
[2]*Department of Technology, Kaunas College, Lithuania*

Abstract

The aim of the present study is to clarify the tendencies of the heat transfer developments in gravitational liquid film flow. Heat transfer in a turbulent film flow on a vertical tube has been investigated in this paper. The analytical study of stabilized heat transfer of turbulent film has been performed. The calculation method for the local heat transfer coefficient of turbulent film falling down a vertical convex surface is proposed. The analytical approach is used to establish the dependence of heat flux variation on the distance from the wetted surface. An experimental investigation of heat transfer in the entrance region of the turbulent film has also been carried out. The methodology involves determining the local heat transfer coefficient and establishing the transfer stabilization length. The description of the experimental set-up and procedure is presented in this study. The experiments have been performed in water film flowing down a surface of vertical tube for Reynolds number ranged from 5850–6700. The results of experiments are discussed with respect to the local heat transfer dependence on the Reynolds number and initial velocity of the film in liquid distributor.
Key words: heat transfer, gravitational liquid film flow, turbulent film, entrance region, vertical tube.

1 Introduction

A lot of industrial processes in chemical, environmental and power engineering employ gravitational liquid film systems that are often designed using the heat transfer phenomena in flows. The application of stabilized liquid film flow in industrial apparatus is perspective from both economic and engineering aspects.

The heat exchangers in which film flow is used have such advantages as relatively high heat transfer and low energy consumption.

Turbulent film flow has an immense technological importance, because it frequently occurs in normal operating conditions in a variety of heating and cooling devices used in such diverse fields as aerospace, naval, nuclear, mechanical and chemical engineering. Turbulent film flows have not been investigated as widely as their laminar counterparts. The main reason for this is that transport equations for the turbulent flow are more complex, requiring a turbulence model to solve the fluid flow and the heat transfer problem. Many useful heat transfer results have been obtained by establishing an analogy between the processes of heat and momentum transfer [1-3].

A number of experimental investigations and theoretical analysis [4,5] have been conducted to determine the hydromechanical and heat transfer characteristics of thin liquid films on vertical surfaces. Heat transfer mechanism of a liquid film flowing down horizontal tubes was investigated in [6]. A method based on the breakdown of the heat boundary layer by longitudinal fins in order to enhance the local heat transfer coefficient has been developed in this study. The comparison of various correlations for calculation of the heat transfer in liquid films with high Prandtl number was carried out in [7]. The questions of how hydromechanical parameters of gravitational turbulent film are affected by initial velocity of the film were investigated in [8]. It was found that shear stress distribution in the entrance region of vertical film flow is a function of Reynolds number and depends on the initial velocity of the film.

2 Analytical method

2.1 Heat transfer determination in a turbulent film

In practice, the operation of real film heat exchangers is based on vertical tubes. Therefore, evaluating the cross curvature of wetted surface, heat flux across the turbulent film can be determined by the expression

$$q = -c\rho\left(1+\varepsilon_R \frac{y}{\delta}\right)(a + a_b + a_t)\frac{dT}{dy} \tag{1}$$

Let us denote that

$$\vartheta = T_w - T \text{ and } \psi = \int_0^{\eta} \frac{(q/q_w)d\eta}{\left(1+\varepsilon_R \dfrac{\eta}{\eta_\delta}\right)\left(1+\dfrac{a_b}{a}+\dfrac{a_t}{a}\right)} \tag{2}$$

By integrating the eqn (2) and making simple rearrangements we obtain the expression defining the temperature field in the film

$$\vartheta = \frac{q_w Pr \psi}{c\rho v^*}. \tag{3}$$

The temperature field and heat flux distribution in the liquid film can be defined by energy equation

$$\left(1+\varepsilon_R \frac{y}{\delta}\right) c\rho w \frac{\partial T}{\partial x} + \frac{\partial q}{\partial y} = 0. \tag{4}$$

By integrating the eqn (4) within the limits from 0 to y one can obtain the ratio of heat flux densities in the film

$$\frac{q}{q_w} = 1 - \frac{c\rho}{q_w} \int_0^y \left(1+\varepsilon_R \frac{y}{\delta}\right) \frac{\partial T}{\partial x} w dy. \tag{5}$$

The dimensionless form of eqn (5) is as follows

$$\frac{q}{q_w} = 1 - \frac{c\rho v}{q_w} \int_0^\eta \left(1+\varepsilon_R \frac{\eta}{\eta_\delta}\right) \frac{\partial T}{\partial x} \varphi d\eta. \tag{6}$$

The temperature gradient can be defined by the following boundary conditions on the wetted surface: $q_w = const$ and $T_w = const$. According to [9]

$$\frac{\partial T}{\partial x} = \frac{dT}{dx}, \text{ for } q_w = const \text{ and } \frac{\partial T}{\partial x} = \frac{\vartheta}{\Delta T}\frac{dT_f}{dx}, \text{ for } T_w = const. \tag{7}$$

The change of the film temperature can be determined by the equation of heat balance in the film

$$\frac{dT_f}{dx} = \frac{q_w - q_s}{c\Gamma} = \frac{4q_w}{c\rho v Re}\left(1 - \frac{q}{q_w}\right). \tag{8}$$

Taking into consideration that

$$\int_0^\delta \left(1+\varepsilon_R \frac{y}{\delta}\right) w dy = \frac{\Gamma}{\rho} = \frac{vRe}{4}, \tag{9}$$

we obtain the following expression of temperature difference between the wetted surface and liquid film

$$\Delta T = \frac{\int_0^{\delta}\left(1+\varepsilon_R\frac{y}{\delta}\right)\vartheta w dy}{\int_0^{\delta}\left(1+\varepsilon_R\frac{y}{\delta}\right)w dy} = \frac{4}{Re}\int_0^{\eta_\delta}\left(1+\frac{\eta}{\eta_\delta}\right)\vartheta\varphi d\eta\,. \tag{10}$$

By substituting eqn (3) for eqn (10), we get

$$\Delta T = \frac{4q_w Pr}{c\rho v^* Re}\int_0^{\eta_\delta}\left(1+\varepsilon_R\frac{\eta}{\eta_\delta}\right)\varphi\psi d\eta\,. \tag{11}$$

Dividing of eqn (3) by eqn (11) leads to the following relationship

$$\frac{\vartheta}{\Delta T} = \frac{\psi Re}{4\int_0^{\eta_\delta}\left(1+\varepsilon_R\frac{\eta}{\eta_\delta}\right)\varphi\psi d\eta}\,. \tag{12}$$

Assume that the ratio q_s/q_w does not vary during the film flow. Then the eqn (7) is valid for stabilized heat transfer in the liquid film. Employing the mentioned above expressions and taking into account eqns (8) and (12), we obtain the following relationships from eqn (6): when $q_w = const$

$$\frac{q}{q_w} = 1-\left(1-\frac{q_s}{q_w}\right)\left[\int_0^{\eta}\left(1+\varepsilon_R\frac{\eta}{\eta_\delta}\right)\varphi d\eta\right] \times\left[\int_0^{\eta_\delta}\left(1+\varepsilon_R\frac{\eta}{\eta_\delta}\right)\varphi d\eta\right]^{-1}, \tag{13}$$

and then $T_w = const$

$$\frac{q}{q_w} = 1-\left(1-\frac{q_s}{q_w}\right)\frac{\int_0^{\eta}\left(1+\varepsilon_R\frac{\eta}{\eta_\delta}\right)\varphi\psi d\eta}{\int_0^{\eta_\delta}\left(1+\varepsilon_R\frac{\eta}{\eta_\delta}\right)\varphi\psi d\eta}\,. \tag{14}$$

In practice, $q_s/q_w = const$ is not frequent. Therefore, eqns (13) and (14) can be used when $q_s \le q_w$. The comparison of the mentioned above equations has showed that heat flux ratio determination is complicated when $T_w = const$. The use of eqn (13) is more convenient for calculation of ratio q/q_w.

Variation of the heat flux ratio in turbulent film on vertical tube surface for the different Reynolds numbers is shown in figure 1.

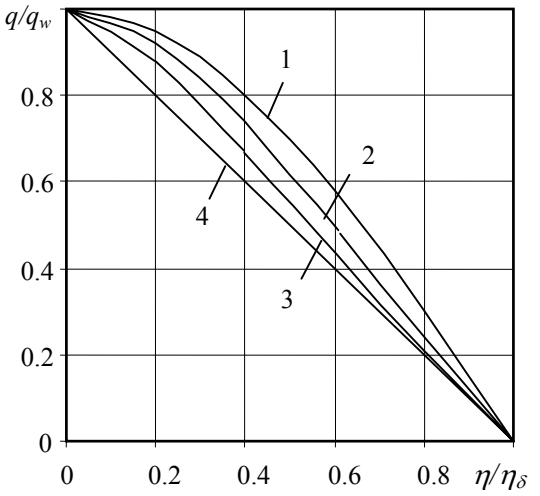

Figure 1: Dependence of heat flux variation on the distance from the wetted surface for the different Reynolds numbers: 1 – Re=1620; 2 – Re= 3123; 3 – Re=9440; 4 – $q/q_w = 1 - \eta/\eta_\delta$.

Dynamic velocity of the film can be defined by equation

$$v^* = \left(0.25 \nu g \eta_d\right)^{1/3}. \tag{15}$$

By substituting eqn (15) for eqn (11), we obtain the relationship for calculation of heat transfer coefficient

$$\alpha = \frac{q_w}{\Delta T} = \frac{c\rho Re\left(0.25\eta_d\right)^{1/3}\left(\nu g\right)^{1/3}}{4\int_0^{\eta_\delta}\left(1+\varepsilon_R\frac{\eta}{\eta_\delta}\right)\varphi\psi d\eta}. \tag{16}$$

In case of heat transfer calculations, it is more reasonable to use dimensionless values. Therefore, eqn (17) can be modified to the following relationship

$$Nu_M = \frac{Re(0.25\eta_d)^{1/3}}{4\int_0^{\eta_\delta}\left(1+\varepsilon_R\frac{\eta}{\eta_\delta}\right)\varphi\psi d\eta}. \quad (17)$$

It should be noted that in case of wavy film flow, the mentioned above method of heat transfer calculation is valid only for small values of the ratio $q_s/q_w \le 0.1$.

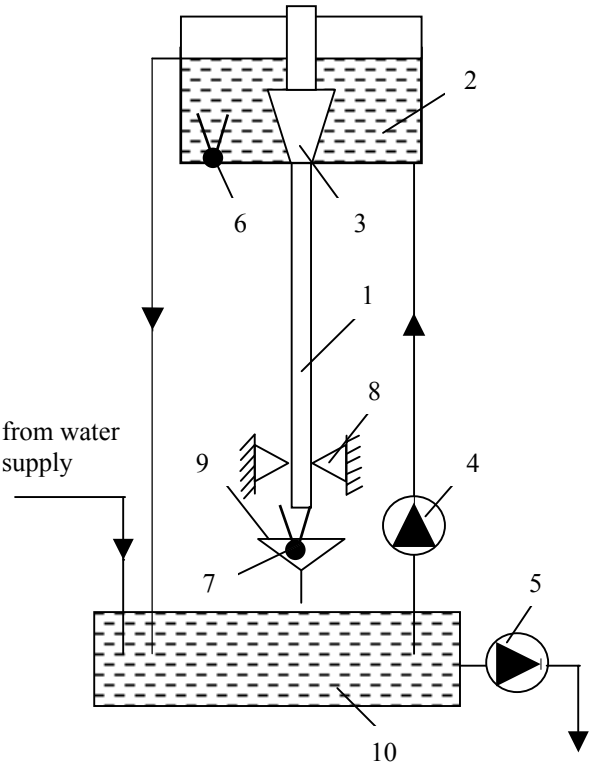

Figure 2: Schematic diagram of experimental set-up: 1 – calorimeter; 2 – liquid distributor; 3 – slot distributive mechanism; 4 – feed-pump; 5 – exhaust-pump; 6 – inlet thermocouple; 7 – outlet thermocouple; 8 – centering bolts; 9 – gutter; 10 – liquid reservoir.

3 Experimental method

3.1 Experimental set-up and procedure

In order to generate the liquid film flow the experimental arrangement was applied fig. 2. The stainless steel tube, 30 mm in outside diameter with the length

of 1000 mm was employed in the experiment as a calorimeter. The fixing bolts at the end of the tested tube provided the possibility to regulate and to guarantee that the tube was in vertical position. Water was pumped up to a liquid distributor by feed-pump. At the top end of the tube a slot distributive mechanism was installed to generate the uniform film flow. After flowing down the test tube, the water was collected back to the reservoir. The gutter at the calorimeter end ensured a smooth falling of the water into the reservoir. The surplus water was discharged to the sewerage by exhaust-pump while the fresh water was supplied directly from water supply.

Preliminary investigation showed that the use of water from plumbing did not influence the demanded experiment accuracy. That is why fresh water was employed in the research. The temperature of falling down film was measured by two calibrated thermocouples. The location of a thermocouple in the liquid distributor ensured the film temperature measurement in the inlet. The thermocouple installed at the end of calorimeter determined film temperature at the exit correspondingly. As heat flux along the tested section did not change, so to the demanded accuracy of the experiment, it was assumed that the bulk mean temperature of the liquid film conform linear regularity. That circumstance has allowed determining the liquid film temperature at any cross-section of the tested section accurately.

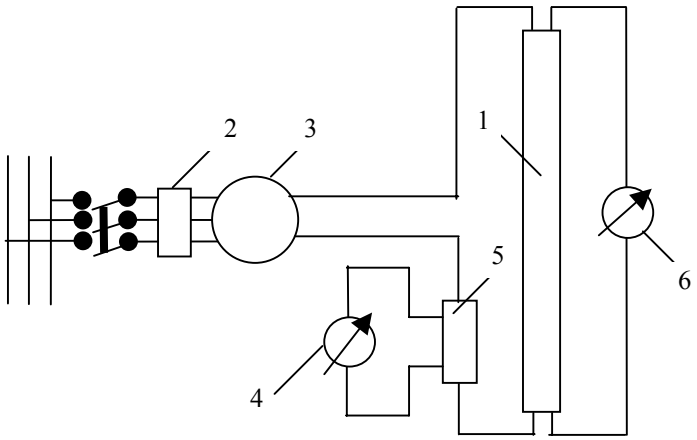

Figure 3: Electric circuit: 1 – calorimeter; 2 – voltage regulator; 3 – rectifier; 4 – millivolmeter; 5 – shunt; 6 – voltmeter.

The electric circuit was applied for the heat transfer research of falling down water film on the surface of vertical tubes, fig. 3. The electric current supplied the calorimeter with a guaranteed steady heat flux on the experimental section. The current ranged from 400 to 600 amperes and voltage from 5 to 10 volts. In order to convert an alternating current into a direct current the rectifier was used. Voltages drop on the known value resistor fitted in as shunt determined the electric current strength in the circuit. Its readings were taken from the

millivoltmeter. Voltage value on the calorimeter has been measured by voltmeter. The resistance of the test section has come to 0.015 ohm/m, while the resistance of water film has not exceeded $28 \cdot 10^6$ ohm/m. So, heat dissipation within the liquid film has been ignored on the assumption that the whole heat flux, determined by the voltage drop and current, has been carried through the surface of tested section exclusively.

3.2 Local heat transfer for a turbulent film flow on a vertical surface

The water film flowing down the surface of vertical tube has been used in experiments. The experiments have been carried out for Reynolds number ranged from 5850 to 6700. The temperature of the tube (calorimeter) surface and the film, electric current, voltage have been measured and recorded during the experiment. After registration of electric current and voltage the heat flux density on the calorimeter surface has been calculated. After heated tube surface and film flow temperatures were recorded, the difference of temperature ΔT (between the mean temperatures of film $\overline{T}_f$ and tube surface T_w) has been calculated. The local heat transfer coefficient was calculated by formula

$$\alpha = q_w / \Delta T \ . \tag{18}$$

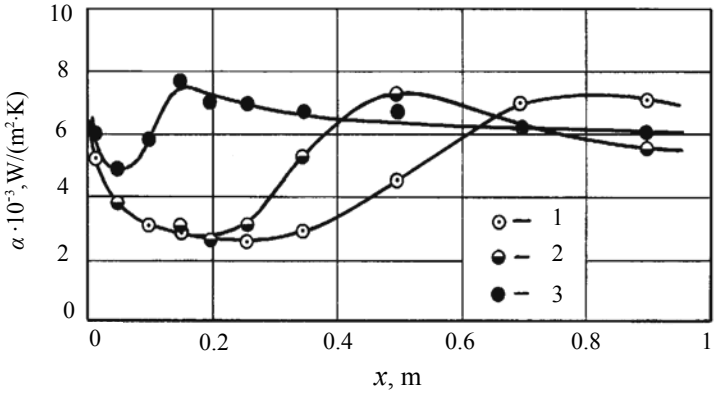

Figure 4: Variation of local heat transfer coefficient in the entrance region of the film flow down a vertical surface: 1 – Re=5850, ε =0.9; 2 – Re=6200, ε =1.27; 3 – Re=6700, ε =1.38.

Experimental data is presented in figure 4. Three different regions may be distinguished along the length of film flow in such a case when initial average velocity of the film in the liquid distributor is less or exceeds an average velocity of stabilized flow. The significant decrease of the local heat transfer coefficient at a certain distance from liquid distributor is seen in the first region while reaching minimal value. This phenomenon one can explain by the development

of thermal boundary layer and its laminar nature. In the second region, fluid fluctuations begin to develop while heat transfer increases up to its maximum value. The beginning of heat transfer stabilization takes place in the third region of the film flow. Augmentation of a thermal boundary layer terminates with the film thickness. The variation of local heat transfer in the entrance region, when initial average velocity of the film exceeds the average velocity of stabilized film, is not high. In all cases the heat transfer stabilization takes place at the distance 0.7 m from the liquid distributor when $Re < 10^4$.

4 Conclusions

Predictions of heat transfer in turbulent liquid film flow on the surface of vertical tubes have been made. The relationships for calculation of local heat transfer coefficient are valid for the following boundary conditions on the wall: $T_w = const$ and $q_w = const$. It has been determined that heat flux intensity in turbulent film decreases as the distance from the wetted surface increases.

The turbulent film flow is very complicated and difficult for theoretical study. The determining effect of film generation on heat transfer takes place in the entrance region of the film flow down the surface of vertical tube. The experimental data has revealed that Reynolds number and initial velocity have a significant influence on local heat transfer. It has been obtained that heat transfer stabilization occurs at 0.7 m distance from the liquid distributor when $Re < 10^4$.

5 Nomenclature

a – thermal diffusivity, m/s^2; a_b – wavy thermal diffusivity, m/s^2; a_t – turbulent thermal diffusivity, m/s^2; c – specific heat, J/(kg·K); d – hydraulic diameter of the film, m; g – acceleration of gravity, m/s^2; Nu_M – modified Nusselt number, $(\alpha/\lambda)(\nu^2/g)$; Pr – Prandtl number, ν/a; q – heat flux density, W/m^2; Re – Reynolds number for liquid film, $4\Gamma/(\rho\nu)$; T – temperature, K; v^* – dynamic velocity, $(\tau_w/g)^{1/2}$; w – film velocity, m/s; x – longitudinal coordinate; y – distance from the wetted surface, m; α – heat transfer coefficient, W/(m^2·K); Γ – wetting density, kg/(ms); δ – liquid film thickness, m; η – dimensionless distance from the wetted surface, v^*y/ν; η_δ – dimensionless film thickness, $v^*\delta/\nu$; η_d – dimensionless film diameter, v^*d/ν, ε – relative film velocity $\overline{w}_d / \overline{w}_{stab}$; ε_R – relative cross curvature of the film, δ/R; λ – thermal conductivity, W/(m·K); ν – kinematic viscosity, m^2/s; ρ – liquid density, kg/m^3; τ – shear stress, Pa; φ – dimensionless film velocity, w/v^*;

Subscripts: b – wavy; d – distributor; f – film flow; s – film surface; $stab$ – stabilized flow; t – turbulent; w – wetted surface.

References

[1] Gimbutis, G., *Heat Transfer of a Falling Fluid Film*, Mokslas Publishers: Vilnius, 1988.

[2] Tananayko, J.M. & Vorontszov, E.G., *Analytical and Experimental Methods in a Fluid Film Flow*, Technika: Kiev, 1975.
[3] Von Karman, T., The analogy between fluid friction and heat transfer. *Trans. ASME,* 61, pp.705–710, 1939.
[4] Alekseenko, S., Cherdantsev, S., Kharlamov, S. & Markovitch, D., Characteristics of liquid film in a vertical pipe with the pressure of gas flow. *Proc. of the 5th World Conference on Experimental Heat Transfer, Fluid Mechanics and Thermodynamics*, Edizioni ETS: Pisa, Vol. 3, pp. 1996–1999, 2001.
[5] Bertani, C. & De Salve, M., On freely falling liquid film along vertical flat plate. *Proc. of the 5th World Conference on Experimental Heat Transfer, Fluid Mechanics and Thermodynamics*, Edizioni ETS: Pisa, Vol.3, pp. 1953–1958, 2001.
[6] Rifert, V., Sidorenko, V., Usenko, V. & Zolotukhin, I., Heat transfer and breakdown of subcooled falling liquid film on a middle size heater, *Proc. 5th World Conference on Experimental Heat Transfer, Fluid Mechanics, and Thermodynamics*, Edizioni ETS: Pisa, Vol. 3, pp. 1997–2000, 2001.
[7] Wadekar, V.V., Heat transfer to falling liquid films with high Prandtl numbers, *Proc. 3rd European Thermal Sciences Conference,* Edizioni ETS: Pisa, Vol. 2, pp. 851–856, 2000.
[8] Sinkunas, S., Influence of cross curvature on hydrodynamic parameters of laminar liquid film. *Mechanics*, 2 (22), pp. 31–35, 2000.
[9] Kays, W.M., *Convective Heat and Mass Transfer,* Energy: Moscow, 1972.

Effects of droplet preferential segregation in turbulent flows on the mixture fraction topology

J. Réveillon & F. X. Demoulin
CORIA, University and INSA of Rouen, Saint Etienne du Rouvray, France

Abstract

The objective of this paper is to determine the simultaneous effects of the turbulence on the dispersion of an evaporating spray and the mixture fraction evolution. Three-dimensional simulations are carried out following two stages leading to various physical analysis. First, the mixing between the initially randomly dispersed phase is considered with non-evaporating particles. Following their Stokes number and the turbulence properties, the formation of clusters of particles is analyzed (formation delay, cluster characteristic size). Once the particles are in dynamical equilibrium with the surrounding turbulent flow, evaporation phenomena are considered through the analysis of the mixture fraction evolution.

1 Introduction

In industrial systems dedicated to transport or energy transformation, a combustion chamber is generally fuelled by a spray of evaporating liquid droplets. The modeling of such chambers, involving the combustion of a two-phase flow or of a gaseous mixture issued from evaporation of a spray, is of primary importance to improve, the output of the considered device and to predict pollutant formation while maintaining a reasonable development cost.

One of the input parameter of any non-premixed turbulent combustion model is the mixture fraction variable Z, which describes locally the mixing between the evaporated fuel and the gaseous oxidizer. The objective of this paper is to determine the simultaneous effects of the turbulence on the spray dispersion and the mixture fraction evolution. Thus, main characteristics of the mixture fraction field (fluctuation intensity levels and characteristic length scales) can be estimated directly from local properties of turbulence (rms, length scales) and spray parameters (Stokes number, liquid equivalence ratio).

WIT Transactions on Engineering Sciences, Vol 50, © 2005 WIT Press
www.witpress.com, ISSN 1743-3533 (on-line)

Multiple interactions may be defined between turbulent flow, spray dispersion and vapor micro-mixing. To reduce the number of varying parameters, a configuration very close to the one used by Eswaran and Pope [1] for their reference study dedicated to the turbulent mixing of purely gaseous flow has been extended to two-phase flow simulations [2]. Thus, a forced isotropic homogeneous turbulence, with statistically stationary properties, is used as carrier phase. A recently developed forcing scheme allowing mean stable properties of the turbulence (energy, dissipation, integral length scale) has been introduced in a spectral formulation describing the evolution of an incompressible gas phase. The dispersed spray evolution is modeled thanks to a Lagrangian formulation describing the position, the velocity and the mass of any droplet embedded in the gas phase. Because of the weak mass loading ratio and to maintain stationary turbulence properties, the coupling between both liquid and gas phases is done through mass exchange terms only and the action of the spray on turbulence is not considered in this work.

2 Numerical system and geometry

Details of computational procedure may be found in [3]. The following three-stage procedure has been employed to analyse all interactions between the turbulent flow and the dispersed phase. Vorticity contours and dispersing particles have been plotted in Fig. 1 to illustrate both Eulerian and Lagrangian resolutions.

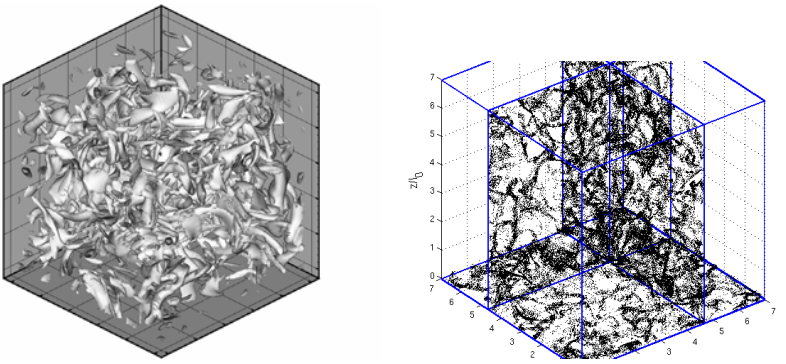

(a) (b)

Figure 1: Examples of (a) vorticity contour and (b) spray dispersion.

Stage 1: statistically stationary turbulence

In this preliminary stage, forced turbulent gaseous phase evolves solely until its statistical properties reach a steady state thanks to the forcing procedure that conserves the mean kinetic energy k equals to the prescribed one [3]. The energy spectrum allows us to determine a reference wave number κ_0 corresponding to turbulence scales that contain most of the kinetic energy.

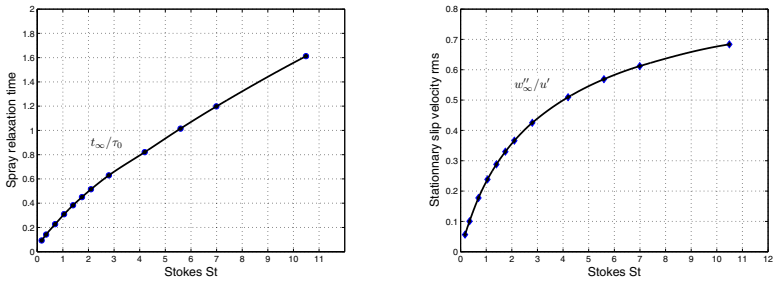

(a) (b)

Figure 2: Statistically stationary spray properties. (a) spray relaxation time (t_∞) necessary for the spray to be in equilibrium with the turbulent carrier phase; (b) final ($t > t_\infty$) stationary level of particles slip velocity rms (w'_∞).

The corresponding physical length $l_0 = 2\pi/\kappa_0$ is an integral scale of the flow that has been used as a reference parameter in this work along with its spectral counterpart κ_0. In all the simulations, $\kappa_0 = 7\Delta\kappa$. $\Delta\kappa$ is the spectral grid size defined by $\Delta\kappa = 2\pi/L$ where L is the cubical domain dimension equals to 3 mm. The maximum energy length scale l_0 is thus equal to $l_0 = L/7$ and remains constant [3]. The constant turbulence velocity root mean square $u' = 1.5\, m/s$ is also used as reference parameter along with the eddy turn over time $\tau_0 = l_0/u'$ and the velocity fluctuation characteristic time $\tau_\kappa = (\nu/\varepsilon)^{(1/2)}$ of the smallest structures. The turbulent Reynolds number of the simulation is $Re_{l_0} = 43$ and the parameters of the filter function [3] are $\kappa_F = 9\,\Delta\kappa$ and $\Delta\kappa_F = 3\,\Delta\kappa$.

Stage 2: spray dynamical equilibrium

Several eddy turn over times after the turbulent flow reaches its stationary state, N_d mono-dispersed non-evaporating particles are randomly embedded in the computational domain with a null initial velocity. The drag force sets particles in motion and very soon the spray reaches a dynamical equilibrium with the turbulence (Fig. 1-(b)). Droplet dispersion is usually characterized by the Stokes number $St = \tau_p/\tau_\kappa$ [4], which indicates the ability of droplets to capture local variations of carrier phase velocity. Turbulence properties being fixed, simulations have been carried out by modifying the τ_p parameter leading to 12 different Stokes numbers varying between 0.025 and 11.

To characterize droplet dispersion and preferential concentration, a density $\xi(\mathbf{x}, t)$, describing the local mass of liquid per unit of volume has been defined. To make easier the spectral analysis of physical properties, the Eulerian computational grid has been used and $\xi(\mathbf{x}, t)$ is determined by considering droplets accumulated in a control volume around each nodes. A mean

reference number density is defined by $\overline{\xi}_0 = N_d/L^3$. Note that in the following $\overline{()}$ stands for the mean over the Eulerian grid whereas $\widetilde{()}$ is the mean over the Lagrangian particles or droplets.

Stage 3: liquid phase evaporation and micro-mixing

Once the spray is in dynamical equilibrium, droplet evaporation start following saturation laws. To describe the mixing between gaseous fuel and oxidizer, a specific definition of the mixture fraction is chosen. A normalization is introduced using the saturation limit: $Z = Y_F/Y^s$. In this non-reactive work, Z is thus bounded between 0 and 1 and it is of practical interest for analyzing the correlations between the evaporating spray and the mixing.

3 Results and discussion

Although homogeneous turbulence is a straightforward configuration, the addition of an evaporating dispersed phase allows us to be at the midpoint of many ill-know interactions between turbulence, spray, mixing and combustion. As described in the introduction, for the sake of clarity this paper focuses on the correlations between mixture fraction topology and droplets preferential segregation. The analysis of flame ignition and propagation or model closures will be the purpose of future works. In a first part, equilibrium regimes of non-evaporating droplets are depicted before evaporation takes place. It leads to the apparition of a gaseous fuel whose mixing with oxidizer is then detailed.

3.1 Solid dispersion

Equilibrium of the spray with its surrounding carrier phase is detected through the Lagrangian statistics of the slip velocity $\mathbf{w}_k = (\mathbf{u}(\mathbf{x}_k, t) - \mathbf{v}_k)$, where $\mathbf{u}$ is the gas velocity at the droplet location and $\mathbf{v}$ is the droplet velocity. Because of the homogeneous nature of the turbulence and the dispersion, the mean value of the slip velocity defined by $\tilde{\mathbf{w}} = N_d^{-1} \sum_{k=1}^{N_d} \mathbf{w}_k$ remains equal to zero. However, the slip velocity root mean square w'' evolves toward a stationary value w''_∞ corresponding to their equilibrium with the surrounding gas. Because particles are initially randomly distributed in the computational domain with a null velocity, w''/u' is equal to one at time $t = 0$, u' stand for the r.m.s. of the gas velocity. Then, depending on particle Stokes number, w'' reaches a steady state (Fig. 2-(a)) in less than $0.2\ \tau_0$ (eddy turn over time) for small Stokes number ($St = 0.35$) and no more than $1\ \tau_0$ are needed for larger values ($St = 7$). This aspect is an important point because, in more complex configurations like combustion chambers, even if delays are short, droplets are most certainly already in equilibrium when evaporation takes place. In figure 2-(b) are plotted the final mean stationary values of the slip velocity rms : w''_∞. It starts from zero when droplets are small enough to follow all the velocity fluctuations of the flow and it increases regularly to reach asymptotically the unity that would correspond to droplets too heavy to be moved by the carrier phase ($St = \infty$).

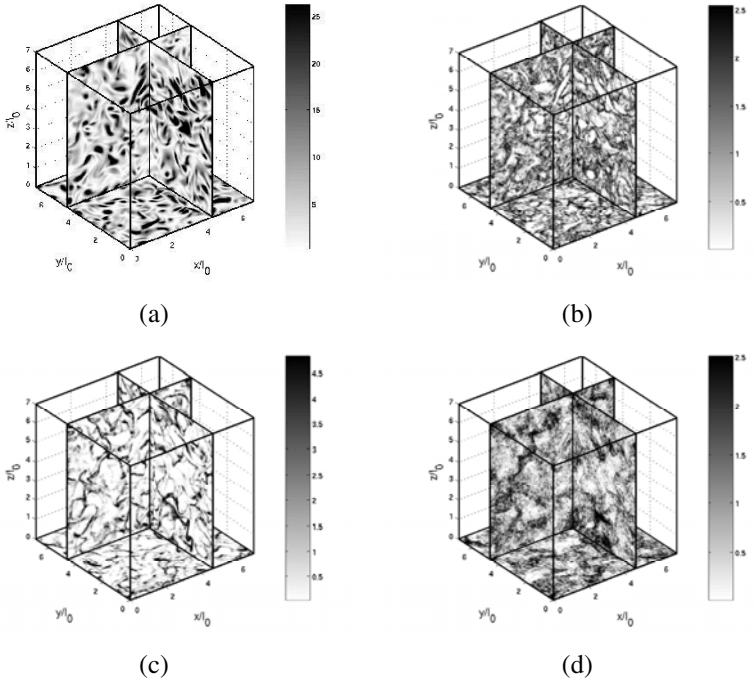

Figure 3: (a) Carrier phase vorticity $\tau_0\sqrt{\omega^2}$ and spray concentration areas $\xi/\overline{\xi}_0$, (b) $St = 0.17$, (c) $St = 1.05$, (d) $St = 5.6$.

To study the preferential concentration of discrete particles in turbulent flows several approaches were used, see for instance [4, 5, 6, 7]. In this study droplets dispersion and preferential segregation have been analyzed from an Eulerian point of view thanks to the local liquid density $\xi(\mathbf{x}, t)$. Instantaneous fields of ξ have been plotted in figure 3 for three Stokes numbers ($St = 0.17$, $St = 1.05$ and $St = 5.6$) along with the corresponding vorticity field. These four fields have been captured at exactly the same time after droplet dispersion has reached a stationary value ($t > t_\infty$). Without any statistical analysis, it is possible to notice the dramatic impact of the particle inertia on their dispersion properties. In fact, even with a small Stokes number, particles tend to leave vortex cores and segregates in weak vorticity areas because of their inertia. This phenomenon may be seen in figure 3-(b) and -(c) where ξ is represented for $St = 0.17$ and $St = 1.05$. This last case shows a normalized liquid density $\xi/\overline{\xi}_0$ ranking between 0 (no droplets) and 5 (five times the mean density). As it will be shown later, density fluctuations reach a maximum when $St = 1$. When $St = 0.17$, segregation is already clearly visible (maximum : 2.5) although there is more intermediates density areas (Fig. 3-(b)). When the $St = 1$ limit is 'broken', the spray topology tends to be totally different than for $St \leq 1$, see Fig. 3-(d) . Indeed, kinetic times become large enough for the

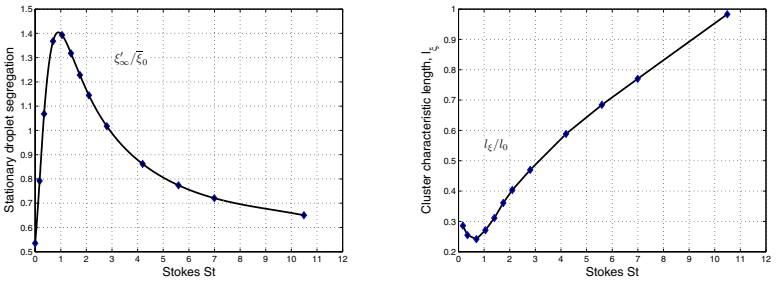

(a) (b)

Figure 4: (a) Final stationary values of the droplet segregation parameter ξ'_∞ normalized by the initial mean value of ξ: $\overline{\xi}_0$. (b) Stationary mean size of the most segregated droplet clusters for various Stokes number.

droplets to cross high vorticity areas leading to a less segregated spray (maximum : 2.5).

The Stokes number dependence of the non-evaporating droplets mean stationary segregation ξ'_∞ has been plotted in figure 4-(a). As defined above, this parameter is the standard deviation of the field ξ when droplet are in dynamical equilibrium with the carrier phase ($t > t_\infty$). Starting from $St = 0.17$ with $\xi'_\infty/\overline{\xi}_0 = 0.8$, a maximum segregation $\xi'_\infty/\overline{\xi}_0 = 1.4$ is observed for a unitary Stokes number before a progressive decay. This parameter informs us on the liquid density level in clusters formed by turbulence. It is also possible to determine their corresponding characteristic size by computing the energy spectrum $E_\xi(\kappa)$ of the variable $\xi(x,t)$ when $t > t_\infty$ and then compute $l_\xi = 2\pi/\kappa_\xi$ where κ_ξ is the position in spectral space of the most energetic (or fluctuating, in physical space) level. Plotting the l_ξ dependence with the Stokes number in figure 4-(b) demonstrates the large scale effects of the turbulence on the spray. Information about mean segregation parameter ξ'_∞ is not sufficient to characterize spray preferential segregation. Indeed for two sprays whose Stokes numbers are 0.17 and 5.6, respectively, a similar mean segregation level equals to 0.8 is found in figure 4-(a) whereas the mean size of the clusters compared to the turbulence integral scale are respectively equal to 0.25 and 0.68. Thus, even if fluctuations levels are similar, liquid density topology is different.

3.2 Evaporation and turbulent mixing

Once dynamic equilibrium is reached between the turbulent gaseous flow and the spray of droplets, the evaporation is activated. The amount of vapour of fuel in the gas phase is characterized by mixture fraction Z. Three cases are chosen that correspond to three initial Stokes numbers. They are recapitulated in table 1, cases B_* has a Stokes number close to unity hence segregation is maximum, cases A_*

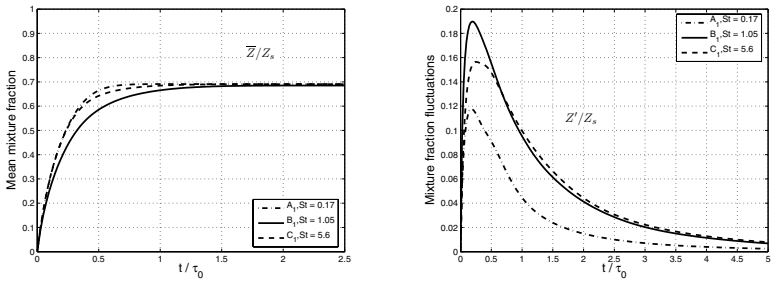

(a) (b)

Figure 5: Evolution of mixture fraction statistics in the domain, characteristic evaporation time : $0.5\tau_0$. Left : mean mixture fraction, right : deviation.

Table 1: Configuration names, St : Stokes number, τ_v : evaporation delay. Non evaporating case : $\tau_v = \infty$.

	$St = 0.17$	$St = 1.05$	$St = 5.6$
$\tau_v = \infty$	A	B	C
$\tau_v = 1/2\tau_0$	A_1	B_1	C_1
$\tau_v = 1\tau_0$	A_2	B_2	C_2
$\tau_v = 2\tau_0$	A_3	B_3	C_3

and C_* correspond respectively to moderately low and high Stokes numbers. Their initial segregation are about the same initially (figure 4-(a)). The evaporation is studied first in case (A_1, B_1 and C_1) where evaporation delay is equal to $0.5\tau_0$.

The evolution of the mixture fraction normalized by the saturation value is represented in figure 5-(a). It is clear from this figure that the most segregated case (B_1) takes the longest time to be evaporated. The clusters that contain a high number density of droplets are transformed in pockets of high vapour concentration. Since the surrounding vapour concentration can be close to its saturation value, the vapour flux leaving the droplet surface is reduced. Thus the evaporation rate decreases for each droplet located in a cluster. It is even stopped if saturation value of vapour concentration is reached in the cluster. Droplets can be evaporated if they are ejected from the cluster by turbulent motion to reach a place where vapour concentration is low enough. Concerning droplets that stay in the cluster, they evaporate only at a rate that permit to sustain the vapour concentration in the cluster at the saturation value.

The standard deviation of the normalized mixture fraction is shown for the three cases in figure 5-(b). Case C_1 clearly evolves from case A_1 to case C_1. Assuming that mixture fraction fluctuations of the variable Z are mainly due to the presence

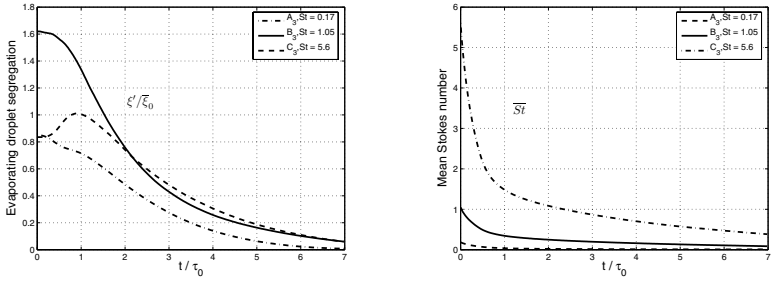

(a) (b)

Figure 6: Droplet mean properties evolution, characteristic evaporation time : $2\tau_0$. Left : droplet number fluctuations, right : mean Stokes number.

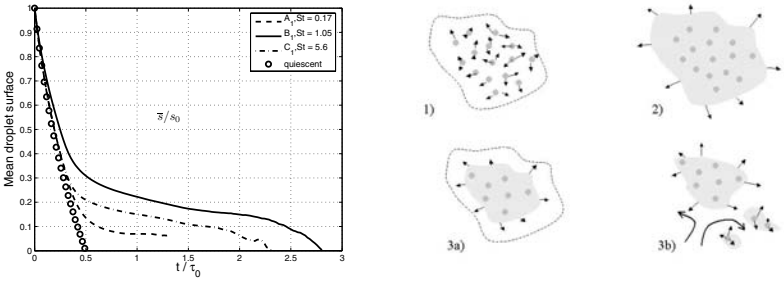

(a) (b)

Figure 7: (a) Droplet mean surface evolution, Symbols : droplet evaporation in a quiescent atmosphere. (b) Mean evaporation rate.

of clusters, it confirmed that clusters segregation of case C_1 is initially similar to case A_1 and then, they become similar to case B_1 as the Stokes number is reduced from 5.7 to 1 and lower. This effect may be imputed to the evaporation time that is chosen lower than the time necessary for clusters formation by preferential concentration effect. From figure 2-(a) it can be seen that the spray relaxation time based on initial Stokes number is respectively $0.12\tau_0$, $0.3\tau_0$ and $0.8\tau_0$ for case A,B and C to be compared with the evaporation time equal to $0.5\tau_0$.

Normalized evolution of ξ' is shown in figure 6-(a) to characterize segregation rate. Choice has been made to plot results for an evaporation time equal to $2\tau_0$ to clearly show the impact of the evaporation on the droplet segregation. The general trend is a decrease of the segregation level during evaporation; this is due to the mean diminution of the droplet number. But it is possible to notice that for the case C_3 segregation is increased first and then decrease. Initial increase of segregation level is due to the evolution of the Stokes number to a level more efficient (close to

the unity) to create cluster. Eventually the segregation level is even bigger for case C_3 than for case B_3.

Figure 6-(b) shows evolution of the Stokes number averaged on the entire set of droplets not yet evaporated for the three cases. Because droplet sizes decrease due to the evaporation, all Stokes numbers decrease. As shown previously, the most efficient Stokes number for the preferential concentration effect is of the order of unity. For cases A_3 and B_3, as their Stokes numbers evolve, the preferential concentration effect diminishes. That means that droplets can be ejected from their clusters by turbulence dispersion to be surrounded by vapor-less gas where they are able to evaporate quickly. On the contrary, for case C_3, as soon as the mean stokes number is reduced and becomes closer to unity, segregation increases and droplets are ejected from zones of high vorticity to join existing clusters. This explains the initial increase of the segregation; the maximum of segregation is obtained for the dimensionless time equal to unity (see figure 6-(a)). This value corresponds exactly to the end of the period when Stokes number is around the unity, the more effective value for preferential concentration effect (see figure 6-(b)).

The evolution of the mean droplet surface divided by its initial value is shown in figure 7-(a) for the three cases. An additional curve, represented by circle symbols, shows the expected evolution that would be obtained if homogeneously distributed droplets (no clusters) were evaporating in a quiescent flow. Then, evaporation is close to a "d-square" law although the curve is not completely straight since the mean value of the vapor concentration seen by each droplet is not anymore constant but increases as the spray is evaporated. In this case, vapor concentration seen by each droplet is the mean value of vapor over the whole domain. Figure 7-(a) shows the important effect of clusters on the evaporation. Even for the smallest droplets (case A_1), an additional time is necessary to complete the evaporation because some droplets are trapped in clusters and cannot be evaporated until they are dismantled.

A possible scenario of evaporation would be: 1) initially the evaporation is very fast since no vapor concentration prevents it. 2) But soon clusters containing a high number density of droplet reach a vapor concentration close to saturation. It reduces dramatically the evaporation rate of the droplets inside the cluster. 3) Droplets leave the saturated area: 3a) they are close to the cluster boundary and because of vapour diffusion, local vapor concentration is lower than the saturation level; 3b) or the turbulent motion ejects the droplet from the cluster, this phenomena is more likely as the droplet Stokes number is large. This scenario is described in figure 7-(b).

References

[1] Eswaran, V. & Pope, S., Direct numerical simulations of the turbulent mixing of the passive scalar. *Phys Fluids*, **31(3)**, pp. 506–520, 1988.

[2] Mashayek, F., Direct numerical simulations of evaporating droplet dispersion in forced low mach number turbulence. *Int j heat mass transfer*, **41(17)**, pp. 2601–2617, 1998.

[3] Guichard, L., Réveillon, J. & Hauguel, R., Direct numerical simulation of statistically stationary one- and two-phase turbulent combustion: a turbulent injection procedure. *Flow, turbulence and combustion*, **73**, pp. 133–167, 2004.
[4] Wang, L. & Maxey, M., Settling velocity and concentration distribution of heavy particles in homogeneous isotropic turbulence. *J Fluid Mech*, **256**, pp. 27–68, 1993.
[5] Fessler, J., Kulick, J. & Eaton, J., Preferential concentration of heavy particles in turbulent channel flow. *Phys Fluids*, **(6)**, pp. 3742–3749, 1994.
[6] Squires, K.D. & Eaton, J., Preferential concentration of particles by turbulence. *Phys Fluids*, **3(5)**, pp. 1169–1178, 1991.
[7] Simonin, O., Fevrier, P. & Laviéville, J., On the spatial distribution of heavy-particle velocities in turbulent flow: from continuous field to particulate chaos. *Journal of Turbulence*, **118**, pp. 97–118, 1993.

Section 6
Injectors and nozzles

This page intentionally left blank

Numerical analysis of three-dimensional two-phase flow behavior in a fuel assembly

K. Takase[1], H. Yoshida[1], Y. Ose[2] & H. Akimoto[1]
[1]*Japan Atomic Energy Research Institute, Japan*
[2]*Yamato System Engineer Co. Ltd, Japan*

Abstract

In order to predict the water-vapor two-phase flow dynamics in a fuel assembly of an advanced light-water reactor, large-scale three-dimensional numerical simulations were carried out. Conventional analysis methods such as subchannel codes and system analysis codes need composition equations based on the experimental data. Because there are no experimental data regarding the thermal-hydraulics in the tight-lattice core, it is difficult to obtain high prediction accuracy on the thermal design of the advanced light-water reactor core. Therefore, a new two-phase flow simulation method has been proposed. The axial velocity distribution in a fuel assembly changed sharply around a spacer. The bridge formation occurred at the position of adjacent fuel rods where an interval is narrow, and the vapor positively flows the triangular region where the interval of adjacent fuel rods is large. From the present results, the high prospect was acquired of the possibility of establishment of a new thermal design method for the advanced light-water reactor cores by the large-scale simulation only.
Keywords: fluid dynamics, large-scale simulation, two-phase flow, fuel assembly, nuclear reactors, thermal design, three-dimensional analysis.

1 Introduction

Subchannel codes [1–3] and system analysis codes [4, 5] are used for the thermal-hydraulic analysis of fuel assemblies in nuclear reactors; from the former, however, many composition equations and empirical correlations based on experimental results are needed to predict the water-vapor two-phase flow behavior. When there are no experimental data such as for an advanced light-

water reactor [6–8] named as the reduced moderation water reactor (RMWR), it is very difficult to obtain highly precise predictions. The authors propose a new thermal design method for nuclear reactors by the large-scale simulation only [9]. Although this method needs a lot of calculation resources, the earth simulator [10] enabled such a request. This paper describes the predicted results of two-phase flow characteristics in a tight-lattice fuel assembly of the RMWR core.

2 Outline of RMWR core

The RMWR can be expected to attain a higher conversion ratio of more than 1 by reducing the moderation of neutrons, i.e. reducing the core water volume. This characteristic is favorable for the long-term energy supply with uranium resources, the high burn-up and long operation cycle achievement, and the multiple recycling of Plutonium. In order to obtain the high conversion ratio, it is expected from the results of the previous studies that a volume ratio of water and fuel must be decreased to about 0.25 or less. To satisfy this condition, the fuel assembly with a triangular tight-lattice arrangement is required: a fuel rod diameter is around 10 mm; and, the gap spacing between each rod is around 1 mm. Although the coolant is 100% liquid water at the core inlet, it changes into a mixture of water and vapor along the flow direction, and then, the vapor occupies 90% or more at the core outlet. Therefore, the RMWR has very severe cooling condition on the viewpoint of the thermal engineering.

3 Numerical analysis

3.1 Governing equations

The two-phase flow analysis method based on the interface-tracking method [11] was developed and is discretized using the CIP method [12]. The surface tension is calculated using the continuum surface force model proposed by Brackbill [13]. The tracking of an interface between the liquid and gas phase is accomplished by the solution of a continuity equation for the volume fraction of a couple of the phases.

The governing equations for the present two-phase flow analysis are written by:

- Mass conservation,

$$\frac{D\rho}{Dt} = -\rho \frac{\partial u_i}{\partial x_i}, \tag{1}$$

$$\rho = \rho_l \phi_l + \rho_g \phi_g, \quad \phi_g = 1 - \phi_l \tag{2}$$

- Density function,

$$\frac{D\rho_l \phi_l}{Dt} = -\rho_l \phi_l \frac{\partial u_i}{\partial x_i}, \qquad \frac{D\rho_g \phi_g}{Dt} = -\rho_g \phi_g \frac{\partial u_i}{\partial x_i} \tag{3}$$

- Momentum conservation,

$$\frac{Du_i}{Dt} = -\frac{1}{\rho}\frac{\partial p}{\partial x_i} + \frac{1}{\rho}\frac{\partial \tau_{ij}}{\partial x_i} + g_i + \sigma_i \tag{4}$$

- Energy conservation,

$$\frac{De}{Dt} = -\frac{p}{\rho}\frac{\partial u_i}{\partial x_i} + \frac{1}{\rho}\frac{\partial}{\partial x_i}\left(\lambda \frac{\partial T}{\partial x_i}\right) + q \tag{5}$$

- Volume fraction,

$$\frac{D\phi_l}{Dt} = 0, \qquad \frac{D\phi_g}{Dt} = 0 \tag{6}$$

3.2 Analytical model and boundary conditions

Figure 1 shows the analytical geometry consisting of 37 fuel rods and a hexagonal flow passage. The geometry and dimensions simulate the experimental conditions [14]. Here, the fuel rod outer diameter is 13 mm and the gap spacing between each rod is 1.3 mm. The length of one hexagonal side is 51.6 mm. An axial length of the fuel bundle is 1260 mm. The water flows upstream from the bottom of the fuel assembly.

Spacers are set to four axial positions in order to keep the gap spacing between fuel rods and also to restrict the movement of a fuel rod to the radial and circumferential directions. The outline of the shape of a currently designed spacer is shown in fig. 2. Its shape is like a honeycomb. The spacer is installed around each fuel rod with a triangular tight-lattice arrangement in the horizontal direction. The fuel rod is supported by three spacer ribs, which are set to the inside of the spacer. In fig. 2 the gap spacing is 1.3 mm and thickness of the spacer is 0.3 mm.

The non-uniform mesh division was applied. The minimum and maximum mesh sizes were 0.01 and 0.3 mm. An example of the calculation mesh division in the horizontal cross-section is shown in fig. 3. In such a case the number of mesh division in the x and y directions are 632 and 555, and the number of mesh division in the z direction is varied from 150 to 600. The maximum number of mesh division in the x, y and z directions was around 210 million. In the present simulation the fuel assembly was divided axially to several sub-domains. First, for the sub-domain located in the upstream of the fuel assembly the two-phase flow analysis was performed. Then, based on this predicted result the next analysis was performed to the adjacent sub-domain located just downstream. Finally, the full assembly size is simulated axially.

Inlet conditions of water are as follows: temperature 283°C, pressure 7.2 MPa, and flow rate 400 kg/m^{2}s. Moreover, boundary conditions are as follows: fluid velocities for x, y and z directions are zero on every wall (i.e., an inner surface of the hexagonal flow passage and outer surface of each fuel rod,

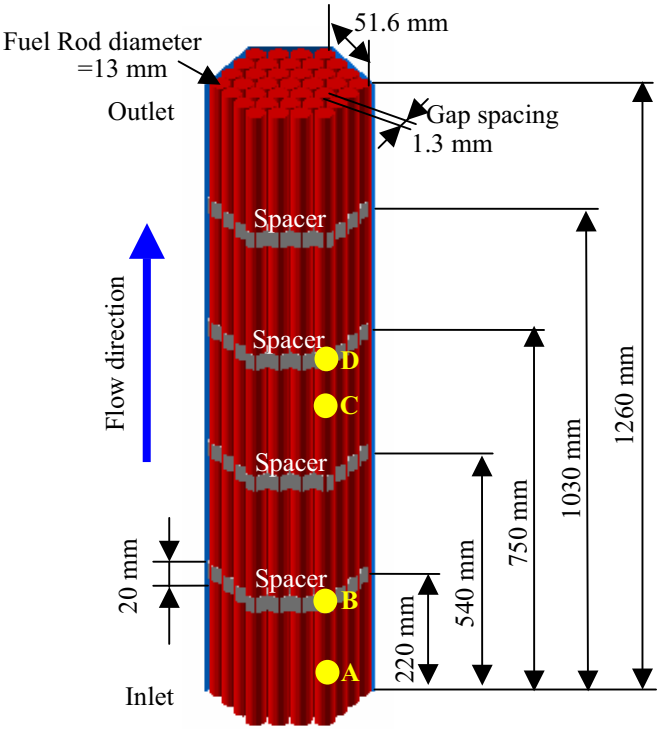

Figure 1: Analytical geometry of a tight-lattice fuel assembly.

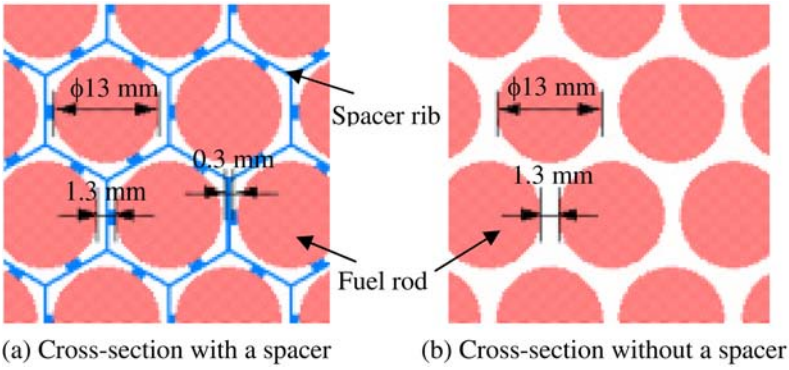

Figure 2: Cross-sectional views of the fuel bundle with and without a spacer.

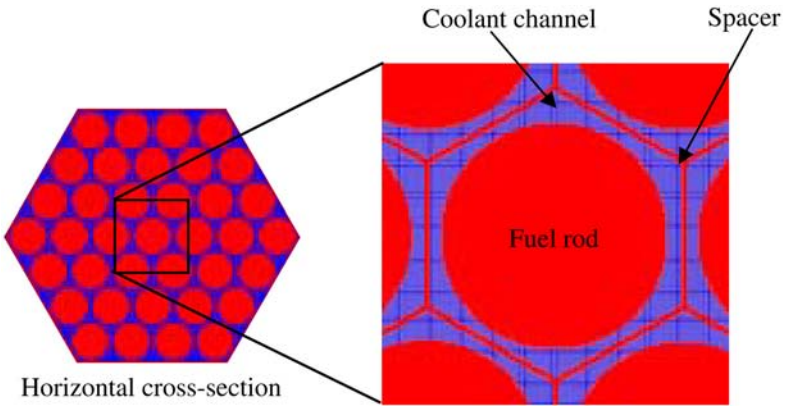

Figure 3: An example of calculation mesh division in a horizontal cross-section.

and surface of each spacer); velocity profile at the inlet of the fuel assembly is uniform. The present three-dimensional two-phase flow simulations were carried out under the non-heated isothermal flow condition in order to remove the effect of heat transfer due to the fuel rods to the fluid. A setup of a mixture condition of water and vapor at the heating was performed by changing the initial void fraction of water and vapor at the inlet of the analytical domain.

4 Analytical results

Predicted axial velocity distributions in the regions with and without a spacer are shown in fig. 4. Here, fig. 4 (a) and (b) represent the predicted results at the axial positions of A and B in fig. 1. Each figure indicates a part of analytical domain which is cut to the axial direction at the exact middle position of the gap spacing between fuel rods. The velocity is shown from blue to red using color gradation; the velocity shows zero when it is blue, and it is 0.8 m/s when red. Fig. 4 (a) shows the predicted result near the inlet of a fuel assembly. The axial velocity develops gradually but it is still underdeveloped. In fig. 4 (b) the axial velocity distribution differs greatly on the upstream and downstream of the spacer position. When there is no spacer, a flow progresses almost uniformly. When there is a spacer, however, the domain in which the axial velocity falls down extremely is formed just behind a spacer. Therefore, the axial velocity distribution at that point is expressed by blue.

Figure 5 shows the void fraction distributions around fuel rods in the horizontal direction. Here, the void fraction is defined as the ratio of the gas flow (i.e., vapor) cross sectional area to the total cross sectional area of the flow channel. In fig. 5 the void fraction is indicated using color gradation from blue to red: 100% liquid water at blue and 100% non-liquid vapor at red. Fig. 5 (a) is the

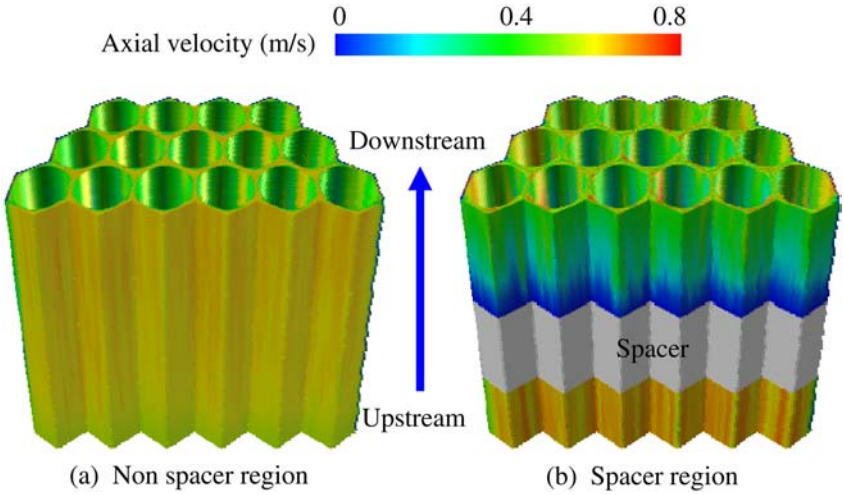

Figure 4: Predicted axial velocity distributions in the regions with and without a spacer.

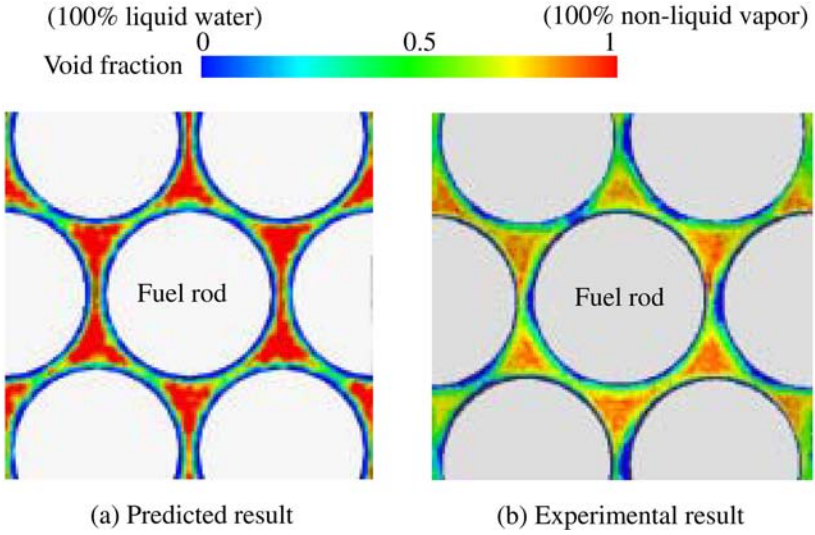

Figure 5: Comparison of predicted and measured void fraction distributions around fuel rods in the horizontal direction.

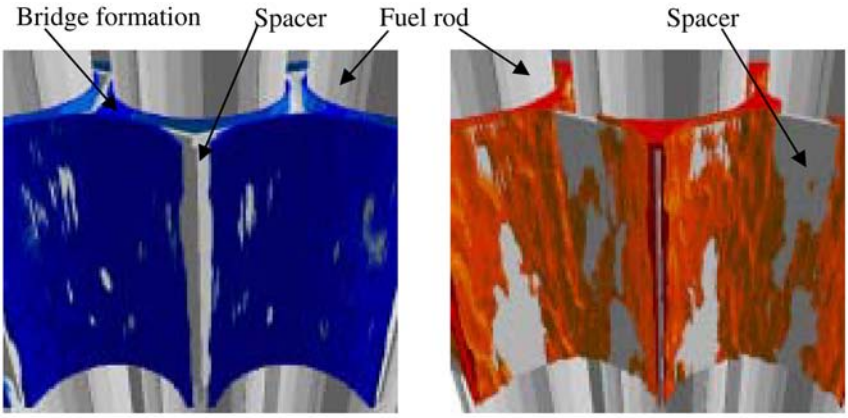

(a) Predicted water distribution (Void fraction in blue is 0.1 or less)

(b) Predicted vapor distribution (Void fraction in red is 0.9 or more)

Figure 6: Predicted water and vapor distributions in the vertical direction around a spacer.

predicted result around the axial position C in fig. 1. Each fuel rod surface shown with a circle is enclosed by thin water film, and vapor flows the outside. In the region where the gap spacing between fuel rods is narrow, the bridge formation of water in which adjacent fuel rods are connected by the water film is confirmed. On the other hand, vapor flows through the center area of the fuel rods arranged in the shape of a triangular pitch. Because it is easier for vapor to flow, since the frictional resistance in this area is low compared with the narrow area.

Figure 5 (b) is an example of the experimental result of the void fraction distribution around the axial position C in fig. 1, which is obtained by an advanced neutron radiography technique which was developed by Kureta [15]. The general neutron radiography technique has been established based on the following features; neutron passes through materials but is blocked by water. It is possible to measure the void fraction inside a fuel bundle by non-contacting using this technology. The result was translated by the experimental result using a new image processing procedure. A tendency of the water and vapor distributions shown in fig. 5 (a) and (b) is in good agreement. Namely,

1) The fuel rod surface is encircled with thin water film;
2) The bridge formation by water film appears in the region where the gap spacing between fuel rods is narrow;
3) Vapor flows the triangular region where the gap spacing between adjacent fuel rods is large; and,
4) These triangular regions exist in the circumference of a fuel rod.

Figure 6 shows the two-phase flow configurations around a spacer of the axial position D in fig. 1. Fig. 6 (a) shows the water distribution. Here, blue represents

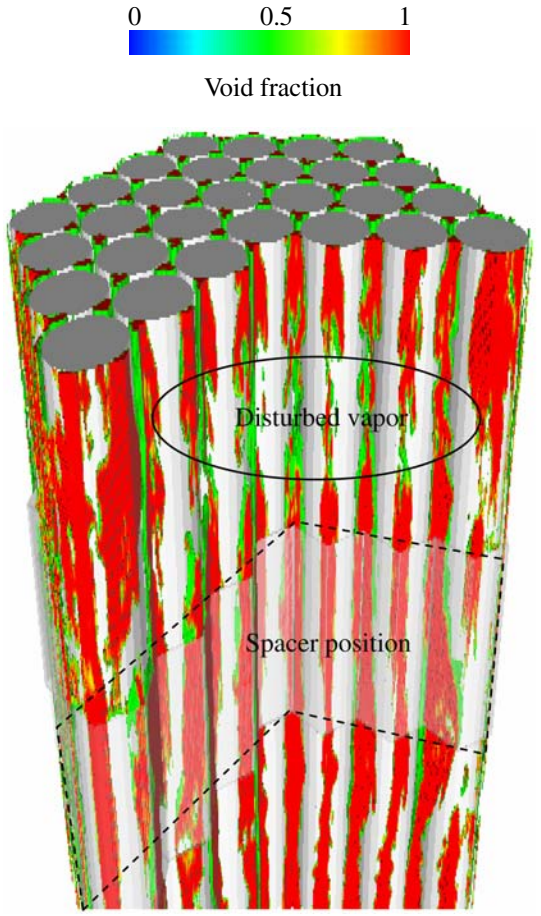

Figure 7: Predicted vapor structure around fuel rods: here, red indicates 100% non-liquid vapor and its void fraction is 1; then, green indicates an interface between water and vapor, and also its void fraction is 0.5.

a region where the void fraction is 0.1 or less and it is occupied with water of about 100%. Moreover, fig. 6 (b) shows the vapor distribution. Here, red represents a region where the void fraction is 0.9 or more and it is occupied with vapor of about 100%. Much water can be seen at to the circumference of a fuel rod. Water exists as the liquid film. A bridge formation can be checked. In addition, much vapor exists along the spacer in the axial direction. Thus, a difference in the water and vapor distributions in the vicinity of the fuel rods and spacer is clear.

Figure 7 shows an example of the predicted vapor structure around the axial position D in fig. 1. Here, the distribution of void fraction within the region from 0.5 to 1 is shown: 0.5 indicates just an interface between the water and vapor and

is shown by green; and 1 indicates the non-liquid vapor and is shown by red. Vapor flows from the upstream to downstream like a streak through the triangular region, and the interaction of the vapor stream to the circumferential direction is not seen. On the other hand, since the vapor is disturbed behind a spacer, the influence of turbulence by existence of the spacer can be predicted.

5 Conclusions

In order to predict the water-vapor two-phase flow dynamics in the RMWR fuel assembly and to reflect them to the thermal design of the RMWR core, large-scale three-dimensional two-phase flow simulations were performed under the simulated fuel assembly condition. Water and vapor distributions around fuel rods and a spacer were clarified precisely. The present results were summarized as follows:

1) The fuel rod surface is encircled with thin water film;
2) The bridge formation by water film appears in the region where the gap spacing between adjacent fuel rods is narrow;
3) Vapor flows into the triangular region where the gap spacing between fuel rods is large.
4) A flow configuration of vapor shows a streak structure along the triangular region.

The authors would like to establish a hybrid thermal design method with higher prediction accuracy, combining the conventional thermal design method and the present numerical method.

Acknowledgements

The authors would like to express their gratitude to the Earth Simulation Center first. Moreover, the present work was conducted under collaboration among Japan Atomic Energy Research Institute (JAERI), Japan Atomic Power Company (JAPC), Hitachi Ltd., Toshiba Corp., Mitsubishi Ltd., Univ. of Tokyo and Univ. of Osaka with the governmental funding from Publicly Invited Research Projects for Development of Innovative Nuclear Technologies by the Ministry of Education, Culture, Sports, Science and Technology (MEXT).

References

[1] Kelly, J. E., Kao, S. P. & Kazimi, M. S., THERMIT-2: A two-fluid model for light water reactor subchannel transient analysis, MIT-EL-81-014, 1981.

[2] Thurgood, M. J., COBRA/TRAC – A thermal-hydraulic code for transient analysis of nuclear reactor vessels and primary coolant systems, equation and constitutive models, NURREG/CR-3046, PNL-4385, Vol. 1, R4, 1983.

[3] Sugawara, S. & Miyamoto, Y., FIDAS: Detailed subchannel analysis code based on the three-fluid and three-field model, Nuclear Engineering and Design, vol. 129, pp. 146–161, 1990.
[4] Taylor, D., TRAC-BD1/MOD1: An advanced best estimated computer program for boiling water reactor transient analysis, volume 1 - model description, NUREG/CR-3633 (1984).
[5] Liles, D., TRAC-PF1/MOD1: An advanced best-estimate computer program for pressurized water reactor analysis, NUREG/CR-3858, LA-10157-MS (1986).
[6] Iwamura, T. & Okubo, T., Development of reduced-moderation water reactor (RMWR) for sustainable energy supply, Proc. 13th Pacific Basin Nuclear Conference (PBNC 2002), Shenzhen, China, pp. 1631–1637, 2002.
[7] Iwamura, T., Core and system design of reduced-moderation water reactor with passive safety features, Proc. 2002 International Congress on Advanced in Nuclear Power Plants (ICAPP 2002), No.1030, Hollywood, Florida, USA, 2002.
[8] Okubo, T. & Iwamura, T., Design of small reduced-moderation water reactor (RMWR) with natural circulation cooling, Proc. International Conference on the New Frontiers of Nuclear Technology; Reactor Physics, Safety and High-Performance Computing (PHYSOR 2002), Seoul, Korea, 2002.
[9] Takase, K., Yoshida, H., Ose, Y., Kureta, M., Tamai, H. & Akimoto, H., Numerical investigation of two-phase flow structure around fuel rods with spacers by large-scale simulations, Proc. 5th International Conference on Multiphase Flow (ICMF04), No. 373, Yokohama, Japan, June, 2004.
[10] Earth Simulator Center, Annual report of the earth simulator center (April 2004–March 2005), Japan Marine Science and Technology Center, 2005.
[11] Yoshida, H. Nagayoshi, T., Ose, Y., Takase, K. & Akimoto, H., Investigation of water-vapor two-phase flow characteristics in a tight-lattice core by large-scale numerical simulation (1), Development of a direct analysis procedure on two-phase flow with an advanced interface tracking method, J. Nuclear Science and Technology, vol. 40, No. 12, pp. 983–988, 2004 (in Japanese).
[12] Yabe, T., The constrained interpolation profile method for multiphase analysis, J. Computational Physics, vol. 169, No. 2, pp. 556–593, 2001.
[13] Brackbill, J. U., A continuum method for modeling surface-tension, J. Computational Physics, vol. 100, No. 2, pp. 335–354, 1992.
[14] Tamai, H., Ohnuki, A., Kureta, M., Liu, W., Sato, T. & Akimoto, H., Current Status of Thermal/Hydraulic Feasibility Project for Reduced-Moderation Water Reactor (1) -Large-scale Thermal/Hydraulic Test-, Proc. 2005 International Congress on Advanced in Nuclear Power Plants (ICAPP 2005), No. 5157, Soul, Korea, May, 2005.
[15] Kureta, M. & Akimoto, H., Void fraction measurement in subcooled-boiling flow using high-frame-rate neutron radiography, Nuclear Technology, vol. 136, pp. 241–254, 2001.

Numerical simulation of spray combustion flows with a linearized real-fluid model

G. C. Cheng[1] & R. C. Farmer[2]
[1]*Department of Mechanical Engineering, University of Alabama at Birmingham, USA*
[2]*SECA, USA*

Abstract

An efficient computational fluid dynamics (CFD) model for simulating spray combustion has been developed and is described. Propellant mixing near the injector has a profound effect on liquid rocket engine performance. Such mixing is extremely complex as it involves supercritical-pressure spray, turbulent mixing, and chemical reactions. Earlier research revealed a homogeneous spray approach coupled with a real-fluid property model accounts for compressibility and evaporation effects such that thermodynamics properties of a mixture over a wide range of pressures and temperatures can be accurately predicted. This spray model successfully simulated uni-element shear coaxial injector spray combustion flows. In the present study a numerical approach is proposed to improve the computational efficiency of predicting thermal properties of a mixture of real-fluid species. The approach is called a linearized real-fluid model (LRFM), and the improved efficiency is achieved by using a combination of a pseudo-liquid species and a gaseous species to represent a real-fluid species. LRFM offers increased efficiency through an improved robustness of the numerical model and a reduction in the overall computational time by an order of magnitude. The methodology of LRFM and thermodynamic properties of some liquid species calculated from the model are presented. The numerical accuracy and computational efficiency of the developed model are assessed by a comparison to benchmark test data.
Keywords: CFD, homogeneous spray approach, real-fluid property model.

WIT Transactions on Engineering Sciences, Vol 50, © 2005 WIT Press
www.witpress.com, ISSN 1743-3533 (on-line)

1 Introduction

The performance and hardware integrity of liquid rocket engines is greatly influenced by the propellant mixing near the injector. Understanding flow characteristics near the injector is thus very crucial in advanced liquid rocket engine design. To describe flow near the injector, researchers rely on indirect experimental data or numerical analyses. Not only it is extremely expensive to conduct hot-fire tests of liquid injectors, but there is no technique available to accurately measure the detailed flowfield of dense spray combustion. Hence, most tests simply measured chamber pressure and thrust. Traditionally, the numerical analysis of liquid injectors has been accomplished by using either 1-D analytical tools, such as CICM code [1], or computational fluid dynamics (CFD) codes with ideal gas properties, such as the TDK code [2]. The effect of multiple phases was accounted for empirically in the 1-D analyses by using cold flow data, neglecting the effects of chemical reactions and spatial non-uniformity. Lately, CFD methodology has become mature enough to effectively analyze detailed flowfield of combustion; however, most of CFD codes use the ideal-gas correlation, leaving the effect of multiple phases unresolved. Traditionally, the operating conditions of liquid rocket engines are transcritical in temperature and well above the critical pressure of propellants. Thus, neither is the perfect-gas law valid, nor is the surface tension stable enough to establish the interface between liquid and gaseous phases. In our previous studies [3–6], a homogeneous spray approach coupled with a real-fluid property model was developed to simulate spray combustion. This approach assumes equilibrium between all phases (i.e. both liquid and gas are treated as continua and there are no momentum and heat transfer lags) and is suitable for near critical and super-critical spray. This approach is computationally efficient because tracking liquid droplets is unnecessary. The homogeneous spray approach coupled with the real-fluid model (RFM) was incorporated into a well-tested pressure-based CFD code, FDNS [7–9], to produce a homogeneous spray combustion CFD model to analyze liquid rocket engines. This model [3–6] successfully predicted the benchmark test cases of the 2nd International Workshop on Rocket Combustion Modeling (IWRCM) [10–12] and other liquid injector configurations [13,14]. Still, this model did not provide adequate computational efficiency. The deficiency is primarily due to the iterative matrix inversions for calculating mixture density and temperature from mixture enthalpy and pressure. The pressure and enthalpy are the independent variables in the CFD solution algorithm, while for RFM the density and temperature are the independent variables. The computational deficiency is worsened by the stiffness of the species equations in reacting flows.

A linearized real-fluid model (LRFM) was developed to improve computational speed by representing a real-fluid species with a combination of a gaseous species and a pseudo-liquid species. The thermal properties of both species were modeled with the perfect-gas type of correlations. With this linearization procedure, the enthalpy of the pseudo-liquid species is a function of temperature only with a known pressure. The matrix inversion process can thus

be avoided, and the computational efficiency is greatly improved. The proposed LRFM was incorporated into the FDNS code to compute thermal properties of local mixtures. The numerical simulation of the RCM test case, previously simulated with the real-fluid model, was repeated with the proposed model to examine its accuracy as well as its computational efficiency. For design studies, no matter how much physics is included in the spray combustion model, if actual injector configurations cannot be simulated, the model is not acceptable. The present study is an initial proof of concept that LRFM is an alternative efficient CFD approach which can be applied to simulate multi-phase spray combustion flows in practical applications.

2 Numerical methodology

Previously [3–6], a real-fluid model was developed to compute the thermal properties (such as density, enthalpy, speed of sound, etc.) of the liquid propellant over a wide range of operating conditions. The real-fluid model was validated for O_2 and H_2 by comparing to the National Institute of Standards and Technology database [15]. In this model, thermal and caloric equations of state, vapor pressure, heat of vaporization, surface tension, and transport properties are modeled with the equations of state proposed by Hirshfelder *et al.* [16,17] (we term these the HBMS equations of state) and with conventional correlations [18], for other properties. These correlations are explicit in density and temperature, and can be expressed as follows.
HBMS thermal equation of state:

$$\frac{P}{P_c} = \sum_{j=1}^{4} T_r^{j-2} \sum_{i=1}^{6} B_{ij}\, \rho_r^{i-2} \quad ; \quad T_r \equiv \frac{T}{T_c} \quad ; \quad \rho_r \equiv \frac{\rho}{\rho_c} \tag{1}$$

HBMS caloric equation of state:

$$\frac{H - H_0}{RT} = Z_c \int_0^{\rho_r} \left[\frac{P}{T_r} - \left(\frac{\partial P}{\partial T_r} \right)_{\rho_r} \right] \rho_r^{-2}\, d\rho_r + Z_c \frac{P}{\rho_r T_r} - 1 \tag{2}$$

where ρ_c, T_c, and P_c are the density, temperature, and pressure at the critical condition, while ρ_r and T_r are the reduced density and temperature which are normalized values with respect to the value at the critical condition. H and H_0 are the real-fluid enthalpy and ideal gas enthalpy of a give species. Z_c is the compressibility for a given species at the critical point. B_{ij} and R are the coefficients of the thermal property polynomial and the gas constant for a given species, respectively. However, for those CFD codes which do not solve density and temperature as the primitive variables, the inversion process from the dependent variables (energy and pressure) to the independent variables (density and temperature) is computationally intensive, especially for the chemically reacting flows, in which a mixture consists of multiple species, and species concentrations of the mixture can change drastically. In this study, a linearized

real-fluid model (LRFM) was developed to resolve this problem by representing a real-fluid species (S) with a mixture of a pseudo-liquid (S_l) and a gaseous (S_g) species, and can be expressed as

$$S = (1 - f)S_l + f S_g \tag{3}$$

where f is the fraction of the gaseous species, and the split between S_l and S_g is defined by

$$\rho = (1 - f)\rho_l + f \rho_g \tag{4}$$

The density (ρ) of the real-fluid species is obtained from the developed real-fluid model. One of the main features of LRFM is that the density-temperature-pressure correlations of both the pseudo-liquid and gaseous species are similar to the perfect-gas law such that the density of pseudo-liquid (ρ_l) and gaseous (ρ_g) species can be explicitly calculated from pressures and temperatures, and thus the computational efficiency can be improved. In addition, for the pseudo-liquid species a compressibility factor (Z_c), which is a function of temperature, and a fictitious molecular weight ($M_{w,l}$) are employed to account for the compressibility effect. With a known pressure, the fictitious molecular weight, the compressibility factor, and the pseudo-liquid density can be calculated as

$$M_{w,l} = \frac{\rho_o R_u T_o}{P} \tag{5}$$

where
$$\begin{cases} T_o = T_c \ , \quad \rho_o = \rho_c & \text{if } P \geq P_c \\ T_o = T_s \ , \quad \rho_o = \rho_{s,L} & \text{if } P < P_c \end{cases}$$

$$\rho_l(T) = \frac{P M_{w,l}}{R_u Z_c T} \qquad Z_c(T) = \frac{\rho(T)}{\rho_o} \tag{6}$$

R_u, T_s, and $\rho_{s,L}$ are the universal gas constant, saturation temperature, and the saturation liquid density, respectively. The correlation of specific enthalpy between real-fluid species (h), pseudo-liquid species (h_l), and gaseous species (h_g) can also be expressed as

$$h = (1 - f)h_l + f h_g \tag{7}$$

The second main feature of the present model is that for a given pressure the specific heat ($C_{p,l}$) and the enthalpy (H_l) of the pseudo-liquid species are polynomial functions of the temperature only similar to those of the gaseous species of the CEC code [19], which can be shown as

$$\frac{C_{p,l}}{R} = \sum_{n=1}^{5} A_n T^{n-1} \quad ; \qquad \frac{H_l}{R} = A_6 + \sum_{n=1}^{5} \frac{A_n}{n} T^n \tag{8}$$

A_n are polynomial coefficients of the pseudo-liquid species, and can be obtained by curve fitting the real-fluid enthalpy for the temperature below either the saturation temperature (at subcritical pressure) or the critical temperature (at supercritical pressure). As a result, the effect of the heat of evaporation can be

accounted for by increasing the fraction of gaseous species as the temperature increases. The last main feature of the present model is the generation of a look-up table for the speed of sound and the ratio of the specific heat based on RFM. These two variables must be defined in order to satisfy the correlation between the density and the pressure changes, which can be shown as

$$\Delta\rho = \begin{cases} \Delta P\left(\dfrac{\partial\rho}{\partial P}\right)_T = \Delta P\dfrac{\gamma}{a^2} & : \text{both liquid and gas} \\ \dfrac{\Delta P M_w}{R_u T} & : \text{ideal gas only} \end{cases} \tag{9}$$

This correlation can be applied to both density-based and pressure-based flow solvers, and it is valid for liquid phase, gas phase, two-phase, and dense fluid regions. In order to apply LRFM to a flow solver, a pre-processor was constructed to generate the thermal properties of the pseudo-liquid species for a range of pressures of interest. In the present model, the temperature is an explicit function of the specific enthalpy at a given pressure, and the fraction of the gaseous species and the density can be directly calculated based on the temperature. As a result, the computational time was greatly reduced, and the time marching step size was increased because the matrix inversion for calculating mixture density and temperature from mixture enthalpy and pressure was avoided.

To test the validity and efficiency of the proposed approach, LRFM was incorporated into the homogeneous spray methodology in the FDNS [7–9] code to simulate the spray combustion problem. The framework of the FDNS code is an elliptic, finite-difference Navier–Stokes flow solver, which employs a predictor plus multi-corrector pressure-based solution algorithm. Higher order upwind, total variation diminishing (TVD), or central difference schemes plus adaptive second-order and fourth-order dissipation terms are used to approximate the convection terms of the transport equations. Various matrix solvers, such as vectorized point implicit, conjugate gradient, and generalized minimal residual [20], are provided in the code such that users can select the appropriate one for a given transport equation. Though the FDNS code is a structured grid code, multi-block, multi-zone grid topology was employed in the code so that problems with complex geometries can be analyzed efficiently. Since the FDNS code is a pressure-based flow solver, a pressure correction (P') equation is derived from the continuity equation and can be expressed as:

$$\frac{\beta_p P'}{\Delta t} + \nabla\cdot(V_i^*\beta_p P') - \nabla\cdot(\rho^*\mathsf{D}_p\nabla P') = -\nabla\cdot(\rho^* V_i^*) - \frac{\rho^* - \rho^n}{\Delta t} \tag{10}$$

$$P^{n+1} = P^n + P' \;;\quad \beta_p = \gamma/a^2 \;;\quad V_i' \approx -\mathsf{D}_p\nabla P'$$

where the superscripts * and n denote the value at the intermediate and previous time steps, respectively. D_p is the inverse of the matrix of the coefficients of the convective terms in the finite-difference form of the inviscid equations of

motion. For the homogeneous spray approach, the speed of sound (a), and the ratio of specific heat (γ) of a multi-component mixture can be calculated from the real-fluid properties of its constituents based on the additive volume method,

$$\gamma = \frac{\sum_i n_i \left(C_p / R\right)_i}{\sum_i n_i \left(C_p / R\right)_i / \gamma_i} \quad ; \quad a^2 = \frac{\gamma / M_w^2}{\sum_i \gamma_i \alpha_i / a_i^2 M_{w,i}^2} \tag{11}$$

where $n_i, \alpha_i, \gamma_i, R_i, (C_p)_i, a_i$, and $M_{w,i}$ are the mole fraction, mass fraction, ratio of specific heat, gas constant, specific heat, speed of sound and the molecular weight of species "i", respectively.

Two approaches of utilizing LRFM are provided. The first approach is called S-P (single-pressure) LRFM, where the parameters and correlations for the thermal property of the pseudo-liquid species are approximated for an anchoring pressure. The single pressure is conveniently taken as the chamber operating pressure, which is approximately constant. The second approach is called M-P (multiple-pressure) LRFM, where a set of the parameters and correlations for the thermal property of the pseudo-liquid species are constructed for a range of pressures such that the parameters and correlations for a specific pressure will be interpolated from the pre-generated database. When compared to M-P LRFM, it is obvious that S-P LRFM has more approximations (i.e. larger errors) but is more computationally efficient because no interpolation based on pressure at each grid point is required. For actual engine simulations, the liquid phase of propellants exists only in the area very close to the injector exit. This study will investigate the difference between these two approaches, and the accuracy of LRFM.

3 Numerical results

In order to utilize LRFM, thermal properties of the pseudo-liquid species as well as the split between gaseous and pseudo-liquid species have to be generated beforehand. A pre-processor was constructed to generate those data needed by the present model. The thermal properties of oxygen, hydrogen and RP-1 generated by the pre-processor were reported in [21]. As an example, oxygen thermal properties of the present model are shown in Figure 1. It can be clearly seen that the thermal properties generated by the pre-processor properly accounts for the compressibility and heat of evaporation effects for oxygen.

To examine the numerical accuracy of the present model, several liquid spray combustion test cases (such as LOX/GH2, and LOX/RP-1, GOX/RP-1) were simulated. The numerical results of two LOX/GH2 uni-element shear coaxial injector test cases, RCM-2 and RCM-3 [3, 11–12] are presented herein. These cases were successfully simulated by RFM in our previous study [3, 5–6]. The accuracy and computational efficiency of the present model were evaluated by comparing the numerical results of S-P LRFM and M-P LRFM and the available test data. Both the experiments and the simulations were essentially axisymmetric.

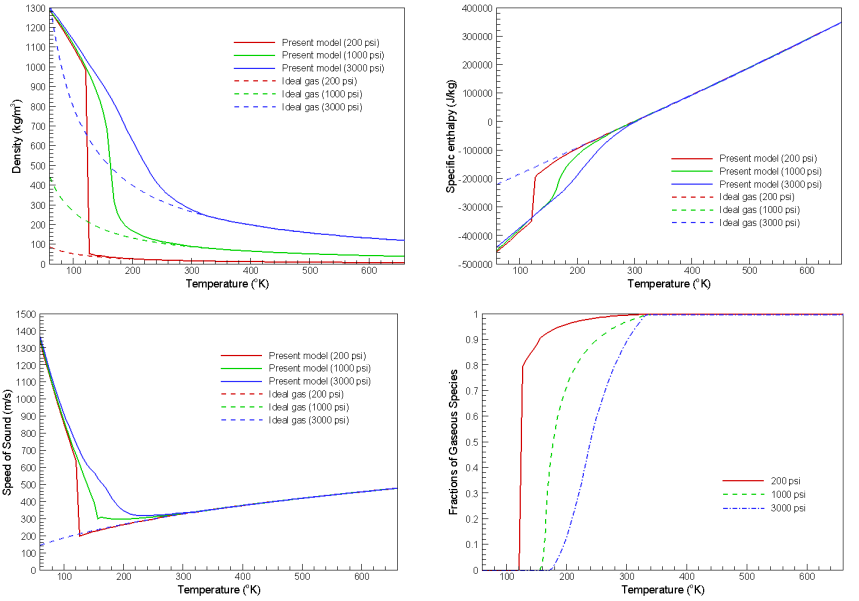

Figure 1: Comparison of oxygen density, specific enthalpy, sonic speed, and fractions of gaseous oxygen at various temperatures and pressures.

3.1 RCM-2 test case

The RCM-2 test case was designed to study the subcritical spray combustion flow of a shear coaxial injector element. The injector orifice diameter for the liquid oxygen (LOX) injection is 5 mm surrounded by an annular gaseous hydrogen (GH_2) jet with channel width of 6.4 mm. The operating conditions and injector configurations of the RCM-2 test case are illustrated in Table 1 and Figure 2. The overall O/F ratio for this case is 2.11. The inlet turbulent kinetic energy level and length scale, as shown in Figure 2 for CFD simulations, were proposed by the IWRCM organizer such that all numerical results can be compared on a similar basis. It is obvious this is a sub-critical spray combustion test case since the critical pressure of oxygen is 5.04 MPa. The grid system is the same as that used in our previous study [3], which has 61x43 grid points for the injector element and 301x101 for the chamber.

In the present study, finite-rate chemistry was employed to model the combustion of hydrogen with oxygen. The temperature profiles predicted by M-P LRFM, S-P LRFM, and RFM are compared at four axial (X=10, 180, 250, and 410 mm) and two radial (r/D=2, and 3) locations, and are plotted as shown in and M-P LRFM are almost identical, but are quite different from that of RFM. Figures 3–4. It can be clearly seen that the numerical results of both S-P LRFM. The primary cause for the difference between RFM and LRFM is the amount of

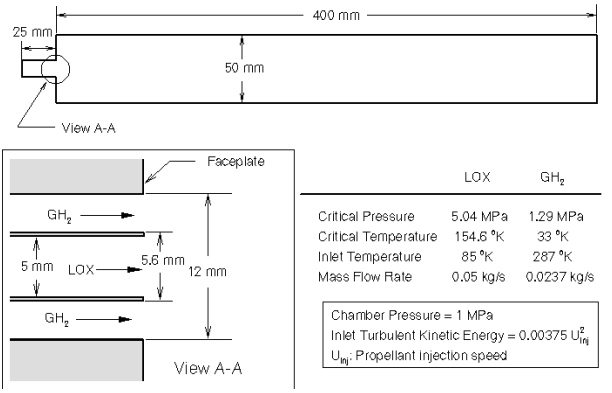

Figure 2: Geometry and inflow conditions for the RCM-2 test case.

Table 1: RCM-2 test case operating conditions.

Conditions	H_2	O_2
Pressure	1 MPa	1 MPa
Mass flow rate	23.7 g/s	50 g/s
Temperature	287 K	85 K
Density	0.84 kg/m^3	1170 kg/m^3
Cp	14300 J/kg/K	1690 J/kg/K
Velocity	319 m/s	2.18 m/s
Viscosity	8.6E-6 kg/m/s	1.94E-4 kg/m/s
Surface Tension	-	1.44E-2 N/m

oxygen involved in the chemical reactions. For RFM, the total amount of oxygen, including gaseous and liquid phases, is used in the calculation of chemical reactions because oxygen is treated as one real-fluid species. However, for LRFM only gaseous oxygen is included in modeling chemical reactions because real-fluid oxygen now consists of gaseous and liquid oxygen. As a result, chemical reactions associated with LRFM near the injector are slower than those with RFM. This effect can be observed in Figure 3, where near the injector faceplate LRFM predicts a thinner shear layer than RFM, which more closely conforms to the test data. However, at the downstream region LRFM predicts larger temperature gradients in the radial direction than the test data, which indicates slower propellant mixing. This is consistent with our understanding that the homogeneous spray approach may underpredict propellant mixing for subcritical spray because of missing dispersion due to droplet atomization. Hence, this approach may require further fine-tuning and study of turbulence mixing for the spray combustion flow at the subcritical

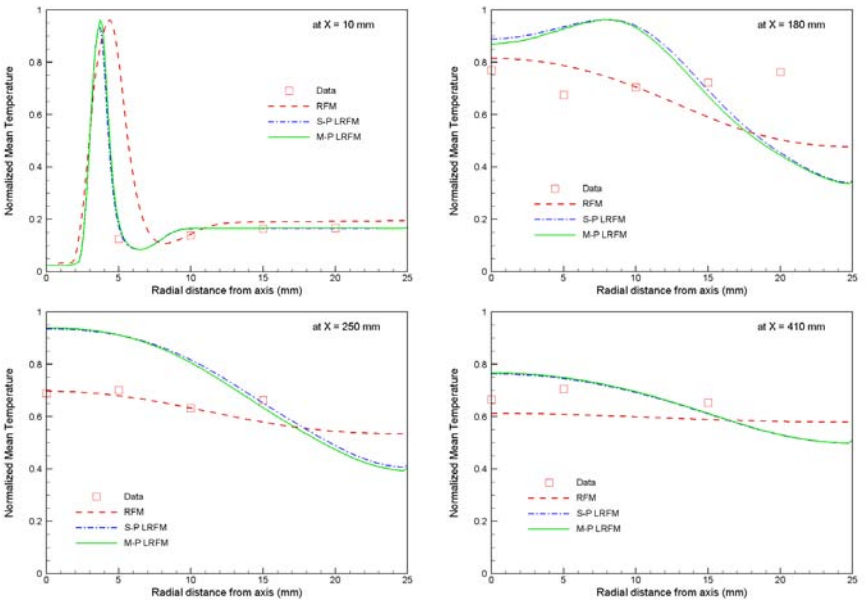

Figure 3: Comparisons of radial temperature profiles at 4 different axial locations for the RCM-2 test case.

condition. It is to be noted that in Figure 3 all models underpredict the temperature in the region towards the wall (outside of the shear layer and in a fuel-rich region), where the test data indicate higher temperature than that in the shear layer. Due to the fuel-rich condition, the temperature outside of the shear layer should be lower than that in the shear layer. Thus, it is suspected that the test data is somewhat in error. It also can be seen that the difference between S-P LRFM and M-P LRFM results is very small, mainly because the pressures of the injected liquid propellant only differ slightly from the operating pressure.

Overall, the characteristics of the shear layer, an indicator of the turbulent mixing and thermal properties, are well simulated by RFM and LRFM with the homogeneous spray approach. Hence, despite the noted discrepancies, either RFM or LRFM models simulate the subcritical spray test case reasonably well. With the cited uncertainties, more definitive test data are needed in order to further fine-tune the numerical models. In addition to the model accuracy, the overall computational time for S-P LRFM is reduced by one order of magnitude compared to that for RFM because the numerical simulation can be conducted with larger time marching step size (from 0.1 μsec to 1 μsec). The computational time for M-P LRFM is about 20% more than that for S-P LRFM due to interpolation of thermal properties. This proves that LRFM is able to relieve the stiffness problem by the utilization of two species representing a real-fluid species, as well as decoupling the process of computing the density and temperature.

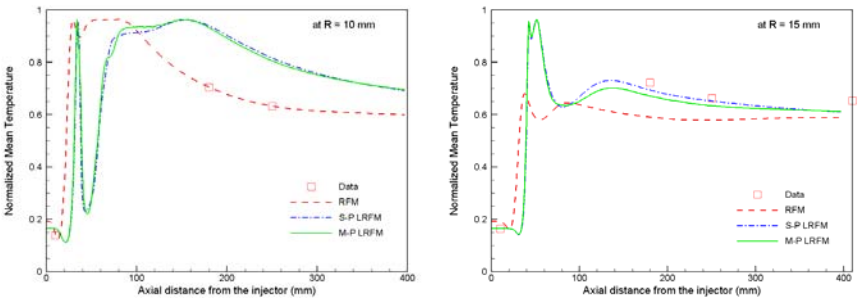

Figure 4: Comparisons of axial temperature profiles at two radial locations for the RCM-2 test case.

Table 2: RCM-3 test case operating conditions.

Conditions	H_2	O_2
Pressure	6 MPa	6 MPa
Mass flow rate	70 g/s	100 g/s
Temperature	287 K	85 K
Density	5.51 kg/m3	1177.8 kg/m^3
Cp	15100 J/kg/K	1660.9 J/kg/K
Velocity	236 m/s	4.35 m/s
Viscosity	8.67E-6 kg/m/s	12.34E-4 kg/m/s

3.2 RCM-3 test case

The operating conditions for the RCM-3 test case are listed in Table 2, which shows this is a super-critical spray combustion test case. Since surface tension is either zero or not well defined for super-critical conditions, drops either do not exist or are very unstable and do not survive very long. Hence, the homogeneous spray model is a rigorous and effective approach for simulating this test case. The injector configuration and flow conditions for the RCM-3 test case are listed in Figure 5. A two-zone mesh system (61x39 and 301x101) was used to model the injector section and the combustion chamber.

Though there is no measured data of this test case available for validating the present model, the OH image obtained from the experimental test compared very well with the homogeneous spray approach with RFM in our previous studies [3–6]. Hence, in the present study, the numerical result of RFM is employed to validate the proposed LRFM (both S-P and M-P approaches).

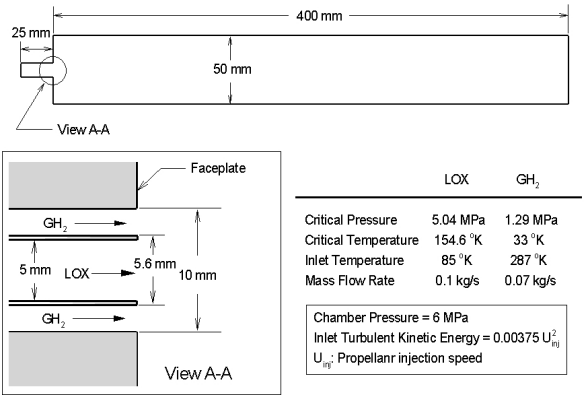

Figure 5: Computational domain and inflow conditions for RCM-3 test case.

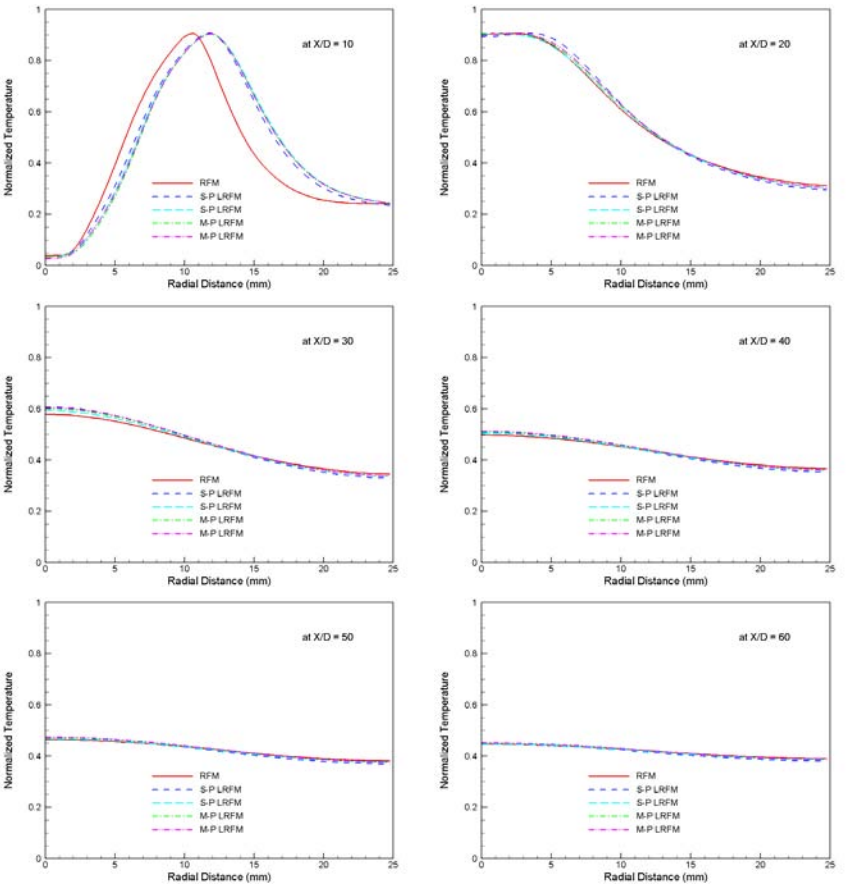

Figure 6: Comparisons of the radial temperature profiles at different axial locations between various real-fluid models for the RCM-3 test case.

The temperature profiles at various axial locations predicted by RFM, S-P LRFM and M-P LRFM are compared in Figure 6, illustrating that the numerical results of these three models are almost identical and within the uncertainty of experimental data acquisitions. The biggest discrepancy between the RFM and LRFM results occurs at the location very close to the injector, which is again attributed to the difference in the amount of reacting species involved in the chemical kinetics. Also, the results of S-P LRFM and M-P LRFM are almost identical, and the main reason for the small difference is that the pressures of the injected liquid propellant only differ slightly from the operating pressure.

Therefore, it is anticipated that the difference between S-P LRFM and M-P LRFM results will be more significant if the pressures of the liquid propellant substantially deviate from the anchoring pressure. Furthermore, similar to the RCM-2 test case, the computational time of S-P LRFM is one order of magnitude less than RFM. The computational time for M-P LRFM is slightly more than S-P LRFM caused by interpolating thermal properties based on local pressures. This demonstrates that both S-P LRFM and M-P LRFM models are able to improve the computational efficiency of the homogeneous spray combustion models to the extent that realistic three-dimensional spray combustion flowfields can be practically simulated.

4 Conclusions

The linearized real-fluid model (with single-pressure and multiple-pressure approaches) is proposed to be an efficient numerical approach for simulation of liquid spray flow. A property pre-processor based on the present model was constructed to generate thermal properties for various pseudo-liquid species. Thermal properties generated by this pre-processor were shown to properly account for the effects of compressibility and the heat of evaporation. The present model has been tested with a well validated CFD code (FDNS), and the results show that LRFM does meet the goal of improving the computational efficiency compared to FRM. Meanwhile, the numerical result of the present model is almost identical to that of RFM for the supercritical spray combustion test case. For the subcritical spray combustion test case, a minor discrepancy exists between the present model and RFM, which may be caused by the difference between these two models in defining the amount of real-fluid species involved in chemical reactions. Differences between S-P LRFM and M-P LRFM are within the uncertainty of experiments and numerical simulations because pressures within the computational domain do not deviate from the operating condition very much. The present study is a proof of concept that the proposed model can be applied to simulate multi-phase spray combustion flows. Further validation and verification are needed to investigate the applicability range of the present model, and to improve the model if needed.

Acknowledgements

The authors would like to express their appreciations to Mr. Kevin Tucker and Dr. Jeff West for their valuable advice and support. This work was performed

under NAS8-02062 for the Marshall Space Flight Center of the National Aeronautics and Space Administration.

References

[1] Sutton, R.B., Schuman, M.D., and Chadwick, W.D., Operating Manual for Coaxial Injection Combustion Model, *NASA CR-129031*, Rocketdyne Division, Rockwell International, Canoga Park, CA, 1 April 1974.

[2] Nickerson, G.R., et al, Two-Dimensional Kinetics (TDK) Nozzle Performance Computer Program, Vols. I-III, *Rpt. No. SN91*, SEA Inc., Mar. 1989.

[3] Cheng, G.C., and Farmer, R.C., CFD Spray Combustion Model for Liquid Rocket Engine Injector Analyses, *AIAA Paper 2002-0785*, 2002.

[4] Farmer, R.C., Cheng, G.C., and Chen, Y.S., CFD simulation of Liquid Rocket Engine Injectors: Test case RCM 1, *Proc. 2nd International Workshop on Rocket Combustion Modeling*, Germany, March 25-27, 2001.

[5] Farmer, R.C., Cheng, G.C., and Chen, Y.S., CFD simulation of Liquid Rocket Engine Injectors: Test case RCM 2, *Proc. 2nd International Workshop on Rocket Combustion Modeling*, Germany, March 25-27, 2001.

[6] Farmer, R.C., Cheng, G.C., and Chen, Y.S., CFD simulation of Liquid Rocket Engine Injectors: Test case RCM 3, *Proc. 2nd International Workshop on Rocket Combustion Modeling*, Germany, March 25-27, 2001.

[7] Chen, Y.S., Compressible and Incompressible Flow Computations with a Pressure Based Method, *AIAA Paper 89-0286*, 1989.

[8] Cheng, G.C., Farmer, R.C., and Chen, Y.S., Numerical Study of Turbulent Flows with Compressibility Effects and Chemical Reactions, *AIAA Paper 94-2026*, 1994.

[9] Cheng, G.C., Chen, Y.S., and Wang, T.S., Flow Distribution Within the SSME Main Injector Assembly Using Porosity Formulation, *AIAA Paper 95-0350*, 1995.

[10] Telaar, J., Schneider, G., Hussong, J., and Mayer, W., Cryogenic Jet Injection: Description of Test Case RCM 1, *Proc. 2nd International Workshop on Rocket Combustion Modeling*, Germany, March 25-27, 2001.

[11] Vingert, L., and Habiballah, M., Test Case RCM 2: Cryogenic Spray Combustion at 10 bar at Mascotte, *Proc. 2nd International Workshop on Rocket Combustion Modeling*, Germany, March 25-27, 2001.

[12] Thomas, J.L., *et al*, Test Case RCM 3: Supercritical Spray Combustion at 60 bar at Mascotte, *Proc. 2nd International Workshop on Rocket Combustion Modeling*, Germany, March 25-27, 2001.

[13] Cheng, G.C., Anderson, P.G., and Farmer, R.C., Development of CFD Model for Simulating Gas/Liquid Injectors in Rocket Engine Design, *AIAA Paper 97-3228*, 1997.

[14] Farmer, R.C., Cheng, G.C., Trinh, H., and Tucker, K., A design Tool for Liquid Rocket Engine Injectors, *AIAA 2000-3499*, 2000.
[15] Reid, R.C., Praunitz, J.M., and Poling, B.E., *The Properties of Gases & Liquids*, 4th ed., McGraw-Hill, 1987
[16] Hirschfelder, J.O., et al, Generalized Equations of State for Gases and Liquids, *IEC*, 50, pp.375-385, 1958.
[17] Hirschfelder, J.O., et al, Generalized Excess Functions for Gases and Liquids, *IEC*, 50, pp.386-390, 1958.
[18] Reid, R.C., et al, *The Properties of Gases & Liquids*, 4th ed., McGraw-Hill, 1987.
[19] Gordon, S., and B.J. McBride, Computer Program for Calculation of Complex Chemical Equilibrium Compositions, Rocket Performance, Incident and Reflected Shocks, and Chapman-Jouget Detonations, *NASA-SP-273*, 1971.
[20] Saad, Y., and Schultz, M.H., *SIAM Journal of Sci. Stat. Comput.*, Vol. 7, pp. 856-869, 1986.
[21] Cheng, G.C., Farmer, R.C., Development of Efficient Real-Fluid Model in Simulating Liquid Rocket Injector Flows, *AIAA Paper 2003-4466*, 2003.

A three dimensional three phase reactive flow for simulating the pulverized coal injection into the channel of the blast furnace raceway

J. A. Castro, A. W. S. Baltazar & A. J. Silva
Post Graduate Program on Metallurgical Engineering-UFF

Abstract

The blast furnace process is a counter current flow reactor whose main purpose is to produce hot metal. This process uses as auxiliary fuel the injection of pulverized coal through the equipment termed the tuyere. However the injection point in the tuyere is of summary importance for the complete combustion of the pulverized coal, which in turn will affect the smooth blast furnace operation. Recently, the price of premium coals became prohibitive for using in the blast furnace, especially in Brazil, where this raw material is imported. Therefore attempts have been made to allow the use of low quality coals partially substituting the premium coals decreasing the production cost of steels. This paper deals with the simulation of the pulverized injection of low-grade coals into the channel of the blast furnace raceway. The analysis was based on a 3D three phase mathematical model, where motion, heat transfer and chemical reactions among chemical species were calculated based on transport equations. Interactions among phases were computed with the help of semi-empirical correlations. The chemical kinetics rates were adapted from the literature by adjusting the constants for representing the industrial process. The finite volume method implemented in a complex computational code written in Fortran 90 was used to solve the highly non-linear system of partial differential equations in a non-orthogonal mesh representing the geometry of a tuyere with different injection points. The comparison between model results for temperature and gas composition and experimental/industrial showed very close agreement. The mathematical model proved to be useful to predict the effect of the injection of different quality coals in the raceway and an efficient tool to evaluate new raw materials for the blast furnace
Keywords: mathematical modelling, pulverized coal and multiphase flow.

WIT Transactions on Engineering Sciences, Vol 50, © 2005 WIT Press
www.witpress.com, ISSN 1743-3533 (on-line)

1 Introduction

Ironmaking is a major energy and raw materials consuming process in the metallurgical industry. In an integrated steel plant, the blast furnace consumes about 70% of the energy input and a major part of this energy is obtained from coal and coke. In the majority of blast furnaces coke is the main fuel. As a result of an increase in the steel production in the last years, the world prices for coke and coals that can be processed to coke have increased dramatically [3]. To reduce the use of coke and to allow the use of less noble coals as fuel in blast furnaces, the technique of pulverized coal injection - PCI - was developed. The PCI technology has achieved maturity and several blast furnaces over the world are operated with pulverized coal rates over 200 kg/thm. However, even PCI demands some especial characteristics of coals to be injected. One important characteristic is the low content of volatile substances, which are released during heating and burning. Therefore, there is a large number of coals that are not appropriated to be used in large scale in PCI. This is the case of some Brazilian coals. The combined injection of different coal types could be useful in order to increase the number and amount of coals used in PCI. To implement this technique, the physical and chemical interaction of different coals injected simultaneously in a blast furnace must be evaluated. Mathematical models are useful, reliable and represent chip tools for the analysis of industrial process, whereas trial and error strategies can lead to very high costs in the implementation of a new operational technique in a smooth operating industrial plant. A mathematical modeling of the blast furnace process is available [9] and its results show excellent agreement when compared with industrial data [5-6-9]. In the present work, the main ideas and concepts of the blast furnace model were extended to compute the chemical interactions of a three phase reactive flow comprising the blast and two kinds of coal powders injected at different sequential points in the tuyere of a blast furnace. Each coal type was modeled as a different phase, interacting chemically, thermally and mechanically with the blast and with each other. This two coal phases approach allowed to characterize the coals by different grain sizes, total carbon, thermal properties, etc.., and, very important, different volatile contents as well. All coal properties, together with the coal genesis affect strongly the coal combustion kinetics. The thermal-chemical efficiency of burning of coals along the tuyere was calculated as a function of the injection rate. The influence of oxygen enrichment was also evaluated. In this numerical experiment, two different sequential injection points were simulated. At the first one, high volatile coal was injected. At the second point, forwards in the tuyere, the low volatile coal was introduced. This combined injection scheme showed a higher efficiency for the burning of the low volatile coal, when compared with injection of low volatile coal alone. The burning of the volatile substances released by the first injected coal preheated the low volatile coal, and this was the main cause found for the increase in the thermal efficiency.

2 Modelling and methodology

The mathematical model is based on differential transport equations of momentum, mass of phases and chemical species, and energy in three phases, which are assumed to co-exist in all points of a calculus domain, representing a blast furnace tuyere, where they interact mutually. All transport equations can be represented by a general form given by Equation (1).

$$\frac{\partial\left(\rho_i \varepsilon_i \phi_{i,k}\right)}{\partial t} + div\left(\rho_i \varepsilon_i \vec{V}_i \phi_{i,k}\right) = div\left(\Gamma_{\phi_{i,k}} grad\left(\phi_{i,k}\right)\right) + S_{\phi_{i,k}} \tag{1}$$

In all differential balances given by eqn (1), ρ_i and ε_i are the absolute density and volume fraction of i'th phase in the whole mixture, respectively, with i varying from 1 to 3. The intensive properties $\phi_{i,k}$ change their meaning according the type of each differential balance. In balances of momentum, the index k has no meaning and ϕ_i, is equivalent to one of components the phase velocity $\vec{\mathbf{V}}_i$. In energy balances, ϕ_i correspond to the phase specific enthalpy, again a property of the whole phase. When mass balances are considered, $\phi_{i,k}$ represent the individual mass fractions of the k'th chemical specie, relative to the mass of the i'th phase. At the right side of eqn (1), $\Gamma_{i,k}$ are diffusive or molecular transport coefficients associated to the intensive property ϕ. In this manner, in momentum balance equations, Γ_i is the phase viscosity. In energy equations, Γ_i represents the i'th phase thermal conductivity, and in mass balance equations, $\Gamma_{\phi i,k}$ should be interpreted as the mass diffusion coefficient of the k'th specie in the i'th phase. In the case of phases representing particles clouds, as pulverised coals, all $\Gamma_{i,k}$ are set to zero, since no molecular transport is possible, and the transport during collisions of two particles can be neglected. $S_{\phi i,k}$ stands for a general non-homogeneous term in the differential balance equations. It can be physically interpreted as a source term of momentum, energy or mass, according the differential balance. Source (or sink) terms are useful to represent several phenomena, including mutual interactions among the phases. In momentum balances, they represent forces per unit of volume as the drag of particles by the gas stream, gravitational forces or pressure gradients

Table 1: Phase contents.

Phase description	Chemical species present
Blast Gas	CO, CO_2, O_2, H_2, H_2O, N_2, SiO
High Volatile Coal HVC	C, SiO_2, high volatile content, SiC, Al_2O_3, MgO, CaO; CaS; FeS; FeS_2
Low Volatile Coal LVC	C, SiO_2, low volatile content, SiC, Al_2O_3, MgO, CaO; CaS; FeS; FeS_2

In energy equations, source terms are used to represent the energy exchange between each two phases and the energy release or consumption due to chemical reactions. In mass balances equations, sources terms take into account the mass exchange between phases due to chemical reactions and eventual phase change phenomena like the transfer of volatile material from pulverised coal to the gas stream.

Each phase has its own initial chemical composition represented by the initial values of mass fractions $\phi_{i,k}$. After the injection, coal composition changes due to the chemical reactions taking place in the tuyere. In this work, three phases were considered: the gas phase, consisting mainly (but not only) of Nitrogen and Oxygen, and the two types of pulverised coal, characterised by their own initial composition and physical properties. The phase contents and coals composition are presented in Tables 1 and 2, respectively.

Table 2: Coal properties.

Coal types		High Volatile Coal	High Volatile Coal
Immediate analysis (% dry)	Ash	2,70	10,50
	Volatiles	41,20	18,90
	carbon	56,10	70,60
Fuel rate		1,36	3,74
Element Analysis (% dry mass, ash free)	C	75,10	88,40
	H	5,20	4,70
	N	1,50	0,80
Ash (% mass as oxides)	SiO_2	50,00	43,40
	AL_2O_3	24,80	26,90
	Fe_2O_3	16,70	9,10
	MgO	1,50	7,50
	CaO	1,80	1,30

Table 3: Combustion reactions of carbon.

(1)	$C_{PC} + 1/2O_{2(g)} \rightarrow CO_{(g)}$ - partial combustion
(2)	$C_{PC} + O_{2(g)} \rightarrow CO_{2(g)}$ - full combustion
$R_{(1)PC} = \frac{a}{1+a} R_{ave}$; $R_{(2)PC} = \frac{1}{1+a} R_{ave}$; $R_{ave} = \left(\frac{\varepsilon_g \rho_g \omega_{O_2(g)}}{M_{O_2}} \right) \left\{ \frac{d_i \varphi_i}{A_i D_{O_2,\omega_2}^{T_{ave}} Sh_i} + \frac{1}{\eta k_{ave}} \right\}^{-1}$	
$a = 2500 \exp\left(-\frac{12400}{1.987 T_i} \right)$; $k_{ave} = 7260 R T_g \exp\left(-\frac{17980}{T_{ave}} \right)$; $T_{ave} = \frac{T_g + T_i}{2}$; $A_i = \frac{6\varepsilon_i}{d_i \varphi_i}$; $\eta = \left[\frac{d_i}{6} \sqrt{\frac{k_{ave} \delta_i}{\zeta_i D_{O_2,N_2}^{T_{ave}}}} \right]^{-1} \left\{ \left[\tanh\left(\frac{d_i}{6} \sqrt{\frac{k_{ave} \delta_i}{\zeta_i D_{O_2,N_2}^{T_{ave}}}} \right) \right]^{-1} - \left[\frac{d_i}{2} \sqrt{\frac{k_{ave} \delta_i}{\zeta_i D_{O_2,N_2}^{T_{ave}}}} \right]^{-1} \right\}$; $\delta_{pc} = 1$; $\zeta_{pc} = 0.2$	

Table 4: Kinetics model for Solution Loss reaction.

(3)	$C_{PC} + CO_{2(g)} \rightarrow 2CO_{(g)}$
$R_{(3)} = \dfrac{\rho_g \omega_{Co_2(g)}}{M_{CO_2}} \left(\dfrac{1}{A_i k_{film,CO_2}} + \dfrac{1}{\eta k_{(3)}} \right)^{-1}$	
$k_{(3)_i} = \dfrac{k_1}{1 + k_2 P_{CO} + k_3 P_{CO_2}} \rho_i \varepsilon_i \omega_i 82{,}056 \times 10^{-3} T_g$; $k_1 = \dfrac{1}{60} \exp\left(19{,}875 - \dfrac{66350}{1{,}987 T_i} \right)$;	
$k_2 = \exp\left(-6{,}688 + \dfrac{21421}{1{,}987 T_i} \right)$; $k_3 = \exp\left(31{,}615 - \dfrac{88168}{1{,}987 T_i} \right)$; $k_{\text{film},CO_2} = D^{T_{ave}}_{CO_2,N_2} \dfrac{Sh_i}{d_i \varphi_i}$	
$P_{\omega_j} = \dfrac{82{,}056 \times 10^{-3} \rho_g T_g \omega_j}{M_{\omega_j}}$;(j=CO,CO2); $A_i = \dfrac{6\varepsilon_i}{d_i \varphi_i}$;	
$\eta = \left[\dfrac{d_i}{6} \sqrt{\dfrac{k_{10_i} \delta_i}{\zeta_i D^{T_{ave}}_{O_2,N_2}}} \right]^{-1} \left\{ \left[\tanh\left(\dfrac{d_i}{6} \sqrt{\dfrac{k_{10_i} \delta_i}{\zeta_i D^{T_{ave}}_{O_2,N_2}}} \right) \right]^{-1} - \left[\dfrac{d_i}{2} \sqrt{\dfrac{k_{10_i} \delta_i}{\zeta_i D^{T_{ave}}_{O_2,N_2}}} \right]^{-1} \right\}$; $T_{ave} = \dfrac{T_g + T_i}{2}$; $\delta_{pc} = 1$;	
$\zeta_{pc} = 0{,}2$	

Table 5: Kinetics model for Water Gas Reaction.

(4)	$C_{PC} + H_2O_{(g)} \rightarrow CO_{(g)} + H_{2(g)}$
$R_{(4)} = \dfrac{\rho_g \omega_{H_2O(g)}}{M_{H_2O}} \left(\dfrac{1}{A_i k_{film,H_2O}} + \dfrac{1}{\eta k_{(4)}} \right)^{-1}$	
$k_{(4)} = \dfrac{k_4}{1 + k_2 P_{CO} + k_3 P_{CO_2} + k_5 P_{H_2O}} \omega_{C_{(i)}} \rho_i \varepsilon_i 82{,}056 \times 10^{-3} T_g$; $k_2 = 10{,}3 \dfrac{M_{H_2O}}{M_{CO}}$;	
$k_{\text{film},H_2O} = D^{T_{ave}}_{H_2O,N_2} \dfrac{Sh_i}{d_i}$; $Sh_i = 1{,}5 Re_g^{0{,}55}$; $k_3 = \dfrac{M_{H_2O}}{M_{CO_2}} \exp\left(14{,}24 - \dfrac{18350}{T_i} \right)$	
$A_i = \dfrac{6\varepsilon_i}{d_i \varphi_i}$; $k_4 = \dfrac{1}{3600 M_C} \exp\left(22{,}35 - \dfrac{26320}{T_i} \right)$; $k_5 = \exp\left(29{,}59 - \dfrac{36760}{T_i} \right)$;	
$P_{\omega_j} = \dfrac{82{,}056 \times 10^{-3} \rho_g T_g \omega_j}{M_{\omega_j}}$	
$\eta = \left[\dfrac{d_i}{6} \sqrt{\dfrac{k_{10_i} \delta_i}{\zeta_i D^{T_{ave}}_{H_2O,N_2}}} \right]^{-1} \left\{ \left[\tanh\left(\dfrac{d_i}{6} \sqrt{\dfrac{k_{10_i} \delta_i}{\zeta_i D^{T_{ave}}_{H_2O,N_2}}} \right) \right]^{-1} - \left[\dfrac{d_i}{2} \sqrt{\dfrac{k_{10_i} \delta_i}{\zeta_i D^{T_{ave}}_{H_2O,N_2}}} \right]^{-1} \right\}$; $\delta_{pc} = 1$;	
$\zeta_{pc} = 0.2$;	

2.1 Chemical models

To simulate the evolution of chemical composition of injected coals, several chemical reactions were considered, which are summarised together with their kinetic models in Tables 3 to 7. For reaction kinetic models from literature [8]

were used. Carbon oxidation was assumed to occur in two ways. In the first one, the oxidation is partial, with generation of CO. In a second stage, CO is fully oxidised to CO_2. The solution loss and water gas shift reactions were considered as taking place at temperatures around 900ºC. Coal combustion data reported by Khairil et al. [5] were use to validate the present model in the scope a Master Thesis Baltazar [8].

Table 6: Kinetics model for Water Shift reaction.

(5)	$CO_{2(g)} + H_{2(g)} \leftrightarrow CO_{(g)} + H_2O_{(g)}$
$R_{(5)} = \frac{1000}{(101325)^2}\varepsilon_s(f_{PC})k_{(5)}\left(P_{CO}P_{H_2O} - \frac{P_{co}P_{H_2O}}{k_{(5)}}\right)$	
$P_{\omega_j} = \frac{82,056\times10^{-3}\rho_g T_g \omega_j}{M_{\omega_j}}$; $k_{(5)} = \exp\left(-3,5414 + \frac{3863,7}{T_i}\right)$; $k_1 = 93,3\exp\left(\frac{-7,32}{8,3146\times10^{-3}T_g}\right)$	
$k_{(5)} = \alpha k_1 + (1-\alpha)k_3$, $\left(P_{CO}P_{H_2O} - \frac{P_{CO_2}P_{H_2}}{K_{12}}\right) \geq 0$; $k_2 = 136\ \exp\left(\frac{-7,75}{8,3146\times10^{-3}T_g}\right)$,;	
$k_{(5)} = \left[\alpha k_2 + (1-\alpha)k_4\ \right]\ k_{(5)}$, $\left(P_{CO}P_{H_2O} - \frac{P_{CO_2}P_{H_2}}{K_{12}}\right) < 0$; $k_3 = 1,83\times10^{-5}\exp\left(\frac{7,84\times10^{-3}}{8,3146\times10^{-3}T_g}\right)$;	
$k_4 = 8,83\times10^{-2}\exp\left(\frac{4,56}{8.,146\times10^{-3}T_g}\right)$	

Table 7: Kinetics model for volatile combustion.

(6) $\text{Volatiles}_{(pc)} + \alpha_1 O_{2(g)} \rightarrow \alpha_2 CO_{2(g)} + \alpha_3 H_2O_{(g)} + \alpha_4 N_{2(g)}$
$R_{(6)} = 23,6\left(\frac{\mu_g\varepsilon_t}{\rho_g k_t}\right)^{1/4}\left(\frac{\varepsilon_t}{k_t}\right)\min\left(\varepsilon_{pc}\rho_{pc}\omega_{MVPC}, \varepsilon_g\omega_{O_2}\frac{M_{MV}}{\alpha_1 M_{O_2}}\right)$
(7) $\text{Volatiles}_{(pc)} + \alpha_5 CO_{2(g)} \rightarrow \alpha_6 CO_{(g)} + \alpha_7 H_{2(g)} + \alpha_8 N_{2(g)}$
$R_{(7)} = 23,6\left(\frac{\mu_g\varepsilon_t}{\rho_g k_t}\right)^{1/4}\left(\frac{\varepsilon_t}{k_t}\right)\min\left(\varepsilon_{pc}\rho_{pc}\omega_{MVPC}, \varepsilon_g\omega_{CO_2}\frac{M_{MV}}{\alpha_5 MC_{O_2}}\right)$; $k_t = \left(0.03\left\lvert\bar{U}_g\right\rvert\right)^2$; $\varepsilon_t = \frac{k_t^{0.5}}{0.01}$

3 Results and discussions

In order to analyze the behaviour of two different pulverized coal injected into two points within the raceway channel the time evolution of the majors distribution variables were plotted. In figure 1 the pressure field and path lines of the gas phase are shown. The pressure drop along the raceway channel is mainly due to the phase interactions with the pulverized phases. Also in Fig. 1 is observed an asymmetric pressure distribution due to the central inclined of 6 degrees of the pulverized flow injection of the two types of pulverized coals.

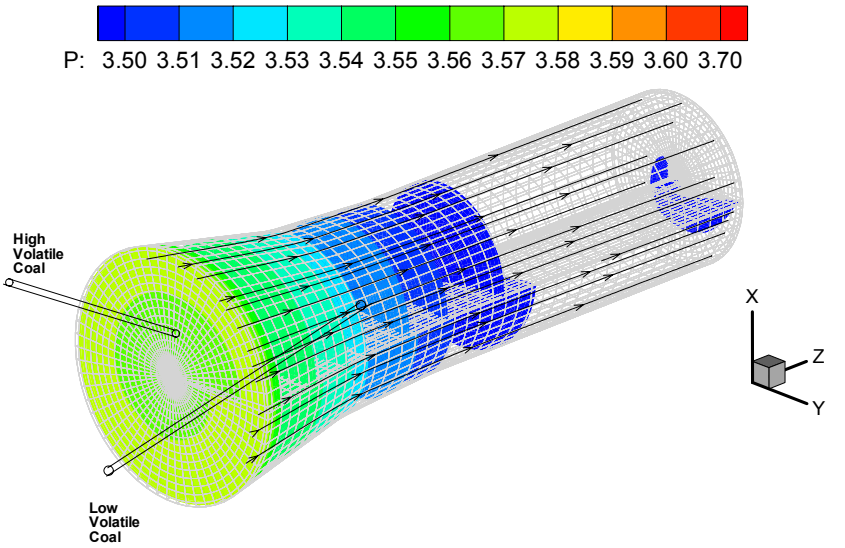

Figure 1: Flow pattern and pressure field for the gaseous phase (time = 0.002 s).

Figure 2 shows the gas temperature pattern for a radial plane and the gas velocity vectors. As can be observed, the gas temperature is increased to around 2000 ^{o}C in the vicinity of the injection points due to the highly exothermic reactions of carbon combustion. On the other hand, just at the injection points the gas temperature decreased because of the strong heat transfer among the gas and the pulverized coals phases, which are injected at the temperature of 30 ^{o}C, while the gas is preheated to 1200 ^{o}C. Figure 3 shows the phase volume fraction of the pulverized coal injected at the first injection point. In figure 4 the temperature distribution of the pulverized coal particle is shown. The temperature of the particle developed very high temperature in the flow stream. This is a technological important parameter since the integrity of the injection device is of fundamental importance for the smooth operation. Therefore the model is an important tool to address the convenient points for the pulverized coal injection without damage of the injection device.

At this point it is import to emphasise the transient behaviour of the blast furnace raceway. In the operation the injection amount and the blast rate is strongly influenced by the inner furnace permeability, which in turn, determines the furnace productivity. Therefore, the results obtained in this study were carried out for the initial condition of no injection and the transient behaviour was predited.

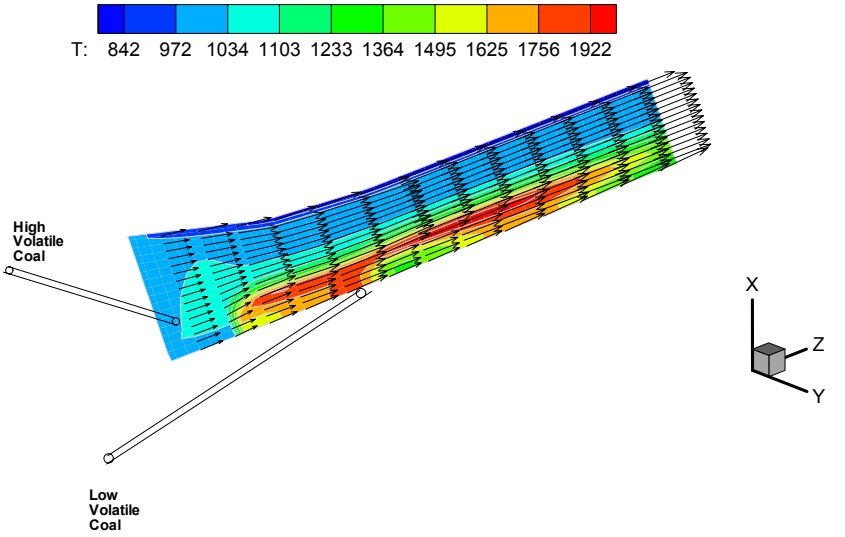

Figure 2: Gas temperature distribution and gas vectors plot (time = 0.002 s).

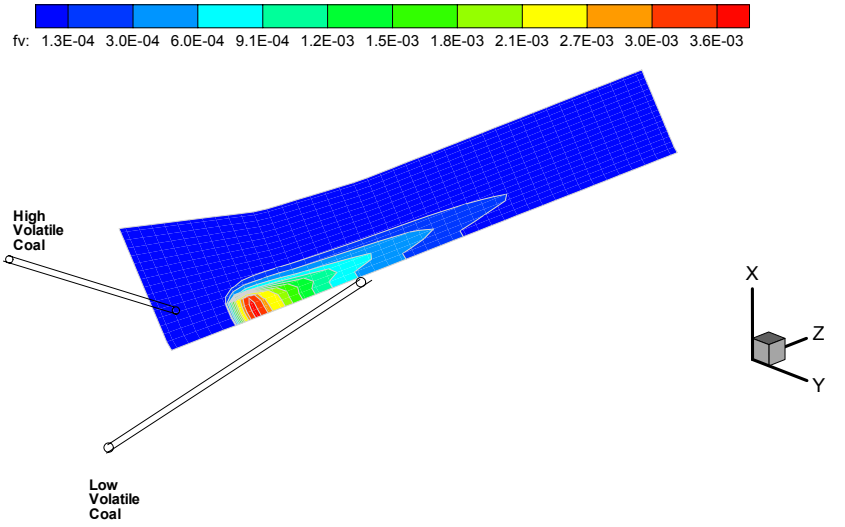

Figure 3: Phase volume fraction for pulverized coal with low volatile matter (time = 0.002 s).

4 Conclusions

A mathematical model for simulating two types of pulverized coal injection has been developed. The model is based on a three phase multi-component system

which interacts with one another exchanging momentum mass and energy. Detailed rate equations for the major chemical reactions taking place in the raceway channel were considered. The governing equations are solved based on the finite volume method for non-orthogonal structured mesh. Transient 3D results were presented for elucidate the flow pattern and temperature distribution of the 3 phases modelled. The model predictions indicted that the inner temperature of the raceway channel could reach around 2000 ^{o}C, which is observed in the actual blast furnace operation.

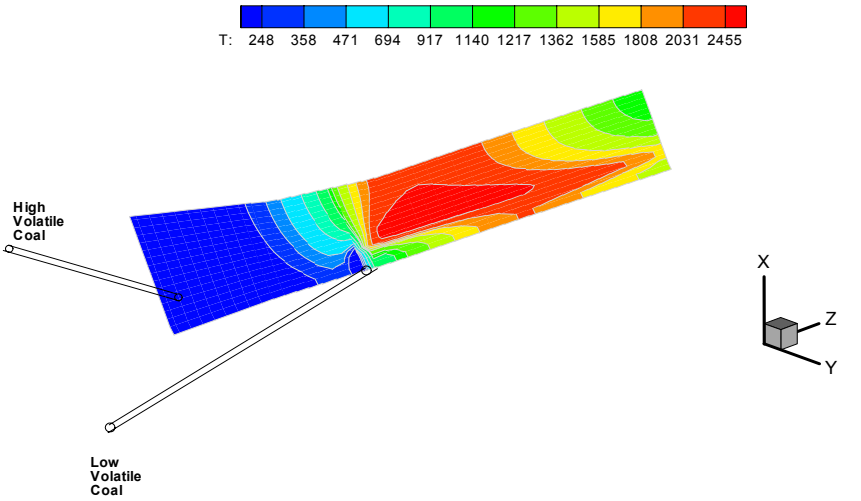

Figure 4: Gas temperature distribution within the raceway channel.

5 Symbol table

A- superficial area (m^2m^{-3})	ωj- Molar fraction of phase j
D- Diffusion coefficient (m^2s^{-1})	η- efficiency factor for reaction
d- Particle diameter (m)	Sϕ - Source terms (various)
Mj – Molecular weight (kg mol^{-1})	Sh - Sherwood number (-)
P- Gas phase pressure (Pa)	φi- Shape factor of phase i
Ri- Reactions rates (mol m^{-3} s^{-1})	ρ- Phase density (kg m^{-3})
T-temperature (K)	Γ_ϕ Transfer coefficient (various)
εi- phase volume fraction(-)	

Acknowledgement

The authors would like to thank CNPq for the financial support for this work (edital Universal 2003 proc: 477240-03-0).

References

[1] Lin, S.Y., Hirato, M., Horio, M., The Characteristics of Coal Char Gasification at around Ash Melting Temperature, *Energy & Fuels*, **8**, pp. 598-606, 1994.

[2] Zolin et al. A comparison of Coal Char Reactivity Determined from Thermogravimetric and Laminar Flow Reactor Experiments, *Energy & Fuels*, **12**, p 268-276,1998.

[3] Castro, J.A., A Multi-dimensional Transient Mathematical Model of Blast Furnace Based on Mult-fluid model, Doctoral Thesis, Tohoku University, Institute for advanced material processing, Japan, 2000.

[4] Austin, P.R., Nogami, H., Yagi, J.I., A mathematical model for blast furnace reaction analysis based on the four fluid model, *ISIJ Int*., **37(8)**, pp. 748-755, 1997.

[5] Khairil et al. Fundamental Reaction Characteristics of Pulverized Coal at High Temperature, *ISIJ Int*., 41**(2)**, pp 136-141, 2001.

[6] Baltazar, A.W.S., Modelamento Matemático e Simulação Computacional de um Ensaio de Combustão de Carvão Pulverizado. Master Thesis, EEIMVR-UFF, Volta Redonda Brazil, 2004.

[7] Castro, J. A., Nogami, H. And Yagi J.: Numerical Investigation of Simultaneous Injection of Pulverized Coal and Natural Gas with Oxygen Enrichment to the Blast Furnace, *ISIJ Int*., **42**, pp 1203-1211, 2002.

[8] Austin, P. R., Nogami, H., And Yagi, J.: A Mathematical Model of Four Phase Motion and Heat Transfer in the Blast Furnace ISIJ *Int*., **37**, pp 458-467, 1997.

[9] Castro, J. A., Nogami, H., And Yagi, J.: Three-dimensional Multiphase Mathematical Modeling of the Blast Furnace Based on the Multifluid Model *ISIJ Int*. **42**, pp. 44-52, 2002.

[10] Austin, P. R, Nogami, H., And Yagi, J.: A Mathematical Model for Blast Furnace Reaction Analysis Based on the Four Fluid Model *ISIJ Int*., **37**,pp.748-755, 1997.

[11] Perry, R. H. And Green, D.: Perry's *Chemical Engineers Handbook*, 6th. Ed., McGraw-Hill, New York, Table 3-5, 1984

[12] Kagaku Kogaku Binran (5th ed.), *Chemical Engineers Handbook* eds. Soc. Chem. Eng of Japan, Maruzen, Tokyo, pp. 232, 1988.

[13] Castro J. A., Nogami, H., And Yagi, J.: Numerical Analysis of Multiple Injection of Pulverized Coal, Prereduced Iron Ore and Flux with Oxygen Enrichment to the Blast Furnace, *ISIJ Int*. **41**, pp. 18-24-, 2001.

Section 7
Particle image velocimetry

This page intentionally left blank

Gas-liquid two-phase flow in a downward facing open channel

D. Toulouse & L. I. Kiss
Département des sciences appliquées,
Université du Québec à Chicoutimi, Québec, Canada

Abstract

There are certain industrial applications where gas is evacuated from below a solid surface by using vertical grooves. To study this phenomenon experimentally, a solid body with a horizontal gas-generating bottom surface is immersed into a liquid. A downward facing open channel in the form of a rectangular groove is cut into the solid. Gas enters at the lower part of the groove and is evacuated at the two ends. The flow is induced by the buoyancy effect in the channel. The morphology and flow pattern in the downward facing open channel is analysed as a function of the gas flow rate entering the groove. Different flow regimes were identified as the volume fraction of the gas inside the channel was increased. High-speed videography and image processing were used to analyse the flow structure inside the channel and to extract quantitative information such as the volume fraction of the gas and the bubble size distribution. Particle image velocimetry (PIV) and bubble image velocimetry (BIV) were used to study the velocity distribution inside the liquid phase and the velocity of the bubbles.
Keywords: two-phase flow, flow pattern, image processing, bubble image velocimetry, gas bubbles.

1 Introduction

There are situations in the industry where gas must be evacuated from below a large partially immersed body. It has been observed that thin grooves cut into the downward face of this body improve the evacuation of the gas. To understand this phenomenon, it is necessary to gather some information on the morphology of buoyancy driven gas-liquid flow in an open channel. As it is the

case for most phenomenon involving a gas and liquid flow, deeper understanding that can lead to the development of a mathematical model requires the measurement of some flow parameters such as the phases volume fractions and their velocity field. Many different techniques have been used to estimate those parameters in gas-liquid flows. For the particular case of a 2D flow within transparent boundaries, non-intrusive techniques based on image analysis are known to give detailed results on the flow variables and have been widely used in the last decades.

Mishima et al. [8] determined the total void fraction in a 2D channel of 5 mm thickness by processing images obtained by neutron radiography. He also estimated the velocity of the largest bubbles inside the flow by the same technique. Wilmarth and Ishii [13] used a CCD camera for visualization and flow regime identification inside a narrow 2 mm channel. Later, Wilmarth and Ishii [12] used image processing and were able to obtain void fraction and interfacial area concentration for the 2D channel flow studied. Chen et al. [2] used a custom developed PIV system for simultaneous measurement of void fraction, liquid velocity and gas velocity inside a 3D bubble column. The same system was used by Lin et al. [7] for the study of gas-liquid flow inside 2D columns of 0.64 cm and 1.27 cm thickness. Void fraction distribution and liquid velocity profile across the channel width were obtained with this technique. Spicka et al [10] studied the flow inside a 2D column of 2 mm gap thickness. LDV was used for measurement of velocity field, turbulence intensity and Reynolds stresses inside the liquid phase. Imaging was used for the measurement of gas volume fraction, interfacial area and bubble size. The use of a shape factor was introduced to correctly estimate void fraction and interfacial area from 2D images.

The present study intends to describe the morphology of gas liquid flow inside a downward facing open channel as a function of the gas velocity. Additionally, information on the void fraction distribution and the velocity field of the phases are needed for a better understanding of the phenomenon. Tests were performed on a transparent water model. High-speed videography was used for flow visualization. Images obtained were processed to obtain void fraction distribution and bubbles velocity. A PIV system was used for measurement of the liquid flow field.

2 Experimental

2.1 Water model

Experimental study of gas-liquid two-phase flow inside a downward facing open channel is performed on the model shown in fig. 1. A solid box 900 mm long and 190 mm thick is immersed into a large reservoir of water. The bottom surface of this box consists of a porous bronze plate that will generate air bubbles under its surface once the chambers are put under pressure. The volume of the box is divided into 6 separate chambers. A flowmeter controls the airflow rate for each of these chambers to ensure a uniform bubble generation along the

horizontal axis x. A 10 mm thick groove is cut into the whole length of the body. The gas generating surfaces are given an inclination of 1 degree toward the groove to ensure that all the gas generated will enter the channel. Entering gas bubbles will rise up the 150 mm high slot and then be evacuated at the two ends. The entry section of 900 mm per 10 mm is used for calculation of the superficial velocity U_{gs} of the gas.

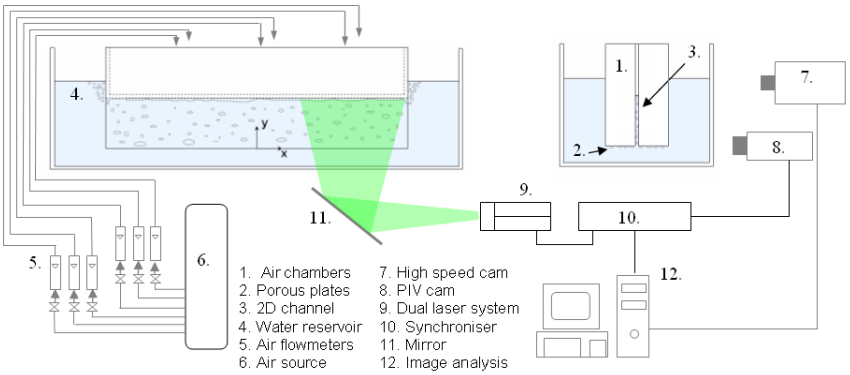

Figure 1: Experimental set up.

Air is used as the gas phase while distilled water at a temperature of 21 ± 1 C is used as the liquid phase. The whole set up is made of acrylic allowing a total visualization of the flow from the side with the exception of the four 6 mm thick walls that divide the sections. The water level in the reservoir is kept constant 50 mm higher than the upper part of the groove. During the experiments, the total gas flow to the chambers is controlled so that U_{gs} inside the channel changes from 0.44 cm/s to 28 cm/s. A high-speed digital camera connected to a PCI board is used for visualization and computation of the void fraction and gas bubbles velocities. A PIV system is used for measurement of the liquid phase velocity field.

2.2 Imaging

A CCD camera with a resolution of 512 X 480 pixels and a maximum shutter speed of 1/10000 s is used for grabbing images of the flow. Two different fields of view are used. In the first one, the camera covers the whole length of the 2D channel. While this yields a relatively poor resolution (0.5 pixels/mm), it allows for visualization of the global behaviour of the flow and is particularly useful at high gas velocity. With the second field of view, the camera covers a smaller part of the channel and the resolution is 1.7 pixels/mm. This allows for a more precise measurement of the gas volume fraction and the gas bubbles velocities. Proper lighting is provided by three 500 W light sources behind a diffuser on the other side of the 2D channel.

Estimation of the void fraction inside the groove is made by analysis of the images captured. Image enhancement by linear filtering is performed to allow the detection of the edges between the gas and liquid phases Yang [14]. Closed contour lines can then be filled to obtain the projected area in the x-y plane for all the bubbles detected. Centroïd position and equivalent diameter are computed for each bubble. The instantaneous 2D gas fraction is equal to the sum of the areas of all the detected objects inside one frame divided by the area of that frame. To be able to estimate the instantaneous gas volume fraction in one frame, it is necessary to assume the 3D shape of the bubbles detected. A method for correcting 2D data was proposed by Spicka et al. [10]. A shape factor is introduced to correct the projected area of a bubble in the x-y plane. This shape factor is defined in eqn. 1 where A_{y-z} is the projected area of the bubble in the y-z plane, l_b is the length of the bubble in the y dimension, t is the thickness of the channel and C is the shape factor for that particular bubble.

$$C = \frac{A_{y-z}}{l_b t} \tag{1}$$

This shape factor was measured experimentally by image analysis for 60 bubbles of d_e ranging from 5 to 40 mm; results are shown in fig. 2. It was found that for bubbles larger than 10 mm (the gap thickness) this shape factor converged to a value of 0.73. Using this shape factor is the same as considering that the average film thickness between the bubble and the walls is 1.3 mm. The value of the shape factor found is slightly higher than the 0.69 proposed by Spicka et al. [10] for a 2 mm gap system. Bubbles with d_e less than the thickness of the channel are considered perfectly spherical. This approximation is chosen for simplicity even if bubbles of d_e close to 10 mm are observed to be oval and will have a shape factor bigger than the spherical ones.

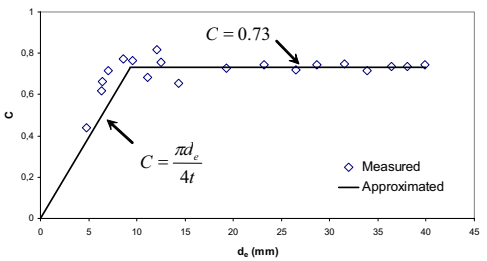

Figure 2: Bubble shape factor.

2.3 PIV

A particle image velocimetry system using dual Nd:YAG lasers for illumination is used to measure the liquid velocity field. The light sheet produced by the lasers is oriented into the thin channel from the bottom by using a mirror. The water is seeded with neutrally buoyant small particles. The CCD camera is moved in ten different positions to totally scan the right half of the channel.

3 Results and discussion

3.1 Macroscopic observations

With U_{gs} increasing from 0.45 cm/s to 28 cm/s, 3 distinct regimes can be observed for the flow inside the groove: a homogeneous regime, a heterogeneous regime and a slugging regime.

For U_{gs} below 0.7 to 0.8 cm/s, the flow inside the channel is in a homogeneous regime. Dispersed bubbles rise regularly until they reach the upper part of the groove. Those bubbles will then form a shallow and discontinuous gas channel along the top of the groove and the gas will evacuate at the sides. This flow is similar to the one observed in a 2D bubble column under the homogeneous regime. PIV imaging shows the liquid rising in the wake of the bubbles and going down between them. The gas being generated under porous plates, bubbles will enter the groove at random locations along the lower part of it. Areas of rising liquid and gas and areas of descending liquid will move with time. Even in the homogenous regime, a few larger bubbles with d_e up to 10 mm will appear, as seen in fig. 5. Those bubbles will adopt a slightly oval shape when rising in the groove and will oscillate as they head for the top of the channel.

As U_{gs} is increased, a transition will occur and the flow will cease to behave homogeneously. It is not easy to define clearly when this transition occurs by observing the images taken with the high-speed camera because of the lack of a standard definition. Previous studies on gas liquid flow inside a wide 2D channel outlined the characteristics of the transition from the homogenous regime for this type of flow. Tzeng et al. [11] and Lin et al. [7] described this transition as the point where the effects of the sidewalls on the flow become important. Those sidewalls will induce a migration of the closest bubbles toward the center of the column that will create the gross circulation pattern where some bubbles are observed to move in clusters. In the case of the studied flow there must be another mechanism that triggers the transition. When U_{gs} reaches values above 0.8 cm/s, coalescence under the porous plate will create large cap shaped bubbles. Those larger bubbles will induce cluster motion when they rise into the channel and will initiate the heterogeneous regime.

For U_{gs} between 0.7-0.8 cm/s and 15-20 cm/s, the flow is in a heterogeneous regime. As the number of the cap shaped bubbles increases, their effect on the flow becomes more important. When a large bubble, initially under the porous plate enters the groove, it will attract in its wake other bubbles that were staying near. In this regime, a great part of the gas will enter the lower part of the channel in large bubble clusters at varying locations along its length. The size of those clusters will increase with U_{gs} and they will periodically form columns of high velocity rising gas and liquid. Between those columns vortices of descending liquid and small bubbles will be created. After the bubbles reach the top of the groove, gas will evacuate by flowing toward the sides in a gas channel. The shape of this upper gas channel is deformed and discontinuous because of the liquid movement induced by the bubble clusters and the irregular

alimentation by the rising columns. The thickness of the gas channel will oscillate between 0 and 20 mm when U_{gs} = 1 cm/s and between 0 and 100 mm at U_{gs} = 15 cm/s.

When U_{gs} reaches a critical value located between 15 and 20 cm/s, a third flow pattern that was called the slugging regime will take place. Coalescence inside the bubble clusters will create gas pockets so large they will occupy the whole height of the channel. Gas will continue to be transported to the upper gas channel but no longer by discrete bubbles. The large pockets will form bridges that will directly link the gas generating surfaces and the upper gas film for a short time. When this phenomenon happens, gas will enter the groove at a much higher rate than it is evacuated at the sides. Consequently, the thickness of the gas film will increase in the whole channel until gas occupies the larger part of it (fig. 3 a). While the thickness of the gas film increases, the liquid and the small bubbles will be pushed down and flow out of the groove through the lower part. When the film reaches a certain thickness, gas will escape suddenly by the sides. The film thickness will diminish rapidly as the groove fills in with liquid from below. This fast liquid flow will entrain small bubbles that are forming under the porous plate (fig. 3 b). The time between the figures 3 a) and b) is 0.38 s.

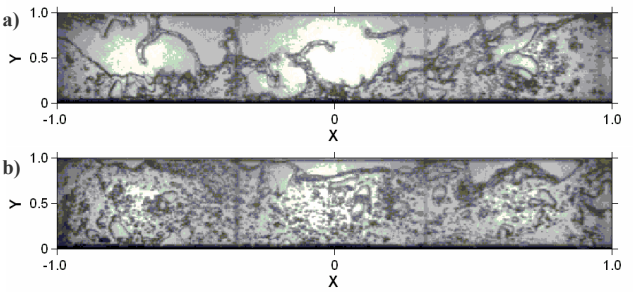

Figure 3: Phases of the slugging regime a) building of gas holdup b) gas evacuation.

3.2 Gas volume fraction measurements

Images showing the whole channel were analysed to measure the instantaneous void fraction. Using this large field of view is not precise but allowed the estimation of the total quantity of gas inside the groove at a given instant in time. Measurements were performed for gas superficial velocities up to 28 cm/s and the data were corrected to account for the film thickness between the bubbles and the wall. It can be seen in fig. 4 a) that a sharp increase in the amplitude of fluctuation will occur between U_{gs} = 0.17 m/s and U_{gs} = 0.28 m/s, when the flow enters the slugging regime. The variation of the total quantity of gas between 2 instants becomes important as large holdups are created and evacuated periodically. As seen in Fig. 4 b) the average gas void fraction will increase monotonically for all regimes.

A smaller field of view allows a more precise measurement of the void fraction. Fig. 7 a) shows the average distribution of the void fraction inside the

right half of the model for U_{gs} = 0.56 cm/s. It can be seen that gas will concentrate in the upper part of the groove where it will slowly exits by the sides.

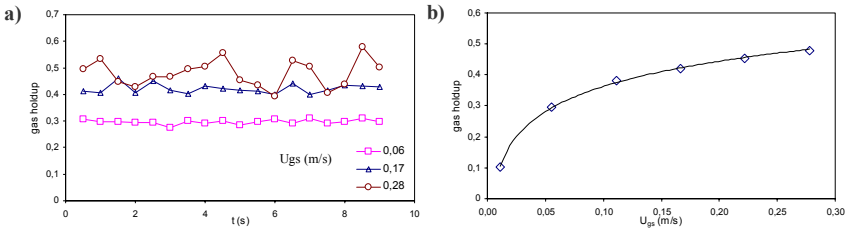

Figure 4: Total gas volume fraction a) Instantaneous b) Average.

3.3 Bubble size and bubble velocity measurement

For different values of the superficial gas velocity, pictures of the flow are analysed by means of the method described earlier. The 2D projection area and the position of the centroïd are computed for each bubble in each frame treated. Fig. 5 presents the number of bubbles detected for each different equivalent diameter range. The data was taken at U_{gs} = 0.56 cm/s in the right half of the model. 20 different images were analysed for each camera position. More than 2000 rising bubbles were identified for these conditions.

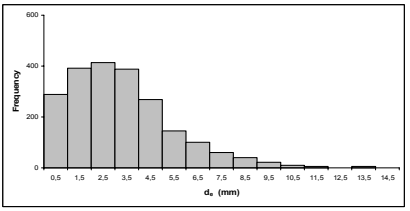

Figure 5: Bubble size distribution, U_{gs}=0.56 cm/s.

As mentioned previously, the bubbles inside the channel tend to have a wide size distribution. Even when U_{gs} is so low that no noticeable coalescence occurs inside the channel, different bubble sizes are detected. This situation is created by the non-uniformity of the pores inside the bronze plate and the coalescence during the creation of the bubbles and their travel under the porous plate.

The results obtained for the bubble size distribution only concern the freely rising bubbles. For each different flow condition, an important part of the gas appears in the form of a gas tube in the upper part of the groove and is not computed in the bubble size distribution.

Using the method described earlier, the instantaneous velocity vectors were calculated for each bubbles detected. The time step between the two frames used

for correlation is 0.016 s. The average rising velocity for these conditions was found to be 0.21 cm/s. The precision of the measurement for the rising velocity of a bubble was estimated with the method proposed by Ho [4]. The digitizing error on the measurement of an average sized bubble's centroïd is estimated to be of ± 0.09 mm with the resolution used. This will yield a precision of ± 0.011 cm/s when calculating the bubble's velocity. Of course, for bubbles smaller or slower than average, the measurement of the velocity will be less precise.

There seems to be no correlation between the bubble size and its rising velocity inside the groove. In fig. 6, bubbles were separated in 11 different classes according to their equivalent diameter. The average rising velocity was then computed for each class. According to Spicka et al. [10] bubbles of the size detected here rising in a 3D column of distillate water are all under the ellipsoidal regime. In this regime, there is no sharp increase of the bubble velocity with the diameter and this could explain the results obtained

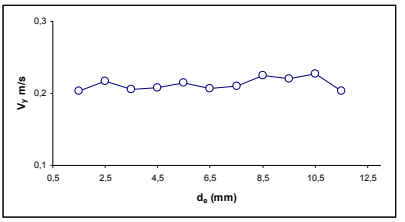

Figure 6: Average rising velocity for different bubble class, U_{gs}=0.56 cm/s.

If a bubble's rising velocity inside the groove was not found to be a function of its size, it will however be influenced by its position along the horizontal axis x. The results obtained for the analysis of the liquid velocities under the homogeneous and the first part of the heterogeneous regimes clearly shows the apparition of a circulation pattern inside the groove. Bubbles rising in areas of fast circulating liquid will have a higher rising velocity than others. Fig. 7 c) shows the average rising velocity for bubbles with d_e between 3 and 4 mm, classified according to their position along x when detected.

3.4 Liquid velocity measurement

A PIV system was used to compute the average liquid velocity for different points inside the right half of the channel. For each different location, 20 images were analysed and averaged. Fig. 7 b) shows the results obtained at U_{gs} = 0.56 cm/s. Although visualization has shown that the major flow structures are transient, there seems to be a global flow pattern inside the groove, at least for low gas velocities. Circulation cells can be observed in the center part of the groove and part of the liquid entrained from below the channel in this area will not be conveyed to the sides. Near the sides, there is no global recirculation within the groove and the rising bubbles will create a continuous liquid flow from below to the sides.

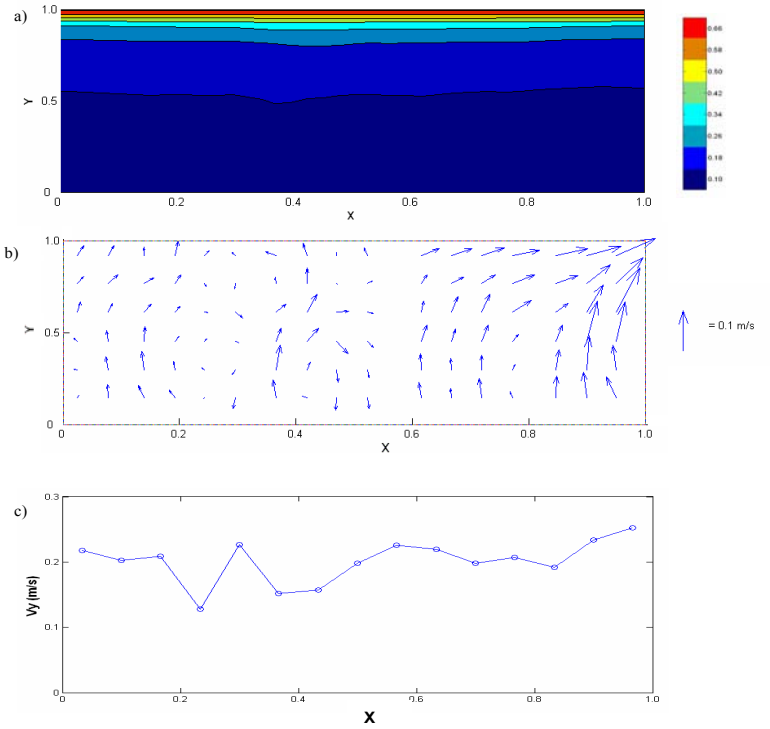

Figure 7: Time averaged distributions for U_{gs} = 0.56 cm/s, a) gas volume fraction b) liquid velocities c) rising velocity of bubbles d_e = 3-4 mm.

4 Conclusions

Gas-liquid flow in a narrow downward facing open channel is studied at various gas velocities. High-speed videography allows the identification of three different flow regimes: homogeneous, heterogeneous and slugging. For each of these regimes a morphological description is made on the base of observations. Image analysis shows a monotonic augmentation in the average void fraction inside the groove as gas velocity is increased. The instantaneous void fraction shows great variations with time for the slugging regime while it is stable for the two others. The measurements of bubble sizes inside the groove in the homogeneous regime shows a population between 0.5 and 12 mm, which is characteristic for the type of injection used. The size of the bubbles generated has a great influence on the flow behaviour, particularly on the transition from homogeneous to heterogeneous regime. Bubbles absolute rising velocity inside the groove for the homogenous regime seems to be more influenced by their position along the length of the channel than by their size. Liquid velocity measurements show the existence of a mean circulation pattern for the same regime.

Acknowledgement

The first author gratefully acknowledges the support of the Natural Sciences and Engineering Research Council of Canada (NSERC) in the form of post-graduate scholarships.

References

[1] Ali M. I., Sadatomi M., Kawaji M., "Adiabatic two-phase flow in narrow channels between two flat plates", *Can. J. Ch. Eng.*, Vol. 71, 1993, pp. 657-666.

[2] Chen R. C., Reese J., Fan L. S., "Flow structure in a three dimensional bubble column and three-phase fluidized bed", AIChE. J., Vol. 40, No. 7, 1994, pp. 1093-1104.

[3] Hetsroni, G., *Handbook of multiphase systems*, Hemisphere Publishing Corporation, New York, 1982, 1165 p.

[4] Ho, C-S., ''Precision of digital vision systems'', IEEE t*ansactions on pattern analysis and machine intelligence,* Vol. PAMI-5, No. 6 1983, pp. 593-601.

[5] Joshi J. B., et al., "Coherent flow structures in bubble column reactors", *Chemical Engineering Science*, Vol. 57, 2002, pp. 3157-3183.

[6] Kleinstreuer, C., *Two-phase flow theory and applications*, Taylor and Francis, New York, 2003, 454 p.

[7] Lin, T. J., Reese J., Hong T., Fan L. S., "Quantitative analysis and computation of two-dimensional bubble columns", *AIChE. J.*, Vol. 42, No. 2, 1996, pp. 301-318.

[8] Mishima K., Hibiki T., Nishihara H., "Some characteristics of gas-liquid flow in narrow rectangular ducts", *Int. J. Multiphase Flow*, Vol. 19, No 1, 1993, pp. 115-124.

[9] Spicka P., Dias M. M., Lopes J. C., "Gas-liquid flow in a 2D column: Comparison between experimental data and CFD modelling", *Chemical Engineering Science*, Vol. 56, 2001, pp. 6367-6383.

[10] Spicka P., Martins A. A., Dias M. M., Lopes J. C., "Hydrodynamics of gas-liquid flow in 2D packed/unpacked rectangular reactor", *Chemical Engineering Science*, Vol. 54, 1999, pp. 5127-5137.

[11] Tzeng, J. W., Chen R. C., Fan L. S., "Visualization of flow characteristics in a 2-D bubble column and three phase fluidized bed", *AIChE. J.*, Vol. 39, No. 5, 1993, pp. 733-744.

[12] Wilmarth T., Ishii M., "Interfacial area concentration and void fraction of two phase flow in narrow rectangular vertical channels", *Tansactions of ASME*, Vol. 119, 1997, pp. 916-922.

[13] Wilmarth T., Ishii M., "Two phase flow regimes in narrow rectangular vertical and horizontal channels", *Int. J. Heat Mass Transfer*, Vol. 37, No. 12, 1993, pp. 1749-1758.

[14] Yang, W., Computer-assisted flow visualization, second generation technology, CRC Press, London, 1994, 342 p.

The effect of two inclined circular plunging jets on air entrainment in an aeration tank

M. S. Baawain, M. Gamal El-Din & D. W. Smith
Department of Civil and Environmental Engineering, University of Alberta, Edmonton, Canada

Abstract

Air entrainment occurs when two or more flowing fluids plunge into each other, or when some sort of turbulence is introduced in a water body. In this study, experiments were conducted to explore some properties of bubble plumes of two inclined circular plunging water jets on a water surface in a cubic tank utilizing particle image velocimetry (PIV). Different combinations of two inclined water jet sizes operating under different flow rates and plunging angles were used to study air entrainment in the aeration tank. The PIV system was used to measure the two-phase jet velocities in both lateral and axial positions. Other parameters of interest, such as penetration depths and the height and width of the two-phase mixture due to the air entrainment, were monitored using a photographic technique. The gas hold-up (ε_G) and the bubble average diameter (d_b) were consequently obtained. Using ε_G and d_b, the specific interfacial area (a) and the overall mass transfer coefficient (k_La) under each operating condition were determined. The obtained results were compared with results obtained under similar operating conditions for vertically aligned jets.
Keywords: air entrainment, plunging jets, particle image velocimetry, gas hold-up, specific interfacial area, overall mass transfer coefficient.

1 Introduction

Liquid plunging jets are moving columns of liquid (water) that pass through some gaseous headspace before impinging into a free surface of the receiving liquid. At the intersection of the plunging jet and the liquid surface, free-surface instabilities develop and gas entrainment may be observed. In order for the gas entrainment to take place, the jet impact velocity has to exceed a characteristic

velocity (onset or threshold velocity) that is a function of the plunging flow conditions [1]. Other factors that control the mechanisms of air entrainment include: physical properties of the liquid, the design of the jet nozzle, the distance from the jet outlet to the liquid surface, and the turbulence of the jet [2, 3].

Air entrainment by plunging liquid jets in water bodies has potential applications in many chemical and waste treatment processes. Examples of such processes include minerals-processing flotation cells and wastewater treatment. This process, referred to as plunging jet entrainment and aeration, can also be observed in natural systems such as self-purification (re-aeration) of rivers and waterfalls [2, 3, 4].

When aeration systems are used in wastewater treatment plants, the ultimate goal is to obtain high mass transfer of oxygen by having the most effective bubbles (i.e. bubbles with small diameter and long residence time). The process of mass transfer of gas to water with time (t) can be expressed using the following equation:

$$\frac{dC}{dt} = k_L a\left(C_s - C\right) \tag{1}$$

where C is the dissolved oxygen concentration in water (mg/L), k_La is the overall mass transfer coefficient (s^{-1}), and C_s is the saturation concentration of oxygen in water. The determination of k_La is very important for the design and performance evaluation of gas-liquid mass transfer processes.

This study explores air entrainment resulted from the use of two inclined circular plunging jets intersecting at the surface of water tank in comparison to the commonly used vertical jets. The research aims at utilizing particle image velocimetery (PIV), which is a well established non-intrusive measuring technique that can provide simultaneous measurements of velocity components of different phases of fluids [5, 6], to evaluate the two-phase jet velocity components in the tank. In addition to the impingement angle, this research work evaluates the use of different jets nozzle size, free jet lengths, and jet outlet velocities.

2 Materials and methods

Air entrainment experiments were performed using a clear walled tank, vertical jet, and a particle image velocimetery, as shown in fig. 1. The inside dimensions of the tank had a width of 0.67 m, a length of 0.67 m, and a depth of 0.67 m. An overflow weir was located on one side to maintain a constant depth in the tank. The water overflow drained into a storage barrel and re-circulated using an electric pump, which also provided a means of varying the discharge.

Water was directed by the pump to two inclined (or vertical) circular jets mounted above the water surface of the tank. This alignment allowed the jets to be moved in three directions and to be rotated from 0^o to 90^o. The diameter of these jets was varied from 2.5×10^{-3} to 0.01 m. Air bubbles entrained by jets

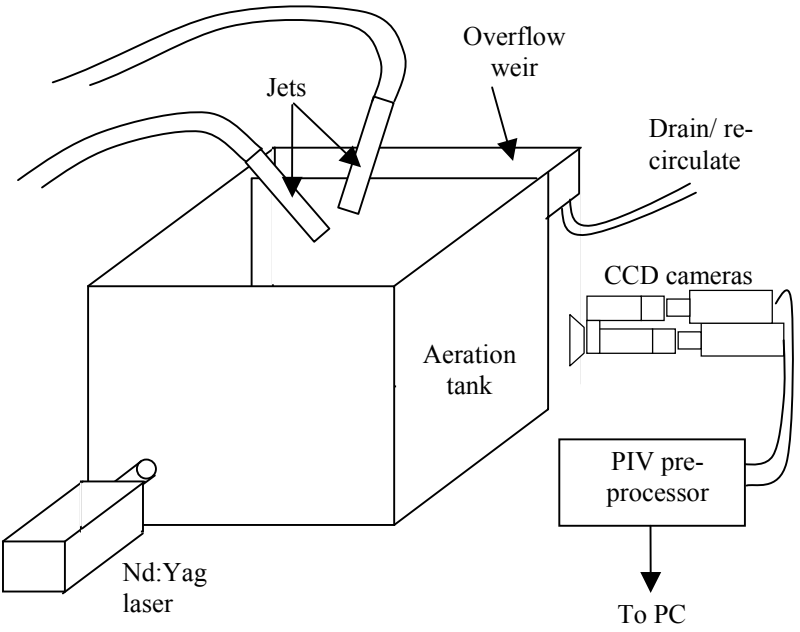

Figure 1: Experimental setup.

were then observed through the transparent tank walls. Two measuring tapes were secured to the tank horizontal and vertical sides in order to monitor the depth and width of the bubble plumes.

The PIV system consisted of a laser source, two charge coupled device (CCD) cameras, and processing units. This study used an Nd:Yag dual cavity laser with a power level of 100 mJ. The emitted wavelength of the Nd:Yag laser was 532 nm with a pulse duration of 10 ns. The time between pulses was set to 100 μs with a maximum repetition rate of 8.0 Hz. The two CCD cameras were configured to use double frames for PIV measurements (velocity measurements) of the two phases (water and air). Melamine-formaldehyde (MF) spheres, coated with Rhodium B (RhB), were used as seeding particles during the liquid velocity measurements. A FlowMap System Hub from Dantec Dynamics was used to record and transfer the data to a PC where FlowMap software was used to analyze the images and export the resulted files to a desired format for further analysis. Two PIV measurements were conducted simultaneously: one for obtaining liquid jet velocity components in the tank and the second for measuring the air (bubble) jet velocity components in the tank. The images captured for the bubble plumes by the CCD camera were used to estimate the average bubble size under each experimental condition.

Table 1: Summary of the experimental operating conditions.

Run #	Q_L x 10^{-5} (m^3/s)	d_o x 10^{-3} (m)	α (deg)	H x 10^{-2} (m)
1	3.15	2.50	90	5.00
2	3.15	2.50	15	7.00
3	3.15	2.50	22.5	8.45
4	6.30	5.00	90	5.00
5	6.30	5.00	15	7.00
6	6.30	5.00	22.5	8.45
7	9.45	5.00	90	5.00
8	12.6	5.00	90	5.00
9	9.45	5.00	15	7.00
10	12.6	5.00	15	7.00
11	6.30	5.00	15	8.60
12	9.45	5.00	15	8.60
13	12.6	5.00	15	8.60
14	6.3	5.00	15	11.20
15	9.5	5.00	15	11.20
16	12.6	5.00	15	11.2
17	9.45	5.00	22.5	8.45
18	12.6	5.00	22.5	8.45
19	9.45	7.50	90	5.00
20	9.45	7.50	15	7.00
21	9.45	7.50	22.5	8.45
22	12.6	10.0	90	5.00
23	12.6	10.0	15	7.00
24	12.6	10.0	22.5	8.45

A summary of the experimental runs conducted for this work is provided in table 1. The jet nozzles were made of copper with an inlet diameter (d_i) of 0.025 m and a cylindrical length (l_i) of 0.015 m. Nozzles outlet diameter (d_o) used in this study ranged from 2.5 x 10^{-3} to 0.01 m yielding a range for the aspect ratio (l_i/d_o) of 1.5 and 6. The monitored water temperature during all experiments was 23 ^{o}C ± 1 ^{o}C. The Liquid flowrate (Q_L) was varied from 3.15 x 10^{-3} to 12.6 x 10^{-3} m^3/s, with the angle at which the jets plunge the surface (α) of 67.5^{o}, 75^{o} (resulted angle between the two jets are 45^{o} and 30^{o}, respectively) and 90^{o}. The vertical distance from the jets outlet to the free water surface (H) was varied from 0.05 to 0.11 m. The rage of H and α used in this study resulted in a free jet length (L_o) that ranged from 0.05 to 0.13 m.

The mean outlet jet velocity (u_o) has to be greater than a threshold value (u_e) at which gas entrainment inaugurates. A rough estimate of u_e in m/s can be obtained using the following relationship [2]:

$$u_e = 5L_o^{0.534} \tag{2}$$

Equation (2) is valid for L_o ranging from 0.015 to 0.4 m. The required u_e for this study ranged from 1.0 to 1.7 m/s. The used u_o was always more than the required u_e in order to ensure air entrainment in the tank under every experimental condition throughout the course of this study. In addition to satisfying the threshold velocity criterion, the water temperature was 23 ^oC (i.e. kinematic water viscosity of 9.34 x 10^{-7} m^2/s) and at the mentioned flow rates and nozzle diameters, the diameter-based Reynolds number (Re_d) was greater than 1.71 x 10^4 indicating turbulent flow conditions which are favourable for air entertainment [2].

Some parameters of interest such as the maximum penetration depth (z_p), the width of the bubble plume, and the height and the width of the two-phase mixture (gas and water) due to the air entrainment were observed using a digital photographic technique and by eye inspection utilizing the measuring tapes fixed to the sides of the tank. The height and width of the two-phase mixture can be used to estimate the gas holdup (ε_G) as follows:

$$\varepsilon_G = \frac{\left(\frac{W_{L-G}}{W_L}\right)\left(H_{L-G} - H_L\right)}{H_{L-G}} \tag{3}$$

where W_{L-G} is the width of the two-phase mixture (m), W_L is the inside width of the tank under no air entrainment (m), H_{L-G} is the height of the two-phase mixture (m), and H_L is the inside depth of the tank under no air entrainment (m). Once ε_G is obtained and the average bubble diameter (d_b) is obtained from the CCD camera images, the specific interfacial area (a) of the bubbles can be determined using the following relationship [7]:

$$a = \frac{6}{d_b}\left(\frac{\varepsilon_G}{1-\varepsilon_G}\right) \tag{4}$$

3 Results and discussion

3.1 Velocity measurements

All PIV measurements obtained for the velocity components of the two phase flow conditions were taken below the region of the break-up length (z_b) (length after which bubbles start to be formed in the water body) of the two-phase jet. The reason for taking the measurements below z_b is related to the inability of the scattered laser sheet from reaching the CCD cameras. Therefore, the CCD cameras were moved up and down to overcome this problem. Measurements of the lateral (radial) distributions (x) of water and bubble jets velocity components were taken at different axial positions (z). At each z, the axial velocity (v) was normalized by its centreline value (v_m), and plotted against the normalized lateral

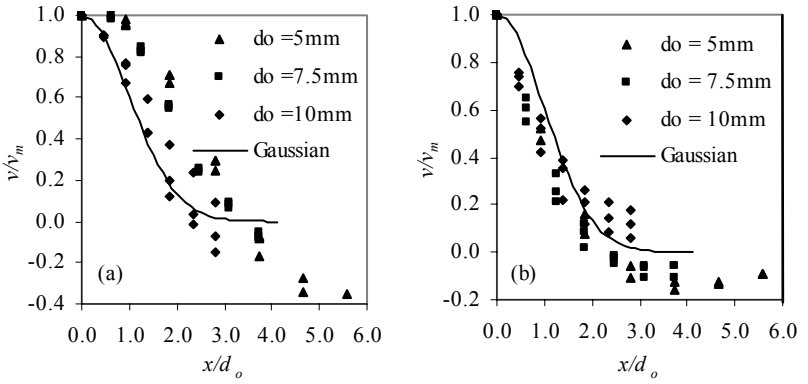

Figure 2: Lateral distributions of the axial mean velocity: (a) gas-phase, (b) liquid-phase.

distance (x/d_0). The data shown in Figure 2 is a result of using same value of Re_d and varying d_o and θ (the angle between the two plunging jets).Fig. 2a, representing the gas phase, shows a fairly good agreement with the Gaussian distribution. However, as d_o decreases (i.e. water jet velocity increases), the deviation from the Gaussian distribution increases. The negative values of v/v_m in the region of $x/d_o > 2$ could be attributed to the fact that bubbles rise up when their buoyancy force overcomes the impingement force. On the other hand, the water phase jet, fig. 2b, showed a very good agreement with the Gaussian distribution in the region of $x/d_o < 2$, which is supported by the observations made by Iguchi *et al* [8], and McKeogh and Ervine [9]. The negative values observed as x/d_o increased further could be related to the effect of the rising bubble.

3.2 Penetration depth

The performance of the aeration process resulted from air entrainment due to plunging jets is highly affected by the residence time of the entrained bubbles. Therefore, the residence time is related to the bubble penetration depth (z_p) into the aeration tank. During all experimental conditions (table 1), penetration depth was always less than the water depth in the tank.

Figure 3a illustrates that under the same turbulence condition and different α, as d_o increases, z_p also increases. It also shows that under the same d_o, z_p at $\alpha = 75^o$ ($\theta = 30^o$) is greater than the ones related to the other two cases ($\alpha = 67.5^o$ and $\alpha = 90^o$). Figure 3b shows the variation of z_p at different water jet outlet velocity at d_o = 5.0 x 10^{-3} m and different α values. Results showed that as jet outlet velocity increases, z_p also increases. For a specific velocity, the highest z_p was obtained when $\alpha = 75^o$ and L_o/d_o ratio was relatively small. The relatively high z_p value under $\alpha = 75^o$ ($\theta = 30^o$) could be related to the combined energy of the two plunging jets that intersect at the surface of the water without much dissipation.

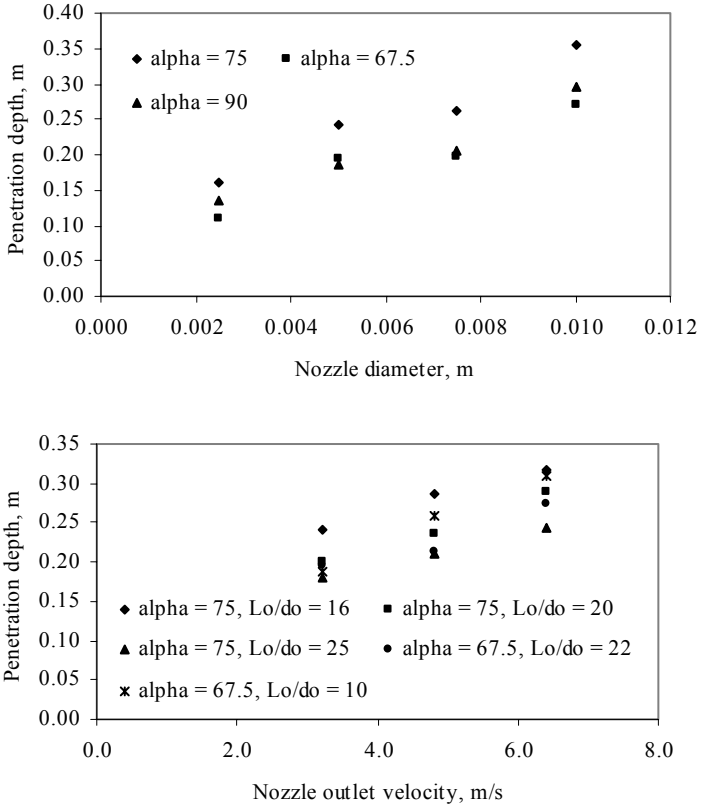

Figure 3: Variation of the penetration depth with nozzles diameter and nozzle outlet velocity.

In the case of $\alpha = 67.5^{o}$, the intersecting jets could be dissipating the energy as the angle of intersection was too wide.

3.3 Gas hold-up and mass transfer coefficient

Gas hold-up (ε_G) is another important parameter in evaluating gas-liquid mass transfer. ε_G was obtained using the measured parameters and applying them to eqn (3). As d_o increases (outlet velocity decreases for the same Re_d), ε_G decreases (see fig. 4a). This can be explained by the reduced amount of bubble entrained under such conditions. On the contrary, for the same d_o as shown in fig. 4b, ε_G increases as outlet velocity increases. This result is expected as for the same nozzle diameter, increasing the jet outlet velocity will increase the turbulence

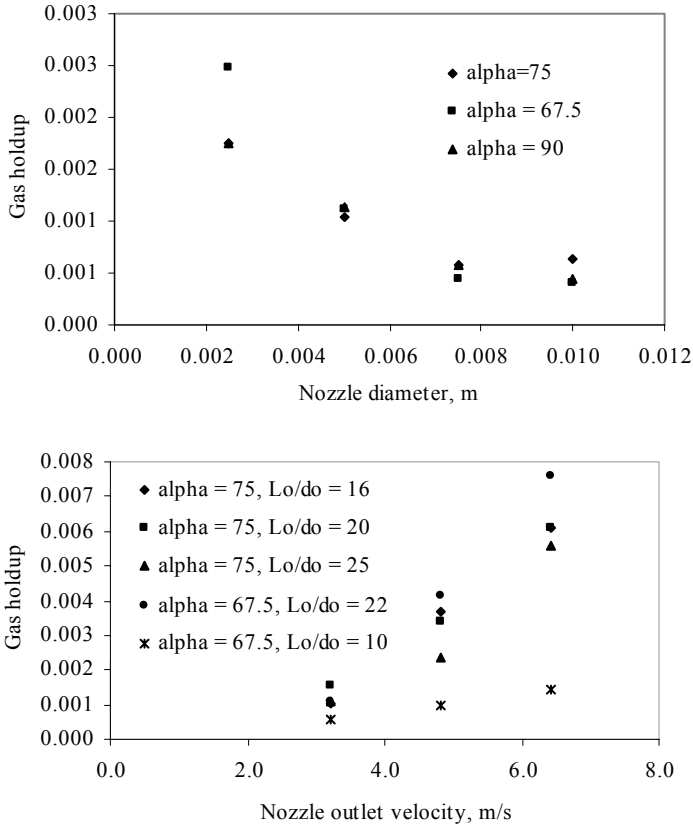

Figure 4: Variation of the gas hold-up with nozzles diameter and nozzle outlet velocity.

further (initial experimental condition was turbulent with $Re_d > 1.7 \times 10^4$). Hence as the turbulence increases, the free-surface instabilities will increase and therefore leading to more air entrainment and eventually higher gas hold-up.

After ε_G was obtained and the average bubble diameter was determined from the CCD images captured during the PIV processing, the specific interfacial area (a) was calculated using eqn (4). The local mass transfer coefficient was then assumed to be 2.0×10^{-4} m/s according to Bin [2] and multiplied by eqn (4) in order to evaluate the overall mass transfer coefficient (k_La). Figure 5 shows the variation of k_La with jet nozzle diameter under the same turbulent condition. The mass transfer mechanism is expected to decrease in this case as the amount of gas entrained decreased under similar conditions (fig. 4a).

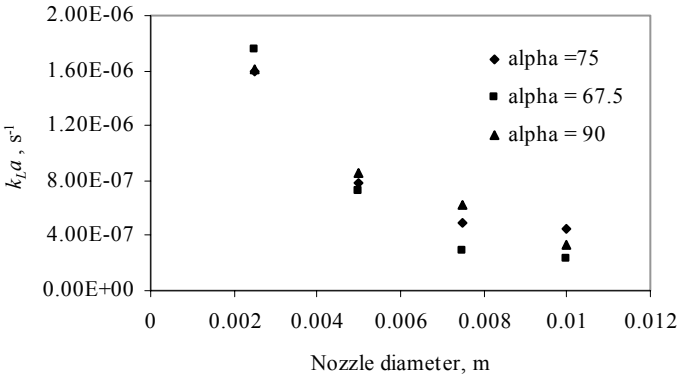

Figure 5: Variation of the overall mass transfer coefficient with nozzles diameter.

4 Conclusions

Gas entrainment utilizing liquid plunging jets has seen many practical applications in chemical and waste treatment processes. The phenomenon can be observed in natural systems such as re-aeration of rivers and streams. Although, such systems can entrain air in water bodies, the process has to be optimized in order to achieve the most effective bubble in the system.

This study explored the air entrainment resulted from the use of two inclined circular plunging jets intersecting at the surface of a water tank with different angles and nozzle diameters in comparison to the vertical plunging jets. Particle image velocimetery (PIV), a non-intrusive measuring technique, was used to measure the lateral and axial velocities of the two-phase jet. Images captured during the PIV process using the charge coupled device (CCD) cameras were used to estimate the average bubble size under each operating condition. Other important parameters such as the maximum penetration depth, the width of the bubble plume, and the height and the width of the two-phase mixture (gas and water) due to the air entrainment were observed using a digital photographic technique and by eye inspection utilizing the measuring tapes fixed to the sides of the tank.

PIV measurements of the normalized axial velocity for the gas and water jets were plotted against normalized lateral distance. Results of both phases showed good agreement with the Gaussian distribution which agrees with the literature. The variation from the Gaussian distribution is related to the amount of bubbles that may block the CCD camera from capturing the scattered laser sheet.

The bubble penetration depth was measured to evaluate the jet combination that will provide the longest bubble residence time. Results obtained under the same turbulence condition and different plunging angle (α) showed that as the

nozzle diameter (d_o) increased the penetration depth (z_p) also increased. Also, under the same d_o, z_p at $\alpha = 75^o$ ($\theta = 30^o$) was found to be higher than the ones obtained under other cases ($\alpha = 67.5^o$ and $\alpha = 90^o$).

Gas hold-up (ε_G) was found to decrease as d_o increases (outlet velocity decreases for the same Re_d). This was related to the reduced amount of bubble entrained under such conditions. On the other hand, when same d_o is used, ε_G increases as outlet velocity increases. This was explained as increasing the jet outlet velocity will increase the turbulence condition further and hence the free-surface instabilities will increase leading to more air entrainment and eventually higher gas hold-up. After ε_G was obtained and the average bubble diameter was determined from the CCD images captured during the PIV processing, the specific interfacial area (a) and the overall mass transfer coefficient (k_La) were calculated.

References

[1] Cummings, P.D., & Chanson, H., An experimental study of individual air bubble entrainment at a planar plunging jet. *Chem. Eng. Res. Des*., **77 (A2)**, pp. 159–164, 1999.

[2] Bin, A.K., Gas entrainment by plunging liquid jets. *Chem. Eng. Sci.*, **48(21)**, 3585–3630, 1993.

[3] Chanson, H., *Air Bubble Entrainment in Free-Surface Turbulent Shear Flows*. Academic Press: London, 1997.

[4] Evans, G.M., Jameson, G.J, & Rielly, C.D., Free jet expansion and gas entrainment characteristics of a plunging jet, *Exp. Therm. Fluid Mech*., **12**, 142–149, 1996.

[5] Raffel, M., Willert, C. & Kompenhans, J., *Particle Image Velocimetry: A Practical Guide*, Springer-Velag: Berlin Heidelberg, N. Y., 1998.

[6] Stanislas, M., Kompenhans, J., & Westerweel, J., *Particle Image Velocimetry: Progress Towards Industrial Application*, Kluwer Academic Publishers: Dordrecht, The Netherlands, 2000.

[7] Jakubowski, C.a., Atkinson, B.W., Dennis, P., & Evans, G.M., Ozone Mass Transfer in a confined plunging liquid jet contactor, *Ozone Sci. & Eng.* **25**, 1–12, 2003.

[8] Iguchi, M., Okita, K., & Yamamoto, F., Mean velocity and turbulence characteristics of water flow in the bubble dispersion region induced by plunging water jet. *Int. J. Multiphase Flow*, **24(4)**, 523–537, 1998.

[9] McKeogh, E.J., & Ervine, D.A., Air entrainment rate and diffusion pattern of plunging liquid jets. *Chem. Eng. Sci.* **36**, 1161–1172, 1981.

Section 8
Macroscale constitutive models

This page intentionally left blank

A fixed coarse-grid thermal-fluid scheme and a heat conduction scheme in the distinct element method

Y. Shimizu
Tokai University, Japan

Abstract

A particle-thermal-fluid coupling scheme with a mixed Lagrangian-Eulerian approach is described by extending the author's previous research (Shimizu, 2004). The scheme solves the continuity, Navier-Stokes (N-S) and thermal energy equations numerically in Eulerian Cartesian coordinates by considering the existence of particles within the cell. On the other hand, in the Distinct Element Method (DEM), driving forces and thermal energy applies to the particles.
Keywords: particle-thermal-fluid coupling, mixed Lagrangian-Eulerian approach, distinct element method.

1 Introduction

Numerical analysis of particle-fluid coupling using a mixed Lagrangian-Eulerian approach is becoming popular, especially in the chemical and mechanical engineering fields [5,6,8]. Also, this approach has many potential applications in the geo-engineering field especially when there is a wide range of fluid velocity and high porosity [7]. In this scheme, the fluid phase is described by using the continuity and momentum (Navier–Stokes) equations to calculate pressure and velocity of fluid, while the movement of the solid phase (particles) is traced by the DEM as a Lagrangian method. Momentum exchange between particles and fluid is considered in the momentum equation for the fluid phase and in the force-displacement law for the solid phase. Here, we extend the mixed Lagrangian-Eulerian approach to include the thermal energy equation to solve for temperature in both fluid and particles. A correlation of forced convection heat transfer by considering particle existence is used for interaction term

between particles and fluid in thermal energy equation for fluid-phase. Also, the interaction term is added as a source term in the heat transfer equation for solid-phase (particles). In this paper, the complete scheme, as implemented on PFC^{2D} and PFC^{3D} [3,4], is described, with especial emphasis on the interaction term. Two-dimensional simulations with forced convection heat transfer are conducted.

2 Interaction between particles and fluid by forced convection heat transfer

Figure 1 shows a fixed control volume $\Delta x \Delta y \Delta z$ in the model, in which N_p spherical particles exist within a flowing fluid, the temperature is T_f. Each particle has a temperature $T_{p_n}(n:1, N_p)$, and the average temperature is $T_b(\equiv \overline{T_{p_n}})$. There is no temperature variation within each particle.

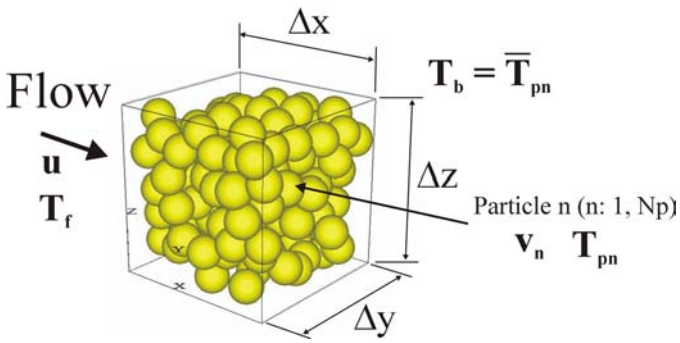

Figure 1: Fluid flow with thermal energy through particle assembly.

Consider thermal energy exchange between the particle assembly (bulk material) and fluid, by forced convective heat transfer. The thermal energy flux per unit volume caused by temperature difference between particle assembly and fluid Q_{int} [W/m^3] is given by eq.(1). Here, the heat-transfer coefficient and average particle temperature are defined in each control volume.

$$Q_{\text{int}} = \frac{h_b\left(T_b - T_f\right)\pi\sum_{n=1}^{N_p} d_{p_n}{}^2}{\Delta x \Delta y \Delta z} = \frac{6h_b\left(1-\varepsilon\right)\overline{d_p{}^2}}{\overline{d_p{}^3}}\left(T_b - T_f\right) \qquad (1)$$

where

d_{p_n} : particle diameter (n=1,N_p)	[m]
h_b : heat-transfer coefficient of particle assembly	[W/m^2.K]
T_b : temperature of particle assembly	[K]
T_f : temperature of fluid	[K]
ε : porosity	[-]

The heat-transfer coefficient of particle assembly h_b is usually provided by empirical equations, which depend on material properties, flow condition and particle arrangement (porosity). One such relation for heat transfer by forced convection is given by eq. (2) [9]. This empirical equation is derived by using air, and is applicable for porosity, ε, below 0.8.

$$h_b = \frac{k_f}{\overline{d_p}} \frac{1-\varepsilon}{\varepsilon} \left(0.5 \left(\frac{\mathrm{Re}}{1-\varepsilon} \right)^{\frac{1}{2}} + 0.2 \left(\frac{\mathrm{Re}}{1-\varepsilon} \right)^{\frac{2}{3}} \right) \mathrm{Pr}^{\frac{1}{3}} \quad \varepsilon \le 0.8 \tag{2}$$

where Re is the particle Reynolds number and Pr is the Prandtl number defined by eq. (3) and (4).

$$\mathrm{Re} = \frac{|\mathbf{u}_{\mathbf{rel}}| \overline{d_p} \varepsilon \rho_f}{\mu_f} = \frac{|\overline{\mathbf{v}} - \mathbf{u}| \overline{d_p} \varepsilon \rho_f}{\mu_f} \tag{3}$$

$$\mathrm{Pr} = \frac{c_f \mu_f}{k_f} \tag{4}$$

c_f : specific heat	[J/kg.K]
$\overline{d_p}$: average particle diameter	[m]
k_f : thermal conductivity	[W/m^2.K]
$\mathbf{u}$: fluid velocity vector	[m/s]
$\overline{\mathbf{v}}$: average particle velocity vector	[m/s]
μ_f : viscosity	[Pa.s]
ρ_f : density of fluid	[kg/m^3]

The thermal energy flux applied to the particle assembly within the control volume, Q_{apb}, is given as a form of preserving the thermal energy exchange between particle assembly and fluid. The Q_{apb} is also sum of the rate of thermal energy applied to each particle. Hence,

$$Q_{apb} \equiv \sum_{n=1}^{N_p} Q_{ap_n} = -Q_{\text{int}} \Delta x \Delta y \Delta z = h_b \left(T_f - T_b \right) \pi \sum_{n=1}^{N_p} {d_{p_n}}^2 \tag{5}$$

Hence, the rate of thermal energy applied to each particle due to convective heat transfer $Q_{ap_n} (n : 1, N_p)$ is given by eq. (6).

$$Q_{ap_n} = h_b \left(T_f - T_b \right) \pi {d_{p_n}}^2 \tag{6}$$

3 Formulation and scheme

The thermal scheme for the fluid-phase is invoked between application of the Law of Motion and the Force-Displacement Law in the mechanical (DEM) calculation, with the interaction forces on particles being added as external body forces in the mechanical calculation. Also, the thermal scheme for the particle-phase is invoked after the thermal-fluid scheme, so that temperatures of all particles are updated.

3.1 Fluid-phase, thermal-fluid scheme

The continuity, Navier Stokes equation and thermal energy equation for fluid-phase in the fluid-solid two-phase flow model (using incompressible fluid with constant density) are given by eqs. (7) and (8) [7]. Also the thermal energy equation is given by eq. (9).

$$\frac{\partial \varepsilon}{\partial t} = -\left(\nabla \cdot \varepsilon \mathbf{u} \right) \tag{7}$$

$$\frac{\partial \left(\varepsilon \mathbf{u} \right)}{\partial t} = -\left(\nabla \cdot \varepsilon \mathbf{u} \mathbf{u} \right) - \frac{\varepsilon}{\rho_f} \nabla p + \frac{\mathbf{f}_{\text{int}}}{\rho_f} \tag{8}$$

$$\frac{\partial \left(\varepsilon T_f \right)}{\partial t} = -\left(\nabla \cdot \varepsilon T_f \mathbf{u} \right) + \frac{k_f}{\rho_f c_f} \nabla^2 \left(\varepsilon T_f \right) + \frac{Q_{\text{int}}}{\rho_f c_f} \tag{9}$$

where

$\mathbf{f}_{\mathbf{int}}$: interaction force per unit volume [N/m^3]

The natural convection term is not included in eq. (8), since forced convection is dominant in the simulations considered here. Also, the viscous term is not included. The interaction force per unit volume is calculated by using a fluid-particle friction coefficient. Also, the driving force applied to a particle is calculated by using the interaction force and pressure gradient [7].

3.2 Particle-phase, thermal scheme

The conduction heat transfer is applied through particle-particle contacts, and is described in the code user's manuals [3,4]. Each particle exchanges thermal energy between neighbor particles through a thermal pipe created between two contacted particles with a thermal resistance (Fig. 2). Also, the rate of thermal energy due to convection heat transfer Q_{ap_n} (eq. (6)) is added to the particle as one of the source term.

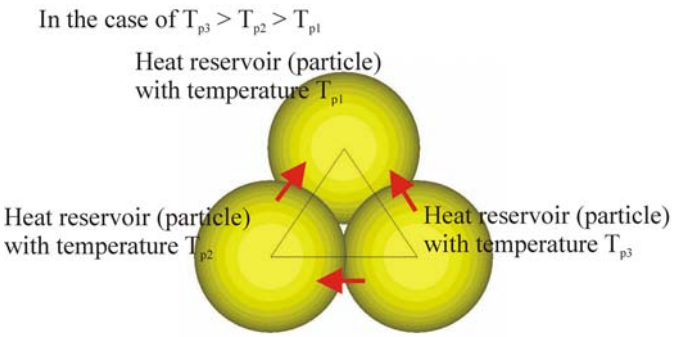

Figure 2: Network of particle assembly.

4 Simulations

Two simulations are performed. The first verifies the interaction term for convective heat transfer. A simple two-dimensional model with regularly arranged particle is created in order to observe the transient particle temperatures and the result is compared with the analytical solution. The other simulation is an application example; a gas-fluidized bed simulation. Gas is introduced into a particle assembly to study the migration and temperature transient of each particle.

4.1 Two-dimensional fixed particles case

Figure 3 shows the particle arrangement and the fluid cells placed in the model. The model dimensions are 0.096 m width and 0.12 m height. 80 particles with 10mm diameter are placed as regular arrangement. There are no contacts between particles, to prevent conduction heat transfer through contact points. 80 fluid cells (8 x 10) are created as occupying one particle in each cell. Extra cells are created at the outside in order to take account of boundary conditions. The dimension of each cell is 12 mm in the x and y direction, and the porosity of each fluid cell is 0.64. Slip-wall boundary (fluid velocity parallel to the boundary surface is non-zero at the boundary) is specified at the side boundary, and a zero pressure boundary is specified at the top boundary, from which fluid discharges. A fluid velocity is specified at the bottom boundary to create a uniform velocity profile. Thermally adiabatic boundary condition: there is no thermal energy transfer across boundaries, is specified at the side boundary. At the bottom boundary, the fluid temperature is set to 100 K. The time step for both of the DEM and the thermal-fluid calculation is taken as 5.0×10^{-5} s.

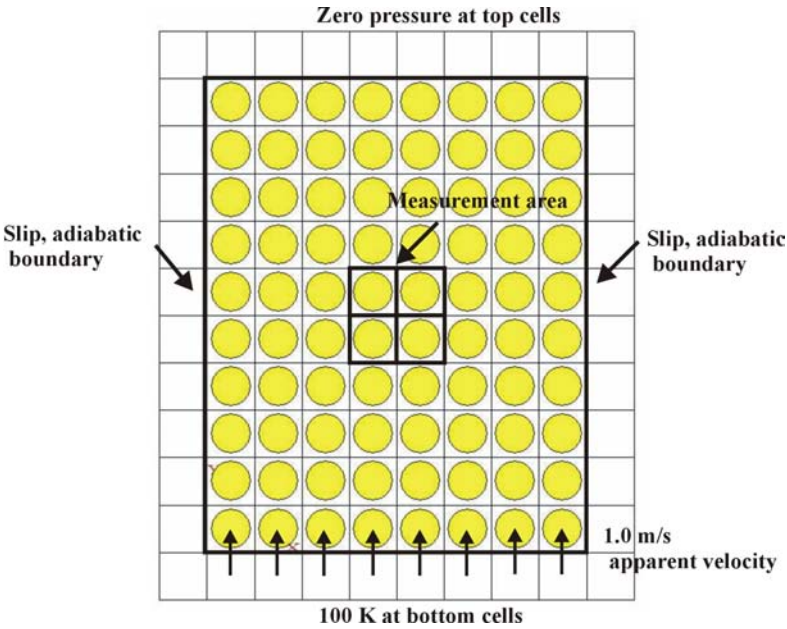

Figure 3: Model: particle assembly and fluid cell.

Table 1 shows the material properties. The material properties for particle are not related to a real material, because the objective of this simulation is to verify heat transfer between particles and fluid in the scheme.

Table 1: Material properties.

(Particle)		(Air)	
Number	800	Density	1.2 kg/m^3
Diameter	10mm	Viscosity	1.8x10^{-5} Pa.s
Density	2000 kg/m^3	Thermal Conductivity	0.025 W/m K
Normal Stiffness	1.0x10^5 N/m	Specific Heat	1.0 kJ/kg K
Thermal Conductivity	50 W/m K		
Specific Heat	0.5 kJ/kg K		

The simulation procedure is as follows. First, particles with 0 K temperature are created in a regular arrangement, with translational and rotational movements being prevented. Second, while heat transfer between particle and fluid is turned off, air is injected at 1.0 m/s of apparent velocity from the bottom boundary during 3000 cycles to make a constant flow profile and 100 K of each fluid cell temperature. After that, by fixing the air temperature for all fluid cells, the heat transfer between particles and fluid is turned on in order to study the evolution of temperature. A measurement area is set, to trace fluid and particle temperatures.

Figure 4 shows the time history of particle and fluid temperature. Solid line shows the analytical value calculated by an equation in the figure, which is derived from the particle thermal equation without conduction heat transfer term. The numerical result is in good agreement with the analytical solution.

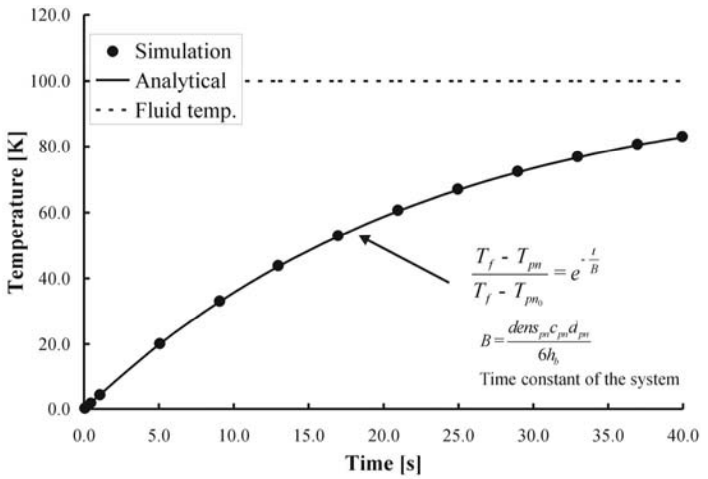

Figure 4: Comparison between simulation result and analytical value: transient of particle temperature, 0–40 s.

4.2 Two-dimensional fluidized bed simulation

Figure 5 shows the particle assembly and the fluid cells placed in the model. The model consists of particles and surrounding walls. The model dimensions are 0.15 m width and 0.6 m height, surrounded by bottom and side walls. 2400 particles with 4 mm diameter are created within the walls. The assembly height is around 0.22 m. 450 fluid cells (15 x 30 (width x height)) are created, with a cell size of 10 and 20 mm respectively. Slip-wall boundary is specified at the side and bottom boundary, and a zero pressure boundary is specified at the top of the boundary. A fluid velocity is specified at the center of the bottom boundary, from which fluid with temperature 1000°C is introduced. Thermally adiabatic boundary condition is specified at the side boundary. Also, temperature of particle and fluid is set 0 °C at the initial stage. The time step for both of the DEM and the thermal-fluid calculation is taken as 1.0×10^{-5}s.

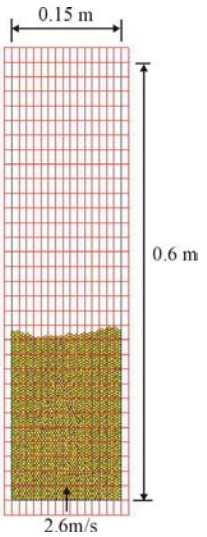

Figure 5: Model: particle assembly and fluid cell.

Table 2 shows the material properties. The normal and shear stiffness for particle and wall are 1.0×10^6 N/m. The friction coefficient for particle-particle contact is 0.5; also that for particle-wall is 0.3. The density of particles is 2650 kg/m^3. Viscous damping without tensile force is used for energy dissipation at contacts. The ratio of the damping constant to the critical damping constant in the normal and shear direction is 0.05, which is equivalent to a restitution coefficient of 0.9. Thermal conductivity of particle assembly is 2.0 W/m.K and specific heat is 800 J/kg.K. Air is used as a fluid, with density and viscosity of 1.2 kg/m^3 and $1.8e^{-5}$ Pa.s, respectively. Thermal conductivity and specific heat of air are 0.03 W/m.K and 1.0 kJ/kg.K respectively.

Table 2: Material properties.

(Particle)		(Air)	
Number	2,400	Density	1.2 kg/m^3
Diameter	4mm	Viscosity	1.8e^{-5} Pa.s
Density	2650 kg/m^3	Thermal Conductivity	0.03 W/m.K
Normal Stiffness	1.0x10^6 N/m	Specific Heat	1.0 kJ/kg.K
Shear stiffness	1.0x10^6 N/m		
Friction coefficient	0.5		
Thermal Conductivity	2.0 W/m.K		
Specific Heat	800 J/kg.K		
Coef. Of Linear Thermal Expansion	3.0x10^{-6} K^{-1}		
(Wall)			
Normal Stiffness	1.0x10^6 N/m		
Shear stiffness	1.0x10^6 N/m		
Friction coefficient	0.3		

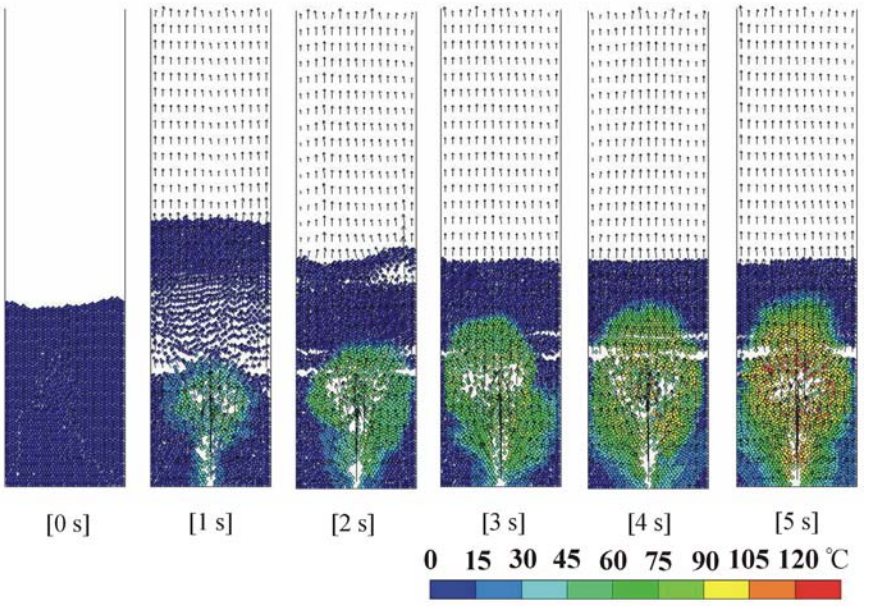

Figure 6: General view; transient of particle temperature and fluid velocity vectors.

The simulation procedure is as follows. First, particles are created randomly within the rectangular space, then dropped by gravity. After reaching a steady-

state condition, air is injected at 2.6 m/s of apparent velocity from the center of bottom boundary for 5 seconds.

Figure 6 shows a general view and fluid velocity vectors for 5 seconds from the initial stage. Colour of each particle shows its temperature. The gas lifts particles near the injection point in the first stage. After that, particles migrate in the box, and the temperature of particles is gradually increased by forced convection and conduction heat transfer.

5 Summary

A particle-thermal-fluid coupling scheme with a mixed Lagrangian-Eulerian approach is developed by extending the author's previous research. The scheme is described, with emphasis on the interaction term between particles and fluid. Two-dimensional simulations with forced convection heat transfer are conducted. As a result, it was found that thermal energy is exchanged correctly between particle and fluid. The scheme is believed to be useful for simulating coupled particle-thermal-fluid systems.

Acknowlegement

I sincerely thank Dr. Peter Cundall at Itasca Consulting Group, Inc. for initiating this project and useful discussion during developing the scheme.

References

[1] Bird, B. R., Stewart, W.E. and Lightfoot, E. N., (1960), "Transport Phenomena", John Wiley & Sons, pp. 71–91.
[2] Holman, J. P., (1976), "Heat Transfer", McGraw-Hill, Chapter 6.
[3] Itasca Consulting Group, Inc. 2004. PFC2D – Particle Flow code in 2 Dimensions Version 3.1, Minneapolis: Itasca.
[4] Itasca Consulting Group, Inc. 2005. PFC3D – Particle Flow code in 3 Dimensions Version 3.1 (to be released). Minneapolis: Itasca.
[5] Kawaguchi, T., Tanaka, T. and Tsuji, Y. (1992), "Numerical Simulation of Fluidized Bed Using the Discrete Element Method (the Case of Spouting Bed)", JSME (B), vol.58, No.551, pp.79-85.
[6] Kawaguchi, T. (2003), PhD thesis, Osaka University.
[7] Shimizu, Y. (2004), "Fluid Coupling in PFC2D and PFC3D", Numerical Modeling in Micromechanics via Particle Methods -2004, Proceeding of 2nd International PFC Conference, Balkema, pp. 281–287.
[8] Tsuji, Y., Kawaguchi, T. and Tanata, T., (1993), "Direct Particle Simulation of Two-Dimensional Fluidized Bed", Powder Technology, 77, pp. 79–87.
[9] Whitaker, S., (1972), "Forced Convection Heat-Transfer Correlations for Flow in Pipes, Past Flat Plates, Single Cylinders, Single Spheres, and for Flow in Packed Beds and Tube Bundles", AIChE J., vol. 18, No.2, pp. 361–371.

Modeling multi-phase flow using CFD with related applications

D. Lin, P. Diwakar, V. Mehrotra, B. Rosendall & J. Berkoe
Bechtel Corporation, USA

Abstract

Concurrent liquid-gas flow manifests itself into different flow regimes depending on fluid properties, flow rates, heat inputs and geometry. The Baker chart has identified at least seven flow regimes, viz. stratified, wavy, plug, slug, annular, dispersed and bubbly flow. Each flow regime exhibits a unique flow pattern and may transition from one to another depending on the flow conditions in the pipe.

Computational Fluid Dynamics (CFD) with multiphase flow equations add a capability by which these flow regimes can be visualized and understood. In this paper stratified and slug flow regimes are studied by using CFD modeling. The modeling results are validated by comparison with published experimental data. The benchmark comparison shows that CFD is successful in predicting the following aspects in two-phase flow:

- Quantitative prediction of stream-wise velocities in both phases.
- Qualitative prediction of flow regime, phase distribution and pressure distribution.
- Transition between certain, but not all, flow regimes.

On the other hand, more research and development is needed to accurately predict pressure drop and vapor/liquid interface location when the velocity difference between phases is relatively large.

The application of the validated CFD model is extended to the same flow regime in a tee joint distributor system. The results demonstrate that the mal-distribution of flow can occur in complex piping systems with sudden transition.

Keywords: validation, transition, stratified flow, slug flow, CFD.

1 Introduction

Two-phase flow is a challenging problem because the interaction of liquid and vapor phase can generate different flow patterns depending on properties of the

fluids, flow rates, heat inputs and geometry. Baker [1] has identified seven flow regimes for concurrent flows in a horizontal pipe: stratified, wavy, plug, slug, annular, dispersed, and bubbly flow. Some of the flow regimes are transient and migrate from one regime to another. Slug flow is intrinsically unsteady and is characterized by a succession of slugs of liquid separated by large gas bubbles whose diameter approaches that of a pipe. It is considered one of the most challenging flow types to model because of its intermittent nature and lack of understanding in the mechanism. Stratified flow is characterized by liquid running at the bottom and vapor at the top of a pipe due to gravity effects. It is considered the simplest flow regime. This study focuses on modeling these two flow regimes.

CFD employs different mechanistic models to predict different flow regimes. It is very important to choose the correct modeling approach that captures the physics of the application. The best mechanistic multi-phase CFD model for predicting the behavior in stratified and slug flows is the VOF (Volume of Fluid) approach (Fluent Manual). The Eulerian-Granular model can successfully predict the level of solid-liquid mixing when compared to experimental tests (Rosendall and Berkoe [5]).

Due to the complex nature of two-phase flows, it is necessary to validate the CFD model with experimental data before applying the analysis to more complex systems. Validation with experimental results for stratified and slug flow regime is covered in Section 3. More complex geometry and some results (flow pattern, velocity and pressure) are presented in Section 4. Finally, some concluding remarks about using CFD to two-phase flow problems are presented in Section 5.

2 CFD multiphase model description

2.1 Governing equations

The Volume of Fluid (VOF) model is a surface-tracking technique applied to a fixed Eulerian mesh. It is designed for two or more immiscible fluids where the position of the interface between the fluids is of interest. In addition to solving the continuity and momentum equations, VOF model solves one additional set of equation for the volume fractions. These equations are listed below (Fluent Manual):

$$\frac{\partial \rho}{\partial t} + \nabla \bullet (\rho \vec{v}) = 0$$

$$\frac{\partial}{\partial t}(\rho \vec{v}) + \nabla \bullet (\rho \vec{v} \vec{v}) = -\nabla p + \nabla \bullet [\mu(\nabla \vec{v} + \nabla \vec{v}^{T})] + \rho \vec{g}$$

$$\frac{\partial \alpha_q}{\partial t} + \vec{v} \bullet \nabla \alpha_q = 0$$

where ρ = density for each phase, $\vec{v}$ = velocity vector that is shared for all the phases, μ = viscosity of each phase, g = gravitation = 9.81 m/s^2, and α_q = the volume fraction for the q^{th} phase of fluid.

2.2 Assumptions

The following assumptions were made for all calculations in this study:

- No phase changes were considered in liquid and vapor.
- Both phases were considered incompressible. The compressibility of the gas phase is not expected to have a significant effect on the results.
- The air and water were assumed of constant density and viscosity.
- The surface tension for the air-water interaction was assumed constant.

3 Validation of CFD Model for various flow regimes

3.1 Slug flow validation

The CFD results presented in this section are compared with experimental results on slug flow in a horizontal 2" pipe (Lewis et al. [2]). This paper provides average velocity profile measurements for comparison.

In the initial CFD testing, it was observed that the generation of small bubbles and the latter regrouping phenomenon are very important in predicting slug flow. These require:

1. High velocity differential and mixing (between vapor and liquid) at the inlet. This can be achieved by using very small injection or impingement (on fences that provide sufficient restriction), which enhances liquid and vapor mixing and ensures the generation of small bubbles.
2. A fine grid throughout so that shear stress is not smeared or smoothed out. This will ensure proper break up and coalesce of bubbles downstream of the inlet.

3.1.1 Geometry, mesh and boundary conditions:

To create a 3D pipe flow model of 200 diameters long with a vapor injection zone of 100mm pores will require millions of calculation cells and take a long time to converge. Based on this consideration, a 2D CFD model was used for this study.

Nine air and water inlets were created along with slots downstream of the inlets to enhance mixing. The fence also creates vapor bubbles in the pipe. It is expected that the simplified CFD model may have a different transition length for a fully developed slug flow and the different pressure drop through the pipe length. These two aspects were not investigated in the experiment, however. The VOF time-dependent segregated solver was used for tracking the break up and coalesces of the vapor bubbles. For a slug flow, the larger bubbles are of interest.

The air inlet velocity is 3.3 m/s, and the water inlet velocity was 2.5 m/s. This translates to air superficial velocity of 1.1 m/s and water superficial velocity

of 1.65 m/s, which corresponds to case (b) in Lewis et al. [2]. The average air volume fraction was calculated to be 0.4. The outlet was specified as outflow boundary condition. The walls were specified as stationary walls. The maximum aspect ratio of the computational cells was about 2 and the total grid was about 210,000 in this calculation.

3.1.2 Analysis and discussion

3.1.2.1 Generation of air and water bubbles The formation of air bubbles is represented by contours of volume fraction as illustrated in Fig. 1. Red color indicates air and blue represents water. As can be seen, air bubbles of different sizes were generated immediately downstream of the slots. Some air accumulated and broke off behind the slots. As the air bubbles traveled downstream, they coalesced and broke again. Influenced by gravity, air bubbles rose up to the top portion of the pipe and water settled towards the bottom of the pipe. Some eventually formed bigger bubbles that resembled the flow pattern shown in Fig. 2.

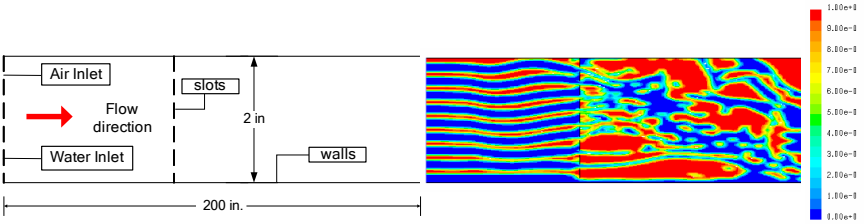

Figure 1: Slug flow creation using slotted inlets and fences.

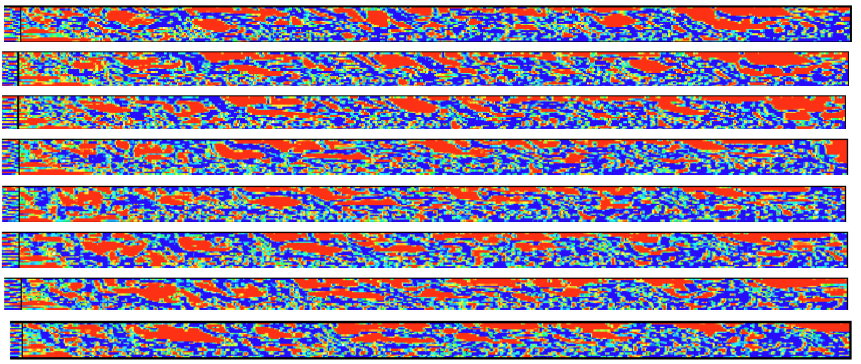

Figure 2: Tracking large bubbles in slug flow.

3.1.2.2 Slug flow downstream of developing zone Fig. 3 shows a snap shot of air and water distribution in the whole length of pipe. Fig. 3(a) shows the first 50 diameters of pipe and 3(b) from 50 to 100 diameters. Starting from about 40 diameters downstream, the air accumulates at the top of the pipe. The water exhibited wavy pattern with small air bubbles trapped inside.

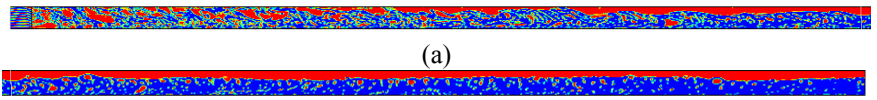

(a)

(b)

Figure 3: (a) Flow pattern in the first 50 diameters; (b) Flow patterns from 50 diameters to 100 diameters.

3.1.2.3 Velocity profile The velocity profile at x/D=75 is shown in Fig. 4 (right), where x is measured along the length of the pipe and D=2". Fig. 4 shows that the calculated air speed is higher than the water speed by about 10%. A similar trend was also observed in the experiment (Lewis et al. [2]).

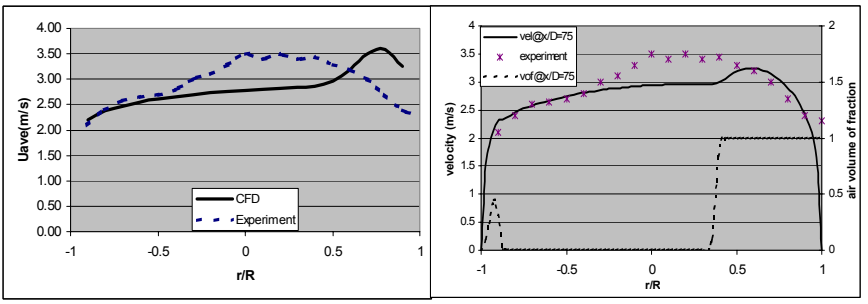

Figure 4: Comparison of calculated time-averaged velocity profile with measurements at x/D=100 and x/D=75.

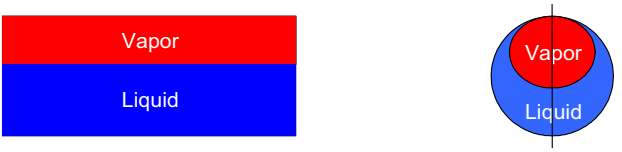

(a) 2D channel flow (b) 3D pipe flow

Figure 5: Illustration of slug distribution in cross-sectional view.

At x/D=100 (Fig.4 left) the air had gained more speed than water by the time it reaches the outlet. For the region of r/R < -0.4, the velocity profile agreed very well with the measurements because this region was occupied by water in both cases. The velocity difference increases for the region r/R > -0.4 due to the difference in locations of vapor/liquid interface. With the same vapor volume fraction, a large slug is expected to displace more water along the vertical centerline in a 3D pipe, whereas a 2D channel is more likely to have a flat interface from a cross-sectional view (Fig. 5). This explains the major discrepancies in velocity profiles between CFD and experiment. The accuracy of the predicted velocity is about ±20%.

3.2 Stratified flow validation

Two-phase stratified flow is one of the simplest flow regimes since the liquid and vapor are just separated by gravity. However, there are some challenges with modeling due the wavy interface between the liquid and vapor layer. Fabre et al. [3] have published experimental results for stratified flows in a closed slightly inclined channel.

In the CFD model, the computational domain for the stratified flow is in a channel that is 12 meters long, 0.2 m wide and 0.1 high. The dimensions are identical to the experimental setup described in Fabre et al. [3].

Velocity inlet boundary conditions are specified at the air and water inlet. The water inlet velocity was 0.476 m/s and air velocity at 5.5 m/s with mean water depth at 0.0315m. This condition corresponded to run #400 in the experiment. Downstream outlet is specified as an outflow. The four sidewalls were specified as stationary walls. A total number of 310,000 calculation cells were generated for this model.

The results of the stratified flow modeling in the form of phase distribution and velocity fields are shown in Fig. 6. The vapor and liquid interface with small wave motion at the interface is clearly seen.

3.2.1 Velocity profile

Time averaged data was recorded at various locations of the flow. A comparison with experimental measurement is shown in Table 1. At Z = 0, the flow is expected of zero velocity due to the non-slip wall boundary condition. Therefore, a location of Z = 0.0125m was chosen in CFD for comparison with experiments. It is suspected that the experimentalist had chosen the measuring points close to the wall but inaccurately presented the location as Z = 0, instead of Z ≈ 0.

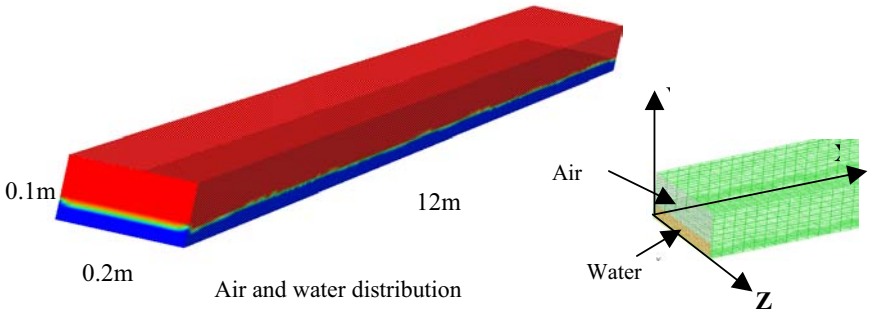

Figure 6: Air and water distribution of the stratified flow. Black represents water and gray represents air.

The y = 40 mm location is close to the liquid and vapor interface. At y > 40, the space is occupied by vapor and below is liquid. Comparing the velocity along the channel, U, the prediction and experiment agrees very well away from the interface. At the interface, large discrepancies occurred. It is possible that

grid might be too coarse at the interface to be able to capture the wavy interface correctly. This might have also affected the velocity component along the y and z direction in the cross sectional area of the channel. This is shown by the large differences in the V velocity in Table 1. It was reported (Fabre, et al. [3]) that there was a secondary swirling motion in the cross sectional area of the channel, caused by the wavy liquid and vapor interface. The model was not able to predict the secondary motions in the pipe. .

Table 1: Comparison of time-average velocity prediction with experiment (X = 9.1 m).

Y(mm)	U (m/s) Experiment @ Z = 0	U (m/s) CFD @ Z = 0.0125m	V (m/s) Experiment @ Z = 0	V (m/s) CFD @ Z =0.0125m
1.2	0.365	0.37	N/A	
13	0.54	0.47	-0.0245	-0.00028
28	0.53	0.51	-0.0226	-0.0003
40	5.96	3.96	0.366	-0.0069
75	5.93	6.02	0.366	-0.0102
96	5.07	5.29	0.067	-0.0058

3.2.2 Pressure loss

The pressure gradient in the gas phase was also compared with experimental data. As shown in Table 2, CFD over predicts the pressure drop by a factor of 1.7. It is expected that the pressure loss is a result of the wall and liquid/vapor interface friction. However, in the Volume of Fluid (VOF) model, only one set of momentum equations are solved and the velocity field shared between phases. It is possible that the velocities were averaged out in the cells that were occupied by both liquid and vapor. In reality, vortices occur in these locations and produce drag force in both phases. The effect of the approximation could have adversely affected the liquid/vapor interface prediction when the velocity difference between the phases is large.

Based on experimental researches (Paras et al. [4] and Levy, [2]), the pressure loss at the liquid/vapor interface was found to be a function of velocity differential between phases, wave height and the properties of both phases. It is not clear how these parameters were taken into account for the pressure calculation in the VOF model.

Table 2: Comparison of pressure gradient in gas phase.

Pressure gradient (Pa/m), Experiment	Pressure gradient (Pa/m), CFD
6.7	11.6

4 Applications of stratified flow and slug flow in piping

This section uses the knowledge base developed during the validation study and applies it to a slightly more complex piping geometry. One example of such

applications is flow through a vertical tee. Section 4.1 presents a slug flow through a tee junction and section 4.2 describes a stratified flow through a tee.

4.1 Slug flow in a tee

Using a similar geometry and boundary conditions described in Section 3.1, the model was extended with a vertical tee at the outlet of the slug flow described. Fig. 7 illustrates the geometry for this model. Due to similar runtime constraints, the model was built in 2-D. The air inlet velocity was 3.3m/s, and the water inlet velocity was 2.5m/s. The top and bottom outlets of the tee were specified as outflow boundary conditions.

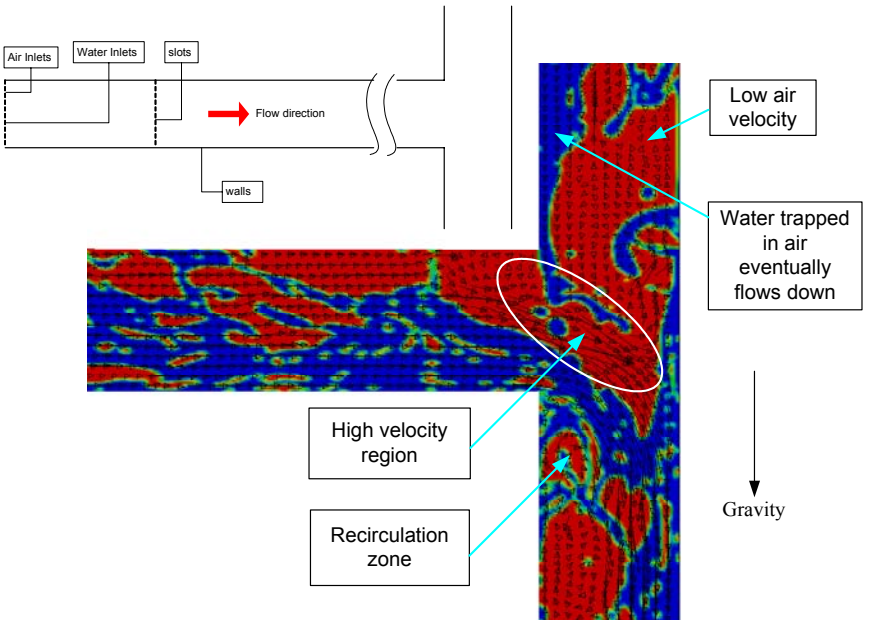

Figure 7: Velocity vectors superimposed on phase distribution at the tee joint. Black arrows indicate velocity vectors. Black color represents water and gray color represents air.

Fig. 7 shows an instantaneous velocity vector plot superimposed with phase distribution in a tee. A high velocity region was predicted at the tee due to the gravity force acting on the water as it flowed into the vertical branch. As water accelerates towards the bottom, a significant amount of air was entrained into the bottom branch. Some air was trapped and re-circulated at the low velocity region at the lower corner. The air in the top branch moves very slowly due to the small pressure gradient in this section.

Fig. 8 shows velocity magnitude and static pressure distribution in the tee joint at the same instance. It is clear that the pressure distribution is not the same

between the top and bottom branch due to gravity and flow distribution. This causes the slow air velocity on the top.

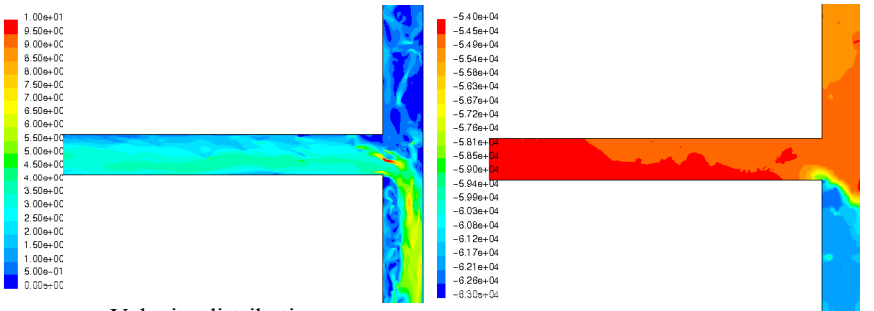

Velocity distribution
(Scale: 0 – 10 m/s)

Static pressure distribution
(Scale: -54000 to –63000 Pascal, gauge).

Figure 8: Instantaneous phase, velocity and pressure distributions in a tee joint.

This CFD model can also show the distribution of phase with time. Due to the unsteady nature of a slug flow, as the mixture impinges at the tee joint, most liquid flow through the bottom branch while some vapor was entrained with liquid. The remaining vapor occupies the top branch. Some liquid was trapped in the vapor flow on the top branch, but influenced by gravity, it eventually attached to the wall and flows downward. A small amount of vapor was re-circulating at the lower left corner of the tee due to the low velocity in this region.

4.2 Stratified flow in a tee joint

The application of a stratified flow running through a tee connection is described in this section. The upstream geometry and boundary conditions are similar to the one used for validation with a vertical tee added at the end. Fig. 9 illustrates the geometry for this model. The air inlet velocity was 5.5m/s, and the water inlet velocity was 0.476m/s. The top and bottom outlets of the tee were specified as outflow boundary conditions. The entire channel and tee joint was also tilted at a slope of 0.001.

The results of the stratified flow through a tee are also shown in Fig. 9 in the form of phase distribution and velocity magnitude distribution in the vertical symmetry plane. As expected, water flows down to the bottom branch at the tee joint due to gravity. Due to the acceleration of the water stream in the vertical branch, water layer was stretched thin and was broken up as it flowed downwards. The breaking of the water layer allowed air to penetrate to the left side of the bottom branch.

Because the pressure at the bottom branch is lower than the top, a significant amount of air is diverted to the lower branch. The highest velocity region was found in the right side of the branch immediately downstream of the tee joint.

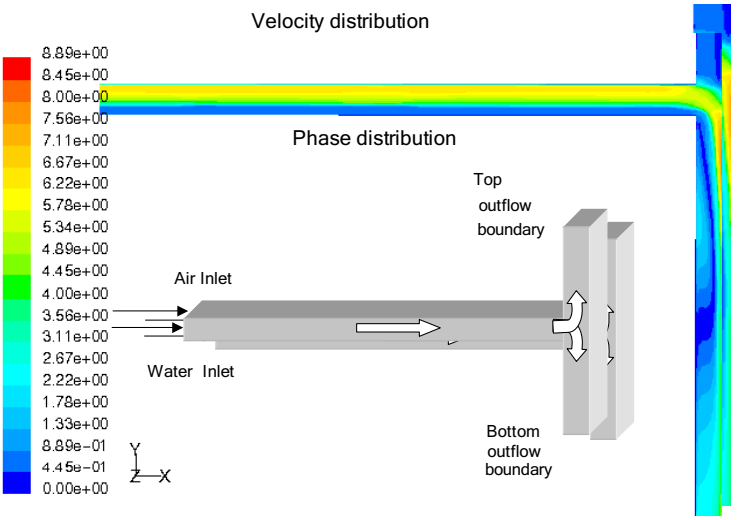

Figure 9: Geometry and velocity magnitude (m/s).

5 Conclusions and recommendations

The complexity of two-phase flow can cause flow mal-distribution, vibration and excess thermal and mechanical stress in equipment. Understanding two-phase flows is important for equipment design with potential multi-phase flow. This study shows that slug and stratified flow patterns can be analyzed with CFD analysis and the results can be used to determine flow mal-distributions in multi-phase applications.

The analysis also shed lights on some of the advantages and limitations of CFD:

Advantages:

- CFD can predict mean stream-wise flow velocities and flow patterns with reasonable accuracy.
- CFD helps in visualizing flow patterns in complex systems and can identify problem zones in design, in terms of flow and phase distribution, re-circulations.
- For unsteady slug flows, CFD helps understand the development and physics of such flows.
- Unsteady reaction forces due to a slug flow may be deduced with reasonable accuracy for equipment support and stress calculations, since the reaction forces are a direct function of stream-wise velocity.
- Qualitatively, CFD can predict the pressure gradient in stratified and slug flow.

Limitations:

- The inaccurate prediction of liquid and vapor wavy interface when the velocity differences between phases are large. Increasing the number of

cells at the interface may minimize the inaccuracy. However, the VOF model may also need to be improved for better prediction.

- More research is needed in CFD for better prediction of pressure gradient in a two-phase flow.

Resolving the limitations in CFD rely on our understanding of two-phase flow behavior, incorporating these inputs into correct boundary conditions in CFD and a good-quality mesh. There are several application areas that need predictions of two-phase flow for design and trouble-shooting purposes. Providing a valid two-phase CFD model will be crucial during the design stage.

References

[1] Baker, O. Multiphase flow in pipes, Oil and Gas Journal, Nov. 1958.
[2] Lewis, S., Fu, W. L., Kojasoy, G. Internal flow structure description of slug flow-pattern in a horizontal pipe, International Journal of Heat and Mass Transfer, 2000.
[3] Fabre, J., Masbernat, L., Suzanne, C. Stratified flow, part I: local structure, Multiphase Science and Technology, volume 3, 1999.
[4] Paras, S.V., Vlachos, N. A., Karabelas, A. J. Liquid layer characteristics in stratified-atomization flow. Int. J. Multiphase Flow, Vol. 20, 1994.
[5] Rosendall, B. and Berkoe, J. Success of computational fluid dynamics (CFD) modeling of fluidics designs using pulsed jet mixers in the Hanford Waste Treatment Plant (WTP). Bechtel WTP project memorandum, CCN: 066517.
[6] Levy, "Two-phase flow in complex systems", Wiley-Interscience, 1999.

This page intentionally left blank

Section 9
Large eddy simulation

This page intentionally left blank

The dispersion of a light solid particle in high-Reynolds number homogeneous stationary turbulence: LES approach with stochastic sub-grid model

M. Gorokhovski & A. Chtab
CORIA/UMR 6614 CNRS/University of Rouen, France

Abstract

In the framework of the LES approach, the simple stochastic model of turbulent cascade with intermittency is introduced in order to represent the interaction between a solid particle and turbulence at sub-grid scales. The computation of the Lagrangian statistics of a light particle in homogeneous stationary turbulence reproduced the results of measurements: (i) for the velocity statistics, the numerical results were in agreement with classical Kolmogorov 1941 phenomenology; (ii) the computation of the velocity increment at different time lags revealed, however, the strong intermittency.
Keywords: dispersion, LES approach, turbulence, intermittency.

1 Introduction

During the past years, it has been recognized that for computation of high-Reynolds turbulent gas flow, the large eddy simulation (LES) approach (integration of 3D filtered Navier-Stokes equations with effective sub-grid eddy viscosity model) provides accurate local estimates of statistical quantities [1]. Recently [2], this approach was rigorously formulated from the group-theoretical analyses. Applying the LES approach to computation of turbulent flow with dispersed phase, one can expect that at each time, the momentum transport from flow to particles can be predicted accurately. However there is a problem: the interactions between gas and small particles are often characterized by length (or time) scales, which are not resolved by LES approach. Such interactions need to be modeled.

The objective of this paper is to simulate the dispersion of light particle in the highly intermittent turbulent flow. This numerical study was motivated by recent experimental work done by Mordant *et al.* [3]. In this experiment, the von Karman swirling flow was generated by two counter-rotating discs. Remote from boundaries, such a flow was considered as a high Reynolds number homogeneous isotropic turbulence. The solid polystyrene sphere ($d = 250\,\mu m$; $\tau_{St} = 3.67 ms$; $\rho_p = 1.06\,g/cm^3$) has been immersed in the flow in order to measure the Lagrangian velocity variations across the inertial range of turbulence. It has been observed that at Reynolds number $\mathrm{Re}_\lambda = 570 - 1200$ (λ is Taylor micro-scale), the velocity auto-correlation function and the time spectrum were in agreement with Kolmogorov, 1941. However, the measured velocity increments revealed the strong intermittency: the periods of weak velocity increments alternated with moments, when the particle was subjected to intense accelerations (going up to $4500 m/s^2$). In this paper, the experiment of Mordant *et al.* [3] is simulated in the framework of LES approach. The particle/turbulence interaction at sub-grid scales is introduced assuming the scaling symmetry in turbulent cascade with intermittency [4]. Along with LES computation, can this model match the observations from [3] - was the question raised before computation.

2 Universalities of fragmentation under the scaling symmetry and turbulent cascade with intermittency

Fragmentation plays an important role in a variety of physical, chemical, and geological processes. Examples include atomization in sprays, crushing of rocks, polymer degradation, turbulence *etc*. Although each individual action of fragmentation is a complex process, the number of these elementary actions is large. In this situation, it is natural to abstract a simple scenario of fragmentation and to represent its essential features, independently of the details of elementary break-up actions. One of the models is the fragmentation under the scaling symmetry. Here each breakup action reduces the typical length of fragments, $r \Rightarrow \alpha r$, by an independent random multiplier α, which is governed by the fragmentation intensity spectrum, say, $q(\alpha)$, $\int_0^1 q(\alpha)d\alpha = 1$. The following question is raised: during the fragmentation under scaling symmetry, how does evolve the distribution $f(r,t)$ to the ultimate steady-state solution $f(r) = \delta(r)$? This question cannot be completely answered since such evolution requires the knowledge of the spectrum $q(\alpha)$, which is principally unknown function. However, as it has been shown in Gorokhovski and Saveliev [5], due to scaling symmetry $r \to \alpha\, r$, the evolution of $f(r,t)$ goes, at least,

through two intermediate asymptotic distributions. Evaluating these distributions does not require the knowledge of entire spectrum $q(\alpha)$ - only its first two logarithmic moments (first universality), and further only the ratio of these moments in the long-time limit (second universality), determine the shape of $f(r,t)$. The first universality leads to the log-normal distribution of $f(r,t)$, and the second one verifies to be power (fractal) distribution (so far, the delta-function distribution is never achieved).

In turbulence, due to intermittency, the energy of large unstable eddy is transferred to the smaller one at fluctuating rate. Here the fragmentation under scaling symmetry can be formulated in terms of Castaing *et al.* [6 – 10]: when the turbulent length scale r gets smaller, the velocity increment, $\delta_r \mathrm{v}(x)=\left|\mathrm{v}(x+r)-\mathrm{v}(x)\right|$, is changed by independent positive random multiplier, $\delta_r \mathrm{v}=\alpha\,\delta_l \mathrm{v}$, with $r\le l$. Let us introduce an evolution parameter $\tau=\ln(L_{LES}/l)$ of penetration towards smaller scales (L_{LES} is typical scale of finite-difference cell and l is a progressively decreasing eddy scale). One can write an equation, which governs the evolution from distribution $f(\delta \mathrm{v},\tau_l)$ at scale l towards distribution $f(\delta \mathrm{v},\tau_r \succ \tau_l)$ at smaller scale r. Such an equation has been established in [5]:

$$\frac{d\,f(\delta \mathrm{v};\tau)}{d\tau}=\left(\hat{I}_+-1\right)f(\delta \mathrm{v};\tau) \tag{1}$$

where

$$\hat{I}_+ f(\delta \mathrm{v};\tau)=\int\frac{d\alpha}{\alpha}q(\alpha)f\left(\frac{\delta \mathrm{v}}{\alpha};\tau\right)$$

is operator of fragmentation.
The long-time limit solution of (1) is verified to be [5]:

$$f(\delta \mathbf{v},\tau)=\int_0^\infty d\,\alpha\,B(\alpha,\tau)\,f(\alpha\,\delta \mathbf{v},\tau_0) \tag{2}$$

where $f(\alpha\,\delta \mathbf{v},\tau_0)$ is the initial distribution and

$$B(\alpha,\tau)=\frac{1}{\sqrt{2\pi\left\langle \ln^2\alpha\right\rangle\tau}}e^{-\left(\ln\alpha+\left\langle \ln\alpha\right\rangle\tau\right)^2/2\left\langle \ln^2\alpha\right\rangle\tau}.$$

In the case of LES, the velocity increment, δV_{LES}, is resolved exactly at L_{LES} and then the initial distribution of the velocity increment

($l = L_{LES} \Rightarrow \tau = 0$) may be represented by the Dirac delta function, $f(\alpha\,\delta\mathrm{v}, \tau = 0) = \delta(\alpha\,\delta\mathrm{v} - \delta\mathrm{V}_{LES})$. In this case, solution (2) yields:

$$f(\delta\mathrm{v};\tau) \underset{t\to\infty}{=} \frac{1}{\delta V_{LES}} \frac{1}{\sqrt{2\pi\left\langle \ln^2\alpha\right\rangle\tau}} \exp\left(-\frac{\left\langle \ln\alpha\right\rangle^2}{2\left\langle \ln^2\alpha\right\rangle}\tau\right) \cdot \exp\left(-\frac{\ln^2\frac{\delta V_{LES}}{\delta\mathrm{v}}}{2\left\langle \ln^2\alpha\right\rangle\tau}\right)\left(\frac{\delta V_{LES}}{\delta\mathrm{v}}\right)^{1-\frac{\left\langle \ln\alpha\right\rangle}{\left\langle \ln^2\alpha\right\rangle}} \tag{3}$$

As it has been noted in [5], the second multiplier in log-normal asymptotic (3) tends to unity, as time progresses further, and *only one universal parameter*, $\left\langle \ln\ \alpha\right\rangle / \left\langle \ln^2\ \alpha\right\rangle$, determines the distribution at largest times (evolution from log-normal distribution towards power function with growing in time pick at small increments and stretched tails at larger increments). This parameter we assumed in the following form: $\left\langle \ \ln^2\ \alpha\ \right\rangle\ /\ \left\langle \ \ln\ \alpha\ \right\rangle = \ln(\lambda_T / L_{LES})$, where λ_T is referred to as local Taylor micro-scale; the first logarithmic moment we introduced as $\left\langle \ \ln\ \alpha\ \right\rangle = A \cdot \ln(\lambda_T / L_{LES})$. Here A is unknown constant. This constant has been adjusted comparing the evolution of the excess in (2), $K(\tau) = \left\langle (\delta\mathrm{v})^4 \right\rangle / \left\langle (\delta\mathrm{v})^2 \right\rangle^2 - 3$, with values measured in Mordant *et al.* [3]. To do this, the distribution, which was measured in [3] at integral turbulent time (Gaussian with variance of $1\,m/s$), has been introduced as initial distribution in (2). The value $\lambda_T = 0.076cm$ taken from [3] also was used. Different fitting curves with $A = 0.007,\ 0.008,\ 0.009$ are shown in fig.1; the value $A = 0.008$ was taken in our further computations.

3 Computational model

In this work, the filtered Navier-Stokes equations were integrated numerically in 3D box with periodic conditions in order to simulate the stationary homogeneous gaseous turbulence. The stationarity and statistical isotropy of turbulent flow was provided by the forcing scheme at large scales proposed by Overholt and Pope [11]. In the computation, the Reynolds number, the kinetic energy, the micro-scales of Kolmogorov and Taylor were close to those mentioned in Mordant *et al.* [3] ($\mathrm{Re}_\lambda = 740$; $\sigma_v^2 = 1m/s$; $\eta_k = 14\mu m$; $\lambda_T = 0.076cm$; $T_{\mathrm{int}} = 23\ ms$; $\tau_K = 0.22ms$). Examples of the flow configuration and the sub-grid viscosity

distribution computed by 32^3 grid points mesh at different times is given in fig. 2. Fig. 3 shows the kinetic energy spectrum compared to the presumed spectrum of Overholt and Pope [11]. It is seen that the presumed spectrum is well represented up to the spatial scale $k = 2.5\,cm^{-1}$. At smaller scales, the computed spectrum deviates from the presumed one; these scales will be simulated.

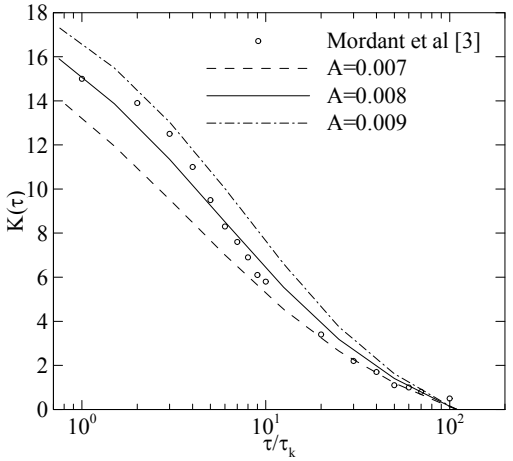

Figure 1: Evolution of the excess in (2) compared to measured values in Mordant *et al.* [3].

Along with LES computation of the flow, the rigid particle, same as in Mordant *et al.* [3], was tracked ($d_P \succ \eta_K$ and $\tau_{St} \succ \tau_K$). To simulate the drag force, one needs to estimate the gas velocity "seen" by the particle. We assume that this velocity is combined from the resolved one and its increment at spatial scales of order of the particle diameter, d_p. The estimation of the last one can be obtained from distribution (3) by setting both the evolution parameter $\tau_p = \ln\left(L_{LES} / d_p\right)$ and the local resolved velocity increment δV_{LES}. Hence, the equation for the dragging particle is:

$$\frac{dU_p}{dt} = \frac{V_{LES} + \delta \mathrm{v} - U_p}{\tau_{st}} \tag{4}$$

with $\delta \mathrm{v} = rnd\left\{ f\left(\delta \mathrm{v} \middle| \delta V_{LES}, \tau_p \right)\right\}$ sampled from (3) after passage of local time $\left|\overline{S}\right|^{-1}$, where $\left|\overline{S}\right| = \left(2\overline{S_{ij}}\,\overline{S_{ij}}\right)^{1/2}$ is the norm of resolved velocity gradients tensor.

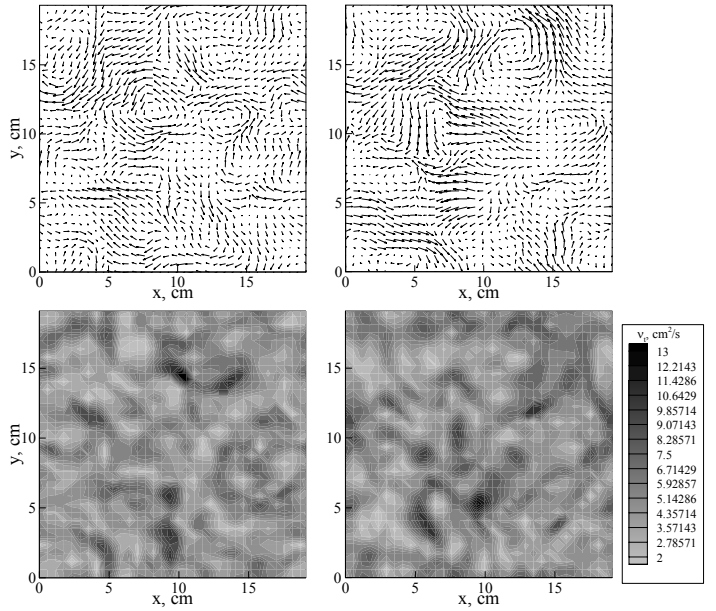

Figure 2: Examples of the flow configuration and the sub-grid viscosity distribution at two different times.

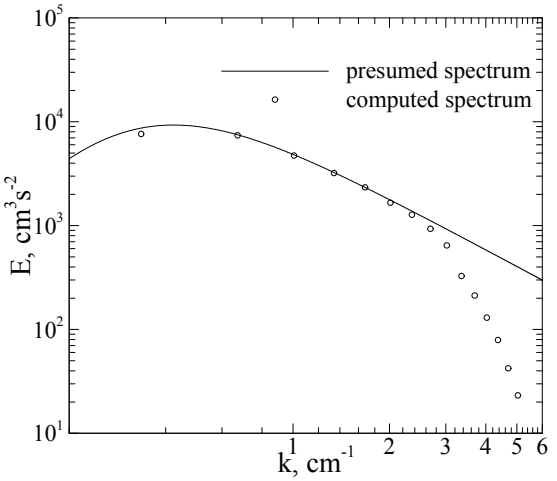

Figure 3: Computed kinetic energy spectrum compared to the presumed shape in Overholt and Pope [11].

4 Numerical results and discussion

In the framework of Kolmogorov 1941 scaling in the inertial range, the second-order structure function, $D_2^L(\tau) = \left\langle \left(\mathrm{v}(t+\tau) - \mathrm{v}(t) \right)^2 \right\rangle$, is expected to be $D_2^L(\tau) \approx \varepsilon\tau \approx 2\sigma_{\mathrm{v}}^2 \tau / T_L$, where σ_{v}^2 is variance of the Eulerian velocity field and T_L provides the measure of the Lagrangian velocity memory. For $\tau << T_L$, this is consistent with Taylor 1921 theory, according to which $D_2^L(\tau) = \left\langle \left(\mathrm{v}(t+\tau) - \mathrm{v}(t) \right)^2 \right\rangle = 2\sigma_{\mathrm{v}}^2 \left(1 - e^{-\tau/T_L} \right)$. At very large times, the second-order structure function tends to its constant magnitude, $D_2^L(\tau) = 2\sigma_{\mathrm{v}}^2$, while at very small times, this function is expected to behave as $D_2^L(\tau) \approx \varepsilon^{3/2} \nu^{-1/2} \tau^2$ [12]. Along with Mordant *et al.* [3], our computation of the second-order structure is in agreement with these classical results. In fig. 4, we show the second-order structure function for tracking particle at different time lags. Here, the time lags are scaled by Kolmogorov's time τ_K and υ_K is the Kolmogorov's velocity scale (a_0 and C_0 are constants, for illustration). The quadratic dependency at small scales, and the linear dependency at larger scales, with saturation towards the prescribed in experiment variance $2\sigma_{\mathrm{v}}^2 / \upsilon_K^2$ can be seen in this figure. Note that the range, where $D_2^L(\tau) \approx \tau$, is not wide. This has been also mentioned by Mordant *et al.* [3]. Another confirmation of Kolmogorov 1941 phenomenology is demonstrated in fig. 5. This figure shows that the computed velocity spectrum, presented as Fourier transform of autocorrelation function, proofs the Lorentz form, which is proportional to ω^{-2}, at small $\omega \approx \tau^{-1}$, and to ω^{-4} at larger frequencies. At the same time, the computed statistics of the velocity increment displayed a strong non-gaussianity. In fig. 6, we show the computed and measured distributions of particle velocity increment at different time lags. It is seen that at integral times, the velocity increment is normally distributed. This confirms the result of Oboukhov's Lagrangian model of turbulence [12, 13]. However at smaller time lags, similar to experimental observation, the distributions exhibit a growing central peak with stretched tails: small amplitude events alternate with events of large acceleration. Such a manifestation of intermittency at small scales is seen also from the computed distribution of the particle acceleration (fig. 7): the accelerations of particle may attain very large values. In the same figure, we present the measured distribution and the distribution, which was computed without sub-grid modeling (zero $\delta_p \mathrm{v}$). One can see that in the last case, the computed acceleration is of order of Kolmogorov's scaling

$a_K \approx \left(\varepsilon^3 / \nu\right)^{1/4} \approx 300 m/s^2$, which is substantially less than the measured one.

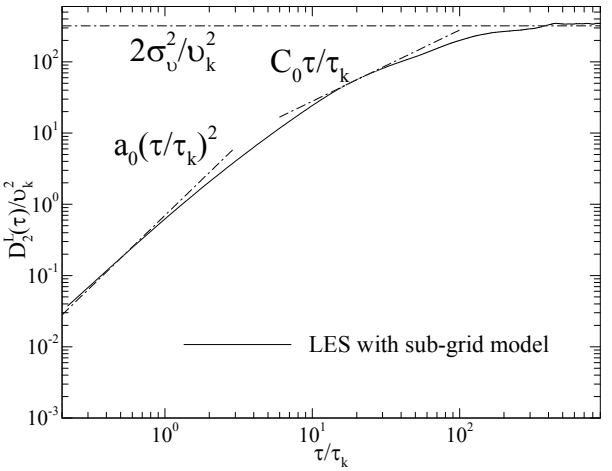

Figure 4: Second order structure function (solid line) at different time lags scaled by Kolmogorov's time τ_K; υ_K is Kolmogorov's velocity scale).

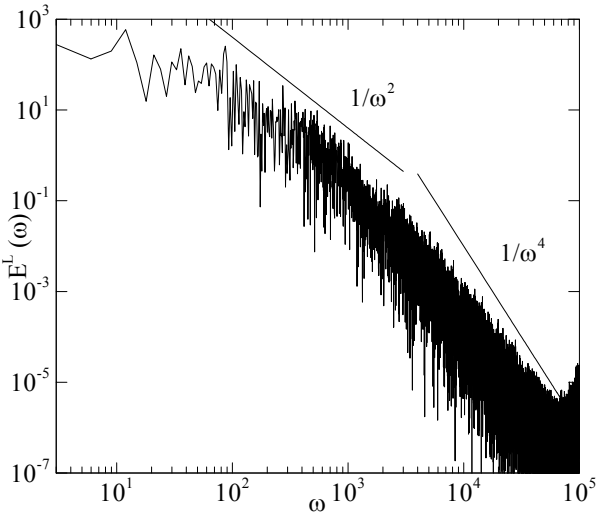

Figure 5: Computed Lagrangian velocity spectrum.

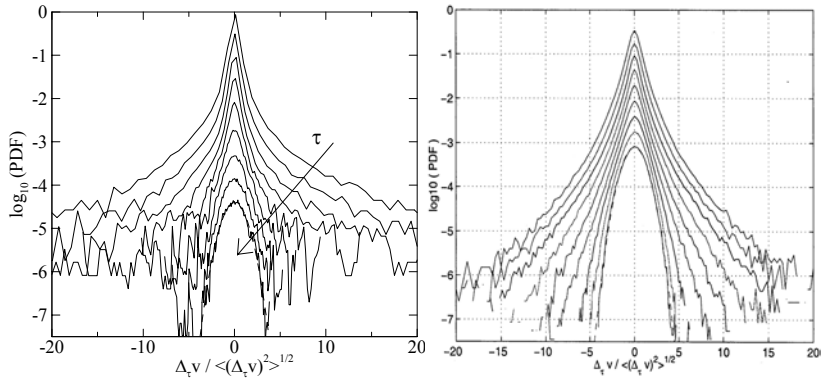

Figure 6: Velocity increment distribution at different time lags (computation - on the left; measurements of Mordant *et al.* [3] at the same lags - on the right).

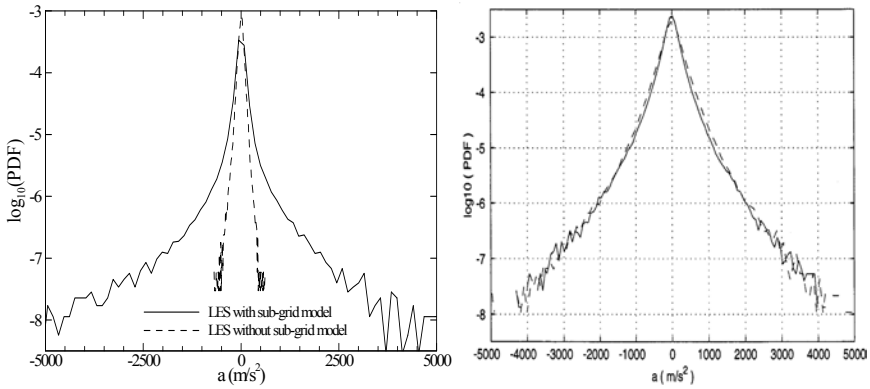

Figure 7: PDF of acceleration (computation - on the left; measurements of Mordant *et al.* [3] - on the right).

References

[1] Moin, P. & Kim, J., Numerical investigation of turbulent channel flow. *J. Fluid Mech.*, **118**, pp. 341-377, 1982.

[2] Saveliev, V.L. & Gorokhovski, M.A., Group-theoretical model of developed turbulence and renormalization of Navier-Stokes equation. *Physical Review E* **72**, 016302, 2005.

[3] Mordant, N., Leveque, E. & Pinton, J.-F., Experimental and numerical study of the Lagrangian dynamics of high Reynolds turbulence. *New Journal of Physics*, **6**, pp. 116, 2004.

[4] Gorokhovski, M., Scaling Symmetry Universality and Stochastic Formulation of Turbulent Cascade With Intermittency. *Annual Research*

Briefs -2003, Center of Turbulence Research, Stanford University, NASA, pp. 197-204, 2003.

[5] Gorokhovski, M & Saveliev, V., Further analyses of Kolmogorov's model of breakup and its application in air blast atomization. *J. Physics of Fluids*, **15(1)**, pp. 184-192, 2003.

[6] Castaing, B., Gagne, Y. & Hopfinger, E.J., Velocity proprobability density functions of high Reynolds number turbulence. *Physica D* **46**, pp 177-200, 1990.

[7] Castaing, B., Gagne, Y. & Marchand, M., Log-similarity for turbulent flows? *Physica D* **68**, pp 387-400, 1993.

[8] Castaing, B., Temperature of turbulent flows. *Journal De Physique II,* **6(1)**, pp 105-114, 1996.

[9] Kahalerras, H., Malécot, Y., Gagne, Y. & Castaing, B., Intemittency and Reynolds number. *Phys.Fluids*, **10(4)**, pp 910-921, 1998.

[10] Naert, A., Castaing, B., Chabaud, B., Hebral, B. & Peinke, J., Conditional statistics of velocity fluctuations in turbulence. *Physica D: Nonlinear Phenomena*, **113(1)**, pp 73-78, 1998.

[11] Overholt, M.R & Pope, S.B., A deterministic forcing scheme for direct numerical simulations of turbulence. *Computers & Fluids*, **27(1)**, pp. 11-28, 1998.

[12] Monin, A.S & Yaglom, A.M., *Statistical fluid mechanics: mechanics of turbulence*, The MIT press, 900 pp., 1981.

[13] Obukhov, A.M., Atmospheric diffusion and air pollution. *Adv. In Geophys.*, **6**, pp. 113-115, 1959.

Formulation of a two-phase filtered density function approach for large eddy simulation

M. D. Carrara & P. E. DesJardin
Department of Mechanical and Aerospace Engineering,
University at Buffalo, The State University of New York, Buffalo, USA

Abstract

Two-phase velocity-scalar filtered density function (FDF) methods have recently been extended for large eddy simulation (LES) of separated two-phase flows [1]. Several terms in the two-phase FDF transport equation are unclosed and must be modeled for practical application of the two-phase FDF theory. Some terms, such as conditional dissipation in momentum, scalar, and momentum-scalar phase spaces are analogous to those in the single-phase velocity-scalar FDF formulation for which closures are readily available. Phase-coupling and interphase conversion terms, however, which are unique to the two-phase FDF formulation are unclosed and must be modeled. There are, then, three distinct types of unclosed terms in the two-phase FDF formulation: conditional dissipation terms, phase-coupling terms and interphase conversion terms. In this study, the mathematical formulation of this approach is presented and conditional dissipation, phase-coupling and interphase conversion terms are identified and their connection to standard LES closures identified.

1 Two-phase FDF transport equation

Two-phase probability density function (PDF) methods have recently been formulated and successfully applied for dispersed/continuum phase flows [2, 3, 4]. Probability density function methods are based on defining a suitable set of flow realizations over which the PDF may be defined in the ensemble statistics context and therefore in practice are devoid of any spatial information about the two-phase flow. That is to say, turbulent flow field information in the PDF approach must be given in the time-averaged or RANS context, and consequently coupling to a RANS calculation for the carrier gas field is common [4, 2]. Filtered density func-

tion (FDF) methods are based on spatial averaging, or filtering, of a fine-grain density function. With appropriate constraints imposed on the filtering kernel, the filtered fine-grain density function has all the mathematical properties of a joint PDF [5, 6, 7], and hence all the advantages of the PDF formulation are retained in the FDF context while large scale spatial information about the flow field is simulated in the large eddy simulation (LES). Filtered density function methods have been successfully applied to single-phase reactive and non-reactive flows in a full velocity-scalar formulation [8] and scalar-only FDF formulations coupled to an LES of the momentum field [9, 10]. Recently, Carrara and DesJardin have extended the FDF approach for separated two-phase flows [1]. In this development, the two-phase velocity-scalar filtered density function (TVSFDF), F_L, is defined in terms of the spatially filtered value of the two-phase fine-grain density function, ξ:

$$F_L(\mathbf{u}_k, \Psi_{\alpha,k}) \equiv \langle \xi(\mathbf{u}_k, \Psi_{\alpha,k}) \rangle$$
$$= \sum_{k=1}^{2} \int_{\infty} d^3x' \rho_k(\mathbf{x}', t) G(\mathbf{x}' - \mathbf{x}) \phi_k(\mathbf{x}', t) \xi_k(\mathbf{u}_k(\mathbf{x}', t), \Psi_{\alpha,k}(\mathbf{x}', t)) \quad (1)$$

where the two-phase fine-grain density function for velocity $\mathbf{u}_k$ and field scalars $\Psi_{\alpha,k}$ is given by,

$$\xi(\mathbf{u}_1, \mathbf{u}_2, \Psi_{\alpha,1}, \Psi_{\alpha,2}) \equiv \phi_1(\mathbf{x}, t) \prod_{i=1}^{3} \delta[v_{1,i}(\mathbf{x}, t) - u_{1,i}] \prod_{i=1}^{\sigma} \delta[\psi_{\alpha,1}(\mathbf{x}, t) - \Psi_{\alpha,1}]$$
$$+ \phi_2(\mathbf{x}, t) \prod_{i=1}^{3} \delta[v_{2,i}(\mathbf{x}, t) - u_{2,i}] \prod_{i=1}^{\sigma} \delta[\psi_{\alpha,2}(\mathbf{x}, t) - \Psi_{\alpha,2}]$$
$$= \phi_1 \xi_1 + \phi_2 \xi_2. \quad (2)$$

In the above equations δ denotes a Dirac delta distribution [11] and ϕ_k is a phase indicator function in phase k [12], defined here as 1 in phase 1 and 0 in phase 2. The filtering kernel G restricts the filtering operation to a compact region in the spatial domain of the flow and is defined for $\mathbf{x} > 0, t > 0$ such that it is parity invariant, non-zero, continuously differentiable and normalized with compact support. The variables $\psi_{\alpha,k}$ and $\mathbf{v}_k$ are sampled values of the random variables $\Psi_{\alpha,k}$ and $\mathbf{u}_k$ at a particular spatial location $\mathbf{x}$ and time t, respectively. For the separated two-phase flow, ξ_1 and ξ_2 are defined as the marginal joint fine-grain density functions in phase 1 and phase 2. As discussed by Carrara and DesJardin, a marginal TVSFDF

transport equation for phase 1 can be derived and given as [1],

$$\begin{aligned}\frac{\partial F_L^1}{\partial t}+\frac{\partial}{\partial \mathbf{x}}\big(\mathbf{u}_1 F_L^1\big)&=\frac{\partial}{\partial \mathbf{x}}\big[\mu_1\frac{\partial(F_L^1/\widehat{\rho_1})}{\partial \mathbf{x}}\big]\\&+\frac{\partial}{\partial \mathbf{x}}\big[\Gamma_{\alpha,1}\frac{\partial(F_L^1/\widehat{\rho_1})}{\partial \mathbf{x}}\big]-\frac{\partial}{\partial \Psi_{\alpha,1}}\big[S_{\alpha,1}F_L^1\big]\\&-\frac{\partial^2}{\partial \mathbf{u}_1\cdot\partial \mathbf{u}_1}\big[\langle\mu_1\phi_1\nabla\mathbf{v}_1\cdot\nabla\mathbf{v}_1\Big|_{\gamma<0^-}\rangle(F_L^1/\widehat{\rho_1})\big]\\&-\frac{\partial^2}{\partial \mathbf{u}_1\partial \Psi_{\alpha,1}}\big[\langle\mu_1\phi_1\nabla\mathbf{v}_1\cdot\nabla\psi_{\alpha,1}\Big|_{\gamma<0^-}\rangle(F_L^1/\widehat{\rho_1})\big]\\&-\frac{\partial^2}{\partial \Psi_{\alpha,1}\partial \Psi_{\beta,1}}\big[\langle\phi_1\Gamma_{\alpha,1}\nabla\psi_{\alpha,1}\cdot\nabla\psi_{\beta,1}\Big|_{\gamma<0^-}\rangle(F_L^1/\widehat{\rho_1})\big]\\&-\frac{\partial^2}{\partial \Psi_{\alpha,1}\partial \mathbf{u}_1}\big[\langle\phi_1\Gamma_{\alpha,1}\nabla\psi_{\alpha,1}\cdot\nabla\mathbf{v}_1\Big|_{\gamma<0^-}\rangle(F_L^1/\widehat{\rho_1})\big]\\&+\frac{\partial}{\partial \mathbf{u}_1}\big[\langle\frac{1}{\rho_1}\nabla(\phi_1 P_1)\Big|_{\gamma<0^-}\rangle F_L^1\big]-\frac{\partial}{\partial \mathbf{u}_1}\big[\langle\phi_1\mathbf{f}_1\Big|_{\gamma<0^-}\rangle F_L^1\big]\\&-\frac{\partial}{\partial \mathbf{u}_1}\big[\langle\frac{1}{\rho_1}P_1^I\mathbf{e}_{n,1}^I a^I\Big|_{\gamma=0^-}\rangle F_L^1\big]+\frac{\partial}{\partial \mathbf{u}_1}\big[\langle\frac{1}{\rho_1}\underset{\sim}{\boldsymbol{\tau}_1}^I\cdot\mathbf{e}_{n,1}^I a^I\Big|_{\gamma=0^-}\rangle F_L^1\big]\\&+\frac{\partial}{\partial \Psi_{\alpha,1}}\big[\langle\frac{1}{\rho_1}\Gamma_{\alpha,1}\nabla\psi_{\alpha,1}^I\cdot\mathbf{e}_{n,1}^I a^I\Big|_{\gamma=0^-}\rangle F_L^1\big]+\langle\Pi_1\Big|_{\gamma=0^-}\rangle F_L^1. \quad (3)\end{aligned}$$

In Eq. (3) a low Mach number flow of a Newtonian fluid is assumed so that μ_1 is the molecular viscosity, $\Gamma_{\alpha,1}$ is the gradient flux transport coefficient for the transported scalar quantity $\psi_{\alpha,1}$, P_1 is the thermodynamic pressure, $\underset{\sim}{\boldsymbol{\tau}_1}$ is the deviatoric stress tensor and $\mathbf{f}_1$ is the body force, all in phase 1. Equation (3) represents the transport of the marginal TVSFDF in phase 1 that is defined through the TVSFDF as [13, 4],

$$F_L^1(\mathbf{u}_1,\Psi_{\alpha,1})\equiv\int d^3u_2 d^\sigma\Psi_{\alpha,2}F_L(\mathbf{u}_1,\mathbf{u}_2,\Psi_{\alpha,1},\Psi_{\alpha,2}). \quad (4)$$

The conditional filtering operator, appearing in Eq. (3) is defined for a field quantity $Q_k(\mathbf{x},t)$ in phase k as,

$$\langle Q_k\big|_{\chi=\varphi}\rangle\equiv\frac{\int d^3x' G\rho_k\xi Q_k}{\int d^3x' G\rho_k\xi}=\frac{\int d^3x' G\rho_k\xi Q_k}{F_L} \quad (5)$$

where the filtered value of Q_k is conditioned upon $\chi=\varphi$ for the sampled fields $\varphi=\{\mathbf{v}_k,\psi_{\alpha,k}\}$ associated with the random phase fields $\chi=\{\mathbf{u}_k,\Psi_{\alpha,k}\}$. The conditional filtered Q_k arises when Q_k is not solely a function of φ; accordingly, if Q_k is completely determined by φ then the field variable appears in the FDF context in *closed form*: $\langle Q_k\big|_{\chi=\varphi}\rangle\equiv\frac{\int d^3x' G\rho_k\xi Q_k(\chi)}{\int d^3x' G\rho_k\xi}=\hat{Q}_k(\varphi)$. One advantage

of PDF/FDF methods over traditional moment closure methods is that reaction source terms appear in closed form as evidenced by the closed $S_{\alpha,1}$ term on the second line of Eq. (3). In Eq. (3) the conditional dissipation decomposition has been has been applied to unclosed conditionally filtered terms in both momentum and scalar-momentum phase spaces (within the fluid phase, $\gamma < 0-$) in the TVSFDF transport equation [13, 14]. The interested reader is referred to the seminal paper by Pope [13] for details.

In a separated two-phase flow, the conditional filter operation must be separated by phase. Consequently, two-phase FDF formulation admits three types of unclosed terms: conditionally filtered terms within the continuum phase (conditioned on $\gamma < 0-$), conditionally surface filtered terms that account for phase coupling in the FDF context (conditioned on $\gamma = 0-$) and the interphase conversion term Π_k, also conditioned on the phase interface $\gamma = 0-$. The closure of these terms will be considered separately in the following sections.

2 Continuum field FDF closures: $\gamma < 0-$

Closure models for single-phase FDF formulations are well developed and applying the work of Sheikhi *et al.* [14], Colucci *et al.* [8], Gicquel *et al.* [15], and O'Brien [16], the generalized Langevin model (GLM) and the linear mean square estimation (LMSE) model for a single-phase flow are applied to those terms in the marginal TVSFDF transport equation that are conditioned within phase $1, \gamma < 0-$. These closures imply,

$$\frac{\partial^2}{\partial\Psi_{\alpha,1}\partial\Psi_{\beta,1}}\Big[\langle\phi_1\Gamma_{\alpha,1}\frac{\partial\psi_{\alpha,1}}{\partial\mathbf{x}}\cdot\frac{\partial\psi_{\beta,1}}{\partial\mathbf{x}}\big|_{\gamma<0}\rangle F_L^1\Big] \overset{\text{modeled}}{=\!=\!=} \frac{\partial}{\partial\Psi_{\alpha,1}}\Big[\Omega_m(\Psi_{\alpha,1}-\langle\psi_{\alpha,1}\rangle)F_L^1\Big] \quad (6)$$

and,

$$\begin{aligned}
&\frac{\partial}{\partial\mathbf{u}_1}\Big[\langle\frac{1}{\rho_1}\nabla(\phi_1 P_1)\big|_{\gamma<0}\rangle F_L^1 - \frac{1}{\langle\rho_1\rangle}\frac{\partial\langle P_1\rangle}{\partial\mathbf{x}}F_L^1\Big] \\
&-\frac{\partial^2}{\partial\mathbf{u}_1\cdot\partial\mathbf{u}_1}\Big[\langle\phi_1\mu_1\frac{\partial\mathbf{v}_1}{\partial\mathbf{x}}\cdot\frac{\partial\mathbf{v}_1}{\partial\mathbf{x}}\big|_{\gamma<0}\rangle F_L^1\Big] - \frac{\partial^2}{\partial\mathbf{u}_1\partial\Psi_{\alpha,1}}\Big[\langle\phi_1\mu_1\frac{\partial\mathbf{v}_1}{\partial\mathbf{x}}\cdot\frac{\partial\psi_{\alpha,1}}{\partial\mathbf{x}}\big|_{\gamma<0}\rangle F_L^1\Big] \\
&-\frac{1}{\langle\rho_1\rangle}\frac{\partial^2}{\partial\Psi_{\alpha,1}\partial\mathbf{u}_1}\Big[\langle\rho_1\phi_1\Gamma_{\alpha,1}\frac{\partial\psi_{\alpha,1}}{\partial\mathbf{x}}\cdot\frac{\partial\mathbf{v}_1}{\partial\mathbf{x}}\big|_{\gamma<0}\rangle F_L^1\Big] \overset{\text{modeled}}{=\!=\!=} \frac{C_o\epsilon}{2}\frac{\partial^2 F_L^1}{\partial\mathbf{u}_1\cdot\partial\mathbf{u}_1} \\
&\qquad+\nu_1\Big(\frac{\partial\langle\mathbf{v}_1\rangle}{\partial\mathbf{x}}\cdot\frac{\partial\langle\mathbf{v}_1\rangle}{\partial\mathbf{x}}\Big)\frac{\partial^2 F_L^1}{\partial\mathbf{u}_1\cdot\partial\mathbf{u}_1} + 2\nu_1\frac{\partial\langle\mathbf{v}_1\rangle}{\partial\mathbf{x}}\cdot\frac{\partial^2 F_L^1}{\partial\mathbf{x}\cdot\partial\mathbf{u}_1} \\
&\qquad\qquad-\frac{\partial}{\partial\mathbf{u}_1}\Big[\underset{\sim}{\mathbf{G}}\cdot(\mathbf{u}_1-\langle\mathbf{v}_1\rangle)F_L^1\Big] \quad (7)
\end{aligned}$$

where, $\underset{\sim}{\mathbf{G}} = -\omega(1/2 + 2C_o/3)\underset{\sim}{\mathbf{I}}$, $\omega = \epsilon/k$ is the turbulent mixing frequency, and $\Omega_m = \underset{\sim}{C_\phi}\omega$. The turbulent dissipation and turbulent kinetic energy are given by $\epsilon = C_\epsilon k^{3/2}/\Delta_f$ and $k = 1/2(\langle \mathbf{v}_1 \cdot \mathbf{v}_1 \rangle - \langle \mathbf{v}_1 \rangle \cdot \langle \mathbf{v}_1 \rangle$ respectively. The parameters C_o, C_ϵ and C_ϕ are modeling constants that must be specified and Δ_f is the LES filter width [14].

3 FDF phase-coupling terms: $\gamma = 0-$

Unique to the two-phase flow formulation of the FDF transport equation are the phase-coupling terms, arising in this context in terms of conditionally surface filtered quantities in Eq. (3). These terms, conditioned on $\gamma = 0-$, shown on the last two lines of Eq. (3), may be expressed in terms of the "local instantaneous interfacial area concentration", a^I, in the conditional average [1, 4]:

$$\langle \phi_k \nabla \phi_k \big|_{\gamma=0-} \rangle = \langle \psi_k^I a^I \mathbf{e}_{n,k}^I \big|_{\gamma=0-} \rangle. \tag{8}$$

The superscript I indicates values on the phase interface is the sense that $\psi_1^I \equiv \lim_{\gamma \to 0-} \psi_1$ and $\phi_2^I \equiv \lim_{\gamma \to 0+} \psi_2$. The interfacial area concentration is given in terms of a Dirac distribution of the characteristic function γ, $a^I \equiv \delta(\gamma)\nabla\gamma$ [12]. Carrara and DesJardin showed that this term may be given in terms of a surface integration of the filtering kernel G in the limit where the support of G approaches zero: $G(\mathbf{x}' - \mathbf{x}) \to \delta(\mathbf{x}' - \mathbf{x})$ [1]. The result is,

$$a^I = \oint_{\partial\Omega_1} d^2x' \delta(\mathbf{x}' - \mathbf{x}) = \delta(\gamma)\nabla\gamma. \tag{9}$$

It is shown in [1] that the two definitions of a^I are mathematically equivalent, and this result is of key importance in proposing closure models for conditionally surface filtered terms. By using Eq. (9) in Eq. (8), it was shown that conditionally surface filtered quantities like those in Eq. (8) can be directly expressed in terms of conditionally surface averaged quantities arising as the source terms in the phase-averaged LES equations [1]. That is, a surface filtered quantity $1/\rho_1 Q_1(\mathbf{x}, t)a^I$ in phase 1 can be written as,

$$\langle \frac{1}{\rho_1} Q_1 a^I \big|_{\gamma=0-} \rangle \equiv \frac{\int_\infty d^3x' G\xi Q_1 a^I}{\int_\infty d^3x' G\rho_1 \xi} = \frac{\oint_{\partial\Omega_1} d^2x' G Q_1^I}{\oint_{\partial\Omega_1} d^2x' G\rho_1^I} = \frac{A_1}{V_1} \frac{\overline{(Q_1)_s}}{\overline{(\rho_1)_s}}. \tag{10}$$

Because the quantity Q_k is filtered on the phase interface, the appropriate jump condition can be applied to relate conditionally surface filtered quantities in one phase to those in the other phase. For a given application these phase-coupling terms are known in the volume-averaged LES context and can be substituted directly for the surface averaged terms $\overline{(Q_1)_s}$, $\overline{(\rho_1)_s}$ [17].

4 Volumetric inter-phase conversion

The last term on the r.h.s. of Eq. (3) is the conditionally surface filtered inter-phase conversion term, $\Pi_1(\mathbf{x}, t)$. Physically $\Pi_1(\mathbf{x}, t)$ tracks how the size of phase

1 changes in response to changes in the size of phase 2 due to momentum transfer between phases, when compressibility of one or both phases are important, and mass and/or energy transfer between phases due to evaporation, condensation or chemical reaction in general. The evolution of Π_k is determined by requiring the streamline derivative of the phase indicator function, ϕ_k, to balance inter-phase transition, yielding [1]

$$\Pi_k(\mathbf{x},t) = \frac{\partial \phi_k}{\partial t} + \mathbf{v}_k \cdot \nabla \phi_k. \tag{11}$$

Previous work has attributed Π_k to coalescence and break-up for a discrete dispersed liquid droplet phase, and subsequently disregarded when the dispersed phase is dilute [18]. Specification of this term and conditions under which it may be disregarded frequently leads to confusion in the multiphase flow literature and is important in this context due to the inclusion of the $\langle \Pi_k|_{\gamma=0-} \rangle$ term in Eq. (3). To develop this argument the standard ansatz is to begin with an assumed conservation equation for the dispersed phase droplet number density, $f(V,\mathbf{x},t)$,

$$\frac{\partial f}{\partial t} + \nabla \cdot (f \mathbf{v}_d) = \frac{df}{dt}\Big|_c + \frac{df}{dt}\Big|_b. \tag{12}$$

Here $f(V,\mathbf{x},t)dVd^3x$ is the probability of finding a droplet with volume between V and $V+dV$ within $d\mathbf{x}$ of $\mathbf{x}$ and $\mathbf{v}_d$ is the velocity associated with droplets of volume V [18]. The total derivatives on the r.h.s. of Eq. (12) correspond to the rate of change of the number of droplets due to coalescence and breakup. In writing this equation it is assumed that if two droplets coalesce or breakup, the original volume of the droplets is conserved and it is the droplet number density that changes. One may multiply Eq. (12) through by V_1/n_1 where $n_1(\mathbf{x},t) = \int_\infty dV f(V,\mathbf{x},t)$ is the droplet number density in phase 1, and integrate over the entire flow domain to obtain,

$$\frac{\partial \theta_1}{\partial t} + \nabla \cdot (\theta_1 \mathbf{v}_1) = n_1 \int_\infty dV \frac{V_1}{n_1} \Big[\frac{df}{dt}\Big|_c + \frac{df}{dt}\Big|_b \Big]. \tag{13}$$

The volume fraction shown in Eq. (13) is given in terms of the droplet PDF via,

$$\theta_1(\mathbf{x},t) = \int_\infty dV V_1 f(V,\mathbf{x},t) = \overline{V_1} n_1(\mathbf{x},t) \tag{14}$$

where $\overline{V_1} = \int_\infty dV f(V,\mathbf{x},t) V/n_1$. Recalling the relationship between the local instantaneous void fraction, ϕ_k, and the volume fraction, θ_k: $\theta_1 = \langle \phi_1 \rangle$, $\theta_2 = 1 - \theta_1$, one may filter Eq. (11) and compare to Eq. (13). Then, the reason for disregarding Π_k is evident: if the droplets are sufficiently dispersed that there are no coalescence or breakup processes to alter the number density in the droplet phase, the r.h.s. of Eq. (13) vanishes. However, Eq. (14) shows directly that the number density alone does not sufficiently describe the inter-phase conversion state as conservation of overall droplet phase volume implied in this development does not hold. Droplets may change volume by virtue of evaporation, condensation or

chemical reaction (*e.g.* combustion). It is not clear then that Π_k should be disregarded, in general, if there is no coalescence or breakup in a given reactive flow. However, it is clear that if the volume of the dispersed phase is much less than that of the carrier phase, *i.e.* low mass loading, one may safely disregard Π_k because the mass exchange between phases is negligible. Under these conditions, the modeled marginal TVSFDF transport equation given in Eq. (3) is a homogeneous Fokker-Planck equation. The homogeneous Fokker-Planck equation admits an equivalent system of stochastic differential equations (SDE) that may be solved in lieu of solving the high dimensional PDF/FDF partial differential transport equation directly [13]. For cases where Π_k cannot be disregarded, the non-homogeneous term creates additional complexities when developing a system of equivalent SDE's. It is therefore advantageous to disregard Π_k for numerical solution reasons but one must carefully consider the validity of this assumption for any given new application.

5 Conclusions

A full two-phase velocity-scalar filtered density function formulation for LES of a separated two-phase flow has been developed recently and is summarized. In contrast to single phase FDF formulations, conditional averages must be separated by phase. This separation leads mathematically to a decomposition yielding unclosed terms conditionally filtered within the fluid phase and on the phase interface. Three types of unclosed terms are identified: conditional dissipation terms conditioned within the fluid phase, $\gamma < 0-$, phase-coupling terms conditioned on the phase interface, $\gamma = 0-$, and interphase conversion terms also conditioned on $\gamma = 0-$. Applying standard closures for single phase FDF formulations to terms conditionally filtered within the fluid phase, $\gamma < 0-$, leaves only conditionally surface filtered terms, accounting for phase coupling, unclosed. Conditionally surface filtered terms can be expressed mathematically in terms of surface averaged terms arising in the volume averaged formulation of the field equations for LES. Consequently, phase coupling models used in volume averaged equations for two-phase LES can be applied directly in the two-phase FDF context to close these terms. It is also shown that the remaining unclosed term representing interphase conversion may be disregarded if the mass loading in the dispersed phase is sufficiently low.

References

[1] Carrara, M. & DesJardin, P., A filtered density function approach for modeling separated two-phase flows for LES I: Mathematical formulation. *Int J of Multiphase Flow*, 2005. In revision.

[2] Minier, J. & Peirano, E., The pdf approach to turbulent polydisperse two-phase flows. *Physics Reports*, **352**, pp. 1–214, 2001.

[3] Zhou, X.Y. & Pereira, J.C.F., Large eddy simulation (2d) of a reacting plane mixing layer using filtered density function closure. *Flow, Turbulence and*

Combustion, **64**, pp. 279–300, 2000.
[4] Zhu, M., *Modeling and Simulation of Spray Combustion with PDF Methods*. Ph.D. Thesis, University of Cambridge, Cambridge, 1996.
[5] Pope, S.B., Computations of turbulent combustion: Progress and challenges. *Proceedings of 23rd Symp. (Int.) on Combustion*, The Combustion Institute: Pittsburgh, PA, pp. 591–612, 1990.
[6] Pope, S., *Turbulent Flows*. Cambridge University Press: Cambridge, UK, 2nd edition, 2000.
[7] Givi, P., Model free simulations of turbulent reactive flows. *Prog Energy Combust Sci*, **15**, pp. 1–107, 1989.
[8] Colucci, P.J., Jaberi, F.A., Givi, P. & Pope, S.B., Filtered density function for large eddy simulation of turbulent reacting flows. *Phys Fluids*, **10(2)**, pp. 499–515, 1998.
[9] Givi, P., Subgrid scale modeling in turbulent reacting flows. AIAA Paper AIAA-03-5081, 2003.
[10] Jaberi, F.A., Colucci, P.J., James, S., Givi, P. & Pope, S.B., Filtered mass density function for large eddy simulation of turbulent reacting flows. *J Fluid Mech*, **401**, pp. 85–121, 1999.
[11] Arfkin, G., *Mathematical Methods for Physicists, 3nd edn.* Acedemic Press: New York, 1985.
[12] Kataoka, I., Local instant formulation of two-phase flow. *Int J Multiphase Flow*, **12**, pp. 745–758, 1986.
[13] Pope, S.B., PDF methods for turbulent reacting flows. *Prog Energy Combust Sci*, **11**, pp. 119–192, 1985.
[14] Sheikhi, M.R.H., Drozda, T.G., Givi, P. & Pope, S.B. *Phys Fluids*, pp. 1196–1214.
[15] Gicquel, L., Givi, P., Jaberi, F. & Pope, S., Velocity filtered density function for large eddy simulation of turbulent flows. *Phys Fluids*, **14(3)**, 2002.
[16] Libby, P.A. & Williams, F.A., (eds.) *Turbulent Reacting Flows*, volume 44 of *Topics in Applied Physics*. Springer-Verlag: Heidelberg, 1980.
[17] Sirignano, W., Volume averaging for the analysis of turbulent spray flows. *Int J Multiphase Flow*, **31**, pp. 675–705, 2005.
[18] Drew, D. & Passman, S., *Theory of Multicomponent Fluids*. Springer: New York, 1998.

Application of the two-phase filtered density function approach for LES of a 2D droplet laden turbulent mixing layer

M. D. Carrara & P. E. DesJardin
Department of Mechanical and Aerospace Engineering,
University at Buffalo, The State University of New York, Buffalo, USA

Abstract

In this study, the two-phase velocity-scalar filtered density function transport equation for large eddy simulation is considered in the limit of a continuum-dispersed phase two-phase flow. For a sufficiently small dispersed particulate phase, all quantities conditionally filtered within the dispersed phase may be disregarded leaving only terms conditionally filtered on the phase interface. These conditionally surface-filtered terms account for phase-coupling between the dispersed and continuum phases of the flow. Closure models are presented and implemented for a two-phase system consisting of a water droplet laden 2d temporally developing mixing layer. Marginal FDF transport equations are presented for each phase and a statistically equivalent set of Ito stochastic differential equations (SDE) are derived from each marginal FDF equation. Simulations are conducted via a full stand-alone Lagrangian particle Monte-Carlo method with closure models to account for subgrid scale (SGS) mixing and inter-phase conversion processes. The effect of variable Stokes number on turbulent dispersion of evaporating and non-evaporating droplets is discussed.

1 Marginal FDF transport equations

Two-phase velocity-scalar filtered density function (TVSFDF) methods have recently been developed for large eddy simulation (LES) of separated two-phase flows [1]. In this approach, unclosed terms arise in the marginal FDF transport equations in three classes: quantities conditionally filtered within the phase, quantities conditionally filtered on the phase interface, and inter-phase conversion terms

WIT Transactions on Engineering Sciences, Vol 50, © 2005 WIT Press
www.witpress.com, ISSN 1743-3533 (on-line)

relating changes in volume across the phase interface [1, 2]. The unclosed marginal FDF transport equation for a dispersed phase will be presented in the following section and closures will be supplied for the case of evaporating droplets. In the carrier phase, standard gas field FDF closures are employed. For both phases systems of ordinary and stochastic differential equations are derived from principles of Ito Calculus that are statistically equivalent to the modeled marginal FDF transport equations in each phase.

1.1 Dispersed phase marginal FDF transport equation: evaporating droplets

If the particulate comprising the dispersed phase is sufficiently small with respect to the flow field domain, flow field information within the particulate phase can be disregarded. For this case a Lagrangian description of the dispersed phase is appropriate and consequently, all terms conditionally filtered *within* the dispersed phase may be disregarded, leaving only conditionally surface filtered terms to be modeled. It can be shown that these conditionally surface filtered terms are mathematically equivalent to the phase-coupling terms that arise in more traditional LES formulations for which models are available [1, 2, 3]. The dispersed phase system chosen here consists of a collection of water droplets. The phase-averaged (filtered) equations governing the conservation of mass, energy and momentum for individual droplets can be written as, (see [4] for a detailed derivation)

$$\frac{dm_p}{dt} = \dot{m}_p = -\pi d_p \frac{\mu_g}{Sc_g} B_M Sh_g \tag{1}$$

$$m_p C_{v,p} \frac{dT_p}{dt} = \pi d_p \frac{\mu_g C_{p,g}}{Pr_g} (T_g - T_p) Nu_g + \dot{m}_p L_{vap} \tag{2}$$

$$m_p \frac{d\mathbf{v}_p}{dt} = \frac{\pi}{8} \rho_g d_p^2 C_D \left|\mathbf{v}_g - \mathbf{v}_p\right| \left(\mathbf{v}_g - \mathbf{v}_p\right) + m_p \mathbf{f}_b. \tag{3}$$

In the above equations d_p is the particle diameter, μ_g is the gas phase molecular viscosity, ρ_g is the gas phase mass density, $C_{p,g}$ and $C_{v,p}$ are the gas and particle phase specific heats, Sc_g is the Schmidt number, Sh_g is the Sherwood number and C_D is the coefficient of drag and is approximated for a sphere as $C_D = 24(1 + Re^{2/3}/6)/Re$ for $Re < 1000$ and $C_D = 0.424$ for $Re \geqslant 1000$. $Pr_g = (C_{p,g}\mu_g/k_g)$ is the gas phase Prandtl number, $Sc_g (= \nu_g/Dm_g)$ is the Schmidt number, $B_M (= (Y_s - Y_g)/(Y_p - Y_s))$ is the Spaulding or mass transfer number and $Re_p (= \rho_g d_p |\mathbf{v}_g - \mathbf{v}_p|/\mu_g)$ is the particle Reynolds number. Using using the Ranz-Marshall correction [5] to extend to a convective environment, the Sherwood number, Sh_g is written as, $Sh_g = 2[1 + Re_p^{1/2} Sc_g^{1/3}/3] log(1 + B_M)/B_M$. A unity Lewis number $Le (= Sc_g/Pr_g)$ is taken here so that the Nusselt number, Nu_g, is equal to the Sherwood number. In the Lagrangian description of the dispersed phase, only 'surface averaged' quantities are present as the droplets are described as point particles with diameter describing the location of the surface with respect to the particle center. Therefore, in light of the equivalence between conditionally surface filtered and phase-averaged coupling terms, considering Eqs. (1)-(3) and

applying the principle of equivalent systems [6], the closed marginal FDF transport equation (in the absence of a diffusion process, the FDF transport equation is actually a Liouvelle equation, but the principle of equivalent systems still holds [7]) yields equivalent statistics to the system of ODE's:

$$d\mathbf{X}_p^+ = \mathbf{U}_p^+ dt \tag{4}$$

$$d\mathbf{U}_p^+ = \frac{\pi \rho_g C_D d_p^2}{8 M_p^+} \big| \langle \mathbf{v}_g \rangle - \mathbf{U}_p^+ \big| \big(\langle \mathbf{v}_g \rangle - \mathbf{U}_p^+ \big) dt \tag{5}$$

$$dT_p^+ = \frac{\pi d_p \mu_g C_{p,g}}{M_p^+ Pr_g C_{v,p}} \big(\langle T_g \rangle - T_p^+ \big) Nu_g dt - \dot{M}_p^+ L_{vap} dt \tag{6}$$

$$dM_p^+ = -\frac{d_p \pi \mu_g B_M}{Sc_g} Sh_g dt \tag{7}$$

In the above equations the super script "+" is written to distinguish between random variables, Ψ^+, and physical variables, ψ. As can be seen above the droplet phase equations are coupled directly to the gas phase momentum and energy in Eqs. (5) and (6) respectively, and indirectly coupled to gas phase momentum through the Reynolds number, and hence the Sherwood number, Nusselt number, and coefficient of drag.

1.2 Gas phase marginal FDF transport equation

Filtered density function methods for single phase reactive flows are fairly well developed and closure models for all terms conditionally filtered within the gas phase $\gamma < 0-$ exist in the single phase case [8, 9]. As a first step these models, namely the generalized Langevin model (GLM) and linear mean square estimation (LMSE) model, will be applied to the gas phase leaving only conditionally surface filtered phase-coupling terms unclosed in the gas phase marginal FDF equation (see ref. [3]). In this equation conditionally averaged quantities at the phase interface require closure. Employing mass, momentum, energy and species mass fraction conservation across the phase interface, the unclosed terms can be modeled as follows:

$$\frac{\partial}{\partial T_g^+} \Big[\langle \frac{k_g}{\rho_g} \nabla T_g^I \cdot \mathbf{e}_{n,g}^I a^I \Big|_{\gamma=0-} \rangle \Big] = -\frac{\partial}{\partial T_g^+} \Big[\frac{\pi N_p k_g \langle r_p \rangle L_{vap}}{\Delta_f^3 \theta_g C_{v,p}} log(1 + B_M) \Big]$$
$$- \frac{\partial}{\partial T_g^+} \Big[\frac{\pi N_p \langle r_p \rangle C_{p,g}}{2 \Delta_f^3 \theta_g C_{v,p} Pr_g} (T_g^+ - \langle T_p \rangle) Nu \Big] \equiv \frac{\partial}{\partial T_g^+} \Big[S_T \Big] \tag{8}$$

$$\frac{\partial}{\partial \mathbf{u}_g}\Big[\langle\frac{1}{\rho_g}P_g^I\mathbf{e}_{n,g}^I a^I\Big|_{\gamma=0^-}\rangle F_L^g + \langle\frac{1}{\rho_g}\underset{\sim}{\boldsymbol{\tau}}_g{}^I\cdot\mathbf{e}_{n,g}^I a^I\Big|_{\gamma=0^-}\rangle F_L^g\Big]$$
$$= -\frac{\partial}{\partial \mathbf{u}_g}\Big[\frac{\langle A_p\rangle^2 C_D N_p}{8\Delta_f^3\theta_g}\Big|\mathbf{u}_g - \langle\mathbf{v}_p\rangle\Big|\big(\mathbf{u}_g - \langle\mathbf{v}_p\rangle\big)$$
$$- \frac{\pi\langle r_p\rangle N_p K_g}{\Delta_f^3\theta_g C_{v,p}} log(1+B_M)\Big] \equiv \frac{\partial}{\partial \mathbf{u}_g}\Big[\mathbf{S}_U\Big] \quad (9)$$

$$\frac{\partial}{\partial Y_{a,g}^+}\Big[\langle\frac{D_{m,g}}{\rho_g}\nabla Y_{a,g}^I\cdot\mathbf{e}_{n,g}^I a^I\Big|_{\gamma=0-}\rangle\Big] =$$
$$- \frac{\partial}{\partial Y_{a,g}^+}\Big[\frac{\pi N_p\langle r_p\rangle}{\Delta_f^3\theta_g}\frac{\mu_g}{\rho_g Sc_g}B_M Sh_g\big(Y_{a,g}^+ - 1\big)\Big] \equiv \frac{\partial}{\partial Y_{a,g}^+}\Big[S_Y\Big] \quad (10)$$

where θ_g is the gas phase volume fraction, Δ_f is the LES filter width, N_p is the number of physical droplets and $\langle r_p\rangle$ is the average particle radius within a filtering volume Δ_f^3, and $\langle A_p\rangle = 4\pi\langle r_p\rangle^2$. Using these closures for the phase coupling terms and the GLM and LMSE models noted above, the principle of equivalent systems yields the following set of coupled nonlinear stochastic differential equations (SDE) for the gas phase:

$$d\mathbf{X}_g^+ = \mathbf{U}_g^+ dt \quad (11)$$

$$d\mathbf{U}_g^+ = \Big[\nabla\langle P_g\rangle + 2\nu_g\nabla^2\langle\mathbf{v}_g\rangle + \underset{\sim}{\mathbf{G}}\cdot\big(\mathbf{U}_g^+ - \langle\mathbf{v}_g\rangle\big)\Big]dt$$
$$+\sqrt{2\nu_g}\nabla\otimes\langle\mathbf{v}_g\rangle\cdot d\mathbf{W}^X + \sqrt{C_o\epsilon}d\mathbf{W}^U + \mathbf{S}_U dt \quad (12)$$

$$dT_g^+ = -C_\phi\Omega_m\big(T_g^+ - \langle T_g\rangle\big)dt + S_T dt \quad (13)$$

$$dY_{a,g}^+ = -C_\phi\Omega_m\big(Y_{a,g}^+ - \langle Y_{a,g}\rangle\big)dt + S_Y dt \quad (14)$$

where, $\underset{\sim}{\mathbf{G}} = -\omega(1/2 + 2C_o/3)\underset{\sim}{\mathbf{I}}$, $\omega = \epsilon/k$ is the turbulent mixing frequency, and $\Omega_m = C_\phi\omega$. The turbulent dissipation and turbulent kinetic energy are given by $\epsilon = C_\epsilon k^{3/2}/\Delta_f$ and $k = 1/2(\langle\mathbf{v}_g\cdot\mathbf{v}_g\rangle - \langle\mathbf{v}_g\rangle\cdot\langle\mathbf{v}_g\rangle$ respectively. The parameters C_o, C_ϵ and C_ϕ are modeling constants that must be specified [9]. The system of equations given by Eqs. (4)-(7) and (11)-(14) are fully closed and describe the two-phase flow of a turbulent gas fully coupled to a dilute dispersed particulate phase.

2 Problem setup – solution methodology

The problem considered here is that of a two-phase flow consisting of water droplets seeded in a 2D temporally developing mixing layer. The domain size is $0.28m$ by $0.28m$ where in the upper gas stream, $U_{max} = 0.65m/s$ with $T_g = 365K$ and in the lower gas stream $U_{min} = -0.65m/s$ with $T_g = 300K$. Droplets are

seeded uniformly and initially at rest in the lower stream with initial temperature $T_p = 300K$. Three droplet diameters of 50, 450 and $3000\mu m$ are considered corresponding to dispersed phase Stokes numbers (ST) of 0.017, 1.2 and 62, respectively. The mass loading (ML) is 0.0225 in all cases. Numerical solution of the modeled marginal FDF transport equations is obtained by a Lagrangian Monte-Carlo procedure. For simulations, each marginal FDF is represented by N_p statistically identical notional Monte-Carlo particles whose time evolution is governed by the appropriate set of ODE/SDE's; Eqs. (4)-(7) for the droplet field and Eqs. (11)-(14) for the gas. Each particle contains information about its position, velocity and scalar value for both droplet and gas phases. Statistical field information is estimated from the particle properties by a non-parametric kernel estimation method based on linear basis functions [10]. The computational domain is 51 by 51 with 302,500 Monte-Carlo particles for each phase resulting in ensemble sizes of 121 realizations and 242 realizations for the gas and droplet phases, respectively. The initial shear layer thickness is 2% of the maximum y dimension and the initial velocity distribution is a hyperbolic tangent profile where small harmonic phase shifted disturbances containing sub-harmonics of the most unstable mode are utilized to facilitate formation of large scale roller structures.

3 Results: droplets evaporating in a mixing layer

Results are presented for water droplets one-way coupled to the carrier gas; thus, gas phase coupling terms are zero, however, droplets are directly coupled to gas field properties. Figure 1 shows a snap shot of droplet temperature contours superimposed with droplet number density isolines for $St = 0.017$ at $t = 0.35sec.$ As the roller structure grows, hot gas is entrained into the droplet stream while individual droplets are centrifuged out of the region of high vorticity, coinciding with the roller center, and congregate in regions of high shear. This trend is in qualitative agreement with previous DNS studies of droplet laden temporally developing mixing layers [11].

Two different types of dispersion are analyzed in Figs. 2-4; termed here 'Dispersion 1' and 'Dispersion 2'. Dispersion 2 is a measure of dispersion of the droplets from their initial seeding location and is therefore given as, $\sum^{Np}[(Xp^+(t) - Xp^+(t_o))^2 + (Yp^+(t) - Yp^+(t_o))^2]/Np$. Dispersion 1 is a measure of dispersion of the droplets from spanning one time step in the calculation for each data point. Thus, Dispersion 1 is calculated as $\sum^{Np}[(Xp^+(t+\delta t) - Xp^+(t))^2 + (Yp^+(t+\delta t) - Yp^+(t))^2]/Np$. Figure 2 shows Dispersion 2 as a function of time for evaporating and non-evaporating droplets. Droplets with smaller Stokes number respond faster to the gas phase momentum, and consequently are dispersed farther up to approximately $t = 0.1sec.$. The sinusoidal nature of the curves for $St = 0.017$ and $St = 1.2$ droplets reflect the fact that droplets are carried circularly following the large scale roller structure of the gas phase as shown in Fig. 1. The $St = 62$ droplets are sufficiently large that they are insensitive to the large scale roller structure of the flow and only respond to the bulk flow of the gas over the time scale presented.

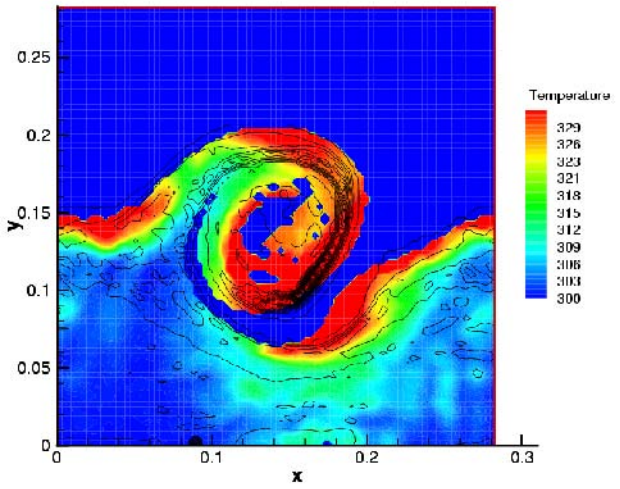

Figure 1: Droplet number density and temperature contour, t=0.35 sec.

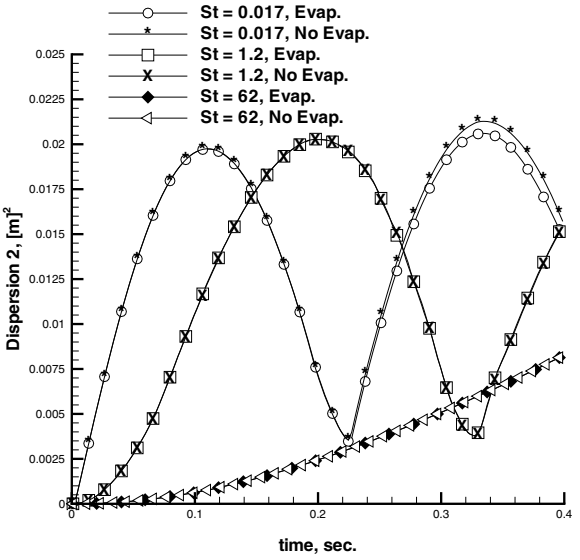

Figure 2: Dispersion 2 vs. time for evaporating and non-evaporating droplets.

Figure 2 also shows that evaporation has an effect on transient droplet dispersion only for the $St = 0.017$ case. Droplet lifetimes, τ_d, can be estimated based on their initial diameter: $\tau_d = d_{p,o}^2/\lambda$ with $\lambda = 8k_g log(B_T + 1)/(\rho_d C_{p,g})$ with B_T estimated as $B_T = C_{p,g}(T_{\infty,g} - T_s)/L_{vap}$ where the thermal transfer number,

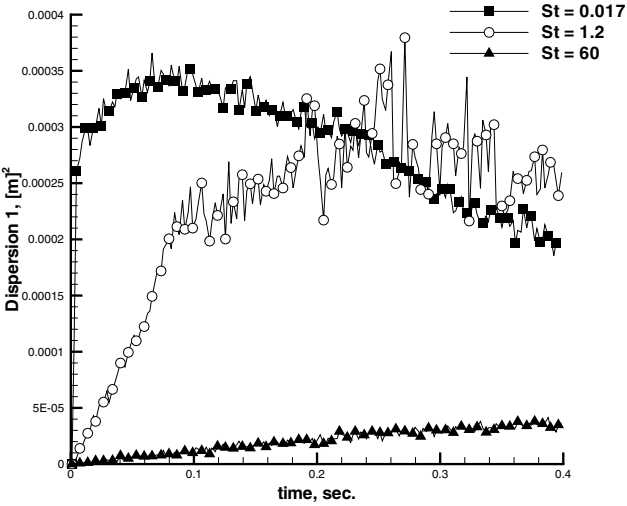

Figure 3: Dispersion vs. time for evaporating droplets.

B_T, is equal to the mass transfer number, B_q, in this case because the Lewis number is taken to be unity. The surface temperature, T_s is estimated as the steady-state temperature on the surface during evaporation. Droplet lifetimes for the droplets in direct contact with the high temperature gas stream are, form smallest to largest, $\tau_d \approx \{4 \times 10^{-3} sec., 0.19 sec., 8.5 sec.\}$, respectively. Based on these estimates, it is clear that the effects of evaporation will have only a pronounced effect on the smallest droplets over the $0.4 sec.$ time period considered. Figure 3 shows Dispersion 1 as a function of time for variable Stokes number for evaporating droplets. The droplet relaxation time τ_V, $(= \rho_p d_p^2/(18\mu_g)$ for the $St = 0.017$ droplets is $1.6 \times 10^{-4} sec.$, thus the smaller droplets adjust faster to the flow momentum and are readily accelerated due to their small inertial mass. This is evidenced in Fig. 3 by immediate increase in dispersion from $t = 0$ and subsequently by the observation that it takes few time steps for the $St = 0.017$ droplets to respond to fluctuations in the momentum field due to turbulence.

For the $St = 1.2$ case, the droplets are small enough to respond to changes in the gas flow field, but their larger inertial mass requires more time to respond to rapid fluctuations. Once the droplets start moving in a given direction their course is subsequently altered only after several time steps in the calculation, resulting in the large observed spatial fluctuations. For $St = 62$, the droplets are sufficiently large that they follow a ballistic trajectory and are insensitive to all but the largest fluid motion. Figure 4 shows the transient dispersion for the $St = 0.017$ case with and without evaporation. Differences in the transient dispersion only appear after sufficient time has passed to allow evaporation to have an appreciable effect, resulting in a decrease in the spatial fluctuations.

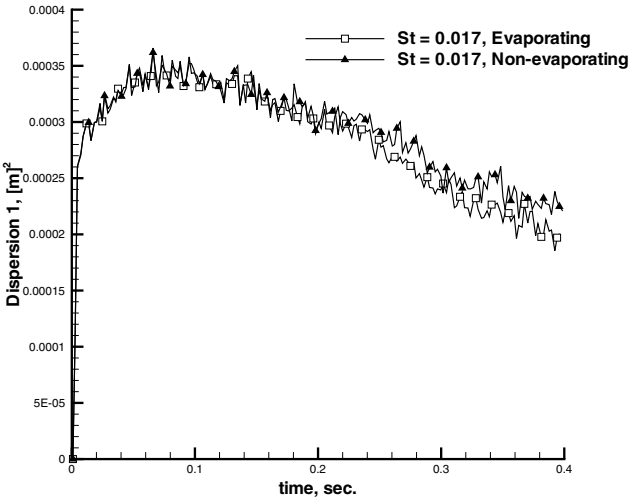

Figure 4: Dispersion vs. time for evaporating and non-evaporating droplets with $St = 0.017$.

4 Conclusions

A two-phase filtered density function method for LES has been applied to a separated two-phase flow of dispersed water droplets immersed in a 2D temporally developing turbulent mixing layer. Closures of gas field terms in the marginal gas phase FDF are taken from single phase FDF theory while closures for phase coupling terms in both the droplet and gas phases are developed. Two different measures of dispersion have been analyzed for three different Stokes numbers for evaporating as well as non-evaporating droplets. It is shown that the dispersion of the droplets increases with decreasing droplet size with local droplet fluctuations being largest when the Stokes number is near unity.

References

[1] Carrara, M. & DesJardin, P., A filtered density function approach for modeling separated two-phase flows for LES I: Mathematical formulation. *Int J of Multiphase Flow*, 2005. In revision.

[2] Carrara, M. & DesJardin, P., On subgrid scale modeling of reactive droplets using probability density function methods. AIAA paper AIAA-05-1426, 2005.

[3] Carrara, M. & DesJardin, P., Formluation of a two-phase filtered density function approach for large eddy simulation. Multiphase Flow 2005 WIT Press, 2005.
[4] Crowe, C., Sommerfeld, M. & Tsuji, Y., *Multiphase Flows with Droplets and Particles*. CRC Press: New York, NY, 1998.
[5] Ranz, W.E. & Marshall, W.R., Evaporation from drops. *Chem Engrg Prog*, **48(3)**, pp. 141–173, 1952.
[6] Pope, S.B., PDF methods for turbulent reacting flows. *Prog Energy Combust Sci*, **11**, pp. 119–192, 1985.
[7] Gardiner, C., *Handbook of Stochastic Methods*. Springer: New York, 1982.
[8] Colucci, P.J., Jaberi, F.A., Givi, P. & Pope, S.B., Filtered density function for large eddy simulation of turbulent reacting flows. *Phys Fluids*, **10(2)**, pp. 499–515, 1998.
[9] Gicquel, L., Givi, P., Jaberi, F. & Pope, S., Velocity filtered density function for large eddy simulation of turbulent flows. *Phys Fluids*, **14(3)**, 2002.
[10] Dreeben, T. & Pope, S., Non-parametric estimation of mean fields with application to particle methods for turbulent flows. Cornell Technical Report FDA 92-13, Cornell University, Ithaca, NY, 1992.
[11] Miller, R. & Bellan, J., Direct numerical simulation of a confined 3d gas mixing layer with one evaporting hydrocarbon-droplet-laden stream. *J Fluid Mech*, **384**, pp. 293–338, 1999.

This page intentionally left blank

Section 10
Finite volumes

This page intentionally left blank

A linearly semi-implicit AMR method for 1D gas-liquid flows

N. Andrianov[1], F. Coquel[2], M. Postel[2] & Q.-H. Tran[1]
[1] *Institut Français du Pétrole, Rueil-Malmaison, France*
[2] *Université Paris VI, France*

Abstract

We consider a drift-flux model for the numerical solution of 1D gas-liquid flows in pipes. The model is given by a set of conservation laws, consisting of two continuity equations for the two phases, and a single momentum equation for the mixture. The model is closed by providing a slip law, i.e., an empirical relation between the velocities of two phases. There are two principal issues concerning the numerical solution of the model. Firstly, for certain slip laws, the model is not hyperbolic. Secondly, there are two very different time scales in the problem: the slow one, related to the transport, and the fast one, related to propagation of acoustic waves. In practical applications, the precise resolution of the fast scale is not important. We employ a relaxation method to deal with potential non-hyperbolicity of the model. In order to account for the different time scales of the model, we use a linearly semi-implicit version of the scheme. Furthermore, we apply the resulting finite volume scheme on a dynamically adaptive grid. This allows us to obtain a significant acceleration of the computation.
Keywords: finite volumes, adaptive mesh refinement, relaxation, drift-flux model, slug flow.

1 Introduction

We consider a two-phase, two-component flow of oil and gas in the pipelines during the offshore oil production. Since the pipeline is typically laid on the sea bottom, the pipeline slope is in general not constant. The change of the slope can lead to the formation of the *slug flow*, which is characterized by abrupt changes in the flow velocity, pressure, etc. The flow becomes highly unsteady, which is undesirable for the oil production. Given the pipeline geometry, the task of the mathematical modeling is to predict the resulting flow regime.

To this goal, we employ a one-dimensional *drift-flux* model, which consists of two continuity equations for the two phases, and a momentum equation for the mixture. The gravity and friction are represented by the source terms. The system of equations is closed by an empirical *slip law*, which gives the difference of phase velocities as a function of the state variables.

It appears to be difficult to solve the resulting system of equations directly: due to complexity of the slip law one cannot provide its characteristic analysis. Also, at the practical implementation, each call to the slip law function appears to be very expensive computationally. To avoid these problems, we employ a relaxation method of Baudin *et al.* [1].

In our applications it is necessary to compute the two-phase transport accurately, whereas the acoustic waves propagation is less important. Since the typical flow velocity is several orders of magnitude slower than the speed of propagation of the acoustic waves, we have to deal with very different time scales of the problem. To address this issue numerically, we employ a *semi-implicit* version of the relaxation method.

In the slug flow simulation, one is typically interested in the accurate representation of the material front. Therefore, it is necessary to use a fine computational mesh in the neighborhood of the front. However, using the same fine mesh everywhere in the domain becomes prohibitively expensive computationally. To deal with this dilemma, we use an adaptive mesh refinement (AMR) technique of Cohen *et al.* [2]. With its help, we obtain up to three-fold acceleration of the calculation, compared to that on the fine mesh everywhere in the domain.

The paper is organized as follows. In Section 2 we present the drift-flux model and discuss its mathematical properties. In Section 3 we present the relaxation method. In Section 4 we provide some details about the AMR algorithm. Finally, Section 5 contains numerical results.

2 The drift-flux model

Denote the phases by the subscripts l (liquid) and g (gas). For $k = l, g$, denote the phase densities by ρ_k, the fraction surfaces (the part of the pipeline cross-section, occupied by the phase k) by R_k, and the velocities by v_k. We suppose the pressure equilibrium between the two phases, $p_l = p_g =: p$. Consider the mixture density $\rho := \rho_l R_l + \rho_g R_g$, the mass fractions $X := \rho_l R_l/\rho$, $Y := \rho_g R_g/\rho$, the mixture velocity $v := Xv_l + Yv_g$, the liquid mass flow $q_l := \rho_l R_l v_l$, and the gas mass flow $q_g := \rho_g R_g v_g$. We have obviously $R_l + R_g = 1$, $X + Y = 1$, $R_{l,g}, X, Y \in [0, 1]$.

The pipeline is characterized by its length L and diameter D. In this work, we only consider the *plane* pipelines, i.e., the geometry of the pipeline is determined by the angle $\theta = \theta(x)$, where the x-axis is oriented along the pipeline. Assuming that $D \ll L$, we can consider the flow as one-dimensional.

The system of governing equations reads

$$\begin{aligned} \rho_t + (\rho v)_x &= 0 \\ (\rho Y)_t + (\rho Y v - \sigma)_x &= 0 \\ (\rho v)_t + (\rho v^2 + P)_x &= -\rho g \sin\theta - C\rho v|v|. \end{aligned} \tag{1}$$

Here $C = 2C_f/D$, C_f is the friction coefficient,

$$\sigma = \rho Y(1-Y)\phi, \quad P = p + \rho Y(1-Y)\phi^2, \tag{2}$$

and the function $\phi = \phi(\rho, Y, v) := v_l - v_g$ is given by the slip law (see below).

We assume that the flow is isothermal. We use the ideal gas equation of state for the gas,

$$\frac{p}{\rho_g} = a_g^2 = \text{const}, \tag{3}$$

where a_g is the constant gas sound speed. The equation of state for the liquid is

$$\frac{p - p^0}{\rho_l - \rho_l^0} = a_l^2 = \text{const}, \tag{4}$$

where p^0 is the atmospheric pressure, ρ_l^0 is the liquid density at $p = p^0$, and a_l is the constant liquid sound speed. If the liquid is incompressible, $\rho_l = \rho_l^0$ and $a_l \to \infty$.

The hydrodynamic closure is given by the slip law. In this work, we use the law of Zuber and Findlay [3]

$$\phi = -\frac{(1-c_0)v - c_1}{c_0 b + 1 - Y}, \tag{5}$$

with $c_0 = 1.07$, $c_1 = 0.2162$ and $b = (1-Y)(\rho/\rho_l - 1)$. One can show that the system (1), closed with the law (5), is hyperbolic with the characteristic speeds of the form

$$c^- = \hat{v} - a_m, \quad c^0 = v_g, \quad c^+ = \hat{v} + a_m, \tag{6}$$

where $\hat{v} = (1-\delta)v_l + \delta v_g$ and a_m is the mixture sound speed. Physically, $a_m \gg \hat{v}$ so that $c^- < 0$, $c^+ > 0$. Similar to the case of the Euler equations, the *fast* characteristic speeds c^- and c^+ are associated with the acoustic waves, whereas the *slow* speed c^0 is associated with the transport. In our applications we are mainly interested in the accurate resolution of the slow waves, since they correspond to the movement of material interfaces.

Note that the Zuber–Findlay law (5) is not valid in case of pure phases $Y = 0$ and $Y = 1$. In these cases we will use the modified Zuber–Findlay law

$$\phi = -\frac{\mu v + \nu}{1 + \mu b}, \tag{7}$$

with $\mu = 0.2 \sin\theta$, $\nu = 0.35\sqrt{gD}\sin\theta$. Due to relative complexity of the law (7), it is impossible to provide the characteristic analysis of the system (1), closed with the law (7).

The flow in the pipeline is governed by the boundary conditions. At the entrance of the pipeline $x = 0$, we impose the mass flows for the liquid and for the gas. $q_g == q_g(t)$, $q_l = q_l(t)$. At the exit $x = L$, we impose the pressure $p := \bar{p}(t)$. Note that the boundary conditions depend on time.

3 The relaxation method

We approach the solutions of the original system (1) by the solutions of the *relaxation system*

$$\mathbf{u}^\epsilon_t + \mathbf{f}(\mathbf{u}^\epsilon)_x = \frac{1}{\epsilon}\mathbf{s}_{\text{rel}}(\mathbf{u}^\epsilon) + \mathbf{s}(\mathbf{u}^\epsilon), \tag{8}$$

where

$$\mathbf{u} = \begin{bmatrix} \rho \\ \rho Y \\ \rho v \\ \rho \Pi \\ \rho \Sigma \end{bmatrix}, \qquad \mathbf{f}(\mathbf{u}) = \begin{bmatrix} \rho v \\ \rho Y v - \Sigma \\ \rho v^2 + \Pi \\ \rho \Pi v + a^2 v \\ \rho \Sigma v - b^2 Y \end{bmatrix}, \tag{9}$$

$$\mathbf{s}_{\text{rel}} = \begin{bmatrix} 0 \\ 0 \\ 0 \\ P(\mathbf{u}) - \Pi \\ \sigma(\mathbf{u}) - \Sigma \end{bmatrix}, \qquad \mathbf{s}(\mathbf{u}) = \begin{bmatrix} 0 \\ 0 \\ -\rho g \sin\theta - C\rho v|v| \\ 0 \\ 0 \end{bmatrix}. \tag{10}$$

Here $P = P(\rho, Y, v)$, $\sigma = \sigma(\rho, Y, v)$ are given by eqns (2), ϵ is the *relaxation parameter*, and a, b are the *relaxation coefficients*. Under certain conditions on a and b, we have $\Pi \to P$ and $\Sigma \to \sigma$ as $\epsilon \to 0$, so the relaxation system (8) reduces to the original system (1), see Baudin *et al.* [1].

The advantage of considering the system (8) instead of (1) is that the mathematical structure of (8) appears to be quite simple. In particular, the system (8) is strictly hyperbolic. Analogous to (6), we can distinguish between the slow transport waves and the fast acoustic waves of (8). For the homogeneous part of (8) (i.e., without the source terms (10)), we can also solve the Riemann problem for (8) (i.e. the initial-value problem with piecewise constant initial data) *exactly*, see Baudin *et al.* [1]. Therefore, we can use Godunov's method for the numerical solution of (8).

Consider a computational mesh in the domain $[0, L]$, consisting of cells j with mesh sizes Δx_j, $j = 1, \ldots, N$. In general, the mesh sizes Δx_j can be different. We will describe the construction of the mesh in Section 4. Denote by $\mathbf{u}^n_j$ the average values at the mesh cell j at time t^n, $j = 1, \ldots, N$. The values at the left and right of the cell interface $j + 1/2$ are denoted by $\mathbf{u}^{n,\mp}_{j+1/2}$. They are obtained from the average values $\mathbf{u}^n_j$ using a modified MUSCL approach, so that the resulting scheme will be of second order. The time step Δt is the same for all cells.

The homogeneous part of (8) is solved as follows. We consider an implicit formulation of the Godunov method for the homogeneous part of (8),

$$\mathbf{u}^{n+1}_j := \mathbf{u}^n_j - \frac{\Delta t}{\Delta x_j}\left[\mathbf{f}(\mathbf{u}^*(\mathbf{u}^{n+1,-}_{j+1/2}, \mathbf{u}^{n+1,+}_{j+1/2})) - \mathbf{f}(\mathbf{u}^*(\mathbf{u}^{n+1,-}_{j-1/2}, \mathbf{u}^{n+1,+}_{j-1/2}))\right], \tag{11}$$

for $j = 1, \ldots, N$. Here $\mathbf{f}(\mathbf{u})$ is given by (9), and $\mathbf{u}^*(\mathbf{u}^{n,-}_{j+1/2}, \mathbf{u}^{n,+}_{j+1/2})$, $j = 0, \ldots, N$, represents the exact solution to the Riemann problem with initial data $\mathbf{u}^{n,-}_{j+1/2}$ et $\mathbf{u}^{n,+}_{j+1/2}$. The Taylor expansion for the Godunov flux $\mathbf{f}(\mathbf{u}^*(\mathbf{u}^{n,-}_{j+1/2}, \mathbf{u}^{n,+}_{j+1/2}))$ gives

$$\mathbf{f}(\mathbf{u}^*(\mathbf{u}^{n+1,-}_{j+1/2}, \mathbf{u}^{n+1,+}_{j+1/2})) = \mathbf{f}(\mathbf{u}^*(\mathbf{u}^{n,-}_{j+1/2}, \mathbf{u}^{n,+}_{j+1/2})) + \nabla\mathbf{f}_{j+1/2}\delta\mathbf{u}^-_{j+1/2} + \nabla\mathbf{f}_{j+1/2}\delta\mathbf{u}^+_{j+1/2}, \qquad j = 0, \ldots, N, \quad (12)$$

with $\delta\mathbf{u}^{\pm}_{j+1/2} := \mathbf{u}^{n+1,\pm}_{j+1/2} - \mathbf{u}^{n,\pm}_{j+1/2}$. In order to calculate the Jacobians in (12), we interpret the Godunov flux as a Roe flux,

$$\mathbf{f}(\mathbf{u}^*(\mathbf{u}^{n,-}_{j+1/2}, \mathbf{u}^{n,+}_{j+1/2})) = \mathbf{F}(\mathbf{u}^{n,-}_{j+1/2}, \mathbf{u}^{n,+}_{j+1/2}) := \frac{1}{2}\left[\mathbf{f}(\mathbf{u}^{n,-}_{j+1/2}) + \mathbf{f}(\mathbf{u}^{n,+}_{j+1/2}) - |\mathbf{A}_{j+1/2}|(\mathbf{u}^{n,+}_{j+1/2} - \mathbf{u}^{n,-}_{j+1/2})\right], \quad (13)$$

where $\mathbf{A}_{j+1/2} = \mathbf{R}_{j+1/2}\mathbf{\Lambda}_{j+1/2}\mathbf{R}^{-1}_{j+1/2}$ is the Roe matrix, $\mathbf{R}_{j+1/2}$ is the matrix of its right eigenvectors, and $\mathbf{\Lambda}_{j+1/2}$ contains the corresponding eigenvalues on the main diagonal and zeros elsewhere. Using (13), we calculate the Jacobians in (12) as

$$\begin{aligned} \frac{\partial\mathbf{F}(\mathbf{u}^{n,-}_{j+1/2}, \mathbf{u}^{n,+}_{j+1/2})}{\partial\mathbf{u}^{n,-}_{j+1/2}} &= \frac{1}{2}\left[\nabla\mathbf{f}(\mathbf{u}^{n,-}_{j+1/2}) + |\mathbf{A}_{j+1/2}|\right] \\ \frac{\partial\mathbf{F}(\mathbf{u}^{n,-}_{j+1/2}, \mathbf{u}^{n,+}_{j+1/2})}{\partial\mathbf{u}^{n,+}_{j+1/2}} &= \frac{1}{2}\left[\nabla\mathbf{f}(\mathbf{u}^{n,+}_{j+1/2}) - |\mathbf{A}_{j+1/2}|\right]. \end{aligned} \quad (14)$$

For the semi-implicit version of the relaxation method, we rewrite the Jacobians in (14) as

$$\nabla\mathbf{f}(\mathbf{u}^{n,\pm}_{j+1/2}) = \mathbf{R}^{\pm}_{j+1/2}\mathbf{\Lambda}^{\pm}_{j+1/2}\left(\mathbf{R}^{\pm}_{j+1/2}\right)^{-1}, \quad (15)$$

where $\mathbf{\Lambda}^{\pm}_{j+1/2}$ and $\mathbf{R}^{\pm}_{j+1/2}$ are the matrices of right eigenvectors and corresponding eigenvalues of $\mathbf{f}'(\mathbf{u})^{n,\pm}_{j+1/2}$. The semi-implicit version of the scheme consists in replacing the eigenvalues in $\mathbf{\Lambda}_{j+1/2}$ and $\mathbf{\Lambda}^{\pm}_{j+1/2}$, corresponding to the transport waves, by zeros. This amounts in solving the slow transport waves explicitly, and the fast acoustic waves — implicitly. The motivation for this approach comes from the linear case, see [1] for details.

Using (13), we substitute (14) in (12). Assuming $\delta\mathbf{u}^+_{j-1/2} := \delta\mathbf{u}_j$, $\delta\mathbf{u}^-_{j+1/2} := \delta\mathbf{u}_j$ for $j = 1, \ldots, N$, we obtain by (11) the linear system for the values of $\delta\mathbf{u}_j$, which is three-diagonal by blocks 5×5. We solve it using the LU-factorization.

The time step is subject to the two CFL constraints: the explicit and the implicit one. We demand that the slow characteristic speeds satisfy the explicit CFL condition with $\text{CFL}_{\text{exp}} := 0.5$. The fast characteristic speeds must satisfy the implicit CFL condition with $\text{CFL}_{\text{imp}} := 20$, for instance.

The source terms $\mathbf{s}_{\text{rel}}(\mathbf{u})$ and $\mathbf{s}(\mathbf{u})$, given by (10), are treated with the splitting technique. Assuming that the relaxation take place instantaneously, the splitting for the relaxation term $\mathbf{s}_{\text{rel}}(\mathbf{u})$ reads

$$\Pi_j^{n+1} := P(\rho_j^{n+1}, Y_j^{n+1}, v_j^{n+1}) \tag{16a}$$

$$\Sigma_j^{n+1} := \sigma(\rho_j^{n+1}, Y_j^{n+1}, v_j^{n+1}). \tag{16b}$$

In practical implementation, it is necessary to solve (16a) *implicitly*, see [1].

4 Adaptive mesh refinement

On the interval $[0, L]$ we introduce the ensemble of uniform grids, which are characterized by the level k, $k = K_c, \ldots, K_f$, with the cell size Δx^k. On the level k, the total number of cells is taken equal to 2^k, so that $\Delta x^k = L/2^k$. The cell i on the level k is defined as $M_i^k := \Delta x^k[i-1, i]$, $i = 1, \ldots, 2^k$. We have therefore an ensemble of $K_f - K_c + 1$ imbricated grids. The grid of the level K_f is the finest, and the grid of the level K_g is the coarsest one.

Consider the solution $\mathbf{u}(x) := \mathbf{u}(x, t^n)$ to the relaxation system (8) at the time instant t^n. We denote by $\mathbf{u}_i^k$ the average value of the solution $\mathbf{u}(x)$ for $x \in M_i^k$. Given the initial condition $\mathbf{u}_i^k$, $i = 1, \ldots, 2^k$ on the fine grid, we compute the solution $\mathbf{u}_i^{k-1}$, $i = 1, \ldots, 2^{k-1}$ on the coarser grid by

$$\mathbf{u}_i^{k-1} := \frac{1}{2}(\mathbf{u}_{2i-1}^k + \mathbf{u}_{2i}^k), \quad i = 1, \ldots, 2^{k-1}. \tag{17}$$

The inverse operation consists in predicting the values $\hat{\mathbf{u}}_{2i-1}^k$, $\hat{\mathbf{u}}_{2i}^k$ on the fine grid by using the values on the coarser grid. Here we use the reconstruction operator, based on the second order polynomials,

$$\hat{\mathbf{u}}_{2i-1}^k := \mathbf{u}_i^{k-1} - \frac{1}{8}(\mathbf{u}_{i+1}^{k-1} - \mathbf{u}_{i-1}^{k-1}), \quad \hat{\mathbf{u}}_{2i}^k := \mathbf{u}_i^{k-1} + \frac{1}{8}(\mathbf{u}_{i+1}^{k-1} - \mathbf{u}_{i-1}^{k-1}), \tag{18}$$

for $i = 2, \ldots, 2^{k-1} - 1$. For the boundary cells, we use the first order polynomials.

We define the *detail* as the difference between the average and the predicted values of the solution,

$$\mathbf{d}_i^{k-1} := \mathbf{u}_{2i}^k - \hat{\mathbf{u}}_{2i}^k, \quad i = 1, \ldots, 2^{k-1}. \tag{19}$$

The absolute value of the detail depends on the local regularity of the solution $\mathbf{u}(x)$, see [4].

The relations (17), (18), and (19) define the algorithms of *coding* and *decoding* the solution. Starting from the *decoded* solution $\mathbf{u}_i^{K_f}$ on the finest grid, we can calculate the *coded* solution, which is given by the average values $\mathbf{u}_i^K$, $i = 1, \ldots, 2^K$ on the grid K, and the details $\mathbf{d}_i^k$, $k = K, \ldots, K_f - 1$, $i = 1, \ldots, 2^k$. Iterating the coding $K_f - K_c$ times, we can get the coded solution on the coarsest level K_c. Inversely, starting from the coded solution on th level K, we can obtain the decoded solution on the finest grid K_f.

The construction of adaptive mesh consists in selecting the grid level, which will be used to represent locally the solution. The decision is taken according to the size of the detail $\mathbf{d}_i^k$. If its norm is below certain *threshold* ϵ, the detail is considered as negligible and the cell M_i^k is marked for the decoding the solution. Otherwise one has to use the coarser level.

During the evolution of the solution to the hyperbolic system (8) the singularities propagate with finite speed. In order to predict the position of singularities at the time t^{n+1} using the solution at the time t^n, we use the idea of Harten [5]. It consists in augmenting the set of marked cells such that if a cell M_i^k is marked, than also the neighbor cells M_{i-1}^k, M_{i+1}^k, M_{2i-1}^{k+1}, M_{2i}^{k+1} will be marked. Finally, the set of marked cells is one again augmented in order to ensure that the set of the marked cells is *gradual*, i.e., the neighbor cells are situated either on the same level, or on the neighbor ones. Also, the marked cells should cover the whole domain $[0, L]$. Now the obtained set of the marked cells forms the *adaptive mesh* over the domain $[0, L]$. We can decode the average values of the solution $\mathbf{u}_i^k$ on the adaptive mesh and use them to evolve the solution to the next time instant.

The adaptive mesh is characterized by the threshold parameter ϵ and the number of refinement levels. The smaller ϵ is, the more details are considered as non-negligible; in the limit case $\epsilon = 0$ all details are non-negligible and the finest mesh is used everywhere in the domain. On the contrary, if ϵ is too big, too many details are considered as negligible and consequently the accuracy of the numerical solution deteriorates. The choice of the optimal ϵ is specific for each class of problems and it has to be fitted manually.

5 Numerical results

5.1 Stationary solution in the W-pipeline

Consider the pipeline with length $L = 4000$, diameter $D = 0.146$, and the inclination $\theta(x) = -30^\circ$ for $0 \le x \le L$ or $L/2 < x \le 3L/4$, and $\theta(x) = +30^\circ$ for $L/4 < x \le L/2$ or $3L/4 < x \le L$.

The gas sound speed is $a_g = 316.22777$. The liquid is compressible, the equation of state is given by (4) with $\rho_l^0 = 1000$, $p^0 = 10^5$ and $a_l = 500$. The friction coefficient $C_f = 0.005$ and the gravity acceleration is $g = 9.81$. We use the Zuber–Findlay slip law (5). Boundary conditions are given by $q_l := 5/A$, $q_g := 0.1/A$, $\bar{p} := 10^6$, where $A = \pi D^2/4$ is the cross-section of the pipeline.

The comparison of the results using the adaptive and uniform grids is shown in Fig. 1. The calculations were done using 256 cells on the finest level with 5 levels of refinement for the the adaptive mesh, and 256 cells for the uniform mesh. We see that the density and pressure are maximal at the lowest points of the pipeline, and minimal at its highest points. On the contrary, the velocity is minimal at the lowest points and maximal at the highest points. The mesh is refined where the solution is less smooth. Note that the adaptive and uniform solutions are almost indistinguishable.

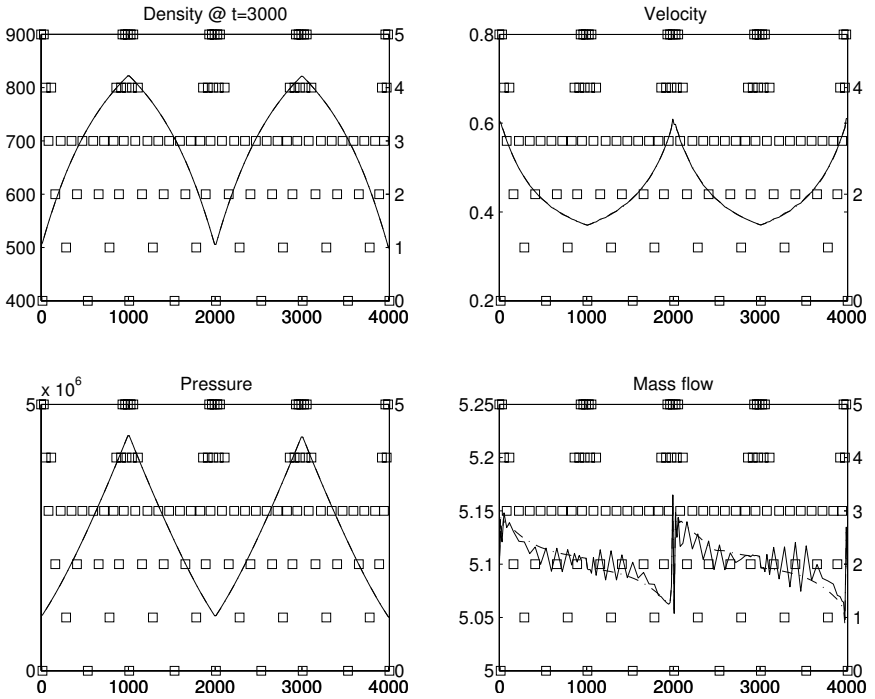

Figure 1: The adaptive solution (solid line) and the uniform one (dash-dot) for the stationary flow in the W-pipeline. The boxes represent the levels of refinement.

Table 1.

	$\epsilon = 0.01$	$\epsilon = 0.001$	$\epsilon = 0.0001$
3 levels	1.82	1.38	1.22
4 levels	1.82	1.50	1.22
5 levels	1.82	1.51	1.23

The speed-up factor of the AMR method with 256 cells on the finest level over the uniform one with 256 cells is shown in Table 1. For the same number of refinement levels, the acceleration diminishes as $\epsilon \to 0$. Indeed, in this case the more and more details are considered as non-negligible, so the solution can be rarely represented on the coarsest grid. For the same value of ϵ, the speed-up factor increases slightly with the number of levels.

5.2 Severe slugging

Consider a pipeline with length $L = 74$, diameter $D = 0.05$, and the inclination $\theta(x) = 0^\circ$ for $0 \le x \le 60$, and $\theta(x) = +90^\circ$ for $60 < x \le L$.

The gas sound speed is $a_g = 316.22777$. The liquid is compressible, the equation of state is given by (4) with $\rho_l^0 = 1000$, $p^0 = 10^5$ and $a_l = 500$. The friction coefficient $C_f = 0.005$ and the gravity acceleration is $g = 9.81$. We use the modified Zuber–Findlay slip law (7). Boundary conditions are given by $q_l := 0.07854/A$, $q_g := 0.000196/A$, $\bar{p} := 10^5$.

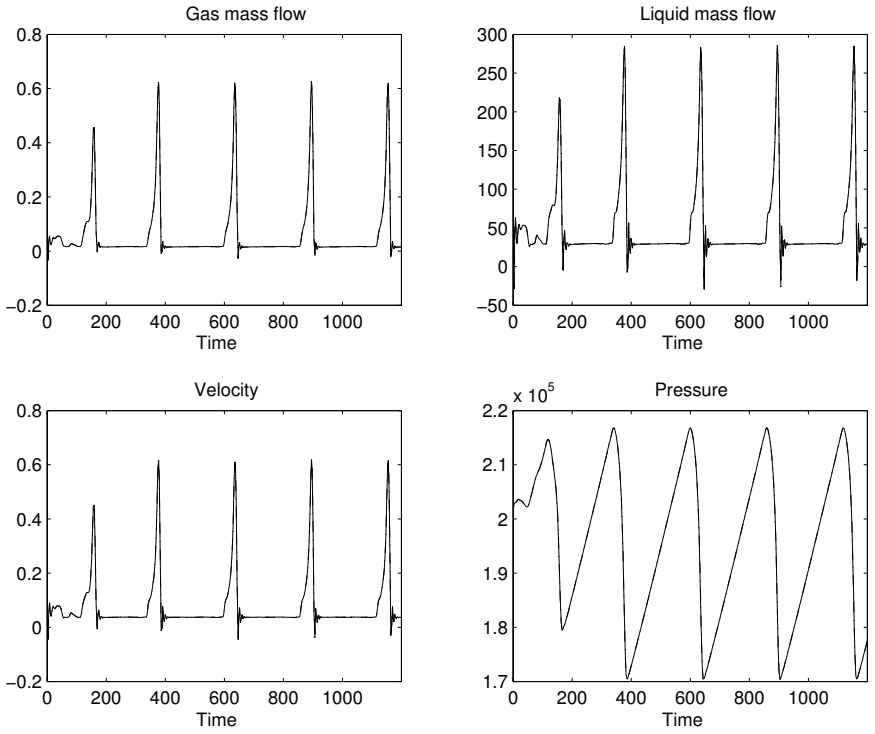

Figure 2: The time evolution of the adaptive and uniform solutions (indistinguishable) for the severe slugging flow.

Fig. 2 shows the time evolution of the flow at the fixed position $x = 60$, with 3 refinement levels, $\epsilon = 0.0001$, and 128 cells on the finest level for the AMR method. The physical situation is the following. The liquid column in the *riser* (the vertical part of the pipeline) blocks the flow, causing the pressure in the horizontal part to augment. When the pressure exceeds a critical value, the pressure difference pushes the mixture towards the pipeline exit. The violent acceleration (over 16-fold in velocity) causes the appearance of the rarefaction zone near the corner. The

liquid in the riser falls down and swings back and forth, finally again blocking the flow.

Table 2.

	$\epsilon = 0.01$	$\epsilon = 0.001$	$\epsilon = 0.0001$
3 levels	2.37	2.27	2.18
4 levels	2.46	2.28	2.07
5 levels	1.58	1.51	1.49

The speed-up factor of the AMR method with 128 cells on the finest level over the uniform one with 128 cells is shown in Table 2. As for the previous test case, the speed-up factor diminishes as ϵ goes to zero. Observe that for the same value of ϵ, the speed-up factor varies non-monotonically with number of levels. The reason is that with more refinement levels, the coding-decoding operations become increasingly expensive. Note that this test is favorable for the AMR method: there are few irregularities in the horizontal part of the pipeline, and therefore the coarsest grid can be used in the most of the domain.

6 Conclusions and outlook

We have demonstrated that the relaxation method can be successfully used for simulating several flow phenomena in pipelines, including the slug formation. Our experience shows that the adaptive mesh refinement technique accelerates the computation by the factor of up to 3. We expect that using more realistic slip laws will increase this factor even more significantly. We are also considering the use of the local time stepping for the further speed-up of the computation.

References

[1] Baudin, M., Coquel, F. & Tran, Q.H., A semi-implicit relaxation scheme for modeling two-phase flow in a pipeline. To appear in *SIAM Journal on Scientific Computing*, 2005.

[2] Cohen, A., Kaber, S.M., Müller, S. & Postel, M., Fully adaptive multiresolution finite volume schemes for conservation laws. *Mathematics of Computation*, **72**, pp. 183–225, 2003.

[3] Zuber, N. & Findlay, J., Average volumetric concentration in two-phase flow systems. *Journal of Heat Transfer*, **87**, pp. 453–468, 1965.

[4] Cohen, A., *Numerical analysis of wavelet methods*. North-Holland: Amsterdam, 2003.

[5] Harten, A., Multiresolution algorithms for the numerical solution of hyperbolic conservation laws. *Communications on Pure and Applied Mathematics*, **48(12)**, pp. 1305–1342, 1995.

Computational fluid dynamics simulation of a very dense liquid-solid flow using a Eulerian model

J. Yang & R. J. Chalaturnyk
Department of Civil and Environmental Engineering, University of Alberta, Canada

Abstract

Segregation in a dense solid-liquid multiphase flow is complicated by its interactions between phases. In this paper, the segregation of dense solid-liquid flow was simulated using the Finite Volume Method. A Euler-Euler multiphase simulation was conducted for the dense solid-liquid flow. The flow in the viscous regime was evaluated using kinetic theory describing the flow of smooth, slightly inelastic, spherical particles. The friction between solid particles which occurs in the plastic regime was evaluated based on the concepts from critical soil mechanics. The challenge of simulating non-segregation behaviour of dense solid-liquid flow was discussed.
Keywords: multiphase flow, segregation, dense solid-liquid flow, finite volume method, computational fluid dynamics (CFD), Euler-Euler multiphase simulation.

1 Introduction

Particle segregation was observed to occur in particles with different size or density under shearing. Depending on the particle properties and shearing conditions, segregation in radial, axial or vertical direction may take place. Since segregation is beneficial to some applications (e.g. sorting of particles with different densities) while it is unfavourable in other fields (e.g. sedimentation of tailing slurry), segregation mechanisms and it's modelling have been studied by researchers in different areas.

Segregation in rapid granular flow has been investigated thoroughly [1,2]. Competition between buoyancy force and geometric force [3], percolation and

convection were believed to contribute to the size segregation effect. On the other hand, few literatures on particle segregation in slow flow regime or under quasi-static condition can be found.

Attempts have been made to simulate the segregation of granular flow by researches. Both Euler-Euler and Euler-Lagrange descriptions have been applied. In Euler-Euler approach, both continuous and dispersed phases are treated as interpenetrating continua. The dispersed phase is tracked using Lagrange approach in Euler-Lagrange method. Choosing one method over the other depends on flow regimes (gas-liquid, liquid-liquid, gas-solid, liquid-solid and three-phase flows), volume fraction of the disperse phase and the confidence on the parameters involved in the models. Generally speaking, Euler-Euler model is suitable for flow with high volume fraction of dispersed phase and Euler-Lagrange model is applicable to the situation where particle size distribution is of importance and the volume fraction of the dispersed phase is low (< 10%).

2 Experiments

A large volume of oil sand tailing composed of water, bitumen, fines and sand, are produced in extracting synthetic crude oil from oil sands. Segregation of this material during transportation and deposition is an unexpected behaviour. Research has been carried out in finding ways to produce non-segregating oil sand tailings. Batch standpipe tests were conducted on tailing slurry with a wide range of solid content (i.e. percent of solid mass) and fine content (i.e. percent of fine mass in solid components), where 44 micron is selected as the boundary between fine and coarse particles. After the slurry was uniformly mixed in mixer then placed into standpipe, an interface between upper clear water and lower suspension develops. The variation of the elevation of the interface with elapsed time was recorded and was used to characterize the properties of the tailing slurry. The observation was ended when the elevation of the interface changed extremely slowly. Then the profiles of the solid content and fine content were obtained by measuring the mass fraction of water, sand and fine. The average solid content [4] was calculated using eqn. (1):

$$S_{avg} = \frac{1}{\frac{1}{S_0} - \left(1 - \frac{H}{H_0}\right)\left(\frac{G_w}{G_s} + \frac{1}{S_0} - 1\right)} \tag{1}$$

where S_{avg} is average solid content, S_0 the initial average solid content, H_0 the initial height of the slurry, and G_w and G_s are specific gravity of water and solid respectively. In order to describe the segregation, Segregation Index is defined as follows:

$$I_s = \sum_{i=1}^{N} \left\{ \frac{1}{2}\left[\frac{S_i}{S_{avg}} - 1\right]\left[\left(\frac{H}{H_f}\right)_{i+1} - \left(\frac{H}{H_f}\right)_{i-1}\right] \right\} * 100\% \tag{2}$$

where S_i is the solid content of layer i at elevation of H, H_f is the total height of the suspension, and N is the total number of layers measured. The fine capture is

define as 100 – I_s and a mix is defined as non-segregation matrix if fine capture is at least 95%.

In order to determine the segregation boundary of the oil tailing slurry, three standpipe tests were conducted on the oil sand tailing with solid and fine content combination shown in Table 1.

Table 1: Initial solid and fine content of oil tailing slurry used for segregation boundary tests.

Tests No.	Initial Solid Content (%)	Initial Fine Content (%)	Fine Capture	Segregating/Non-segregating
SB1	45	25	55.50	Segregating
SB2	55	25	92.09	Non-Segregating
SB3	65	25	98.41	Non-Segregating

2.1 CFD Simulation

ANSYS CFX-5.7 and FLUENT 6.1 were used to simulate the segregation of the oil sand tailing slurry. Euler-Euler method was applied in simulating the segregation process and the slurry was simulated using three phases flow composed of continuous phase of water and dispersed phases of sand and clay.

2.1.1 Conservation equations

The continuity equations and momentum equations for each phase are derived by assuming that phases can be treated as interpenetrating continua [5,6]. The continuity equation for each phase is expressed as follows:

$$\frac{\partial}{\partial t}(\alpha_q \rho_q) + \nabla \cdot (\alpha_q \rho_q \vec{v}_q) = 0 \tag{3}$$

where α_q, ρ_q and $\vec{v}_q$ are volume fraction, density and velocity of phase q, respectively. The volume fraction of the phases is restrained by the condition that volume fraction of all phases sums up to unity at any time.

The momentum equation for continuous phase q is expressed as follows:

$$\frac{\partial}{\partial t}(\alpha_q \rho_q \vec{v}_q) + \nabla \cdot (\alpha_q \rho_q \vec{v}_q \vec{v}_q) = -\alpha_q \nabla p + \nabla \cdot \bar{\bar{\tau}}_q + \sum_{p=1}^{n} (\vec{R}_{pq} + \dot{m}_{pq} \vec{v}_{qp}) + \alpha_q \rho_q \vec{F}_q \tag{4}$$

where $\bar{\bar{\tau}}_q$ is the q[th] phase stress-strain tensor,

$$\bar{\bar{\tau}}_q = \alpha_q \mu_q (\nabla \vec{v}_q + \nabla \vec{v}_q^{\,T}) + \alpha_q (\lambda_q - \frac{2}{3} \mu_q) \nabla \cdot \vec{v}_q \bar{\bar{I}} \tag{5}$$

where μ_q and λ_q are the shear and bulk viscosity of phase q, $\vec{F}_q$ is an external body force, and p is the pressure shared by all phases. The $\vec{R}_{pq}$ is the interphase force between liquid phase q and solid phase p, which depends on the friction, pressure, cohesion and other factors. It is expressed as following form in Fluent:

$$\sum_{p=1}^{n} \vec{R}_{pq} = \sum_{p=1}^{n} K_{pq}(\vec{v}_p - \vec{v}_q) \tag{6}$$

where K_{pq} (= K_{qp}) is the solid-liquid momentum exchange coefficient. Gidaspow model [7] is a combination of the Wen and Yu and the Ergun equation and is suitable for dense solid-liquid flow. In this model, the fluid-solid exchange coefficient K_{pq} is of the following form:

$$K_{pq} = \begin{cases} \frac{3}{4} C_D \frac{\alpha_p \alpha_q \rho_p \left|\vec{v}_p - \vec{v}_q\right|}{d_p} \alpha_q^{-2.65} & (\alpha_q > 0.8) \\ 150 \frac{\alpha_p (1-\alpha_q)\mu_q}{\alpha_q d_p^2} + 1.75 \frac{\rho_q \alpha_p \left|\vec{v}_p - \vec{v}_q\right|}{d_p} & (\alpha_q \le 0.8) \end{cases} \tag{7}$$

where

$$C_D = \begin{cases} \frac{24}{\mathrm{Re}_p}\left[1 + 0.15\,\mathrm{Re}_p^{0.687}\right] & \mathrm{Re}_p < 1000 \\ 0.43 & \mathrm{Re}_p \ge 1000 \end{cases} \tag{8}$$

The general momentum equation for solid phase s is expressed as follows:

$$\frac{\partial}{\partial t}(\alpha_s \rho_s \vec{v}_s) + \nabla \cdot (\alpha_s \rho_s \vec{v}_s \vec{v}_s) = -\alpha_s \nabla p - \nabla p_s + \nabla \cdot \overline{\overline{\tau}}_s + \alpha_s \rho_s \vec{g} + \alpha_s \rho_s \vec{F}_s + \sum_{l=1}^{N} (K_{ls}(\vec{v}_l - \vec{v}_s)) \tag{9}$$

where p_s is the s^{th} solids pressure, $K_{ls} = K_{sl}$ is the momentum exchange coefficient between fluid or solid phase l and solid phase s, N is the total number of phases.

The implementation of momentum equations for solid phase differs in CFX 5.7 and Fluent 6.1. The model due to Gidaspow was incorporated into CFX 5.7, in which the solid stress tensor is ignored and the solid pressure is expressed as a function of solid volume fraction in the following form:

$$\nabla P_s = G_0 \exp(c(\alpha_s - \alpha_{sm}))\nabla \alpha_s \tag{10}$$

where α_{sm} is the packing limit for solid phase s, G_0 and c are reference elasticity and compaction modulus respectively.

In Fluent 6, the solid stress tensor is expressed in the similar form to that for liquid phase (eqn. 5). Solid shear viscosity is expressed as collisional viscosity $\mu_{s,col}$, kinetic viscosity $\mu_{s,kin}$ and frictional viscosity $\mu_{s,fr}$:

$$\mu_s = \mu_{s,col} + \mu_{s,kin} + \mu_{s,fr} \tag{11}$$

where:

$$\mu_{s,col} = \frac{4}{5}\alpha_s \rho_s d_s g_{0,ss}(1+e_{ss})\left(\frac{\Theta_s}{\pi}\right)^{1/2} \tag{12}$$

$$\mu_{s,kin} = \frac{10\rho_s d_s \sqrt{\Theta_s \pi}}{96\alpha_s (1+e_{ss}) g_{0,ss}}\left[1 + \frac{4}{5}\alpha_s g_{0,ss}(1+e_{ss})\right]^2 \tag{13}$$

$$\mu_{s,fr} = \frac{p_s \sin\phi}{2\sqrt{I_{2D}}} \tag{14}$$

In eqn. (12) and (13), $g_{0,ss}$ is the radial distribution function, e_{ss} is restitution coefficient, Θ_s is the granular temperature for solid phase s. I_{2D} is the second invariant of the deviatoric stress tensor, ϕ is the internal friction angle of solid particles.

The solid-solid exchange coefficient K_{ls} between solid phase s and l in Fluent has the following form:

$$K_{ls} = \frac{3(1+e_{ls})(\frac{\pi}{2} + C_{fr,ls}\frac{\pi^2}{8})\alpha_s \rho_s \alpha_l \rho_l (d_l + d_s)^2 g_{0,ls}}{2\pi(\rho_l d_l^3 + \rho_s d_s^3)} |\vec{v}_l - \vec{v}_s| \tag{15}$$

where $C_{fr,ls}$ is the coefficient of friction between the l^{th} and s^{th} solid phase particles, d_l and d_s are the diameter of the particles of solid l and s respectively. e_{ss} is the restitution coefficient between phase s particles, $g_{0,s}$ is the radial distribution function. The radial distribution function due to Lebowitz [12] was used:

$$g_{0,sl} = \frac{1}{\alpha_q} + \frac{3(d_s + d_l)}{\alpha_q^2 (d_s + d_l)} \sum_{\lambda=1}^{M} \frac{\alpha_{s\lambda}}{d_{s\lambda}} \tag{16}$$

2.2 Simulation setup and results

2.2.1 CFX 5.7 setup

SB1 and SB3 are chosen to verify the Euler-Euler Multiphase model in CFX 5.7 since mixture in SB1 experiments is segregating matrix and that in SB3 is non-segregating. Three phase simulations were conducted in ANSYS CFX 5.7 using a mesh composing of 20,114 tetrahedron elements. The properties of each phase are listed in Table 2. The flow in standpipe was assumed to be laminar. The initial volume fraction of sand, clay and water is shown in Table 3. The top of the standpipe was set to be free-slip wall boundary and the wall and bottom of the standpipe were assigned as non-slip walls.

Table 2: The properties of material.

Name	Density (kg/m^3)	Diameter (micron)
Water	1000	
Sand	2700	120
Clay	2600	22

Table 3: Initial volume fraction.

Tests	Water VOF	Sand VOF	Clay VOF
SB1	0.7657	0.1740	0.0602
SB3	0.5902	0.3044	0.1054

2.2.2 Fluent 6.1 setup

The material properties listed in Table 2 were used in Fluent simulation. The same initial and boundary conditions as those used in CFX 5.7 were applied in

Fluent. The mesh with the same element distribution was used in Fluent 6.1. The granular temperature of the solid phases was solved using algebraic equations. Frictional viscosity was enabled and the internal friction angles of sand and clay were set to be 30 and 25 degree respectively.

2.2.3 Comparison of simulation results

Figure 1 showed the simulated solid and fine content profiles for SB1 from CFX and Fluent at flow time of 300 seconds. The measured solid and fine content profiles for SB1 also were demonstrated in Figure 1. One can observe that the predicted solid content profile was close to that obtained from experiment, while the predicted fine content profile deviated from experiment result. Both CFX and Fluent predicted that almost all sand particles settle down to the lower part of the standpipe and all the solid particles are clay particles at the elevation of 0.12m up to the top of the standpipe. The segregation indexes calculated from the solid and fine content profiles obtained from CFX and Fluent simulation are 23.5 and 57.6 compared with a value of 69.6 from experiments.

Comparison of solid and fine content profiles for SB3 was shown in Figure 2. Segregation Index calculated from experiment result was 1.59 while Segregation Indexes of 24.7 and 31.7 were obtained from CFX and Fluent simulation. From Figure 2 it can be seen that sand settled at the bottom of the standpipe while clay particles were suspended in the upper part of the fluid. The development of the level of interface between supernatant and suspension was shown in Figure 3. A higher rate of the interface progress in simulations than that in experiments was observed although Fluent predicted that the interface developed at a lower speed than in CFX. From Figure 1 – 3 one can see that similar solid and fine content profiles were obtained in CFX and Fluent. However, one main difference is that CFX cannot limit the solid volume fraction at compaction zone (Figure 1 and 2). For this reason, the following simulation was done in Fluent only.

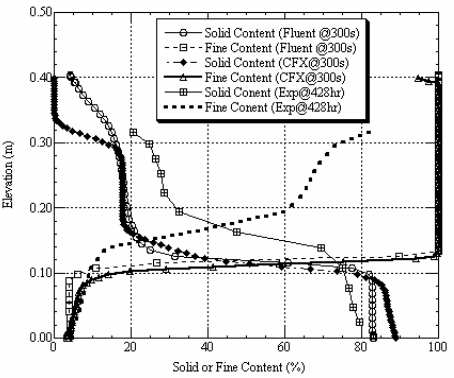

Figure 1: Comparison of solid and fine content profiles from CFX and Fluent and experiment for SB1 test.

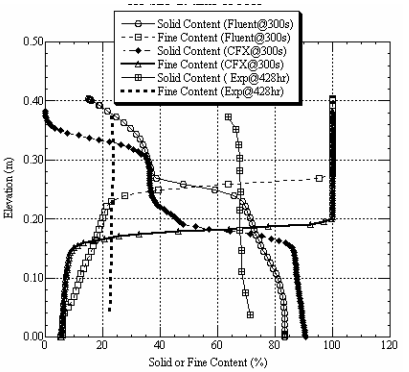

Figure 2: Comparison of solid and fine content profiles obtained from CFX, Fluent and experiment for SB3 test.

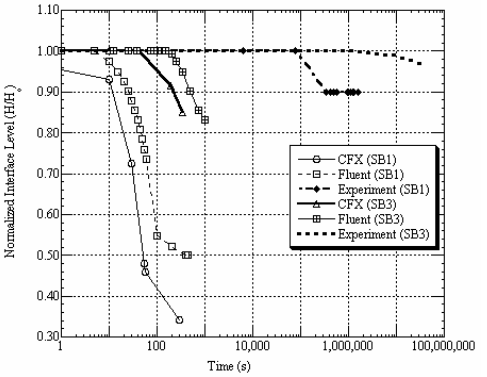

Figure 3: Comparison of interface development process in CFX and Fluent simulation as well as in experiment for SB3.

2.2.4 Modification of solid-solid exchange coefficient

Both cases indicated that the above Euler-Euler model in Fluent and CFX is not capable of capturing the non-segregation behaviour of very dense solid-liquid flow under quasi-static conditions. This was similar to the finding by Gera et al. [8]. They argued that the model of Goldschmidt et al. [9] cannot predict the non-segregation phenomena at a low fluidization velocity. Then they added a term, which is proportional to solid pressure, into solid-solid drag exchange coefficient. They found the modified model can predict no segregation at low fluidization velocities. In following their idea, another term was added into solid-solid exchange coefficient. The magnitude of this term depends on the relative volume fraction of sand and clay and the location of the segregation boundary shown in Figure 4. If the combination of sand volume fraction and clay volume fraction lies above the segregation boundary curve and below the compacting limit line, then the additional term is 1000.0 times the vertical distance of this point to the point on the segregation boundary curve at current clay volume

fraction. The effects of the additional term on the sand and clay volume fraction profile were shown in Figure 5. It can be seen that the added solid-solid exchange term had little effect on prohibiting the occurrence of segregation.

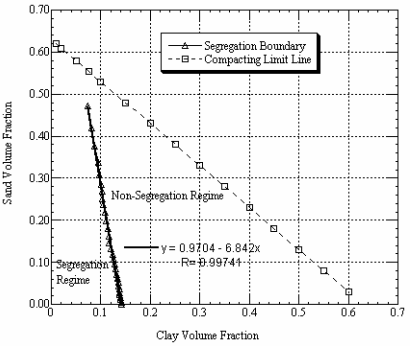

Figure 4: Segregation boundaries for tailing slurry.

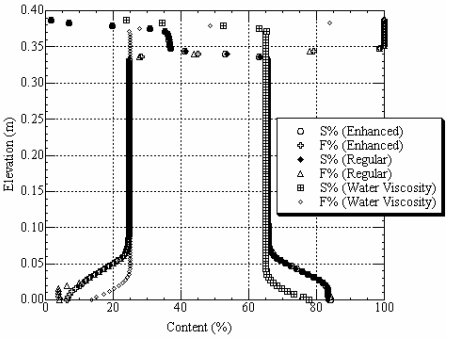

Figure 5: Comparison of Solid and Fine Content Profile at Time of 250s. The solid and fine content profile for simulations using enhanced solid-solid drag coefficient, regular solid-solid drag coefficient and enhanced water viscosity were shown.

2.2.5 Modification of the viscosity of water phase

There must be other mechanisms that are not included in the momentum exchange mechanisms in the models above. Since rheological properties result from momentum transfer due to Brownian, hydrodynamic, packing, colloidal and inertial effects [10], modification of the rheological properties of suspending fluid may capture some of these unincorporated interactions.

According to Thomas [11], the viscosity of the suspension can be expressed via:

$$\mu_m = \mu_0(1 + 2.5\Phi + 10.05\Phi^2 + A\exp(B\Phi)) \tag{17}$$

where μ_m, μ_0 and Φ are viscosity of suspension, viscosity of suspending medium and the volume fraction of solids, and A and B are parameters. We adopted the

suggested value of 0.00273 and 16.6 for these two parameters in the simulation. The solid and fine content profiles at flow time of 250s were shown in Figure 5. It can be seen that increasing the viscosity of the suspending medium hindered the happening of segregation.

2.2.6 Two-phase simulation

Above simulations demonstrated that some interactions between solid and solid as well as between solid and liquid were not captured in the current models. In order to circumvent the considerations of the clay-clay and clay-water interactions, clay and water can be considered as a single phase with varying viscosity and density, which can reflect the distribution of clay particles in water due to segregation or non-segregation. For non-segregation mixture, the clay volume fraction almost remains constant, which simplify the simulation.

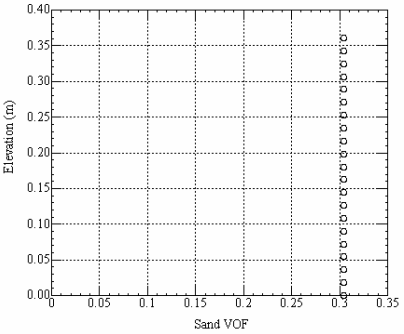

Figure 6: Sand volume fraction at flow time of 2500 s.

The slurry viscosity was measured using a Brookfield DV-II+ Programmable Viscometer. Cylindrical spindles were used for these tests. Logarithmic model in the following form was used to correlate viscosity with shear strain rate:

$$\mu = 10^{(a+b*\log(\dot{\gamma}))} \tag{18}$$

in which μ and $\dot{\gamma}$ are viscosity and shear strain rate respectively, a and b are curve-fitting parameters which are functions of solid content. The parameters can be related to solids content by regression as follows:

$$a = -2.3885 + 0.12102s - 0.0008079s^2 \tag{19}$$

$$b = -0.7666 - 0.002714s \tag{20}$$

where s is the solid content of the slurry (%). The simulation result was shown in Figure 6. It can be seen that the sand volume fraction remains almost constant even at time of 2500s.

3 Conclusion

Compared with segregation, non-segregation behaviour of the solid-liquid system brought more challenge in numerical simulation. The interactions between clay and clay as well between clay and water are critical to solution of this problem. One solution to this is to modify the suspending medium viscosity to reflect the influence of the interactions. Considering the clay-water as a single phase can be another way to evade the complexity of the interactions

Acknowledgements

The authors would like to acknowledge the financial and technical support provided by Suncor Energy Ltd. and the Oil Sands Tailings Research Facility. The individual support provided by Dr. Don Sheeran and Mr. Mike Agnew in establishing this research effort is also very much appreciated.

References

[1] Williams JC. The segregation of powders and granular materials. *Fuel Soc. J.* 14:29–34, 1963.
[2] Trujillo, L., Herrmanna, H.J., Hydrodynamic model for particle size segregation in granular media. *Physica A*, vol. 330, pp. 519 – 542, 2003.
[3] Trujillo, L., Alam, M., Herrmann H.J., Segregation in a fluidized binary granular mixture: Competition between buoyancy and geometric forces. *Europhysics Letters*, **64 (2)**, pp. 190-196 OCT 2003.
[4] Chalaturnyk, R.J. and Scott, J.D., Soil structure behaviour diagram. *High Density and Paste Tailings 2001*, Edmonton, Canada, 2001.
[5] Ansys, Inc., Ansys CFX 5.7.1: *Solver Theory*, 2004.
[6] Fluent, Inc., Fluent 6.1: *Fluent User's Guide*, February 2003.
[7] Gidaspow, D., 1994. *Multiphase Flow and Fluidization, Continuum and Kinetic Theory Description*. Academic Press, 1994.
[8] Gera, D., Syamlal, M., and O'Brien, T.J., Hydrodynamics of Particle Segregation in Fluidized Beds. *International Journal of Multiphase Flow*, vol. 30, pg. 419-428, 2004.
[9] Goldschmidt, M.J.V., Kuipers, J.A.M., van Swaiij, W.P.M., 2001. Segregation in dense gas-fluidised beds: validation of multi-fluid continuum model with non-intrusive digital image analysis measurements. In: *10th Engineering Foundation Conference on Fluidization*, Beijing, China, May 20–25, pp. 795–802.
[10] Coussot, P., *Mudflow rheology and dynamics*. International Association for Hydraulic Research. A.A. Balkema, 1997.
[11] Thomas, D.G., Transport characteristics of suspensions: Application of different rheological model to flocculated suspension data. *American Society Mech. Engineers*, Chapter 64, 704-717, New York, 1962.
[12] Lebowitz, J.L. Exact Solution of Generalized Percus-Yevick Equation for a Mixture of Hard Spheres. The Phy. Rev., 133(4A):A895-A899, 1964.

Section 11
Interface tracking methods

This page intentionally left blank

The liquid-liquid interface under planetary rotation

C. S. König & I. A. Sutherland
Brunel Institute for Bioengineering, Brunel University, UK

Abstract

Countercurrent chromatography is a liquid-liquid partition chromatography method allowing high-resolution purifications. It utilises the hydrodynamic behaviour of two immiscible liquid phases in coil columns undergoing a planetary motion generated by a synchronous coil planet centrifuge.

In this study planetary rotation is applied to liquid-liquid flows in two types of ring geometries. The influence of the epicyclic force field is studied by applying a variety of different operating conditions, namely rotational speed and the ratio of the planet and sun radii known as the beta value. The results show that variation of the beta value has far greater influence on phase distribution than variation of the rotational speed.

1 Introduction

Countercurrent chromatography (CCC) separates compounds from mixtures on the basis of their partition or distribution between two immiscible solvents. The process utilises the hydrodynamic behaviour of the two liquid phases in coil columns undergoing a planetary motion generated by a synchronous coil planet centrifuge. The centrifugal force field applied to the coiled columns promotes the retention of stationary phase against a continuous flow of mobile phase, while providing efficient mixing between the two solvent phases to enable the partition process. A series of simultaneous mixing and settling zones occur along the length of the tubing. This mixing and settling process and the mass transfer between the phases are the key elements for successful high-resolution liquid-liquid chromatography [1,2]. Although phase distribution and phase-mixing phenomena, which are fundamental to CCC, are directly linked to the gravity field, its influence is still not fully understood [2-4].

WIT Transactions on Engineering Sciences, Vol 50, © 2005 WIT Press
www.witpress.com, ISSN 1743-3533 (on-line)

The current need for developing industrial scale CCC [5,6] is assisted by applying CFD (Computational Fluid Mechanics) modelling. Process scale CCC machinery will allow continuous processing of samples in the order of tonnes per annum as required by the pharmaceutical industries. The experimental and empirical determination of the optimal design parameters and operating conditions of such machinery can be aided by CFD modelling.

Prior to this study the authors numerically investigated the influence of the gravity field on the interface between two immiscible liquids in straight, both fixed, inclined [4] as well as oscillating [7] tubes for one typical CCC phase system. Comparisons with experimental data in the former case showed that the interface motion was generally well predicted. Subsequently other CCC phase systems of different ranges of interfacial tension were modeled numerically and experimentally in the suddenly tilted and then fixed, inclined straight tube [8]. Also the models were extended to circular and coiled tubes undergoing a circular rotation [8].

In the present study the influence of the differential g-field, as exerted by planet centrifuges, on the liquid-liquid interface is investigated in circular tubes. Fig. 1 shows the motion of a coil planet centrifuge. The central sections experience mixing due to the higher tangential accelerations whereas the outer sections, as a result of the higher centrifugal forces, result in settling zones, see Fig. 2 from [2]. The magnitude of the g-forces is governed by the rotation speed and beta value.

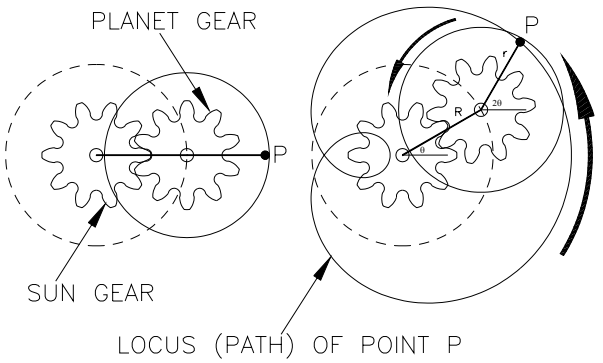

Figure 1: The motion of a planet centrifuge.

2 Numerical models

The numerical ring tube models are a 2D representation of existing experimental open and closed ring glass models. Whereas the closed model has a single internal wall, the open one has none. The experimental ring models have an inner diameter (inner wall to inner wall) of 100mm with a circular cross-section of

10mm diameter. The two-dimensional models (not shown) consist of four blocks and 32,000 cells with 40 subdivisions in radial direction. The radial grid resolution is approximately similar to previously modelled 3D rings [8].

The unsteady fluid flow is treated as laminar, Newtonian, isothermal and buoyant. The software used in this study to solve the governing equations (CFX-4 by AEA Technology Engineering Software Limited, Release 4.4) is based on the finite volume method. (CFX-Meshbuild and CFX-View were used for pre- and post-processing, respectively). A homogeneous two-fluid model based on mass and momentum conservation was used. The homogeneous model is a simplified multi-fluid model in that that it assumes the transported quantities for that process are the same for all phases, i.e.

$$\Phi_\alpha = \Phi \qquad 1 \le \alpha \le N_P \tag{1}$$

However, the volume fractions are still assumed distinct and hence the individual phase continuity equations are solved to determine the volume fractions. The individual transport equations are summed over all phases to give a single transport equation for Φ

$$\frac{\partial}{\partial t}(\rho\Phi) + \nabla \bullet (\rho \mathbf{U}\Phi - \Gamma \nabla\Phi) = S \tag{2}$$

where

$$\rho = \sum_{\alpha=1}^{N_P} r_\alpha \rho_\alpha, \quad \mathbf{U} = \frac{1}{\rho}\sum_{\alpha=1}^{N_P} r_\alpha \rho_\alpha \mathbf{U}_\alpha, \quad \Gamma = \sum_{\alpha=1}^{N_P} r_\alpha \Gamma_\alpha \tag{3}$$

with r_α being the volume fraction for each phase. In particular, the homogeneous model for momentum transport assumes $\mathbf{U}_\alpha = \mathbf{U}$, $1 \le \alpha \le N_P$, in the momentum equation

$$\frac{\partial}{\partial t}(\rho \mathbf{U}) + \nabla \bullet \left(\rho \mathbf{U} \otimes \mathbf{U} - \mu\left(\nabla \mathbf{U} + (\nabla \mathbf{U})^T\right)\right) = \mathbf{B} - \nabla p \tag{4}$$

and the continuity equation

$$\frac{\partial}{\partial t}(r_\alpha \rho_\alpha) + \nabla \bullet (r_\alpha \rho_\alpha \mathbf{U}_\alpha) = \sum_{\beta=1}^{N_P} (\dot{m}_{\alpha\beta} - \dot{m}_{\beta\alpha}) \tag{5}$$

where $\dot{m}_{\alpha\beta}$ is the mass flow rate per unit volume into phase α from phase β and

$$\rho = \sum_{\alpha=1}^{N_P} r_\alpha \rho_\alpha, \quad \mu = \sum_{\alpha=1}^{N_P} r_\alpha \mu_\alpha \tag{6}$$

The surface tension force is modeled based on the continuum surface model of Brackbill et al. [9]. To avoid a smeared interface, that may develop due to numerical diffusion in time, a surface-sharpening algorithm was employed [10].

The modelled CCC phase system, known as 4B and of intermediate hydrophobicity, is made up from heptane, ethyl acetate, methanol and water in the proportion 1.4:0.6:1:1. After mixing the components the system will separate into two immiscible liquids (ρ_1=713.68 kg m^{-3}, μ_1=0.3549E-3 kg m^{-1}s^{-1}, ρ_2=923.84 kg m^{-3}, μ_2=1.3406E-3 kg m^{-1}s^{-1}, σ=6.0569 E-3 Nm^{-1}).

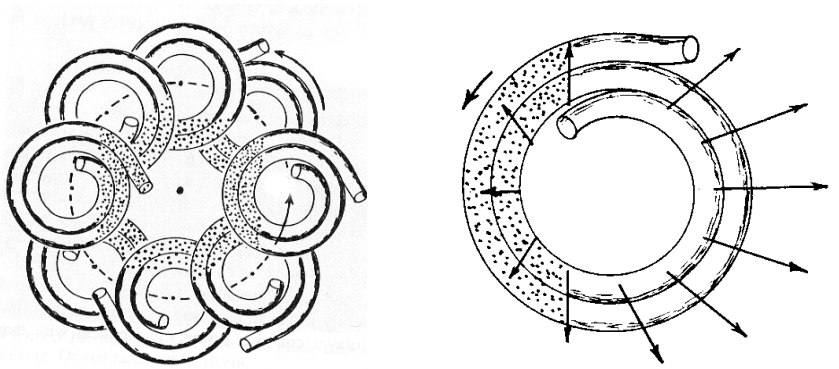

a) b)

Figure 2: a) Illustrated mixing and stratification zones in CCC; b) accelerations exerted on the liquid phases from [2].

3 Initial and boundary conditions

The models were filled radially by 50% with the heavier phase located in the outer half of the models. In all cases the flow field had initially zero velocity in the entire domain. The no-slip boundary condition was applied to all walls.

The planetary motion of the computational grid was incorporated using user Fortran. The rotational speeds were varied between 120, 300 and 600 rpm. The beta value ranged from 0.3, 0.5 to 0.7.

4 Computational details

Each time step uses the solution (phase volume fractions, velocities and pressure) of the previous time step as initial conditions. The pressure was obtained using the SIMPLEC algorithm. The differencing schemes used are a fully implicit backward differencing procedure for time, central differencing for pressure, upwind differencing for the phase volume fractions and hybrid

differencing for the velocity variables. The under-relaxation factors were set to 0.65 for the velocity components and to 1.0 for the volume fractions and the pressure. The runs were performed for a wall contact angle of 90°. The surface sharpening level was set to 2. The computations were performed for fixed time stepping in the order of 1E-4 s, which was adjusted with respect to the set rotational speed. The results were dumped at appropriate intervals. The minimum reduction of the mass source residuals per time step was one order of magnitude. The achieved total mass source residuals were of the order of 1E-5 kg/s. At this point in the computation the residuals for the velocity components and the volume fractions were also reduced to acceptable levels. The simulations were carried out on a SUN Blade 1000 workstation.

5 Results and discussion

As for circular rotation [8] it has been observed for planetary rotation that in stratification regions the heavier liquid will be found along the outer ring wall. Due to the centrifugal action the greater density fluid is subjected to a higher centrifugal force which will cause it to move away from the centre of curvature while the less dense fluid will be displaced towards the centre of curvature. When comparing the general differences in flow behaviour between the open and the closed ring it is most notable that instability occurs much earlier in the closed ring. This had also been observed in the case of the circular rotation [8]. For both types of rotation of the open ring, as a result of the differential velocities between the inner and the outer wall and the different inertia and viscosity of the two liquids, the resulting shear at the interface triggers the onset of instability. In planetary rotation though, the non-uniformly acting centrifugal forces result in an uneven radial distribution of the two phases already in the early stages.

In case of the closed ring it was observed that in positions where the internal wall is located on the outer locus, distinct wave formation is present in central regions, similarly as indicated in Fig. 2a. The mixing zone is shown very well in the 2nd rotation of the closed ring rotating at 120rpm with β=0.5 in Fig. 3, see steps 9&10 and 15&16. Note also the more stratified interface in the outer region of e.g. step 11&12. This agrees well with experimental findings in [1]. An increase in rotational speed resulted in a more undercut wave pattern in the mixing zone and greater stratification in outer regions (not shown).

In case of the open ring model the flow pattern development differs significantly from the one shown in Fig. 3. For any of the three speeds a typical Helmholz-type wave instability was not observed. For β=0.5 at 120rpm the centrifugal force proved too low to move the heavier phase out of the lower part of the ring. The wall shear pulls the heavier phase up to a certain point but not beyond. The phase distribution remains fairly constant through successive cycles and the heavier phase remains attached to the outer wall albeit being only a thin film in places (not shown). For both higher rotational speeds of 300 and 600rpm, a region of ~120º contains mostly heavier phase. For both speeds this phase bulk moves slowly anti-clockwise, see Figs. 4&5. At both speeds fluid fingers develop which develop earlier and more distinctly at 300rpm.

A decrease in beta value shows overall similar flow trends in the beginning. A significant difference is, however, that island areas of one phase dispersed in the other start to develop, see Fig. 6 in comparison with Figs. 4&5. Also the heavier phase does not remain contained in a single-phase bulk, see for example step 20 in Fig. 6. The formation of the phase island areas suggests a far more violent form of mixing. It is surprising that these islands are not formed in the central region. In fact, in some instances the flow appears highly stratified in this region, see for example step 17&21 in Fig.6. An increase in beta value from 0.5 to 0.7 was found to have less influence on phase distribution than a decrease.

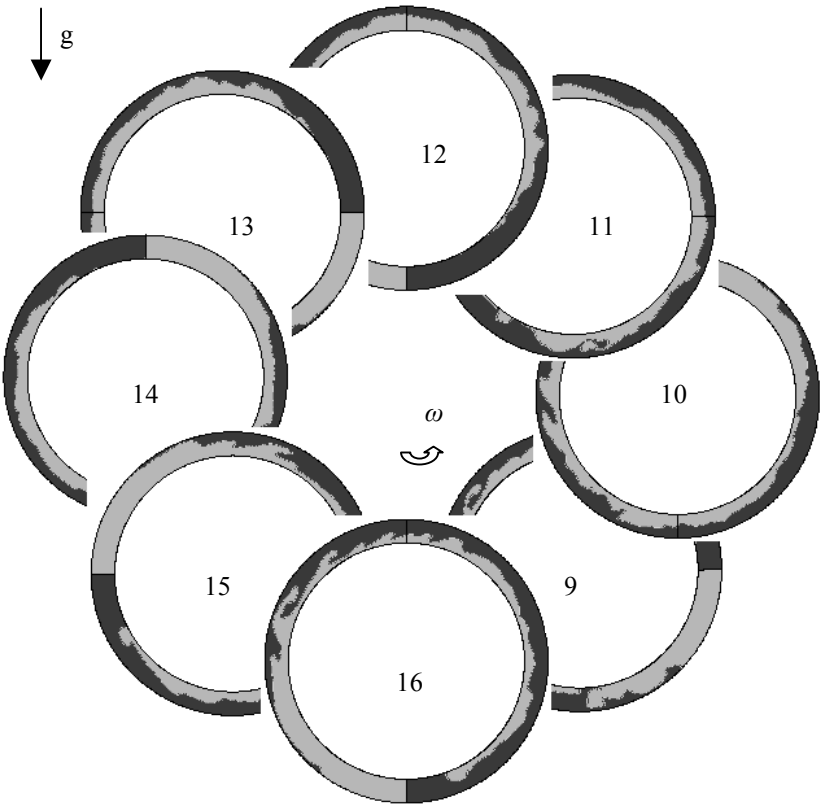

Figure 3: Phase distribution for the closed ring during 2nd rotation at 120rpm and β=0.5.

Another difference for the variation in beta value is the velocity development in the ring. For β≥ 0.5 the wall velocities at the proximal point remain ≥ 0, whereas for β<0.5 they become negative with respect to the rotation [13]. For any of the three beta values, the absolute velocity in the flow though is negative with respect to the rotation though its relative magnitude varies. As the wall

velocities are always greatest in the distal region, the resulting shear forces there are responsible in accelerating the flow in positive rotation direction. The inertia of the liquids causes the absolute velocity maintaining this direction throughout, but at the proximal end this then is negative with respect to the rotation. For β=0.5 and β=0.7 the velocity in the core area remains fairly constant throughout the ring with a fairly flat profile, its magnitude being approximately midway between the outer proximal and inner distal wall velocity. For β=0.3, however, the core velocity profile is distinctly more parabolic resulting in different shear. In all cases the core velocity is higher in the proximal region and lower in the distal region. While for β=0.5 and β=0.7, the difference in core velocity at the two different locations is very small, it is significantly increased for β=0.3 due to the different nature of the velocity profile.

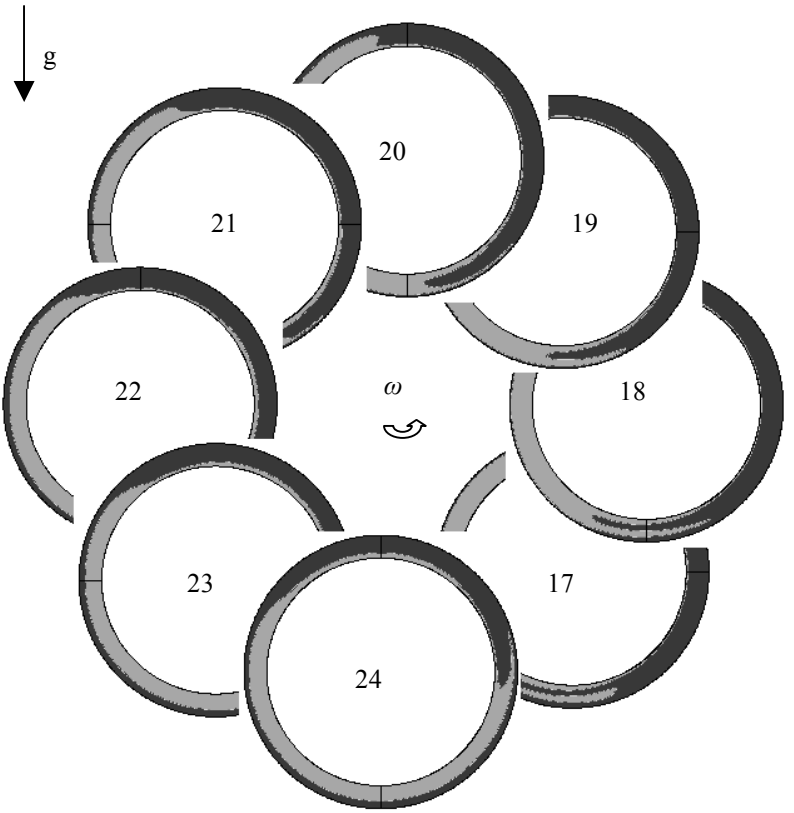

Figure 4: Phase distribution for the open ring during 3rd rotation at 300rpm and β=0.5.

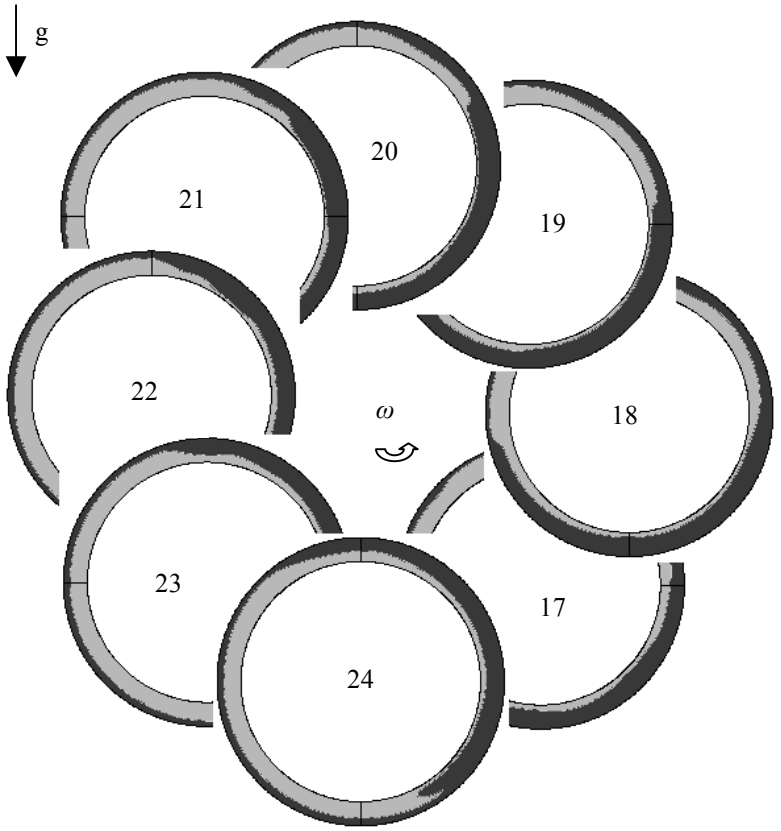

Figure 5: Phase distribution for the closed ring during 3rd rotation at 600rpm and β=0.5.

6 Conclusions and future work

The most significant finding of this study is the influence beta value has on phase distribution. Smaller beta values tend to result in areas of more violent mixing. The core velocity is found to show different characteristics for different beta values.

Future numerical experiments are planned with refined beta steps in both ring and coil geometries. It is also planned to compare these numerical results with experimental ones for verification. An experimental test rig is currently being built.

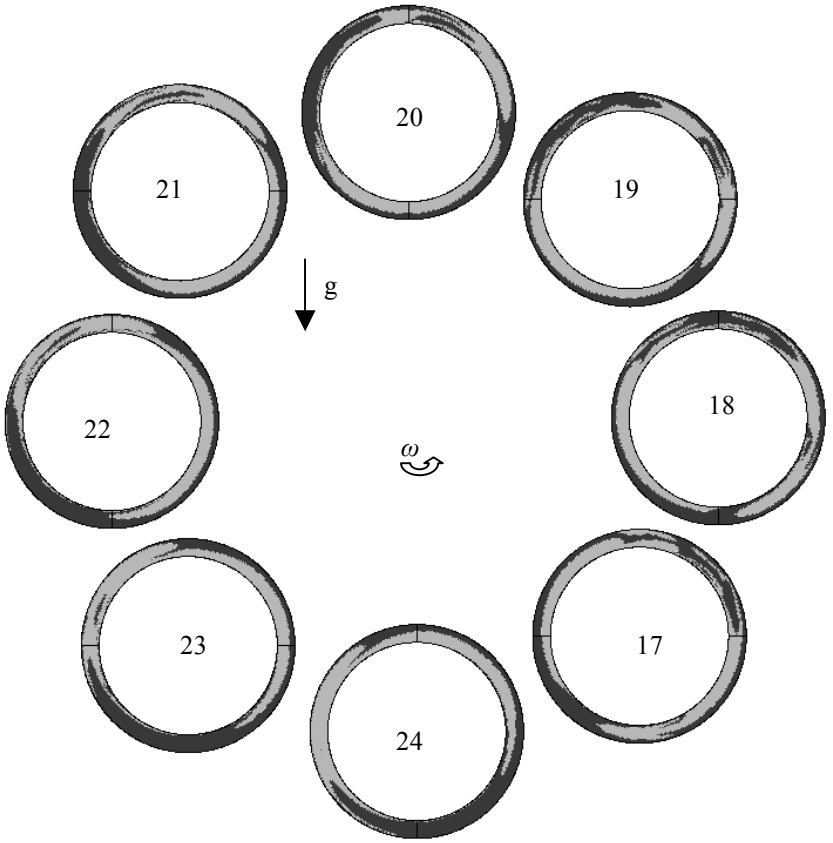

Figure 6: Phase distribution for the closed ring during 3rd rotation at 600rpm and β=0.3.

References

[1] Sutherland, I.A., Muytjens, J., Prins, M., Wood, P. A new hypothesis on phase distribution in countercurrent chromatography, J. Liq. Chrom. & Rel. Technol,. 2000, **23(15)**, 2259-2276.

[2] Conway, W.D. *Countercurrent Chromatography: Apparatus, Theory and Applications*, VCH Publishers, 1990, ISBN 0-89573-331-5.

[3] Wood, P.L., Jaber, B., and Sutherland, I.A. A new hypothesis on the hydrodynamic distribution of the upper and lower phases in CCC, J. Liq. Chrom. & Rel. Technol., 2001, ***24*(11&12)**, 1629-1654.

[4] Carola S. König & Ian A. Sutherland. An investigation of the influence of the gravity field on the interface of two immiscible liquids - a computational study comparing prediction with experiment, J. Liq. Chrom. & Rel. Technol., 2003, 26(9&10), 1521-1535.

[5] Sutherland, I.A., Booth, A.J., Brown, L., et al., Industrial scale-up of countercurrent chromatography, J. Liq. Chrom. & Rel. Technol., **24(11&12)**, pp. 1533-1553, 2001.
[6] Sutherland, I.A., Brown, L., Forbes, S., et al., Countercurrent chromatography (CCC) and its versatile application as an industrial purification & production process, *J. Liq. Chrom. & Rel. Technol.*, **21(3)**, pp. 279-298, 1998.
[7] König, C.S. & Sutherland, I.A., 'Numerical visualization of the interface of immiscible liquids in an oscillating pipe'. *Proc. of the 10th International Symposium on Flow Visualization*, Kyoto, Japan, 26-29 August, Paper no. F0203, ISBN 4-906497-82-9, pp. 1-6., 2002.
[8] König, C.S. & Sutherland, I.A., ‘'Numerical modelling of liquid-liquid flow related to countercurrent chromatography (CCC) '. In: Advances in Fluid Mechanics - Computational Methods in Multiphase Flow II, **37**, pp. 63-73.
[9] Brackbill, J., Kothe, D.B., Zemach, C., A continuum method for modelling surface tension, *J. Comp. Phys.*, **100**, 335-354, 1992.
[10] Anonymous, CFX-4 Release 4.4, Solver manual, CFX International, Harwell Laboratory, Oxfordshire, UK.
[11] Wood, P., The hyrdodynamics of countercurrent chromatography in J-type centrifuges, PhD thesis, Brunel University, Uxbridge, UK, 2002.
[12] Scardovelli, R. & Zaleski, S., Direct numerical simulation of free-surface and interfacial flow, *Annu. Rev. Fluid Mech*., **31**, pp. 567-603, 1999.
[13] Wood, P.L., Jaber, B., Janaway, L., Sutherland, I.A. and Terlinden, N., ‘Effect of β-value on the head and tail distribution of the upper and lower phases in helical coils’, J. Liq. Chrom. & Rel. Technol., in print.

Development of low-diffusion flux-splitting methods for gas-liquid flows with interface propagation and phase variation

D. Mao[1], A. D. Harvey[2] & J. R. Edwards[3]
[1]*The Dow Chemical Company*
[2]*Shell Exploration and Production Company*
[3]*Department of Mechanical and Aerospace Engineering, North Carolina Sate University, USA*

Abstract

The development of a class of low-diffusion upwinding methods for computing gas-liquid flows with interface propagation and phase variation is presented in this work. An artificial compressibility/low-Mach preconditioning strategy is developed for a hyperbolic two-phase mixture system. The eigenvalues of this system are used to devise extensions of the low-diffusion flux-splitting scheme (LDFSS) method that provide high resolution capturing of interface propagation and phase variation in the gas-liquid system. These schemes are utilized in a polymer injection molding application involving the flow and growth of both chemical and physical foams. In physical foaming processes, a gas is dissolved into the polymer as a physical blowing agent and at a specified temperature and pressure creates foams. Once the dissolution is completed, either the pressure is reduced or the temperature is increased so as to liberate the dissolved gas to create foam. In chemical foams, the blowing agent is created by a chemical reaction as a dissolved gas which vaporizes into a bubble phase creating foam. The foam expansion rate is determined by fundamental physical parameters such as diffusion coefficient, bulk viscosity, bubble radius, bubble number density and dissolved gas concentration at the bubble edge. Foam growth dynamics is modeled using an influence volume approach which is fully coupled into a two-phase (gas-liquid) Navier-Stokes solver. The resulting three-phase foam flow formulation (polymer liquid mixture, foam bubble gas and air phases) provides polymer/air interface tracking as well as quantitative bubble scale and macro-scale flow information. Bubble scale information includes bubble number density and bubble radius; and macro-scale information includes bubble void fraction, mixture mass density and temperature, liquid species mass fraction, and velocity distribution. The method is demonstrated on both a continuous (flow-through) application and a semi-batch (or closed) foam flow system.

Keywords: upwind discretisation, time-derivative preconditioning, interface tracking, phase variation, physical foam, chemical foam, bubble growth, influence volume approach.

1 Introduction

There are several basic characteristics of a foaming flow that we attempt to consider as we develop a model. The first is the expansion of the bubble gas phase. In physically-blown foams, the gas used in the expansion process is present initially in the liquid as dissolved gas and is released thermodynamically by a sudden drop in pressure. In chemically-blown foams, the dissolved gas is first produced through a chemical reaction, and the diffusion of the gas into an initial population of bubbles (generated through homogeneous or heterogeneous nucleation) drives the bubble-growth process. The bubble-growth process may be influenced by viscoelastic effects and is generally halted at the gel point due to the dramatic increase in viscosity. The second characteristic of foam flows is the presence of a moving interface between the foaming mixture and the environment. As the liquid polymeric material is injected through a die or into a mold, it displaces air, and the modeling of the interface between these two phases must be considered.

There has been a great deal of interest in modeling and simulation of foaming flows. Most of the foaming work found in the literature is based on Lagrangian techniques. Some examples include: [1-27]. Lagrangian models are more suited for detailed analysis of single-bubble growth and are less applicable to complex mold-filling problems.

Examples of some foaming flow modeling based on Eulerian methods include Lo *et al.* [28, 29]; Kim and Macosko, [30]; Shimoda *et al.* [31]; Malkin and Kuznetsov [32]; Polushkin *et al.* [33], Mitani and Hamada [34], and Seo *et al.* [35]. Many of these usually attempt to capture the moving interface, but do not consider the foaming expansion or the bubble growth process in much detail. Kim and Macosko [30] considered the dependence of conversion, temperature and average molecular weight on mixture viscosity during foam processing. Shimoda *et al.* [31] did numerical simulations of polymeric foaming for extrusion applications; however, the governing equations were solved in a non-conservative form. Of these works, that of Seo *et al.* [35] is closest to the present approach. This work, however, assumes a time-dependent variation in density and viscosity without attempting to connect this variation to the dynamics of the foaming process itself. These assumptions would appear to limit the applicability of their approach. Han *et al.* [36] did a foaming simulation based on modeling polymer / dissolved gas-phase equilibrium using the Sanchez-Lacombe equation of state, rather than Henry's law. They reported having trouble with the multi-phase implementation in the Fluent CFD package.

The moving interface between the polymeric mixture and the environment (usually air) is a general characteristic in reaction injection molding and foaming applications. The question of how to capture a moving interface accurately is still a challenging area of research. In our work, we use techniques similar to those used in gas-dynamic shock-capturing to resolve the interface across a few mesh cells. An advantage of this approach is that it conserves mass and requires only minor modifications for multiple spatial dimensions. A disadvantage is that

"sharp" interfaces may be spread over a number of mesh cells. This number can be reduced to 3 or 4 by applying higher-order upwind methods or contact-discontinuity sharpening techniques

It is also important to consider that the melt viscosity often changes by orders of magnitude during foam processing. The presence of an increasing viscosity results in the creation of high stresses, which have dramatic influences on bubble growth rate and bubble shape.

In this paper, we develop this general foaming model and apply to chemical and physical foaming.

2 Governing equations and model development

2.1 Conservation equations for general foam modeling

The general foaming model is represented as a system of conservation laws in Eqs (1), (2a), and (2b). The development is presented for chemically-blown polyurethane foaming; physically-blown foams may be simulated by eliminating liquid-phase chemical reactions and by imposing a fixed initial concentration of the dissolved gas in the polymer liquid.

$$\frac{\partial U}{\partial t}+\frac{\partial\left(E-E_v\right)}{\partial x}+\frac{\partial\left(F-F_v\right)}{\partial y}+\frac{\partial\left(G-G_v\right)}{\partial z}=S \tag{1}$$

The equations describe a three-phase system consisting of a polymer liquid phase (subscript "L") which may consist of multiple components, a bubble gas phase (subscript "g"), and an external air phase (subscript "a"). A "mixture" formulation is used, meaning that velocity slip effects are neglected and that a mass-averaged "mixture" velocity is used for all phases.

In these equations, U is the vector of conserved variables, E, F, and G are the inviscid flux vectors in each of the Cartesian coordinate directions, and E_v F_v and G_v are the viscous / diffusive flux vectors. The mixture density is ρ_B; Y_L^F is the polymer liquid mass fraction in the mixture, and Y_g^F is the bubble-gas mass fraction in the mixture. For polyurethane foaming, the polymer liquid contains components of polyol, water, isocyanate, polyurethane, and carbon dioxide, with mass fractions (relative to the liquid mass) denoted as X_L^1, X_L^2, X_L^3, X_L^4, X_L^5, respectively. The bubble-gas void fraction is α_g^F; the liquid void fraction is α_L^F; and the external air void fraction is α_A.

$$U=\begin{bmatrix}\rho_B Y_g^F\\ \rho_B\\ \rho_B u\\ \rho_B v\\ \rho_B w\\ \rho_B H-p\\ \rho_B Y_L^F X_L^1\\ \rho_B Y_L^F X_L^2\\ \rho_B Y_L^F X_L^3\\ \rho_B Y_L^F X_L^4\\ \rho_B Y_L^F X_L^5\\ \rho_B Y_L^F\\ \rho_g^F\\ n\end{bmatrix}=\begin{bmatrix}\rho_g \alpha_g^F\\ \rho_B\\ \rho_B u\\ \rho_B v\\ \rho_B w\\ \rho_B H-p\\ \rho_L^F \alpha_L^F X_L^1\\ \rho_L^F \alpha_L^F X_L^2\\ \rho_L^F \alpha_L^F X_L^3\\ \rho_L^F \alpha_L^F X_L^4\\ \rho_L^F \alpha_L^F X_L^5\\ \rho_L^F \alpha_L^F\\ \rho_g^F\\ n\end{bmatrix}\quad E=\begin{bmatrix}\rho_B Y_g^F u\\ \rho_B u\\ \rho_B uu+p\\ \rho_B uv\\ \rho_B uw\\ \rho_B Hu\\ \rho_B Y_L^F X_L^1 u\\ \rho_B Y_L^F X_L^2 u\\ \rho_B Y_L^F X_L^3 u\\ \rho_B Y_L^F X_L^4 u\\ \rho_B Y_L^F X_L^5 u\\ \rho_B Y_L^F u\\ \rho_g^F u\\ nu\end{bmatrix}\quad F=\begin{bmatrix}\rho_B Y_g^F v\\ \rho_B v\\ \rho_B vu\\ \rho_B vv+p\\ \rho_B vw\\ \rho_B Hv\\ \rho_B Y_L^F X_L^1 v\\ \rho_B Y_L^F X_L^2 v\\ \rho_B Y_L^F X_L^3 v\\ \rho_B Y_L^F X_L^4 v\\ \rho_B Y_L^F X_L^5 v\\ \rho_B Y_L^F v\\ \rho_g^F v\\ nv\end{bmatrix}\quad G=\begin{bmatrix}\rho_B Y_g^F w\\ \rho_B w\\ \rho_B wu\\ \rho_B wv\\ \rho_B ww+p\\ \rho_B Hw\\ \rho_B Y_L^F X_L^1 w\\ \rho_B Y_L^F X_L^2 w\\ \rho_B Y_L^F X_L^3 w\\ \rho_B Y_L^F X_L^4 w\\ \rho_B Y_L^F X_L^5 w\\ \rho_B Y_L^F w\\ \rho_g^F w\\ nw\end{bmatrix} \tag{2a}$$

$$S=\begin{bmatrix}S_{pg}\\ 0\\ S_x\\ S_y\\ S_z\\ S_{energy}\\ S_L^1\\ S_L^2\\ S_L^3\\ S_L^4\\ S_L^5-S_{pg}\\ -S_{pg}\\ S_{rhogf}\\ 0\end{bmatrix}\quad E_v=\begin{bmatrix}0\\ 0\\ \tau_{xx}\\ \tau_{yx}\\ \tau_{zx}\\ u_i\tau_{ix}-q_x-q_x^{sp}\\ -\rho_B Y_L^F X_L^1 u_1^d\\ -\rho_B Y_L^F X_L^2 u_2^d\\ -\rho_B Y_L^F X_L^3 u_3^d\\ -\rho_B Y_L^F X_L^4 u_4^d\\ -\rho_B Y_L^F X_L^5 u_5^d\\ 0\\ 0\\ 0\end{bmatrix}\quad F_v=\begin{bmatrix}0\\ 0\\ \tau_{xy}\\ \tau_{yy}\\ \tau_{zy}\\ u_i\tau_{iy}-q_y-q_y^{sp}\\ -\rho_B Y_L^F X_L^1 v_1^d\\ -\rho_B Y_L^F X_L^2 v_2^d\\ -\rho_B Y_L^F X_L^3 v_3^d\\ -\rho_B Y_L^F X_L^4 v_4^d\\ -\rho_B Y_L^F X_L^5 v_5^d\\ 0\\ 0\\ 0\end{bmatrix}\quad G_v=\begin{bmatrix}0\\ 0\\ \tau_{xz}\\ \tau_{yz}\\ \tau_{zz}\\ u_i\tau_{iz}-q_z-q_z^{sp}\\ -\rho_B Y_L^F X_L^1 w_1^d\\ -\rho_B Y_L^F X_L^2 w_2^d\\ -\rho_B Y_L^F X_L^3 w_3^d\\ -\rho_B Y_L^F X_L^4 w_4^d\\ -\rho_B Y_L^F X_L^5 w_5^d\\ 0\\ 0\\ 0\end{bmatrix} \tag{2b}$$

The Cartesian velocity components are u, v, and w. The total enthalpy of the mixture is given as H, and T is the mixture temperature. ρ_A is the external air density, ρ_g^F is the bubble mass density, and n is the bubble number density. The last liquid species, urea, is not included explicitly, as it is accounted for by the constraint that the liquid-species mass fractions sum to unity. For the case of physically-blown foams, only one liquid species equation for the dissolved gas concentration in the polymer liquid is solved.

The mixture density and total enthalpy are defined in terms of the phasic densities, enthalpies, and void fractions:

$$\rho_B = \rho_g^F \alpha_g^F + \rho_L^F \alpha_L^F + \rho_A \alpha_A \tag{2d}$$

$$\rho_B H = \left(\rho_g^F \alpha_g^F C_g^F + \rho_L^F \alpha_L^F C_L^F + \rho_A \alpha_A C_A\right) T + \frac{1}{2}\rho_B \left(u^2 + v^2 + w^2\right) \tag{2e}$$

In this, C_g^F, C_L^F and C_A are specific heats for bubble gas, liquid and external air, respectively. Here, we assume that enthalpies of the liquid mixture, as well as the gases, may be represented by a linear dependence on the temperature and constant specific heats. Enthalpy changes due to chemical conversion are dealt with separately.

Components of the viscous / diffusive fluxes include the stress tensor

$$\tau_{ij} = \mu\left(\frac{\partial u_i}{\partial x_j} + \frac{\partial u_j}{\partial x_i}\right) \tag{2f}$$

the heat flux vector

$$q_i = -\lambda \frac{\partial T}{\partial x_i} \tag{2g}$$

and the effective heat flux due to diffusion of reactants

$$q_j^{sp} = \sum_{k=1}^{N} h_k J_{k,j} = \sum_{k=1}^{N} h_k \rho_k u_{k,j}^d = \sum_{k=1}^{N} h_k \rho Y_k u_{k,j}^d = \sum_{k=1}^{N} C_{p,k} T \rho Y_k u_{k,j}^d \tag{2h}$$

The molecular diffusion velocities are expressed using Fick's law as

$$u_{i,j}^d = -\frac{D_i}{X_L^i}\frac{\partial X_L^i}{\partial x_j} \tag{3a}$$

$$-\rho_B Y_L^F X_L^i u_{i,j}^d = -\frac{\mu_L \alpha_L}{Sc}\frac{\partial X_{L,i}}{\partial x_j} \tag{3b}$$

$$Sc = \frac{\mu_L}{\rho_L^F D} \tag{3c}$$

In these equations, μ is the viscosity of the polymer, λ is the thermal conductivity, and Sc is the Schmidt number. In the cases presented in the following section, the diffusion coefficient and the thermal conductivity are set to zero. Other closure relationships are as follows.

$$\frac{1}{\rho_B} = \frac{Y_L^F}{\rho_L^F} + \frac{Y_g^F}{\rho_g^F} + \frac{Y_a}{\rho_a} \tag{4a}$$

$$1 = Y_L^F + Y_g^F + Y_a^F \tag{4b}$$

$$\alpha_a = 1 - \alpha_p^F - \alpha_g^F \tag{4c}$$

$$\alpha_k = \frac{\rho_B Y_k}{\rho_k}, \left(k = a, L^F, g^F\right) \tag{4d}$$

$$\rho_a = \frac{P M_{air}}{RT} \tag{4e}$$

Because the density differences among polyol, water, isocyanate, polyurethane, and urea are small, their densities are assumed to be same as the polymer melt density ρ_L^F.

2.2 Chemical reaction dynamics

For chemically-blown polyurethane foaming, Baser and Khakhar [11] considered two simplified reactions. The first governs the polymerization process, which generates heat, increases average molecular weight, and induces an increase in viscosity up to the gel-point. The second chemical reaction generates carbon dioxide, which foams the polymer. It is assumed that carbon dioxide generated by this reaction is initially dissolved in the polymer melt and then is diffused into bubble gas phase after the liquid becomes saturated.

$$R - NCO_{(Isocyanate)} + R'\text{–}OH_{(Polyol)} \rightarrow R - NH - COOR'_{(Polyurethane)} \quad (5a)$$

$$2R - NCO_{(Isocyanate)} + H_2O_{(Water)} \rightarrow R - NH - CONH - R_{(Urea)} + CO_2 \quad (5b)$$

Chemical reaction rates for the above two reactions are listed below. Rate constants and other parameters of interest are listed in Table 1.

$$\begin{aligned} \frac{d[OH]}{dt} &= -R_1 = -A_{OH} \exp\left(-\frac{E_{OH}}{RT}\right)[NCO][OH] \\ \frac{d[W]}{dt} &= -R_2 = -A_W \exp\left(-\frac{E_W}{RT}\right)[W] \end{aligned} \quad (5c)$$

Table 1: Material parameters [11].

Parameter	Value
Polyurethane	
ρ_P	$1100\,kg/m^3$
C_P	$1800\,J/kg\,K$
M_{no}	615
Carbon Dioxide	
M_{CO_2}	44
C_{PCO_2}	$836.6\,J/kg\,K$
$D_{(CO_2)_D}$	4.4×10^{-4}
Polyurethane kinetic parameters	
A_{OH}	$1.7348 m^3/g-equiv/s$
E_{OH}	$4.04\times10^4 J/g-mol$
$(-\Delta H)_{OH}$	$7.075\times10^4 m^3/g-equiv$
Water-Isocyanate reaction kinetic	
A_W	$1.385\times10^3\ \mathrm{sec}^{-1}$
E_W	$3.266\times10^4 J/g-mol$
$(-\Delta H)_W$	$8.6\times10^4 m^3/g-equiv$

$$\begin{aligned} [OH] &= \frac{\rho_L^F \alpha_L^F X_L^1 \cdot 1000}{M_{Polyol}} \\ [NCO] &= \frac{\rho_L^F \alpha_L^F X_L^3 \cdot 1000}{M_{Isocyanante}} \\ [W] &= \frac{\rho_L^F \alpha_L^F X_L^3 \cdot 1000}{M_{Water}} \end{aligned} \tag{5d}$$

The factor of 1000 converts the concentration variables to gram-equivalent or gram-moles, as our model is formulated in SI units.

The source terms in Eq. (2) are developed as in Equation 6. In this, M_{Polyol}, M_{Water}, $M_{Isocyanate}$, $M_{Polyurethane}$, and M_{CO2} are equivalent weights of the reactants (g/g-equiv) and are assigned values of 153.7, 18, 135, 288.7, and 44, respectively. Momentum source terms S_x, S_y, and S_z in Eq. (2) are comprised of gravitational acceleration terms and Brackbill's [37] continuum model for surface tension between the foam and air phases.

The source term for the bubble gas phase is denoted by S_{pg}, which is driven by mass diffusion from the liquid carbon dioxide and derived based on Influence Volume Approach (IVA). The concentration profile is linear and taken from Koopmans *et al.* [23]. Because the bubble gas mass increases at the expense of mass losses from the carbon dioxide dissolved in the polymer liquid phase, the sign of the source term is positive in the bubble gas phase equation and negative in both the continuity equation for carbon dioxide in the liquid phase (X_L^5) and the continuity equation for the liquid phase. The concentration of carbon dioxide in the liquid phase grows through the chemical reactions listed above. S_{energy} is the source term in the energy equation and accounts for heat generated by chemical reaction or phase change.

$$\begin{aligned} S_L^1 &= -\alpha_p^F \frac{M_{Polyol}}{1000} R_1 \\ S_L^2 &= -\alpha_p^F \frac{M_{Water}}{1000} R_2 \\ S_L^3 &= -\alpha_p^F \frac{M_{Isocyanate}}{1000} (R_1 + 2R_2) \\ S_L^4 &= \alpha_p^F \frac{M_{Polyurethane}}{1000} R_1 \\ S_L^5 &= \alpha_p^F \frac{M_{CO2}}{1000} R_2 \\ S_{pg} &= 3\frac{\alpha_g^F}{R} D_{pg} \left.\frac{\partial C}{\partial R}\right|_{r=R} \\ S_{energy} &= -\alpha_p^F \left[(\Delta H)_{OH} R_1 + (\Delta H)_W R_2\right] + S_{pg}(h_g - h_p) - S_{pg}(h_g - h_{p,CO_2}) \\ S_{rhogf} &= -\rho_g^F \left(\frac{3}{R}\frac{DR}{Dt} - \left[\frac{\partial u}{\partial x} + \frac{\partial v}{\partial y} + \frac{\partial w}{\partial z}\right]\right) + 3\frac{D_{pg}}{R}\left.\frac{\partial C}{\partial R}\right|_{r=R} \end{aligned} \tag{6}$$

2.3 Bubble growth dynamics

The model for bubble growth dynamics is based on an influence-volume approach, and some of the parameters used are taken from Koopmans *et al.* (23). The concentration profile within the influence volume is assumed to be linear, following den Doelder et al. [24], Koopmans et al. [23]. Details of the bubble dynamics model are presented below.

A rate law for growth of an average bubble of radius R is

$$\frac{DR}{Dt} = \frac{\left(p_g^F - p\right)R - 2\sigma}{4\eta} \tag{7a}$$

with the bubble pressure defined in terms of the bubble gas density and temperature:

$$p_g^F = \rho_g^F R_{CO2} T \tag{7b}$$

The average radius is related to the bubble number density n and the bubble gas void fraction α_g^F as follows,

$$R = \left[\frac{3}{4\pi}\left(\frac{\alpha_g^F}{n}\right)\right]^{1/3} \tag{7c}$$

while a characteristic radius of the influence volume is defined by considering the volume occupied by both the bubble gas phase and the liquid phase:

$$S = \left[\frac{3}{4\pi}\left(\frac{\alpha_g^F + \alpha_p^F}{n}\right)\right]^{1/3} \tag{7d}$$

A linear distribution of gas concentration within the influence volume is assumed, with the concentration at the bubble edge given by Henry's Law:

$$C(R) = K_h p_g^F \tag{7e}$$

The requirement that the average concentration within the influence volume (based on the assumed linear distribution) be equal to the average concentration as extracted from the continuity equation for carbon dioxide within the liquid phase gives a form for the concentration gradient at the bubble edge $\left.\frac{\partial C}{\partial r}\right|_{r=R}$. This provides the mass source for the bubble gas phase:

$$\left.\frac{\partial C}{\partial r}\right|_{r=R} = \frac{\left[\overline{C} - C(R)\right]}{\Delta r} \tag{7f}$$

$$\Delta r = \frac{0.75\left(S^4 - R^4\right) - R\left(S^3 - R^3\right)}{\left(S^3 - R^3\right)} \tag{7g}$$

The above equations are extended to a generalized coordinate system for use in analyzing flows in complicated geometries and are incorporated into a version of Dow Chemical's CHEM3D flow solver. CHEM3D solves the equation system using implicit preconditioning methods.

3 Initial and boundary conditions

At the start of a simulation, the initial position of the liquid-air interface is specified on the computational mesh, and the appropriate initial conditions for

the thermodynamic variables are provided for each phase. The pressure is held constant, and the velocities are initially set to zero. No-slip, adiabatic wall boundary conditions are used in the present simulation for all phases. Due to the polymeric liquid structure, a slip wall or partial slip wall should actually occur. We will consider this complexity in future work [38, 39].

4 Results and discussions

4.1 Validation in one dimensional continuous tube

To demonstrate the model performance, a chemical foam in a 1-D continuous tube is considered. Fresh liquid mixture enters the tube from left inlet section as shown in Figure 1a. With the polymerization and blowing agent reaction, liquid mixture mass density decreases with foam growing. Thus, liquid mixture gets acceleration in the tube. Transferring this information from spatial coordinate into temporal coordinate based on local residence time, which is calculated by the local space position and local velocity, makes the comparison between Eulerian frame and Lagrangian one possible. For example, Figures 1b and 1c show a good comparison in temperature and liquid mixture mass density between Lagrangian experiments from Baser and Khakhar [10] and the present simulation from Eulerian frame. Tables 1 and 2 provide parameters needed in the present simulation.

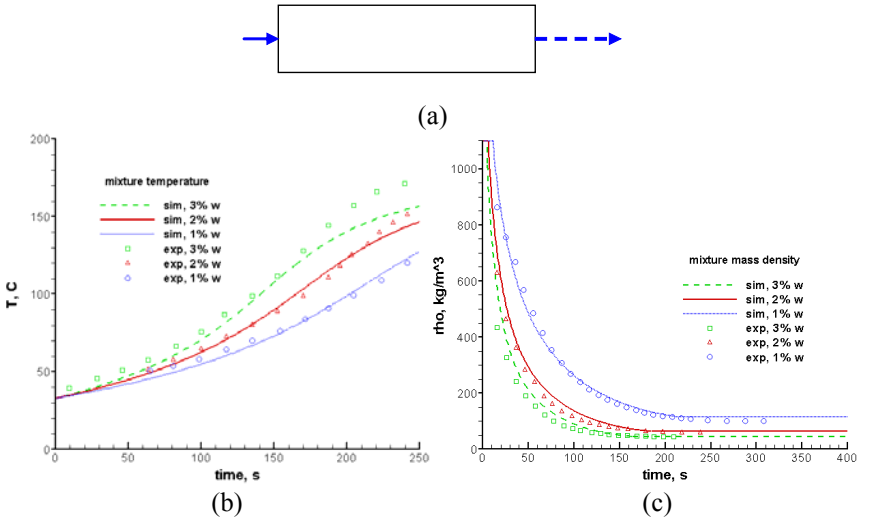

Figure 1: (a) Tube geometry. (b) mixture temperature. (c) mixture mass density.

4.2 Chemical and physical foam expansion in Hele-Shaw flow

The left figure in Fig. 2 shows a channel geometry containing an "L" shape cross-section used in the simulation of Hele-Shaw flow. This cavity extends 1

meter in the z-direction (streamwise direction), 0.06 or 0.03 meters in the y-direction, and 0.15 or 0.30 meters in the x-direction. Initially, 0.5% dissolved carbon dioxide and 3% water are set at the bottom with the height of 0.1 meters. Due to viscous effect close to the wall, the evolving foam mixture will travel with a different velocity in locations where the cross-section is wide compared to the material located in the narrower cross-section.

Table 2: Bubble formation parameters (some from Koopmans *et al.* [23]).

Parameters	Values
Ambient pressure, P_o	1.0E5 Pa
Diffusion coefficient, D_{pg}	1.0E-7 m^2/s
Dissolved gas mass fraction, X_g^0	0.01
Henry coefficient, K_H	5.0E-7 s^2/m^2
Initial bubble radius, R_0	1.0E-8 m
Initial bubble number density, n_0	1.0E15 $\#/m^3$
Initial temperature, T	420 K
Polymer density, ρ_p	1050 kg/m^3
Surface tension, σ	0.02 N/m
Viscosity, η	6,000 Pa s

Table 3: Initial parameters for chemically-blown Polyurethane foam.

Parameter	3% water
T, K	306.0
n_0, $\#/m^3$	1.0E15
R_0, m	1.0E-6
X_L^1 (Polyol)	0.42403
X_L^2 (water)	0.01272
X_L^3 (isocyanate)	0.56325

The middle figure in Fig. 2 shows bubble voidage fraction in three dimensions at 0.3. It can be found that interface moves faster in the wide cross-section where it is 0.06 meters in width compared to that in the narrow cross-

section where it is 0.03 meters in width. This is clearly shown in right Figure in Fig. 2 which illustrates the evolution of the interface through a sequence of snapshots of the flow in a three-dimensional plane at 15.0 seconds, respectively. Close to the beginning, the bubble voidage fraction is small and the interface shape is almost flat. With foaming growth, bubble void fraction increases and the interface shape changes due to the viscous resistance at the wall. Material in the wider cross-section moves faster than that located in the narrower cross-section. Mitani and Hamada [34] performed experiments in a similar geometry and also found that the interface moves faster in the wider section. They also performed numerical simulations based on steady Stokes flow but using an unsteady continuity equation and assuming a prescribed foam volume expansion rate as 0.3 or a linear profile over the foaming time. But they regarded that the viscosity was allowed an arbitrary value and a viscosity value of 100 $Pa \cdot s$ was provided just to make sure that Reynolds number was much smaller than unity. Their predicted cross-stream velocity profile in the channel is much flatter than that measured in the experiments.

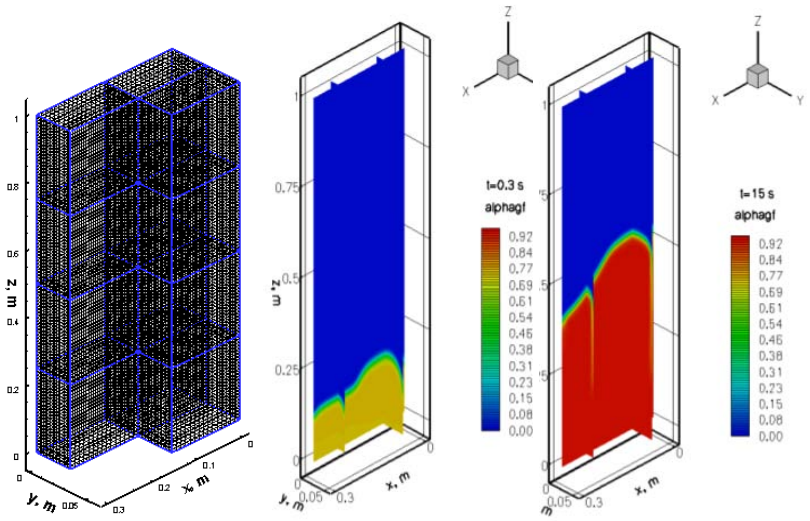

Figure 2: Hele-Shaw flow.

4.3 Chemical and physical foam expansion in 3D box

Figure 3 shows a three-dimensional box geometry for physical and chemical foam. This 3D box is a continuous reactor for physical foam and a semi-batch reactor for the combination of physical and chemical foam. Ninety blocks are utilized in the box for parallelization simulation. Fresh mixture liquid is injected into the box through left inlet section. Only the top is open to the air.

Figure 4a shows distribution of bubble radius in the surface of 3D box at 1.0 seconds. The box is filled up with mixture liquid when shooting time is 1.0

seconds and it works like a continuous reactor. Bubble radius is smaller in the surface close to the injection inlet section when local residence time is shorter and it is larger in the surface where liquid has longer residence time.

Figure 4b shows distribution of bubble voidage in a continuous reactor at 0.3 seconds from the beginning of injection. In this physical foam, 1% dissolved gas (carbon dioxide) is shot into the box through injection inlet section with 7.0 m/s of velocity. Interface between mixture liquid and external air is found at the front. Bubble voidage fraction is larger close to the interface because bubbles have longer residence time to grow. It is also larger close to the wall. This is due to the low velocity of the boundary layer results in the longer residence time, and longer residence time means bubble has grown for a longer time. Close to the injection inlet section, bubble voidage fraction is smaller because local residence time is shorter and bubbles do not have enough time to grow.

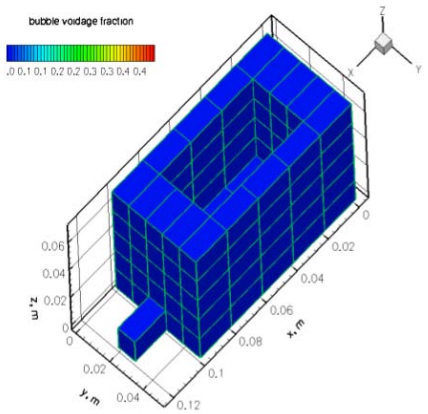

Figure 3: Geometry of 3D box.

Figure 4c shows distribution of mixture liquid mass density at 0.3 seconds. Mixture liquids mass density is the function of bubble voidage fraction as shown in Equation (2d). When bubble voidage fraction is zero, mixture liquid is pure liquid and mixture mass density is the maximum. When liquid voidage fraction is close to zero, mixture liquid is almost composed of bubble gas and its mass density is the minimum. Mixture mass density is smaller close to the wall and the interface where liquid has longer local residence time, and it is larger close to the injection inlet section for local residence time is shorter.

For the combination of physical and chemical foam, 0.1% physical blowing agent, carbon dioxide, dissolved in the liquid mixture and 1.2% chemical blowing agent, water, are shot at the injection inlet section for 0.1 seconds. After 0.1 seconds, the shooting stops and foam rise freely. Figures 5a and 5b show distributions at the end of the shooting for liquid voidage fraction and water mass fraction, respectively. It can be found that liquid touch the end of the box at 0.1 seconds.

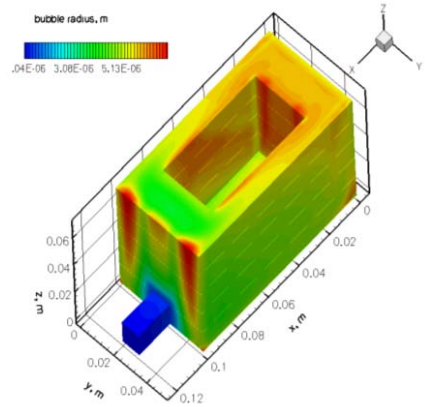

(a)

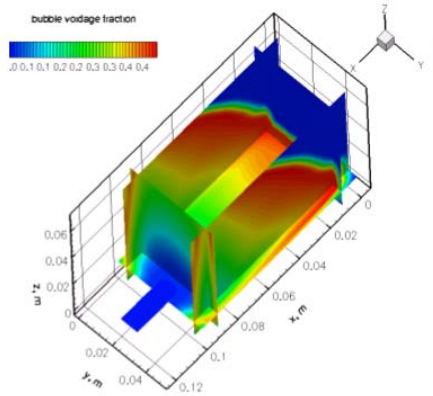

(b)

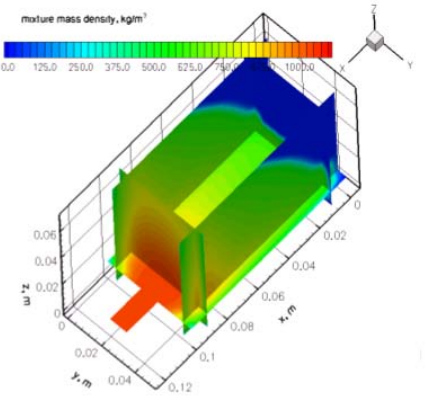

(c)

Figure 4: (a) Bubble radius at 1.0 s. (b) Bubble voidage fraction at 0.3 s. (c) mixture mass density at 0.3 s.

Figures 5c and 5d show distributions of liquid voidage fraction and water mass fraction at 2.2 seconds, respectively. It can be found more homogeneous in the present semi-batch reactor than that in the continuous reactor shown in Figures 4a to 4c. Liquid voidage fraction is much smaller at 2.2 seconds than that at 0.1 seconds with foaming processing. For example, it is about 0.9 and 0.09 at 0.1 seconds and 2.2 seconds, respectively. So does water mass fraction. It is about 0.012 and 0.005 at 0.1 seconds and 2.2 seconds, respectively.

5 Conclusion

A Eulerian approach for simulating physically- and chemically-blown foams has been presented. The computational model can provide variables such as species composition, bubble gas void fraction, mixture velocity, mixture density, and mixture temperature as functions of time and space. By combining the model

with an influence volume approach (IVA), distributions of bubble size and bubble number density can also be obtained. Simulations in one and three spatial dimensions have been performed to assess the new methodology. Future work will include the addition of viscoelastic effects, improved influence-volume modeling, bubble nucleation, and velocity slip effects, along with a more detailed assessment versus experimental data.

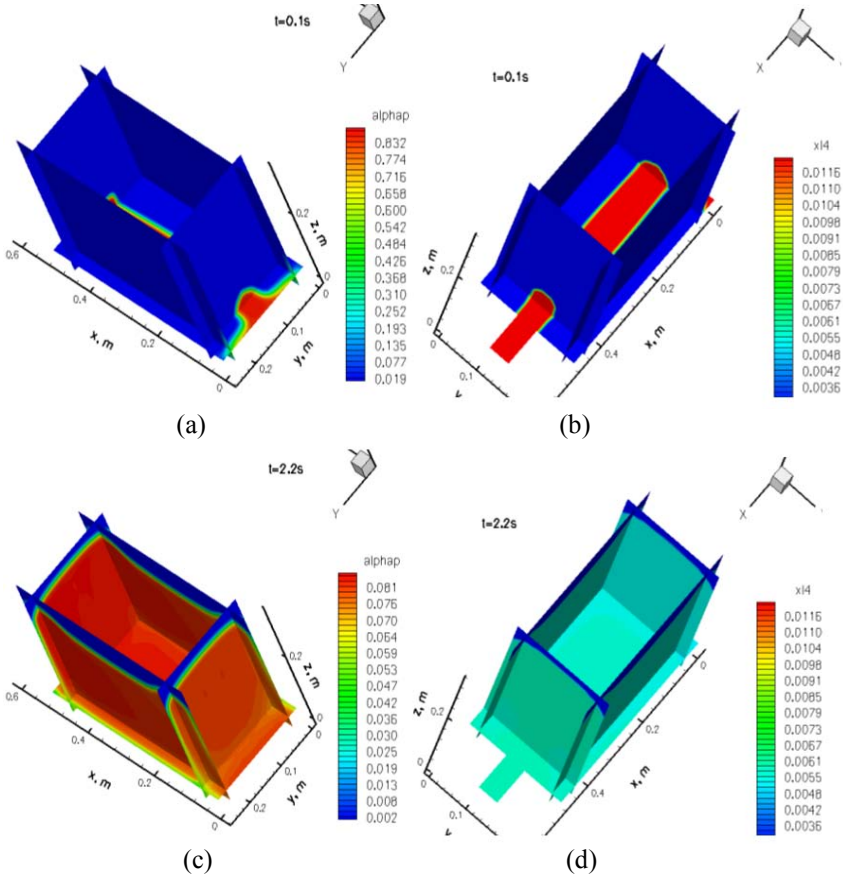

Figure 5: (a) Liquid voidage fraction at 0.1 s. (b) Water mass fraction at 0.1 s. (c) Liquid voidage fraction at 2.2 s. (d): Water mass fraction at 2.2 s.

References

[1] Rojas, A.J., Marciano, J.H. and Williams, R.J., *Polymer Engineering and Science*, **22**, 840 (1982).

[2] Amon, M. and Denson, C. D., *Polymer Engineering and Science*, **24**, 1027 (1984).

[3] Han, J.H. and Han, C.D., *Polymer Engineering and Science*, **28**, 1616 (1988).
[4] Tighe, S.C. and Manzione, L. T., *Polymer Engineering and Science*, **28**, 949 (1988).
[5] Han, J. H. and Han, C. D., *Journal of Polymer Science: Part B: Polymer Science*, **28**, 711 (1990).
[6] Han, J.H. and Han, C.D., *Journal of Polymer Science: Part B: Polymer Science*, **28**, 743 (1990).
[7] Ramesh, R.S., Rasmussen, D.H. and Campbell, G. A., *Polymer Engineering and Science*, **31**, 1657 (1991).
[8] Niyogi, D., Kumar, R. and Gandhi, K. S., *AIChE Journal*, **38**, 1170 (1992).
[9] Niyogi, D., Kumar, R. and Gandhi, K. S., *Polymer Engineering and Science*, **39**, 199 (1999).
[10] Baser, S. A. and Khakhar, D. V., *Polymer Engineering and Science*, **34**, 632 (1994).
[11] Baser, S.A. and Khakhar, D. V., *Polymer Engineering and Science*, **34**, 642 (1994).
[12] Ramesh, N.S., Rasmussen, D.H. and Campbell, G. A., *Polymer Engineering and Science*, **34**, 1685 (1994).
[13] Ramesh, N.S., Rasmussen, D.H. and Campbell, G. A., *Polymer Engineering and Science*, **34**, 1698 (1994).
[14] Arefmanesh, A. and Advani, S.G., *Polymer Engineering and Science*, **35**, 252 (1995).
[15] Shafi, M.A. and Flumerfelt, R. W., *Chemical Engineering Science*, **52**, 627 (1997).
[16] Shafi, M.A., Joshi, K. and Flumerfelt, R.W., *Chemical Engineering Science*, **52**, 635 (1997).
[17] Venerus, D. C. and Yala, N., *AIChE Journal*, **43**, 2948 (1997).
[18] Han, C.D., Sun, J., Chuang, H.K. and Lee, J.K., *Polymer Engineering and Science*, **38**, 1154 (1998).
[19] Joshi, K., Lee, J.G., Shafi, M.A. and Flumerfelt, R. W., *Journal of Applied Polymer Science*, **67**, 1353 (1998).
[20] Alsoy, S., *Journal of Cellular Plastics*, **35**, 247 (1999).
[21] Favelukis, M., Tadmor, Z. and Semiat, R., *AIChE Journal*, **45**, 691 (1999).
[22] Ramesh, N.S. and Malwitz, N., *Journal of Cellular Plastics*, **35**, 199 (1999).
[23] Koopmans, R. J., den Doelder, J.C.F., and Paquet, A.N., *Adv. Mater.*, **12**, 1873 (2000).
[24] den Doelder, C.F.J., Sammler, R.L., Koopmans, R.J. and Paquet, A.N., *Cellular Polymers*, **21**, 99 (2002).
[25] Chen, L., Blizard, K., Straff, R. and Wang, X., *Journal of Cellular Plastics*, **38**, 139 (2002).
[26] Pai, V. and Favelukis, M., *Journal of Cellular Plastics*, **38**, 403 (2002).
[27] Venerus, D.C., *Cellular Polymers*, **22**, 89 (2003).

[28] Lo, Y. W., Reible, D. D., Collier, J.R. and Chen, C.H., *Polymer Engineering and Science*, **34**, 1393 (1994).
[29] Lo, Y. W., Reible, D.D., Collier, J. R. and Chen, C.H., *Polymer Engineering and Science*, **34**, 1400 (1994).
[30] Kim, D. S. and Macosko, C., *Polymer Engineering and Science*, **40**, 2205 (2000).
[31] Shimoda, M., Tsujimura, I., Tanigaki, M. and Ohshima, M., Polymeric foaming simulation for extrusion processes, *Journal of Cellular Plastics*, **37**, 517 (2001).
[32] Malkin, A. Y.A. and Kuznetsov, V. V., *Polymer Engineering and Science*, **41**, 850 (2001).
[33] Polushkin, E. Y.U., Polushkina, O.M., Malkin, A.Y.A., Kulichikhin, V.G., Michaeli, Kleba, I. and Blaurock, J., *Polymer Engineering and Science*, **42**, 846 (2002).
[34] Mitani, T. and Hamada, H., *Polymer Engineering and Science*, **43**, 1603 (2003).
[35] Seo, D., Youn, J. R., and Tucker III, C.L., *Int. J. Num. Methods in Fluids*, **42**, 1105 (2003).
[36] Han, X., Koelling, K. W., Tomasko, D.L. and Lee, L.J., *Polymer Engineering and Science*, **42**, 2094 (2002).
[37] Brackbill, J. U., Kothe, D.B. and Zemach, C., *Journal of Computational Physics*, **100**, 335 (1992).
[38] Finn, R. and Shinbrot, M., *Journal of Mathematical Analysis and Applications*, **123**, 1 (1987).
[39] Cuvelier, C. and Schulkes, R.M.S.M., SIAM Review, **32,** 355 (1990).

Primary break-up: DNS of liquid jet to improve atomization modelling

T. Ménard, P. A. Beau, S. Tanguy, F. X. Demoulin & A. Berlemont
CNRS-UMR6614-CORIA, Rouen University, France

Abstract

Two different approaches for numerical simulations of primary break-up of liquid jet are described. In the ELSA model (Eulerian Lagrangian Spray Atomization) the liquid and the gas are considered as two species of a same mixture, but without necessarily the same velocity. The drift velocity and the liquid mass dispersion are exactly related to the turbulent liquid mass flux. To describe the topology of the spray the liquid/gas interface density per unit of volume is used instead of the droplet diameter that has no meaning in the dense part of the spray. To establish definitely the model for the turbulent liquid mass flux and for the liquid/gas interface density equation, DNS simulations are carried out to obtain information in the dense zone of the spray where nearly no experimental data are available. Interface tracking is ensured by the Level Set Method and the Ghost Fluid Method (GFM) is used to capture accurately sharp discontinuities for pressure, density and viscosity. Coupling between the Level Set and VOF method is used for mass conservation. Fluid motion is predicted with a projection method for incompressible flows.
Keywords: Level Set, Ghost Fluid Method, VOF, DNS, atomization modelling, liquid jet.

1 Introduction

Extensive studies have been devoted to the transport of spray of droplets, but the atomization process remains a challenging topic of research. It clearly appears that specific approaches must be developed when it is necessary to describe interface behavior. In recent years a number of studies have been proposed for the modelling and numerical simulation of moving interfaces. Two approaches are described in this paper. Vallet et al [1] proposed a new approach that permits to compute all the atomization process and that included the primary break-up zone: the ELSA

model [1, 2]. The model is based on a single-phase Eulerian model, and describes the whole process from inside the injector to the final dilute spray region. The classical transport equations of the mean mixture variable are considered. Unclosed correlation terms appear in the set of equations. A $k - \epsilon$ model is used to model the turbulence. The liquid turbulent diffusion discussed in previous papers [3], will be treated using a classical gradient law since the purpose of this paper is to study the transport equation for the mean liquid/gas interface density. We will focus our work on this original equation first introduced by Vallet et al [1]. This equation was postulated in comparison with the flame surface density equation. Despite initial successes of the method there is a lack of experimental data to establish definitely the model for the turbulent liquid mass flux and for the liquid/gas interface density equation. DNS simulations are carried out to obtain information in the dense zone of the spray where nearly no experimental data are available.We are here concern by the primary break-up of a jet: a lot of topological changes occur (interface pinching or merging, droplet coalescence or secondary break-up) and the Level Set Method thus appears well designed for our purpose. Osher and Sethian [9] proposed a Level Set method which describes the interface with the zero level curve of a continuous function defined by the signed distance to the interface. To describe the interface discontinuities, we use the ghost fluid method (GFM), which has been derived by Fedkiw et al [5] to capture jump condition on the interface. A projection method is used to solve incompressible Navier-Stokes equations that are coupled to a transport equation for the level set function. It is well known that numerical computations in the re-distancing algorithm of the method can generate mass loss in under-resolved regions. This is the main drawback of level set methods, but to improve mass conservation extension of the method can be developed, namely a coupling between VOF and Level Set (Sussman and Puckett [11]). Specific care has been devoted to improve simulation capabilities with MPI parallelization. The numerical methods have been applied to investigate physical processes, involved during the primary break-up of an atomizing jet. The chosen configuration is close as possible of Diesel injection.

2 Overview of the Eulerian Lagrangian Spray Atomization (ELSA)

2.1 The mean liquid/gas interface density transport equation

The ELSA model is an atomization model. It means that this modelling has to predict the characteristics of the liquid droplets or blobs in the dense part of the spray. Concerning the diameter, Vallet et al [1]. introduced a more general equation than an equation for the diameter: the mean liquid/gas interface density equation. This equation avoids us to assume the shape of the droplets and allows us to describe complex liquid topology like liquid ligaments. This variable $\bar{\Sigma}$ (in m^{-1}) corresponds to the quantity of liquid/gas interface per unity of volume. In this part, we

rather use the quantity of liquid/gas interface per unity of mass $\tilde{\Omega}$ (in $m^2.kg^{-1}$) to simplify the equations and most especially the treatment of the diffusive term.

The transport equation for the mean liquid/gas interface density has the following general form:

$$\frac{\partial \bar{\rho}\tilde{\Omega}}{\partial t} + \frac{\partial \bar{\rho}\tilde{\Omega}\tilde{U}_j}{\partial x_j} = \frac{\partial}{\partial x_j}\left(\bar{\rho} D_t \frac{\partial \tilde{\Omega}}{\partial x_j}\right) + \bar{\rho}\left(\dot{\tilde{\Omega}}_{mixture} + \dot{\tilde{\Omega}}_{stress} + \dot{\tilde{\Omega}}_{breakup} + \dot{\tilde{\Omega}}_{coalescence}\right) \quad (1)$$

with $\tilde{U}$ the mean mixture velocity, D_t the turbulent diffusivity and $\bar{\rho}$ the mixture density.

2.2 Initialization $\dot{\tilde{\Omega}}_{mixture}$

This first term corresponds to a production of liquid/gas interface due to the mixing of liquid and gas phases. In fact, if the liquid and the gas phases are mixed together, there is obviously production of liquid/as interface.

$$\begin{aligned} \dot{\tilde{\Omega}}_{mixture} &= 2D_t \frac{6\bar{\rho}}{\rho_1 \rho_2 L_t} \frac{\partial \tilde{X}_2}{\partial x_i} \frac{\partial \tilde{X}_2}{x_i} && \text{if} \quad \tilde{X}_2(1-\tilde{X}_2) \leq 0.001 \\ \dot{\tilde{\Omega}}_{mixture} &= 2D_t \frac{\tilde{\Omega}}{\tilde{X}_2(1-\tilde{X}_2)} \frac{\partial \tilde{X}_2}{\partial x_i} \frac{\partial \tilde{X}_2}{x_i} && \text{otherwise} \end{aligned} \quad (2)$$

where L_t is the turbulent length scale and $\tilde{X}_2$ is the liquid mass fraction, ρ_1 and ρ_2 stands respectively for the gas and liquid densities. By introducing this term, we assume that the first scale of the liquid blob produced is the turbulent length scale.

2.3 Production due to the turbulent stress $\dot{\tilde{\Omega}}_{stress}$

The second term represents the production of the interface due to the turbulent stretching. This term expresses that the liquid/gas interface is wrinkled by the turbulent flow. The simplest model is:

$\dot{\tilde{\Omega}}_{stress} = \frac{\tilde{\Omega}}{\tau_t}$ with τ_t the turbulent time scale.

2.4 Production due to the break-up $\dot{\tilde{\Omega}}_{breakup}$

The third term deals with the effect of the droplet break-up due to collisions. This phenomenon seems to be the most important one in the dense spray region. The break-up phenomenon is not only controlled by the turbulence but mainly by the collisions occurring in the dense part of the spray.

$\dot{\tilde{\Omega}}_{breakup} = \frac{\tilde{\Omega}}{\tau_{coll}}$ with $\tau_{coll} = \frac{L_{coll}^3}{S_{eff}\Delta v}$ the collision time scale.

The characteristic collision length scale is L_{coll}, the characteristic collision velocity is Δv and the effective section of the colliding droplets is S_{eff}.

2.5 Destruction due to the coalescence $\dot{\tilde{\Omega}}_{coalescence}$

The fourth term stands for the coalescence effects. This is a destruction term of the liquid/gas interface. The liquid/gas interface density equation must reach an asymptotic state, i.e. the destruction term must balance the production terms. It means that the Sauter mean diameter tends to a steady value. Vallet et al [1] propose a critical diameter given by:

$$D_{crit} = \frac{\sigma_l^{3/5} L_t^{2/5}}{\tilde{k}} \frac{(\bar{\rho}\tilde{X}_2)^{2/15}}{\rho_2^{11/15}} \quad \text{and} \quad \Omega_{crit} = \frac{6\tilde{X}_2}{\rho_2 D_{crit}} \tag{3}$$

The characteristic time scale of the coalescence is the collision time scale because coalescence occurs only if there is collision. We obtained for the coalescence destruction term:

$$\dot{\tilde{\Omega}}_{coalescence} = -\frac{1}{\tau_{coll}} \frac{\tilde{\Omega}^2}{\Omega_{crit}} \tag{4}$$

3 Overview of DNS simulation

3.1 The Level Set method

Level Set methods are based on the transport of a continuous function ϕ which describes the interface between two mediums (Sussman et al [12] and Sethian [10]). That function is defined by the algebraic signed distance ($|\nabla\phi| = 1$) between any point of the domain and the interface. The interface is thus described by the 0 level of the level set function. Solving a convection equation determines the evolution of the interface in a given velocity field $\boldsymbol{U}$ [10]:

$$\frac{\partial\phi}{\partial t} + \boldsymbol{U} \cdot \nabla(\phi) = 0 \tag{5}$$

Particular attention must be paid to this transport equation. Some problems may arise when the level set method is developed, namely a high velocity gradient can produce large spreading and stretching of level set, such as ϕ will no longer remains a distance function. A re-distancing algorithm [12] is then applied to keep ϕ as the algebraic distance to the interface. The algorithm is based on the iterative resolution of the following equation:

$$\frac{\partial d}{\partial \tau} = \text{sign}(\phi)(1 - |\nabla d|) \qquad \text{where} \quad d(\boldsymbol{x}, t, \tau)_{\tau=0} = \phi(\boldsymbol{x}, t) \tag{6}$$

where τ is a fictitious time. We solve equation (6) until steady state is reached, thus close to the exact steady state solution namely either $sign(\phi) = 0$, meaning that we are on the droplet interface, or ($|\nabla d| = 1$) which mathematically defines a distance function. In our simulations two or three iterations per physical time step of re-distancing algorithm are sufficient to ensure that d is a signed distance. The main advantage of the above algorithm is to provide us with the required

property for ϕ without changing its zero level set. Equations (5) and (6) are hyperbolic types. Specific care must be devoted to the discretization method, as discontinuities are often observed in the results. To avoid singularities in the distance function field, we thus use a 5th order WENO scheme for convective terms Jiang and Shu [6]. Temporal derivatives are at least computed with a second order Runge Kutta scheme.

One advantage of the level set method is its ability to represent topological changes both in 2D or 3D geometry quite naturally. Moreover, geometrical information on the interface, such as normal vector $\boldsymbol{n}$ or curvature κ, are easily obtained through:

$$\boldsymbol{n} = \frac{\nabla\phi}{|\nabla\phi|} \quad \kappa(\phi) = \nabla \cdot \boldsymbol{n} \tag{7}$$

As previously mentioned, mass loss can occur in under-resolved regions when eqns. (5, 6) are solved. Two main extensions of the method can be developed, namely the particle level set (Enright et al. [4]) or a coupling between VOF method and Level Set method (Sussman and Puckett [11], Van Der pijl et al. [14]). Our choice is to develop Level Set Method with GFM and coupling with VOF approach.

3.2 Coupling VOF and Level Set method

We recall here the main ideas of the CLSVOF method extensively discussed by Sussman and Puckett [11]. To couple the VOF method and the Level Set method, we first define the volume fraction F, in a grid cell Ω of the domain, at time t, as a function of ϕ (assuming 2D formalism for simplicity):

$$F(\Omega, t) = \frac{1}{|\Omega|} \int_{\Omega} H(\phi(x, y, t))\, dx\, dy \tag{8}$$

where H is the Heaviside function :

$$H(\phi) = \begin{cases} 1 & \text{if } \phi > 0 \\ 0 & \text{otherwise} \end{cases} \tag{9}$$

Discretization of eqn. (8) requires to define the interface in a cell $\Omega_{(i,j)}$. We thus introduce a reconstructed level set function (ϕ^R), that is defined by a line in 2D (a plane in 3D) :

$$\phi^R_{i,j} = a_{i,j}(x - x_i) + b_{i,j}(y - y_j) + c_{i,j} \tag{10}$$

The coefficients $c_{i,j}$ represent the normal distance form the interface to the points (x_i, y_j). The coefficient of eqn. (13) are determined by the minimization of the error (for a nine point stencil):

$$E_{i,j} = \sum_{i'=i-1}^{i'=i+1} \sum_{j'=j-1}^{j'=j+1} w_{i',j'} \delta_\epsilon(\phi_{i',j'})(\phi_{i',j'} - a_{i,j}(x_{i'} - x_i) - b_{i,j}(y_{j'} - y_j) - c_{i,j})^2 \tag{11}$$

$\delta_\epsilon(\phi_{i',j'})$ is a smoothed Dirac distribution with thickness ϵ ($\epsilon = \sqrt{2}dx$) and $w_{\alpha,\beta}$ are weighting factors which are maximal on the cell central point (i, j). One advantage of the approach is that we can choose the number of points in the stencil. For example, when two interfaces are in the nine point stencil but only one interface is in the considered cell, the approximation can be unrealistic. A six point or four point stencil is then used in eqn. (11).

Equation (8) then reads :

$$F_{i,j} = \frac{1}{\Delta x \Delta y} \int_{y_{j-1/2}}^{y_{j+1/2}} \int_{x_{i-1/2}}^{x_{i+1/2}} H(a_{i,j}(x-x_i)+b_{i,j}(y-y_j)+c_{i,j})\, dx\, dy \quad (12)$$

In order to calculate the above integral a change of coordinate system is first applied such as the origin of the new coordinate system is on the lower left hand corner of the cell and the normal to interface points towards the origin. In other terms we will always have liquid in the lower left hand corner and the new coefficient $c'_{i,j}$ is the distance from the new origin to interface. A new equation is obtained for interface:

$$a'_{i,j}(x - x_{i-1/2}) + b'_{i,j}(y - y_{j-1/2}) + c'_{i,j} = 0 \quad (13)$$

and eqn. (12) is now the sum of two parts (figure 1): the area I is calculated with geometrical rules and the area II is estimated by $\frac{1}{dxdy}\int(y(x)dx$ which now represents the liquid volume under the line. In 3D geometries the same steps are applied with a little bit more calculus.

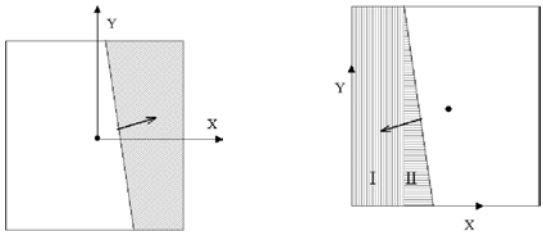

(a) initial configuration

(b) Configuration for the Volume fraction calculation

Figure 1: Illustration to determinate the Volume Fraction in a cell.

Note that the above coupling between VOF and Level Set method is applied in two cases. When we want to verify mass conservation in the level set transport and

re-distancing algorithm, we assume that the volume fraction $F^n_{i,j}$ is known and the following constraint at time n, is applied:

$$\frac{1}{\Delta x \Delta y}\int_{y_{j-1/2}}^{y_{j+1/2}}\int_{x_{i-1/2}}^{x_{i+1/2}} H(a_{i,j}(x-x_i)+b_{i,j}(y-y_j)+c_{i,j})\,dx\,dy = F^n_{i,j} \quad (14)$$

We use an iterative Newton method with a given precision to get the final value of $c'_{i,j}$ and then $c_{i,j}$. Finally we write:

$$\phi^n(i,j) = c_{i,j} \quad (15)$$

But the transport of the liquid volume fraction is also solved with the above coupling. In order to get the value $F^{n+1}_{i,j}$, eqn. (12) is used but the integral limits are modified, namely the velocity is used to determine the volume of liquid passing from one cell to a neighboured cell. Detailed information can be found in Sussman and Puckett [11].

3.3 Projection method for Navier-Stokes

Incompressible Navier-Stokes equations can be written as:

$$\frac{\partial \boldsymbol{U}}{\partial t} + \boldsymbol{U}\cdot\nabla(\boldsymbol{U}) = -\frac{\nabla(p)}{\rho(\phi)} + \frac{\nabla\Big(2\mu(\phi)\boldsymbol{D}\Big)}{\rho(\phi)} + \boldsymbol{g} \quad (16)$$

$$\nabla\cdot\boldsymbol{U} = 0 \quad (17)$$

p is the pressure, ρ and μ are the fluid density and viscosity respectively. Spatial derivatives are estimated with 2^{nd} order central scheme, but convective terms are approximated by 5^{th} order WENO scheme discretization in order to get a robust behavior of the solution. Temporal derivatives are approximated by Adams Bashforth formulation. Linear system deduced from Poisson equation is solved with a multigrid algorithm for preconditioning conjugate gradient method (Tanguy [13])

3.4 Ghost Fluid Method

To handle interface discontinuities we use a Ghost Fluid Method which has been derived by Fedkiw et al [5] to capture jump condition on the interface. For example, the pressure jump related to surface tension σ and to the interface curvature reads :

$$[p] = \sigma\kappa(\phi) + 2[\mu](\nabla u\cdot\boldsymbol{n}, \nabla v\cdot\boldsymbol{n}, \nabla w\cdot\boldsymbol{n})\cdot\boldsymbol{n} \quad (18)$$

The Ghost Fluid Method formalism respects jump discontinuities across the interface, and avoids an interface thickness. Discretization of discontinuous variables is more accurate, and spurious currents in the velocity field are thus much lower than with other approach such Continuous Surface Force method. We have used this procedure to discretize all discontinuous variables, namely density, viscosity, pressure and viscous tensors. Details can be found in Fedkiw [5], Tanguy [13], Kang et al [7].

3.5 Simulation

All the simulations presented here are thus carried out with the Level Set Method, with Ghost Fluid Method for interface discontinuities and coupling with VOF Method for mass conservation. Numerical codes have been developed for 2D, 2Daxi and 3D geometries, and MPI parallelization is used.

4 Turbulent liquid jet

We present a comparison between these two approaches. We perform a simulation in 3D with the DNS method in the primary atomization zone of a turbulent jet where conditions are given in Tab. (1). The uniform mesh size is $128 \times 128 \times 896$ and dimensions of the domain are (0.0003, 0.0003, 0.0021) in the (x, y, z) directions.

Generation of turbulent inflow boundary conditions is still a challenging task for studying turbulent spatially developing flow like jet with DNS or LES. Here we use a method, devised by Klein et al [8], which consists in generating random velocities with a prescribed length scale. In our computation that scale is equal to the turbulent integral scale L_t of the cylindrical channel flow ($L_t = 0.1D$). Turbulence intensity is 0.05 of inlet mean velocity.

Table 1: Characteristics of the spray.

Diameter (D)	velocity	turbulent intensity	turbulent length scale
100 μm	$100m.s^{-1}$	$\frac{u'}{U} = 0.05$	0.1D
phase	Density	viscosity	surface tension
liquid	696 $kg.m^{-3}$	$1.2.10^{-3}$ $kg.m^{-1}.s^{-1}$	0.06 $N.m^{-1}$
gas	25 $kg.m^{-3}$	1.10^{-5} $kg.m^{-1}.s^{-1}$	

For the RANS simulation, the model is implemented in CFD code STARCD V 3.15 through user-subroutines. Since only mean values are computed, a 2D non-uniform mesh is sufficient for the modelling part. The total number of cells is 100×55 and the dimension of the domain are (0.046, 0.097) in the (x,y) direction. There are 10 cells along the diameter of the injector hole. The aspect ratio of the cells near the orifice is close to one in order to achieve good numerical accuracy.

5 Results

Typical result for both methods are represented on figure 2. Figure 2.a shows an instantaneous 3D result using the level set method. From the injector nozzle, the

turbulence initiates some perturbations of the liquid surface, that are enhanced by the mean shear between the liquid jet and the surrounding air. The interface becomes very wrinkled and some break-up are initiated. The induced liquid parcels show a wide range of shapes. The surface is not organized and no clear process of break-up seems dominant. On the figure 2.b and 2.c a cut through the middle of the jet is used to show the mean value of the liquid volume fraction. Figure 2.b is obtained by averaging the level set results and figure 2.c is the result of the ELSA model. The global behavior is well captured by the model even if the length of the liquid core is overestimated. These results imply that the representation of the initial liquid break-up and dispersion by a turbulent flux is an appropriate model in such atomization process, even if it has to be improved.

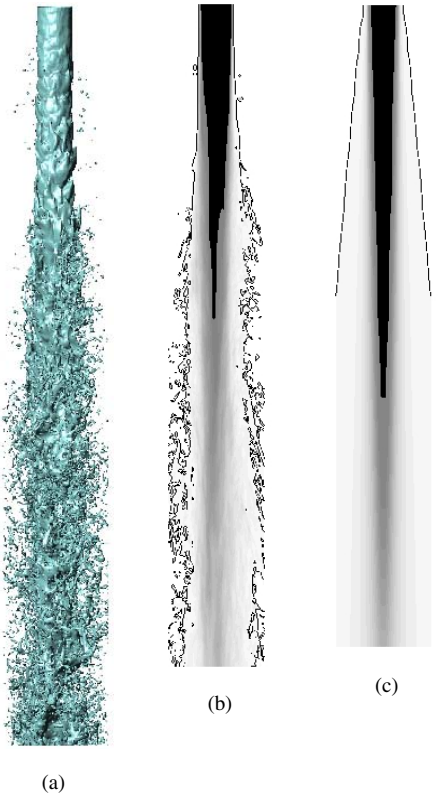

Figure 2: Comparison between DNS and ELSA results. (a) instantaneous DNS result at $t = 40\mu s$; (b) center cut, mean liquid volume fraction (DNS); (c) center cut, mean liquid volume fraction (ELSA model). (b), (c) Black area correspond to liquid core ($\phi_{VOL} > 0.99$), line: external contour of the spray ($\phi_{VOL} = 0.01$).

Extensive numerical simulations are still carried out to compare other means quantities. Space limitation, however, does not allow us to discuss all of the results in this paper.

References

[1] Vallet A., Burluka A.A., Borghi R., Development of a Eulerian model for the atomization of a liquid jet, *Atomization and Sprays*, vol. 11, pp. 619-642, 2001.
[2] Blokkeel G. et al., A continuous modeling approach for describing the atomization process from inside the injector to the final spray, *ICLASS*, 2003.
[3] Beau P.-A., Lebas R., Funk M., Demoulin F.-X., A multiphase flow approach and a single phase flow approach in the context of an Euler model for primary break-up, *ILASS Nottingham*, 2004
[4] Enright D., Fedkiw R., Ferziger J., Mitchell I., A hybrid particle level set method for improved interface capturing, *J. Comp. Phys.*, 183, 83-116, 2002
[5] Fedkiw R., Aslam T., Merriman B., Osher S., A non-oscillatory eulerian approach to interfaces in multimaterial flows (The Ghost Fluid Method). *J. Comp. Phys.* 152, 457-492, 1999
[6] Jiang G.S., Shu C.W., Efficient implementation of weighted essentially non-oscillatory schemes. *J. Comp. Phys.* 126, 202-228, 1996
[7] Kang M Fedkiw R Liu X D A Boundary Condition Capturing Method for Multiphase Incompressible Flow. *J. Sci. Comput.* 15, 323-360,2000
[8] Klein, Sadiki, Janicka, A digital filter based generation of inflow data for spatially developing direct numerical or large eddy simulations. *J. Comp. Phys.*, 186, 652-665, 2003
[9] Osher S., Sethian J.A. Fronts propagating with curvature-dependent speed : algorithms based on Hamilton-Jacobi formulations. *J. Comp. Phys.* 79, 12-49, 1988
[10] Sethian J. A Level Set Method and fast marching methods. Cambridge Univ.Press, 1999
[11] Sussman M., Puckett E.G., A coupled level set and volume-of-fluid method for computing 3D and axisymmetric incompressible two-phase flows. *J. Comp. Phys.* 162, 301-337,2000
[12] Sussman M Fatemi E Smereka P Osher S, An improved Level Set method for incompressible two-phase, *Computers and fluids*, 27, 1997
[13] Tanguy S. Développement d'une méthode de suivi d'interface. Applications aux écoulements diphasiques. *PhD thesis*, Université Rouen, Laboratoire CORIA CNRS UMR 6614, 2004
[14] S. P. van der Pijl, A. Segal, C. Vuik and P. Wesseling, A mass-conserving Level-Set method for modelling of multi-phase flows, *Int. J. Numer. Meth. Fluids*, 47:339-361, 2005

A coupled interface-tracking/ interface-capturing technique for free-surface flows

M. Watts, S. Aliabadi & S. Tu
School of Engineering, Jackson State University, Jackson, MS, USA

Abstract

In this paper we will present a new computational approach to simulate free-surface flow problems efficiently. The finite element solution strategy is based on a combination approach derived from fixed-mesh and moving-mesh techniques. Here, the free-surface flow simulations are based on the Navier-Stokes equations written for two incompressible fluids where the impact of one fluid on the other one is extremely small. An interface function with two distinct values is used to locate the position of the free-surface in regions near the floating object, while mesh-moving is used to move the free-surface in regions where wave breaking is not expected. The stabilized finite element formulations are written and integrated in an arbitrary Lagrangian-Eulerian domain. In the mesh-moving scheme, we assume that the computational domain is made of elastic materials. The linear elasticity equations are solved to obtain the displacements for each computational node. The numerical example includes a 3D simulation of flow past a sphere with a Reynolds number of 5000 and a Froude number of 0.5.
Keywords: finite element method, parallel simulation, free-surface flows, interface-tracking, and interface-capturing.

1 Introduction

The numerical simulations of free-surface flows require the coupling between the equations governing the dynamics of the fluid and the free-surface. Generally, there are two distinct approaches in the numerical simulation of free-surface flows. Depending on the physical characteristics of the problem, either "interface-tracking" or "interface-capturing" techniques are used. In the

interface-tracking technique, to absorb the motion of the free-surface, the nodal coordinates on the free-surface are usually moved with either the normal component of the fluid velocity to the free-surface or the fluid velocity itself [1]. The space-time finite element method is an example of the interface-tracking technique [2].

In the interface-tracking methods, the computational nodes need to be moved to account for the motion of the free-surface [3-8]. In the applications where the deformation of the free-surface is large, the moving-mesh methods usually result in element distortion. As the element distortion grows and becomes unacceptable, the generation of a new mesh and the projection of the solution from the old mesh to the new mesh is essential. In complex 3D applications, this procedure is extremely difficult and time consuming. In such cases, computations using the interface-capturing technique over fixed meshes are more desirable.

Most of the interface-capturing techniques are based on the volume of the fluid (VOF) approach [1, 9-19]. In the VOF approach, the Navier-Stokes equations are solved over a non-moving mesh. An interface function with two distinct values serves as a marker identifying the location of the free-surface. This function is transported throughout the computational domain with a time-dependent advection equation. Generally, the accuracy of the interface-capturing techniques depends on how accurate the free-surface function is represented. Therefore, mesh resolution becomes a prime factor in determining the accuracy of this technique [1, 10].

Clearly, both techniques have inherent advantages and disadvantages specific to the class of problems being solved. In this article, we present a new finite element technique for the simulation of free-surface flows, which combines these two techniques, each eliminating the disadvantages of the other. This finite element method is based on advanced computational technologies we have developed in the past several years for simulation of free-surface flows. Our free-surface computational technology is very user friendly and has been applied to many applications including sloshing in tanker-trucks [1], waves interacting with marine vessels in motion [9], and flow in open channels [13]. Our free-surface flow solver has gone through extensive communication and performance optimization [10].

In our new finite element technique, we will keep track of the free-surface in the region close to the floating object using an interface function based on the VOF method. In the far field regions where wave breaking and mixing is not expected we use an interface tracking method. Figure 1 shows the subdomains where the interface-tracking and interface-capturing techniques will be used.

Due to the presence of breaking waves, interface-capturing technique will be used in domain Ω_A, as shown in Figure 1. Consequently, this volume will be substantially more refined than the rest of the computational domain. In domain Ω_B shown in Figure 1, mesh-moving will be used to allow the free-surface to translate in the vertical direction only. In domain Ω_A, the new finite element method is based on the implementation of the Interface-Sharpening/Global Mass Conservation (IS-GMC) [1, 3-8] flow solver in the Arbitrary Lagrangian-

Eulerian (ALE) moving-mesh frame. The advantage of the IS-GMC over other VOF approaches is the enforcement of the conservation of mass not only locally, but also globally. In domain Ω_B, the automatic mesh-moving scheme is also used to absorb the motion of the free-surface. This scheme is based on the solution of the linear elasticity equations [4-7]. Here, we assume that the computational domain is made of elastic materials. The displacement of the free-surface will be the boundary conditions of the elasticity equations. The linear elasticity equations are coupled with the governing equations of the fluid and the interface function equation, which are solved simultaneously.

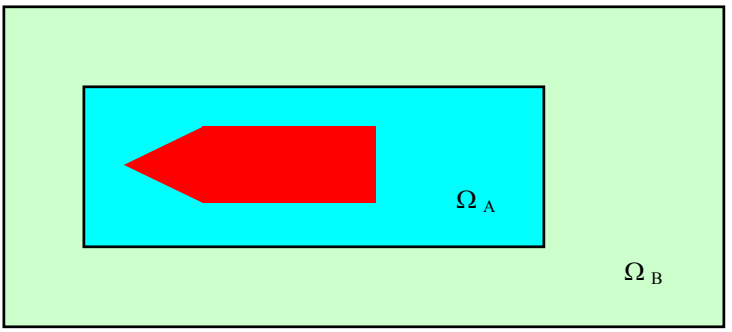

Figure 1: Top view of generic ship.

The discretization of the finite element formulations results in a coupled, non-linear system of equations, which need to be solved at every time step. Using the Newton-Raphson iteration algorithm, we solve the linearized systems of equations with the Generalized Minimal RESidual (GMRES) update technique [3-8]. For very large systems of equations, we use a matrix-free iteration strategy to obtain the solution of the non-linear system. This vector-based computation strategy totally eliminates a need to form any matrices, even at the element-levels and therefore minimize the memory requirements in large-scale computations. This new finite element technique is implemented in parallel using the message passing interface (MPI) libraries and METIS [20] mesh partitioning package reducing the inter processors communication.

2 Governing equations

To simulate free-surface flow problems, we assume there are two fluids interacting with each other where the dynamic impacts of one fluid on the other one is very small. For example, in water flows, air is constantly interacting with water. Since the density of the air is almost 1000 times less than the water, its effect on the water is negligible.

We consider the governing equations for two interacting fluids in the spatial domains Ω_A and Ω_B, and their boundaries Γ_A and Γ_B, respectively. Here we assume that the spatial domains and boundaries are functions of time, t. The two fluids are incompressible (e.g. air-water) and separated with an interface. Along the interface, the traction force is continuous (surface tension is negligible).

The governing equations are the incompressible Navier-Stokes equations written for two fluids in the Arbitrary Lagrangian-Eulerian (ALE) frame. These equations are:

$$\rho\left[\left.\frac{\partial \mathbf{u}}{\partial t}\right|_{\zeta} + (\mathbf{u}-\mathbf{u}_{mesh})\cdot\nabla\mathbf{u} - \mathbf{g}\right] - \nabla\cdot\boldsymbol{\sigma} = 0\,, \tag{1}$$

$$\nabla\cdot\mathbf{u} = 0\,, \tag{2}$$

where

$$\boldsymbol{\sigma} = -\mathrm{p}\,\mathbf{I} + 2\mu\boldsymbol{\varepsilon}(\mathbf{u})\,, \tag{3}$$

$$\boldsymbol{\varepsilon} = \frac{1}{2}(\nabla\mathbf{u} + \nabla\mathbf{u}^{\mathrm{T}})\,. \tag{4}$$

Here $\mathbf{u}$, $\mathbf{u}_{mesh}$, p, ρ, $\mathbf{g}$, and μ are the fluid velocity, mesh velocity, pressure, density, gravitational force, and dynamic viscosity, respectively. The strain tensor is denoted by $\boldsymbol{\varepsilon}$ and $\mathbf{I}$ represents the identity tensor. Eqns (1-2) are completed by an appropriate set of boundary and initial conditions.

In domain Ω_{A}, the interface function ϕ has two distinct values (0, 1) and is used to differentiate between the two fluids [1-8]. A time-dependent advection equation transports this function throughout the computational domain with the fluid velocity. This equation can be written as:

$$\left.\frac{\partial \phi}{\partial t}\right|_{\zeta} + (\mathbf{u}-\mathbf{u}_{mesh})\cdot\nabla\phi = 0\,. \tag{5}$$

Using ϕ, the density and viscosity can be calculate as:

$$\rho = \phi\rho_A + (1-\phi)\rho_B\,, \tag{6}$$

$$\mu = \phi\mu_A + (1-\phi)\mu_B\,, \tag{7}$$

where the subscripts A and B denote the fluid A and fluid B. Initially, ϕ is set to 0 in Fluid A and 1 in Fluid B.

Our mesh-moving scheme will be used to allow the free-surface to move in the vertical direction only in regions where wave breaking and mixing is not expected, i.e. domain Ω_{B}. The equation used to translate the interface nodes in the vertical direction is:

$$\frac{\partial \eta}{\partial t} + \mathrm{u}\frac{\partial \eta}{\partial x} + \mathrm{v}\frac{\partial \eta}{\partial y} = \mathrm{w}\,. \tag{8}$$

where η is the free-surface elevation. Here, η is initially equal to the free-surface static height. In this approach, it is clear that the need for high-resolution grids in domain Ω_B becomes less significant. Therefore, we can use significantly coarse mesh in domain Ω_B.

In our mesh-moving scheme, we assume that the computational domain is made of an elastic material. We solve linear elasticity equations to obtain the displacements for every computational node in domain Ω_B. These equations are:

$$\nabla . \left[\lambda_1 (\nabla . \mathbf{d})\, \mathbf{I} + 2\lambda_2 \nabla \boldsymbol{\kappa}(\mathbf{d})\right] = \mathbf{0}\,, \tag{9}$$

$$\boldsymbol{\kappa} = \frac{1}{2}(\nabla \mathbf{d} + \nabla \mathbf{d}^{\mathrm{T}})\,, \tag{10}$$

where $\mathbf{d}$ is the displacement, $\boldsymbol{\kappa}$ is the strain tensor, and λ_1 and λ_2 are the linear elasticity coefficients. Here our objective is have a mechanism for moving the computational nodes around, rather than finding the exact displacements. To have a better control over the movements of nodes, we set the coefficients λ_1 and λ_2 inversely proportional to the volume of each element. This makes the smaller elements stiffer than the larger ones and allows the motion of the physical boundary to be absorbed more in the larger elements, which delays the mesh distortion.

3 Finite element formulation

We use classical Galerkin formulation for linear elasticity equations and stabilized finite element formulation for the Navier-Stokes and interface function equations. The stabilizations are based on the stabilized-upwind/Petrov-Galerkin (SUPG), pressure-stabilization/Petrov-Galerkin (PSPG), and the artificial diffusion techniques. The SUPG term allows us to solve flow problems at high speeds [1, 3-8] and the PSPG term eliminates instabilities associated with the use of linear interpolation functions for both pressure and velocity. The artificial diffusion stabilization technique is used for the interface function for over stabilization [1]. Later, we will see that this feature allows us to enforce the conservation of mass not only locally, but also globally.

In the finite element formulations, we first define appropriate sets of trail solution spaces $S^h_{\mathbf{u}}$, S^h_p, S^h_ϕ and $S^h_{\mathbf{d}}$ and weighing function spaces $V^h_{\mathbf{u}}$, V^h_p, V^h_ϕ and $V^h_{\mathbf{d}}$ for the velocity, pressure, the interface function and displacements, respectively. The finite element formulation of Eqns (1-2, 5, 8) can then be written as follows: for all $\mathbf{w}^h \in V^h_{\mathbf{u}}$, $q^h \in V^h_p$, $\psi^h \in V^h_\phi$, $\gamma^h \in V^h_\eta$ and $\boldsymbol{\pi}^h \in V^h_{\mathbf{d}}$, find $\mathbf{u}^h \in S^h_{\mathbf{u}}$, $p^h \in S^h_p$, $\phi^h \in S^h_\phi$, $\eta^h \in S^h_\eta$ and $\mathbf{d}^h \in S^h_{\mathbf{d}}$ such that:

$$\int_\Omega \mathbf{w}^h \cdot \rho[\frac{\partial \mathbf{u}^h}{\partial t} + (\mathbf{u}^h - \mathbf{u}^h_{mesh}) \cdot \nabla \mathbf{u}^h - \mathbf{g}] d\Omega + \int_\Omega \boldsymbol{\varepsilon}(\mathbf{w}^h) : \boldsymbol{\sigma}(p^h, \mathbf{u}^h) d\Omega$$
$$+ \int_\Omega q_p^h \nabla \cdot \mathbf{u}^h d\Omega + \sum_{e=1}^{ne} \int_{\Omega^e} \frac{\tau_m}{\rho} \left[(\mathbf{u}^h - \mathbf{u}^h_{mesh}) \cdot \nabla \mathbf{w}^h - \nabla \cdot \boldsymbol{\sigma}(q_p^h, \mathbf{w}^h) \right] \cdot$$
$$\left[\rho[\frac{\partial \mathbf{u}^h}{\partial t} + (\mathbf{u}^h - \mathbf{u}^h_{mesh}) \cdot \nabla \mathbf{u}^h - \mathbf{g}] - \nabla \cdot \boldsymbol{\sigma}(p^h, \mathbf{u}^h) \right] d\Omega$$
$$+ \sum_{e=1}^{ne} \int_{\Omega^e} \tau_c \nabla \cdot \mathbf{w}^h \rho \nabla \cdot \mathbf{u}^h d\Omega = \int_{\Gamma_{h_u}} \mathbf{w}^h \cdot \mathbf{h} \, d\Gamma \,, \tag{11}$$

Eqn (11) is solved throughout the computational domain. In domain Ω_A we solve the following equation:

$$\int_\Omega \psi^h \left[\frac{\partial \phi^h}{\partial t} + (\mathbf{u}^h - \mathbf{u}^h_{mesh}) \cdot \nabla \phi^h \right] d\Omega + \sum_{e=1}^{ne} \int_{\Omega^e} \tau_i \nabla \psi^h \cdot \nabla \phi^h d\Omega = 0 \,. \tag{12}$$

However, in domain Ω_B we solve:

$$\int_\Omega \gamma^h \left[\frac{\partial \eta^h}{\partial t} + \mathrm{u} \frac{\partial \eta^h}{\partial x} + \mathrm{v} \frac{\partial \eta^h}{\partial y} - \mathrm{w} \right] d\Omega$$
$$+ \sum_{e=1}^{ne} \int_{\Omega^e} \tau_{II} \left[\mathrm{u} \frac{\partial \gamma^h}{\partial x} + \mathrm{v} \frac{\partial \gamma^h}{\partial y} \right] \left[\frac{\partial \eta^h}{\partial t} + \mathrm{u} \frac{\partial \eta^h}{\partial x} + \mathrm{v} \frac{\partial \eta^h}{\partial y} - \mathrm{w} \right] d\Omega. = 0 \tag{13}$$

$$\int_\Omega \boldsymbol{\kappa}(\boldsymbol{\pi}^h) : \left[\lambda_1 (\nabla . \mathbf{d}^h) \mathbf{I} + 2\lambda_2 \nabla \boldsymbol{\kappa}(\mathbf{d}^h) \right] d\Omega = 0 \,, \tag{14}$$

The parameters τ_m, τ_c, τ_i, and τ_{II} are the stabilization parameters defined as:

$$\tau_m = \left[\left(\frac{2}{\Delta t} \right)^2 + \left(\frac{2 \| \mathbf{u} \|}{h} \right)^2 + \left(\frac{4\mu}{\rho h^2} \right)^2 \right]^{-\frac{1}{2}}, \tag{15}$$

$$\tau_c = \frac{h}{2} \| \mathbf{u} \| z, \qquad z = \begin{cases} R_u / 3 & R_u \le 3 \\ 1 & 3 < Ru \end{cases} \tag{16}$$

$$\tau_i = \frac{h}{2} \| \mathbf{u} \|, \tag{17}$$

$$\tau_{II} = \left[\left(\frac{2}{\Delta t} \right)^2 + \left(\frac{2\sqrt{\mathrm{u}^2 + \mathrm{v}^2}}{h} \right)^2 \right]^{-\frac{1}{2}}, \tag{18}$$

where h is the element length, Δt is the time increment and R_u is the cell Reynolds number [1].

In Eqn (11), the first three integrals together with the right-hand-side term represent the Galerkin formulation of the governing equations of fluid. The first and second series of element-level integrals in the same equation are the SUPG and PSPG stabilization for the momentum equation, and the least-square stabilization of the continuity equation, respectively. In Eqn (12), the first integral is the Galerkin formulation of the interface function equation and the second integral (element-level) is the artificial diffusion stabilization. The diffusive formulation for the interface function eliminates the numerical undershoots (below 0) and overshoots (above 1) of the interface function around the interface. In the IS-GMC algorithm, we recover the sharpness of the interface in such a way that the global conservation of mass for each fluid is enforced. In Eqn (13) the first integral represents the Galerkin formulation of the elevation equation. Eqn (14) is the Galerkin formulation of the linear elasticity equations. The element-level integral in the same equation is the SUPG stabilization for the elevation equation.

4 Numerical example

Here we simulate water flow past a sphere using our coupled interface-tracking/interface capturing technique. The mesh consists of approximately 13 million tetrahedral elements. The Reynolds number for this case is 5000, with a Froude number of 0.5. Figure 2 below, depicts the solution at time steps 1 and 10, respectively. Domain Ω_A contains approximately 9 million unstructured elements, which includes almost 300,000 prism elements on the sphere surface. Domain Ω_B contains approximately 4 million elements. The free-surface in domain Ω_B consists of 65,000 triangular elements. Also, domain Ω_B is approximately 7 times larger in volume than domain Ω_A.

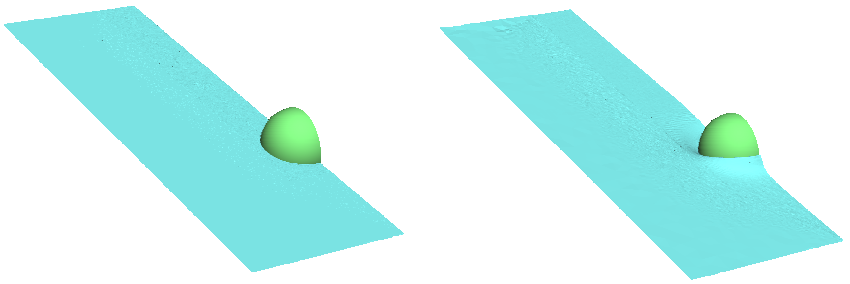

Figure 2: Flow past a sphere at time steps 1 and 10, respectively.

Acknowledgements

Work is funded by Northrop Grumman Ship Systems. The computations are carried out using Cray supercomputers located at the Army High Performance Computing Research Center. Partial support is provided by NASA –AMES.

References

[1] S. Aliabadi and T. Tezduyar, "Stabilized-Finite-Element/Interface-Capturing Technique for Parallel Computation of Unsteady Flows with Interfaces", Computer Methods in Applied Mechanics and Engineering, 190, 243-261, 2000.

[2] S. K. Aliabadi and T.E. Tezduyar, "Space-time Finite Element Computation of Compressible Flows Involving Moving Boundaries and Interfaces", Computer Methods in Applied Mechanics and Engineering, 107, 209-223, 1993.

[3] S. Aliabadi and T. Tezduyar, "Parallel Fluid Dynamics Computations in Aerospace Applications", International Journal for the Numerical Methods in Fluids, 21, 783-805, 1995.

[4] A.A. Johnson and T.E. Tezduyar, "Simulation of Multiple Spheres Falling in a Liquid-Filled Tube", Computer Methods in Applied Mechanics and Engineering, 134, 351-373, 1996.

[5] A.A. Johnson and T.E. Tezduyar, "3D Simulation of Fluid-Particle Interactions with the Number of Particles Reaching 100", Computer Methods in Applied Mechanics and Engineering, 145, 301-321, 1997.

[6] A.A. Johnson and T.E. Tezduyar, "Parallel Computation of Incompressible Flows with Complex Geometry", International Journal for Numerical Methods in Fluids, 24, 1321-1340, 1997.

[7] A. Johnson and T. Tezduyar, "Advanced Mesh Generation and Update Methods for 3D Flow Simulations", Computational Mechanics, 23,130-143, 1999.

[8] A. Johnson and S. Aliabadi, "Application of Automatic Mesh Generation and Mesh Multiplication Techniques to Very Large Scale Free-Surface Flow Simulations", Proceeding of the 7th International Conference on Numerical Grid Generation in Computational Field Simulations, Whistler, British Columbia, Canada, September 2000.

[9] S. Aliabadi, B. Zellars, J. Abedi, A. Johnson, C. Berger and J. Smith, "Implicit, Large-Scale, Parallel 3D Simulations of Waves Impacting on Floating Vessels", Proceedings of the LACSI 2001 Symposium, Los Alamos National Laboratory, October 16-17, 2001.

[10] Shahrouz Aliabadi, Andrew Johnson, and Bruce Zellars, "Finite Element Simulations of Free-Surface Flows Using Unstructured Meshes with One Billion Tetrahedral Elements", Proceeding of Users Group Conference 2001, Biloxi, MS, June 18-21, 2001.

[11] S. Aliabadi, J. Abedi, B. Zellars and K. Bota "New Finite Element Technique for Simulation of Wave-Object Interaction", AIAA Paper 2002-0876.

[12] S. Aliabadi and S. Shujaee, "Two-Fluid Flow Simulations Using Parallel Finite Element Method", *Simulation*, Volume 76, No. 5, pp. 257-262, ISSN 0037-5497/01, (2001).
[13] Shahrouz Aliabadi, Andrew Johnson, Bruce Zellars, Ade Abatan, and Charlie Berger, "Parallel Simulation of Flows in Open Channels", *Journal of Future Generation Computer Systems*, Vol. 18/5, Pages: 627-637 (2002).
[14] T. Tezduyar and S. Aliabadi, "EDICT for 3D Computation of Two-Fluid Interfaces", *Computer Methods in Applied Mechanics and Engineering,* 190, 403-410, 2000.
[15] M. Sussman, P. Smareka and S. Osher, "A level Set Approach for Computing Incompressible Two-Phase Flows", Journal of Computational Physics, 114, 146-168, 1994.
[16] J. A. Sethian, "Level Set Method", *Cambridge Monographs On Applied and Computational Mathematics*, Cambridge University Press, 1996.
[17] Y. C. Chang, T. Y. Hou, B. Merriam and S. Osher, "A Level Set Formulation of Eulerian Interface Capturing Methods for Incompressible Fluid Flows", *Journal of Computational Physics,* 124, 449-464, 1996.
[18] W. Hirt and B. D. Nichols, "Volume of Fluid (VOF) Method for the Dynamics of Free Boundaries", *Journal of Computational Physics*, 39:201-225, 1981.
[19] Shahrouz Aliabadi, Andrew Johnson and Jalal Abedi, "Comparison of Finite Element and Pendulum Models for Simulation of Sloshing", accepted for publication in the *Journal of Computer and Fluids.*
[20] G. Karypis and V. Kumar, "Parallel Multilevel k-Way Partitioning Scheme for Irregular Graphs", SIAM Review, 41 (2), 278-300, 1999.

This page intentionally left blank

Author Index

This page intentionally left blank

This page intentionally left blank

This page intentionally left blank

This page intentionally left blank

This page intentionally left blank